

**-PET- Vol. 59**

**ISSN : 1737-9934**

**Studies & Applications  
on Renewable Energy**

**Proceedings of Engineering & Technology  
-PET-**

**Editor :**

Dr. Ahmed Rhif (Tunisia)

International Centre for Innovation & Development  
**-ICID-**



# ICID

ISSN: 1737-9334

-PET- Vol. 59

**International Centre for Innovation & Development**

## Proceedings of Engineering & Technology -PET-

Studies & Applications  
on Renewable Energy

**Editor:**

Dr. Ahmed Rhif (Tunisia)

International Centre for Innovation & Development

**-ICID-**



## **Editor in Chief:**

Dr. Ahmed Rhif (**Tunisia**)

[Ahmed.rhif@gmail.com](mailto:Ahmed.rhif@gmail.com)

Dean of International Centre for  
Innovation & Development (**ICID**)

## **Editorial board:**

Prof. Georges Descombes, **France**

Dr. Mohamed Becherif, **France**

Prof. Mohammed El Hadi Zaim, **France**

Prof. El Mati Khoumri, **Maroc**

Dr. Sophie Simonet, **France**

Prof. Abdelmounaïm Tounzi, **France**

Prof. Djeghlal Mohammed Elamine, **Algérie**

Prof. Hassane Mahmoudi, **Maroc**

Dr. Nachida Kasbadji Merzouk, **Algérie**

Prof. Nektarios Benekos, **Grèce**

Dr. Saoussen Hammami, **Tunisie**

Prof. Abdellah El Fadar, **Maroc**

Prof. Djamila Rekioua, **Algérie**

Dr. Haitham Saad Mohamed Ramadan, **France**

Prof. Kamal Reklaoui, **Maroc**

Dr. Sara Zatir, **Algérie**

Prof. Abdellah Mechaqrane, **Maroc**

Prof. Abdelkader Aissat, **Algérie**

Prof. Adnan Yassine, **France**

Prof. Abdelfettah Barhdadi, **Maroc**

Prof. Ali Haddi, **Maroc**

Dr. Berbaoui brahim, **Algérie**

Dr. Hatem Trabelsi, **Tunisie**

Dr. Khouloud Bedoud, **Algérie**

Prof. Khenfer Nabil, **Algérie**

Dr. Mustapha Hatti, **Algérie**

Dr. Mohamed Gherbi, **Algérie**

Dr. Mimi Belatel, **Algérie**

Dr. Rafika Boudries, **Algérie**

Prof. Salma El Aimani, **Maroc**

Prof. Sellam Mebrouk, **Algérie**

Prof. Souad Tayane, **Maroc**

Prof. Tahar Bahi, **Algérie**

Dr. Toufik Madani Layadi, **Algérie**

Prof. Touria Barradi, **Maroc**

Dr. Youcef Soufi, **Algérie**

Prof. Youssef Errami, **Maroc**

Prof. Zohra Ameer, **Algérie**

# Summary

- Differential cross section for the ionization of CH<sub>4</sub> by proton impact. **Page 1**  
*Askri Souhaila, Sahlaoui Mohammed, Ferouani Abdel Karim, Lalia Aïci, El Habib Ghedda.*
- Study of the Asymptotic Stability of a Motor Electronic Circuit under the Effect of Different Voltages. **Page 5**  
*Lassouani fatiha, A. Ghomri, D. Kherbouche.*
- Experimental Investigations and Model optimisation of Thermal Operated of Bubble Pump. **Page 10**  
*Raoudha Garma, Doniazied Sioud, Khelifa Mejbri, Ahmed Bellagi.*
- Cascade Refrigeration Systems Involving CO<sub>2</sub> sub-cycles. **Page 17**  
*Doniazied Sioud, Yosra Ben Salem, Ahmed Bellagi.*
- Modelling of a classical absorption-diffusion cycle. **Page 23**  
*Ikram Saâfi, Ahmed Taieb, Yosra Ben Salem, Khalifa Mejbri, Ahmed Bellagi.*
- The impact of the transaction costs per hedging effectiveness ratio on renewable energy's hedging decisions. **Page 29**  
*Asma Abdallah, Ahmed Ghorbel.*
- Elimination of Metronidazole from Synthetic Wastewater by Coagulation and Electrocoagulation. **Page 49**  
*Chérifi Mouna, Mécibah Wahiab, Grid Azeddine, Abrane Rahma, Hazourli Sabir.*
- Evaluation of Acceptance Angle for High Concentration Photovoltaics Based on Triple Junction Solar Cells. **Page 53**  
*Nouamane Kellil, Abd Elkader Aissat, Sakina Atoui, Belkacem Bouzidi, Adel Mellit.*
- Performance Comparison of STATCOM and SVC Controllers for Static Voltage Stability Enhancement and Reactive Power Compensation. **Page 57**  
*Mimi Belatel.*
- A new harmonic reduction approach based on signal filtering in solar inverter's controllers. **Page 64**  
*Walid Rahmouni, Ghalem Bachir, Michel Aillerie.*
- Effect of Catalysts On the production of Biodiesel from Used Domestic Waste Oils. **Page 71**  
*D.KHERBOUCHE, A. GHOMRI, F. LASSOUANI, BIBI TRIKI, BENMOUSSA.*
- Faults Detection and Isolation of DC-AC Static Converter Feeding Induction Machine. **Page 75**  
*K. Bedoud, T. Bahi, H. Merabet, D. Drici, B. Oudjani.*
- The influence of Mn in structure of hydrotalcite-derived catalysts on the activity of dry reforming of methane. **Page 80**  
*F. Touahra, F. Bali, B. Djebbari, N. Aider, Z. Abdelsadek, K. Bachari, D. Halliche.*

Design of a Permanent Magnet Synchronous Generator for Wind Turbines. <i>Zina Larabi, Kaci Ghedamsi, Djamel Aouzellag.</i>	<b>Page 84</b>
Characterization of Protease milk clotting Obtained from Turkey proventriculus (Meleagris gallopavo). <i>MEKHANEG B, GIRARDET J-M, BELLAL M-M.</i>	<b>Page 90</b>
Voltage Control of a Self Excited Induction Generator in a Wind Turbine: Implementation and Simulation. <i>Rachid El Bachtiri, Imane Idrissi, Mohamed Salhi, Tariq Riouch.</i>	<b>Page 93</b>
Preparation and characterization of nickel-based catalysts deposited on ZrO <sub>2</sub> for methane steam reforming. <i>Akila BELHADI, Ouiza CHERIFI.</i>	<b>Page 99</b>
Environment and Technology for Architecture and Cultural Heritage. <i>Amri Khaoulaa, Alkama Djamel.</i>	<b>Page 103</b>
Biogas production from algal wastes. <i>Nadjla CHAIB, Sabrina LAMRAOUI, Sabrina DZIZI.</i>	<b>Page 112</b>
Preparation and characterization of nickel-based catalysts deposited on vanadium oxide for hydrogen production by methane steam reforming. <i>A. Belhadi, A. Boudjema, S. Boumaza, M.Trari, O. Cherifi.</i>	<b>Page 116</b>
An air cooler system for retrofitted PV panels in a Mediterranean climate. <i>Amel F. Boudjabi, Abderrahmane Dib, Thabet Lebeche, Kamal Rezgui, Chafik Tamrabet.</i>	<b>Page 119</b>
CFD analysis of wind loads on Linear Fresnel Concentrator. <i>H.Bendjebbas, A.Mezidi.</i>	<b>Page 124</b>
Optimization of two level production distribution systems with stock and transportation costs. <i>Bensakhria Mohamed, Samir Abdelhamid.</i>	<b>Page 128</b>
Olive pomace steam gasification for production of syngas/hydrogen : sensitivity analysis. <i>Rim Tilouche, Raoudha Garma, Doniazed Sioud, Housam Binous, Ahmed Bellagi.</i>	<b>Page 134</b>
METHANE DECOMPOSITION over NICKEL SUPPORTED on ACID TREATED HZSM-5. <i>Lilia ALALGA, Aicha BENAMAR.</i>	<b>Page 141</b>
Hybrid Power System Optimization of the Emission Antenna of Beni Chograne FM-Radio (Cherb-Errih,Mascara, Algeria). <i>Hamza SIYOUCEF, Benameur AFIF, HabibAllah BOUHAMIDA, Boualem MERABET.</i>	<b>Page 147</b>
A two dimensional numerical study of an evaporative cooler with a wet return surface. <i>Amel F. Boudjabi, Chadi Maalouf, Kamal Rezguia, Fabien Beaumont, Guillaume Polidori, Djamila Rouag.</i>	<b>Page 152</b>
Comparative Study on Modeling of Heavy Duty Gas Turbines. <i>Djamila Talah, Hamid Bentarzi.</i>	<b>Page 156</b>

Improved absorbance of the mixed Fe <sub>2</sub> O <sub>3</sub> / V <sub>2</sub> O <sub>5</sub> PSi structure. <i>H. Cheraga, S.Friha, S.Achacha.</i>	<b>Page 161</b>
IoT and lighting control for smart greenhouse . <i>Anouar BELKADI, Dhafer MEZGHANI, Abdelkader MAMI.</i>	<b>Page 164</b>
Robust Speed Control of a Doubly Fed Induction Motor. <i>Lekhchine Salima, Bahi Tahar.</i>	<b>Page 170</b>
Effects of the Cl-edge shape and the width on the structural, electronic and magnetic properties of silicene nanoribbons. <i>M. T. Kadri, I. Djabri, H. Belkhir.</i>	<b>Page 176</b>
Etanolysis of sunflower oil overhomogeneous and heterogeneous heteropolyacid catalysts. <i>Yasmina Idrissou, Tassadit Mazari, Chérifa Rabia.</i>	<b>Page 181</b>
Modeling of transport phenomena in laser welding of dissimilar metals Al/Mg. <i>Sabrine Ben Halim, Sana Bannour, Kamel Abderrazek, Wassim Kriaa, Michel Autric.</i>	<b>Page 188</b>
Feasibility study of a solar brackish water desalination system plant in Algeria. <i>Mohamed Abbas, Asma Adda, Djilali Tassalit, Hanane Aburdeh, Zahia Tgrine.</i>	<b>Page 193</b>
Modeling and Simulation of Low Voltage Power MOSFET for DC-DC Converter Applications. <i>Smail toufik, Belmili hocine.</i>	<b>Page 197</b>
Evaluation of wind park performances located At Algerian East Highlands. <i>A. Mezidi, H. Bendjebbas, K. Mohammedi.</i>	<b>Page 203</b>
Energy Flow Management for a Standalone Hybrid PV/Wind Power System. <i>Sabri Boulouma, Hachemi Rahmani, Boualem Bendib, Hocine Belmili, Naoual Seddaoui.</i>	<b>Page 208</b>



# Differential cross section for the ionization of CH<sub>4</sub> by proton impact

Askri Souhaila  
 LEVRES, Université Echahid Hamma  
 Lakhdar  
 El Oued  
 Algeria  
 askrisouha@gmail.com

Sahlaoui Mohammed  
 Laboratoire de Physique Théorique  
 Ecole Supérieure en Sciences Appliquées  
 Tlemcen  
 Algeria  
 mohammed.sahlaoui@gmail.com

Ferouani Abdel Karim  
 Laboratoire de Physique Théorique  
 Ecole Supérieure en Sciences Appliquées  
 Tlemcen  
 Algeria  
 ferouani\_karim@yahoo.fr

Lalia Aïci  
 Laboratoire de Physique Théorique  
 Tlemcen  
 Algeria  
 Université abou bekr belkaid  
 Tlemcen  
 Algeria  
 lalia\_aci@yahoo.fr

El Habib Ghedda  
 LEVRES, Université Echahid Hamma  
 Lakhdar  
 El Oued  
 Algeria  
 elh\_ghedda@yahoo.fr

**Abstract**—In the present paper, we study the single ionization of methane molecule by proton impact in high incident energy range. In the theoretical model presented here, the initial state is composed from projectile and methane wave functions. The target is described by means of a molecular wave function centered on the heavy nuclei. The final state is constituted from the ejected electron and the scattered proton. This electron is described by Coulomb wave function and the fast and heavy proton is described by a plane wave function. The obtained results are compared to the available experimental data.

**Keywords**—Cross section, methane molecule, ICW model, Born approximation.

## I. INTRODUCTION

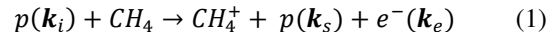
Studying the ionization of atoms and molecules by charged particles is important for a large number of areas, such as plasma physics, radiation physics, astrophysics, radiation therapy, and planetary atmospheres [1-6]. Cross sections, differential in energy and emission angle, give important information about the different ionization processes. This is why interactions of charged particles with molecules have actually important consideration, especially for the irradiation of living matter [7,8] destined for cancer treatment [9]. The methane molecule is the simplest organic molecule, so, mastering the problem of the ionization of this molecule by charged particles allows us to study more complex biological molecules. Without forgetting that the CH<sub>4</sub> molecule is a critically important molecule in the atmosphere of some planetary and the interstellar medium [10-12].

Several works have been interested to the interaction of CH<sub>4</sub> with ions [13,14]. In this work, we are interested to the single ionization of this molecule by proton impact. This problem is a true challenge. This is why we want in this paper, to present an analytical formalism based on the computation of the triple differential cross section in the frame of the first Born approximation for the treatment ionization of molecules by swift proton impact. Our formalism has proved its worth previously in the study of the single ionization of water, methane and ammonia by

electron impact [15-21]. This formalism allows to gain accuracy and computation time. In this formalism, the molecular target is described by Slater-type functions centered at the carbon atom, according to the description proposed by Moccia [22]. The continuum of the ejected electron is described by Coulomb wave function. The incidence and scattering state of the proton are described by plane wave functions.

## II. THEORY

The single ionization of the CH<sub>4</sub> molecule by proton impact can be presented as:



where  $\mathbf{k}_i$  is the projectile momentum,  $\mathbf{k}_s$  is the scattered proton momentum and  $\mathbf{k}_e$  is the ejected electron momentum. In atomic unit, we have

$$k_i^2 = 2\mu E_i, \quad k_s^2 = 2\mu E_s \quad \text{and} \quad k_e^2 = 2E_e \quad (2)$$

$\mu$  is the mass of the proton. The double differential cross section (DDCS) of the ejection process can be deduced from the triple differential cross section (TDCS) by integration over the scattering solid angle  $\hat{\mathbf{k}}_s$ :

$$\frac{d^{(2)}\sigma}{d\hat{\mathbf{k}}_e dE_e} = \int d\hat{\mathbf{k}}_s \frac{d^{(3)}\sigma}{d\hat{\mathbf{k}}_s d\hat{\mathbf{k}}_e dE_e} \quad (3)$$

$$\frac{d^{(3)}\sigma}{d\hat{\mathbf{r}}_s d\hat{\mathbf{r}}_e dE_e} = \mu^2 \frac{k_e k_s}{k_i} |\langle \psi_f | V | \psi_i \rangle|^2 \quad (4)$$

where  $V$  is the interaction potential energy:

$$V = \sum_{j=1}^N \frac{Z_j}{|\mathbf{r}_0 - \mathbf{R}_j|} - \sum_{i=1}^n \frac{1}{|\mathbf{r}_0 - \mathbf{r}_i|} \quad (5)$$

$Z_j$  is the charge of the nuclei  $j$ ,  $\mathbf{r}_i$  is the position of the  $i$ <sup>th</sup> electron of the molecular target,  $\mathbf{R}_j$  is the position of the  $j$ <sup>th</sup> nuclei. The initial and final states can be written in the following forms:

$$|\psi_i\rangle = |\phi_i(\mathbf{k}_i, \mathbf{r}_0) \varphi_i(\mathbf{r}_1, \mathbf{r}_2, \dots, \mathbf{r}_n)\rangle \quad (7)$$

$$\langle \psi_f | = \langle \phi_s(\mathbf{k}_s, \mathbf{r}_0) \varphi_f(\mathbf{r}_1, \mathbf{r}_2, \dots, \mathbf{r}_n) | \quad (8)$$

$\phi_i(\mathbf{k}_i, \mathbf{r}_0)$  and  $\phi_s(\mathbf{k}_s, \mathbf{r}_0)$  are the wave functions of the incident and scattered proton chosen here as plane wave functions

$$\phi(\mathbf{k}_s, \mathbf{r}_0) = (2\pi)^{-\frac{3}{2}} \exp(\mathbf{k}_s \cdot \mathbf{r}_0) \quad (9)$$

Using the so-called frozen core approximation (FCA), we can reduce the initial and final states to the following forms:

$$|\psi_i\rangle = |\phi_i(\mathbf{k}_i, \mathbf{r}_0)\varphi_i(\mathbf{r}_1)\rangle \quad (10)$$

$$\langle\psi_f| = \langle\phi_s(\mathbf{k}_s, \mathbf{r}_0)\varphi_f(\mathbf{r}_1)| \quad (11)$$

where only the molecular active electron is considered. If the origin of the reference is chosen in the carbon nuclei, using the FCA, we can reduce the potential energy to the form:

$$V = \frac{1}{r_0} - \frac{1}{|\mathbf{r}_0 - \mathbf{r}_1|} \quad (12)$$

The molecular electrons are distributed among the five orbitals  $1A_1$ ,  $2A_1$ ,  $1T_{2x}$ ,  $1T_{2y}$  and  $1T_{2z}$ . Each molecular orbital is defined by linear combinations of Slater-type functions centered over the carbon atom [22]:

$$\varphi_i(\mathbf{r}_1) = \sum_{k=1}^{N_i} a_{ik} \Phi_{n_{ik}l_{ik}m_{ik}}^{\xi_{ik}}(\mathbf{r}_1) \quad (12)$$

$a_{ik}$  is the contribution magnitude of the basis element  $\Phi_{n_{ik}l_{ik}m_{ik}}^{\xi_{ik}}$  given in the molecular frame, as follows:

$$\Phi_{n_{ik}l_{ik}m_{ik}}^{\xi_{ik}}(\mathbf{r}_1) = R_{n_{ik}}^{\xi_{ik}}(r_1) S_{l_{ik},m_{ik}}(\hat{\mathbf{r}}_1) \quad (13)$$

$R_{n_{ik}}^{\xi_{ik}}$  is the radial part chosen as a Slater function and  $S_{l_{ik},m_{ik}}$  is a real spherical harmonic,

$$S_{l_{ik},m_{ik}}(\hat{\mathbf{r}}_1) = \left(\frac{m_{ik}}{2|m_{ik}|}\right)^{\frac{-1}{2}} \{Y_{l_{ik}-|m_{ik}|}(\hat{\mathbf{r}}_1) + (-1)^{m_{ik}} \times \left(\frac{m_{ik}}{|m_{ik}|}\right) Y_{l_{ik}|m_{ik}|}(\hat{\mathbf{r}}_1)\} \quad (14)$$

with  $S_{l_{ik},0}(\hat{\mathbf{r}}_1) = Y_{l_{ik},0}(\hat{\mathbf{r}}_1)$ . The molecular wave function given in equation (13) is defined in a molecular reference frame. We need to make a transformation to the laboratory reference frame thanks to the relationship

$$Y_{l_{ik},m_{ik}}(\hat{\mathbf{r}}_1) = \sum_{\mu=-l_{ik}}^{l_{ik}} D_{\mu_{ik},m_{ik}}^{l_{ik}}(\alpha, \beta, \gamma) Y_{l_{ik},\mu_{ik}}(\hat{\mathbf{r}}_1) \quad (15)$$

where  $D_{\mu_{ik},m_{ik}}^{l_{ik}}$  is a rotation operator,  $\alpha$ ,  $\beta$  and  $\gamma$  are the Euler angles. Since the target is randomly oriented, the measured cross section is an average over all the possible orientations. This is why we need to average the theoretical cross section over all the Euler angles

$$\frac{d^{(2)}\bar{\sigma}}{d\hat{\mathbf{r}}_e dE_e} = \frac{1}{8\pi} \int d\beta \sin\beta \int d\alpha \int d\gamma \frac{d^{(2)}\sigma}{d\hat{\mathbf{r}}_e dE_e} \quad (16)$$

In the present formalism the ejected electron is described by a Coulomb wave:

$$\varphi_f(\mathbf{k}_e, \mathbf{r}_1) = (2\pi)^{-\frac{3}{2}} \exp\left(\frac{\pi}{k_e}\right) \Gamma\left(1 + \frac{i}{k_e}\right) \exp(\mathbf{k}_e \cdot \mathbf{r}_1) \times {}_1F_1\left[\frac{-i}{k_e}, 1, -i(\mathbf{k}_e \cdot \mathbf{r}_1 + k_e r_1)\right] \quad (17)$$

where the effective ionic charge is taken equal to 1.

### III. RESULTS AND DISCUSSIONS

In figure (a), we present the double differential cross section concerning the ejected electron for the ejection energies  $E_e = 11.3, 20, 50, 100, 200$  and  $1000$  eV and for an impact proton energy  $E_i = 2$  MeV. Our results are compared to the theoretical results of Tachino *et al* [13] and the experimental data of Senger [21]. In the work of Tachino *et al* [13], the continuum distorted wave-eikonal initial state (CDW-EIS) model is used to compute the DDCS, where the Moccia [22] description of the molecular wave function is used. However, in order to simplify the computation of the DDCS, Tachino *et al* [13] have truncated the original basis set, leaving out from the calculation the contribution of Slater-type orbitals (see equation (12)) corresponding to values of the principal number  $n \geq 7$ . The other Slater-type orbitals are considered as negligible contribution to the molecular orbitals. In our analytical formalism, all the basis elements have been considered in goal to describe the molecular target accurately. We note that when we use the present analytical formalism, we resolve the problem of times computation (numerical integration of the TDCS).

Instead of presenting the results of the DDCS only in the logarithmic scale, we have presented in figure (a) all the results in both logarithmic and linear scales. We see that, in this way, the comparison of the theoretical and experimental results becomes clearer. Generally speaking, when we compare the present and previous results of Tachino *et al* [13], we can see that our results are close to the experimental data in the peaks. We can also remark that our results are in well agreement with the experimental data and our curves are more close to the experience in the interval from  $30^\circ$  to  $100^\circ$ . Outside these intervals, several effects can be the cause of the discrepancy between the experiment and the theory. One of the effects is the distortion of the ejected electron that can be deduced from the comparison between our results and that of the CDW-EIS model (see curves in the intervals from  $0^\circ$  to about  $30^\circ$ ), where a distorted wave function has been used to describe the ejected particle. We must not forget that we are studying a reaction between a proton and molecular target. This reaction differs from the one where the projectile is an electron by the fact that the proton has a positive electric charge and an important mass compared to the electron. In this case, the interaction between the proton and the active electron can induce the so-called capture phenomenon. This phenomenon is considered as unimportant when the projectile comes with a very fast velocity. However, under certain energetic and geometric conditions, this phenomenon is going to have an important effect. We believe that, this is why for a small ejection energies ( $E_e = 20$  and  $11.3$  eV), our theoretical

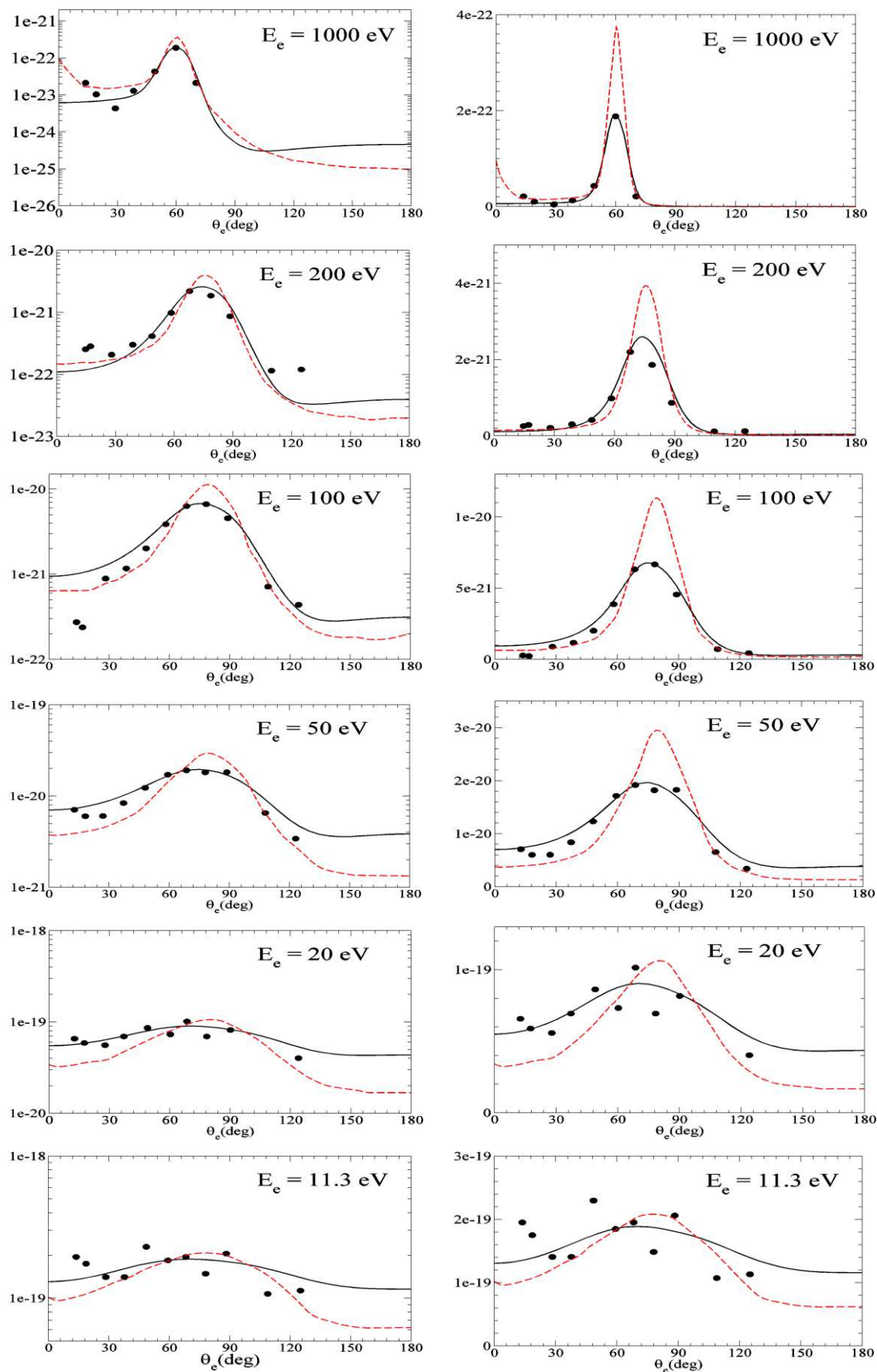


**Figure (a).** Double differential cross section of the single ionization of the CH<sub>4</sub> molecule by 2 MeV proton impact. Solid-line corresponds to our results. Dashed-line for the CDW-EIS model of Tachino *et al* [13]. Solid circles the experimental data of Senger [21]. The left and right results are presented in logarithmic and linear scales, respectively.

results and those of Tachino *et al* [13] are in poor agreement with the experimental data. Without forgetting that the more the ejection energy is small, the more the error on the experimental data becomes important.

#### IV. CONCLUSION

Single ionization of methane molecule by 2 MeV proton impact was considered for 6 ejection energies. Our results are compared to the theoretical results of Tachino *et al* [13] obtained from the CDW-EIS model and to the experimental data of Senger [21]. We find generally that our results are in well agreement with the experiment better than those of Tachino *et al* [13].

This proves once more that our simple formalism can provide very accurate results, under certain geometric and energetic conditions. However, certain corrections are needed to improve the accuracy of the formalism. As for example, the consideration of the distortion effect of the ejected electron by the residual molecular ion. We may also take into account the capture phenomenon.

#### V. REFERENCES

- [1] C.S. Enos, A.R. Lee, and A.G. Brenton, *Int. J. Mass Spectrom. Ion Process.* **104**, 137, 1991.
- [2] K. Mitsuke, T. Takami, K. Ohno, *J. Chem. Phys.* **91**, 1618J, 1989.
- [3] D.H. Katayama, R.E. Huffman, C.L. O'Bryan, *J. Chem. Phys.* **59**, 4309, 1973.
- [4] K. Tachibana, M. Nishida, H. Harima, Y. Urano, *J. Phys. D: Appl. Phys.* **17**, 1727, 1984.
- [5] R. Zellner, G. Weibring, *Z. Phys. Chem.* **161**, 167, 1989.
- [6] S.P. Khare, M. K. Sharma, S. Tomar, *J. Phys. B: At. Mol. Opt. Phys.* **32**, 3147, 1999.
- [7] Z. Nikitaki et al. *Free Radical Res.* **50**, S64–S78, 2016.
- [8] S. Meylan, S. Incerti, M. Karamitros, N. Tang, M. Bueno, I. Clairand and C. Villagrasa, *Sci. Rep.* **7**, 11923, 2017.
- [9] E. Alizadeh, T. M. Orlando and L. Sanche, *Annu. Rev. Phys. Chem.* **66** 379–398, 2015.
- [10] L. Xianming, D. F. Shemansky, *J. Geophys. Res.* **111**, A04303, 2006.
- [11] Y. L. Yung, M. Allen and J. P. Pinto, *Astrophys. J. Suppl.* **55**, 465–506, 1984.
- [12] E. H. Wilson, and S. K. Atreya, *J. Geophys. Res.* **109**, E06002, 2004.
- [13] C. A. Tachino, J. M. Monti, Fojon O A, Champion C and Rivarola R D, *J. Phys: Conf. Ser.* **583** 012020, 2015.
- [14] N. B. Malhi, I. Ben-Itzhak, T. J. Gray, J. C. Legg, V. Needham, K. D. Carnes and J. H. McGuire, *J. Chem. Phys.* **87** 6502, 1987.
- [15] A. Boukhikhi, M. Sahlaoui, B. Lasri, A. Sekkal and M. Bouamoud, *J. Phys B : At. Mol. Opt. Phys.* **52**, 015201, 2019.
- [16] M. Sahlaoui, B. Lasri and M. Bouamoud, *Can. J. Phys.* **92**, 136–140, 2014.
- [17] M. Yavuz, N. Okumus, Z. N. Ozer, M. Ulu, M. Dogan, M. Sahlaoui, N. H. Benmansour, M. Bouamoud, *J. Phys.: Conf. Ser.* **488**, 052031, 2014.
- [18] M. Sahlaoui, M. Bouamoud, B. Lasri and M. Dogan, *J. Phys. B: At. Mol. Opt. Phys.* **46**, 115206, 2013.
- [19] M. Sahlaoui and M. Bouamoud, *J. Phys. B: At. Mol. Opt. Phys.* **45**, 085201, 2012.
- [20] M. Sahlaoui and M. Bouamoud, *Can. J. Phys.* **89**, 723–727, 2011.
- [21] M. Sahlaoui and M. Bouamoud, *Can. J. Phys.* **88**, 905–910, 2010.
- [22] R. Moccia, *J. Chem. Phys.* **40**, 2164, 1964.
- [23] B. Senger, *Z. Phys. D: At. Mol. and Clusters.* **9**, 5631, 1988.

# Study of the Asymptotic Stability of a Motor Electronic Circuit under the Effect of Different Voltages

Lassouani fatiha<sup>#,\*1</sup>, A. Ghomri<sup>\*2</sup>, D. Kherbouche<sup>\*3</sup>

<sup>#</sup> *Laboratoire d'Automatique de Tlemcen, Université de Tlemcen-Algerie*  
<sup>\*</sup> *Ecole Supérieure en Science Appliqués, BP 165 RP Bel horizon, Tlemcen-Algerie*

<sup>1</sup>fatiha\_lass@yahoo.fr

<sup>2</sup>ghomriamina@yahoo.fr

<sup>3</sup>djamila\_kh@yahoo.fr

**Abstract** — Linearization methods play a very important role in the study of nonlinear systems which are generally modeled by ordinary nonlinear differential equations. While many systems may admit a linear behavior domain, linearity is always an approximation of reality. The most classical approximation is that determined by the Fréchet derivative of the nonlinear equation.

In this paper, we applied the optimal derivative method to a physical system of a motor electronic circuit. This system is described by ordinary nonlinear differential equations. We are interested in studying the asymptotic stability of this system.

The approximation obtained by optimal derivation gives satisfactory results with respect to the exact results while respecting the dynamics of the initial problem.

**Keywords**—Electric motor circuit, Ordinary differential equation, Fréchet derivation, Optimal derivative, Asymptotic stability.

## I. INTRODUCTION

In 1892, Lyapunov published his thesis (General Problem of the Stability of the movement) where he introduced a very rigorous definition of the problem of the stability of movement. This method is based on the search for a scalar function of sign defined at real value. In some classes of physical systems, it can be chosen as the energy of the system. Unfortunately, the difficulty of the research constitutes a real handicap since we do not know of a method for the construction in the general case; however, there are construction techniques applicable to particular cases. So, we can say that the study of stability in the case of nonlinear systems poses a very difficult problem; this is why we use the most classical method based on linearization.

In this paper, we apply some concepts of stability for solving and studying the stability of a nonlinear system. Then, we search a numerical method destined to modeling the proposed nonlinear system. The optimal derivative can reveal emerging behaviors.

## II. CONTINUOUS CURRENT MOTOR

The mathematical model of continuous current motor is given by:

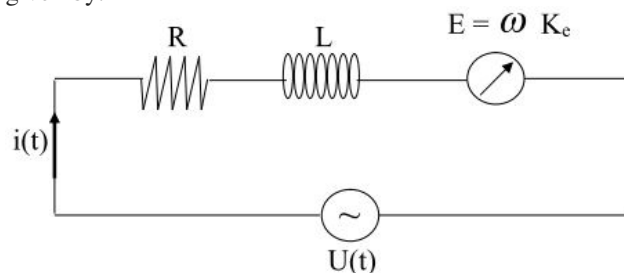


Fig.1 Motor electronic circuit

The application of Kirchof laws gives:

$$U(t) = R i(t) + L \frac{di(t)}{dt} + \omega K_e \quad (1)$$

and

$$I_m \frac{d\omega(t)}{dt} = C_m - C_f \quad (2)$$

$$C_m = K_e i \quad C_f = F_m \omega$$

$I_m$ : Moment of inertia of the motor shaft,  $F_m$ : Viscous coefficient of friction,  $C_m$ : Engine couple,  $i$ : Induced current and  $C_f$ : Viscous friction torque.

Equations (1) and (2) result in a differential system of two equations whose variables are the induced current and the angular velocity  $\omega$ .

The electromechanical parameters of the motor are:

$$R = 5 \Omega, \quad L = 50 \text{ mH}, \quad K_e = 0.2 \text{ v/rad.s}, \quad K_c = 0.1 \text{ Nm/A}, \\ F_m = 0.01 \text{ Nms/rad}, \quad I_m = 5.10^{-2} \text{ kgm}^2.$$

A. In the absence of tension

The system is reduced to:

$$\begin{cases} \frac{di}{dt} = -100i - 4\omega \\ \frac{d\omega}{dt} = 2i - 0.2\omega \end{cases} \quad (3)$$

The associated matrix has two real eigenvalues

$$\begin{cases} \lambda_1 = -99.9198 \\ \lambda_2 = -0.2802 \end{cases}$$

The system is asymptotically stable, showing the origin as an improper stable node.

In this case, the matrix A is diagonalizable. After a basic change, we can assume:

$$A = \begin{pmatrix} \lambda_1 & 0 \\ 0 & \lambda_2 \end{pmatrix}$$

and the system is reduced to:

$$\begin{cases} \frac{di}{dt} = \lambda_1 i \\ \frac{d\omega}{dt} = \lambda_2 \omega \end{cases} \quad (4)$$

The solution of the Cauchy problem, with  $M(0) = (0.4, 0.5)$ , is written then:

$$\begin{cases} i(t) = 0.4 e^{\lambda_1 t} \\ \omega(t) = 0.5 e^{\lambda_2 t} \end{cases}$$

So that the integral curves are those defined below:

$$y = C \left| x \right|^{\frac{\lambda_1}{\lambda_2}} \quad C \in \mathbf{R} \quad \text{and the line of equation } X = 0.$$

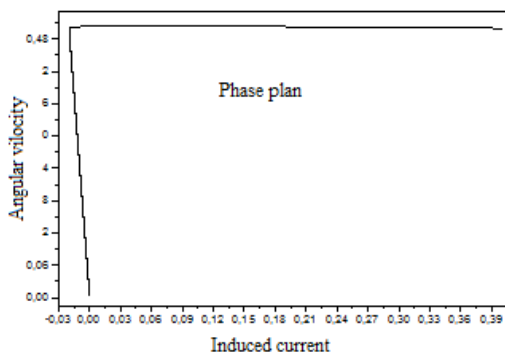


Fig. 2 Variation of the angular velocity with respect to the induced current.

B. By applying to the motor a voltage in the form of a 5v slot

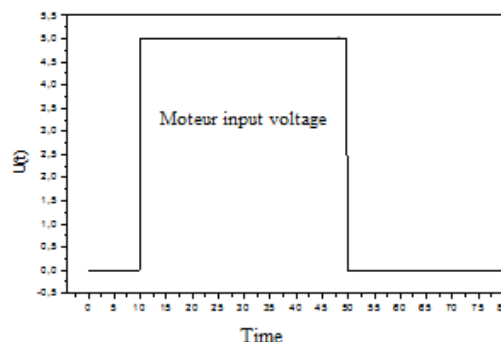


Fig. 3 Input voltage of the motor.

If  $t \in [10, 50]$ , the system is written:

$$\begin{cases} \frac{di}{dt} = -100i - 4\omega + 100 \\ \frac{d\omega}{dt} = 2i - 0.2\omega \end{cases} \quad (5)$$

$X_{eq} \left( i = \frac{5}{7}, \omega = \frac{50}{7} \right)$  is a point of equilibrium.

After a basic change we get:

$$\begin{cases} \frac{di}{dt} = -100 \left( i - \frac{5}{7} \right) - 4 \left( \omega - \frac{50}{7} \right) \\ \frac{d\omega}{dt} = 2 \left( i - \frac{5}{7} \right) - 0.2 \left( \omega - \frac{50}{7} \right) \end{cases} \quad (6)$$

The associated matrix has the same eigenvalues.

$$\begin{cases} \lambda_1 = -99.9198 \\ \lambda_2 = -0.2802 \end{cases}$$

The system is asymptotically stable; the  $X_{eq}$  equilibrium is a stable node.

If  $t \notin [10, 50]$ , the corresponding system is identical to the system (1). So the properties of stability do not change [1].

If one chooses  $M_0 = [0.4, 0.5]$  like initial conditions of the system (1), the other conditions of the systems (5) and (6) will be respectively:

$$\begin{aligned} & [-1.2373021e-3, 3.0848322e-2] \quad \text{et} \\ & [7.1417968e-1, 7.1427626] \end{aligned}$$

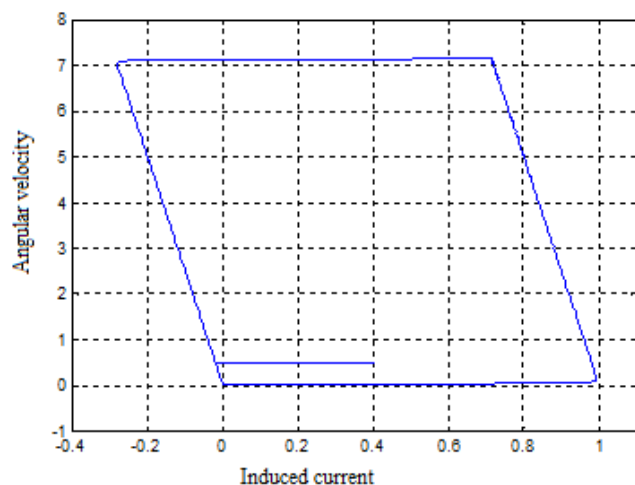


Fig. 4 Phase Plan.

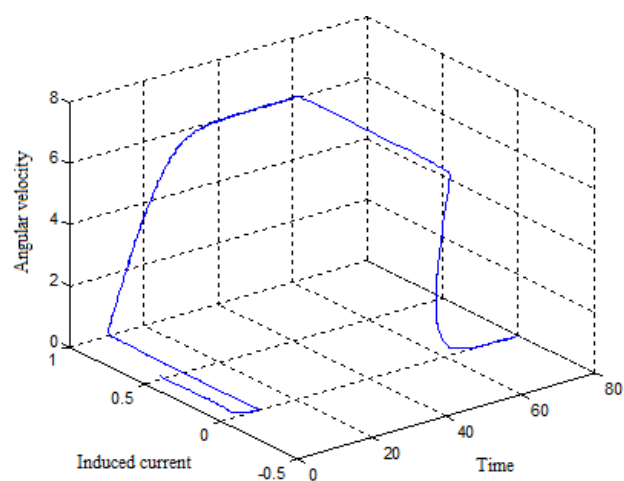


Fig. 5 Espace of movement

C. If  $U(t)$  and  $E(t)$  are variables

The system of dynamic equations becomes as follows:

$$\begin{cases} \frac{di}{dt} = -100i - 4\omega + \frac{40 \omega i}{|i| + \frac{25}{\omega}} \\ \frac{d\omega}{dt} = 2i - 0.2\omega \end{cases} \quad (7)$$

We will use the optimal derivative method which is in fact an overall approximation, which differs from the classical linear approximation of a stationary point [2], [3], [4].

As regards the study of the behavior of the solutions of a nonlinear equation around a singular point, the classical

linearization does not make it possible to answer in the following cases

- Si  $DF(0)$  n'existe pas (cas où la fonction non linéaire définissant une équation non régulière et donc non différentiable).
- Si  $DF(0)$  est stable, mais non pas asymptotiquement stable.

### III. RRÉSENTATION DE LA METHOD DE DÉRIVATION OPTIMALE

Consider a nonlinear ordinary differential problem of the form On considère l'équation différentielle ordinaire non linéaire de la forme:

$$\begin{cases} \frac{dx}{dt} = F(x(t)) \\ x(0) = x_0 \end{cases} \quad (8)$$

$x \in \mathbb{R}^n$ ,  $F$  is a given function on an open subset  $\Omega \subset \mathbb{R}^n$ , with the assumptions:

- H1)  $F(0) = 0$ .
- H2) the spectrum  $\sigma(DF(x))$  is contained in the set  $z : \text{Re}z < 0$  for every  $x \neq 0$  in a neighborhood of 0 for which 0, où  $DF(x)$  exists.
- H3)  $F$  is  $\gamma$ . Lipschitz continuous.

-First step: Calculation of  $A_0 = DF(x_0)$

-Second step: Calculation of  $A_1$  from the solution of equation (9):

$$\begin{cases} \frac{dy}{dt} = A_0 y(t) \\ y(0) = y_0 \end{cases} \quad (9)$$

we minimize the functional

$$G(A) = \int_0^{+\infty} \|F(y(t)) - A y(t)\|^2 dt.$$

$A_1$  is uniquely determined by the formula:

$$A_1 = \left[ \int_0^{+\infty} [F(x(t))] [x(t)]^T dt \right] [\Gamma(x)]^{-1}$$

where  $x$  is the solution of equation (9). We thus see that apart from the initial matrix, the matrices determined by the procedure are not the Jacobian matrices of  $F$  at a given point.

Subsequently, it is necessary that the conditions at the beginning of this section are satisfied at each step. If we assume that this is true, then the procedure works as follows:

-Third step

To calculate  $A_j$  from  $A_{j-1}$ , one must first solve:

$$\begin{cases} \frac{dy}{dt} = [A_{j-1}] y(t) \\ y(0) = x_0 \end{cases} \quad (10)$$

We denote by  $y_j(t)$  the solution of equation (10).

Minimizing the functional

$$G_j(A) = \int_0^{+\infty} \|F(y_j(t)) - A y_j(t)\|^2 dt.$$

and assuming that  $\Gamma(y_j)$  and invertible, we end up with:

$$A_j = \left[ \int_0^{+\infty} [F(y_j(t))] [y_j(t)]^T dt \right] [\Gamma(y_j)]^{-1}$$

Si  $A_j$  converge vers une matrice  $A$ , on dit que  $A$  est la dérivée optimale de  $F$  en  $x_0$ .

To evaluate and judge the quality of the approximation, we plot the squared error as a function of time. To do this, the expression of the latter is given by:

$$E_Q = \sum_{i=1}^n \|x_i(t) - y_i(t)\|^2$$

or

$x(t)$  represents the solution of the nonlinear system.

$y(t)$  represents the solution of the linear system.

#### IV. MAIN RESULTS OF THE DIGITAL STUDY

To prove that the origin is a point of equilibrium, it suffices to use the following theorem:

We consider a function  $F$  defined in a domain  $\Omega$ , undefined and non-continuous at the point  $N(\alpha_1, \alpha_2)$ .

If  $\lim_{(x,y) \rightarrow (\alpha_1, \alpha_2)} F(x, y) = l$  exists, we say that  $F(x, y)$  admits an

extension by continuity in  $N$ .

Let the function  $G(x, y)$  be such that

$$G(x, y) = \lim_{(x,y) \rightarrow (\alpha_1, \alpha_2)} F(x, y) = \begin{cases} F(x, y) & \text{si } (x, y) \neq (\alpha_1, \alpha_2) \\ l & \text{si } (x, y) = (\alpha_1, \alpha_2) \end{cases}$$

For our example, the problem is to show that  $\lim_{(x,y) \rightarrow (0,0)} F_1(x, y)$

exists.

$$\text{Now, we have } \lim_{(x,y) \rightarrow (0,0)} F_1(x, y) = \lim_{(x,y) \rightarrow (0,0)} \frac{xy}{|x| + \frac{25}{y}} = 0.$$

This confirms that the origin is a point of singular equilibrium.

The procedure for calculating the optimal derivative gives the result of 7 iterations:

$$A = \begin{bmatrix} -98.6067 & -3.9898 \\ 2 & -0.2 \end{bmatrix}$$

$A$  is obtained for initial conditions  $(x_0, y_0) = (0.03, 1.2)$ . The eigenvalues are

$\lambda_1 = -98.5256, \lambda_2 = -0.2812$ . So, the system is asymptotically stable, and makes equilibrium  $O$  appear as a stable node.

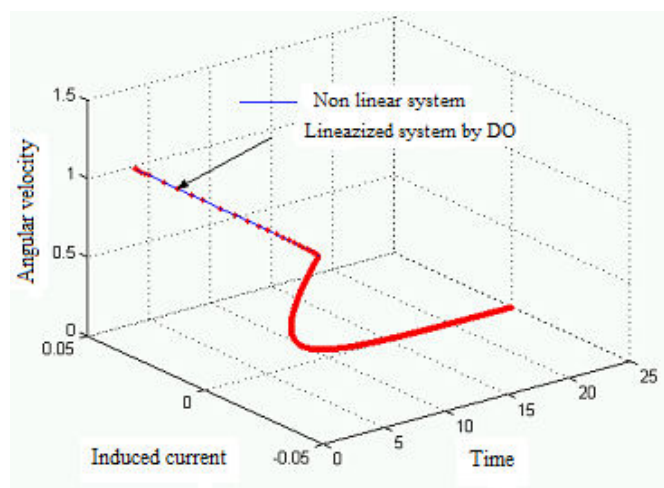


Fig. 6 The solution  $(x(t), y(t), z(t))$  in the phase space for the initial conditions  $(x_0, y_0) = (0.03, 1.2)$ .

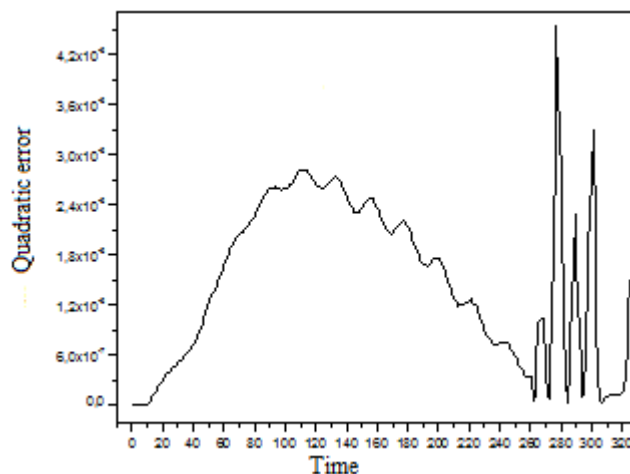


Fig. 7 Quadratic error due to the optimal derivation



## V. CONCLUSION GENERAL

Ordinary differential equations model a large family of phenomena that manifests itself in several domains (electronics, biology [5], mechanics, etc.). They are often non-linear and innumerable and usually appear complex and surprising effects.

So, we can say that the study of stability in the case of nonlinear systems poses a very difficult problem; this is why we use the most classical method based on linearization (optimal derivative).

It is an overall approximation, as opposed to the nonlinear perturbation of a linear equation that differs from the classical linear approximation near a point of equilibrium. The approach followed is of the least squares optimization type.

We also presented a study of stability using the concepts of stability for the study of physical linear systems.

Regarding the study of the behavior of the solutions of a nonlinear equation (4) around a singular point where the classical linearization does not make it possible to answer in this case. We therefore arrive at the conclusion that:

The example presented shows the good agreement of the optimal derivation with the nonlinear system (4) since the layout of the solutions confirms the similarity of the two trajectories.

On the other hand, the calculation of errors shows that the optimal derivative is a good approximation near the starting point.

## REFERENCES

- [1] T. Benouaz, S.M.A. Bekkouche, N.Gouali, Modelling of the Non linear Systems by Optimal Derivative, Computational Procedure and Proprieties, International Journal of Nonlinear Science, V.1.15(2013, N°3, pp. 271-283,ISSN 1749-3889 (print),1749-3897.
- [2] T. Benouaz, *Optimal Derivative of a Non-Linear Ordinary Differential Equation*, Equadiff 99, International Conference on Differential equations, Berlin (Germany) 1-7 August, Vol.2, pp.1404-1407, World scientific Publishing Co. Pte. Ltd, 2000.
- [3] T. Benouaz, O. Arino, Determination of the Stability of a Nonlinear Ordinary Differential Equation by Least Square Approximation. Computational Procedure, Appl. Math. and Comp sci., N°1, Vol.5, pp.33-48, 1995.
- [4] T. Benouaz and Martin Bohner, "On the Relationship between the Classical Linearization and Optimal Derivative", Advances in Dynamical Systems and Applications (ADSA), V. 2, N°1, pp. 41-57, 2007.
- [5] T.Benouaz, F.Lassouani, S.M.A.Bekkouche,M. Bohner, Application of the optimal derivative to the study of a ratio-dependent model describing the evolution of HIV in Canada", Advances in Dynamical Systems and Applications,( A.D.S.A.) Volume 6, Number 1, pp. 3-12S, 2011.

# Experimental Investigations and Model optimisation of Thermal Operated of Bubble Pump

Raoudha Garma<sup>#1</sup>, Doniazied Sioud<sup>#2</sup>, Khlifa Mej bri<sup>#3</sup>, Ahmed Bellagi<sup>#4</sup>

<sup>#</sup>*L.R. Thermique & Thermodynamique des Procédés Industriels*

*Ecole Nationale d'Ingénieurs de Monastir-ENIM, University of Monastir, Monastir, Tunisia*

<sup>1</sup>raoudhagarma83@gmail.com

<sup>2</sup>siouddoniazied@gmail.com

<sup>4</sup>Ahmedbellagi@enim.rnu.tn

**Abstract**—Bubble pump is the key component for single pressure refrigeration systems. In order to estimate the performance of these systems, the performance of the bubble pump must first be predicted. Successful analytical model of bubble pumps which better predict the required tube diameters, heat input, and submergence ratio enhance the whole absorption refrigeration system performance. In the present work, an experimental study and a new theoretical model are presented to estimate the bubble pump mass flow rate for different heat flux inputs and then compared to the performance of experimental investigated bubble pump for different tube diameters and submergence ratio.

**Keywords**—Bubble pump, Experimental validation, Analytical Model, Heat input, Tube diameter, Submergence ratio

## I. INTRODUCTION

The diffusion absorption technique is invented by the Swedish engineers von Platen and Minters [1] in the 1920s. The corresponding thermodynamic cycle is based on a refrigerant/absorbent pair mixture as working fluids and an inert gas for pressure equalization. The most used working fluids for this called diffusion absorption refrigerator is the ammonia/water system with ammonia as refrigerant and water as absorbent. To maintain a uniform pressure throughout the machine, either hydrogen or helium is used as an auxiliary gas in the cold compartment [2]. Helium is proved to be preferable to hydrogen as auxiliary gas for the cycle [3]. The circulation of the working fluids is carried out by a thermally driven bubble pump which can be powered by waste heat or solar thermal energy. As a result of the absence of any mechanical moving part, the refrigerator is silent and very reliable [4] in addition to an economical and environmental friendly devise.

Thermal driven bubble pump simply consists of a vertical tube that is heated causing the formation of bubbles. The rising bubbles act as small gas pistons lifting liquid slugs to the tube's top. Heat can be supplied at the bottom of the tube [5-10] with a separate heating element where the pipe section is assumed to be insulated and vapor is supposed to be produced only at the surface of the heating element and the pumping tube serves simply as vapor/liquid riser. Heat may be also

applied along all the tube length (pump with direct heating) [11, 12] liquid is vaporized in the pumping tube. Bubbles increase in size and coalescence as they rise along the tube and finally push the liquid up.

This apparently simple devise is quite complex from the point of view of analysis and modeling.

Pfaff et al. [5] developed a mathematical model using the hydrostatic principle (manometer principle) to evaluate the bubble pump's performance. In order to validate the mathematical model, an experimental system was built and tested.

Delano [13, 14] proposed an analytical model to evaluate the bubble pump performance. The model was based on the air-lift pump analysis developed by Stunning and Martin [15] which uses conservation equations of mass and momentum and assigns a value to the slip ratio ( $S=VG/VL$ ) between phases velocities. The influence of the heat input, tube diameter and submergence ratio ( $H/L$ ) on the bubble pump performance were investigated. To validate the analytical model, Delano conducted experiments with water, and it was shown experimentally to provide a good estimation of the heat input required to produce a desired liquid flow rate.

A single pressure absorption heat pump analysis was presented by Schaefer [16]. She was also concerned by the Einstein refrigeration generator design and in particular by the bubble pump configuration. Her study builds on the work of Delano. She used a methodical approach to increase the efficiency of the Einstein cycle, therefore the relationship of the diameter, submergence ratio, mass flow rate, and heat input have been analyzed for the bubble pump, and its physical geometry has been altered to maximize its performance.

White [17] performed experimental studies and analytical modeling of bubble pump using air-lift pump theory which operates on the same principals as a vapor bubble pump. The model (verified by the experimental data of the air-water system) was then used to analyze the design considerations of a bubble pump using an ammonia-water mixture (Einstein cycle).

## II. EXPERIMENTAL STUDY

### A. experimental setup

For the purposes of the present study, an experimental prototype was built in order to investigate the performance of a bubble pump operated diffusion absorption refrigerator based on water-acetone.

Fig. 2 presents a schematic assembly diagram of the experimental set up. The system design allows investigating the bubble pump behavior and the absorber efficiency.

The design of the main component is as table I:

TABLE I  
 EXPERIMENTAL TECHNICAL DATA

Pump characterisation	
Pump tube diameter	8 mm
Pump tube length	1.4 m
Submergence ratio H/L	0.25/0.27

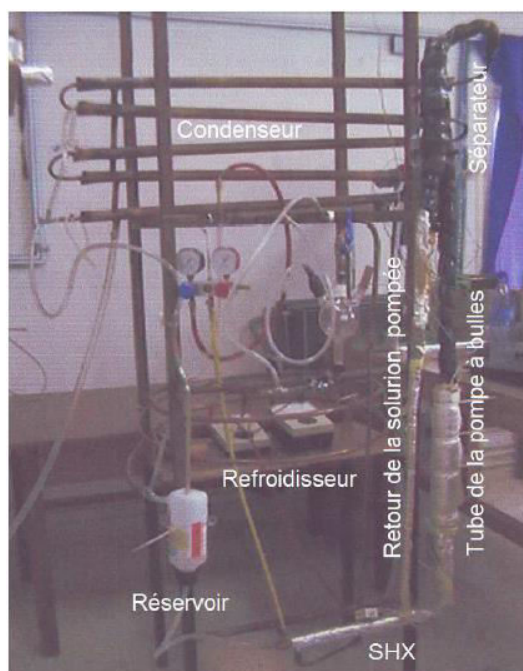


Fig 1. Experimental set up.

As shown in Fig. 1, the boiler and the bubble pump are not combined in one unit as in a classical DAR but separated in order to investigate each of both machine components independently from one another. Therefore the generator consists of:

- a single vertical, the heat input is restricted to a small zone in the bottom,
- a vapor-liquid separator
- a boiler.
- Solution heat exchanger
- Bubble pump
- Phase separator
- Condenser
- Cooler
- Tank

### B. Experimental Results and discussion

#### 1. Heat flux effect

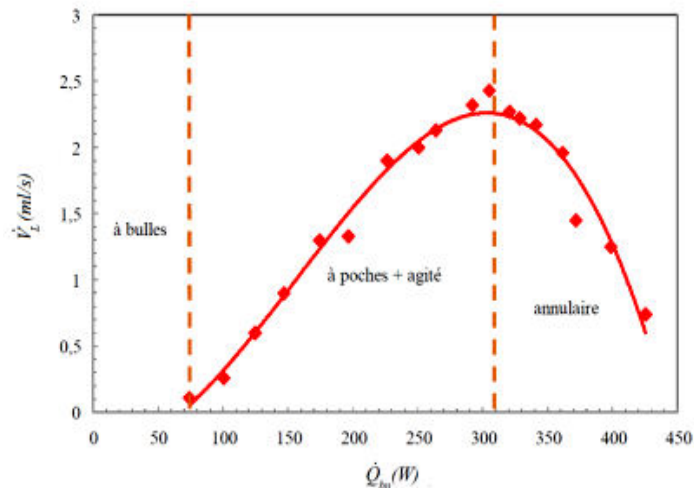


Fig. 2 Effect of heat flux on the pumped solution flow rate.

For a tube diameter of 8/10 mm and 1.4 m of length, first the minimum required heat, enough to start the pumping process, was determined. Rising heat power and noticing the pumped solution flow rate leads to a found value of heat of 75 W for a level of 38 cm.

Figure 2 shows that the pumped solution flow rate depends highly on the given heat power/flux. In fact rising this heat starting from 75 W which is the pumping start point the liquid pumped flow rate rises until it reaches a maximum for a value of 305W. Progressive increase of heat flux as input is associated to an increase of the number of bubble created and of the pumped liquid flow rate. Figure 2 shows that like in the bubbly flow, bubbles are dispersed continuously in the liquid flow phase, having a small size as compare to the tube diameter and the liquid level remains almost constant. Once the starting bubble heat is reached, large size bubbles with frame of slug holding the hole diameter of the tube are created moving the liquid to the tube top, until it is pumped to the liquid-vapor separator. The downline in figure 2 is formed due to the increase of the flow rate, losses inside tube become important which reduce the capacity of bubble to pump the liquid. Transition to the annular flow explain also the performances drop, the velocity of the vapor occupy become more important, occupy total tube volume where only small droplets of liquid are entrained.

#### 2. Initial liquid level effect

Figure 3 shows experimental results of variation of pumped flow rate as function of heat flux, for two initial rich solution values. The flow rate of pumped solution have the same shape (represented via the liquid velocity) for the two submergence ratio tested and the pumped solution flow rate is more important when the solution initial level is higher. Curve shapes is similar to literature study. It is seen that the heat flux is reduced when the initial level is more important. In fact

when the level rise from 35 to 38 cm the minimum required heat is reduced from 100 to 75 W.

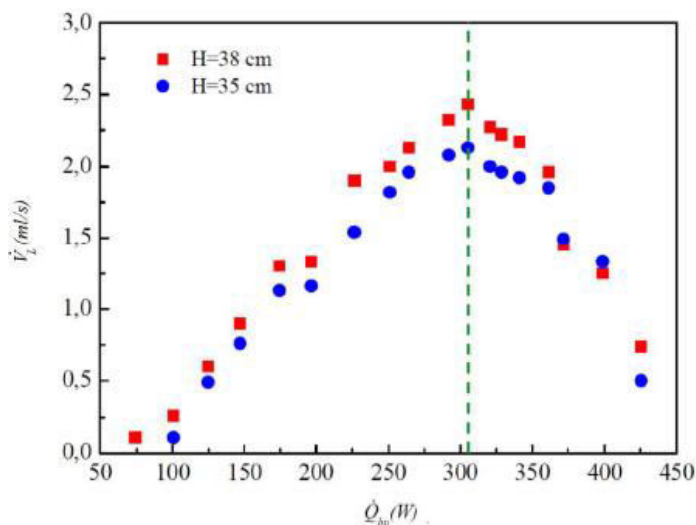


Fig 3. Effect of Heat on pumped solution flow rate as function of submergence ratio

Figure 4 illustrates the behavior of bubble pump temperature as function of motive heat, for H=35 et 38 cm. It is noticed that when the introduced heat increases, the temperature of solution at the feed of this equipment is unchangeable for the two tested level H (H: initial level of acetone rich solution) until  $Q_{bp}=305$  W which is the required experimental value for reaching a maximum of pumped solution flow rate. When the heat flux is increased in pump feed, its temperature rise. The pumped solution flow rate rises with the heat, the rise of the flow rate will oppose the pumped temperature rises.

According to the heat corresponding to the maximum pumped solution flow rate, the temperature rise because of the decrease of the pumped flow rate which increase the mixture heating time in the tube inlet.

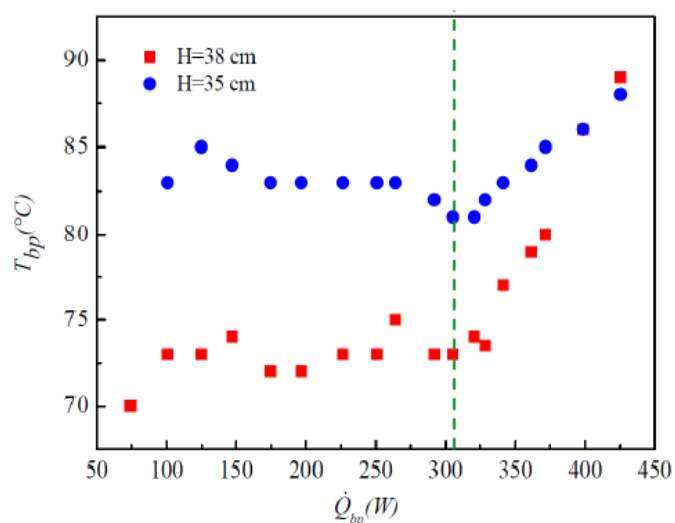


Fig 4. Bubble pump temperature variation with generator heat

### III. ANALYTICAL STUDY

#### A. Mathematical Model

Experimental and theoretical studies on a bubble pump for a diffusion-absorption refrigeration system was carried out by Sathe [18] using Delano's [13] methodology applied to the Platen-Munters' bubble pump, fig. 5. He concluded that a correction of loss factor K is necessary for the model. The correlation is found out by applying the experimental results (methanol based bubble pump) to the analytical model for a given pump tube diameter and a given submergence ratio.

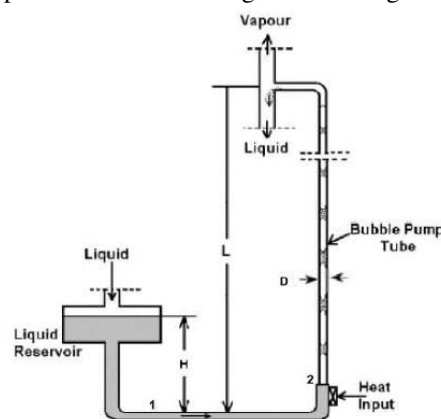


Fig 5. Mathematic model of bubble pump.

The correlation established for one pump tube diameter is not valid for another pump tube diameter:

$$K = A\dot{V}_g^4 + B\dot{V}_g^3 + C\dot{V}_g^2 + D\dot{V}_g \quad (1)$$

Where A, B, C, D and E are constants and are functions of the pump tube diameter, and  $\dot{V}$  volume flow rate.

Mathematical model for vapor bubble pump was provided by Akeel et al. [19] and used to simulate the thermal driving mechanism of LiBr-water absorption refrigerator. It had been generally developed and then tested based on water properties. The obtained results was then correlated to express the maximum pumping capacity as a function of the bubble pump configuration, but it was limited for water properties only.

Experimental investigation of water vapor-bubble pump characteristics and mathematical model was performed by Abduwadood et al. [20]. An improved correlation of K is found out such that the obtained value of the maximum liquid flow rate based on the corrected model matches that value obtained from the experimental test at the same operating conditions pump.

$$K = \left[ 1095 \left( \frac{H}{L} \right) - 4089.4 \right] d + \left( -105.37 \left( \frac{H}{L} \right) + 46.669 \right) \quad (2)$$

Keng Wai et al. present a new model based on the pumping characteristics of bubble pump. This model is used to estimate the mass flow rate of a water based bubble pump at atmospheric pressure. The critical parameters such as submergence ratio, tube diameter and heat input were varied to examine the validity of the new presented model.

In this paper, an improved analytical model for bubble pump is reconstructed and verified. The model is based on Delano's Methodology. Experimental results of the water based bubble pump tested by Abduwadood et al. [20] and those of the methanol based bubble pump studied by Sathe [18] were used to perform a new correlation of the loss factor K as function of the tube diameter and the submergence ratio. The comparison between the proposed analytical model and the practical experiments results was much acceptable in order to be used to analyze the bubble pump performance.

The bubble pump model is based on Delano methodology. He suggested that the submergence ratio of the bubble pump (H/L), which describes the average pressure gradient along the lift tube, can be expressed in terms of velocities, geometrical parameters, and fluid properties by using Bernoulli's equation, the continuity equation and momentum conservation equation.

Point 1 in Fig.1 represents the inlet of the bubble pump. Applying Bernoulli's equation between the surface of the lower reservoir and point 1 yields:

$$P_1 = P_{sys} + \rho_f g H - \rho_f \frac{V_1^2}{2} \quad (3)$$

Mass continuity is applied between point 1 and point 2 (where heat is applied). Assuming that the mixture of vapor bubbles and the liquid exit at a mixture velocity V2, continuity of mass yields:

$$\dot{m}_1 = \dot{m}_2 \quad (4)$$

or,  

$$\frac{AV_1}{v_1} = \frac{AV_1}{v_f} = \frac{AV_2}{v_2} \quad (5)$$

Thus,  

$$V_2 = \frac{v_2 V_1}{v_f} \quad (6)$$

The specific volume at point 2 is assumed to be the specific volume of a vapor liquid mixture with a quality, x, where:

$$v_2 = v_f + x(v_g - v_f) = v_f \left( 1 + \left( \frac{v_g - v_f}{v_f} \right) \right) \quad (7)$$

and,  

$$x = \frac{\dot{m}_g}{\dot{m}_f + \dot{m}_g} \quad (8)$$

Combining equations (4), (5), and (6) yields:  

$$V_2 = V_1 \left( 1 + \left( \frac{\dot{m}_g}{\dot{m}_f + \dot{m}_g} \right) \left( \frac{v_g - v_f}{v_f} \right) \right) \quad (9)$$

The mass flow rate of vapor is assumed negligible relative to the mass flow rate of liquid, and the specific volume of the liquid is assumed negligible relative to the specific volume of the vapor. Equation (7) now becomes:

$$V_2 = V_1 \left( 1 + \frac{\dot{V}_g}{\dot{V}_f} \right) \quad (10)$$

Momentum conservation is then applied between point 1 and point 2. Neglecting friction pressure losses over this short distance yields:

$$P_2 = P_1 - \rho_f V_1 (V_2 - V_1) \quad (11)$$

Substituting equation (8) into equation (9) yields:  

$$P_2 = P_1 - \frac{\rho_f V_1 \dot{V}_g}{A} \quad (12)$$

Now, equations (10) and (1) are combined:

$$P_2 = P_{sys} + \rho_f g H - \frac{\rho_f V_1^2}{2} - \frac{\rho_f V_1 \dot{V}_g}{A} \quad (13)$$

Next, the momentum conservation is applied to the pipe connecting the lower and upper reservoir.

$$P_2 - P_{sys} = \frac{1}{2} f \rho_f V_2^2 \left( \frac{L.B}{A} \right) + \frac{W}{A} \quad (14)$$

Where B is the perimeter of the bubble pump tube and W is the weight of fluid in the bubble pump tube. W can be expressed as the combined weight of liquid and vapor in the tube.

$$W = Lg(\rho_f A_f + \rho_g A_g) \quad (15)$$

Where Af is a superficial area through which the liquid flows and Ag is a superficial area through which the vapor flows. By assuming that the density of the vapour phase is negligible as compared to that of the liquid equation (13) can be simplified as follow:

$$W = Lg\rho_f A_f \quad (16)$$

We can also write down the following equations:

$$\dot{V}_f = \rho_f A_f = AV_1 \quad (17)$$

$$\dot{V}_g = A_g V_g \quad (18)$$

$$A = A_f + A_g \quad (19)$$

Substituting these equations into equation (14),

$$\frac{W}{A} = Lg \frac{\rho_f}{1 + \left( \frac{A_g}{A_f} \right)} \quad (20)$$

$$\frac{W}{A} = Lg \frac{\rho_f}{1 + \left( \frac{\dot{V}_g}{S\dot{V}_f} \right)} \quad (21)$$

Where

$$S = \frac{\dot{V}_g}{\dot{V}_f} \quad (22)$$

Substituting equation (19) into equation (12),

$$P_2 - P_{sys} = \frac{1}{2} f \rho_f V_2^2 \left( \frac{L.B}{A} \right) + Lg \frac{\rho_f}{1 + \left( \frac{\dot{V}_g}{S\dot{V}_f} \right)} \quad (23)$$

And substituting equation (8) into equation (21),

$$P_2 = P_{sys} + \frac{4fL}{d} \cdot \frac{\rho_f V_1^2}{2} \left( 1 + \frac{\dot{V}_g}{\dot{V}_f} \right)^2 + Lg \frac{\rho_f}{\left( 1 + \frac{\dot{V}_g}{S\dot{V}_f} \right)} \quad (24)$$

Finally, equation (22) is equated with equation (11) to complete the momentum model of the bubble pump:

$$\frac{H}{L} - \frac{1}{\left( 1 + \frac{\dot{V}_g}{S\dot{V}_f} \right)} = \frac{V_1^2}{2gL} \left[ 1 + 2 \frac{\dot{V}_g}{\dot{V}_f} + K \left( 1 + \frac{\dot{V}_g}{\dot{V}_f} \right)^2 \right] \quad (25)$$

Where

$$K = \frac{4fL}{d} \quad (26)$$

Several correlations for calculation the slip, S, are presented in literature. One of the best known of these is the so-called CISE correlation (developed at the CISE laboratories in Milan) which is presented by Premoli et al. The correlation has the form:

$$S = 1 + E_1 \sqrt{\frac{y}{1 + yE_2}} - yE_2 \quad (27)$$

Where

$$y = \frac{\dot{\epsilon}_g}{1 - \dot{\epsilon}_g} \quad (28)$$

In equation (26)  $\dot{\epsilon}_g$  is the volume flow ratio:

$$\dot{\epsilon}_g = \frac{\dot{V}_g}{\dot{V}_g + \dot{V}_f} \quad (29)$$

E1 and E2 are given by:

$$E_1 = 1.578 \text{Re}_{10}^{-0.19} \left( \frac{\rho_f}{\rho_g} \right)^{0.22} \quad (30)$$

$$E_2 = 0.0273 \text{We}' \text{Re}_{10}^{-0.51} \left( \frac{\rho_f}{\rho_g} \right)^{-0.08} \quad (31)$$

Where  $\text{Re}_{10}$  and  $\text{We}'$  are defined as:

$$\text{Re} = \frac{\dot{m}D}{\mu_f} \quad (32)$$

$$\text{We}' = \frac{\dot{m}^2 D}{\sigma \rho_f} \quad (33)$$

Where  $\dot{m}$  is the mass flow flux,  $D$  the equivalent diameter of the channel,  $\mu_f$  the liquid phase viscosity, and  $\sigma$  the surface tension.

#### IV. MODELLING RESULTS AND DISCUSSION

##### B. Model optimization

With the aim to optimize the analytical bubble pump model developed by Delano, based on parameters Regression, a new correlation of the loss factor parameter  $K$ , eq.(34), is proposed based on the experimental investigation of the thermally operated vapor lift bubble pump carried out by Abduwaddood and et al using water as working fluid and that conducted by sathe using methanol. The correlation is found out using TableCurve 2D by applying the experimental results to the analytical model for a given tube diameter and a given submergence ratio and inserted in the analytical model equation (23). Next, the rectified model is developed using FORTRAN program coding the ODRPACK algorithm. The theoretical liquid mass flow is so calculated and then compared with the experimental results.

The  $K$  is a function of  $(d/L)$  and  $(H/L)$  and it has the form:

$$K = A + \frac{B}{\text{Re}_g^{0.5}} + \frac{C}{\text{Re}_g^{1.5}} \quad (34)$$

Where

$$A = \beta_1 + \beta_2 \left( \frac{H}{L} \right) + \beta_3 \left( \frac{H}{L} \right)^2 \quad (35)$$

$$B = \beta_4 + \beta_5 \left( \frac{H}{L} \right) + \beta_6 \left( \frac{H}{L} \right)^2 \quad (36)$$

$$C = \beta_7 + \beta_8 \left( \frac{H}{L} \right) \quad (37)$$

Where

$$\beta_1 = \delta_{10} + \delta_{11} \left( \frac{d}{L} \right) \quad (38)$$

$$\beta_2 = \delta_{20} + \delta_{21} \left( \frac{d}{L} \right) \quad (39)$$

$$\beta_3 = \delta_{30} + \delta_{31} / \left( \frac{d}{L} \right)^2 \quad (40)$$

$$\beta_4 = \delta_{40} + \delta_{41} \left( \frac{d}{L} \right) \quad (41)$$

$$\beta_5 = \delta_{40} + \delta_{51} \left( \frac{d}{L} \right) \quad (42)$$

$$\beta_6 = \delta_{60} + \delta_{61} / \left( \frac{d}{L} \right)^2 \quad (43)$$

$$\beta_7 = \delta_{70} + \delta_{71} \left( \frac{d}{L} \right) \quad (44)$$

$$\beta_8 = \delta_{80} \quad (45)$$

and

$$\text{Re}_G = 4 \frac{\rho_G \dot{V}_G}{\pi d^2 \mu_G} \quad (46)$$

The correlation parameters in the two cases, water based and methanol based bubble pump are summarized in the table 2.

TABLE2 VALUE OF COEFFICIENT OF CORRELATION K (WATER)

Coef	Value	Coef	Value
$\delta_{10}$	-6.34168851E+00	$\delta_{50}$	-9.43075199E+02
$\delta_{11}$	9.52881153E+02	$\delta_{51}$	1.13622783E+05
$\delta_{20}$	1.51417591E+01	$\delta_{60}$	-3.13213006E+02
$\delta_{21}$	-2.07270761E+03	$\delta_{61}$	8.78401748E-03
$\delta_{30}$	6.84549802E+00	$\delta_{70}$	-1.39667124E+05
$\delta_{31}$	-1.83113118E-04	$\delta_{71}$	1.01373745E+07
$\delta_{40}$	3.89222704E+02	$\delta_{80}$	3.04800171E+05
$\delta_{41}$	-5.43738808E+04	-	-

##### C. New model validation

The Model verification of bubble pump for is based in the use of water in order to discuss the Dependence of mass flow rate on submergence ratio.

The submergence ratio is one of the influencing parameter on the bubble pump performance. For the same tube diameter, increasing the submergence ratio leads to increase the liquid flow rate. Therefore, the bubble pump is more efficient when the submergence ratio increases.

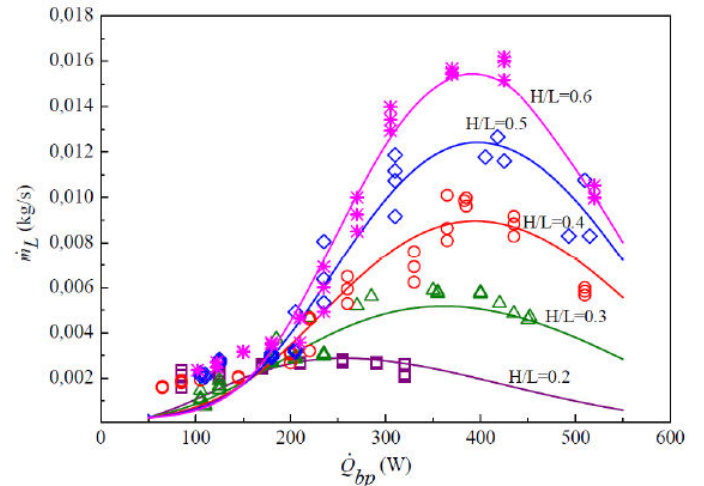


Fig. 6 Mass flow rate of the pumped liquid as a function of the driving power for the  $\varnothing$  8mm tube and different submergence rates. Symbol: experimental data, Line: theoretical model corrected

Figs. 6, 7 and 8 illustrate the comparison between the improved analytical model and the experimental result of the water based bubble pump performance when varying the submergence ratio for fixed tube diameter. One can see that the predictions show the same behavior as the experimental results. In fact, the increasing of the heat input leads to a higher liquid flow rate until a maximum value is reached. Heating the fluid beyond this limit will simply generates more vapor and the produced high vapor velocity will change the

flow pattern from slug to annular flow which causes the expected decrease in pumping capacity.

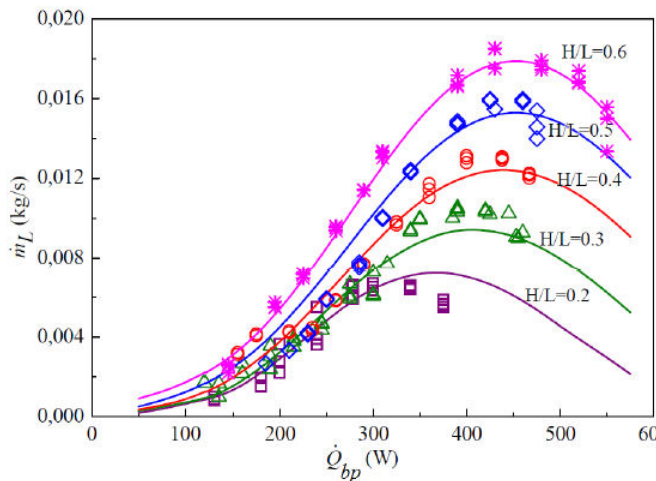


Fig. 7 Mass flow rate of the pumped liquid as a function of the driving power for the Ø 10mm tube and different submersion rates. Symbol: experimental data, Line: theoretical model corrected

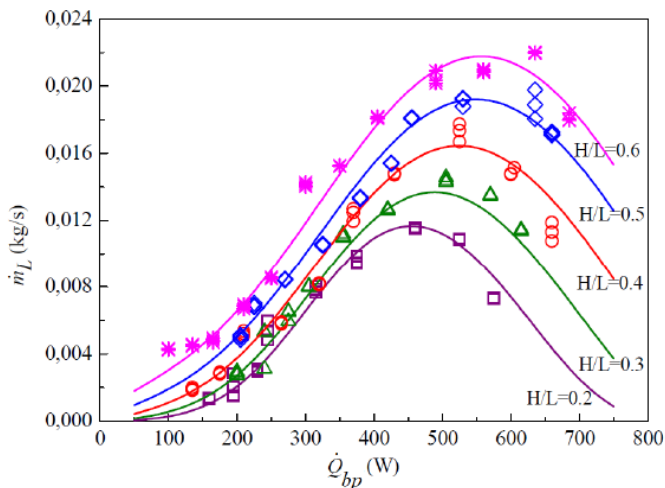


Fig. 8 Mass flow rate of the pumped liquid as a function of the driving power for the Ø 10mm tube and different submersion rates. Symbol: experimental data, Line: theoretical model corrected

According to Fig. 6, the theoretical model shows a little under-prediction of pumping capacity when decreasing the bubble pump driving heat under 175 W. Nevertheless, one can observe (cf. Figs. 7 and 8) that this model proves a very good agreement with the experimental points for different diameter and submersion ratio. So we can conclude that the model describes very well the pump performance.

#### D. Model comparison

Referring to Fig.9, one can realize that the predicted maximum bubble pump capacity in the present work show a great similarity with the experimental data [19]. When compared to abduwadood work, one can remark that experiments are better described by the present model ( $H/L =$

0.4 and 0.6), hence it can be suited to describe bubble pumps behavior.

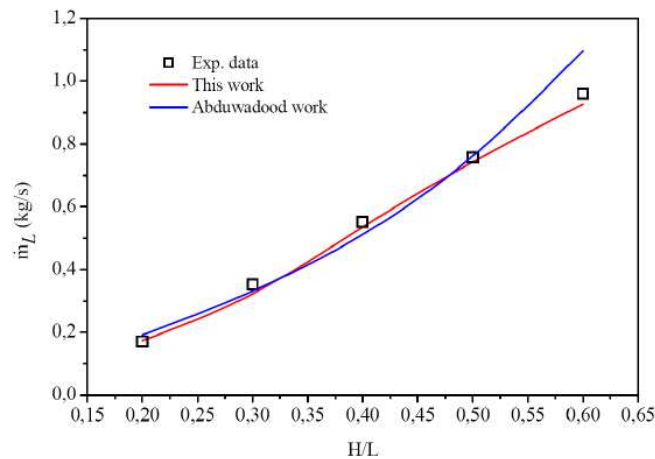


Fig. 9 Comparison of the present model with Abduwadood's model and experiments

#### V. CONCLUSIONS

Bubble pump is a crucial component of the Platen-Munter [1] and Einstein-Szilard [22] single pressure absorption refrigeration cycles. First, an experimental work has been conducted to investigate bubble pump for different tube diameters and submersion ratio. Second, as bubble pumps have the same fundamental working principle as air-lift pumps, a new theoretical model based on Delano work is presented to estimate the bubble pump mass flow rate. In this model a new correlation of the loss factor parameter  $K$  is proposed. Compared to the experimental and theoretical investigated bubble pump [20] for different tube diameters and submersion ratio, the new developed model show an excellent estimation of the bubble pump performances.

#### REFERENCES

- [1] Von Platen BC, Munters CG. US Patent 1, 685,764; 1928.
- [2] Jakob U, Eicker U, Schneider D, Taki AH, Cook MJ. Simulation and experimental investigation into diffusion absorption cooling machines for air conditioning applications. *Applied Thermal Engineering* 2007.
- [3] Zohar A, Jelinek M, Levy A, Brode I. Numerical investigation of a diffusion-absorption refrigeration cycle. *International Journal of Refrigeration* 2005;28(4):515–25.
- [4] Koyfman A, Jelinek M, Levy A, Borde I. An experimental investigation of bubble pump performance for diffusion absorption refrigeration system with organic working fluids. *Applied Thermal Engineering* 2003;23:1881–94.
- [5] Pfaff M, Saravanan R, Maiya MP, Srinivasa M (1998) Studies on bubble pump for a water-lithium bromide vapor absorption refrigeration. *Int J Refrig* 21:452–462
- [6] White SJ 2001 Bubble pump design and performance. M.Sc Thesis, Georgia Institute of Technology
- [7] Koyfman A, Jelinek M, Levy A, Borde I (2003) An experimental investigation of bubble pump performance for diffusion absorption refrigeration system with organic working fluids. *App Ther Eng* 23:1881–1894
- [8] Vicatos G, Bennett A (2007) Multiple lift tube pumps boost refrigeration capacity in absorption plants. *J Energy S Afr* 18:49–57
- [9] Siyoung Jeong, Sang-Kyun Lee, Kee-Kahb Koo: Pumping characteristics of a thermosyphon applied for absorption refrigerators

- with working pair of LiBr/water. *Applied Thermal Engineering* 18 (1998) 1309-1323
- [10] Ben Ezzine N., Garma R., Bourouis M., Bellagi A., Experimental Studies on Bubble Pump Operated Diffusion Absorption Machine Based on Light Hydrocarbons for Solar Cooling, *Renewable Energy*, 35 (2010), 2, pp. 464-470
- [11] A. Benhmidene, B. Chaouachi, M. Bourouis, and S. Gabsi. 2011. Effect of Operating Conditions on the Performance of the Bubble Pump of Absorption-Diffusion Refrigeration Cycles. *Thermal Science*, Vol. 15, No. 3, pp. 793-806
- [12] A. Benhmidene, B. Chaouachi, M. Bourouis, and S. Gabsi. 2011. Modelling of heat flux received by a bubble pump of absorption-diffusion refrigeration cycles. *Heat Mass Transfer*. 47: 1341-1347
- [13] A. Delano, Analysis of the Einstein Refrigeration Cycle, M.Sc Thesis, Georgia Institute of Technology, 1997.
- [14] A. Delano, Design Analysis of the Einstein Refrigeration Cycle, PhD Dissertation, Georgia Institute of Technology, 1998.
- [15] Stenning, A. and Martin, C. 1968. An analytical and Experimental Study of Airlift Pump Performance. *ASME Journal of Engineering for Power* pp. 106-110,
- [16] L.A. Schaefer, Single Pressure Absorption Heat Pump Analysis, PhD Dissertation, Georgia Institute of Technology May 2000.
- [17] White, S.J., Bubble Pump Design and Performance: M.Sc. Thesis, Georgia Institute of Technology, 2001.
- [18] Sathe, A. 2001. Experimental and Theoretical Studies on A bubble Pump for A diffusion Absorption Refrigeration System. Master of Technology Project Report, Universitat Stuttgart.
- [19] Akeel, M.A., S., Abdulwadood., S.A., Asiem. (2010). Theoretical Analysis of a Thermally Operated Vapor Bubble Pump. In *Proceeding, F.T.E. Scientific Int. Conf. Tech.-College – Najaf. Iraq*, 12-13/ April, 2010.
- [20] Abdulwadood S.S., Akeel M.A., (2012), Experimental Investigation of Water Vapor Bubble Pump Characteristics and its Mathematical Model Reconstruction, *Eng. & Tech. Journal*, Vol. 30, No.11, 2012
- [21] Keng Wai Chan , Malcolm McCulloch, Analysis and modelling of water based bubble pump at atmospheric pressure, *International journal of refrigeration* 36 (2013), 1521-1528
- [22] Einstein, A., Szilard, L., 1930. Refrigeration. U.S. Patent 1781541.



# Cascade Refrigeration Systems Involving CO<sub>2</sub> sub-cycles

Doniazed Sioud<sup>#1</sup>, Yosra Ben Salem<sup>#2</sup>, Ahmed Bellagi<sup>#3</sup>

<sup>#</sup>*L.R. Thermique & Thermodynamique des Procédés Industriels*

*Ecole Nationale d'Ingénieurs de Monastir-ENIM, University of Monastir, Monastir, Tunisia*

<sup>1</sup>siouddoniazed@gmail.com

<sup>2</sup>yosraissetkelibia@gmail.com

<sup>3</sup>a.bellagi@enim.rnu.tn

**Abstract**—In this study, two cascade refrigeration configurations involving CO<sub>2</sub> sub-cycles are thermodynamically analyzed. In both systems a single-effect lithium bromide/water absorption unit is used as upper cycle. Two different CO<sub>2</sub> sub-cycles are combined in a cascade with this absorption unit: a trans-critical one in the first configuration and a conventional cycle in the second configuration. Whereas the driving heat for the absorption unit in the former system is supplied solely by the hot carbon dioxide gas exiting the compressor, the heat of this hot gas covers only partially the energy needs of the absorption unit in the latter configuration. Numerical simulations of these refrigeration systems are performed for heat rejection temperature of 35°C and –35°C evaporator temperature. It is found that refrigeration system with a trans-critical CO<sub>2</sub> sub-cycle is more performant than the system including a conventional CO<sub>2</sub> cycle.

**Keywords**—Cascade refrigeration, Trans-critical CO<sub>2</sub> cycle, LiBr–Absorption cooling, Numerical simulations.

## I. INTRODUCTION

The adoption of natural working fluids for refrigeration systems is now the focus of research in this field and considered as sustainable solution of environmental matter such as global warming of the atmosphere and ozone depletion of the stratosphere [1,2]. Many regulations have been developed in this direction (for instance EU F-Gas Regulation 517/2014 (European Commission, 2014 [3]) with the purpose of substituting the old generation of harmful refrigerants. Main usual natural refrigerants are CO<sub>2</sub>, butane, propane, ammonia, water and air. However carbon dioxide is particular: nontoxic, non-flammable, stable and cheap [4,5]. Research is performed to investigate the CO<sub>2</sub> refrigeration systems in order to increase their performance for the reason that it is generally low when compared to other conventional refrigerants mainly because of the low-critical point of the CO<sub>2</sub> (31.1°C). This fact is associated with high compression (electrical) energy. Especially in the warm climates, such as in Tunisia, this problem is more important where the refrigeration cycle has to be operated in trans-critical mode with a further decrease of performance [6,7]. Many researchers have considered the optimization of the high pressure in the trans-critical mode in order to enhance the performance of CO<sub>2</sub> refrigeration systems. (Kauf [8] and Liao *et al.* [9]). An internal heat exchanger used

for sub-cooling after the gas cooler as well as cascade systems have been considered [10-12]. An external device for creating a devoted sub-cooling after the gas cooler was also studied and was found as an important choice to improve the COP by around 30% [13]. Studies of mechanical sub-cooling (M-SC) are also present in the literature. Llopis *et al.* [14,15] investigated the use of R134a as working fluids in the (M-SC) system and they found that the COP was increased by 30%. Gullo *et al.* (2016) studied the use of the same refrigerant and they calculated the total equivalent warming impact to be reduced compared to a supermarket booster system about 10% for Greece and 25% for Spain climate. A comparative study [17] is carried out to state that the use of a mechanical subcooling system could increase the system COP up to 75% as compared to simple system. The use of a thermos-electrical sub-cooling is another practical technique. Sarkar [18] calculated a COP enhancement of 25% compared to the conventional system. Moreover, Dai *et al.* [19] found that the combination of a thermos-electrical sub-cooling device with an expander to enhanced the COP by about 38%. Heat input from solar systems, waste heat or biomass boiler can be used in these systems in order to feed the absorption machine. Salajeghe and Ameri [20] investigated the use of a LiBr-H<sub>2</sub>O absorption chiller for sub-cooling purposes. The heat input for the chiller is set by a solid oxide fuel cell and they also investigated the incorporation of an internal heat exchanger in this system. They found that the use of the dedicated sub-cooling with the absorption chiller is effective than internal heat exchanger for sub-cooling. However, the combination of the two ways was found to be a totally optimum method. In another study [21], comparison of an absorption chiller and a mechanical vapour compression system as sub-cooling devices in a CO<sub>2</sub> refrigeration system is performed. It was concluded that the use of the absorption chiller may reduce the consumption of electric power by 84% while the use of the (M-SC) by 41%, but the use of the absorption chiller requires an extra heat source input. Mohammadi [22] investigated various configurations of the CO<sub>2</sub> refrigeration systems coupled to absorption machines. The objective was to produce refrigeration in temperature range (–30°C to –80°C). Novel designs were proposed. They studied the use of two-stage machines in order to decrease the compressor work due to the

important pressure ratio. In their case, the absorption machines were fed with the waste heat after the compressors. They concludes that the *COP* of the studied configurations can be increased by 200% in some cases. The use of an absorption machine in the high-stage of a CO<sub>2</sub> cascade system has been studied by Mohammadi and Mc-Gowan [23], Cyklis [24]. In addition, the incorporation of absorption machines in CO<sub>2</sub> power cycles has been studied by Li *et al.* [25] and Arora *et al.* [26]. Another effective way for enhancing the CO<sub>2</sub> refrigeration system is the use of a vortex tube expansion component after the gas cooler. This design has been studied by Sarkar [27] and enhancement by up to 18% have been found. The previous literature review makes clear that it is interesting to use sub-cooling as a means for enhancing the performance of the CO<sub>2</sub> refrigerators in the trans-critical mode. A similar idea had been studied by Mohammadi [28] to produce temperatures from -35°C up to 5°C. Basing on these findings, we propose in the present paper the scheme combining a single-effect LiBr-H<sub>2</sub>O absorption cycle with a CO<sub>2</sub> refrigeration unit in trans-critical and in conventional mode. In the trans-critical mode, the waste heat after the compressor is supplied to the generator of the absorption chiller as unique energy source.

## II. DESCRIPTION AND ANALYSIS OF THE CYCLE

Two cascade systems, A and B, have been investigated.

Fig. 1 depicts the configuration A which contains a trans-critical CO<sub>2</sub> subsystem (11-12-13-14-15-16-11) for low-temperature refrigeration and a LiBr absorption cycle (1-2-3-4-5-6-7-8-9-10-1) for subcooling the CO<sub>2</sub> after the gas cooler. The subcooling is performed by the produced refrigeration capacity in the evaporator (9-10) of the absorption sub-cycle. The driving heat for the absorption unit is provided by the hot CO<sub>2</sub> exiting the compressor (12). The CO<sub>2</sub> with reduced temperature exiting the generator (13) enters to the gas cooler in order to be further cooled.

Fig. 2 represents schematically cascade B. The system consists of an electricity-driven conventional vapor compression refrigeration CO<sub>2</sub>-subunit, coupled in series with a LiBr-absorption cooler.

Fig. 3 shows the trans-critical CO<sub>2</sub>-cycle of refrigeration system A on the pressure-specific enthalpy ( $p-h$ ) diagram. It depicts how the enthalpy of the hot gas exiting the compressor is used or rejected: by process (11 → 13) heat is supplied to the generator of the absorption subunit, process (13 → 14) is heat rejection to ambient through the gas cooler, and process (14 → 15) is the subcooling.

Fig. 4 shows the pressure-specific enthalpy ( $p-h$ ) diagram of the CO<sub>2</sub> cycle for the configuration B. It depicts in particular that the enthalpy of the hot gas here is simply rejected as heat to the ambient in process (12 → 13).

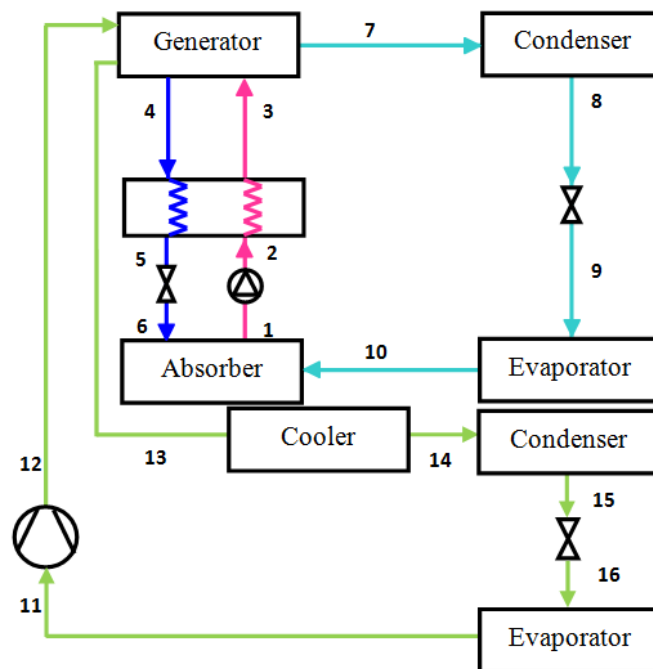


Fig. 1. Compression-absorption cascade A.

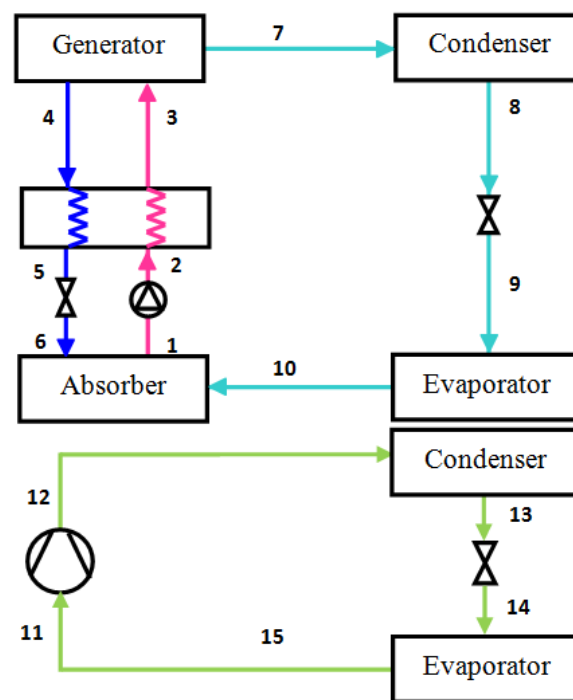


Fig. 2. Compression-absorption cascade B.

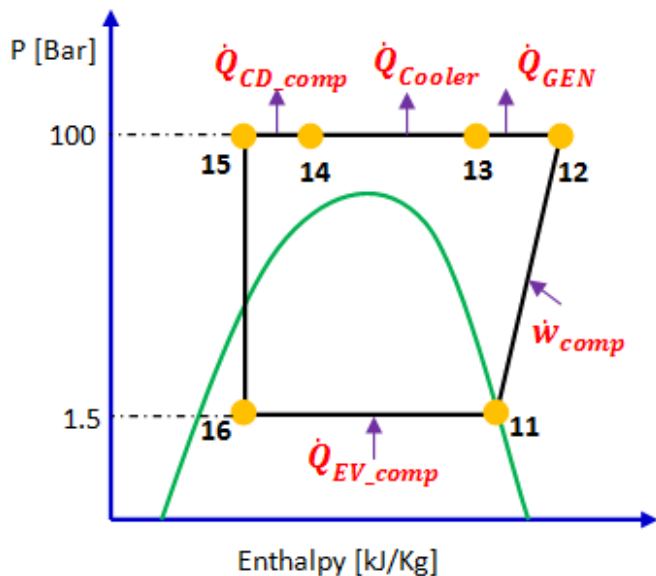


Fig. 3. Trans-critical CO<sub>2</sub> sub-cycle of configuration A in (P-h)-diagram.

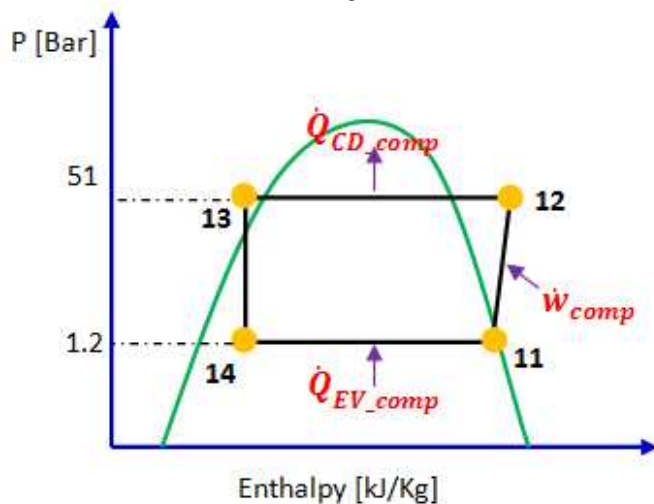


Fig. 4. CO<sub>2</sub> sub-cycle of configuration B in (P-h)-diagram.

### III. MATHEMATICAL MODEL

During developing of mathematical models of configurations A et B following assumptions were made:

- Analyses are made under steady state conditions.
- Heat losses to the surroundings are assumed negligible at generator, condenser absorber and evaporator.
- Pressure losses in pipes and components are negligible.
- Flows exiting condenser (liquid), evaporator (vapor), absorber (liquid) or generator (liquid & vapor) are saturated.
- Solution and refrigerant valves are isenthalpic.
- Evaporator energy of absorption cycle is equal to the condenser energy of compression cycle.
- Effectiveness of heat exchangers is set to  $\epsilon_{HX} = 0.7$ .
- The isentropic efficiency of pumps is  $\eta_{pumps} = 100\%$ .

The thermodynamic models of the components of the absorption subunit cycle is based on mass and energy balances as follows.

Mass balance

$$\sum \dot{m}_{in} = \sum \dot{m}_{out} \quad (1)$$

LiBr-Mass balance

$$\sum \dot{m}_{in} X_{in} = \sum \dot{m}_{out} X_{out} \quad (2)$$

Energy balance

$$\sum \dot{Q} - \sum \dot{W} = \sum \dot{m}_{out} h_{out} - \sum \dot{m}_{in} h_{in} \quad (3)$$

Where  $\dot{m}_{in}$  and  $\dot{m}_{out}$  are the mass flow rates of inlet and outlet streams.  $X$  stands for salt mass fraction in the LiBr/water solution,  $\dot{Q}$  is the heat transfer rate from/to the unit component and  $\dot{W}$ , the work transfer rate to/from that component, and  $h$ , the specific enthalpy of refrigerant or solution mixture.

*Model of absorption subunit of configuration A*

$$\dot{Q}_{EV-abs} = \dot{m}_9 (h_9 - h_{10}) \quad (4)$$

$$\dot{Q}_{CD-abs} = \dot{m}_9 (h_8 - h_7) \quad (5)$$

$$\dot{Q}_{AB} = (\dot{m}_{10} h_{10} + \dot{m}_6 h_6) - \dot{m}_1 h_1 \quad (6)$$

$$\dot{Q}_{GEN} = (\dot{m}_4 h_4 + \dot{m}_7 h_7) - \dot{m}_3 h_3 \quad (7)$$

$$\dot{Q}_{GEN} = \dot{m}_{11} (h_{13} - h_{12}) \quad (8)$$

$$\dot{Q}_{EV-abs} = \dot{Q}_{CD-comp} \quad (9)$$

*Model of vapor-compression subunit of configuration A*

$$\dot{Q}_{EV-comp} = \dot{m}_{11} (h_{16} - h_{11}) \quad (10)$$

$$\dot{Q}_{CD-comp} = \dot{m}_{11} (h_{14} - h_{15}) \quad (11)$$

$$\dot{Q}_{Cooler} = \dot{m}_{11} (h_{13} - h_{14}) \quad (12)$$

$$\dot{W}_{comp} = \dot{m}_{11} (h_{12} - h_{11}) \quad (13)$$

*Model of absorption subunit of configuration B*

$$\dot{Q}_{EV-abs} = \dot{m}_9 (h_9 - h_{10}) \quad (14)$$

$$\dot{Q}_{CD-abs} = \dot{m}_9 (h_8 - h_7) \quad (15)$$

$$\dot{Q}_{AB} = (\dot{m}_{10} h_{10} + \dot{m}_6 h_6) - \dot{m}_1 h_1 \quad (16)$$

$$\dot{Q}_{GEN} = (\dot{m}_4 h_4 + \dot{m}_7 h_7) - \dot{m}_3 h_3 \quad (17)$$

$$\dot{Q}_{EV-abs} = \dot{Q}_{CD-comp} \quad (18)$$

*Model of vapor-compression subunit of configuration B*

$$\dot{Q}_{EV-comp} = \dot{m}_{11} (h_{14} - h_{12}) \quad (19)$$

$$\dot{Q}_{CD-comp} = \dot{m}_{11} (h_{11} - h_{13}) \quad (20)$$

$$\dot{W}_{comp} = \dot{m}_{11} (h_{11} - h_{12}) \quad (21)$$

The coefficient of performance (*COP*) a subunit and of the whole configuration is given by the ratio of the refrigeration load and the energy supplied to the cycle, *i. e.*

*COP* of an absorption subunit

$$COP_{ABS} = \frac{\dot{Q}_{EV-ABS}}{\dot{Q}_{GEN} + \dot{W}_p} \quad (22)$$

*COP* of a vapor compression subunit

$$COP_{COMP} = \frac{\dot{Q}_{EV-comp}}{\dot{W}_{comp}} \quad (23)$$

*COP* of configuration A

$$COP_A = \frac{\dot{Q}_{EV-comp}}{\dot{W}_p + \dot{W}_{comp}} \quad (25)$$

*COP* of configuration B

$$COP_B = \frac{\dot{Q}_{EV-comp}}{\dot{Q}_{GEN} + \dot{W}_p + \dot{W}_{comp}} \quad (24)$$

For the numerical simulations, computer codes have been realized using the software Engineering Equation Solver, *EES*, [29]. The refrigeration capacity of each configuration is set to 100 kW for a low temperature evaporator of  $-35^{\circ}\text{C}$ . The evaporation of the refrigerant water in the absorption subsystem is assumed to take place at  $10^{\circ}\text{C}$ . The temperature of  $\text{CO}_2$  in that element (sub-cooler or condenser) is supposed to be  $5^{\circ}\text{C}$  higher, *i.e.*, at  $15^{\circ}\text{C}$ .

TABLE I  
 OPERATING CONDITIONS FOR SIMULATIONS

ABSORPTION SUB-CYCLE		
Input variable	Unit	Value
Generator temperature (Configuration B)	$^{\circ}\text{C}$	83
Evaporator temperature	$^{\circ}\text{C}$	10
Condensation temperature	$^{\circ}\text{C}$	35
Absorber temperature	$^{\circ}\text{C}$	35
Solution heat exchanger efficiency, $\epsilon_{HX}$		0.7
COMPRESSION SUB-CYCLE		
Input variable	Unit	Value
Capacity	kW	100
Cooler temperature	$^{\circ}\text{C}$	$T_{CD-abs}$
Evaporator temperature	$^{\circ}\text{C}$	-35
Condensation temperature/Sub-cooler outlet temperature	$^{\circ}\text{C}$	15
Heat exchanger efficiency, $\epsilon_{HX}$		0.7
Isentropic efficiency of compressor		0.68

Table I summarizes the assumed operating conditions for configurations A et B.

#### IV. RESULTS AND DISCUSSION

Simulation results for case A are shown in Tables II and III. It should be mentioned that in order to accommodate the enthalpy of the hot  $\text{CO}_2$  exiting the compressor to the energy needs of the absorption subunit, the pressure ratio must exceeds 8. Otherwise, the energy of hot gas at (12) wouldn't be large enough to activate the generator of absorption sub-cycle. In the present simulations, we set in a first approach the high pressure at 12 to 100 bar instead of at the minimum of 96 bar. An optimization procedure would reveal the appropriate compression ratio to maximize the coefficient of performance,  $COP_A$ . It must be noticed also that a better heat integration scheme, *e.g.* using part of the rejected heat in the cooler to preheat the salt solution coming from the absorber and flowing to the generator, would enhance the *COP* of this configuration.

It is interesting to notice that a refrigeration unit constituted solely of the trans-critical system would achieve the same *COP*, namely 1.35. But in that case, an exergy analysis would reveal a major destruction of exergy due heat rejected to environment represented by the process between points 12 and 13 in Fig. 3 (temperature decrease from  $107^{\circ}\text{C}$  to  $15^{\circ}\text{C}$ ). Further, a cold source would be necessary to cool  $\text{CO}_2$  gas from point 14 ( $35^{\circ}\text{C}$ ) to 15 ( $15^{\circ}\text{C}$ ) and that would again necessitate a second refrigeration cycle which then would reduce the *COP* of the combined system. To avoid the cooling between 14 and 15, one may lead directly flow 14 into the expansion valve. In this case however, the enthalpy change per kg  $\text{CO}_2$  associated to the evaporation is reduced and, by fixed cooling capacity, the mass flowrate of the refrigerant has to be increased, reducing thus the thermal and exergetic performance of the unit.

TABLE II  
 CASCADE A: STATE POINT RESULTS.

Point	Parameters			
	$P$ [kPa]	$T$ [ $^{\circ}\text{C}$ ]	$\dot{m}$ [kg/s]	$X$ [%]
1	1.2	35	0.067	61.64
2	5.6	49	0.067	61.64
3	5.6	60	0.079	52.19
4	5.6	83	0.067	61.64
5	5.6	35	0.079	52.19
6	1.2	35	0.079	52.19
7	5.6	83	0.012	0
8	5.6	35	0.012	0
9	1.2	10	0.012	0
10	1.2	10	0.012	0
11	1202	-35	0.485	-
12	10000	164	0.485	-
13	10000	107	0.485	-
14	10000	35	0.485	-
15	10000	15	0.485	-
16	1202	-35	0.485	-

TABLE III  
 CASCADE A: ENERGY RESULTS.

ABSORPTION SUB-CYCLE		
Parameter	Unit	Value
$P$ low	kPa	1.23
$P$ high	kPa	5.68
$\dot{Q}$ evaporator	kW	28.8
$\dot{Q}$ condenser	kW	30.4
$\dot{Q}$ absorber	kW	34.2
$\dot{Q}$ generator	kW	35.9
$COP_{ABS-A}$	-	0.8
COMPRESSION SUB-CYCLE		
Parameter	Unit	Value
$P$ low	bar	12.02
$P$ high	bar	100
$\dot{Q}$ evaporator	kW	100
$\dot{Q}$ condenser	kW	28.8
$\dot{Q}$ cooler	kW	109.2
$\dot{W}$ compressor	kW	73.9
$COP_{COMP-A}$	-	1.35
WHOLE CYCLE		
$COP_A$		1.35

Similarly to Tables II and III, Tables IV and V give the simulation results for case B. The value of the high pressure in the compression sub-cycle is now deduced from the condensation temperature of CO<sub>2</sub> at 15°C, less than its value in the trans-critical subunit.

The coefficient of performance of this configuration is equal to 0.53, much lower than that of each of its constituting sub-units. Clearly, when no heat integration is realized as it is the case for this configuration, the energetic as well as the exergetic performance of the unit are expectedly low. To enhance the performance of such a scheme one can try to use part of the rejected heat between compressor and condenser to preheat the solution 3 (Fig. 2) on its way to the generator.

TABLE IV  
 CASCADE B: STATE POINT RESULTS.

Point	Parameters			
	$P$ [kPa]	$T$ [°C]	$\dot{m}$ [kg/s]	$X$ [%]
1	1.2	35	0.262	61.64
2	5.6	49	0.262	61.64
3	5.6	60	0.310	52.19
4	5.6	83	0.262	61.64
5	5.6	35	0.310	52.19
6	1.2	35	0.310	52.19
7	5.6	83	0.048	0
8	5.6	35	0.048	0
9	1.2	10	0.048	0
10	1.2	10	0.048	0
11	1202	-35	0.509	-
12	5087	92	0.509	-
13	5087	15	0.509	-
14	10000	35	0.509	-

The  $COP$  of the configuration A is larger than that of configuration B because all the driving heat for the absorption unit in the former configuration is recovered from the energy already supplied to the compressor, whilst in system B an auxiliary heat source is needed to activate the absorption subunit.

TABLE V  
 CASCADE B: ENERGY RESULTS.

ABSORPTION SUB-CYCLE		
Parameter	Unit	Value
$P$ low	kPa	1.3
$P$ high	kPa	5.6
$\dot{Q}$ evaporator	kW	112.7
$\dot{Q}$ condenser	kW	119.2
$\dot{Q}$ absorber	kW	134.3
$\dot{Q}$ generator	kW	140.8
$COP_{ABS-B}$	-	0.8
COMPRESSION SUB-CYCLE		
Parameter	Unit	Value
$P$ low	bar	50.9
$P$ high	bar	12.0
$\dot{Q}$ evaporator	kW	100
$\dot{Q}$ condenser	kW	112.7
$\dot{Q}$ cooler	kW	-
$\dot{W}$ compressor	kW	48.9
$COP_{COMP-B}$	-	2.04
WHOLE CYCLE		
$COP_B$		0.53

## V. CONCLUSIONS

The objective of this work was to examine and compare two cascade refrigeration units involving a CO<sub>2</sub> cycle as bottom subunit and a LiBr single-effect absorption cycle as upper subunit. In the first system, A, the CO<sub>2</sub> cycle is trans-critical, and in the second system B, a conventional refrigeration cycle. The numerical simulations of these schemes show that system A is more energy efficient than system B as all the heat needed for the activation of the absorption section is covered by the energy recuperated from the hot carbon dioxide exiting the compressor. A  $COP$  of 1.35 is achieved for 35°C heat rejection temperature and cold production at -35°C. The  $COP$  of scheme B for same heat rejection and cold production temperatures is just 0.53. It should be noted that neither of the schemes is yet optimized in respect to operating conditions and/or heat integration. Addressing these issues is our current research objective. Even if we expect an enhancement in the performance of both systems, we anticipate that the scheme A will remain superior.

## REFERENCES

- [1] S. Khan mohammadi, M. Goodarzi, S. Khan mohammadi, H. Ganjehsarabi, "Thermoeconomic modeling and multi-objective evolutionary-based optimization of a modified trans-critical CO<sub>2</sub> refrigeration cycle". *Thermal Sci. Eng. Prog.* 5, pp. 86–96, 2018.
- [2] N. Purohit, V. Sharma, S. Sawalha, B. Fricke, R. Llopis, M. S. Dasgupta, "Integrated supermarket refrigeration for very high ambient temperature". *Energy* 165 (A), pp. 572–590, 2018.
- [3] European Commission. Regulation (EU) No 517/2014 of the European Parliament and of the Council of 16th April 2014 on fluorinated greenhouse gases and repealing Regulation (EC) No 842/2006, 2014.
- [4] N. Purohit, P. Gullo, M. S. Dasgupta, "Comparative assessment of low-GWP based refrigerating plants operating in hot climates". *Energy Procedia* 109, pp. 138–145, 2017.
- [5] R. Ciconkov, "Refrigerants: there is still no vision for sustainable solutions". *Int. J. Refrig.* 86, pp. 441–448, 2018.
- [6] K.M. Tsamos, Y.T Ge, I. Santosa, S.A. Tassou, G. Bianchi, Z. Mylona, "Energy analysis of alternative CO<sub>2</sub> refrigeration system configurations for retail food applications in moderate and warm climates". *Energy Convers. Manag.* 150, pp. 822–829, 2017.
- [7] P. Gullo, B. Elmegaard, G. Cortella, "Energy and environmental performance assessment of R744 booster supermarket refrigeration systems operating in warm climates". *Int. J. Refrig.* 64, pp. 61–79, 2016.
- [8] F. Kauf, "Determination of the optimum high pressure for trans-critical CO<sub>2</sub>-refrigeration cycles". *Int. J. Thermal Sci.* 38 (4), 325–330 (1999).
- [9] S.M. Liao, T.S. Zhao, A. Jakobsen, "A correlation of optimal heat rejection pressures in trans-critical carbon dioxide cycles". *Appl. Therm Eng.* 20 (9), pp. 831–841, 2000.
- [10] D. Sanchez, R. Llopis, R. Cabello, J. Catalán-Gil, L. Nebot-Andrés, "Conversion of a direct to an indirect commercial (HFC134a/CO<sub>2</sub>) cascade refrigeration system: energy impact analysis". *Int. J. Refrig.* 73, pp. 183–199, 2017.
- [11] K. Megdoui, B.M Tashtoush, Y. Ezzaalouni, E. Nahdi, A. Mhimid, L. Kairouani, "Performance analysis of a new ejector expansion refrigeration cycle (NEERC) for power and cold: exergy and energy points of view". *Appl. Therm. Eng.* 122, pp. 39–48, 2017.
- [12] M. Ma, J. Yu, X. Wang, "Performance evaluation and optimal configuration analysis of a CO<sub>2</sub>/NH<sub>3</sub> cascade refrigeration system with falling film evaporator-condenser". *Energy Convers. Manag.* 79, pp. 224–231, 2014.
- [13] R. Llopis, L. Nebot-Andrés, D. Sánchez, J. Catalán-Gil, R. Cabello, "Subcooling methods for CO<sub>2</sub> refrigeration cycles: a review". *Int. J. Refrig.* 93, pp. 85–107, 2018.
- [14] R. Llopis, R. Cabello, D. Sánchez, E. Torrella, "Energy improvements of CO<sub>2</sub> transcritical refrigeration cycles using dedicated mechanical subcooling". *Int. J. Refrig.* 55, pp. 129–141, 2015.
- [15] R. Llopis, L. Nebot-Andrés, R. Cabello, D. Sánchez, J. Catalán Gil, "Experimental evaluation of a CO<sub>2</sub> transcritical refrigeration plant with dedicated mechanical subcooling". *Int. J. Refrig.* 69, pp. 361–368, 2016.
- [16] P. Gullo, B. Elmegaard, G. Cortella, "Advanced exergy analysis of a R744 booster refrigeration system with parallel compression". *Energy* 107, pp. 562–571, 2016.
- [17] E. Bellos, C. Tzivanidis, "A comparative study of CO<sub>2</sub> refrigeration systems". *Energy Convers. Manag.* X1, 100002, 2019.
- [18] J. Sarkar, "Performance optimization of trans-critical CO<sub>2</sub> refrigeration cycle with thermoelectric sub-cooler". *Int. J. Energy Res.* 37 (2), pp. 121–128 (2013).
- [19] B. Dai, S. Liu, K. Zhu, Z. Sun, Y. Ma, "Thermodynamic performance evaluation of trans-critical carbon dioxide refrigeration cycle integrated with thermoelectric sub-cooler and expander". *Energy* 122, pp. 787–800, 2017.
- [20] M. Salajeghe, M. Ameri, "Effects of further cooling the gas cooler outlet refrigerant by an absorption chiller, on a trans-critical CO<sub>2</sub>-compression refrigeration system". *Int. J. Exergy* 21 (1), pp. 110–125, 2016.
- [21] E. Bellos, C. Tzivanidis, "A theoretical comparative study of CO<sub>2</sub> cascade refrigeration systems". *Appl. Sci.* 9, 790, 2019.
- [22] S. M. Hojjat Mohammadi, "Theoretical investigation on performance improvement of a low-temperature trans-critical carbon dioxide compression refrigeration system by means of an absorption chiller after-cooler". *Appl. Therm. Eng.* 138, pp. 264–279, 2018.
- [23] K. Mohammadi, J.G. McGowan, "A thermo-economic analysis of a combined cooling system for air conditioning and low to medium temperature refrigeration". *J. Clean. Prod.* 206, 580–597, 2019.
- [24] P. Cyklis, "Two stage ecological hybrid sorption-compression refrigeration cycle". *Int. J. Refrig.* 48, pp. 121–131, 2014.
- [25] H. Li, W. Su, L. Cao, F. Chang, W. Xia, Y. Dai, "Preliminary conceptual design and thermodynamic comparative study on vapor absorption refrigeration cycles integrated with a supercritical CO<sub>2</sub> power cycle". *Energy Convers. Manag.* 161, pp. 162–171, 2018.
- [26] A. Arora, N.K. Singh, S. Monga, O. Kumar, "Energy and exergy analysis of a combined trans-critical CO<sub>2</sub> compression refrigeration and single effect H<sub>2</sub>O-LiBr vapor absorption system". *Int. J. Exergy* 9 (4), pp. 453–471, 2011.
- [27] J. Sarkar, "Cycle parameter optimization of vortex tube expansion trans-critical CO<sub>2</sub> system". *Int. J. Thermal Sci.* 48 (9), 1823–1828, 2009.
- [28] S.M. Hojjat Mohammadi, "Theoretical investigation on performance improvement of a low-temperature trans-critical carbon dioxide compression refrigeration system by means of an absorption chiller after-cooler". *Appl. Therm. Eng.* 138, pp. 264–279, 2018.
- [29] S. A. Klein, F. Alvarado, Engineering equation solver. Middleton, WI: F-chart software.

# Modelling of a classical absorption-diffusion cycle

Ikram Saâfi<sup>#\*1</sup>, Ahmed Taieb<sup>#\*2</sup>, Yosra Ben Salem<sup>#\*3</sup>, Khalifa Mej bri<sup>#\*4</sup>, Ahmed Bellagi<sup>#\*5</sup>

<sup>#</sup> L. R. Thermique et Thermodynamique des Procédés Industriels,  
Ecole Nationale d'ingénieurs de Monastir (E.N.I.M.), University of Monastir - Tunisia

<sup>1</sup>[Ikram.saafi@gmail.com](mailto:Ikram.saafi@gmail.com)

<sup>2</sup>[hmed.taieb@gmail.com](mailto:hmed.taieb@gmail.com)

<sup>3</sup>[yosraissetkelibia@gmail.com](mailto:yosraissetkelibia@gmail.com)

<sup>4</sup>[mej bri\\_khalifa@yahoo.fr](mailto:mej bri_khalifa@yahoo.fr)

<sup>5</sup>[a.bellagi@enim.rnu.tn](mailto:a.bellagi@enim.rnu.tn)

<sup>\*</sup>*Institut Supérieure des études technologiques de Kelibia, Route Oued el Khatf 8090*

**Abstract**— This document proposes a simulation model of an absorption-diffusion refrigerator using ammonia/water/hydrogen as working fluids, developed to describe and predict the behavior of the device under different operating conditions. The system is supposed to be cooled in the ambient air and operated with a free thermal source. Based on the results obtained, a thermodynamic analysis of the system is carried out in order to evaluate the contribution of the various components of the machine to the loss of machine performance. In addition, thermals conductances of the internal and external heat flows that take place in the machine are evaluated. The model is then modified by replacing the thermal pinches of the different heat exchangers with thermals conductances and used to perform a parametric study of the cycle.

**Keywords**— Diffusion-absorption refrigerator. Model and simulation. Water-ammonia.

## I. INTRODUCTION

The Diffusion Absorption Refrigerator (DAR) introduced by Platen and Munters in 1928 [1] has been recognized as one of the most encouraging sustainable technologies for production of cold. The cycle of the machine operates at a constant total pressure level and uses ammonia as refrigerant, water as absorbent and hydrogen or helium as non-absorbable auxiliary inert gas. This inert gas is necessary to reduce the partial pressure of the refrigerant in the evaporator and the absorber and to allow the processes of evaporation and absorption to take place in the uniform pressure device.

DAR operates only with thermal energy, no mechanical and then no electric power is needed. This energy can be provided by the fossil fuel combustion (gas, fuel, etc), but also, for temperatures varying between 90 and 200°C, by solar thermics, or the thermal discharges, etc. The growing concerns about worldwide energy and environmental sustainability in recent years enlarge the development of DAR [2].

The DAR systems have been experimentally and theoretically investigated by various researchers.

Chen et al. [3], designed a new generator including a heat-exchanger that reuses the waste heat. The new configuration of the cycle showed a slightly improvement of the COP (5%).

Srikhirin et al. [4] carried out an experimental study on an NH<sub>3</sub>-H<sub>2</sub>O DAR cycle using helium as the auxiliary gas. They developed a mathematical model to determine the maximum performance for the appropriate operating conditions. They observed that the evaporator and absorber mass transfer performances have a strong effect on the system performance [5]. They also showed that the COP of the machine varies in the range 0.09 - 0.15.

Maiya [6]; showed that helium is more advantageous than hydrogen as inert gas although it requires a larger size of propulsion because of its greater viscosity. This study proved also that a higher pressure of operation causes a reduction in the COP.

Zohar et al. [7] studied two configurations of a DAR with and without condensate sub-cooling before the entry of the evaporator. The results showed that the COP of the cycle without subcooling is higher by approximately 14-20% than that of the cycle with subcooling. The best performances are obtained when the mass fraction of ammonia of the rich solution varies in the range (0.25-0.4).

Ben Ezzine et al. [9] reported that the R124-DMAC DAR gives a higher COP at lower driving temperatures compared with the NH<sub>3</sub>-H<sub>2</sub>O system; they also experimentally investigated a DAR using C<sub>4</sub>H<sub>10</sub>-C<sub>9</sub>H<sub>20</sub> as the working fluid and helium as the auxiliary gas [10].

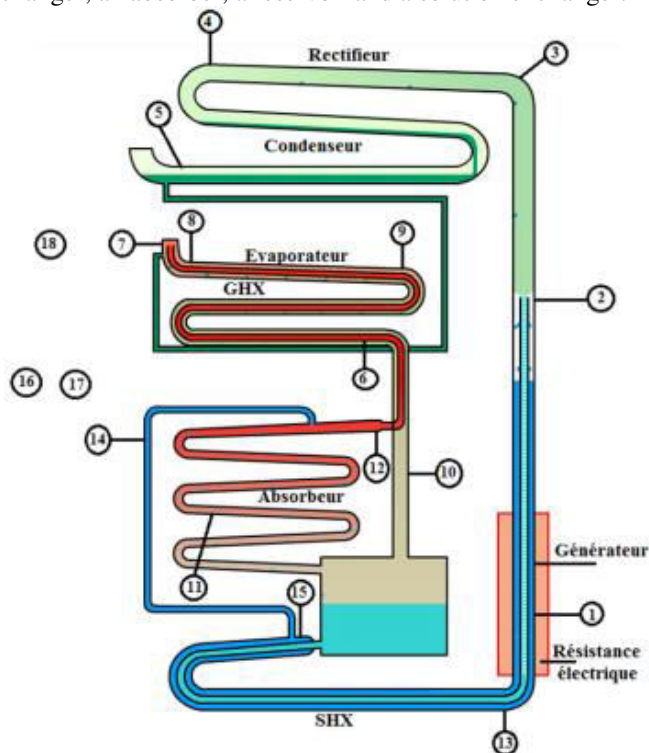
In the present paper a thermodynamic model for an ammonia-water diffusion absorption refrigeration, with hydrogen as inert gas is developed. The performances of cycle are theoretically analyzed and evaluated. The effects of the characteristics of bubble pump with various power inputs, heating temperatures and other parameters are investigated. In addition, an exergy analysis is carried out to evaluate the percentages of irreversibilities created in the different parts of the machine

## II. DESCRIPTION OF THE CYCLE

The figure 1 shows a commercial low-power absorption-diffusion machine that operates according to the diffusion-

absorption cycle. This cycle uses the refrigerant/absorbent: ammonia/water in combination with hydrogen as an inert gas.

The absorption-diffusion cycle consists mainly of a generator, a rectifier, a condenser, an evaporator, a gas exchanger, an absorber, a reservoir and a solution exchanger.



### III. THERMODYNAMIC PROPERTIES

The properties of the ammonia / water binary mixture (refrigerant / absorbent) are described by the PC-SAFT state equation. The model obtained is in agreement with the constraints of the equality of the chemical potential in the liquid-vapor equilibrium. The inert gas is supposed to be immiscible with the liquid phase and exists only in the gas phase. This is considered an ideal solution of real gases. The properties of hydrogen are taken from the NIST databank [11] and have been put into an empirical model using the Younglove state equation [12].

### IV. MODEL OF THE MACHINE

#### A. RECTIFIER

The rectifier is equivalent to a continuous contact column which provides cooling and partial condensation of the vapor produced by the ambient air. The saturating steam leaving the rectifier goes into the condenser, while the liquid falls back into the boiler. The vapor flow from the generator enters the rectifier. The liquid returning to the boiler is supposed to be saturated, and is in equilibrium with the vapors. The upstream flows, will be cooled and undergo partial condensation.

The rectifier is necessary to purify the ammonia vapor to the desired composition  $y_1$ . The corresponding temperature  $T_1$  is deduced from the liquid-vapor equilibrium. The flow rate of refrigerant vapor is deduced from the molar flow rate of the gases  $\dot{n}_{10}$  flowing in the gas circuit. The energy balance makes it possible to determine the heat released to the rectifier.

$$\begin{aligned} \dot{n}_{13V} + \dot{n}_{16} &= \dot{n}_1 + \dot{n}_{17} \\ r &= \dot{n}_{10} / \dot{n}_1 = y_{H_2,7} / (y_{H_2,10} - y_{H_2,7}) \\ \dot{Q}_R &= \dot{n}_1 h_1 + \dot{n}_{17} h_{17} - \dot{n}_{13V} h_{13V} - \dot{n}_{16} h_{16} \\ \dot{S}_{gen,R} &= \dot{n}_1 s_1 + \dot{n}_{17} s_{17} - \dot{n}_{13V} s_{13V} - \dot{n}_{16} s_{16} - \dot{Q}_R / \tilde{T}_{air} \end{aligned}$$

#### B. CONDENSER

The condenser, shown in figure 6, is cooled to ambient air. It is characterized by a deviation of the condensation temperature and air temperature:  $\Delta T_{C-air}$ . The liquid refrigerant at the outlet of the condenser is assumed to be saturated. The mass, energy and entropy balances are given by the following equations,

$$\begin{aligned} T_2 &= T_C = \tilde{T}_{air} + \Delta T_{C-air} \\ \dot{n}_1 &= \dot{n}_2 ; y_1 = x_2 \\ \dot{Q}_C &= \dot{n}_2 h_2 - \dot{n}_1 h_1 \\ \dot{S}_{gen,C} &= \dot{n}_2 s_2 - \dot{n}_1 s_1 - \dot{Q}_C / \tilde{T}_{air} \end{aligned}$$

#### C. EXPANSION CHAMBER

The liquid / vapor equilibrium is estimated by considering the equalities of the chemical potentials and the energy balance. The molar flow rates of liquid and vapor as well as the molar composition of the inert gas at the outlet are determined from the material balances. Entropy creation is computed using the entropy balance.

$$\begin{aligned} \dot{n}_{5L} + \dot{n}_{5V} &= \dot{n}_4 + \dot{n}_{10} \\ \dot{n}_{5L} x_{5L} + \dot{n}_{5V} x_{5V} &= \dot{n}_4 x_4 + \dot{n}_{10} x_{10} \\ \dot{n}_{5V} y_{H_2,5} &= \dot{n}_{10} y_{H_2,10} \\ \dot{n}_{5L} h_{5L} + \dot{n}_{5V} h_{5V} - (\dot{n}_4 h_4 + \dot{n}_{10} h_{10}) &= 0 \end{aligned}$$

#### D. EVAPORATOR AND GAS EXCHANGER (GHX)

The evaporator and the GHX are composed of three independent circuits as shown in figure 8. The evaporator is immersed in the refrigerator cabinet at a  $T_{Cab}$  temperature while the GHX is isolated. In the evaporator, the temperature of the four output streams is determined, with respect to this temperature, with the aid of the thermal tips.

The liquid refrigerant is cooled in the circuit (3 - 4) essentially by the cold chamber. The temperature  $T_4$  is determined with respect to the temperature of the cold



room. Evaporation of the refrigerant (5 - 6) cools the inert gas (9 - 10) circulating countercurrently and produces the cooling effect in the refrigerator cabin. Therefore, the temperatures  $T_{10}$  and  $T_6$  are determined by pinches with respect to  $T_5$  and  $T_{Cab}$ , respectively. Unvaporated liquid circulates in (9'). In the GHX, the temperature of the liquid refrigerant (3) is characterized by a nip  $\Delta T_{SR3}$  and the outlet temperature of the inert gas  $T_9$  is set with respect to the inlet temperature  $T_6$ . The temperature  $T_7$  is evaluated using the energy balance of GHX. The water-rich liquid returning to the absorber (8') is assumed to be at the same inlet temperature of the inert gas  $T_8$ .

The inert gas flow rate from the absorber to the evaporator is cooled, which allows it to be purified by the condensation of most of the remainder of water and ammonia which returns to the absorber (8'). The partial pressure  $P_9^*$  (9-9') of the ammonia/water mixture vapor-liquid phase is calculated using the chemical potential equalities described by equations 66 to 68. A similar calculation is made for the flux (10) using the equations 69 to 71. Mass balances are calculated for all independent evaporator and GHX circuits using the following equations.

$$\begin{aligned} \dot{n}_{5V} + \dot{n}_{5L} &= \dot{n}_{6V} + \dot{n}_{6L} \\ \dot{n}_{5V}y_5 + \dot{n}_{5V}x_5 &= \dot{n}_{6V}y_6 + \dot{n}_{6L}x_6 \\ \dot{n}_{6V}y_{H_2,6} &= \dot{n}_{5V}y_{H_2,5} \\ \dot{n}_{6V} + \dot{n}_{6L} &= \dot{n}_7 \\ \dot{n}_{6V}y_6 + \dot{n}_{6L}x_6 &= \dot{n}_7y_7 \\ \dot{n}_{6V}y_{H_2,6} &= \dot{n}_7y_{H_2,7} \\ \dot{n}_8 + \dot{n}_{9'} &= \dot{n}_8' + \dot{n}_9 \\ \dot{n}_8y_8 + \dot{n}_{9'}x_{9'} &= \dot{n}_8'x_{8'} + \dot{n}_9y_9 \\ \dot{n}_9y_{H_2,9} &= \dot{n}_8y_{H_2,8} \\ \dot{n}_9 &= \dot{n}_{9'} + \dot{n}_{10} \\ \dot{n}_9y_9 &= \dot{n}_{9'}x_{9'} + \dot{n}_{10}y_{10} \\ \dot{n}_9y_{H_2,9} &= \dot{n}_{10}y_{H_2,10} \end{aligned}$$

$$\dot{n}_3 = \dot{n}_2; x_3 = x_2; \dot{n}_4 = \dot{n}_3; x_4 = x_3$$

$$\dot{Q}_E = \dot{n}_4h_4 + \dot{n}_{6L}h_{6L} + \dot{n}_{6V}h_{6V} + \dot{n}_9h_9 + \dot{n}_{10}h_{10} - \dot{n}_3h_3 - (\dot{n}_{5L}h_{5L} + \dot{n}_{5V}h_{5V}) - \dot{n}_8h_8$$

$$\dot{S}_{gen,E} = \dot{n}_4s_4 + (\dot{n}_{6L}s_{6L} + \dot{n}_{6V}s_{6V}) + \dot{n}_9s_9 + \dot{n}_{10}s_{10} - \dot{n}_3s_3 - (\dot{n}_{5L}s_{5L} + \dot{n}_{5V}s_{5V}) - \dot{n}_8s_8 - \dot{Q}_E/T_{air}$$

$$\dot{S}_{gen,GHX} = \dot{n}_2h_2 + (\dot{n}_{6L}h_{6L} + \dot{n}_{6V}h_{6V}) + \dot{n}_8h_8 + \dot{n}_9h_9 - \dot{n}_3h_3 - \dot{n}_7h_7 - \dot{n}_8'x_{8'} - \dot{n}_9y_9$$

$$\dot{S}_{gen,GHX} = \dot{n}_2s_2 + (\dot{n}_{6L}s_{6L} + \dot{n}_{6V}s_{6V}) + \dot{n}_8s_8 + \dot{n}_9s_9 - \dot{n}_3s_3 - \dot{n}_7s_7 - \dot{n}_8's_8' - \dot{n}_9s_9$$

### E. ABSORBER

The absorber is cooled in the ambient air. It is supposed to be isothermal at the temperature  $T_8 = T_{air} + \Delta T_{A-air}$  where  $\Delta T_{A-air}$  is the thermal nip with respect to the air temperature. In fact, the absorber of the absorption-diffusion machine is a falling-film absorber which ensures a continuous contact between the liquid and gaseous phase flowing in countercurrent.

$$\dot{n}_8 + \dot{n}_{11} = \dot{n}_7 + \dot{n}_{15} + \dot{n}_8'$$

$$\dot{n}_8y_8 + \dot{n}_{11}x_{11} = \dot{n}_7x_7 + \dot{n}_{15}x_{15} + \dot{n}_8'x_{8'}$$

$$\dot{Q}_A = \dot{n}_8h_8 + \dot{n}_{11}h_{11} - (\dot{n}_{15}h_{15} + \dot{n}_7h_7 + \dot{n}_8'h_{8'})$$

## V. RESULTS

Simulation the machine in basic operating conditions

A number of basic data used as input for the simulations is reported in Table 1. The values are based on experimental measurements made in our commercial refrigerator research laboratory.

TABLE 1: Basic simulation data.

Variable	Valeur	Variable	Valeur
$T_{air}$ (°C)	26	$\Delta T_{A-air}$ (°C)	20
$T_{cf}$ (°C)	5	$\Delta T_{GHX}$ (°C)	12
$x_{12}$	1	$\Delta T_{4-CF}$ (°C)	20
$y_1$	0.99	$\Delta T_{6-CF}$ (°C)	10
$d$ (mm)	4	$\Delta T_{5-10}$ (°C)	10
$h/H$	3	$E_{ABS}$	0.8
$\phi$	1.3	$E_{SHX}$	0.7
$\Delta T_{SR3}$ (°C)	15	$\dot{Q}_m$ (W)	63
$\Delta T_{C-air}$ (°C)	25		

The machine studied is cooled in the ambient air whose temperature is fixed at 26°C, assuming that the space containing the installation is air-conditioned. The cabin is supposed to be at a temperature of 5°C. The diameter of the bubble pump tube is equal to 4mm and the submergence rate is set to 3. The power  $\dot{Q}_m$  supplied to the generator is 63 W. The refrigerant vapor produced in the generator is purified in the air-cooled rectifier to  $y_1 = 0.99$ . The condenser and absorber are cooled by air in natural convection. Their characteristic thermal nips  $\Delta T_{C-air}$  and  $\Delta T_{A-air}$  are respectively set at 25°C and 20°C. The efficiency of the absorber is set at  $E_{ABS} = 0.8$ . The coefficient  $\phi$ , the ratio of the slopes of the real and minimum operating lines (Figure 10) is set to 1.3, and the efficiency of the solution exchanger  $E_{SHX}$  is equal to 0.7. To determine the outlet temperatures in the evaporator and the GHX, the following values are adopted for thermal nip:  $\Delta T_{SR3} = 15^\circ\text{C}$ ,  $\Delta T_{GHX} = 12^\circ\text{C}$ ,  $\Delta T_{4-CF} = 20^\circ\text{C}$ ,  $\Delta T_{6-CF} = 10^\circ\text{C}$  and  $\Delta T_{5-10} = 10^\circ\text{C}$ .

The energy performance of the refrigerator is evaluated by its coefficient of performance:

$$COP = \frac{\dot{Q}_E}{\dot{Q}_m}$$

Table 2 provides the simulation results for the conditions in Table 1. The solution rich in ammonia leaves the reservoir with a molar composition  $x_{11} = 0.334$  and a molar flow rate imposed by the thermal bubble pump  $n_{11} = 0.0111$  mol/s

equivalent to a mass flow rate of 0.196 g/s. In the SHX, the rich solution is preheated by the lean solution at a temperature  $T_{12} = 126 \text{ }^\circ\text{C}$ , close to its saturation temperature equal to  $129.7 \text{ }^\circ\text{C}$ . In the heating zone in the lower part of the bubble pump, the power provided  $Q_p$  allows the evaporation of 8.6% of the liquid solution, the vapor produced for pumping the rest of the liquid. The vacuum ratio corresponds to a two-phase flow in the bubble pump tube is estimated with the CISE correlation [13] at about 0.283; this value corresponds to a Slug flow. At the top of the bubble pump, the saturated liquid and the vapor phase at temperature  $T_{13} = 140.8 \text{ }^\circ\text{C}$  are separated; the liquid is further heated in the boiler at a temperature  $T_{14} = 189.7 \text{ }^\circ\text{C}$ . The steam, with an average ammonia molar composition of 0.634, is generated at 78.7% in the boiler and 21.3% in the bubble pump. In the rectifier, the refrigerant vapor flow rate is  $\dot{n}_1 = 0.00257 \text{ mol/s}$  (0.0438 g/s) is purified to a molar ammonia composition of  $y_1 = 0.99$ . The liquid rich in water ( $x_{17} = 0.156$ ) returns to the boiler with a flow rate  $\dot{n}_{17} = 0.0019 \text{ mol/s}$ . The power  $Q_R = 30.34 \text{ W}$  is rejected from the rectifier to the outside environment. The condensing power released to the ambient air is  $Q_C = -21 \text{ W}$ .

The liquid refrigerant is at the temperature  $T_4 = 25 \text{ }^\circ\text{C}$  and injected into the expansion chamber, where 34.3% of the liquid is evaporated by reducing its hydrogen composition to  $y_{H_2,5} = 0.9357$ . The two-phase flow is now at the very low temperature  $T_5 = 27.4 \text{ }^\circ\text{C}$ . The expansion chamber is equivalent to an isenthalpic expansion in a vapor compression refrigerator. The liquid refrigerant continues its evaporation in the annular space of the evaporator producing the useful cold  $Q_E = 8.42 \text{ W}$ . The temperature at the outlet (6) of the evaporator reaches  $T_6 = 5 \text{ }^\circ\text{C}$ , 9.7% of refrigerant is still in the liquid state. In the annulus of the GHX, all the liquid refrigerant is evaporated and the superheated gas at  $T_7 = 34 \text{ }^\circ\text{C}$ . The absorber is equivalent to 4 theoretical stages. The ammonia-rich gas at the bottom of the absorber is characterized by a molar composition of hydrogen  $y_{H_2,7} = 0.8346$  and a molar flow  $\dot{n}_7 = 0.01545 \text{ mol/s}$ . At its top is injected the liquid poor solution with a molar composition  $x_{15} = 0.1362$  and at a temperature  $T_{15} = 85.2 \text{ }^\circ\text{C}$  and with a flow rate  $\dot{n}_{15} = 0.00852 \text{ mol/s}$ . Due to the absorption process, a power  $Q_A = -30.85 \text{ W}$  is rejected in the external environment. The ammonia-rich solution is stored in the reservoir at a molar composition  $x_{11} = 0.334$ . The ammonia-poor gas leaves the head of the absorber with a flow rate  $\dot{n}_8 = 0.0136 \text{ mol/s}$  and at a temperature  $T_8 = 46 \text{ }^\circ\text{C}$ . At this point, the molar compositions of hydrogen, ammonia and water are  $y_{H_2,8} = 0.9460$ ,  $y_{NH_3,8} = 0.0317$  and  $y_{H_2O,8} = 0.0223$ , respectively. It should be noted here that water is transferred from the liquid phase to the gaseous phase during the absorption process. During subcooling of the inert gas in the central tube of the GHX, its temperature is reduced to  $T_9 = 23.6 \text{ }^\circ\text{C}$ , and most of its ammonia and water content is condensed ( $y_{H_2,9} = 0.99659$ ) and returned to the absorber with a molar flow rate of  $\dot{n}_{9r} = 0.00073 \text{ mol/s}$ . The inert gas

continues its subcooling in the central tube of the evaporator to  $T_{10} = -17.4 \text{ }^\circ\text{C}$ . The gas flow at the inlet of the expansion chamber is composed of almost pure hydrogen ( $y_{H_2,10} = 0.99985$ ). The circulation rate of the inert gas and the refrigerant in the gas loop is  $r = 5.05$ .

It should be noted that a significant amount of cold is dissipated during the purification and subcooling of the inert gas in the GHX and evaporator (15.8W). On the other side, and under the specified operating conditions, the degassing of the refrigerant in the generator is small, and therefore the flow rate of the rich solution is large compared to that of the refrigerant (4.3 times). This means that the amount of heat supplied to the generator is important in relation to the cooling power. For all these reasons, the COP of an absorption-diffusion refrigerator is normally low: In this case, it is equal to 0.126.

TABLE 2: Basic simulation results.

Variable	Value	Variable	Value
$P_{sys}$ (bar)	20.7	$\dot{n}_{10}$ (mol/s)	0.012872
$T_1$ ( $^\circ\text{C}$ )	81.8	$\dot{n}_{11}$ (mol/s)	0.011096
$T_4$ ( $^\circ\text{C}$ )	25.0	$\dot{n}_{15}$ (mol/s)	0.008522
$T_5$ ( $^\circ\text{C}$ )	-27.4	$\dot{n}_{17}$ (mol/s)	0.001900
$T_6$ ( $^\circ\text{C}$ )	-5.0	$\alpha_{13}$	0.086
$T_7$ ( $^\circ\text{C}$ )	34.0	$\tau_{void,13}$	0.283
$T_8$ ( $^\circ\text{C}$ )	46.0	$x_{11}$	0.33427
$T_9$ ( $^\circ\text{C}$ )	23.6	$x_{15}$	0.13619
$T_{10}$ ( $^\circ\text{C}$ )	-17.4	$y_{H_2,5}$	0.93570
$T_{12}$ ( $^\circ\text{C}$ )	126.0	$y_{H_2,7}$	0.83456
$T_{13}$ ( $^\circ\text{C}$ )	140.8	$y_{NH_3,8}$	0.03169
$T_{14}$ ( $^\circ\text{C}$ )	189.7	$y_{H_2O,8}$	0.02228
$T_{15}$ ( $^\circ\text{C}$ )	85.2	$y_{H_2,8}$	0.94603
$r$	5.05	$y_{H_2,9}$	0.99659
$\alpha_5$	0.343	$y_{H_2,10}$	0.99985
$\alpha_6$	0.903	$Q_E$ (W)	8,42
$\dot{n}_1$ (mol/s)	0.002574	$Q_C$ (W)	-21,08
$\dot{n}_8$	0.013605	$Q_A$ (W)	-30,85
$\dot{n}_{8r}$	0.000733	$Q_R$ (W)	-30,34
$\dot{n}_{9r}$	0.000017	$COP$	0.126

### Parametric study

Based on the results of the previous section, the refrigerator is now studied for various operating conditions. The evolution of the molar flow rate of the refrigerant and

that of the inert gas  $\dot{n}_{11}$  and  $\dot{n}_{10}$  as a function of the heat input supplied to the generator is illustrated in Figure 14. Indeed, by increasing the motive power, enough ammonia vapor is generated which enters the condenser to liquefy and then goes to the evaporator. As demonstrated in section II, that the flow rate of hydrogen required for the evaporation of the liquid condenser  $\dot{n}_{11}$  from the condenser is proportional, this latter flow rate is equal to 5 times the first.

In figure 15, the COP is calculated under the basic conditions, but by varying the motive power supplied to the generator (boiler and bubble pump),  $Q_m$ . It is found that the variation of the COP with  $Q_m$  has a maximum, but the cooling capacity  $Q_E$  increases regularly to finally stabilize in the drop range of the COP.

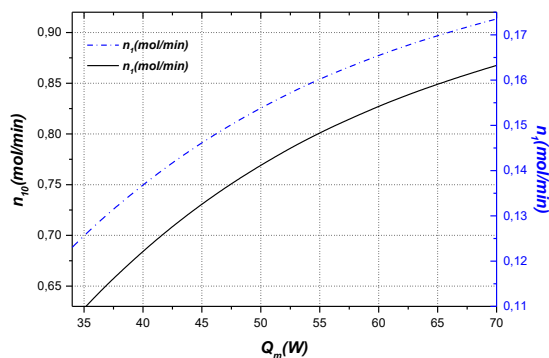


Figure 2: Variation of the molar flow rate of the refrigerant and the inert gas as a function of  $Q_m$ .

When  $Q_m$  is low, the molar flow rate of the refrigerant,  $\dot{n}_1$ , is relatively low. As  $Q_m$  increases,  $\dot{n}_1$  also increases. Thus, the amount of ammonia that evaporates in the evaporator is larger, and therefore, increases. Thus, the COP increases rapidly in the left region of the optimal point ( $Q_m = 55W$  and  $T_{14} = 190^\circ C$ ). As  $Q_m$  increases further, the driving temperature  $T_{14}$  also increases generating evaporation of a quantity of steam richer in water. The evaporated water condenses in the rectifier and returns to the boiler. As a result, more and more of the heat supplied to the boiler is released into the atmosphere as a heat of condensation. As a result, the COP gradually decreases.  $Q_E$  increases very slightly and then stabilizes.

In order to better explain this phenomenon, Figure 4 shows that the growth of the driving temperature has an effect on the impoverishment of the poor solution going from the boiler to the absorber. On the other hand, it can also be noted that the growth of the motive power (i.e. the driving temperature) produces more ammonia vapor. However, above  $190^\circ C$ , the additional heat supplied is released into the atmosphere without contributing proportionately to the improvement in the production of cold, hence the degradation of the COP.

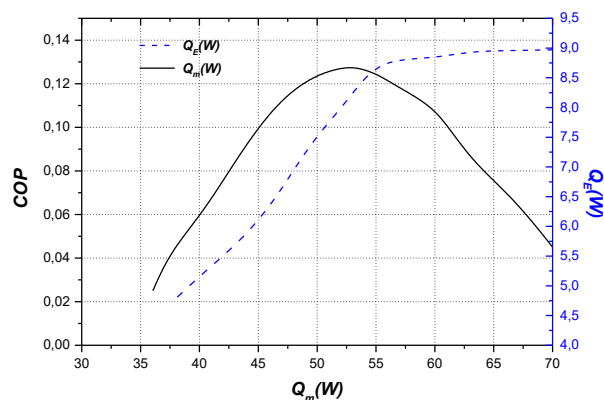


Figure 3: Variation of the COP and the cooling capacity according to the driving power.

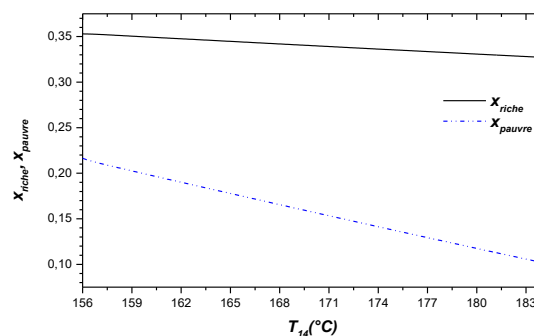


Figure 4: Effect of the driving temperature on the composition of the lean liquid solution at the inlet and the outlet of the absorber.

To validate the simulation model, figures 5 and 6 show the performances of the machine found by the numerical simulation and those deduced from the experimental results for the tested motor power range. Above all, we can see that the two results are in good agreement since the curves are similar.

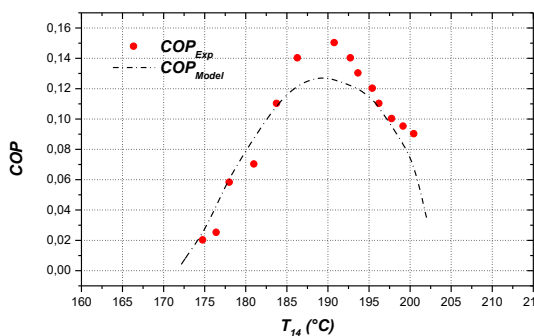


Figure 5: Variation of the experimental and theoretical COP as a function of the driving temperature.

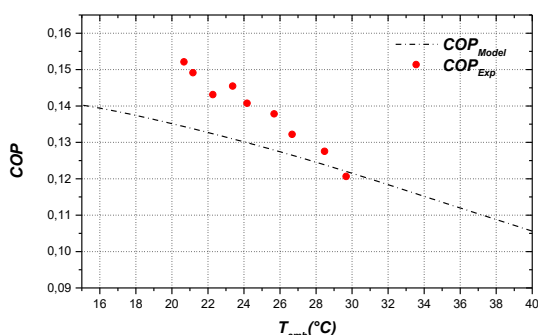


Figure 6: Variation of the experimental and theoretical COP as a function of the ambient temperature.

Figure 6 shows the effect of the driving temperature on the COP. As can be noted, the minimum motive power found by the simulation is lower than that measured experimentally. Indeed, the generator is not ideally isolated and therefore the power supplied is actually acquired by the rich solution and is smaller than that measured experimentally. The maximum value of the theoretical COP is reached for a lower motive power. This maximum is 0.127 for a driving temperature of 189 °C.

The various experiments carried out for different values of the ambient temperature made it possible to compare the performances of the refrigerator found by the simulation and those deduced from the experimental results. Figure 5 shows the variation of the experimental and theoretical COP as a function of the ambient temperature. Note that the two results are in good agreement since the shape of the curves is identical in the common range of temperatures. As can be noted, the COP predicted by the model decreases continuously from 0.14 to 0.09 for ambient temperatures between 15 and 40 °C. Indeed, this decrease is mainly due to the increase of the total pressure of the system when the ambient temperature increases which makes the evaporation of the ammonia vapor more difficult.

## VI. CONCLUSIONS

In this paper, we have carried out a theoretical simulation of the absorption-diffusion machine. For this purpose, an advanced model of thermodynamic simulation is developed to predict the performance and the operating conditions of the machine. This model takes into account the flows in the bubble pump and the absorber-evaporator gas circuit. The laws of conservation of mass and energy are established for each organ.

The experimental results are used as basic data for the simulation. Validation of the established model has shown that it accurately describes the behavior of the machine. Indeed, the performance of the machine found by numerical simulation and those deduced from experimental results are in good agreement for the range of engine power and tested ambient temperatures. A parametric study, also carried out in this context, made it possible to identify the best performances.

## REFERENCES

- [1] B.C. Von Platen, C.G. Munters, Refrigerator, US Patent 1 (1928) 685-764.
- [2] H.C. Steirlin, J.R. Ferguson, Diffusion absorption heat pump
- [3] S. Mazzouz, Fonctionnement des cycles à mono-pression pour le froid solaire : étude théorique et expérimentale d'un pilote, PhD Thesis, ENIM-University of Monastir, Tunisia, 2014.
- [4] R. Garma, Machines frigorifiques à absorption à monopression : Etude de la pompe à bulle, PhD Thesis, ENIM-University of Monastir, Tunisia, 2015.
- [5] R. ben Jemaa, PhD Thesis, Cycle de Platen et Munters : étude expérimentale et théorique d'un pilote et analyse en dynamique de l'installation, ENIM-University of Monastir, Tunisia, 2014.
- [6] J. Chen, KJ. Kim, KE. Herold. Performance enhancement of a diffusion-absorption refrigerator. International Journal of Refrigeration 1996; 19:208-18.
- [7] P. Srihirin, S. Aphornratana, Investigation of a diffusion absorption refrigerator, Applied Thermal Engineering 22 (2002) 1181-1193.
- [8] L. S. Wilson, A. C. Carlos, A. T. Ednildo, C. S. Jacques, C. M. Evania, Exergoeconomic analysis of a single pressure absorption refrigeration cycle, 20th International Congress of Mechanical Engineering (2009)
- [9] A. Zohar, M. Jelinek, A. Levy, I. Borde, The influence of diffusion absorption refrigeration cycle configuration on the performance, Applied Thermal Engineering 27 (2007) 2213-2219.
- [10] A. Zohar, M. Jelinek, A. Levy and I. Borde, 'Performance of Diffusion Absorption Refrigeration Cycle With Organic Working Fluids', International Journal of Refrigeration, Vol. 32, N°6, pp. 1241 - 1246, 2009.
- [11] N. Ben Ezzine, R. Garma, A. Bellagi, A numerical investigation of a diffusion-absorption refrigeration cycle based on R124-DMAC mixture for solar cooling, Energy 35 (2010) 1874-1883.
- [12] N. Ben Ezzine, R. Garma, M. Bourouis, A. Bellagi, Experimental studies on bubble pump operated diffusion absorption machine based on light hydrocarbons for solar cooling, Renewable Energy 35 (2010) 464-470.
- [13] A. Benhmidene, B. Chauouachi, M. Bourouis, S. Gabsi, Effect of operation conditions on the performance of the bubble pump of absorption-diffusion refrigeration cycles, Thermal science Vol. 15, N°3, pp. 793 - 806, 2011.
- [14] R. Garma, Y. Stiriba, M. Bourouis, A. Bellagi, Numerical investigations of the heating distribution effect on the boiling flow in bubble pumps, International Journal of Hydrogen Energy, Vol. 39 (2014) 15256-15260.
- [15] B.A. Younglove, "Thermophysical Properties of Fluids. I. Argon, Ethylene, Parahydrogen, Nitrogen, Nitrogen Trifluoride, and Oxygen," J. Phys. Chem. Ref. Data, Vol. 11, Suppl. 1, pp. 1-11, 1982

# The impact of the transaction costs per hedging effectiveness ratio on renewable energy's hedging decisions

Asma Abdallah<sup>#1</sup>, Ahmed Ghorbel<sup>#2</sup>

<sup>#</sup> *Department of Quantitative Methods  
CODECI Laboratory*

*Faculty of Economics and Management (FSEG) of Sfax,  
B.P.3018 Sfax, Tunisia*

<sup>1</sup>abdallah.asma25@gmail.com

<sup>2</sup>ahmed\_isg@yahoo.fr

**Abstract**— Coupled with global warming, increasing oil prices and CO2 emissions are identified as the most important factors behind the considerable evolution of clean energy sector which is, recently, taking a significant role in the energy industry. Accordingly, investors need to assess the potential risks, volatility dynamics and transaction costs in order to hedge their investment in renewable energy equities.

In this paper, based on daily data covering the period from December 19, 2007 to October 17, 2018, the time-varying optimal hedge ratios are estimated by applying three versions of multivariate GARCH models (DCC, ADCC and GO-GARCH) for the purpose of whether the Wilder Hill New Energy Global Innovation (NEX) can be hedged by Crude Oil, CDS, BOND, GOLD, VSTOXX, Euro\_Stoxx\_50, OVX, VIX and its volatility (VVIX). Moreover, our study examines the effect of the tradeoff between transactions costs and hedging effectiveness on optimal portfolio and its implications on hedging decisions.

Our empirical findings show that the VIX is the best hedge for clean energy stocks as it has the biggest hedging effectiveness index value in most cases, followed by VSTOXX, then Euro Stoxx 50. However, the TC/HE results indicate that the VSTOXX is the best hedging instrument since it yields the lowest TC/HE ratio of all assets.

**Keywords**— Optimal hedge ratios, renewable energy indices, Euro\_Stoxx\_50, VIX, VSTOXX, Multivariate GARCH models, transaction costs, hedging effectiveness.

## I. INTRODUCTION

From the beginning of the 21st century, investment in renewable energy stocks has attracted a sustainable amount of international and significant interest in order to move to the area of green economy and reducing environment related risks [1,2,11]. Recently, it has become on the top of our agenda in world-wide economy, not only due to concerns over climate change, global warming, sustainable economic development, pollution, emerging CO2 emissions or growth energy consumption and energy security issues, but also due to new technologies and ecologically conscious consumers as well as the need for moving away from conventional energy resources to clean energies, which are available almost worldwide [1, 3, 4, 5]. Consequently, the international Energy outlook predicts that global investment in clean energy sources will drastically increase the most till 2040, by providing around 14% of total primary energy [6].

In the mean time, analyzing clean energy performance has attracted significant attentiveness among researchers and investors in different countries or areas due to the high-speed growth in renewable energy investment. In this context, and as the progressively development, the growth in the number of clean energy firms, which become more and more bigger, and the volatility of renewable energy assets, it is necessary, nowadays, for investors to hedge their investment and manage risks beyond volatility dynamics [7,8].

By using various methods, several methods as Sadorsky [9], Sanchez [10], Ahmad [1], Ahmad et al. [7], and Bouri [11] are focused on the evaluation of the time-varying hedge ratios

and the estimation of hedging effectiveness, but they forgot the effect of the tradeoff between transaction costs and effectiveness hedging on the portfolio decision. The main novelty of our paper is to examine firstly the time varying optimal hedging ratios from rolling window analysis among three MGARCH models (DCC, ADCC and GO-GARCH). Then we investigate the impact of the tradeoff between transaction costs and hedging effectiveness measured by the ratio (TC/HE) on portfolio hedging decisions. The current

paper can be considered as the first paper that aims to fulfill this gap in the literature and analyzing, therefore, its value and implication on renewable hedging strategies [7, 12].

The reminder of this paper is laid as follow: Section 2 reviews briefly the previous empirical studies. Section 3 provides data descriptions. Section 4 describes estimation methodology. Section 5 details the empirical results. Finally, concluding remarks, implications and future research opportunities are presented in the last section.

## II. RELEVANT LITERATURE

**Table 1: Related Review**

Authors	Purposes	Methodology		Main findings
		Model	Data period	
Henriques and Sadorsky [13]	Analyze the relationship between stock prices of clean energy and technology companies, oil prices and interest rates.	Vector Autoregression (VAR) model	From 2001 to 2007	They find that interest rates and technology stocks have a larger influence on alternative energy stock prices than oil prices which holds a little significant impact on stock prices of clean energy firms.
Sadorsky [14]	Studying conditional correlations and volatility spillovers between oil prices, clean energy stock prices and technology stock prices.	Multivariate generalized autoregressive conditional heteroskedasticity (GARCH)model	From 2001 to 2007	-Clean Energy Index Combined with Crude Oil Offers Better Investment Opportunities and Portfolio Coverage. -Alternative energy firms' stock prices correlate more exhaustively with technology companies' stock prices than with oil prices.
Kumar et al. [4]	Analyze the relationship between oil prices and alternative energy prices.	Vector autoregressive approach (VAR-Causality)	From 2005 to 2008	-Movements in oil prices, interest rates and technology stock prices affect clean energy stock prices. -There is no impact of carbon allowance prices on renewable energy variations.
Ferstl et al. [15]	investigates the impact of the Fukushima disaster on the daily nuclear and clean energy stock prices in France, Germany, Japan, and U.S.A.	The Fama and French (1993) three-factor model.	From 2008 to 2011	- Finding positive abnormal returns for alternative energy stock returns in France, Germany and Japan, against significantly negative cumulative abnormal returns for nuclear companies in the same countries.
Sadorsky [9]	Identify some of the key drivers of systematic risk for U.S.-listed renewable energy companies.	Variable beta model	From 2001 to 2007	-Rising oil prices provide a positive effect on clean energy stock prices.
Broadstock et al. [16]	Investigated the relationship between international fossil fuel prices and energy related stocks in China.	Time-varying correlation	From 2000 to 2011	-They demonstrated a much stronger association, especially after the onset of the global financial crisis between 2007 and 2008. -This significant linkage suggest that China's new energy stocks were influenced by oil prices dynamics, particularly when correlation increased noticeably.
Managi and Okimoto [17]	Analyzing the relationships among oil prices, clean energy stock prices, and technology stock prices (By extending then developing the study of Henriques and Sadorsky (2008)).	Markov-switching vector autoregressive models (MSVAR)	From 2001 to 2010	-Strong co-movement / strong convergence between clean energy stocks and oil prices. -A positive relationship between oil prices and clean energy stock prices was founded.
Bohl et al. [18]	studied the performance of German renewable energy stocks by analyzing the impact of global stock market returns	Multifactor asset pricing model	From 2004 to 2011	- Between 2004 and 2007, German renewable energy stocks presented a sustainable systematic risk given by a significant and strongly positive beta.

	on clean energy stock prices.			<ul style="list-style-type: none"> <li>-After the outbreak of the 2008–2009 global financial crises, they found risk-adjusted returns.</li> <li>- Detection of speculative bubbles, presented in Germany’s renewable energy stocks, by the ADF test.</li> </ul>
Ortas and Moneva [19]	Measure the financial behavior of 21 primary clean-technology equity indices.	State-space market model	From 2002 to 2011	-Clean techs indices yielded higher risk levels during market stability's period, resulting a clear and positive interaction between financial and environmental performance.
Wen et al. [20]	Documented return and volatility spillover effects between Chinese renewable energy stock prices and fossil fuel companies.	An asymmetric Baba–Engle–Kraft–Kroner (BEKK) model	From 2006 to 2012	<ul style="list-style-type: none"> <li>-Results indicate that fossil fuel and alternative energy stocks are considered as competing assets.</li> <li>-Investments in renewable energy are riskier than fossil fuels investments.</li> </ul>
Inchauspe et al [21]	Examining the impact of oil prices, technology stocks and the MSCI World Stock Index on renewable energy stocks.	State-space multi-factor model with time-varying coefficients	From 2001 to 2014	-There is a positive connection between clean energy and oil prices as well as a high correlation with MSCI World Index and technology stock returns
Reboredo [22]	Investigating systematic risk and dependence structure between oil prices and various alternative energy sector equity indexes.	Time-varying Copulas and the CQ approach	From 2005 to 2013	<ul style="list-style-type: none"> <li>-Reported evidence of a significant association between oil and renewable energy stock prices.</li> <li>- Oil price dynamics contribute to nearly 30% of clean energy stock price risk.</li> </ul>
Sanchez [10]	<ul style="list-style-type: none"> <li>-Calculating in-sample optimal hedge ratios</li> <li>-Investigating volatility spillovers between oil prices and stock prices of alternative energy and technology.</li> </ul>	Multivariate GARCH models	From 2002 to 2015	<ul style="list-style-type: none"> <li>-Alternative energy hedge ratios vary considerably over the sample period.</li> <li>-Volatility spillovers founding between clean energy and technology stock prices are stronger than those between renewable energy and oil prices.</li> <li>-The best hedge ratio for alternative energy is providing by technology global markets.</li> </ul>
Bondia et al. [23]	Exploring the long-term dependence structure between clean energy and technology stock prices, the returns of global oil prices and US interest rate.	VECM (Vector Error Correction Model)	From 2003 to 2015	-They find a significant short-run linkage between stock prices of alternative energy, technology companies, crude oil and US interest rate, while, in the long-run there is no significant relationship.
Reboredo et al [24]	Analyzing dynamic correlation and causality in an alternative time-frequency setting between international oil prices and new energy stocks prices.	Wavelet approach	From 2006 to 2015	-Finding a weak short-term linkage between oil prices and renewable energy stock prices, but in the long run the interaction is getting stronger.
Ahmad [25]	Testing the dynamic interdependence and investment performance between clean energy, oil and technology stock prices.	The directional spillover approach and the Dynamic Conditional Correlation Models	From 2005 to 2015	<ul style="list-style-type: none"> <li>-There is a high interdependence structure moving from technology to alternative energy.</li> <li>-However, crude oil displays a restricted association renewable energy stocks and technology firms.</li> <li>- Crude oil, when combined with clean energy and technology indices, provides better profitable hedge and portfolio investment diversification.</li> </ul>
Dutta A. [26]	Investigating the impact of oil price uncertainty, as measured by the crude oil volatility index (OVX) on the variance of clean energy stocks.	Employing three different range-based estimators proposed by Parkinson (1980) (henceforth RVP), Rogers and Satchell (1991) (Hence forth RVRS) and Alizadeh et al.	From 2007 to 2016	-Oil market uncertainty, emerged as a positive, statically and highly significant variable for modeling, forecasting and predicting the realized volatility of renewable energy stock returns, especially during the subprime crisis.

		(2002) (henceforth RVABD).		
Asma A, Ahmed G. [27]	Studying correlations and volatility spillovers between Brent oil and clean energy stock prices then analyzing the optimal weights and hedge ratio for management risk and building optimal portfolio.	Four multivariate GARCH model (BEKK, CCC, DVEC and DCC)	From 2005 to 2016	-Hedging ratio varies from pair Oil/Renewable Energy to another, from one period to another and from one MGARCH version to another. - The BEKK model is found as the best and the most efficient model on reducing Oil/Renewable energy portfolio risk.
Ahmad et al. [7]	Estimating the time-varying optimal hedging ratios between clean energy equities and various other financial instruments such as oil, bonds, gold, VIX, OVX and Carbon prices.	Three variants of multivariate GARCH models: DCC, ADCC and GO-GARCH	From 2008 to 2017	-Showing that VIX provides the most effective hedge for alternative energy stocks followed by crude oil and OVX respectively.
Bouri [11]	Investigating whether gold and crude oil can act as safe haven mechanism against the clean energy stocks fluctuations.	Copulas	From 2003 to 2018	-Their findings indicate that both gold and crude oil are qualified as no more than weak safe-haven investment against extreme price drops of clean energy market. -Although crude oil serves as an upper weak safe haven asset than gold.
Linh Pham [8]	Exploring the heterogeneous volatility co-movements between oil prices and different clean energy sub-sectors, as well as examining its implications on portfolio diversifications strategies.	The GVAR model: Three multivariate GARCH models; DCC, ADCC and GO-GARCH	From 2010 to 2018	-Results document that interactions between oil prices and alternative energy stocks is obviously homogenous and various significantly over time and across renewable energy stock sub-sectors, which means that hedging cost and effectiveness of clean energy investment portfolio depends especially on clean energy types.

Our Sample has maintaining a detailed description as follow:

### III. DATA

#### A. NEX: the WilderHill New Energy Global Innovation:

Our dataset is composed of daily time series observations for the WilderHill New Energy Global Innovation Index (NEX), oil prices represented by (Crude Oil), the credit default swap index(CDS), the VIX, the VIX volatility (VVIX), Euro Stoxx 50 and its volatility index (VSTOXX), as well as the oil volatility index (OVX), Bond and Gold prices. The entire dataset is collected from Thomson DataStream and covers the period ranging from December 19, 2007 to October 17, 2018; making up a total of 2826 available daily observations. The data analysis and treatment are essentially prepared by the R Studio program.

In order to avoid model dependencies, and reducing heteroskedasticity, each data series is converted into logarithmic differences calculated as  $100 \cdot \ln(P_t / P_{t-1})$  where  $P_t$  is the daily closing price at time t. All data are in dollars.

Created by WilderHill New Energy Finance, is an equal modified dollar weighted index. Since 2006, it has been the first, leading and best known global index for clean, renewable and alternatives energy stocks [28]. This international stock index, contains 106 constituents from 25 countries, mostly from outside the U.S. whose activities focuses not only on renewable energy, but also on solving climate change and on the reduction of carbon dioxide emissions relative to traditional fossil fuel use, as clever solution in order to avoid greenhouse gases. According to Inchaupse et al. [21], this index dispose of a diversified portfolio through clean energy which is composed of: Solar energy (20,6%), Wind energy (15,1%), Biofuel and Biomass (13,9%), renewable energy efficiency (34,8%), energy storage and conversion (3.4%) and (12,2%) for other renewable energy projects. The investments are distributed by regions with weights of 43.8% for the Americas, 29.1% for



Asia and Oceania and 27.1% for Europe, the Middle East and Africa

### B. CDS: Credit Default Swap

The Credit Default Swap (CDS) is a credit derivative contract between two counterparties which bring protection against credit losses. More precisely, the developed credit default swap (CDS) market allows CDS buyers to transfer Credit risk to CDS sellers.

More importantly, a CDS can also act as a hedge.

### C. Crude Oil

Oil, conventional fossil fuel energy, is the most heavily traded physical commodity in the world. In this paper, oil price returns (dollars per barrel) are measured by using the average of the closing prices on the West Texas Intermediate (WTI) nearest Crude Oil futures contract which exchanges on the New York Mercantile Exchange (NYMEX).

### D. OVX: Crude Oil Volatility

In 2008, Chicago Board Option Exchange (CBOE) introduced OVX as a new barometer to examine the systematic behaviour of crude oil market uncertainty. As the VIX, the idea of OVX is to measure the market's expectation of 30-day volatility of crude oil futures prices.

### E. GOLD

For Gold, options data are treated on Chicago Mercantile Exchange 100 ounces Continuous futures contracts settlement price. Many previous studies Tully and Lucey [29]; Shahzad et al. [30] have shown that gold has been usually used as an efficient asset to store value and still treated as a significant valuable metal in modern economies.

### F. VIX: Implied volatility of S&P500 on US Stock index

Introduced by the Chicago Board Options Exchange (CBOE) in 1993, the VIX is used as a RISK-Neutral forward measure of the US stock market volatility.

As such, the VIX is compiled from a portfolio of S&P500 index options in order to measure the implied aggregate volatility in options markets of the S&P500 index during the next 30-Calender day period and is commonly used as a proxy. Based on previous findings, Higher values of the VIX index denote a much riskier stock market, whilst, lower values showed a less risky market. On a worldwide scale, it is one of the most recognized measures of volatility.

### G. VVIX: Volatility VIX Index

Constructed at the aggregate market and represented by Chicago Board Options Exchange (CBOE), we can look at the VVIX as the volatility of volatility index calculated from a portfolio of VIX options (VVIX portfolio) through the same algorithm used to measure the VIX.

Moreover, the VIX index can be viewed as an important indicator of market expectations regarding the future distribution of the implied volatility.

### H. Euro Stoxx 50: The European stock market index

Euro\_Stoxx\_50 index used for the Euro Area was introduced on February 1998.

This index considered as Europe's leading Blue-Chip index specialist aims to provide a blue-Chip representation of super sector leaders in the Eurozone.

In principal, the Euro\_Stoxx\_50 is a composite index represents the performance of the 50 most important companies of up to 11 Eurozone countries (20 companies from France, 14 from Germany, 5 each from Spain and Netherlands, 3 from Italy, and the remaining 3 are respectively from Belgium, Finland and Ireland).

It is the one of the most liquid European equity indices and the most followed in the Eurozone.

### I. VSTOXX: Euro Stoxx 50 Volatility Index

VSTOXX is a Measure of the implied volatility of Euro Stoxx 50 in the Euro Area Market. Additionally, according to Zghal, R. et al. [31], the VSTOXX index helps to capture the equity risk as a whole, since it relies heavily on equity-based options.

## IV. METHODOLOGY: EMPIRICAL MODELS

Recently, modelling the volatility dynamics and correlations are highly relevant in finance.

In this context, two models belonging to the DCC family (DCC model of Engle [32] and ADCC model of Cappiello et al. [33]) as well as the GO-GARCH model of Van der Weide [34] have been applied for the purpose of modelling volatilities, conditional correlations and hedge ratios between NEX, CDS, Crude Oil, GOLD, Bond, Euro\_Stoxx\_50, VSTOXX, VIX, VVIX and OVX.

Let  $\mathbf{r}_t$  be a  $n \times 1$  vector of series of returns. The specification of the multivariate GARCH models, with AR (1) process for

$r_t$  conditional on the information set  $\Omega_{t-1}$ , is defined as follows:

$$r_t | \Omega_{t-1} = \mu_t + \varepsilon_t$$

Where the vector of residuals  $\varepsilon_t$  can be modelled as:

$$\varepsilon_t = H_t^{1/2} z_t; z_t \sim \text{iid}(0, I_n)$$

$H_t$  Represents the  $n \times n$  conditional covariance matrix of  $r_t$ ,  $z_t$  is a  $n \times 1$  i.i.d random vector of errors and  $I_n$  denotes an  $n \times n$  identity matrix.

### 1) The DCC-GARCH model

The Engle [32] Dynamic Conditional Correlation (DCC) model, generalization of CCC model, follows two step procedures. In the first step, the GARCH parameters are estimated followed by correlations in the second step such as:

$$H_t = D_t R_t D_t$$

Where  $D_t = (h_{11t}^{1/2}, \dots, h_{nn}^{1/2})$  is a diagonal matrix that includes varying standard deviations on the diagonal and  $R_t$  which composed as follow is the conditional correlation matrix:

$$R_t = \text{diag}(Q_t)^{-1/2} Q_t \text{diag}(Q_t)^{-1/2}$$

Where  $Q_t$  is a  $n \times n$  symmetric positive definite matrix given by:

$$Q_t = (1 - \theta_1 - \theta_2) \bar{Q} + \theta_1 z_{t-1} z_{t-1}^T + \theta_2 Q_{t-1}$$

$\bar{Q}$  Denotes the  $n \times n$  unconditional correlation matrix of the standardized residuals  $z_{i,t} = \varepsilon_{i,t} / \sqrt{h_{i,t}}$  and  $Q_t$  is its conditional variance-covariance matrix of the residuals  $\varepsilon_t$ .

The parameters  $\theta_1$  and  $\theta_2$  are non-negative scalar parameters satisfying  $\theta_1 + \theta_2 < 1$  which implies that  $Q_t > 0$ .

Under the DCC specification, the time-varying conditional correlation series are described by:

$$\rho_{ij,t} = \frac{q_{ij,t}}{\sqrt{q_{ii,t}} \sqrt{q_{jj,t}}}$$

Where  $q_{ij,t}$  denotes the covariance between asset returns  $i$  and  $j$  at time  $t$ , and  $q_{ii,t}$  as well as  $q_{jj,t}$  are the conditional variance estimates of  $i$  and  $j$  respectively both at time  $t$ .

### 2) The ADCC-GARCH model

By extending the DCC model and the asymmetric GARCH model of Glosten et al. [35], the asymmetric DCC (ADCC) model have been built by Capiello et al. [33] on this models by adding an asymmetric term. In order to beat the problem of asymmetry effects, the ADCC model serves to elaborate either the positive and negative news are of same magnitude

or have different impacts on conditional standard deviations and correlations. Thus, it is described as follow:

$$Q_t = (1 - \alpha - \beta) \bar{Q} + \lambda \bar{Z} + \alpha z_{t-1} z_{t-1}^T + \beta Q_{t-1} + \lambda \zeta_{t-1} \zeta_{t-1}^T$$

Where the coefficient  $\lambda$  indicate the asymmetric effect or “leverage effect” in the model. It tends to explain the role of bad news in increasing volatility than do good news during downturn period.

$\bar{Q}$  and  $\bar{Z}$  are the unconditional matrices of  $z_{t-1} z_{t-1}^T$  and  $\zeta_{t-1} \zeta_{t-1}^T$  respectively.

The variable  $\zeta_t$  defined as Hadamard product of an indicator function and residuals  $\varepsilon_t$  is formally given by  $\zeta_{t-1} = I[\varepsilon_{t-1} < 0] \odot \varepsilon_{t-1}$ . The indicator function which is expressed by  $I[\varepsilon_t < 0]$  is equal to one if the standardized residuals  $\varepsilon_t$  is negative, and 0 otherwise.

Leverage effects tend to explain the role of bad news in increasing volatility than do good news during downturn period. Besides, both models DCC and ADCC are estimated by a maximum likelihood estimator.

### 3) The GO-GARCH model

Under the GO-GARCH model, the residual  $\varepsilon_t$  is modeled as follows:

$$\varepsilon_t = A f_t$$

Where  $f_t$  denotes a set of invisible independent factors ( $f_t = (f_{1t}, f_{2t}, \dots, f_{nt})$ ).  $A$  is an invertible and time-invariant  $n \times n$  and can be decomposed into an unconditional covariance matrix  $\Sigma$  and an orthogonal matrix  $U$ .

$$A = \Sigma^{1/2} U$$

The matrix  $A$  is composed into rows which represent the factor weights assigned to each time series and columns of representing the factors  $f$ . The factors of  $f_t$  can be specified as:

$$f_t = H_t^{1/2} u_t$$

Where  $u_t$  is a random variable satisfying  $E[u_{it}] = 0$  and  $E[u_{it}^2] = 1$ .  $H_t$  is a diagonal matrix with elements  $h_{1t}, h_{2t}, \dots, h_{nt}$  being the conditional variances of the factors.

The factor conditional variance  $h_{it}$  can be modeled using the GARCH process in equation (11) ( $i=1, 2, \dots, n$ ). Furthermore, the unconditional distribution of the factors  $f$  satisfies  $E[f_t] = 0$  and  $F[f_t f_t^T] = I$ . It follows that the returns  $r_t$  can be expressed as:

$$r_t = u_t + A H_t^{1/2} u_t$$

Finally, the conditional covariance matrix of the returns

$$r_t - u_{tis}$$

$$\Sigma_t = A H_t A^T$$

4) *The hedging effectiveness*

The hedging effectiveness (HE) index (e.g. Ku et al. [36] and Chang et al. [37]), described by the following equation, is used to evaluate the hedging performance of hedge ratio and optimal portfolio.

$$HE = \frac{var_{unhedged} - var_{hedged}}{var_{unhedged}}$$

The larger HE index value means the most favorable hedging effectiveness.

5) *The tradeoff between transaction costs and hedging effectiveness.*

According to Chen and Sutcliffe [38], we can measure the transaction cost (TC) as the sum of the absolute changes in the dynamic hedge ratios. Then we calculate the TC/HE ratio as a measure of the tradeoff between hedging effectiveness and transaction cost. A low TC/HE ratio indicates a better hedging instrument.

V. RESULTS AND DISCUSSION

First of all, we analyze, as shown below in table 2, the descriptive statistics of the returns of each series in the natural logarithm from over the period 2007-2018.

**Table 2: Preliminary statistics**

	NEX	CDS	Crude_Oil	GOLD	BOND	Euro_Stoxx_50	VSTOXX	VIX	VVIX	OVX
<b>Mean</b>	-0.0328	0.0325	-0.0044	0.0148	0.0014	-0.0099	-0.0065	-0.0077	0.0095	-0.0039
<b>Median</b>	0.0234	0.0000	0.0000	0.0000	0.0000	0.0000	-0.2374	-0.2919	-0.2473	-0.1811
<b>Std. dev.</b>	1.4851	2.8456	2.1678	1.1629	0.3850	1.4594	6.5320	7.4383	5.0225	4.7163
<b>Min.</b>	-10.485	-32.1330	-16.7095	-9.8233	-2.7373	-9.0111	-43.4376	-35.0588	-23.6414	-43.9905
<b>Max.</b>	12.070	25.3664	17.9691	8.5889	3.5661	10.4376	47.0666	76.8245	37.3161	42.4968
<b>Q1</b>	-0.6530	-0.8733	-1.0734	-0.5029	-0.2012	-0.6685	-3.8065	-3.9941	-2.7529	-2.5016
<b>Q3</b>	0.6736	0.8438	1.0852	0.5772	0.2105	0.6760	3.1236	3.2537	2.2389	2.1002
<b>Skewness</b>	-0.4680	0.0962	0.1864	-0.3865	-0.1202	-0.0498	0.5613	1.0685	0.9459	0.6585
<b>Kurtosis</b>	8.5689	14.5229	5.5904	7.5714	5.6903	6.0269	4.3152	7.3226	5.3219	10.1832
<b>JB test</b>	8746	2483	3695.1	6818.3	3818.2	4276.9	2340.2	6849.3	3755.1	1241
<b>P-Value</b>	0.000*	0.000*	0.000*	0.000*	0.000*	0.000*	0.000*	0.000*	0.000*	0.000*
<b>Q (12)</b>	135.79	29.954	9.9302	24.145	25.453	29.994	29.818	47.211	41.731	80.644
<b>P-Value</b>	0.000*	0.002*	0.622	0.019*	0.012*	0.002*	0.002*	0.000*	0.000*	0.000*
<b>Q<sup>2</sup> (12)</b>	3496.9	405.06	590.65	276.08	308.48	1293.4	363.25	200.83	182.47	337.21
<b>P-Value</b>	0.000*	0.000*	0.000*	0.000*	0.000*	0.000*	0.000*	0.000*	0.000*	0.000*
<b>N obs</b>	2825	2825	2825	2825	2825	2825	2825	2825	2825	2825

N.B.\* denotes 5% significance level. JB test indicates Jarque-Bera statistics and Q(12) and Q(12)<sup>2</sup> are the Ljung-Box statistics. The ARCH-LM test reports the LM-statistic.

CDS exhibits the highest average daily returns among the series (0.032), while NEX have the lowest average return (-0.032), while the lowest average return (-0.032) is observed in case of NEX. The mean daily return is positive for CDS (0.032), GOLD (0.0148), Bond (0.0014), and for VVIX (0.0095), whereas it is negative for NEX (-0.032), Crude Oil (-0.0044), Euro Stoxx 50 (-0.0099), VSTOXX (-0.0065), VIX (-0.0077) and OVX (-0.0039).

VIX shows the greatest volatility designed by its high standard deviation (7,438), while Bonds have the lowest standard deviation (0.3850). The nullity of normal distribution is decisively rejected by the Jarque-Bera (JB) test for each one of the variables at the 5% significance level. Besides maximum and minimum values indicate that the volatility of all sample series was similar in magnitude, with the exception of GOLD, Bond, and Euro Stoxx 50 which had lower volatility.

For the Ljung-Box Q-statistics on returns, we find that only the Crude Oil doesn't exhibit significantly high serial correlation, unless on squared returns, Q-statistics indicate that all sample variables present significant serial correlation and strong volatility clustering effects. The Skewness values are negative for returns of NEX, Gold, Bond, and Euro Stoxx 50; however, they are positive for the other series. This means that negative (positive) Skewness denotes lack of higher negative (positive) returns without corresponding

opportunities of positive (negative) returns. Kurtosis statistics suggest that all variables have kurtosis greater than 4, and as we know that kurtosis for a normal distribution is 3, so we can deduce that all series display of fat or heavy tails in their distributions (leptokurtic). Our observations are confirmed by graphs of the time series and squared returns (Figure 1 and 2 respectively).

Figure 1 reveals that there is some heterogeneity in price co-movements of each index. For example, during the subprime crisis (2007 – 2009) and 2011 – 2014 periods, Crude Oil and NEX, Gold, Bond, Euro Stoxx 50 tends to move together with a strong trend. Although, CDS, VSTOXX, VIX, VVIX and OVX show a similar time series patterns but display of a little increase trend around the 2007 – 2009 financial crisis. Moreover, visual inspection of figure 1 also reveals that NEX and Crude Oil commove jointly during higher and lower phases of the latter one.

Time series plots of the squared time series shown in Figure 2 exhibit how volatility has changed over time. We can observe that all variables present a strong volatility clustering around the Subprime Mortgage crisis with the exception of CDS, VIX and VVIX which show a little clustering effect at the same period.

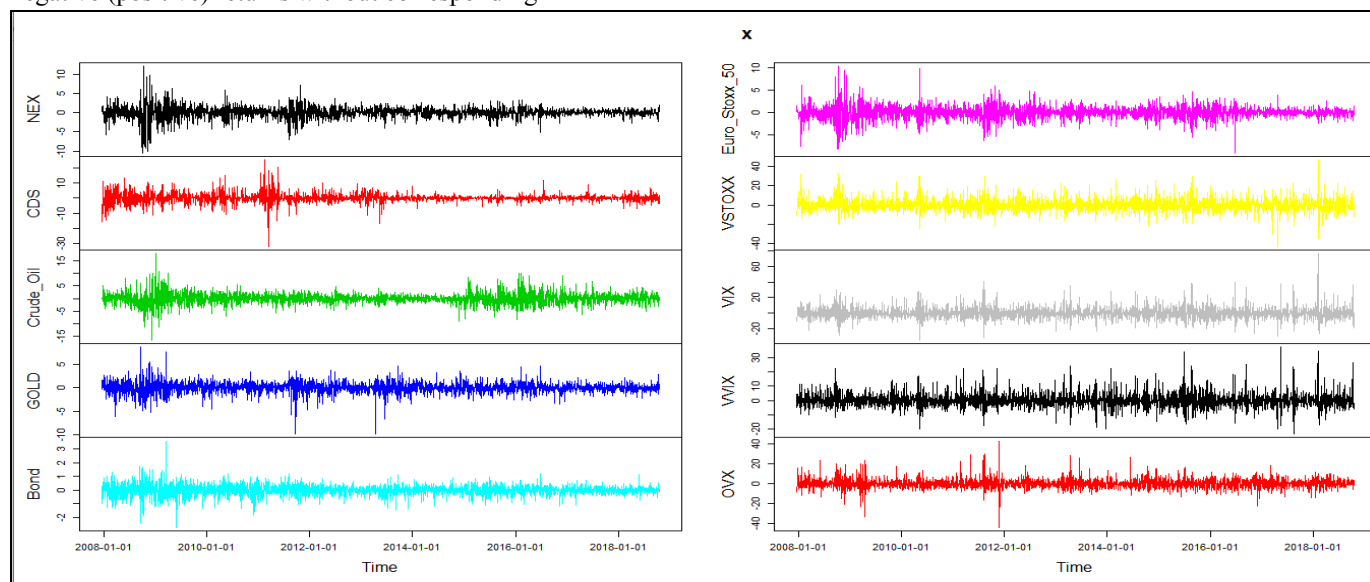
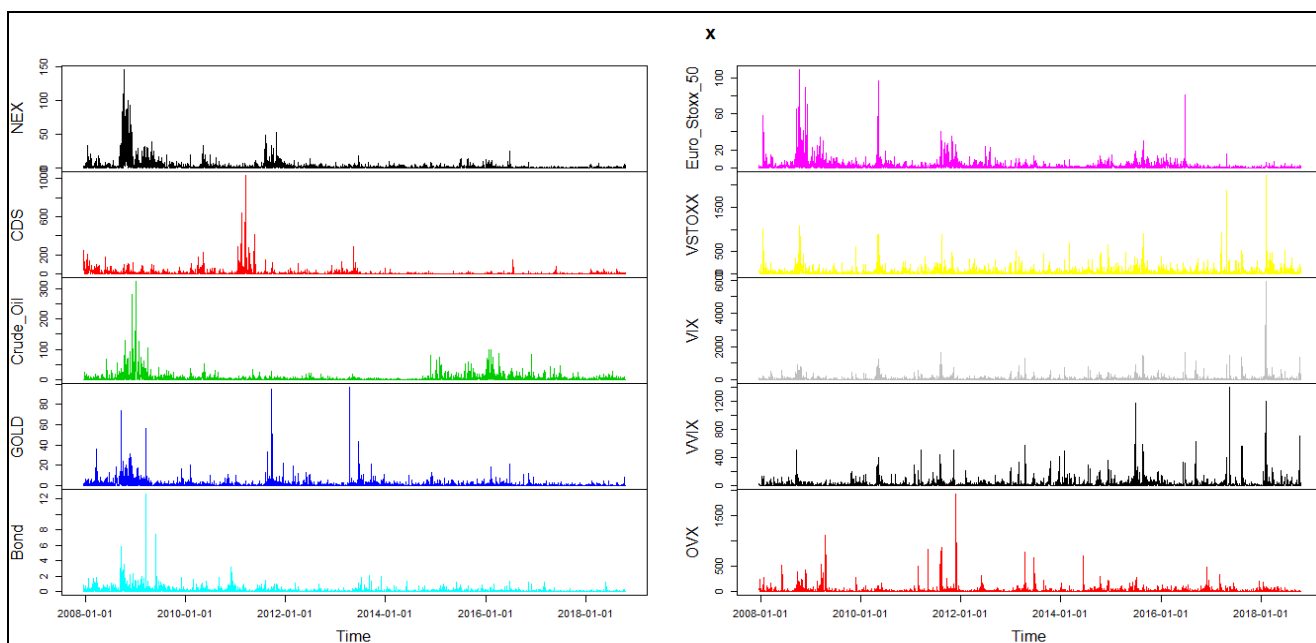


Figure 1: Time series of sample variables



**Figure 2: Squared daily returns**

Now, we turn to examine the unconditional correlation between raw returns and squared returns which are summarized in table 3 and 4 respectively.

From table 3, we find that NEX correlates positively with CDS, Crude Oil, GOLD and Euro Stoxx 50 and negatively with the other indexes. The Euro Stoxx 50 tend to have a stronger correlation (0,7194) than the other variables, followed by the VSTOXX (-0,5269). Whereas, the lowest correlation is found between NEX and CDS (0,0955).

**Table 3: Unconditional correlation between raw returns**

	NEX	CDS	Crude Oil	GOLD	BOND	Euro Stoxx 50	VSTOXX	VIX	VVIX	OVX
NEX	1	0.0955	0.3831	0.1208	-0.2800	0.7194	-0.5269	-0.5255	-0.3879	-0.3181
CDS	0.0955	1	0.0509	-0.0272	-0.0266	0.0967	-0.0859	-0.0238	-0.0200	-0.0354
Crude Oil	0.3831	0.0509	1	0.1888	-0.2005	0.3710	-0.2592	-0.1831	-0.1261	-0.2430
GOLD	0.1208	-0.0272	0.1888	1	0.1368	-0.0178	0.0121	0.0075	0.0145	-0.0190
BOND	-0.2800	-0.0266	-0.2005	0.1368	1	-0.3475	0.2627	0.2871	0.2274	0.1620
Euro Stoxx 50	0.7194	0.0967	0.3710	-0.0178	-0.3475	1	-0.7415	-0.4850	-0.3739	-0.2903
VSTOXX	-0.5269	-0.0859	-0.2592	0.0121	0.2627	-0.7415	1	0.5368	0.4382	0.3146
VIX	-0.5255	-0.0238	-0.1831	0.0075	0.2871	-0.4850	0.5368	1	0.8132	0.4305
VVIX	-0.3879	-0.0200	-0.1261	0.0145	0.2274	-0.3739	0.4382	0.8132	1	0.3431
OVX	-0.3181	-0.0354	-0.2430	-0.0190	0.1620	-0.2903	0.3146	0.4305	0.3431	1

Table 4, show a positive correlation between NEX and each squared asset return, where the strongest correlation occurs for NEX/Euro Stoxx 50 (0,5176) while the pairwise NEX/CDS have the weakest correlation (0,0091).

Overall, Table 4 denotes positive correlation among the squared returns. However, the degree of correlation varies widely among both raw returns (between 0,7 and 0,09), and squared returns (between 0,5 and 0,009).

**Table 4: Unconditional correlation between squared returns**

	NEX	CDS	Crude Oil	GOLD	BOND	Euro Stoxx 50	VSTOXX	VIX	VVIX	OVX
NEX	1	0.0091	0.1468	0.0145	0.0784	0.5176	0.2777	0.2761	0.1505	0.1011
CDS	0.0091	1	0.0025	0.0007	0.0007	0.0093	0.0073	0.0005	0.0004	0.0012
Crude Oil	0.1468	0.0025	1	0.0356	0.0402	0.1377	0.0671	0.0335	0.0159	0.0590
GOLD	0.0145	0.0007	0.0356	1	0.0187	0.0003	0.0001	0.0386	0.0002	0.0003
BOND	0.0784	0.0007	0.0402	0.0187	1	0.1207	0.0690	0.0824	0.0517	0.0262
Euro Stoxx 50	0.5176	0.0093	0.1377	0.0003	0.1207	1	0.5499	0.2353	0.1398	0.0843
VSTOXX	0.2777	0.0073	0.0671	0.0001	0.0690	0.5499	1	0.2881	0.1920	0.0989
VIX	0.2761	0.0005	0.0335	0.0386	0.0824	0.2353	0.2881	1	0.6613	0.1853
VVIX	0.1505	0.0004	0.0159	0.0002	0.0517	0.1398	0.1920	0.6613	1	0.1177
OVX	0.1011	0.0012	0.0590	0.0003	0.0262	0.0843	0.0989	0.1853	0.1177	1

Following, the table 5 (See annex) presents the estimated results of the DCC and ADCC models. First of all, for all time series, the short-term persistence ( $\alpha$ ) and the long-term persistence ( $\beta$ ) are statistically significant and for each case  $\alpha$  is less than  $\beta$ , their sums are close to unity providing evidence of volatility clustering in all variables which is proves in fig2.

Secondly, as known, if the shape parameters ( $\lambda$ ), the equivalence of the degrees of freedom in the distribution, tend to infinity, the t-distribution tends to the normal distribution. In this case, crude oil shows the highest estimated shape (7,26) followed by NEX (6,84) and Bond (6,22), while the lowest shape parameter is found by CDS (3,12).

Thirdly, we find that the estimated coefficients on  $\theta_1$  and  $\theta_2$  are each positive and statistically significant at the 1% significance level and the sum of both parameters is less than one meaning that the dynamic conditional correlations are mean-reverting.

Table 6 presents the GO-GARCH model results. Panel I of the table shows the rotation matrix U which is orthogonal as  $U^T U = 1$ , the second panel II denotes the mixing matrix A and third panel III shows the parameters estimates.

As considered an estimator of factors, the GO-GARCH model does not create any standard errors. For each time series, the estimated short-run persistence ( $\alpha$ ) is significantly

lower than the long-run persistence ( $\beta$ ) which is agreed with DCC and ADCC results. Moreover, “The DCC model is mean reverting as long as  $\alpha+\beta<1$ ”, based on the expression above, we calculate the sum of the persistence parameters ( $\alpha$  and  $\beta$ ), we found that is less than one, which proof the mean-reverting of volatility process.

**Table 6: The GO-GARCH results for NEX**

<b>The rotation matrix U</b>										
	<b>U(1)</b>	<b>U(2)</b>	<b>U(3)</b>	<b>U(4)</b>	<b>U(5)</b>	<b>U(6)</b>	<b>U(7)</b>	<b>U(8)</b>	<b>U(9)</b>	<b>U(10)</b>
<b>U(1)</b>	-0.6610	-0.3590	-0.0862	0.0041	0.0201	-0.5035	0.0736	0.1041	0.2419	0.3128
<b>U(2)</b>	-0.5060	0.1387	0.3123	-0.0685	-0.0201	0.7191	-0.0909	0.0709	0.0447	0.2991
<b>U(3)</b>	0.1950	0.0627	0.0765	0.0261	-0.0109	0.0962	0.1198	0.0902	0.9497	-0.1321
<b>U(4)</b>	0.0094	-0.0711	0.0793	0.9860	0.0783	0.0569	-0.0192	-0.0407	-0.0199	0.0672
<b>U(5)</b>	-0.3872	-0.2516	0.0960	0.0297	0.0048	0.1116	0.0582	-0.0164	-0.0505	-0.8705
<b>U(6)</b>	-0.1200	0.2414	-0.0490	0.0122	0.0710	-0.1688	-0.9107	-0.1690	0.14607	-0.1088
<b>U(7)</b>	-0.2981	0.8219	-0.0041	0.0898	-0.0725	-0.2542	0.3423	-0.1682	-0.0126	-0.1085
<b>U(8)</b>	0.0257	0.1954	0.0830	0.0573	-0.0294	-0.1152	-0.1183	0.9506	-0.1032	-0.0916
<b>U(9)</b>	-0.1205	0.0473	-0.9252	0.0766	-0.1046	0.3096	0.0043	0.1073	0.0473	-0.0248
<b>U(10)</b>	-0.0188	0.0717	-0.0903	-0.0642	0.9852	0.0439	0.0870	0.0432	-0.0011	-0.0083
<b>The Mixing Matrix A</b>										
	<b>A(1)</b>	<b>A(2)</b>	<b>A(3)</b>	<b>A(4)</b>	<b>A (5)</b>	<b>A (6)</b>	<b>A (7)</b>	<b>A (8)</b>	<b>A (9)</b>	<b>A (10)</b>
<b>A (1)</b>	0.2040	1.3074	-0.2792	0.0530	-0.1086	0.3489	-0.1765	-0.2480	-0.1603	-0.1542
<b>A (2)</b>	-0.0497	0.2695	-0.1181	-2.8071	-0.2338	0.1705	0.0749	0.1066	-0.0602	-0.1137
<b>A (3)</b>	0.0861	0.4941	-0.0044	-0.1189	0.1318	0.2232	-2.0640	-0.2121	-0.2381	0.0092
<b>A (4)</b>	-0.0863	-0.0285	-0.0122	-0.0284	0.0809	-0.0055	-0.1298	-1.1382	0.1111	0.1071
<b>A (5)</b>	-0.0576	-0.1380	-0.0100	0.0211	-0.3395	-0.0517	0.0213	-0.0673	0.0342	0.0312
<b>A (6)</b>	0.1988	1.0811	0.7511	-0.0449	-0.0355	0.4982	-0.2264	-0.0329	-0.1820	-0.1341
<b>A(7)</b>	-1.3194	-2.1636	-1.7498	0.1134	0.1819	-5.6649	0.5178	0.1836	0.6065	0.5564
<b>A (8)</b>	-6.3392	-2.4786	0.0876	-0.0544	0.1194	-2.0252	0.2165	0.7542	1.1420	1.6219
<b>A (9)</b>	-2.9602	-0.9141	-0.0545	-0.1058	0.0414	-1.1028	0.1503	0.5612	0.3837	3.7184
<b>A (10)</b>	-0.9145	-0.5092	0.1047	0.0273	0.0126	-0.8044	0.4212	0.6083	4.4062	0.5134
<b>GO-GARCH parameters</b>										
	<b>F1</b>	<b>F2</b>	<b>F3</b>	<b>F4</b>	<b>F5</b>	<b>F6</b>	<b>F7</b>	<b>F8</b>	<b>F9</b>	<b>F10</b>
<b>Omega</b>	0.1681	0.0046	0.0091	0.0109	0.0018	0.0940	0.0027	0.0051	0.1398	0.1643
<b>Alpha</b>	0.1652	0.0743	0.0613	0.1394	0.0229	0.1183	0.0410	0.0321	0.1081	0.1111
<b>Beta</b>	0.6582	0.9203	0.9298	0.8595	0.9745	0.7867	0.9563	0.9622	0.7383	0.7304
<b>Skew</b>	-0.1771	0.0181	0.0157	-0.0667	0.2102	-0.1953	-0.0194	0.0958	0.2476	0.2755
<b>Shape</b>	1.7192	2.7872	2.4955	0.4475	1.5198	1.0692	2.3265	0.9274	0.9762	1.1700

Turning to the correlations between correlations reported in table 7, we find that dynamic conditional correlations realized by DCC and ADCC models are similar. Furthermore, for each pair of correlations, the correlations between DCC/GO-GARCH or ADCC/GO-GARCH are significantly less correlated. Otherwise, the lowest correlation between DCC/GO-GARCH and ADCC/GO-GARCH is found among NEX/Crude Oil followed by NEX/GOLD and NEX/CDS. However, we note a higher correlation for NEX/Bond,

NEX/OVX and NEX/VVIX. In either case, OVX present a negative association with NEX which means that our model exhibits a higher level of interdependence in this case. Summary findings of correlations between hedge ratios estimated from three MGARCH models (DCC, ADCC and GO-GARCH) are presented in table 8, which suggest that hedge ratios obtained from DCC and ADCC models show a perfect high correlation. Beyond this,

**Table 7: Correlations between correlations**

NEX	CDS	Crude Oil	GOLD	BOND	Euro Stoxx 50	VSTOXX	VIX	VVIX	OVX
<b>DCC/ADCC</b>	0.9094	0.9640	0.9904	0.9784	0.7206	0.9539	0.9435	0.9245	0.9570
<b>DCC/GOGARCH</b>	0.6535	0.4161	0.4623	0.9056	0.8557	0.8457	0.7952	0.8447	0.8472
<b>ADCC/GOGARCH</b>	0.6201	0.4147	0.4187	0.8824	0.5320	0.7660	0.6997	0.6993	0.7864

**Table 8: Correlations between hedge ratios**

NEX	CDS	Crude Oil	GOLD	BOND	Euro Stoxx 50	VSTOXX	VIX	VVIX	OVX
<b>DCC/ADCC</b>	0.9240	0.9968	0.9986	0.9979	0.9825	0.9561	0.9802	0.9816	0.9905
<b>DCC/GOGARCH</b>	0.1812	0.4677	0.5385	0.6160	0.4736	0.0924	0.2038	0.3640	-0.4857
<b>ADCC/GOGARCH</b>	0.0662	0.4601	0.5296	0.6186	0.4653	0.1267	0.2141	0.3544	-0.4669

Summary statistics of hedge ratio and hedging effectiveness are reported in table 9, in order to examine the robustness of our findings with the change in the number of model refits. Our results find that, for each pair, hedging effectiveness values estimated with a student distribution are extremely similar beyond all three model refits and for each GARCH model specification. As example, hedging effectiveness values presented by the DCC model for the pair NEX/VVIX are equal for all models (0.2276), the same thing for the ADCC model, where HE values are equals to 0,2145.

Taking another example, the case of NEX/CDS hedge, the hedging effectiveness values obtained by the DCC model are 0.0155, 0.0153 and 0.0145 for the refits 10, 20 and 60 days respectively. In the case of NEX/VIX, the ADCC model

shows the following values of HE: 0.3006, 0.3010 and 0.3015 respectively for the refits 10, 20 and 60 days. Thus, it means that all hedging results are robust to model refits.

According to the table 9, Refit=10, the average value of the hedge ratio between NEX and VIX is 0,40 for th GO-GARCH model, this means that a \$1 long position in NEX can be hedged for 40 cents with a short position in the VIX market.

Moreover, results show that ADCC hedge provide the highest hedging effectiveness for CDS, Gold and Euro Stoxx 50 and GO-GARCH hedge provide the highest HE for the other indices with the exception of NEX/Bond pair series which imply that its highest HE is achieved with DCC model. Opposed to what have been reported by Ahmad et al [7], we



find that both ADCC and GO-GARCH are chosen over DCC model. Additionally, our analysis suggest that NEX/VIX has the highest HE ratio (HE= 0,40) which means that VIX is the best hedge for clean energy stocks followed by VSTOXX (HE= 0,37) and Euro Stoxx 50 (HE= 0,36). Overall, as for investment and hedging their risk inside portfolio creation, investors who are looking for higher returns from NEX should join it with VIX. This finding is compatible with those of Ahmad et al. [7] and Hood and Malik [39] who prove that VIX is the best hedge for ECO and US equities respectively.

For each GARCH model specification, Hedging effectiveness, transaction cost, and the TC/HE ratio produced from model refits every 10days, 20 days and 60 days are summarized in table 10. Based on the above, our findings suggest that the VSTOXX is the most appropriate hedging instrument due its lowest TC/HE ratio= 0,09 of all variables with the DCC model followed by the VIX index (TC/HE=0,11). However, GOLD is the least suitable hedging instrument due its highest TC/HE ratio = 4,32.

**Table 9: Summary statistics of hedge ratios ( $\beta$ ) and hedge effectiveness (HE) for NEX investors – MVT**

	Refit=10				Refit=20				Refit=60			
	mean	min	max	HE	mean	min	max	HE	mean	min	max	HE
<b>NEX/CDS</b>												
DCC	0.0717	0.0150	0.2325	0.0155	0.0713	0.0150	0.2325	0.0153	0.0686	0.0018	0.2325	0.0145
ADCC	0.0440	0.0121	0.1984	<b>0.0158</b>	0.0437	0.0121	0.1984	<b>0.0158</b>	0.0417	0.0088	0.1984	<b>0.0148</b>
GOGARH	0.0670	-0.0526	0.0836	0.0090	0.0671	-0.0526	0.0829	0.0090	0.0707	-0.0448	0.5459	0.0090
<b>NEX/Crude Oil</b>												
DCC	0.1048	-0.0387	0.3881	0.0891	0.1050	-0.0343	0.3881	0.0891	0.1057	-0.0343	0.3877	0.0892
ADCC	0.1141	-0.0419	0.3888	0.0957	0.1143	-0.0376	0.3888	0.0957	0.1151	-0.0376	0.3888	0.0959
GOGARH	0.7663	0.3585	1.4717	<b>0.1489</b>	0.7740	0.3585	1.4746	<b>0.1554</b>	0.7714	0.3608	1.5144	<b>0.1516</b>
<b>NEX/GOLD</b>												
DCC	0.0485	-0.8271	0.6082	0.0463	0.0486	-0.8271	0.6082	0.0458	0.0490	-0.8211	0.6082	0.0455
ADCC	0.0655	-0.8638	0.8278	<b>0.0466</b>	0.0656	-0.8638	0.8193	<b>0.0462</b>	0.0655	-0.8586	0.8060	<b>0.0459</b>
GOGARH	0.2529	-0.2155	0.5371	0.0411	0.2586	0.0028	0.5348	0.0396	0.1467	0.0167	0.1796	0.0401
<b>NEX/BOND</b>												
DCC	-0.7984	-2.4314	0.3467	<b>0.0714</b>	-0.8000	-2.4314	0.3334	<b>0.0714</b>	-0.8054	-2.4463	0.3334	<b>0.0718</b>
ADCC	-0.7848	-2.4459	0.4512	0.0679	-0.7860	-2.4459	0.4376	0.0679	-0.7903	-2.4611	0.4376	0.0683
GOGARH	-0.1905	-0.7619	-0.0048	0.0542	-0.2491	-0.3208	-0.0250	0.0542	-0.2515	-0.3204	-0.0555	0.0544
<b>NEX/Euro Stoxx 50</b>												
DCC	0.4591	0.2458	0.7096	0.3445	0.4594	0.2497	0.7096	0.3446	0.4607	0.2570	0.7050	0.3459
ADCC	0.4934	0.2487	0.8101	<b>0.3638</b>	0.4936	0.2519	0.8129	<b>0.3637</b>	0.4952	0.2572	0.8084	<b>0.3653</b>
GOGARH	0.8448	0.7043	0.9421	0.3247	0.3888	0.1090	0.7547	0.3249	0.8374	0.6866	0.9255	0.3232
<b>NEX/VSTOX X</b>												
DCC	-0.0709	-0.1730	-0.0227	0.2908	-0.0709	-0.1731	-0.0232	0.2896	-0.0713	-0.1731	-0.0232	0.2898
ADCC	-0.0717	-0.1657	-0.0280	0.2787	-0.0717	-0.1655	-0.0280	0.2787	-0.0721	-0.1655	-0.0280	0.2793
GOGARH	-0.3128	-0.5966	-0.1536	<b>0.3703</b>	-0.3130	-0.5956	-0.1537	<b>0.3707</b>	-0.3143	-0.5955	-0.1540	<b>0.3712</b>
<b>NEX /VIX</b>												
DCC	-0.0671	-0.1642	-0.0155	0.3187	-0.0672	-0.1642	-0.0155	0.3192	-0.0676	-0.1642	-0.0156	0.3198
ADCC	-0.0680	-0.1786	-0.0208	0.3006	-0.0681	-0.1786	-0.0208	0.3010	-0.0684	-0.1786	-0.0211	0.3015
GOGARH	-1.3149	-7.2498	-0.5511	<b>0.4065</b>	-1.3134	-7.2479	-0.5528	<b>0.4073</b>	-0.3409	-0.6472	-0.1192	<b>0.4092</b>
<b>NEX /VVIX</b>												

DCC	-0.0813	-0.1946	-0.0240	0.2276	-0.0814	-0.1946	-0.0237	0.2276	-0.0817	-0.1946	-0.0237	0.2276
ADCC	-0.0824	-0.1962	-0.0232	0.2145	-0.0824	-0.1978	-0.0232	0.2145	-0.0826	-0.1944	-0.0232	0.2145
GOGARH	-1.1675	-7.1408	-0.3309	<b>0.2966</b>	-1.1671	-7.1407	-0.3309	<b>0.2965</b>	-0.2823	-0.5352	-0.1129	<b>0.2970</b>
<b>NEX /OVX</b>												
DCC	-0.0641	-0.1828	-0.0035	0.1098	-0.0642	-0.1828	-0.0033	0.1099	-0.0645	-0.1828	-0.0037	0.1100
ADCC	-0.0616	-0.1619	-0.0001	0.1011	-0.0617	-0.1619	0.0001	0.1010	-0.0618	-0.1619	-0.0003	0.1012
GOGARH	-0.2375	-0.3846	-0.1746	<b>0.1623</b>	-0.2422	-1.1264	-0.1746	<b>0.1640</b>	-0.7089	-1.8406	-0.2874	<b>0.1619</b>

**Table 10: The hedging effectiveness (HE), the transaction cost TC, and the TC/HE ratio under different model refits**

	Refit=10			Refit=20			Refit=60		
	HE	TC	$\frac{TC}{HE}$	HE	TC	$\frac{TC}{HE}$	HE	TC	$\frac{TC}{HE}$
<b>NEX/CDS</b>									
DCC	1.55%	4.15	2.67	1.53%	4.18	2.72	1.45%	4.34	2.98
ADCC	1.58%	3.95	<b>2.49</b>	1.58%	3.90	<b>2.46</b>	1.48%	3.85	<b>2.60</b>
GOGARH	0.91%	2.48	2.73	0.90%	2.47	2.72	0.90%	4.59	5.06
<b>NEX/Crude Oil</b>									
DCC	8.91%	5.10	<b>0.57</b>	8.91%	5.08	<b>0.57</b>	8.92%	5.08	<b>0.56</b>
ADCC	9.57%	6.10	0.63	9.57%	6.09	0.63	9.59%	6.08	0.63
GOGARH	14.89%	26.76	1.79	15.54%	27.62	1.77	15.16%	26.75	1.76
<b>NEX/GOLD</b>									
DCC	4.63%	24.36	5.26	4.58%	24.31	5.29	4.55%	24.26	5.32
ADCC	4.66%	25.85	5.53	4.62%	25.79	5.57	4.59%	25.71	5.59
GOGARH	4.11%	17.80	<b>4.32</b>	3.96%	17.11	<b>4.31</b>	4.01%	2.69	<b>4.67</b>
<b>NEX/BOND</b>									
DCC	7.14%	40.08	5.61	7.14%	40.05	5.60	7.18%	39.96	5.56
ADCC	6.79%	45.59	6.70	6.79%	45.55	6.70	6.83%	45.54	6.66
GOGARH	5.42%	13.61	<b>2.50</b>	5.42%	5.64	<b>1.03</b>	5.44%	5.52	<b>1.01</b>
<b>NEX/Euro Stoxx 50</b>									
DCC	34.45%	14.10	0.40	34.46%	14.07	0.40	34.59%	13.97	0.40
ADCC	36.38%	22.61	0.62	36.37%	22.56	0.62	36.53%	22.55	0.61
GOGARH	32.48%	6.98	<b>0.21</b>	32.49%	20.01	<b>0.21</b>	32.32%	6.65	<b>0.20</b>
<b>NEX/VSTOXX</b>									
DCC	29.08%	2.83	<b>0.09</b>	28.96%	2.84	<b>0.09</b>	28.98%	2.84	<b>0.09</b>
ADCC	27.87%	3.52	0.12	27.87%	3.52	0.12	27.93%	3.54	0.12
GOGARH	37.03%	9.52	0.25	37.07%	9.55	0.25	37.12%	9.68	0.26
<b>NEX /VIX</b>									
DCC	31.87%	3.81	<b>0.11</b>	31.92%	3.82	<b>0.11</b>	31.98%	3.85	<b>0.12</b>
ADCC	30.06%	4.55	0.15	30.10%	4.56%	0.15	30.15%	4.57	0.15
GOGARH	40.65%	153.60	3.77	40.73%	153.51	3.76	40.92%	17.55	0.42
<b>NEX /VVIX</b>									
DCC	22.76%	5.31	<b>0.23</b>	22.77%	5.31	<b>0.23</b>	22.76%	5.30	<b>0.23</b>

ADCC	21.45%	6.08	0.28	21.46%	6.09	0.28	21.45%	6.08	0.28
GOGARH	29.66%	150.41	5.07	29.65%	150.16	5.06	29.70%	10.48	0.35
<b>NEX/OVX</b>									
DCC	10.98%	3.41	<b>0.31</b>	10.99%	3.42	<b>0.31</b>	11.00%	3.40	<b>0.30</b>
ADCC	10.11%	3.76	0.37	10.10%	3.77	0.37	10.12%	3.75	0.37
GOGARH	16.23%	5.08	0.31	16.40%	6.58	0.40	16.19%	44.46	2.74

In order to investigate the robustness of our findings on different forecast length, we calculate hedge ratio from fixed length rolling window analysis. To this end, we fix, firstly, our rolling window and refit the DCC, ADCC and GO-GARCH models every 20 observations, results are shown in table 11 (see **Annex**). The forecasts lengths chosen are of 500, 1000 and 1500. We estimate GARCH models (DCC and ADCC) with a student distribution (MVT). The GO-GARCH estimated using a multivariate affine negative inverse Gaussian (MANIG) distribution. Results show that Euro Stoxx 50 provides the most effective hedge for NEX only for 500 forecast length, however, for the 1000 and 1500 forecast length, the VIX is the best hedge ratio. Additionally, for the NEX/VIX hedge, the DCC model is preferred (largest HE value) across all forecast horizons. The same case for the NEX/VSTOXX, NEX/VIX and NEX/Crude Oil hedges. For the NEX/CDS hedge, the DCC model is preferred for forecasts lengths of 500 and 1000, and ADCC is preferred for 1500 forecast. For the pair NEX/GOLD hedge the DCC model is preferred for 500 and 1000 forecast length, while the GO-GARCH model is preferred for 1500 forecast length. However, for the NEX/OVX, the DCC model is chosen only for 500 forecast and GO-GARCH model for 1000 and 1500.

The table 12 (see **Annex**) report the transaction costs, the hedging effectiveness and the TC/HE of the rolling window estimations with different forecasts length. Results show that the VIX is the best hedge ratio for NEX in all cases. Moreover, in most situations the GO-GARCH model makes the best hedge decision with the exception of VSTOXX, VIX, and VVIX where the DCC yields the best hedge ratio.

## VI. CONCLUSIONS

Facing to the rapid growth of the world's population industrialization, urbanization, the energy demand and carbon dioxide emissions are expected to have an important increase over the next twenty years all over the world. Thus allowing, the scientific community has reported that increasing the usage of clean energy is the greatest solution on reducing world's dependence on fossil fuels as well as fighting climate change by reducing greenhouse gas emissions. Based on the previous challenges, investors need to hedge their investments against risk fluctuations of renewable energy assets. This paper, estimate time-varying optimal hedge ratio for the aim of whether an investment in clean energy can be

hedged by CDS, Crude Oil, Bond, GOLD, Euro Stoxx 50, VSTOXX, VIX, VVIX and OVX. Based on several multivariate GARCH models refitted every 10, 20 and 60 observations, our findings suggest that the VIX is the best hedge ratio for renewable energy as it has the highest HE, followed by VSTOXX and Euro Stoxx 50 which robust through the different forecast length.

While previous studies focuses on estimating time varying hedge rat, our paper takes a new approach and analyzing the effect of the tradeoff between transaction costs and effectiveness hedging on the portfolio decisions, which is considered as new insight into hedging strategies for clean energy investors. Our significantly different results show that the VSTOXX is the best hedging instrument for renewable energy since it yields the lowest TC/HE followed by the VIX.

## ACKNOWLEDGMENT

I gratefully thank an anonymous referee for the helpful comments and suggestions that have improved the quality of the paper.

## REFERENCES

- [1] Ahmad, W. (2017). On the dynamic dependence and investment performance of crude oil and clean energy stocks. *Research in International Business and Finance*, 42, 376-389.
- [2] Broadstock, D. C., Cao, H., & Zhang, D. (2012). Oil shocks and their impact on energy related stocks in China. *Energy Economics*, 34(6), 1888-1895.
- [3] Bamati, N., & Raoofi, A. (2019). Development level and the impact of technological factor on renewable energy production. *Renewable Energy*.
- [4] Kumar, S., Managi, S., & Matsuda, A. (2012). Stock prices of clean energy firms, oil and carbon markets: A vector autoregressive analysis. *Energy Economics*, 34(1), 215-226.
- [5] Bouraiou, A., Necaibia, A., Boutasseta, N., Mekhilef, S., Dabou, R., Ziane, A., ... & Touaba, O. (2019). Status of renewable energy potential and utilization in Algeria. *Journal of Cleaner Production*, 119011.
- [6] International Energy outlook 2017, U.S. Energy Information Administration, September 14, 2017. [www.eia.gov/ieo](http://www.eia.gov/ieo).
- [7] Ahmad, W., Sadorsky, P., & Sharma, A. (2018). Optimal hedge ratios for clean energy equities. *Economic Modelling*, 72, 278-295.
- [8] Pham, L. (2019). Do all clean energy stocks respond homogeneously to oil price?. *Energy Economics*, 81, 355-379.
- [9] Sadorsky, P. (2012). Correlations and volatility spillovers between oil prices and the stock prices of clean energy and technology companies. *Energy Economics*, 34(1), 248-255.
- [10] Sánchez, E. R. (2015). VOLATILITY SPILLOVERS AMONG ALTERNATIVE ENERGY, OIL AND TECHNOLOGY GLOBAL

- MARKETS (Doctoral dissertation, Universidad de Castilla-La Mancha).
- [11] Elie, B., Naji, J., Dutta, A., & Uddin, G. S. (2019). Gold and crude oil as safe-haven assets for clean energy stock indices: Blended copulas approach. *Energy*, 178, 544-553.
- [12] Jitmaneeroj, B. (2018). The effect of the rebalancing horizon on the tradeoff between hedging effectiveness and transaction costs. *International Review of Economics & Finance*, 58, 282-298.
- [13] Henriques, I., & Sadorsky, P. (2008). Oil prices and the stock prices of alternative energy companies. *Energy Economics*, 30(3), 998-1010.
- [14] Sadorsky, P. (2012). Modeling renewable energy company risk. *Energy Policy*, 40, 39-48.
- [15] Ferstl, R., Utz, S., & Wimmer, M. (2012). The effect of the Japan 2011 disaster on nuclear and alternative energy stocks worldwide: An event study. *Business Research*, 5(1), 25-41.
- [16] Broadstock, D. C., Cao, H., & Zhang, D. (2012). Oil shocks and their impact on energy related stocks in China. *Energy Economics*, 34(6), 1888-1895.
- [17] Managi, S., & Okimoto, T. (2013). Does the price of oil interact with clean energy prices in the stock market?. *Japan and the World Economy*, 27, 1-9.
- [18] Bohl, M. T., Kaufmann, P., & Stephan, P. M. (2013). From hero to zero: Evidence of performance reversal and speculative bubbles in German renewable energy stocks. *Energy Economics*, 37, 40-51.
- [19] Ortas, E., & Moneva, J. M. (2013). The Clean Techs equity indexes at stake: Risk and return dynamics analysis. *Energy*, 57, 259-269.
- [20] Wen, X., Guo, Y., Wei, Y., & Huang, D. (2014). How do the stock prices of new energy and fossil fuel companies correlate? Evidence from China. *Energy Economics*, 41, 63-75.
- [21] Inchauspe, J., Ripple, R. D., & Trück, S. (2015). The dynamics of returns on renewable energy companies: A state-space approach. *Energy Economics*, 48, 325-335.
- [22] Reboredo, J. C. (2015). Is there dependence and systemic risk between oil and renewable energy stock prices?. *Energy Economics*, 48, 32-45.
- [23] Bondia, R., Ghosh, S., & Kanjilal, K. (2016). International crude oil prices and the stock prices of clean energy and technology companies: Evidence from non-linear cointegration tests with unknown structural breaks. *Energy*, 101, 558-565.
- [24] Reboredo, J. C., Rivera-Castro, M. A., & Ugolini, A. (2017). Wavelet-based test of co-movement and causality between oil and renewable energy stock prices. *Energy Economics*, 61, 241-252.
- [25] Ahmad, W. (2017). On the dynamic dependence and investment performance of crude oil and clean energy stocks. *Research in International Business and Finance*, 42, 376-389.
- [26] Dutta, A. (2017). Oil price uncertainty and clean energy stock returns: new evidence from crude oil volatility index. *Journal of Cleaner Production*, 164, 1157-1166.
- [27] Asma A, Ahmed G. Hedging Oil Prices with Renewable Energy Indices: A Comparison between Various Multivariate Garch Versions. *Biostat Biometrics Open Acc J*. 2018; 6(3):
- [28] <http://www.wildershires.com/stock.php>
- [29] Tully, E., & Lucey, B. M. (2007). A power GARCH examination of the gold market. *Research in International Business and Finance*, 21(2), 316-325.
- [30] Shahzad, S. J. H., Raza, N., Shahbaz, M., & Ali, A. (2017). Dependence of stock markets with gold and bonds under bullish and bearish market states. *Resources Policy*, 52, 308-319.
- [31] Zghal, R., Ghorbel, A., & Triki, M. (2018). Dynamic model for hedging of the European stock sector with credit default swaps and EURO STOXX 50 volatility index futures. *Borsa Istanbul Review*, 18(4), 312-328.
- [32] Engle, R. (2002). Dynamic conditional correlation: A simple class of multivariate generalized autoregressive conditional heteroskedasticity models. *Journal of Business & Economic Statistics*, 20(3), 339-350.
- [33] Cappiello, L., Engle, R. F., & Sheppard, K. (2006). Asymmetric dynamics in the correlations of global equity and bond returns. *Journal of Financial econometrics*, 4(4), 537-572.
- [34] Van der Weide, R. (2002). GO-GARCH: a multivariate generalized orthogonal GARCH model. *Journal of Applied Econometrics*, 17(5), 549-564.
- [35] Glosten, L. R., Jagannathan, R., & Runkle, D. E. (1993). On the relation between the expected value and the volatility of the nominal excess return on stocks. *The journal of finance*, 48(5), 1779-1801.
- [36] Ku, Y. H. H., Chen, H. C., & Chen, K. H. (2007). On the application of the dynamic conditional correlation model in estimating optimal time-varying hedge ratios. *Applied Economics Letters*, 14(7), 503-509.
- [37] Chang, C. L., McAleer, M., & Tansuchat, R. (2011). Crude oil hedging strategies using dynamic multivariate GARCH. *Energy Economics*, 33(5), 912-923.
- [38] Chen, F., & Sutcliffe, C. (2012). Better cross hedges with composite hedging? Hedging equity portfolios using financial and commodity futures. *The European Journal of Finance*, 18(6), 575-595.
- [39] Hood, M., & Malik, F. (2013). Is gold the best hedge and a safe haven under changing stock market volatility?. *Review of Financial Economics*, 22(2), 47-52.
- [40]

**ANNEX :**

**Table 5: Estimation results from DCC and ADCC models**

	DCC				ADCC			
	Coeff.	SE	t-value	Prob.	Coeff.	SE	t-value	Prob.
$\eta_{NEX}$	0.0408	0.0204	1.9984	0.0456	0.0191	0.0221	0.8642	0.3874
$\delta_{NEX}$	0.1885	0.0186	10.0983	0.0000	0.1905	0.0183	10.3655	0.0000
$\omega_{NEX}$	0.0076	0.0042	1.7897	0.0734	0.0135	0.0053	2.5189	0.0117
$\alpha_{NEX}$	0.0746	0.0174	4.2688	0.0000	0.0716	0.0173	4.1335	0.0000
$\beta_{NEX}$	0.9241	0.0174	52.9593	0.0000	0.9333	0.0168	55.4445	0.0000
					0.5689	0.1019	5.5808	0.0000
$\lambda_{NEX}$	6.8474	0.7404	9.2479	0.0000	7.1522	0.6230	11.4794	0.0000
$\eta_{CDS}$	0.0415	0.0208	1.9895	0.0466	0.0487	0.0208	2.3421	0.0191
$\delta_{CDS}$	-0.0107	0.0189	-0.5682	0.5698	-0.0157	0.0203	-0.774	0.4388
$\omega_{CDS}$	0.0835	0.0480	1.7392	0.0819	0.066121	0.0281	2.3494	0.0188
$\alpha_{CDS}$	0.1425	0.0347	4.1066	0.0000	0.2837	0.0596	4.75860	0.0000
$\beta_{CDS}$	0.8564	0.0447	19.1560	0.0000	0.8524	0.0313	27.1688	0.0000
					0.0342	0.0657	0.5203	0.6028
$\lambda_{CDS}$	3.1267	0.1274	24.5337	0.0000	2.3601	0.0407	57.9273	0.0000
$\eta_{Crude\ Oil}$	0.0164	0.0297	0.5514	0.5813	-0.0082	0.0304	-0.2720	0.7855
$\delta_{Crude\ Oil}$	0.0281	0.0181	1.5483	0.1215	0.0266	0.0120	2.2030	0.0275
$\omega_{Crude\ Oil}$	0.0100	0.0043	2.3066	0.0210	0.0058	0.0024	2.3910	0.0168
$\alpha_{Crude\ Oil}$	0.0409	0.0025	15.8787	0.0000	0.0409	0.0019	20.5665	0.0000
$\beta_{Crude\ Oil}$	0.9575	0.0010	933.6031	0.0000	0.9661	0.0004	2411.8898	0.0000
					0.5459	0.0995	5.4856	0.0000
$\lambda_{Crude\ Oil}$	7.2684	0.9173	7.9237	0.0000	8.1356	1.1478	7.0876	0.0000
$\eta_{GOLD}$	0.0273	0.0149	1.8293	0.0673	0.0305	0.0145	2.0929	0.0363
$\delta_{GOLD}$	-0.0301	0.0153	-1.9643	0.0494	-0.0313	0.0155	-2.0217	0.0432
$\omega_{GOLD}$	0.0050	0.0019	2.6489	0.0080	0.0053	0.0020	2.6639	0.0077
$\alpha_{GOLD}$	0.0309	0.0026	11.4900	0.0000	0.0464	0.0031	14.8321	0.0000
$\beta_{GOLD}$	0.9669	0.0006	1575.9395	0.0000	0.9628	0.0003	2599.6359	0.0000
					-0.1609	0.1070	-1.5034	0.1327
$\lambda_{GOLD}$	4.0247	0.2794	14.4039	0.0000	4.0191	0.2769	14.5112	0.0000
$\eta_{BOND}$	0.00314	0.0053	0.5857	0.5580	0.0030	0.0056	0.5440	0.5864
$\delta_{BOND}$	-0.0292	0.0186	-1.5667	0.1171	-0.0292	0.0175	-1.6678	0.0953
$\omega_{BOND}$	0.0002	0.0001	1.8772	0.0604	0.0012	0.0005	2.3139	0.0206
$\alpha_{BOND}$	0.0274	0.0019	14.2146	0.0000	0.0406	0.0024	16.7819	0.0000
$\beta_{BOND}$	0.9703	0.0009	1065.1186	0.0000	0.9657	0.0003	2598.4020	0.0000
					-0.0451	0.1119	-0.4030	0.6868
$\lambda_{BOND}$	6.2265	0.6231	9.9917	0.0000	6.1271	0.6026	10.1664	0.0000

$\eta_{Euro\ Stoxx\ 50}$	0.0407	0.0182	2.2299	0.0257	0.0023	0.0158	0.1504	0.8804
$\delta_{Euro\ Stoxx\ 50}$	-0.0317	0.0184	-1.7191	0.0855	-0.0218	0.0172	-1.2630	0.2065
$\omega_{Euro\ Stoxx\ 50}$	0.0174	0.0069	2.5028	0.0123	0.0242	0.0070	3.4610	0.0005
$\alpha_{Euro\ Stoxx\ 50}$	0.0927	0.0170	5.4501	0.0000	0.0845	0.0116	7.2541	0.0000
$\beta_{Euro\ Stoxx\ 50}$	0.9045	0.0163	55.2967	0.0000	0.9176	0.0129	71.0612	0.0000
					1.0000	0.0852	11.7246	0.0000
$\lambda_{Euro\ Stoxx\ 50}$	5.7800	0.6096	9.4815	0.0000	6.8810	0.8834	7.7884	0.0000
$\eta_{VSTOXX}$	-0.3298	0.0982	-3.3582	0.0007	-0.2023	0.0946	-2.1373	0.0325
$\delta_{VSTOXX}$	-0.0123	0.0188	-0.6556	0.5120	-0.00244	0.0188	-0.1297	0.8967
$\omega_{VSTOXX}$	3.3758	1.2242	2.7575	0.0058	0.3035	0.0794	3.8194	0.0001
$\alpha_{VSTOXX}$	0.0993	0.0234	4.2337	0.0000	0.0721	0.0119	6.0455	0.0000
$\beta_{VSTOXX}$	0.8281	0.0453	18.2606	0.0000	0.8980	0.0186	48.0341	0.0000
					-0.9999	0.2024	-4.9385	0.0000
$\lambda_{VSTOXX}$	4.4813	0.3289	13.6222	0.0000	4.694234	0.3642	12.8869	0.0000
$\eta_{VIX}$	-0.3901	0.0994	-3.9227	0.0000	-0.2189	0.1045	-2.0935	0.0363
$\delta_{VIX}$	-0.0628	0.0185	-3.3921	0.0006	-0.0632	0.0191	-3.3008	0.0009
$\omega_{VIX}$	7.4052	1.6436	4.5054	0.0000	0.4678	0.0975	4.7942	0.0000
$\alpha_{VIX}$	0.1748	0.0314	5.5623	0.0000	0.1058	0.0125	8.4552	0.0000
$\beta_{VIX}$	0.7099	0.0471	15.0428	0.0000	0.8561	0.0201	42.5314	0.0000
					-0.9999	0.1373	-7.2833	0.0000
$\lambda_{VIX}$	4.0119	0.2720	14.7467	0.0000	4.3257	0.3342	12.9413	0.0000
$\eta_{VVIX}$	-0.2930	0.0699	-4.1919	0.0000	-0.1933	0.0826	-2.3386	0.0193
$\delta_{VVIX}$	-0.0300	0.0203	-1.4809	0.1386	-0.0214	0.0245	-0.8738	0.3822
$\omega_{VVIX}$	5.0313	1.4783	3.4033	0.0006	0.4967	0.0991	5.0093	0.0000
$\alpha_{VVIX}$	0.2143	0.0428	5.0042	0.0000	0.1136	0.0184	6.1563	0.0000
$\beta_{VVIX}$	0.6240	0.0812	7.6787	0.0000	0.8164	0.0287	28.4237	0.0000
					-1.0000	0.2018	-4.9536	0.0000
$\gamma_{VVIX}$	3.7410	0.2356	15.8774	0.0000	3.8765	0.2624	14.7711	0.0000
$\eta_{OVX}$	-0.2378	0.0641	-3.7062	0.0002	-0.2040	0.0688	-2.9638	0.0030
$\delta_{OVX}$	-0.0367	0.0191	-1.9216	0.0546	-0.0362	0.0201	-1.8005	0.0717
$\omega_{OVX}$	1.8563	0.6504	2.8540	0.0043	0.2326	0.0690	3.3709	0.0007
$\alpha_{OVX}$	0.0935	0.0211	4.4205	0.0000	0.0690	0.0141	4.8866	0.0000
$\beta_{OVX}$	0.8254	0.0438	18.8065	0.0000	0.8990	0.0213	42.1825	0.0000
					-0.6710	0.2040	-3.2882	0.0010
$\gamma_{OVX}$	3.8468	0.2489	15.4516	0.0000	3.793325	0.2415	15.7032	0.0000
$\theta_1$	0.0137	0.0022	6.1294	0.0000	0.0136	0.0023	5.9024	0.0000
$\theta_2$	0.9597	0.0098	97.7030	0.0000	0.9614	0.0095	100.97545	0.0000
$\theta_3$					0.0006	0.0005	1.2401	0.2149
$\lambda$	7.0383	0.2749	25.5941	0.0000	6.4757	0.2369	27.3320	0.0000
$AIC$	38.753				38.967			
$BIC$	38.980				39.218			

<i>Shibata</i>	38.750	38.964
<i>H-Q</i>	38.835	39.058
<i>LL</i>	-54630.72	-54922.55
<i>Nobs</i>	2825	2825

**Table 11: Summary statistics of hedge ratios ( $\beta$ ) and Hedging Effectiveness (HE) for NEX investors under alternative forecast length**

	Forecast length= 500				Forecast length= 1000				Forecast length= 1500			
	mean	min	max	HE	mean	min	max	HE	mean	min	max	HE
<b>NEX/CDS</b>												
DCC	0.0485	-0.0963	0.2343	<b>0.0096</b>	0.0543	-0.0377	0.2343	<b>0.0105</b>	0.0619	-0.0271	0.2343	0.0119
ADCC	0.0330	-0.0250	0.2006	0.0095	0.0350	-0.0119	0.2006	0.0103	0.0389	-0.0105	0.2006	<b>0.0120</b>
GOGARH	0.0689	-1.2063	1.5832	0.0076	0.1088	-0.0137	0.6195	0.0081	0.0670	-0.0641	0.0828	0.0091
<b>NEX/Crude Oil</b>												
DCC	0.2301	-0.0668	1.0334	0.1408	0.1832	-0.0668	0.8780	0.1009	0.1140	-0.0668	0.3880	0.0736
ADCC	0.2283	-0.0618	0.9754	0.1455	0.1831	0.0103	0.7553	0.1074	0.1224	-0.0618	0.3899	0.0806
GOGARH	0.3701	0.1468	1.7304	<b>0.1836</b>	0.3405	0.1468	1.4826	<b>0.1772</b>	0.2701	0.1468	0.7834	<b>0.1618</b>
<b>NEX/GOLD</b>												
DCC	0.1330	-1.0938	0.8862	0.0677	0.1133	-0.8265	0.8106	0.0571	0.0440	-0.8265	0.6126	0.0364
ADCC	0.1465	-1.1444	0.9811	<b>0.0678</b>	0.1263	-0.8630	0.9576	<b>0.0571</b>	0.0546	-0.8630	0.8328	0.0366
GOGARH	0.1520	-1.0978	0.2884	0.0646	0.1554	0.0502	0.1869	0.0476	0.2794	0.0167	0.8705	<b>0.0451</b>
<b>NEX/BOND</b>												
DCC	-0.9658	-2.5751	0.3289	<b>0.0860</b>	-0.9348	-2.4287	0.3289	<b>0.0807</b>	-0.7716	-2.4287	0.3289	<b>0.0662</b>
ADCC	-0.920	-2.5475	0.4353	0.0793	-0.9065	-2.5475	0.4353	0.0759	-0.7463	-2.4430	0.4353	0.0615
GOGARH	-0.2361	-1.1139	-0.0020	0.0707	-0.2686	-0.3406	-0.0271	0.0714	-0.2503	-0.3196	-0.0271	0.0521
<b>NEX/Euro Stoxx 50</b>												
DCC	0.5699	0.2506	1.1414	0.4275	0.5303	0.2506	0.9443	0.3876	0.4854	0.2506	0.8614	0.3501
ADCC	0.6140	0.2540	1.1822	<b>0.4425</b>	0.5792	0.2540	1.1647	<b>0.4064</b>	0.5286	0.2540	0.9909	<b>0.3704</b>
GOGARH	0.8550	0.5774	1.1323	0.3917	0.4365	0.1046	1.3443	0.3645	0.8442	0.6759	0.9389	0.3328
<b>NEX/VSTOXX</b>												
DCC	-0.1056	-0.3288	-0.0216	0.3311	-0.0938	-0.3288	-0.0216	0.3140	-0.0766	-0.1730	-0.0216	0.2900
ADCC	-0.1054	-0.3158	-0.0277	0.3174	-0.0947	-0.3118	-0.0277	0.3020	-0.0777	-0.1654	-0.0277	0.2818
GOGARH	-0.3652	-1.1997	-0.1536	<b>0.3829</b>	-0.3592	-1.1999	-0.1536	<b>0.3853</b>	-1.2500	-4.5260	-0.4900	<b>0.3780</b>
<b>NEX/VIX</b>												
DCC	-0.0966	-0.2815	-0.0155	0.3548	-0.0870	-0.2463	-0.0155	0.3435	-0.0752	-0.1642	-0.0155	0.3397
ADCC	-0.0972	-0.3267	-0.0207	0.3368	-0.0873	-0.3073	-0.0207	0.3245	-0.0759	-0.1784	-0.0207	0.3215
GOGARH	-0.3775	-1.0042	-0.1178	<b>0.4137</b>	-0.3793	-0.9238	-0.1178	<b>0.4278</b>	-0.3459	-0.6472	-0.1178	<b>0.4206</b>
<b>NEX/VVIX</b>												
DCC	-0.1103	-0.3970	-0.0245	0.2212	-0.1006	-0.3970	-0.0245	0.2264	-0.0869	-0.1946	-0.0245	0.2327
ADCC	-0.1105	-0.4311	-0.0232	0.2100	-0.1005	-0.3047	-0.0232	0.2143	-0.0877	-0.1970	-0.0232	0.2200
GOGARH	-0.2807	-0.9639	-0.1129	<b>0.2594</b>	-0.2873	-0.9648	-0.1129	<b>0.2827</b>	-1.1917	-7.1704	-0.3309	<b>0.2985</b>
<b>NEX/OVX</b>												
DCC	-0.0870	-0.3836	-0.0033	<b>0.1343</b>	-0.0780	-0.3836	-0.0033	0.1246	-0.0667	-0.1827	-0.0033	0.1102
ADCC	-0.0826	-0.3665	0.0035	0.1246	-0.0743	-0.3665	0.0001	0.1161	-0.0634	-0.1616	0.0001	0.1016
GOGARH	-0.5673	-2.4910	-0.0826	0.1272	-0.6503	-2.4910	-0.2147	<b>0.1517</b>	-0.2403	-0.3843	-0.1748	<b>0.1574</b>

	Forecast length = 500			Forecast length= 1000			Forecast length= 1500		
	<i>HE</i>	<i>TC</i>	$\frac{TC}{HE}$	<i>HE</i>	<i>TC</i>	$\frac{TC}{HE}$	<i>HE</i>	<i>TC</i>	$\frac{TC}{HE}$
<b>NEX/CDS</b>									
DCC	0.96%	12.99	13.48	1.05%	9.26	8.81	1.19%	7.51	6.28
ADCC	0.95%	9.61	<b>10.12</b>	1.03%	5.86	<b>5.64</b>	1.20%	5.77	4.80
GOGARH	0.76%	21.54	28.08	0.81%	12.31	15.18	0.91%	1.56	<b>1.71</b>
<b>NEX/Crude Oil</b>									
DCC	14.08%	18.60	1.32	10.09%	15.97	1.58	7.36%	9.01	1.22
ADCC	14.55%	18.93	<b>1.30</b>	10.74%	15.73	1.46	8.06%	9.76	1.21
GOGARH	18.36%	25.20	1.37	17.72%	21.40	<b>1.20</b>	16.18%	10.31	<b>0.63</b>
<b>NEX/GOLD</b>									
DCC	6.77%	38.34	5.65	5.71%	30.66	5.36	3.64%	26.25	7.20
ADCC	6.78%	42.31	6.23	5.71%	33.75	5.90	3.66%	27.37	7.46
GOGARH	6.46%	12.83	<b>1.98</b>	4.76%	1.25	<b>0.26</b>	4.51%	18.71	<b>4.14</b>
<b>NEX/BOND</b>									
DCC	8.60%	51.53	5.99	8.07%	39.63	4.90	6.62%	37.78	5.70
ADCC	7.93%	70.68	8.91	7.59%	47.83	6.30	6.15%	43.93	7.14
GOGARH	7.07%	21.93	<b>3.09</b>	7.14%	4.00	<b>0.56</b>	5.21%	5.14	<b>0.98</b>
<b>NEX/Euro Stoxx 50</b>									
DCC	42.75%	20.06	0.46	38.76%	17.66	<b>0.45</b>	35.01%	15.78	0.45
ADCC	44.25%	31.67	0.71	40.64%	30.46	0.74	37.04%	26.54	0.71
GOGARH	39.17%	16.78	<b>0.42</b>	36.45%	32.06	0.87	33.28%	7.71	<b>0.23</b>
<b>NEX/VSTOXX</b>									
DCC	33.11%	6.08	<b>0.18</b>	31.40%	4.58	<b>0.14</b>	29.00%	3.94	<b>0.13</b>
ADCC	31.74%	7.68	0.24	30.20%	5.87	0.19	28.18%	4.81	0.17
GOGARH	38.29%	19.72	0.51	38.53%	16.42	0.42	37.80%	70.08	1.85
<b>NEX /VIX</b>									
DCC	35.48%	4.99	<b>0.14</b>	34.35%	4.66	<b>0.13</b>	33.97%	4.69	<b>0.13</b>
ADCC	33.68%	6.42	0.19	32.45%	5.64	0.17	32.15%	5.49	0.17
GOGARH	41.37%	19.74	0.47	42.78%	18.50	0.43	42.06%	18.63	0.44
<b>NEX /VVIX</b>									
DCC	22.12%	6.95	<b>0.31</b>	22.64%	5.74	<b>0.25</b>	23.27%	6.33	<b>0.27</b>
ADCC	21.00%	7.37	0.35	21.43%	5.98	0.27	22.00%	6.80	0.30
GOGARH	25.94%	11.15	0.43	28.27%	10.76	0.38	29.85%	132.62	4.44
<b>NEX /OVX</b>									
DCC	13.43%	7.91	<b>0.58</b>	<b>12.46%</b>	4.41	<b>0.35</b>	11.02%	4.08	<b>0.37</b>
ADCC	12.46%	8.20	0.65	11.61%	4.53	0.39	10.16%	4.37	0.43
GOGARH	12.72%	18.56	1.45	15.17%	40.91	2.69	15.74%	6.00	0.38

**Table 12: The Hedging Effectiveness, the Transaction Cost, and the TC/HE ratio for different forecast lengths**



# Elimination of Metronidazole from Synthetic Wastewater by Coagulation and Electrocoagulation.

Chérifi Mouna<sup>#1</sup>, Mécibah Wahib<sup>\*2</sup>, Grid Azeddine<sup>°3</sup>, Abrane Rahma<sup>#4</sup> Hazourli Sabir<sup>#5</sup>

<sup>#</sup>Laboratoire de Traitement des Eaux et Valorisation de Déchets Industriels, Université Badji Mokhtar Annaba, Algérie

[cherifimoun@gmail.com](mailto:cherifimoun@gmail.com)  
[rahmaabranel148@gmail.com](mailto:rahmaabranel148@gmail.com)  
[hazourlisab@yahoo.fr](mailto:hazourlisab@yahoo.fr)

<sup>\*</sup>Département de technologie, université 20 Aout 1955, skikda, Algérie

[mecibahwahiba@yahoo.fr](mailto:mecibahwahiba@yahoo.fr)

<sup>°</sup>Researche center in Industrial Technologies CRT, P.O. Box 64, Cheraga 1514. Algiers, Algeria  
[grid.azzou23@gmail.com](mailto:grid.azzou23@gmail.com)

**Abstract-**Metronidazole is an antibiotic drug for the treatment of anaerobic infections. When discharged in water after use, it reacts with living organisms thus causing adverse effects for their lives. This kind of residue must be removed from wastewater.

In this work, the elimination of metronidazole is carried using coagulation-flocculation and electrocoagulation techniques in batch mode.

The first part of this work is devoted to the study of the degradation of metronidazole by coagulation-flocculation. The results obtained indicate that degradation rates do not exceed 14.13% with the optimal dose of the coagulant  $Al_2(SO_4)_3$  but they increase to 73.84% for a pH 9.

The second part of this work deals with the study of the elimination of the considered antibiotic by electrocoagulation process. The coagulant provided from aluminum electrodes led to a reduction of 77.12% with 1A of applied current, the optimal pH conditions increase this yield to 80.10%.

An improvement in yields even with high initial concentrations of drug in water was recorded with electrocoagulation compared to coagulation.

Overall, after conducting an economic study, the cost is lower in coagulation-flocculation than in electrocoagulation. This trend is mainly related to aluminum consumption which is higher in electrocoagulation system.

**Keywords-** Elimination, Metronidazole, Coagulation-flocculation, Electrocoagulation.

## I. Introduction

The presence of pharmaceutical products in our water resources has raised great concern among scientists worldwide due to their persistence in nature via different ways including modern medicine and veterinary industries, agricultural runoff, direct discharge from refineries of urban and hospital wastewater, human waste [1,2]. Due to their highly polluting nature, it is not possible to discharge treated and untreated waste either into water course or in the soil without causing great damage [3]. In order to treat this pollution, several

methods can be used to remove residues in wastewater [4]. Coagulation-flocculation processes have been mainly used for wastewater treatment to separate suspended and/or fatty particles, the main function of coagulants widely used like aluminum and iron salts is to flocculate colloidal particles into larger particles that can be removed by precipitation or flotation [5].

Currently, electrocoagulation is another process drawing the attention from the scientific community due to the many advantages it offers, it is referred to as an environmental technology owing to the fact that it uses a clean reagent (electron) for the abatement of organic and recalcitrant pollutants [6].

In this perspective, the present study investigates the removal of metronidazole from synthetic wastewater by coagulation-flocculation and electrocoagulation.

## II. Experimental design, materials and methods

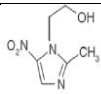
### A. Chemicals

-Pharmaceutical compound: Metronidazole solid with the properties given in table 1. 30mg was added to 1L of distilled water, the mixture was homogenized by slight magnetic stirring for 24h.

-  $Al_2(SO_4)_3 \cdot 16H_2O$  was used as coagulant  
- "SP6" is a cationic polymer was used as flocculent.

TABLE I

Physical and chemical properties of metronidazole [4]

Molecular formula	$C_6H_9N_3O_3$
Usage	Antibiotic
Molecular weight (g/mol)	171,2
Solubility in water (g/mol)	9,5
pK <sub>a</sub>	2,55
Melting point	159-163
Molecular structure	

**B. Experimental Setup**

Runs of coagulation-foculation treatment were realized in Jar test, whereas Fig. 1 describes the electrocoagulation apparatus.

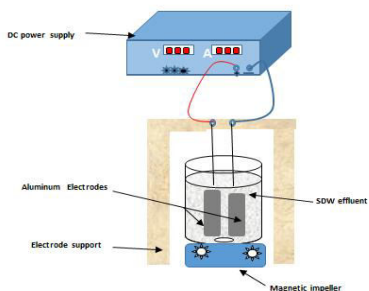


Fig .2 Electrocoagulation apparatus

**C. Experimental procedure**

**1) Jar test coagulation:**

Coagulation-flocculation treatment was carried out in a conventional jar test apparatus (model Velp Scientifica C6F). The experimental procedure is as follow:

- (1) **Dosing stage:** Water sample was put into the 1L beaker. After adjusting pH solution, if needed, coagulant and flocculent were added then the mixture was stirred for 15min with a speed of 120rpm
- (2) **Coagulation stage:** After 15 min rapid mixing, the stirring speed was reduced to 45 rpm and continued to stir 45 min.
- (3) **Settling stage:** After 30min stationary, the water samples were taken to analysis by spectrophotometry UV visible.

**2) Electrocoagulation :**

Electrocoagulation runs were carried out in a batch mode (**Figure1**). 1,5 g of NaCl was added, the pH was adjusted to the desirable values using Hcl and NaOH solutions. A pair of aluminum electrodes of size 12 cm×3 cm×0.5 cm, separated by a space of 1 cm and dipped in the wastewater. The current was provided by a GW GPR3030D, 3A-30 VDC power supply. The effluent under treatment was homogenized by gentle magnetic stirring at 300 rpm which allows the separation of gasses formed from the solution, thus avoiding the formation of foam which can affect the course of the batch process. After runs, samples are subjected to settling for 30 min.

The analysis of the samples is carried out before and after experimentation by UV-visible spectrophotometry (Model 2300UV spectrophotometer) at the absorption wavelength of metronidazole (320 nm). The calibration line is plotted by measuring the absorbances of a series of standard solutions obtained by diluting the stock solution of metronidazole.

**D. Operating parameters processes**

A total of 29 experimental runs were performed to investigate the influence of different parameters (i.e., coagulant mass, pH, initial metronidazole concentration and current density) on the removal rate of studied pharmaceuticals (Table 2)

TABLE 2  
 Experimental runs

Process Parameter	Coagulation-flocculation					
Coagulant dose(mg/l)	100	120	150	175	200	250
pH <sub>solution</sub>	1	3		5		9
Initial [Metronidazole]	10	20	30	40	50	
Process Parameter	Electrocoagulation					
Current intensity (A)	0,25	0,5	0,75	1	1,25	
pH <sub>solution</sub>	1	3		5		9
Initial [Metronidazole]	20	30	40	50	60	

**E. Calculations**

Evaluation of coagulation – flocculation/ electrocoagulation efficiency is given as

$$R\% = \frac{C_0 - C_e}{C_0} \times 100 \quad (1)$$

C<sub>0</sub>: Initial metronidazole concentration

C<sub>e</sub>: The equilibrium concentration.

The calculation of the operational cost of the two water treatment processes takes into account the consumed aluminum sulphate and the electrical energy consumed by the flocculator. According to the author [5], the calculation equations used are the following:

$$operational\ cost = aC_{energy} + bC_{Al^{3+}electrodes} \quad (2)$$

$$C' = b CAI^{3+}Al_2(SO_4)_3 \cdot 18 H_2O \quad (3)$$

Where, (a) and (b) are ratios for the price calculation of the international market on energy and chemicals for the year 2011, they are successively 0.05 US \$/kWh, and 3.08 \$/kg of aluminum.

For coagulation treatment, the value of aluminum consumed is calculated by the knowledge of the Al<sup>3+</sup> concentration introduced in the form of Al<sub>2</sub>(SO<sub>4</sub>)<sub>3</sub> salt. For electrocoagulation, the theoretical concentration of dissolved aluminum by unit of treated wastewater volume (KgAl/m<sup>3</sup>) is given by Faraday law:

$$CAI^{3+}(electrode) = \frac{IM}{ZFV} \quad (4)$$

Where, M the aluminum molecular weight (27 g/mol), I the current intensity applied (A), t the mean residence time in the reactor, Z the number of electrons involved in reaction of dissolution (Z = 3

for aluminum),  $F$  the constant of Faraday (96500 C/mol) and  $V$  the volume of the reactor (1L).  
 The consumed energy by unit of treated wastewater volume (KWh/m<sup>3</sup>), is given by Eq 5,

$$SEEC \left( \frac{\text{KWh}}{\text{m}^3} \right) = \frac{I \int_0^t U dt}{V^3} \quad (5)$$

$U$  is the average cell voltage

$I$  is current intensity in ampere

$T$  is time in hour

$V$  is volume of the solution (m<sup>3</sup>)

### III. Results

#### 1. Elimination of metronidazole by coagulation-floculation

##### A) Effect of coagulant dose

Coagulation-floculation tests are carried out on synthetic wastewater containing 50g/l of Metronidazole without regulating pH solution. The temperature is at 20 to 25<sup>0</sup> C and the coagulant dosage is of 100 to 250 mg/l.

The results presented in fig.2 showed that increasing the dose of coagulant increases the removal rate of metronidazole. However, when the dosage is more than a certain value and continues to be added, the removal efficiency will reduced. The optimum coagulant dose was found to be 150 mg/l at which the concentration of metronidazole decreased from 50 mg/l to 37mg/l but this removal yield insufficient. The sorption of micro-pollutants including pharmaceuticals, depends mostly on the compounds propensity to be sorbet on the surface of adsorbent. As a result, hydrophobic compounds with high octanol–water partition coefficient (logK<sub>ow</sub>) can potentially be removed by coagulation/floculation [6].

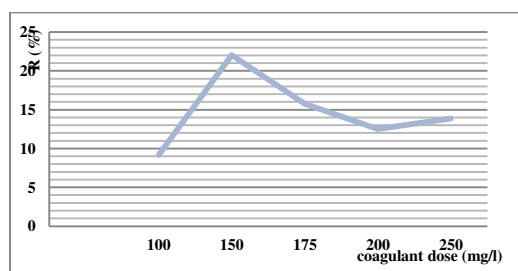


Fig.2 Effect of coagulant dose on the removal of Metronidazole by coagulation-floculation.

##### B) Effect of pH

The sorption of micro-pollutants including: pharmaceuticals, personal care products (PPCPs) and endocrine (EDCs) by solids, depends mainly on their physic-chemical properties, such as lipophilicity or acidity. For this reason, runs with different initial pH (1 to 9) solution containing 30g/l of Metronidazole were conducted to investigate the effect of this parameter. The coagulant dose was thus already optimized 150mg/l.

From Fig.3, we deduced that the pH variation has an important influence on the removal yield. When de solution pH take the value 9, the removal yield take it's high level of 73,84%.

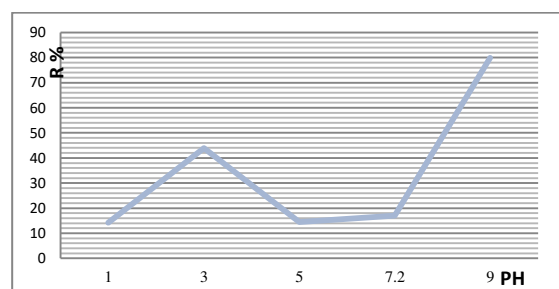


Fig.3 Effect of pH on the removal of Metronidazole by coagulation-floculation.

##### C). Effect of initial Metronidazole concentration

At room temperature, coagulant dose of 150 mg / l and pH = 9, we calculated after coagulation treatment the residual concentrations of metronidazole in solution in function of different initial concentrations. Obtained results are shown in fig.4

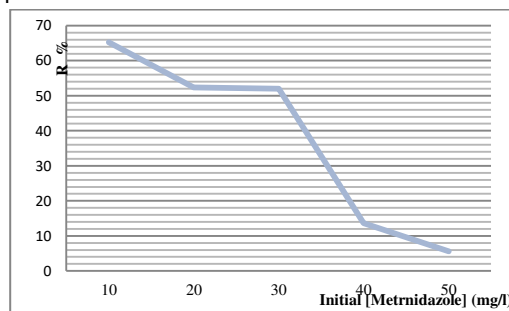


Fig.4 Effect of initial concentration on the removal of Metronidazole by coagulation-floculation.

According to the fig.4, the removal yields are higher for initial Metronidazole concentrations inferior to 30 mg/l where it varies between 58% and 73%, at higher concentrations the elimination efficiencies of metronidazole decreases.

#### 2. Elimination of metronidazole by electrocoagulation

##### A. Effect of current intensity

The current density is the most important operational parameter in the electrochemical processes because it is directly proportional with the reaction rate taking place on the electrode surfaces.

Fig.5 shows the effect of current density on the electrocoagulation treatment of Metronidazole from synthetic wastewater of 30 mg/L initial concentration without adjusting the initial pH of the solution (pH=7,2) to simulate the typical pH of municipal wastewater.

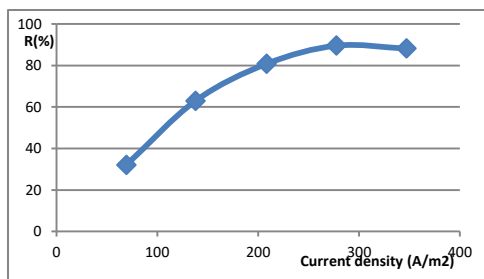


Fig.5 Effect of current density on the removal of Metronidazole by electrocoagulation

It can be seen from the fig.5 that in the range 69,44-277,77 A/m<sup>2</sup>, the Metronidazole removal efficiency yield increased significantly achieving a 89.53 %. The increase of density up to a value of 277,77 A/m<sup>2</sup> did not lead to a significant improvement of Metronidazole reduction. From data analysis it can be stated that the optimum current density is 277,77 A/m<sup>2</sup>.

#### B. Effect of pH

The initial synthetic wastewater pH is a key parameter of the electrocoagulation process. To study the pH influence on Metronidazole removal, the pH of synthetic wastewater was adjusted to the desired value that ranges from 3 to 9. Fig.6 shows the results obtained, standing out that in the process stage at pH 6 and respectively 7 and 9, removal efficiency reached its maximum level.

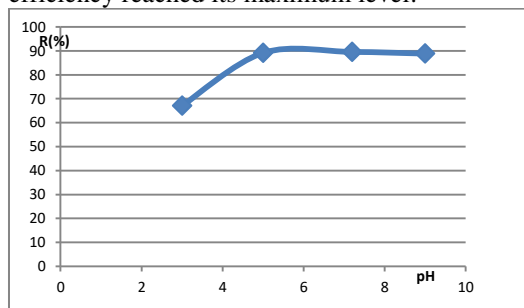


Fig.6 Effect of pH on the removal of Metronidazole by electrocoagulation.

#### c) Effect of initial concentration on elimination of metronidazole by electrocoagulation

The effect of varying initial concentration of Metronidazole (20 to 60 mg/L) on efficiency removal was investigated using the following operating parameters: current density of 277,77A/m<sup>2</sup> mA/cm<sup>2</sup> and reel pH solution.

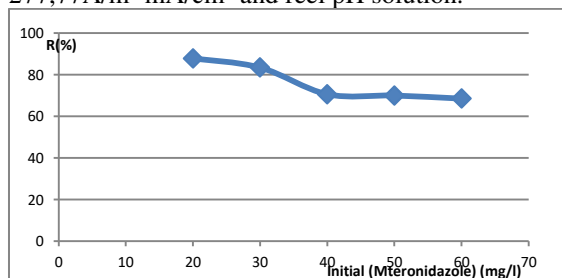


Fig.7 Effect of initial concentration on the removal of Metronidazole by coagulation-flocculation.

From Fig.7 that shows the removal yield of metronidazole versus of initial concentration, the initial concentration has a remarkable effect on Metronidazole removal which ranged from 87,73% to 68,46 % going to high concentrations. Such behavior was observed by authors [7, 8].

### 3. Optimization of treatment removal and cost analysis

At the optimum conditions, calculations done with equations mentioned above are presented in table 2.

TABLE II  
Operational cost of coagulation and electrocoagulation

	Consumed Al(g/m <sup>3</sup> )	Consumed Energy(KWh/m <sup>3</sup> )	Cost DZD/m <sup>3</sup>	Removal Efficiency (%)
CC	12,159	/	2918	79,95
EC	335,54	18700	76142,12	89,53

### IV. Conclusion

The aim of this work was to eliminate a pharmaceutical antibiotic "metronidazole" in a synthetic effluent by means of two processes: coagulation-flocculation and electrocoagulation.

It can be observed that the application of coagulation-flocculation gave almost no reduction with an optimal mass of the coagulant Al<sub>2</sub>(SO<sub>4</sub>)<sub>3</sub>, knowing that the yield reached 22,03 % at real pH solution. This yield is enhanced from 32% to 89% by electrocoagulation even with low applied current values and without adjusting pH solution. For the effect of initial pH, it's remarkable in the case of coagulation, the yield pass to 79,95% and without significant effect on electrocoagulation.

It should be noted that the study of the effect of initial Metronidazole concentration on treatment processes is significantly better with electrocoagulation than with coagulation-flocculation.

### References

- [1] Kummerer, K, "Pharmaceuticals in the Environment: Sources, Fate, Effects, and Risks", second ed. Springer, New York, 2004.
- [2] Beausse, J, "Selected drugs in solid matrices: a review of environmental determination, occurrence and properties of principal substances", Trends Anal. Chem. 23, 753-761, 2004.
- [3] Jjemba, P.K., "Excretion and ecotoxicity of pharmaceutical and personal care products in the environment". Ecotoxicology. Environ. Saf. 63, 113-130, 2006.
- [4] Homem V., Lúcia S, "Degradation and removal methods of antibiotics from aqueous matrices. A review". Journal of Environmental Management. 92 : 2304-2347, 2011.
- [5] A. Amirtharajah, C.R. O'Melia, "Coagulation process: destabilization, mixing, and flocculation", Chap. 4. In: Water Quality and Treatment: A Handbook of Community Water Supplies, 4th ed. AWWA, New York, 1990.
- [6] Lia, T., Zhua, Z., Wanga, D., Yaob, C., Tang, H., "Characterization of floc size, strength and structure under various coagulation mechanisms". Powder Technol. 168, 104-110, 2006.
- [7] Alexandra raluca miron, Ana-maria Andreea Chivu and al, "Pharmaceutical industry wastewater treatment through electrocoagulation"; revista de chimie. 65(12):1399-1406, 2014
- [8] Benny Marie Band and al, "Removal of Pharmaceuticals from Wastewater by Intermittent Electrocoagulation"; Water 9(2) 85; 2017.

# Evaluation of Acceptance Angle for High Concentration Photovoltaics Based on Triple Junction Solar Cells

Nouamane Kellil <sup>#1</sup>, Abd Elkader Aissat <sup>\*2</sup>, Sakina Atoui <sup>#3</sup>, Belkacem Bouzidi <sup>#4</sup> and Adel Mellit <sup>##5</sup>

<sup>#</sup> *Development Unit of Solar Equipment, (UDES)*

*Renewable Energy Development Center (CDER), 42004, Tipasa, Algérie*

<sup>1</sup>n.kellil@yahoo.com

<sup>3</sup>atouisakina@gmail.com

<sup>4</sup>bouzidi.belkacem@udes.dz

<sup>\*</sup> *Saad Dahleb University,*

*POB 270 BLIDA 09000. ALGERIA*

<sup>2</sup>sakre23@yahoo.fr

<sup>##</sup> *Mohamed Seddik Benyahia University,*

*POB 98 Ouled Aïssa 18000. Jijel ALGERIA*

<sup>5</sup>adelmellit2013@gmail.com

**Abstract**— High Concentration Photovoltaics (HCPV), can be considered as a new technology in the field of solar energies, is in continuous progress. The use of less expensive optical components in the design of HCPV systems reduce significantly the capital costs of the PV power plant installations and, subsequently, the levelized cost of electricity (LCOE). However, the major disadvantage of these systems is the need of a high level tracking accuracy systems. In this paper, we focus on the characteristic of Triple-Junction solar cell (TJSC) InGaP/InGaAs/Ge, with n-on-p polarity on Ge substrate at different angles of incidence of solar direct irradiation, relative to the plane of the concentrator surface for two groups of TJSC; with a secondary optic element (SOE) and without SOE., The solar simulator (SAV-HELIOS3198) of the University of Jaén, Spain was used to simulate the sun spectrum.

**Keywords**— Multijunction, CPV, Concentrator, Photovoltaic, Generator,

## I. INTRODUCTION

The MJSCs were developed in the 1990s for space applications [1]. The manufacturing cost of this type of solar cells is relatively, high (~10.000\$/kg) [2]. Nowadays, MJSC are gaining popularity in terrestrial photovoltaic applications [3]. The concentration photovoltaic systems (CPV) are one of these applications. The MJSCs are formed by a stack of different sub-cells (usually 3), with different bandgap each one, to absorb a broader range of wavelengths of the solar spectrum for a high conversion into electrical energy. These sub-cells are formed of an alloy of semiconductor elements (III and V family of the periodic table). The choice of semiconductor materials with their

concentration levels in the sub-cell is based on the value of the desired bandgap. Due to the complexity and to the high costs of manufacturing this type of solar cell, researchers have used optical concentrators, such as Fresnel lenses [4] or parabolic mirrors [5], which are less expensive and concentrate the flow of sunlight on a reduced active area of a high efficiency MJSC. CPVs generators convert direct normal irradiation (DNI), provided by the sun, into electric power [6]. This means that a dual axis sun tracker must be mounted on the CPV module (MJSC + concentrator), to maintain the concentrator surface and the DNI flux in permanent perpendicularity. This is one of the disadvantages of the CPVs. The higher the concentration rate is, the more accurate of the sun tracking systems are required. High precision is expensive and requires additional maintenance costs, which affects the cost of energy production. Here, precision is defined by the parameter of the acceptance angle. The main objective of this work is to evaluate the impact of adding the SOE to the concentrator on the electrical performance of the CPV module. This is done by characterizing the current - voltage I - V of the MJSC solar cells at different angles of tilt.

## II. MATERIAL AND RESULTS

### A. Optical devices

We used two TJSC type: 3C44A from AZUR SPACE® (Fig.1), coated with a multi-layer antireflective giving low reflectance over wavelength range 0.3 to 1.8µm, and were optimized for HCPV applications, under concentrated incident illumination (up to 300 Suns).

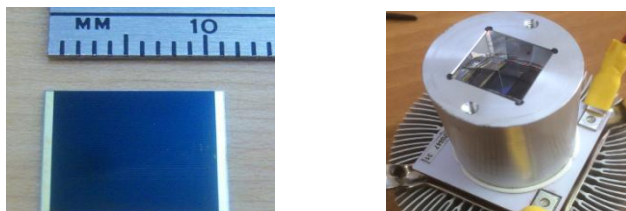


Fig. 1 Triple-junction solar cell (active area = 1cm<sup>2</sup>)

The primary optic element (POE) is a refractive square concentrator with Fresnel lens (Fig.2). The dimension of the POE is 250 x 250 mm<sup>2</sup> and a focal length of 25 cm. The second optic element (SOE) is a glass square pyramid (fig.2), which is glued on the active area of one of the two TJSC.

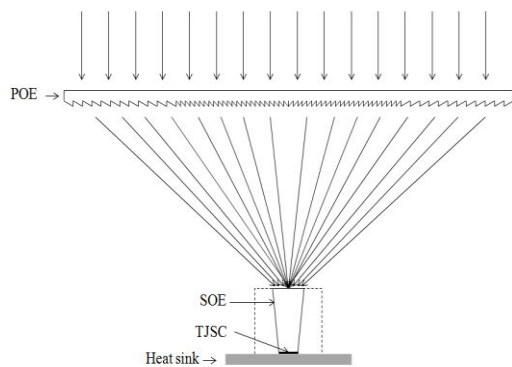


Fig. 2 CPV module with SOE.

### B. Solar Simulator

The SAV-HELIOS3198 was developed to offer adjustable DNI: from 750 to 1000 W/m<sup>2</sup>, with illuminated area of Φ2m. The spectrum is equivalent to AM1.5D.

Before starting measurements, the solar simulator spectral distribution of the luminous flux was calibrated, in order to get a similar sun spectrum. We determined an important index: the Spectral Matching Ratio (SMR), which quantifies a particular irradiance spectrum by comparing it to a reference spectrum [7]. SMR can be defined as the ratio between currents photo-generated by two sub cells under studied spectrum divided by the same ratio under reference spectrum (eq 1), which is close to AM1.5D reference conditions.

$$SMR_j^i = \frac{I_L^i / I_L^j}{I_{Lref}^i / I_{Lref}^j}$$

Where  $I_L^i$  represents the photocurrent of subcell  $i$  when illuminated with a particular spectral irradiance distribution and  $I_{Lref}^i$  stands for the photocurrent of subcell  $i$  under the reference spectrum.

Experimentally, SMR is measured by using 3 isotype cells (Fig. 3), which are spectrally calibrated. In order to simulate the sun spectral distribution, we maintained, in first step, SMR ~1, for different DNI by using different cups and different filters (table 1).

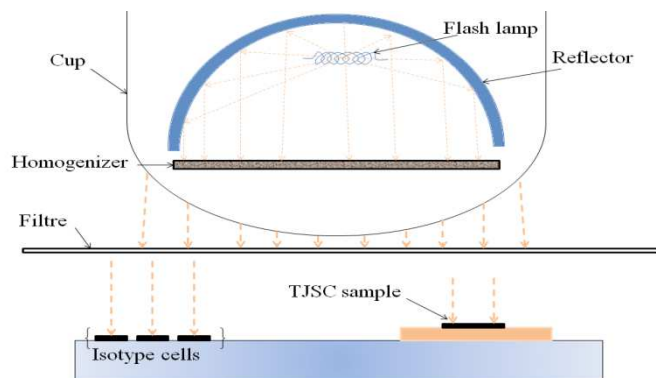


Fig. 3 Solar simulator schema [8].

TABLE I DIFFERENT CUPS WITH DIFFERENT FILTERS

Cups	Filters		
	No	00	50
Std	X	X	X
Brilliant	X	-	-
Transparent	-	X	X

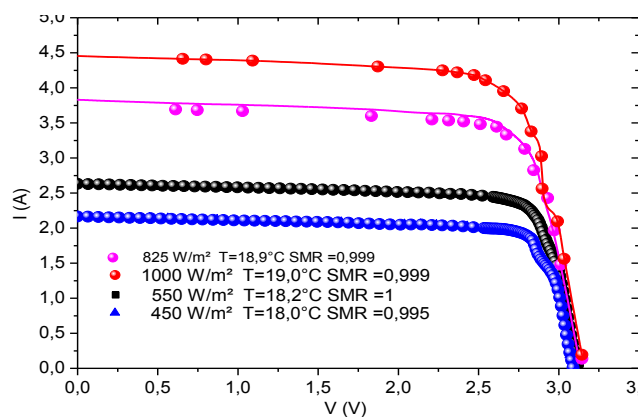


Fig. 4. TJSC I-V curves for different DNI

Fig.4 shows the behaviour of the TJSC I-V curves at different calibrated DNI.

### A. Acceptance angle

After having calibrated the spectral distribution of the light flash produced by the solar simulator to have the same distribution of the solar spectrum, (SMR ~ 1), a laser pointer was installed perpendicularly to the capture surface of the CPV module, in order to tilt, with precision (0.1°), the CPV module with respect to the incident light beam. The red dot of the laser pointer was projected on a graduated sheet, placed at 4m from the CPV module. A distance of 2cm represents a tilt of 0.1°. The acceptance angle represents the angle of tilt of the CPV module with respect to the incident light beam at which the TJSC loses 10% of its maximum power point (MPP) when the CPV module is at the normal incidence of the luminous flux (at tilt angle = 0°).

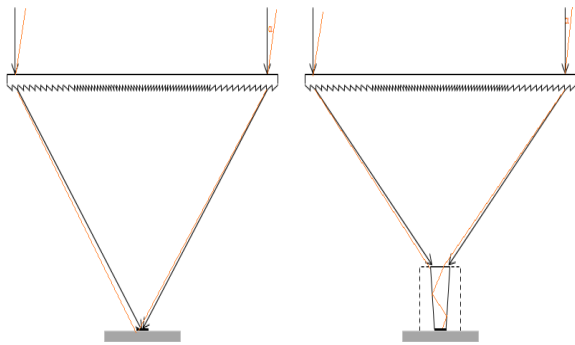


Fig.5 Acceptance angle for CPV module with SOE and without SOE

The different I-V curves of the TJSC characterization was done in ambient temperature  $T_{amb}=18^{\circ}C$ . According to the calibration of spectral distribution tests done before (Fig.4.), we choose  $DNI=850W/m^2$  ( $SMR=1$ ) to characterize the two CPV modules (with SOE and without SOE), at different angles of tilt. Fig.6. and Fig.7. show the behaviour of the I-V curves for the TJSC of the CPV module without SOE and the CPV module with SOE, respectively.

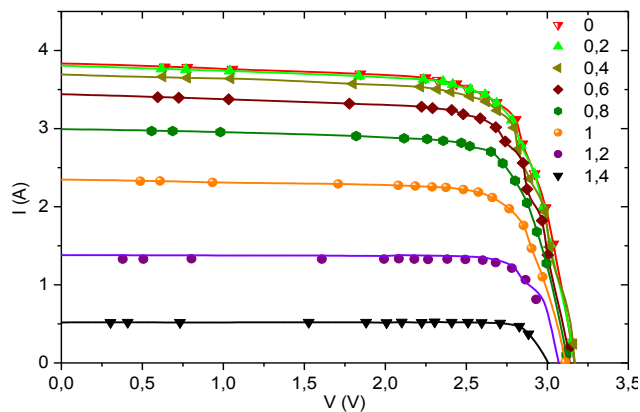


Fig.6. I-V curve for the TJSC without SOE at different tilt angle

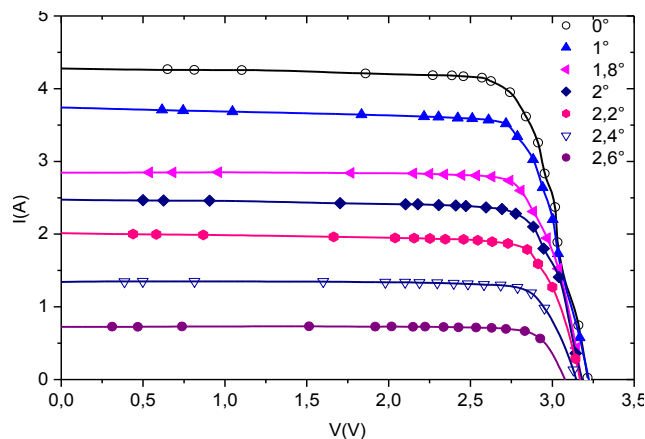


Fig.7. I-V curves for the TJSC with SOE at different tilt angle

The comparison of the normalized values of the MPP of the two CPV modules for different tilt angles is presented in Fig.8. Nevertheless, the sensitivity of the  $V_{oc}$  and the form factor (FF) of the two CPV modules to the tilt angle is not obvious (Fig.9).

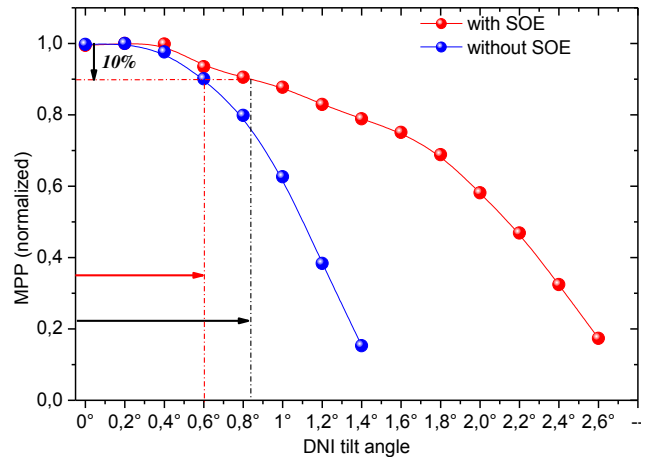


Fig.8. variation of the MPP for the two CPV modules at different tilt angle

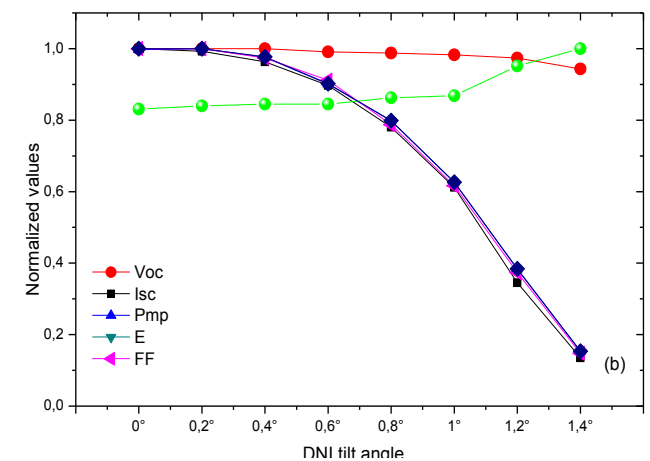
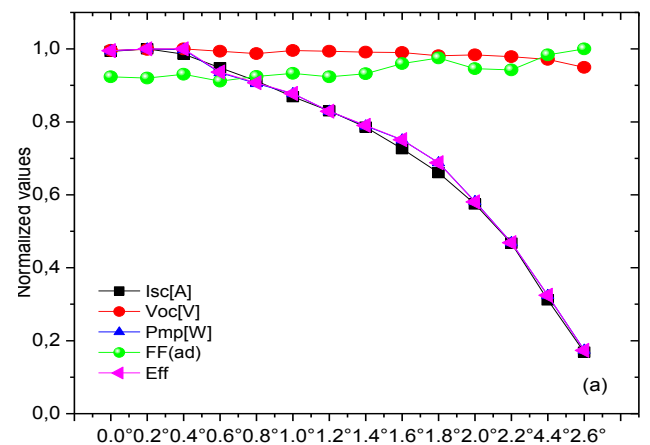


Fig.9 . Behavior of different electrical parameters of TJSC, a) with SOE (up) and b) without SOE (down) at different tilt angle ( $DNI=850W/m^2$ )

All hypertext links and section bookmarks will be removed from papers during the processing of papers for publication. If you need to refer to an Internet email address or URL in your paper, you must type out the address or URL fully in Regular font.

### III. CONCLUSION

In this work, a CPV module with secondary optical element was characterized with a concentration of 650 suns, using a solar simulator with 1.5D AM spectrum. It has been shown that SOE can increase the acceptance angle up to 40%, compared to the CPV module without SOE. This gives more tolerance to the tracking systems, which has a direct impact on the costs of electricity production using the CPV generators.

### ACKNOWLEDGMENTS

This work was conducted at the Jaen University (Spain), with the help of the members of the IDEA Solar Energy Research Group and CEAEM.

### REFERENCES

- [1] J. E. Granata, J. H. Ermer, P. Hebert, M. Haddad, R. R. King, D. D. Krut, M. S. Gillanders, N. H. Karam, and B. T. Cavicchi, “Advancements in GaInP/GaAs/Ge Solar Cells Production Status, Qualification Results and Operational Benefits,” Proc. 29th IEEE Photovoltaic Specialist Conf. (IEEE, New York, 2002), p. 824.
- [2] S. G. Bailey, R. Raffaele and K. Emery”, Progress in Photovoltaics: Research and Applications”, 10, 399 (2002).
- [3] Law, D.C.; King, R.; Yoon, H.; Archer, M.; Boca, A.; Fetzer, C.; Mesropian, S.; Isshiki, T.; Haddad, M.; Edmondson, K., “Future technology pathways of terrestrial III–V multijunction solar cells for concentrator photovoltaic systems”. Sol. Energy Mater. Sol. Cells 2010, 94, 1314–1318.
- [4] D. Romyantsev, V. M. ANDREEV, A. W. Bett, F. Dimroth, M. Hein, G. Lange, M. Z. Shvarts, and O. Sulima “, Progress in Development of All-Glas Terrestrial Concentrator Modules Based on Composite Fresnel Lenses and III-V Solar Cells” in Proceedings of the 28th IEEE Photovoltaic Specialists Conference, 1169-1172 (2000).
- [5] M Dreger, Maik Wiesenfarth, Tobias Schmid and Andreas W. Bett, “Analysis of high concentration passively cooled cpv module designs using mirror optics”, Conference: 28th EU-PVSEC 2013
- [6] Francisco J. Gómez-Gil, Xiaoting Wang and Allen Barnett “,Analysis and Prediction of Energy Production in Concentrating Photovoltaic (CPV) Installations”. Energies 2012, 5, 770-789 ; doi:10.3390/en5030770, ISSN 1996-1073
- [7] R. Núñez, C. Jin, I. Antón and G. Sala Instituto ”, Spectral Classification of Worldwide Locations Using SMR Indexes,” 12th International Conference on Concentrator Photovoltaic Systems (CPV-12), AIP Conf. Proc. 1766, 090007-1–090007-8; doi: 10.1063/1.4962113
- [8] Domínguez C., García-Linares P. (2015) Characterization of Multijunction Concentrator Solar Cells. In: Pérez-Higueras P., Fernández E. (eds) High Concentrator Photovoltaics. Green Energy and Technology. Springer, Cham.



# Performance Comparison of STATCOM and SVC Controllers for Static Voltage Stability Enhancement and Reactive Power Compensation

Mimi Belatel

*LEC Laboratory, Department of Electrotechnics  
University Mentouri Brothers of Constantine, Algeria  
belatelmimi2002@yahoo.fr*

**Abstract—** This paper compares the shunt controllers and considers the impacts of the Static Var Compensator (SVC) and Static Synchronous Compensator (STATCOM) on stability of voltage and reactive power compensation. The objective of this work is to improve the dynamic voltage control specially with increasing use of nonlinear loads; this study compares the voltage regulating system stability, the reactive power and the economical of this device. We present a modeling and simulation of STATCOM and SVC in Matlab/Simulink dynamic voltage and reactive power control. It is found that these controllers behave better than simple shunt capacitors. These FACTS provide better behavior in terms of loss reduction; voltage profile and reactive power compensation but STATCOM have a much better performance as compared to SVC.

**Keywords—** Comparison; FACTS, STATCOM; SVC; Control; Voltage stability; Power compensation.

## I. INTRODUCTION

The Modern electric power utilities are facing many challenges problems due to ever increasing demand and voltage is attending instability by increases in loss and various power quality problems [1]. In recent years, the increase in peak load demand and power transfers between utilities has elevated concerns about system voltage security. Voltage collapse has been deemed responsible for several major disturbances and significant research efforts are under way in an effort to further understand voltage phenomena. Voltage stability is the ability of a power system to maintain adequate voltage magnitude so that when the system nominal load is increased, the actual power transferred to that load will increase. The main cause of voltage instability is the inability of the power system to meet the demand for reactive power. Voltage instability is the cause of system voltage collapse, in which the system voltage decays to a level from which it is unable to recover. Voltage collapse may lead to partial or full power interruption in the system. There are two types of voltage stability based on simulation time; static voltage stability and dynamic voltage stability. Static analysis involves only the solution of algebraic equations and therefore is computationally less extensive than dynamic analysis. Static voltage stability is ideal for the bulk of studies in which a voltage stability limit for many pre-contingency and post

contingency cases must be determined. Voltage instability is mainly associated with reactive power imbalance [2-3].

Reactive Power, also known as use-less/watt-less power, is the power merely absorbed and returned in load due to its reactive properties; in this case, energy is first stored and then released in the form of magnetic or electrostatic field in inductors and capacitors. It is measured in Volt-Ampere reactive [4]. Advances in power electronic technologies together with sophisticated electronic control methods made possible the development of fast static compensators namely Flexible AC Transmission Systems. The FACTS technology has become one of the most valuable compensation techniques, because it applies the latest advances in power electronics to achieve additional and more effective control of the parameters of the electrical systems. This represents the most efficient combination of conventional primary equipment, high power semiconductor devices, microelectronics and telecommunications equipment, allowing a most flexible power electric system [5]. The role of FACTS devices such as SVC and STATCOM in system performance improvement is specified: stability improvement of network system, power swings damping, voltage regulation, increase of power transmission and chiefly as a supplier of controllable reactive power to accelerate voltage recovery after fault occurrence, are considered as improvement factors [6]. In this paper a comparison of performances between SVC and STATCOM controllers are presented. The objective is to compare the merits and demerits of two FACTS devices, namely, SVC and STATCOM. A large portion of this work is concentrated on the study of voltage stability and reactive power compensation.

## II. DESCRIPTION OF STATCOM AND SVC

One of the major causes of voltage instability is the reactive power limit of the system. Improving the system's reactive power handling capacity via Flexible AC transmission System (FACTS) devices is a remedy for prevention of voltage instability [2].

### A. Static Synchronous Compensator (STATCOM)

The STATCOM is a main member of the FACTS family of power electronic based controllers. It has been studied for many years and probably the most widely used FACTS device

in today's power system [7]. The STATCOM is shunt connected reactive power compensation device that is capable of generating and or absorbing reactive power and in which the output can be varied to control the specific parameters of an electric power system [8]. The STATCOM is made up of a shunt transformer, a voltage source converter (VSC), a DC capacitor and a controller. If there is no energy storage device coupled to the DC link and the losses are neglected, neither shunt converter is capable of absorbing or generating real power so that only operating in the reactive domain is possible. The reactive power exchange of STATCOM with the AC system is controlled by regulating the output voltage amplitude of VSC. If the amplitude is increased above that of the AC system, the current flows through the shunt transformer from the STATCOM to the AC system, and the device generates reactive power (capacitive). If the amplitude is decreased to a level below that of the AC system, then the current flows from the AC system to STATCOM. The capacitor is used to maintain DC voltage to the VSC which itself keeps the capacitor charged to the required levels. Thus, by controlling the VSC output voltage lead or lag with respect to the AC system voltage, the capacitor DC voltage can be decreased or increased, respectively, to control the reactive power output of the device. The structure of a STATCOM with phase and voltage controls is depicted in Fig 1 [9].

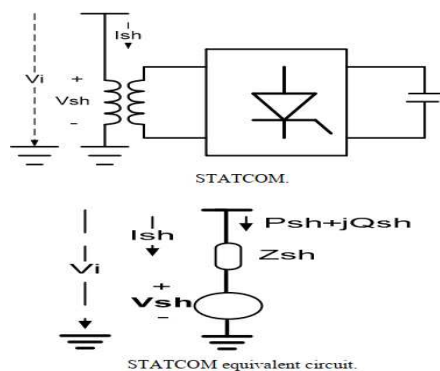


Fig. 1. Structure of STATCOM

The first STATCOM has been designed in 1990. This is a voltage converter based on GTO or IGBT powered by batteries of capacitors. The assembly is connected in parallel to the network through a coupling transformer.

$$Q_{sh} = \frac{|V_k|^2}{X_{sh}} - \frac{|V_k||V_{sh}|}{X_{sh}} \cos(\theta_k - \theta_{sh}) \quad (1)$$

- $|V_k| > |V_{sh}|$  then  $Q_{sh}$  becomes positive and the STATCOM absorbs reactive power.
- $|V_k| < |V_{sh}|$  then  $Q_{sh}$  becomes negative and the STATCOM supplies reactive power.

STATCOM is a generator whose capacitive or inductive output current can be controlled independent of the AC system voltage. It is a solid state switching converter capable to generate or absorb reactive power at its output terminals. The steady state V-I characteristics of the STATCOM are shown in Fig. 2: [7], [10].

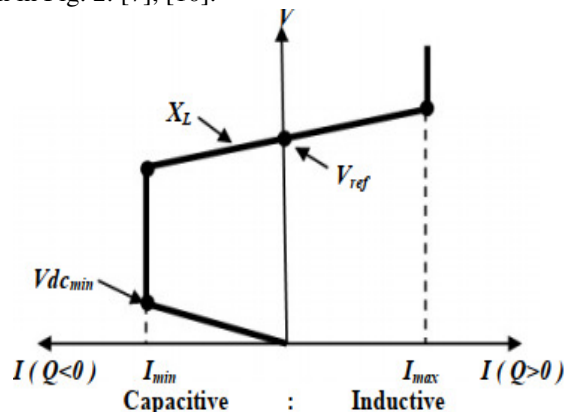


Fig. 2. Terminal characteristic of STATCOM

### B. Static Var Compensator (SVC)

The Static Var Compensator (SVC), is a first generation FACTS controller, it is a variable impedance device where the current controlled using back to back connected thyristor valves. The application of thyristor valve technology to SVC is an offshoot of the developments in HVDC technology. SVC provides an excellent source of rapidly controllable reactive shunt compensation for dynamic voltage control through its utilization of high-speed thyristor switching/controlled devices. Typical TSC-TCR type SVC configuration is shown in Fig 3.

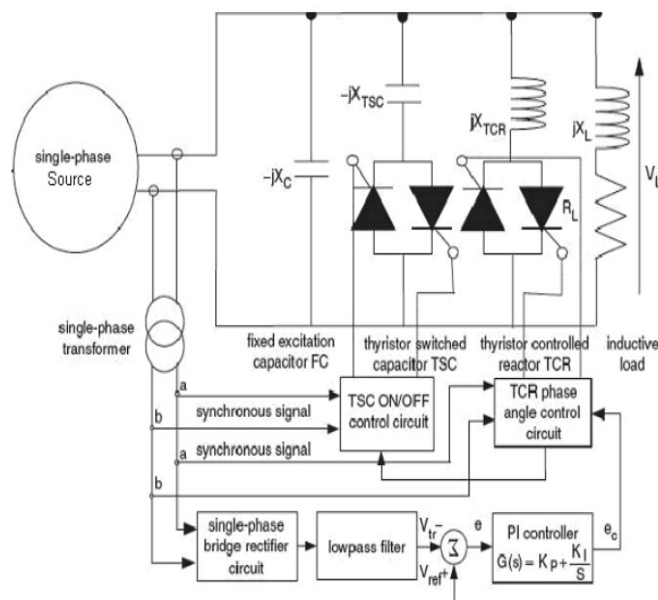


Fig. 3. TCR-TSC type SVC with control circuit

Hence SVC can supply dynamic reactive power support for maintaining the constant voltage which will enhance the generator and voltage stability margins tremendously.

$$Q_c = \frac{V^2}{X_c} \quad (2)$$

Therefore  $X_c = \frac{V^2}{Q_c}$  and  $X_c = \frac{1}{2\pi fC}$

In SVC circuit  $X_c$  is in parallel with  $X_1$

$$Q_{tcr(\alpha)} = Q_{ref} - Q_{min} \quad (3)$$

$$X_1 = \frac{V^2}{Q_{tcr(\alpha)}} \quad (4)$$

$$Q_{SVC} = Q_c - Q_{tcr(\alpha)} \quad (5)$$

The SVC steady-state response will follow the voltage-current (V-I) characteristic curve shown in Fig. 4. The voltage-current characteristic is used to illustrate the SVC rating and steady-state performance with the typical steady state operating region [11-14].

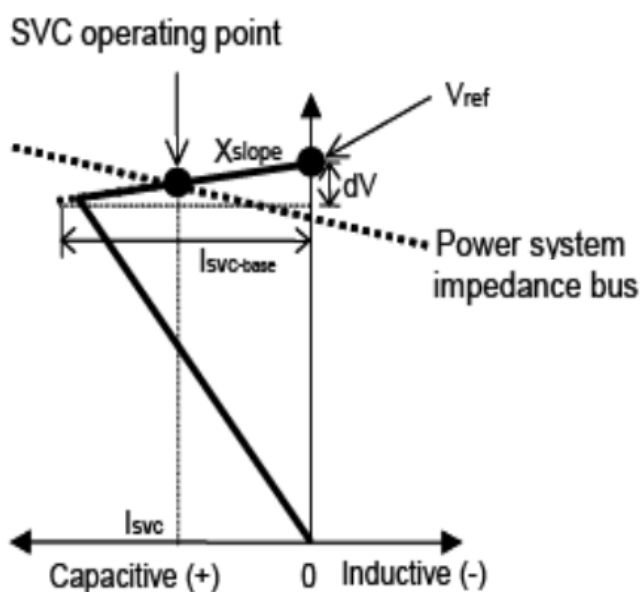


Fig.4. Steady state volt-current (V-I) characteristic of a SVC

### III. COMPARISON BETWEEN STATCOM AND SVC

Until now, the STATCOM and SVC systems are the FACTS most connected to power systems; however, while sharing the same operating principle, they present a significant technology gap [15].

#### A. General evaluation of STATCOM and SVC

Evaluation of STATCOM and SVC devices is shown in table I below [4]:

TABLE I. Evaluation of STATCOM and SVC

Criteria	STATCOM	SVC
<b>Operating principle</b>	Controlled voltage source	Controlled shunt impedance
<b>Reactive power regulation</b>	2x ±50 MVar	±100 MVar
<b>Space requirement</b>	Smaller than SVC (59x45 m <sup>2</sup> )	Large (60x85 m <sup>2</sup> )
<b>Pack solution</b>	Containerized solution	Open pack solution
<b>Dependency of the current output from the voltage level in the point of connection</b>	Non-Linear	Linear
<b>Dependency of the reactive power output from the voltage level in the point of connection</b>	Linear	Quadratic
<b>Reactive Power generation during the three phase short circuit scenario</b>	Moderate	Low
<b>Overload capability</b>	Yes (±25% for 1s)	No
<b>Response time</b>	Faster than SVC	Fast
<b>Maintenance and service requirements</b>	Low	High
<b>Cost</b>	\$55 to \$70 per kVar	from \$40 to \$60 per kVar
<b>Reduce Harmonics</b>	Additional control methods with complementary circuits	Multilevel pulse width modulation and 3 levels inverter technique

**B. Comparison of VI and VQ curves in STATCOM and SVC**

Considering the curves which relate voltage magnitude to current (VI) or reactive power (VQ) for the aim of voltage support capabilities is common. A decrement in system load level results in an increase in voltage magnitude at all system nodes. Both the SVC and the STATCOM holds the voltage magnitude by absorbing inductive current. On the other hand, an increase in the system load level produces a decrease in nodal voltage magnitudes. For this condition, the devices maintain the voltage magnitude by injecting a capacitive current. In Fig 5, there are the VI and VQ curves for the STATCOM and the SVC.

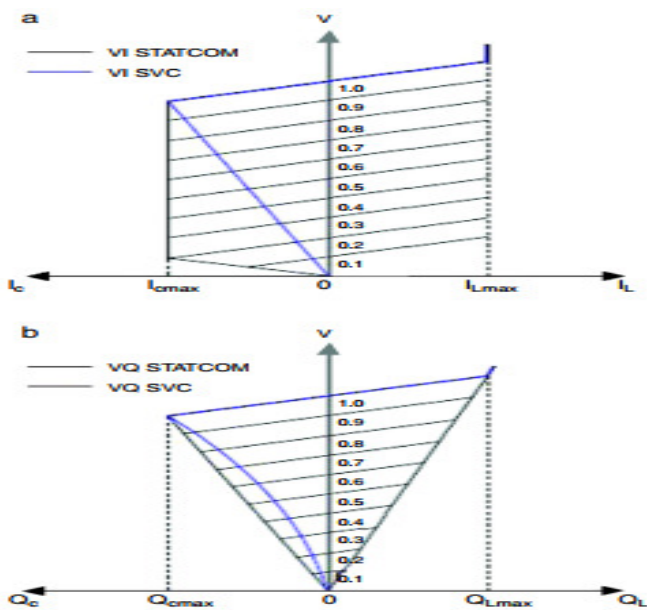


Fig. 5. (a) VI and (b) VQ curves for STATCOM and SVC

We see that STATCOM's ability to provide current compensation is more extensive than the SVC's; even at low voltages levels the STATCOM can continue to supply the full rated reactive current to the system, i.e., the output current is independent of the system voltage, whereas the compensating current of the SVC decreases linearly with the system voltage [15].

**C. Simulation model of STATCOM and SVC**

STATCOM and SVC are connected approximately middle point of the transmission line. In that test model two generators are connected both end side. The three phase mutual inductance connected in series with the first generator. B1, B2 and B3 are used for measurement of voltage and current of transmission line. We are considering in test model the three phase section line and three phase distributed parameter line. The three loads are connecting parallel with transmission line that is 100MW, 2MW, 300MW. We are also connected a fault for creating unbalance in transmission line by manually. After creating a fault the disturbances in

transmission line can be compensated by STATCOM and SVC [16-17].

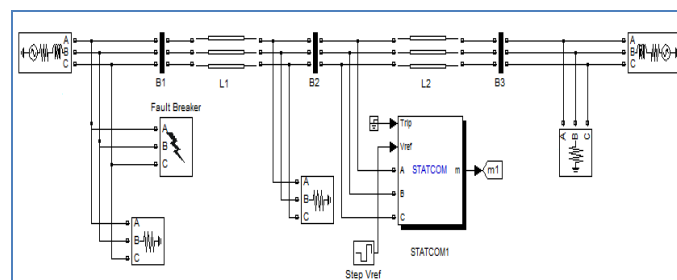


Fig. 6. Simulink model of STATCOM for voltage regulation

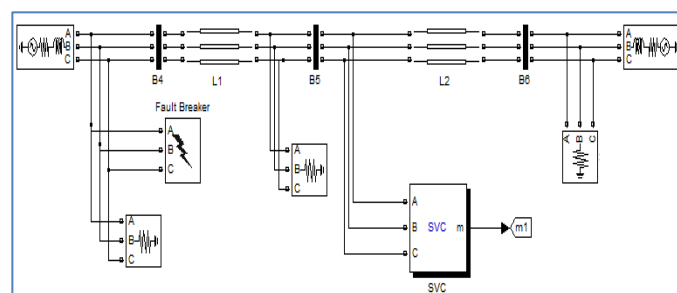


Fig. 7. Simulink model of SVC for voltage regulation

Figure 8 displays the  $V_{ref}$  and  $Q_{ref}$  signals at the (STATCOM/SVC) bus.

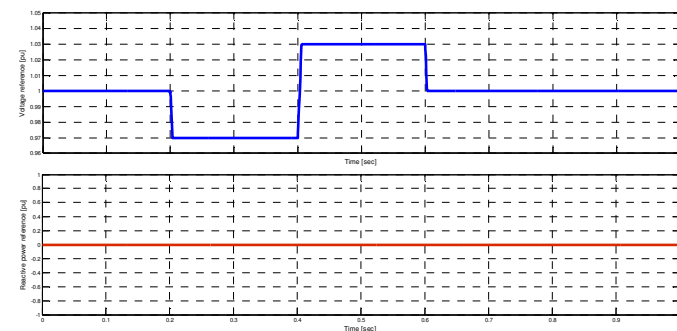


Fig. 8. Dynamic references at the (STATCOM/SVC) bus

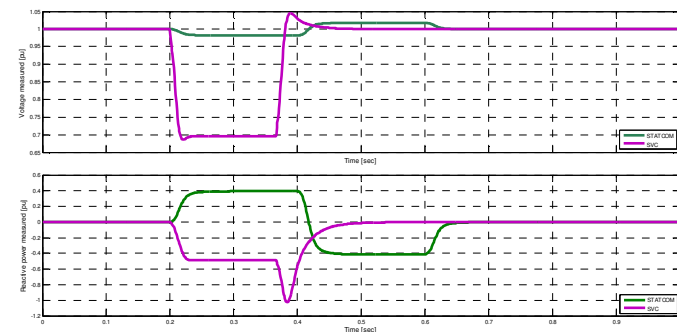


Fig. 9. STATCOM and SVC dynamic responses (loads without fault)

Figure 9, shows that the STATCOM measured voltage  $V_m$  follows the reference value  $V_{ref}$ . This implies that STATCOM is a very good voltage regulator. The reactive power absorbed/generated by the STATCOM,  $Q_m$  together with the reference one,  $Q_{ref}$ . Positive value of  $Q_m$  represents the reactive power absorbed by the STATCOM while negative value indicates the reactive power generated. The two Figures certify that the STATCOM absorbs reactive power when the AC system voltage rises and generates reactive power when the AC system voltage falls. The SVC voltage tries to behave like a reference voltage, If the transmission line voltage decreases, at that time SVC act as a capacitive and vice-versa.

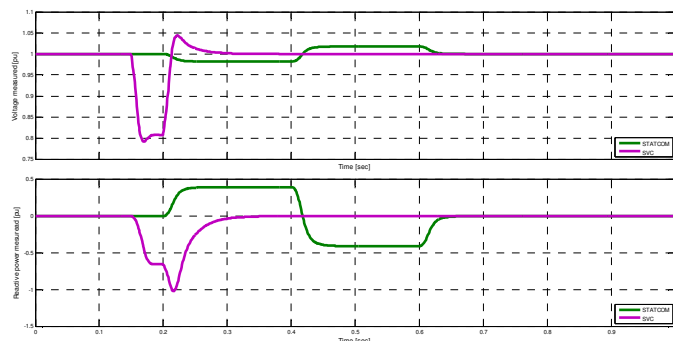


Fig. 10. STATCOM and SVC dynamic responses (fault in phase A)

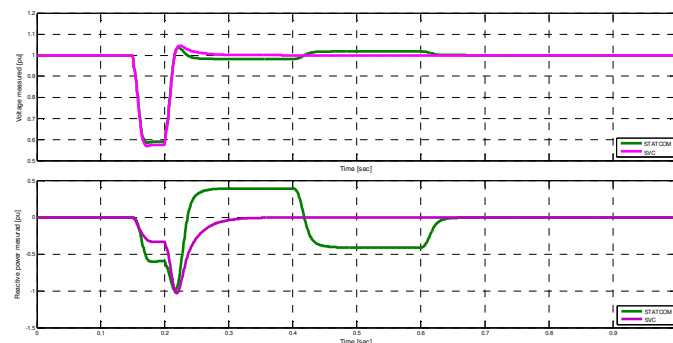


Fig. 11. STATCOM and SVC dynamic responses (fault in phases A, B)

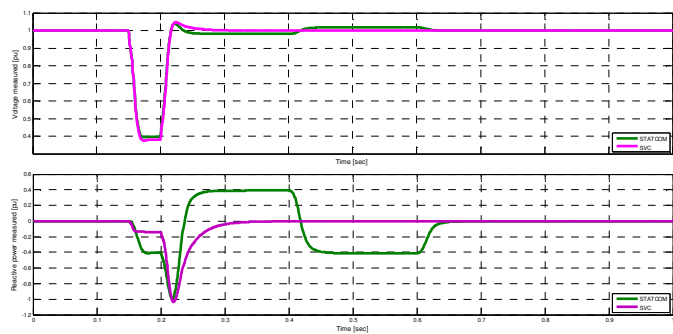


Fig. 12. STATCOM and SVC dynamic responses (fault in phases A, B, C)

From figures 9 to 12, we can see that the STATCOM provides a better voltage profile compared to SVC. The best location for reactive power compensation as far as improvement of static voltage stability margin is concerned.

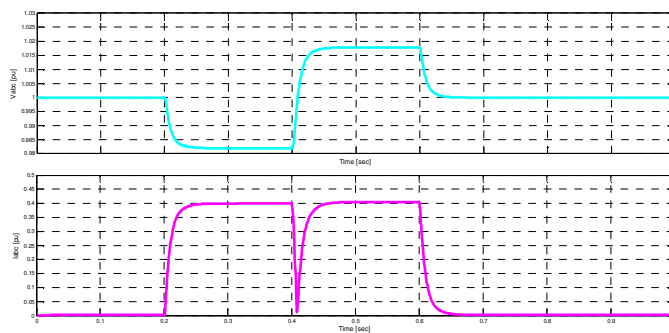


Fig. 13. Voltage and current in STATCOM (fault in phase A)

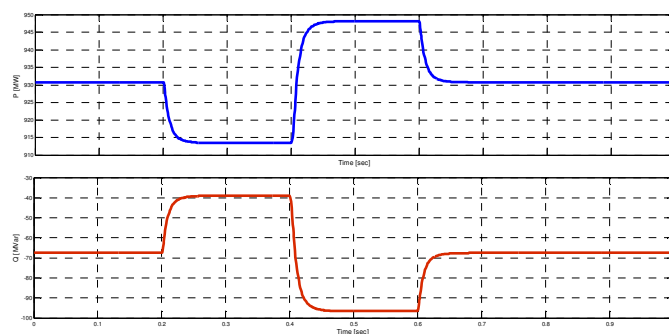


Fig. 14. P and Q in STATCOM (fault in phase A)

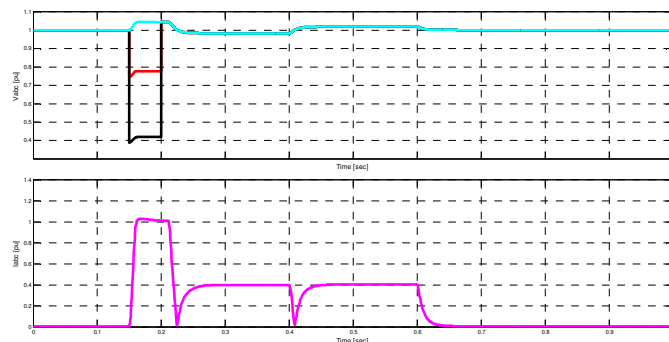


Fig. 15. Voltage and current in STATCOM (fault in phases A and B)

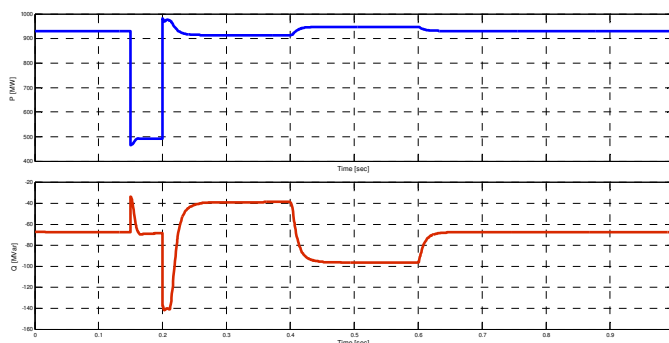


Fig. 16. P and Q in STATCOM (fault in phases A and B)

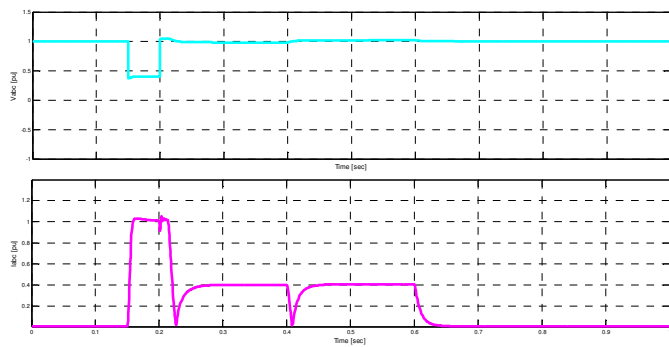


Fig. 17. Voltage and current in STATCOM (fault in phases A, B and C)

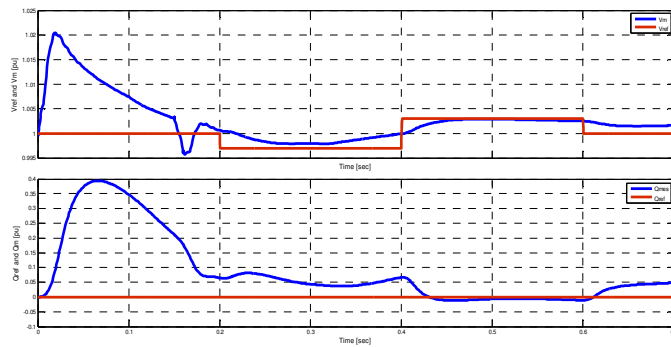


Fig. 20. STATCOM Voltage and reactive power (fault in phases A, B and C)

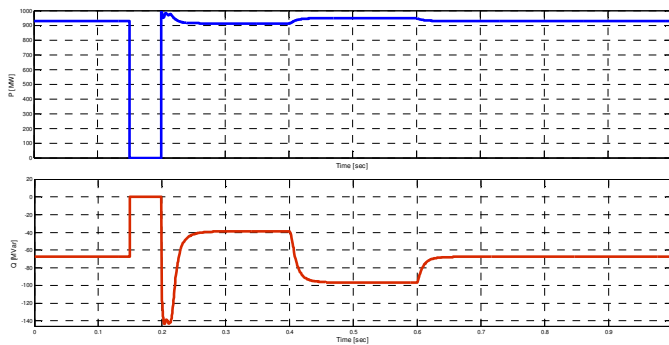


Fig. 18. P and Q in STATCOM (fault in phases A, B and C)

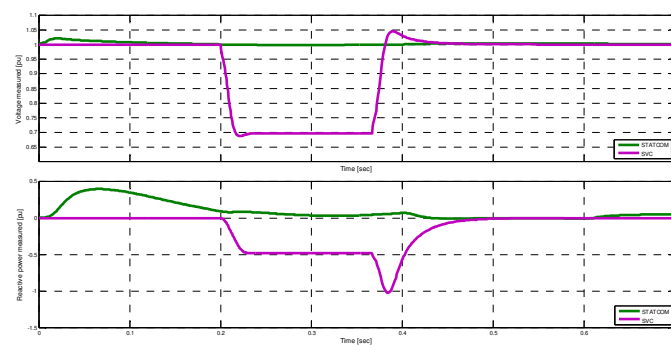


Fig. 21. STATCOM and SVC dynamic responses (fault in phase A, B and C)

Figures 13 to 18, determine the response of the voltage, current, active and reactive power system and determine the stability of the network. Three studies of power network are modeled for transient stability to obtain the operating performance of STATCOM during the disturbance with fault in phase A, in phases B and C and in the three phases. It is found that these controllers significantly increase the load ability margin of power system. And it also shows that STATCOM has the ability to provide more capacitive power during fault situation over SVC. Hence, STATCOM exhibits faster response than SVC.

One of the major causes of voltage instability is the reactive power limit of the electric system. Improving the system's reactive power handling capacity via STATCOM and SVC is a remedy for prevention of voltage instability and hence voltage collapse. Figures 20 and 21, compares the shunt compensator, STATCOM and SVC in static voltage and reactive power stability improvement in network presented in Fig. 19 (expanded test network of the grid presented in Fig. 6 and Fig.7). Performance results are compared under different operating system conditions for the second network test system.

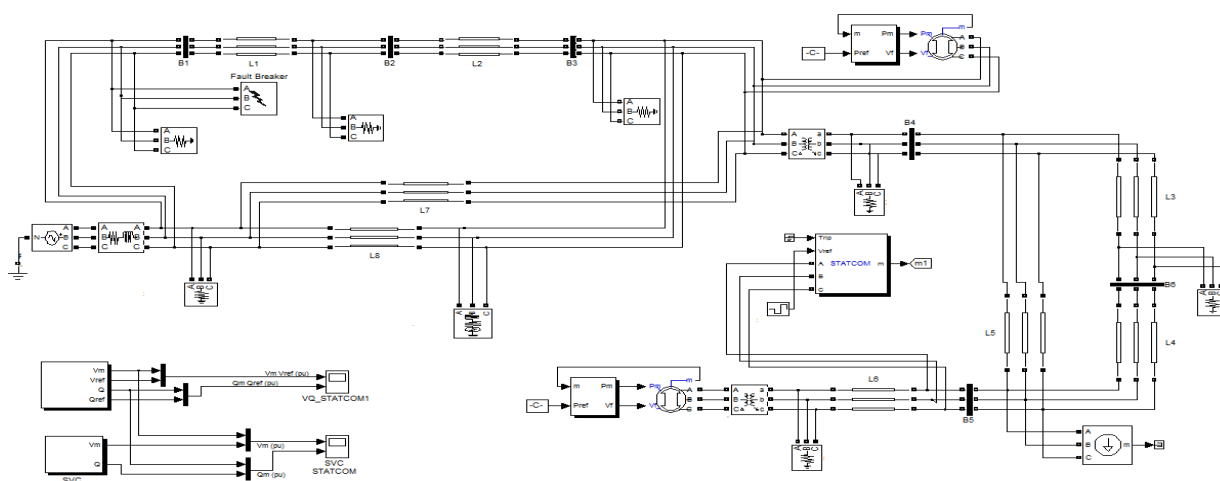


Fig. 19. Simulink model of (STATCOM/SVC) for voltage and reactive power regulation

#### IV. CONCLUSION

The FACTS technology has become one of the most valuable compensation techniques. A comparison study of STATCOM and SVC in static voltage stability improvement is presented. Various merits and demerits of the shunt compensation devices are presented. STATCOM and SVC increase the static voltage stability margin and power transfer capability. But these controllers are expensive when compared to the shunt capacitor. Simulations using Matlab/Simulink are carried out to verify the performance of the proposed controllers. We can see that STATCOM is better compared with that the conventional SVC. The ability to provide more reactive power during fault situations is one of the most important advantages of the STATCOM over the SVC, which helps for faster recovery of the system during faults situations.

#### REFERENCES

- [1] S.O.Farees, M.T.L. Gayatri and K. Sumanth, "Performance comparison between SVC and STATCOM for reactive power compensation by using fuzzy logic controller", *International Journal of Innovative Technology and Research*, Vol. 2, Issue 3, 2014, pp. 991-994.
- [2] M.A. Kamarposhti and M. Alinezhad, "Comparison of SVC and STATCOM in static voltage stability margin enhancement", *World Academy of Science, Engineering and Technology, International Journal of Electrical and Computer Engineering*, Vol.3, No.2, 2009, pp. 297-302.
- [3] A.S.Yome and N. Mithulananthan, "Comparison of shunt capacitor, SVC and STATCOM in static voltage stability margin enhancement", *International Journal of Electrical Engineering Education*, Vol. 41, N°. 2, 2004, pp. 158-171.
- [4] A.S. Sengar, R. Chhajjer, G. Fandi and F.O. Igbinovia, "Comparison of the operational theory and features of SVC and STATCOM", *Poster 2015*, Prague, May 2014, pp. 1-6.
- [5] E.B. Martinez and C.A. Camacho, "Technical comparison of FACTS controllers in parallel connection", *Journal of Applied Research and Technology*, Vol. 15, 2017, pp. 36-44.
- [6] M. Sedighzadeh, A. Rezazadeh and M. Parayandeh, "Comparison of SVC and STATCOM impacts on wind farm stability connected to power system", *International Journal of Engineering and Applied Sciences (IJEAS)*, Vol.2, Issue 2, 2010, pp.13-22.
- [7] A. Bhargava, B. Das and V. Pant, "Load flow study of large power systems with multiple STATCOMs", *National Power System Conference, NPSC 2014, Indian Institute of Technology, Madras*, 2014, pp. 31-35.
- [8] C. Nandi, S. Deb, M.D. Barma, and A.K. Chakraborty, "Study and simulation of the SVC and STATCOM effect on voltage collapse and critical fault clearing time", *International Journal of Modeling and Optimization*, Vol. 2, No. 4, 2012, pp. 462-465.
- [9] E.K. Abharian, M. Karimi, and P. Farhadi, "STATCOM controller design based on MLP for power flow control", *International Journal of Modeling and Optimization*, Vol. 1, No. 4, 2011, pp. 327-333.
- [10] M. Laouer, A. Mekkaoui and M. Younes, "STATCOM and capacitor banks in a fixed-speed wind farm", *The International Conference on Technologies and Materials for Renewable Energy, Environment and Sustainability, TMREES14, Published in Energy Procedia*, Vol. 50, 2014, pp. 882-892.
- [11] V. Yarlagaadda, B.V.S. Ram and K.R.M. Rao, "Testing and control of TSC-TCR type Static Var Compensator (SVC) using microcontroller", *International Journal of Control and Automation*, Vol. 5, N°. 3, 2012, pp. 277-286.
- [12] M. Biswas and K. Das, "Voltage level improving by using Static VAR Compensator SVC", *Global Journal of Researches in Engineering*, Vol. 11, Issue 5, 2011, pp. 13-18.
- [13] M.A. Kamarposhti and M. Alinezhad, "Comparison of SVC and STATCOM in static voltage stability margin enhancement", *International Journal of Electrical and Electronics Engineering*, Vol. 4, Issue. 5, 2010, pp. 323-328.
- [14] B. R. Rajeev and G.N. Madhu, "Voltage enhancement assessment using SVC FACTS controller", *International Journal of Electrical, Electronics and Data Communication*, Vol. 2, Issue. 10, 2014, pp. 40-45.
- [15] E.B. Martínez and C.Á. Camacho, "Technical comparison of FACTS controllers in parallel connection", *Journal of Applied Research and Technology*, Vol. 15, 2017, pp. 36-44.
- [16] P. Kumar, A.S. Mane, P.P. Patil, R.M. Hatkar, N.P. Pangam and S.V. Sawant, "Application of FACTS device via STATCOM and SVC with comparison", *Proceedings of National Conference on Emerging Technologies in Electrical and Electronics Engineering under TEQIPII*, February 2014, pp. 1-5.
- [17] N.B. Kadandani and Y.A. Maiwada, "Simulation of static synchronous compensator (STATCOM) for voltage profile improvement", *Innovative Systems Design and Engineering*, Vol.6, No.7, 2015, pp. 1-8.

# A new harmonic reduction approach based on signal filtering in solar inverter's controllers

Walid Rahmouni

Laboratoire de Développement Durable  
de l'Énergie Electrique (LDDEE)  
Université des Sciences et de la  
Technologie d'Oran (USTO-MB)  
Oran, Algeria  
walid.rahmouni@univ-usto.dz

Ghalem Bachir

Laboratoire de Développement Durable  
de l'Énergie Electrique (LDDEE)  
Université des Sciences et de la  
Technologie d'Oran (USTO-MB)  
Oran, Algeria  
ghalem.bachir@yahoo.fr

Michel Aillerie

Laboratoire Matériaux Optiques,  
Photonique et Systèmes (LMOPS)  
Université de Lorraine  
Metz, France  
aillerie@metz.supelec.fr

**Abstract**— Grid-connected photovoltaic technology has gained an increasing interest worldwide as a clean source of energy. Such system has one major drawback which is the harmonics it generates. Therefore, optimal control is of utmost importance for power quality improvement and low harmonic injection. The most widely used controllers are the Proportional-Integral controllers based on synchronous reference frame. These controllers are affected by the signal noises and interferences which can generate undesired control activity. This in turns lowers the power quality.

This paper proposes a simple harmonic reduction strategy based on signal filtering. A first order filter is implemented on the main inputs of the controller; which are the set-point, the feedback current and the feed-forward voltage. An overview of the system's main components is presented. Then, the validity of the proposed method is proved through various simulations carried out on Simulink-Matlab. The Fast Fourier Transformation is used for power quality assessment.

The results obtained clearly show the validity of the proposed strategy.

**Keywords**—FFT, PI Controller, Grid-tied PV system, Filter, Harmonic reduction (key words)

## I. INTRODUCTION

Nowadays renewable energy sources become more and more important due to energy costs and environmental issues [1]. Currently, special attention is given to the photovoltaic technology. It has grown more than 40% per year since last decades and it is expected to experience larger growth in the future due to cost reduction and increasing efficiencies [2 3].

Power converters play a vital role in photovoltaic power generation systems [4]. An inverter based interface is usually implemented for grid connection [5 6]. Their control is often based on an outer active-reactive power control loop and an inner Current control loop. A Phase-Locked Loop (PLL) technique ensures the grid synchronization [7]. The Synchronous Reference Frame (SRF) based Proportional-Integral (PI) controller is commonly used for the inverters' current control [1]. It is the most popular type of controller due to its ability to decouple the active and reactive components of the current [8].

One serious power quality issue in photovoltaic Systems is the harmonics it generates. Consequently, providing a high quality sinusoidal output with minimal distortion is a major requirement for the controllers [9]. However, Most of the measured converters' signals are affected by switching noises and other disturbances which can generate undesired control activity. The performances are then reduced and the harmonics are worsen [10 11].

A natural idea to attenuate the effect of these noises is to remove them before measured signals are used in the controller. This idea has been realized in PID controllers by filtering methods where low-pass filters are employed to filter out the high frequency component of noise [12].

In this paper, the filter based approach is extended to the PI controllers used in photovoltaic systems. The effect of filtering techniques is investigated over the Total Harmonic Current Distortion with Fast Fourier Transformation (FFT). The proposed strategy focuses on the major input signals of the PI controller which are the set-point from the DC-link voltage, the measured current and the grid voltage in feed-forward. Simulations through Simulink-Matlab are carried out to assess the impact on harmonics generation.

## II. SYSTEM'S STRUCTURE

Photovoltaic is the technology that converts solar energy into electricity [13]. The system under consideration represents a two-stage topology of the grid-tied PV system. The PV array converts solar irradiation into electrical energy. The DC-DC boost converter with a Maximum Power Point Tracker (MPPT) optimizes the PV output. A DC-link capacitor enhances the DC output voltage stability, and therefore, reduces the effect of fluctuation on the AC output [14]. A two-level three-phase inverter transfers the generated PV power from the boost converter to the main grid through a passive filter [15].

Fig 1 depicts a typical transformer-less PV system.

### A. Photovoltaic array

A PV array is mainly constituted of PV cells, which converts the sunlight falling on it directly into electricity by photovoltaic effect [16]. The simplest equivalent circuit of a solar cell is a current source in parallel with a diode. The output of the current source is directly proportional to the light falling on the cell [17].

The single diode model of PV cell is shown in fig 2.

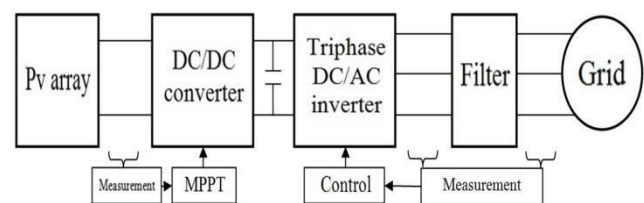


Fig. 1. Grid connected PV system



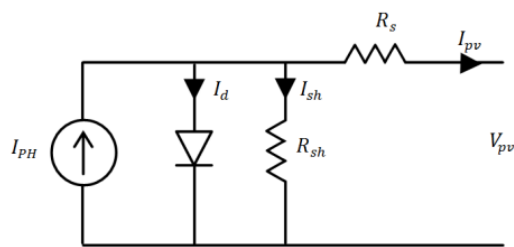


Fig. 2. Equivalent model of a photovoltaic cell

The mathematical model of the PV cell can be presented by the following equations [18 19]

$$I_{pv} = I_{PH} - I_d - I_{sh} \quad (1)$$

When supposing the parallel shunt resistor  $R_{sh}$  is not infinite, the shunt current  $I_{sh}$  can be calculated as follows:

$$I_{sh} = \frac{V_d}{R_{sh}} = \frac{V_{pv} + I_{pv} R_s}{R_{sh}} \quad (2)$$

The Shockley diode equation is:

$$I_d = I_{sat} \left[ \exp \left( \frac{V_{pv} + (I_{pv} R_s)}{A U_T} \right) - 1 \right] \quad (3)$$

The expression of the current supplied by the cell  $I_{pv}$  is then defined by:

$$I_{pv} = I_{PH} - I_{sat} \left[ \exp \left( \frac{V_{pv} + (I_{pv} R_s)}{A U_T} \right) - 1 \right] - \frac{V_{pv} + (I_{pv} R_s)}{R_{sh}} \quad (4)$$

Knowing that :

- $I_{sat}$  : Diode Current (A);
- $I_{ph}$  : The photo-generated current;
- $R_s$  : The series resistor;
- $R_{sh}$  : The shunt resistor;
- $U_T$  : The thermal potential;
- $A$  : Ideality factor;

### B. DC/DC – Boost converter

The power output of the Solar PV module varies with solar irradiation and solar cell temperature [16].

To extract the maximum power from the panel, a DC-DC converter is used. It's the interface that allows adaptation between the PV panel and the load or the grid [19]. The topology of a DC-DC boost converter is shown in Fig 3.

The most commonly used MPPT technique is the Perturb and Observe algorithm (P&O), due to its ease of implementation in its basic form [17]. Its flow chart is given in Fig 4.

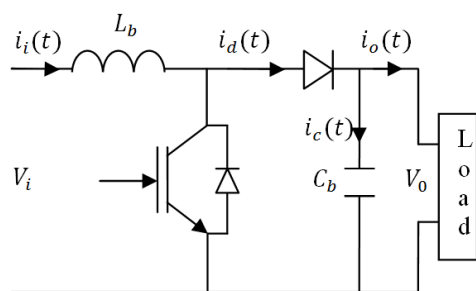


Fig. 3. DC-DC boost converter

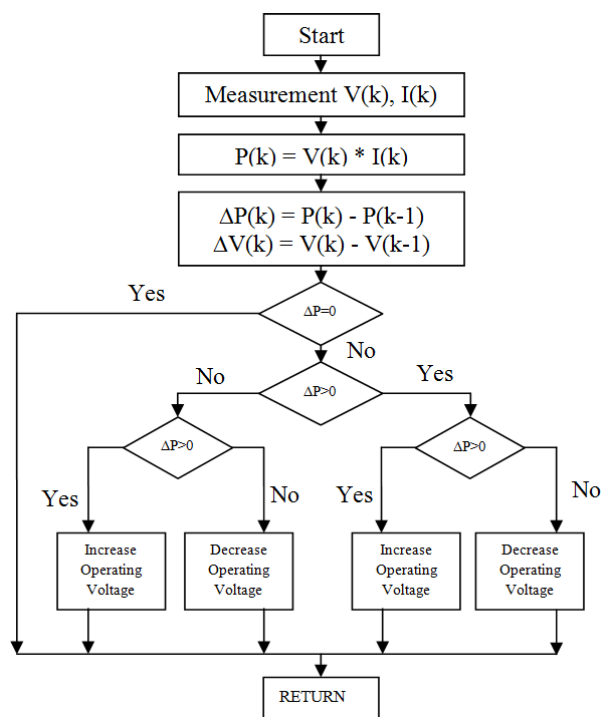


Fig. 4. Flowchart of P&O algorithm

### C. DC/AC- Inverter

An inverter is a power electronic device, which generates a sinusoidal AC output with controllable frequency and magnitude from a DC input. The inverter in the grid-tied PV system acts as an interface between energy sources and the utility grid [14]. In our work a voltage source inverter (VSI) is used, its general structure is shown in Fig 5.

The power circuit of the three-phase inverter consists of six bidirectional switches to connect the three-phase grid through a passive filter. The two switches of each inverter leg must operate in a complementary mode to avoid the short circuit of the DC-Link [15].

The switch is controlled by a PWM generator in order to obtain the same waveform as the reference signal. The PWM signal is obtained by comparing a triangular signal (carrier) to the reference signal obtained from the controller as shown in Fig 6 [20].

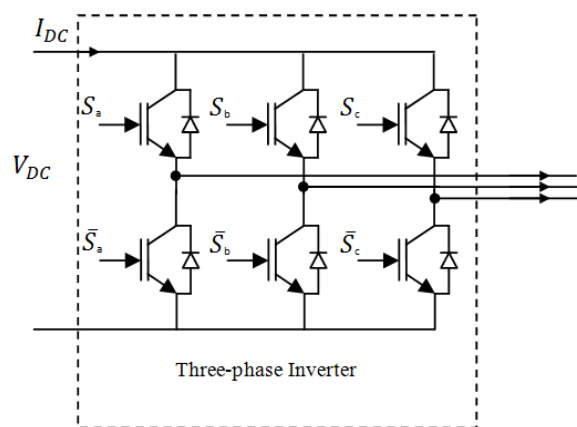


Fig. 5. Three phase Voltage Source Inverter

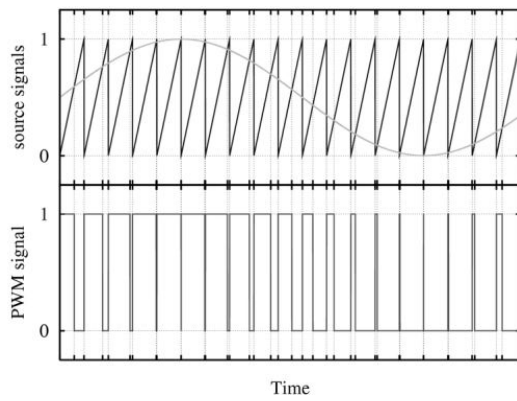


Fig. 6. PWM generator waveform

#### D. LCL filter

A filter is usually placed between the inverter and the grid to attenuate the switching frequency harmonics produced by the grid-connected inverter [21]. There are several types of filters. The LCL filter has good current ripple attenuation (60db/decade) even with small inductance values. Therefore LCL-filter fits to our application. In the technical literature we can find many articles on the design of the LCL filters [22]. Fig 7 shows a three-phase LCL filter.

The filter values will be referred to in a percentage of the base value (p.u).

$$Z_b = \frac{U_n^2}{S_n}, C_b = \frac{1}{\omega_n Z_b} \quad (5)$$

The subscript "n" refers the nominal values and the subscript "b" to the base values.

The inverter side inductance  $L_i$  limits the current ripple by up to 10%, it can be calculated according to (6):

$$L_i = \frac{U_{DC}}{16 f_s \Delta I_{L-max}} \quad (6)$$

Where  $F_s$  is the switching frequency,  $U_{DC}$  is the Dc-link voltage and the  $\Delta I_{L-max}$  is the 10% current ripple specified by:

$$\Delta I_{L-max} = 0.1 \left( \frac{P_n \sqrt{2}}{U_n} \right) \quad (7)$$

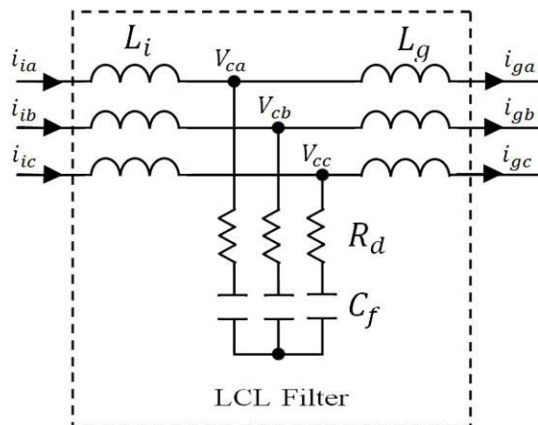


Fig. 7. Basic LCL Filter

The value of the capacitor  $C_f$  is chosen so as to maximize the power factor. The reactive power generated by this capacitor must be less than or equal to five percent of the rated active power. The filter capacity can therefore be calculated as a multiplication of system base:

$$C_f = 0.05 C_b \quad (8)$$

The grid side inductance  $L_g$  can be calculated as:

$$L_g = r L_i \quad (9)$$

In this paper  $r$  taken equals 0.6 according to [21].

The cut-off frequency  $f_{res}$  can be calculated as:

$$f_{res} = \frac{1}{2\pi} \sqrt{\frac{L_i + L_g}{L_i L_g C_f}} \quad (10)$$

The cut-off frequency must have a sufficient distance from the grid frequency. [21]

$$10 f_g < f_{res} < f_s / 10 \quad (11)$$

Where  $f_g$  is the grid frequency and  $f_s$  is the switching frequency

A damping resistance  $R_d$  is added in series with the filter capacitor in order to limit the resonance effects of the filter. This resistance can also be connected in parallel with the capacitor [23].

It can be determined by:

$$R_d = \frac{1}{3 \omega_{res} C_f} \quad (12)$$

The described system will serve as base case for testing the controller response and noise filtering method as a mean to improve the power quality.

### III. THE CONTROL SCHEME

The PID controller is the standard controller used in many engineering areas. Together with a process section, the PID controller forms the basic feedback loop [24]. A drawback of using feedback is that measurement noise is injected into the system [11].

In this paper, the design of a PI controller incorporating a noise filter will be approached as a trade-off between, noise injection and robustness based on the ideas presented in [24]

#### A. PI controller

The control strategy applied to the grid-side converter consists mainly of two cascaded loops. Usually, there is a fast internal current loop, which regulates the grid current, and an external voltage loop, which controls the DC-link voltage [25]. The DC-link voltage control aims at balancing the active power flow in the system [26].

The AC current is decoupled into active and reactive power components through a Synchronous reference frame transformation [27].

$$\begin{bmatrix} d \\ q \\ 0 \end{bmatrix} = \frac{2}{3} \begin{bmatrix} \cos(\theta) & \cos(\theta - \frac{2\pi}{3}) & \cos(\theta + \frac{2\pi}{3}) \\ -\sin(\theta) & -\sin(\theta - \frac{2\pi}{3}) & -\sin(\theta + \frac{2\pi}{3}) \\ \frac{1}{2} & \frac{1}{2} & \frac{1}{2} \end{bmatrix} \begin{bmatrix} a \\ b \\ c \end{bmatrix} \quad (13)$$

In this way,  $I_d$  and  $I_q$ , respectively are regulated using a Proportional-Integral (PI) controller. In order to eliminate the error between the reference and measured values of the active and reactive powers, the current controller generates a proper switching state for the inverter and produces the desired AC current waveform [26].

The synchronization of the system is done by a Phase-Locked Loop (PLL) [23].

For improving the performance of the controller, cross-coupling terms and voltage feed-forward are usually used [25]. The controller is depicted in Fig 8.

The PI controller used in the grid tied PV system gets its control variables directly from measurement of the grid voltage and current values. This means they are subject to the effect of noises coming from the grid. To reduce this effect on the controllers' performance, filtering techniques are adopted in our work.

### B. Noise filtering

Most of the measured converters' signals are affected by switching noise and other disturbances [10]. Adding a filter reduces their effects on the undesired control activity but performance can be degraded [11].

The major input signals to the controller are set point, process output, and, if available, measurable load disturbance [24]. In our work the signal treated are the direct current set-point " $i_d^*$ " (obtained from the Dc-link controller), measured direct current " $i_d$ " and quadratic current " $i_q$ " and the measured feed-forward voltages' direct and quadratic components " $E_d$ " and " $E_q$ " respectively.

The basic feedback loop is shown in fig 9-a and the feedback loop with filtering in fig 9-b.

Set-point filter  $F_r$  may be chosen in several different ways.

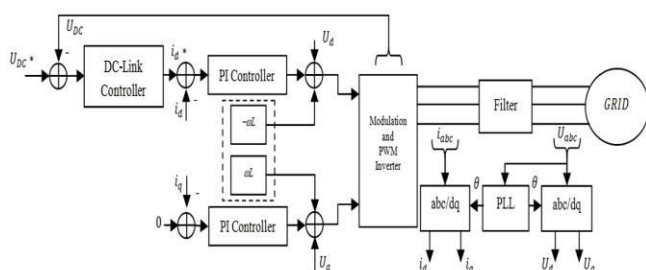


Fig. 8. PI Controller model for grid tied inverter

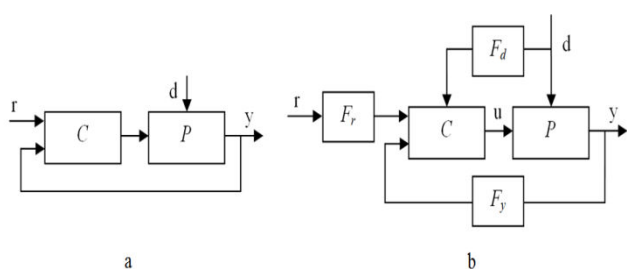


Fig. 9. controller structure a) without filter, b) with filters

It has normally a low-pass character, but not always. It must have the property  $F_r(0) = 1$  to ensure that the process output equals the set-point in steady state.

Filter  $F_y$  is used to improve the information about the process provided by measurement signal  $y$ . Noise can be removed from the signal by giving  $F_y$  low-pass character, and undesired features of the dynamics can be removed by giving  $F_y$  compensating features.

In this work a simple first order filter structure is adopted as suggested in [24]. Equation (14) refers to its transfer function and its Bode plot is given in Fig 10.

$$F_y = \frac{1}{1+sT_f} \quad (14)$$

The filter have only one tuning parameter, Filter-time constant  $T_f$ . One way to determine the filter time constant  $T_f$  is to design ideal controllers and to add the filter afterwards. In this paper, an iterative procedure also known as trial and error is used [10]. Controllers with different filter constants will be designed. The value of  $T_f$  will be chosen as a trade-off between robustness and noise attenuation [11]

Fig 11 shows a random system's step response without filter and with filter of different  $T_f$  values.

The filters described in this section will be used in a grid tied photovoltaic system with a PI controller in order to improve the systems response and mostly to reduce the noise effect on harmonic generation.

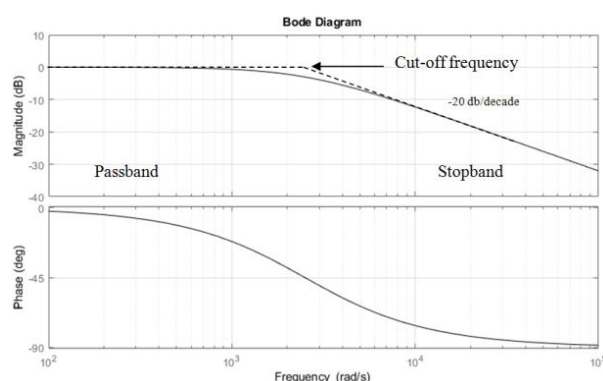


Fig. 10. Bode plot of a first order filter

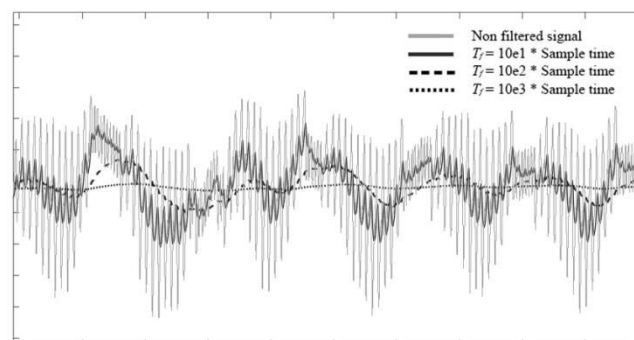


Fig. 11. Random noise signal filtered.

## IV. RESULTS AND DISCUSSION

The performances of the proposed method are assessed with simulations in Simulink-Matlab. The test system and the controller used are shown in fig 12 and 13 respectively.

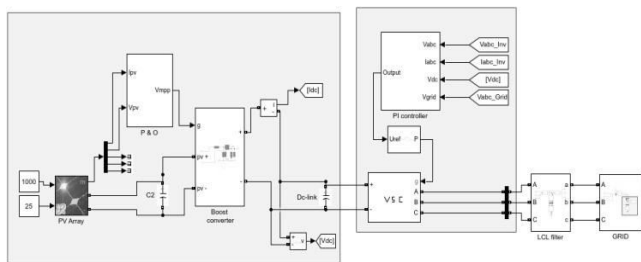


Fig. 12. Test system in Simulink-Matlab environment

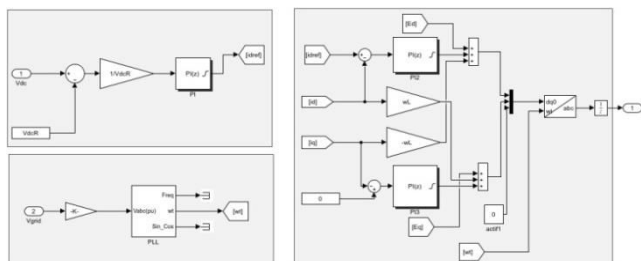


Fig. 13. System's controller in Simulink-Matlab environment

A *Soltech 1Sth-215-P* solar array is chosen for this study. Its data are borrowed from [28]. The module is made of 60 cells in series and provides 213.15W of nominal maximum power. The system is designed to deliver 8.5Kw to the grid at unity power factor. Its specifications are given in table 1.

The harmonic spectrum is investigated through Fast Fourier Transformation (FFT). The base case current waveform and FFT are shown in Fig 14 and 15 respectively.

The first case corresponds to the system with DC-link voltage filtered. The system's transient response is compared for different time constants  $T_f$  in fig 16 and a close-up of the steady state part is shown in fig 17.

Over-filtering is investigated in fig 18 where the filtering constants used are higher. Heavy filtering slows the system response which means that high filtering constants are not suited.

An optimal  $T_f$  is found to be  $T_f = 5e-5s$  which yields a THD of 2.15% as shown in fig 19.

TABLE I. STUDIED SYSTEM SPECIFICATIONS

<b>Pv array</b>	
Open circuit voltage ( $V_{oc}$ )	36.3 [V]
Optimum operating voltage ( $V_{mpp}$ )	29.0 [V]
Short circuit current ( $I_{oc}$ )	7.84 [A]
Optimum operating current ( $I_{Mpp}$ )	7.35 [A]
Maximum power ( $P_{mpp}$ )	213.15 [W]
Number of cells connected in series ( $N_s$ )	60
Number of panels connected in series ( $N_{ss}$ )	10
Number of panels connected in parallel ( $N_{pp}$ )	5
<b>Boost converter</b>	
Inductance ( $L_b$ )	0.250 [mH]
Input capacitor ( $C_b$ )	564 [ $\mu$ F]
Output capacitor ( $C_{dc}$ )	200 [ $\mu$ F]
<b>LCL filter</b>	
Input inductance ( $L_i$ )	1.69 [mH]
Filter Capacitor ( $C_f$ )	16.56 [ $\mu$ F]
Damping resistor ( $R_d$ )	2.05 [ $\Omega$ ]
Grid-side inductance ( $L_g$ )	0.001 [H]
<b>Simulation</b>	
Switching frequency ( $f_s$ )	5 [KHz]
Grid frequency ( $f_g$ )	50 [Hz]
Simulation time-step ( $t$ )	1e-6 [s]

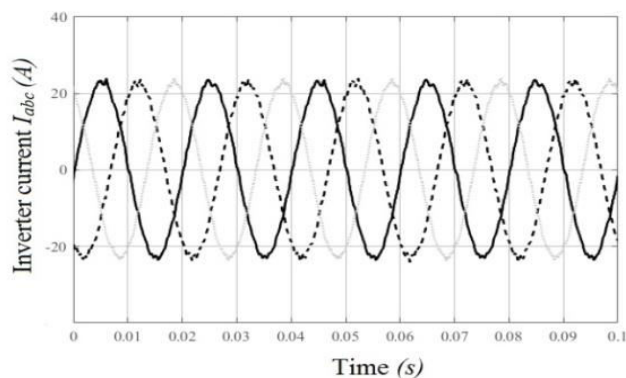


Fig. 14. Base case current waveform on steady state.

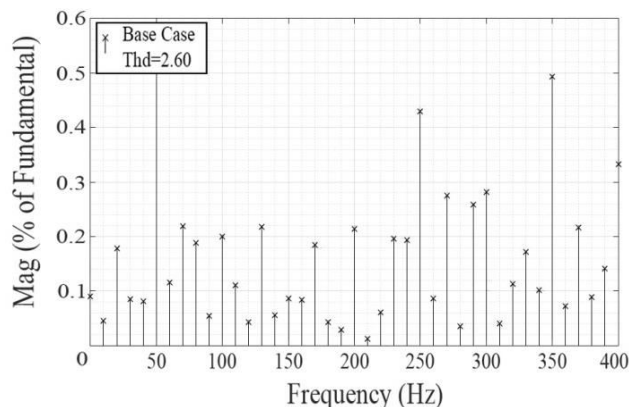


Fig. 15. base case harmonic spectrum

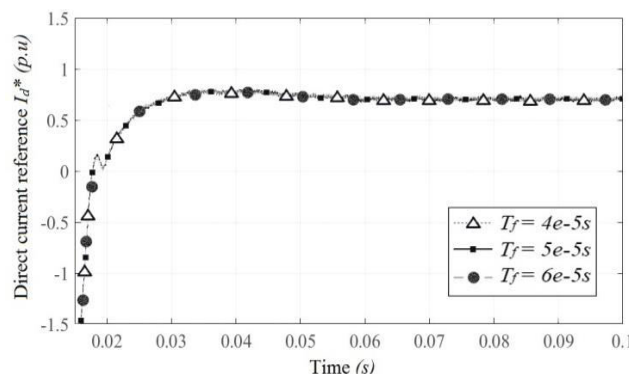


Fig. 16. Transient response of the DC-link controller with Dc-link voltage filtered

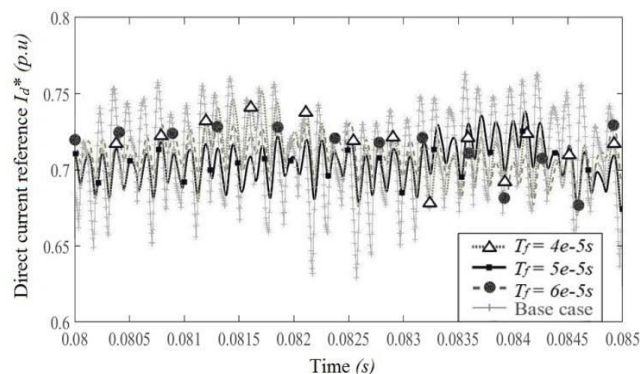


Fig. 17. Steady state response of the DC-link controller with Dc-link voltage filtered compared to base case

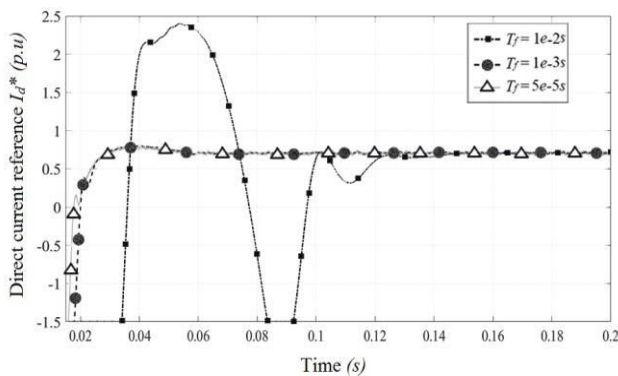


Fig. 18. Transient response of the DC-link controller with Dc-link voltage excessively filtered

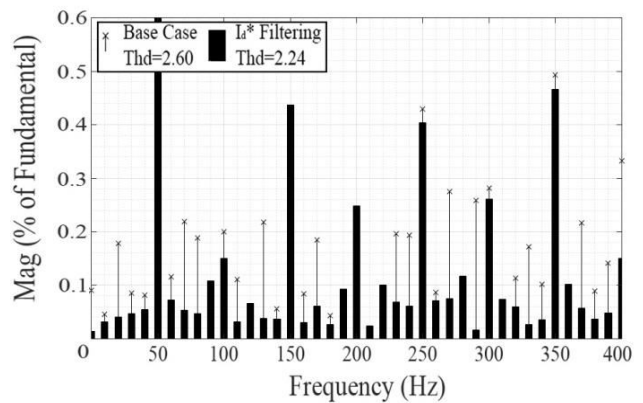


Fig. 20. FFT of the system with set-point filtering

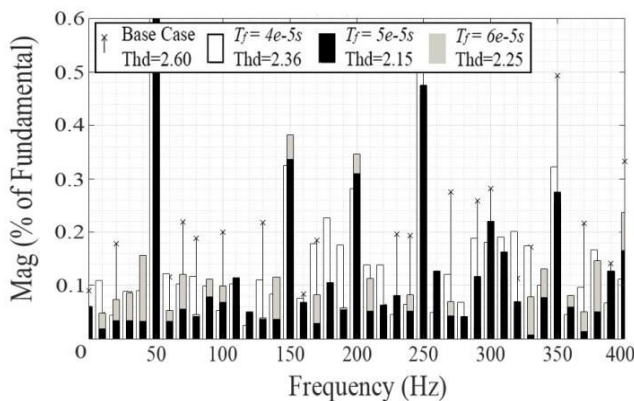


Fig. 19. FFT of the system with DC-link voltage filtering

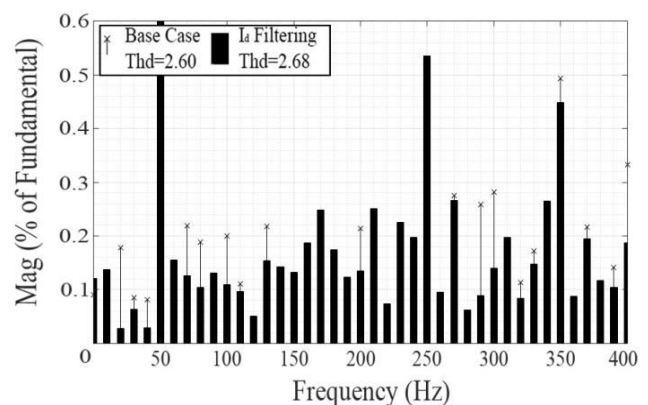


Fig. 21. FFT of the system with input filtering

In the second case, the proposed strategy is implemented for the current controller set-point ( $I_d^*$ ) and the current signal ( $I_d$ ). Their FFT is shown in Fig 20 and 21 respectively.

The third case focuses on the Feed-forward voltage. It is compared to the base case and to the system without Feed-forward signal in term of harmonics generated as presented in fig 22.

From the different simulations with the DC-link voltage, it is noticed that the system's response is not affected when the filter constant is small enough. The noise is reduced without loss in the information carried by the signal. Heavy filtering on the other hand deteriorates the response. This must be considered when determining the filtering time constant.

When applied to the DC-link voltage the proposed strategy proved to be suitable with a THD reduction of about 17.3% compared to the base case.

Filtering the current set-point ( $I_d^*$ ) had a positive impact on the THD (13.8% improvement). Filtering the current signal ( $I_d$ ) on the other hand generated more harmonics and the THD was 3.1% higher. Being the main control signal it might be more sensitive to the delays induced by the filters.

The feed-forward signal improves the controller's response and should not affect the steady state. Because of the background harmonics it contains, filtering it yields a better attenuation of the harmonics with a 22.7% improvement at no cost on the overall performances of the system.

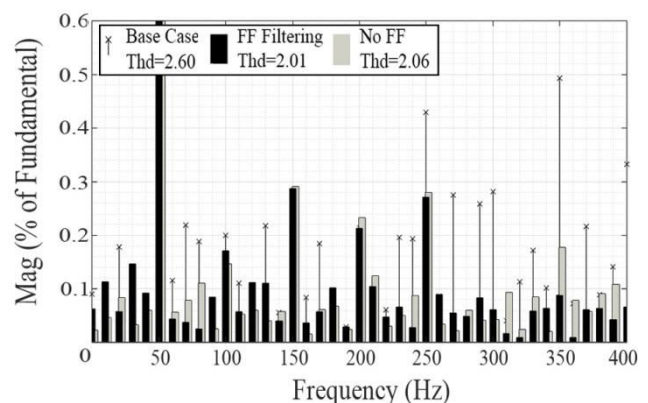


Fig. 22. FFT of the system with Feed-forward filtering

## V. CONCLUSION

In this paper, a new approach harmonic reduction strategy for grid tied photovoltaic systems has been investigated. The DC-link voltage, the current set-point, the current signal and the feed-forward voltage signal were processed with a first order filter to minimize the noise's impact on the controller's output.

The impact of the filtering time constant on the system's response was investigated. An optimum was chosen to maximize the noise reduction without affecting the system response.

The proposed strategy offers a great improvement when applied to the DC-link voltage and the current set-point signals. The implementation on the Feed-Forward signal offers the best results, due to the signal being fed directly to

the controller's output. From the simulation results it can be seen that filtering the current signal is not suitable, possibly because of the delay induced by the filters.

We have shown that the system is affected by the noise injected through the input signals. Filtering these signals is found to be a simple yet very effective way to reduce the harmonics generated by photovoltaic systems.

Furthermore, future work would focus on optimization techniques to design the filters. In addition, more tests on complex power systems would give insights about the controller's behavior with the proposed strategy implemented.

#### REFERENCES

- [1] E. Avci, M. Ucar, "PR Control of grid-connected 3-level inverter with LCL filter", V. International energy technologies conference, ENTECH'17, Istanbul, 2017.
- [2] H. Khalfalla, S. Ethni, M. Al-Greer, V. Pickert, and M. Armstrong, "An adaptive proportional resonant controller for single phase PV grid connected inverter based on band-pass filter technique," in *Compatibility, Power Electronics and Power Engineering (CPE-POWERENG)*, 2017 11th IEEE International Conference on, 2017, pp. 436-441.
- [3] S. Alsadi and T. Khatib, "Photovoltaic Power Systems Optimization Research Status: A Review of Criteria, Constrains, Models, Techniques, and Software Tools", *Applied Sciences*, vol. 8, no. 10, p. 1761, 2018. Available: 10.3390/app8101761.
- [4] K Sekar and V Duraisamy's "Efficient Energy Management System for Integrated Renewable Power Generation Systems" *JSIR Vol 74*, June 2015, pp. 325-329
- [5] B. Kim, J. Cho, J. Kim, J. Lee and C. Won, "An enhanced control strategy for seamless transfer of grid-connected single-phase inverter in synchronous rotating frame," 2017 20th International Conference on Electrical Machines and Systems (ICEMS), Sydney, NSW, 2017, pp.1-6. doi: 10.1109/ICEMS.2017.8056258
- [6] M. Parvez, M. F. M. Elias, N. A. Rahim, "Performance analysis of PR current controller for single-phase inverters", 4th IET Clean Energy and Technology Conference (CEAT 2016), pp. 1-8, 2016.
- [7] Z. Ali, N. Christofides, L. Hadjidemetriou, E. Kyriakides, "An Advanced Current Controller with Reduced Complexity and Improved Performance under Abnormal Grid Conditions" in *Proceedings IEEE PowerTech*, Manchester, pp. 1-6, 2017.
- [8] M. W. Alzahlan, K. M. Alawasa and H. D. Al-Majali, "Performance Evaluation of Different Optimal-Tuned Current Controllers for Voltage-Source Converter Connected to a Weak AC Grid," 2019 IEEE Jordan International Joint Conference on Electrical Engineering and Information Technology (JEEIT), Amman, Jordan, 2019, pp. 198-203. doi: 10.1109/JEEIT.2019.8717376.
- [9] D. Zammit, C. Spiteri Staines, M. Apap, J. Licari, "Design of PR current control with selective harmonic compensators using matlab", *J. Elect. Syst. Inf. Technol.*, vol. 4, no. 3, pp. 347-358, Jan. 2017.
- [10] S. Haitao, M.J. Mnati, M.N. Ibrahim, A. Van der Bossche, "A Tuning Method for PID Controller for an Integrating System with Time Delay", *MATEC Web of Conferences*, vol. 249, 2018, p. 03007, 10.1051/mateconf/201824903007.
- [11] V.R. Segovia, T. Hägglund, K.J. Aström, "Measurement Noise Filtering for PID Controllers", *Journal of Process Control*, vol. 24, no. 4, Apr. 2014, pp. 299-313, 10.1016/j.procont.2014.01.017.
- [12] Y. Zhu, B. Zhu, H. Hong-Tao Liu and K. Qin, "An Estimator-Based Feedback Control Approach for Measurement Noise Rejection," 2018 IEEE 14th International Conference on Control and Automation (ICCA), Anchorage, AK, 2018, pp. 167-172. doi: 10.1109/ICCA.2018.8444317.
- [13] L. Atik et al, "Maximum power point tracking algorithm based on sliding mode and fuzzy logic for photovoltaic sources under variable environmental conditions", 2017. Available: 10.1063/1.4976282.
- [14] M. Shayestegan, "Overview of Grid-Connected Two-Stage Transformer-Less Inverter Design" *Journal of Modern Power Systems and Clean Energy*, vol. 6, no. 4, 29 Jan. 2018, pp. 642-655, 10.1007/s40565-017-0367-z.
- [15] A. Kihal, F.krim, B.Talbi, A. Laib, A.Sahli, "A Robust Control of Two-Stage Grid-Tied PV Systems Employing Integral Sliding Mode Theory." *Energies*, vol. 11, no. 10, 17 Oct. 2018, p. 2791, 10.3390/en11102791.
- [16] A.Ahlatwat, D. Gupta, S.K. Gupta, "Modeling of a pv array and implementation of an efficient MPPT based control mechanism in stand-alone photovoltaic systems", *I-Manager's Journal on Circuits and Systems*, vol. 5, no. 2, 2017, p. 51, 10.26634/jcir.5.2.13665.
- [17] N. Derbel and Q. Zhu, "Modeling, Identification and Control Methods in Renewable Energy Systems." edited by Green Energy and Technology, Singapore, Springer Singapore, 2019.
- [18] M. Fares, L. Atik, G. Bachir and M. Aillerie, "Photovoltaic panels characterization and experimental testing", *Energy Procedia*, vol. 119, pp. 945-952, 2017. Available: 10.1016/j.egypro.2017.07.127.
- [19] L. Atik, et al, "Comparison of Four MPPT Techniques for PV Systems", *AIP Conference Proceedings* 1758, 030047, 2016; doi: 10.1063/1.4959443
- [20] T. Z. Touhami, P. Petit, G. Bachir, M. Aillerie, "New Topology of Photovoltaic Microinverter Based on Boost Converter", *Energy Procedia*, vol. 119, July 2017, pp. 938-944, 10.1016/j.egypro.2017.07.106.
- [21] A.E.Kahlane, L.Hassaine, M.Kherchi, "LCL filter design for photovoltaic grid connected systems, *Revue des Energies Renouvelables SIENR'14* Ghardaia, pp 227-232, 2014
- [22] J. Lettl, J.Bauer, L.Linhart, "Comparison of different filter types for grid connected inverter". *Progress in Electromagnetics Research Symposium*, pp 1426-1429, 2011.
- [23] M. Chabakata M. Petit, F. Costa, R. Marouani, A. Mami, "Optimized Design of an LCL Filter for Grid Connected Photovoltaic System and Analysis of the Impact of Neighbors' Consumption on the System. *Journal of Electrical Systems*, 13, pp 618-632, 2017.
- [24] Hägglund, Tore. "Signal Filtering in PID Control, " *IFAC Proceedings Volumes*, vol. 45, no. 3, 2012, pp. 1-10, 10.3182/20120328-3-it-3014.00002.
- [25] F.Blaabjerg, R.Teodorescu, M.Liserre, A.V.Timbus, "Overview of Control and Grid Synchronization for Distributed Power Generation Systems", *IEEE Transactions on Industrial Electronics*, vol. 53, no. 5, Oct. 2006, pp. 1398-1409, 10.1109/tie.2006.881997.
- [26] L.Hassaine,E.Olias, J.Quintero, V.Salas, "Overview of Power Inverter Topologies and Control Structures for Grid Connected Photovoltaic Systems." *Renewable and Sustainable Energy Reviews*, vol. 30, Feb. 2014, pp. 796-807, 10.1016/j.rser.2013.11.005.
- [27] S. Kim, "Electric motor control : DC, AC, and BLDC motors", Chapter 4 Modeling of alternating current motors and reference frame theory, Elsevier, pp.153-202, 2017.
- [28] A.M. Farayola, A.N. Hasan, A. Aili, "Comparison of Modified Incremental Conductance and Fuzzy Logic MPPT Algorithm Using Modified CUK Converter", 8th International Renewable Energy Congress (IREC), Mar. 2017, 10.1109/irec.2017.7926029.

# Effect of Catalysts On the production of Biodiesel from Used Domestic Waste Oils

D.KHERBOUCHE<sup># 1,2</sup>, A. GHOMRI<sup>1,3</sup>, F. LASSOUANI<sup>1,4</sup> BIBI TRIKI<sup>2,5</sup>, and BENMOUSSA<sup>2,5</sup>

<sup>1</sup>High School of Applied Sciences ESSA Tlemcen, BPN 165 Belhorizon, Tlemcen, Algeria

<sup>2</sup>Research Unit Materials and Renewable Energy, Department of Physics,  
 University of Tlemcen, Algeria  
<sup>#</sup> *djamila\_kh@yahoo.fr*

<sup>3</sup> Natural and Bioactive Substances Laboratory LASNABIO, Chemistry department,  
 University of Tlemcen, Algeria.

<sup>4</sup> Automatic Laboratory, Physic department, University of Tlemcen, Algeria.

<sup>5</sup> University of Tlemcen, Algeria

**Abstract**—The energy challenge was and is always interesting a big community of researchers, indeed, researchers and scientists are interested in other proper and secured energy sources such as biofuel. In this work, we present the catalyst influence on the production of biodiesel from used domestic oil basing on the transesterification reaction. It turn out from our study, that the use of KOH as catalyst gives very good performance of biodiesel regardless of the type of used vegetable used oil, and that the KOH is more effective than NaOH.

**Keywords**— Renewable Energies, Biodiesel, catalysts, NaOH, KOH.

## I. INTRODUCTION:

Biodiesel is a renewable fuel who can be used as a transport fuel, solvent and for energy generation with the advantage to reduce the CO<sub>2</sub>, SO<sub>2</sub>, CO and HS emissions, compared to fossil fuels [1].

Biodiesel is produced by the transesterification reaction (scheme 1) of triglycerides of refined/edible type oils using methanol as solvent and catalyzed by homogeneous or heterogeneous catalysts [2]. Indeed, catalyst plays a crucial role in the reaction yields, the most used catalyst in producing biodiesel are the homogeneous alkaline catalyst such as NaOH, KOH, CH<sub>3</sub>ONa and CH<sub>3</sub>OK [3]. The choice of these catalysts is due to their higher kinetic reaction rates [4]

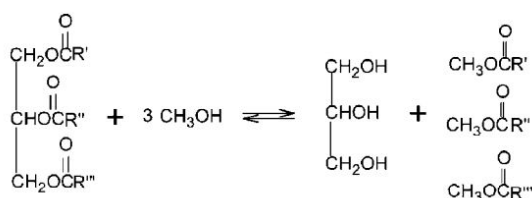


Fig 1: Transesterification reaction mechanism

Actually, the development and optimization of biodiesel production processes involve much experimental works, as well as the application of kinetic models that try to describe the process in a more comprehensive and realistic way. Some

of the variables that are commonly studied in the development of kinetic models are the reaction temperature, the feedstock composition [5], including different contents of free fatty acids (FFAs), the alcohol-to-oil molar ratio [6], the mixing speed [7] and the reaction time. The internal and external mass transfer limitations [8] when using solid catalysts have also been studied [9].

Our aim in the present work is to, elaborate an experimental study of the catalyst type effect on the reaction yields, reaction condition namely the time and the solvent type and the alcohol-to-oil molar ratio where also investigated to confirm our results [10]. Our obtained results show that even with the reaction condition changing the KOH catalyst with methanol as solvent remain most efficient to leads to the best yield.

## II. Material and methods :

### A. The materials

Products	The materials
<ul style="list-style-type: none"> <li>• methanol</li> <li>• ethanol</li> <li>• KOH</li> <li>• oil used</li> <li>• NaOH</li> </ul>	<ul style="list-style-type: none"> <li>• Bulb wasdecanted 1000 ml</li> <li>• The beakers 50 and 100 ml</li> <li>• A scale</li> <li>• acruet</li> <li>• Magnetic agitator</li> </ul>

Tables 1. The materials and products.

### B. The method :

Biodiesel production process occurs through several stages and in our work we proceed as flow:

First we put 50ml of used frying oil UFO in a 100ml beaker, the beaker is placed on the magnetic agitator, the temperature was kept at 50 ° C, with the average stirring speed. On the other hand, a quantity of alcohol is added with the chosen catalyst (NaOH or KOH), after mixing the catalyst and the alcohol previously prepared the mixture is added to the first beaker

containing the UFO with agitation conserved. To ensure a good homogenization of the mixture, magnetic stirrer is set at stirring level 3 and at a temperature of 50 ° C.

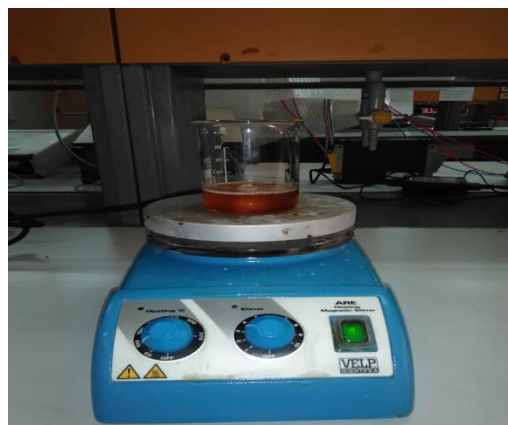


Figure 1: The mixture beaker on the agitator

The mixture is left on the magnetic stirrer for 1 hour, and then the solution is added to the separating funnel aiming to separate the mixture components rest biodiesel and glycerin, as biodiesel is less dense than glycerin, the biodiesel form the top layer so the two layers are completely separated and then decanted the bottom layer of glycerin until the end of glycerin.



Figure 2: The mixture after a day

After settling the biodiesel, the washing step must be carried out to remove the impurities. Finally, we Added a quantity of distilled water to the separating funnel with the biodiesel and agitate well, we left for one day the mixture was separated

into two layers, biodiesel and impurities, and then we will decant two solutions (see Figure 3.3).



Figure.3 Biodiesel after washing step

### III. Results And Discussion:

A. Influence of the mass ratio MeOH / FVO on the biodiesel yield of the transesterification reaction and on the catalyst effect:

To elucidate the MeOH/FVO ratios effect on the reaction yield we change the ratio(solvent/catalyst) results obtained for KOH and NaOH are given in table 2. The corresponding ratios were used 1/4;1/5 ;1/6 ;1/7 with a mass percentage of KOH/oil of 1%.

Table 2: Results of the influence of the mass ratio MeOH / FVO for KOH and NaOH, ρ (biodiesel volumic mass) (g/ cm<sup>3</sup>), ρ'(glycerin volumic mass) (g/ cm<sup>3</sup>),η (reaction yield)

	1	2	3	4	5	6	7	8
	<b>KOH</b>				<b>NaOH</b>			
Catalyst /oil Ratio	1/4	1/5	1/6	1/7	1/4	1/5	1/6	1/7
ρ	0.86	0.89	0.87	0.84	0.86	0.86	0.87	0.84
ρ'	0.13	0.86	2.55	0.85	0.13	0.85	2.55	0.85
η	89	92	91	92	61	76	52	43

We note that the reaction yield is obtained as follow:

$$\eta = \frac{m}{m'} \times 100$$

η : the reaction yield  
 m: the biodieselmass  
 m': the oilmass

Results presented in table 2 show that, the best obtained yields for the tow catalysts are obtained for the ratio of 1/5, on the other hand, for all the treated ratios it is the KOH catalyst use



which leads to the best yields, indeed, for KOH ratios are conserved between 89 and 92 which is a very good yield compared to the yields obtained for in the case of NaOH used as catalyst, ratios in this case are between 43 and 76. Our results, reveals that even if we change the solvent/oil ration it is the KOH catalyst which remain the better for getting a good biodiesel yield.

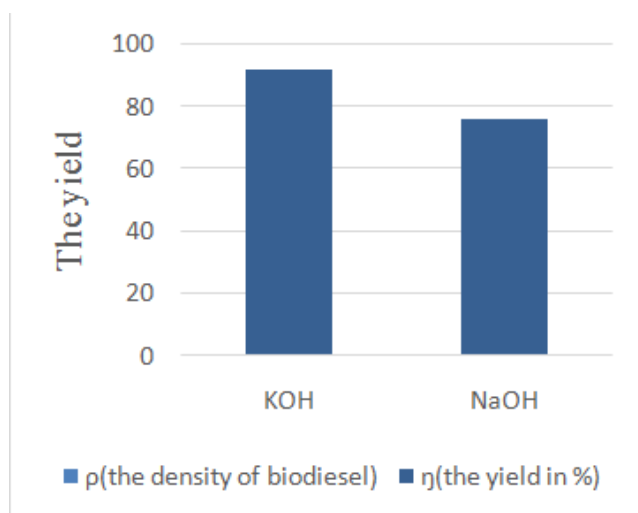


Figure 4: Comparison of KOH and NaOH catalysts

**B. The alcohol type effect:**

In this part we aimed to explain the alcohol type effect on the catalyst efficacy, for this we used two different alcohols namely ethanol and methanol. Obtained results are given in table 3 and figure 1. We note that the quantity of oil remains fixed 50ml

Table 3: Obtained results one changing the alcohol type

	1h		2h	
	1/7	1/4	1/7	1/4
Mass ratio				
Catalyst	KOH	NaOH	KOH	NaOH
$\rho$ (biodiesel volumic mass) (g/cm <sup>3</sup> )	0.83	0.81	0.88	0.85
$\rho'$ (glycerin volumic mass)(g/cm <sup>3</sup> )	2.99	0.74	0.83	0.83
$\eta$ (reactionyield)	87	63	97	85

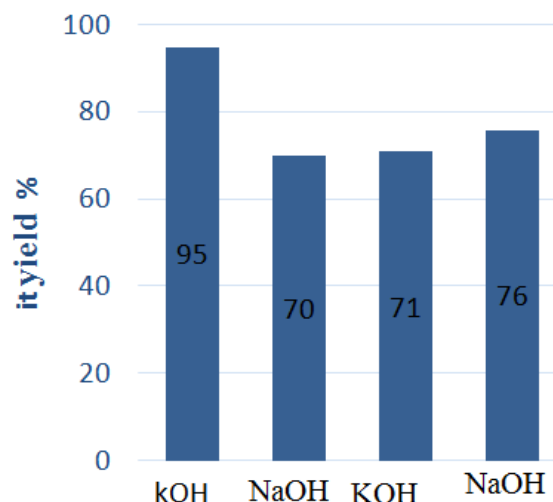


Fig.1. Alcohol influence on the reaction yield

It turn out from the obtained results that the maximum biodiesel yield is 95% obtained in the case of ethanol solvation , which corresponds to the mass ratio EtOH / FUO of 1/2. And this is obtained for KOH as catalyst. Nevertheless, the lowest yield of 21% is obtained for 0.3 NaOH corresponds to the mass ratio EtOH / FUO of 1/5.

**C. Reaction time influences on the reaction yield**

To verify the influences of the reaction time on the reaction yields we calculate the reaction yields by changing the reaction time from 1hour to two hours, reaction temperature was kept at 60°C and the (mass ratioscatalyst / FUO of 1/7 and 1/4). Results are presented in table 4 and figure 2,3.

Table 4: Results of the influence of transesterification reaction time (1, 2 hours)

	1h		2h	
	1/7	1/4	1/7	1/4
Mass ratio				
Catalyst	KOH	NaOH	KOH	NaOH
$\rho$ (biodiesel volumic mass) (g/cm <sup>3</sup> )	0.83	0.81	0.88	0.85
$\rho'$ (glycerin volumic mass)(g/cm <sup>3</sup> )	2.99	0.74	0.83	0.83
$\eta$ (reactionyield)	87	63	97	85

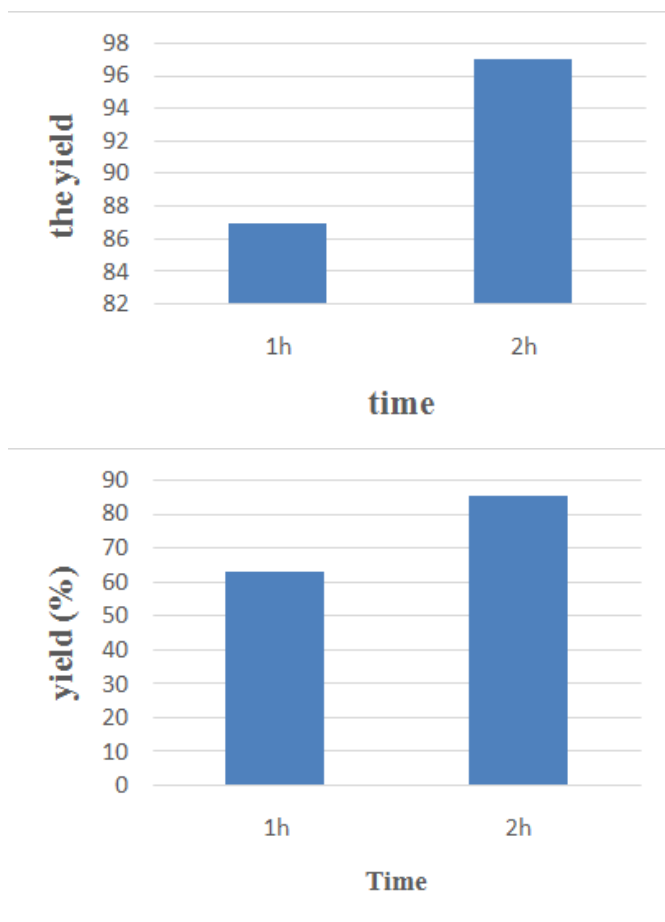


**Figure 2:** Evolution of biodiesel yield as a function of reaction time (mass ratio MeOH /function of. reaction time (mass ratio MeOH / FUO :7/1 KOH: 1% by weight, 60°C)FUO: 4/1 NaOH: 1% by weight, 60°C).

The obtained results show that the time reaction of two hours is the better for the two catalysts. However, the KOH catalyst gives the best reaction yield of 97% compared with the NaOH with the reaction yield of 85%.

**Conclusion:**

In this work we studies the catalyst effect on the used oil transesterification to produce biodiesel, the used frying oils react with alcohol (ethanol/methanol) in different mass ratio (MeOH / UFO or EtOH/UFO).

Our obtained results show that the use of KOH as a catalyst gives a very good biodiesel yield regardless of the type of the mass ratio and the temperature time. Indeed, the maximum obtained yield of 97% of biodiesel is generated with a mass ratio MeOH/ HFU of 1/7 and 1% by mass KOH with a reaction time of 2 hours. We note also that the 95% biodiesel

yield is obtained in the EtOH/HFU ethanol experiment of 1/2 and 3% by mass of KOH. We conclude from our study that regardless on the reaction conditions the KOH catalyst remain better than NaOH catalyst.

REFERENCES

- [1] 1. Luque, R. and J.A. Melero, *Advances in biodiesel production : processes and technologies*. 2011, Oxford ; Philadelphia: Woodhead Pub Ltd. xvi, 288 p.
- [2] 2. Vicente, G., M. Martinez, and J. Aracil, *Integrated biodiesel production: a comparison of different homogeneous catalysts systems*. *Bioresource technology*, 2004. **92**(3): p. 297-305.
- [3] 3. Di Serio, M., et al., *Heterogeneous catalysts for biodiesel production*. *Energy & Fuels*, 2007. **22**(1): p. 207-217.
- [4] 4. Zabeti, M., W.M.A.W. Daud, and M.K. Aroua, *Activity of solid catalysts for biodiesel production: a review*. *Fuel Processing Technology*, 2009. **90**(6): p. 770-777.
- [5] 5. Zhang, Y., et al., *Biodiesel production from waste cooking oil: 1. Process design and technological assessment*. *Bioresource technology*, 2003. **89**(1): p. 1-16.
- [6] 6. Sirisomboonchai, S., et al., *Biodiesel production from waste cooking oil using calcined scallop shell as catalyst*. *Energy Conversion and Management*, 2015. **95**: p. 242-247.
- [7] 7. Sánchez-Cantú, M., et al., *Biodiesel production under mild reaction conditions assisted by high shear mixing*. *Renewable energy*, 2019. **130**: p. 174-181.
- [8] 8. Aboelazayem, O., M. Gadalla, and B. Saha, *Biodiesel production from waste cooking oil via supercritical methanol: Optimisation and reactor simulation*. *Renewable Energy*, 2018. **124**: p. 144-154.
- [9] 9. Sarno, M. and M. Iuliano, *Biodiesel production from waste cooking oil*. *Green Processing and Synthesis*, 2019. **8**(1): p. 828-836.
- [10] 10. SEBAH, *diagnosis Low model: application to a turbocharged diesel engine with direct injection pdf'sd*.

# Faults Detection and Isolation of DC-AC Static Converter Feeding Induction Machine

K. Bedoud<sup>1,2\*</sup>, T. Bahi<sup>2</sup>, H. Merabet<sup>1</sup>, D. Drici<sup>1</sup>, B. Oudjani<sup>1</sup>

<sup>1</sup> Research Center in Industrial Technologies (CRTI) P.O.Box 64, Cheraga, Algeria

<sup>2</sup> Automatic Laboratory and Signals (LASA) Badji Mokhtar University, Annaba, Algeria

\* Mail : [k.bedoud@crti.dz](mailto:k.bedoud@crti.dz)

**Abstract**— This paper focuses on the detection and isolation of faults that may appear on three-phase inverters. We are particularly interested on the stator currents acquisition to develop decision algorithms based on  $d$ - $q$  Park's vector components, for the monitoring of latent faults that shorten the life of the installations and damage them in the short term. This Fault Detection and Isolation (FDI) method, allows the detection and localization of IGBT semiconductor open circuit fault using only motor phase currents. The drive chain modeling (Power Inverter-Machine) and the monitoring algorithm are developed under Matlab / Simulink environment where the results are presented and analyzed. The simulation results obtained the effectiveness and validity of the considered algorithm.

**Keywords**- fault detection, fault isolation, modeling, FDI, diagnosis, AC-DC, Converter

## I. INTRODUCTION

Faults detection and localization are two essential tasks in the industrial field. They can detect a fault in an early manner to avoid unexpected installation shutdowns, this, to ensure a quick and timely maintenance avoiding expenses. The most used methods are those based on the mathematical models. These use the redundancy existing between the different variables measured in terms of static or dynamic relations. Fig.1 presents the structural diagram of 3-phase PWM inverter induction motor drive. As shown, the induction machine (IM) in the studied system is connected directly to the 3-phase PWM inverter to allow an efficient control of IM. The converter is controlled by Pulse Width Modulation (PWM). According to the research that has been done on conversion system failures, power converters and its control circuits have a high failure rate [1-5]. Semiconductors are an essential elements of converters, can caused 34% of the total power converters failures [5, 6]. Today, the diagnosis methods within the components of electrical drive chain develop significantly [7]. These methods have as objective, a possible fault detection and isolation in an early manner, in order to avoid unexpected shutdowns of the installation and thus caused substantial funded losses. Static converters, has become industrial standard in many applications. The faults of one of semiconductor component of static converters: either, that it hangs continuously in open or closed position are one of faults that can appear [8-10], causing a malfunction of conversion chain, which degrades the power

quality and can cause potential secondary faults in other components [11]. Since the protective equipment intervenes only at the last stage of defect, it is obvious that the investment in the field of the detection of malfunctions seems an unavoidable solution. Currently, a large number of research is oriented towards monitoring the state of static converters [12, 13]. An open switch fault diagnosis in three phase inverter using diagnostic variable method is proposed by Mala R. Ubale and all [14], which they used average current of three phase inverter for the detection of single as well as multiple faulty switches. In [15], diagnosis methods for IGBT (Insulated Gate Bipolar Transistor) open switch fault applied to 3-phase AC/DC PWM converter are given. Indeed, these methods are based on the modification of established fault diagnostic methods for DC/AC inverters. The types of faults that can happen in converters and a comparative study among different converters used in wind energy conversion systems are presented in [16].

The work presented in this paper is based on the detection and isolation of open switch faults of semiconductors (IGBT). The paper is organized as follows. Section 2, describes the modeling of drive chain. The principles of FDI approach will be presented in section 3. In Section Conclusion, computer simulation results obtained under Matlab/Simulink are shown and discussed. Finally, the reported work is concluded.

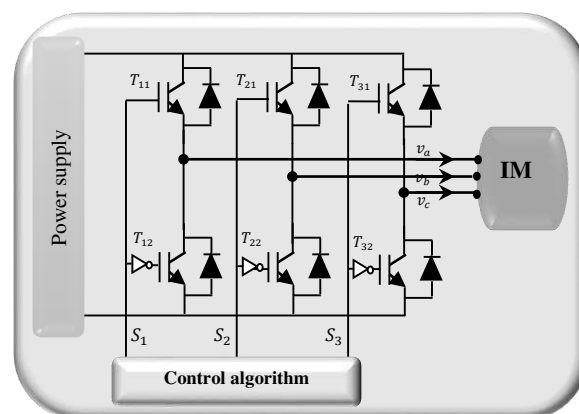


Fig.1. Structural diagram of 3-phase PWM inverter induction motor drive

## II. DRIVE CHAIN MODELLING

### A. Induction motor modelling

Induction motor (IM) model is presented and controlled in synchronous d-q reference frame where the d-axis is aligned with the stator flux linkage vector. It is controlled by acting on the direct and quadrature components of the rotor voltage. In effect, it enables the decoupled control between the electrical torque and the rotor excitation current is obtained.. Furthermore, the electromagnetic torque and the stator reactive power can be controlled by means of the rotor currents  $i_{rq}$  and  $i_{rd}$ , respectively. The mathematical model of the induction motor expressed in a d-q synchronously rotating reference frame, are presented as follow [17]:

$$\begin{cases} \dot{X} = A.X + B.U \\ Y = C.X \end{cases} \quad (1)$$

Where, the state vectors  $X$ ,  $Y$  and  $U$  are respectively:

$$X = Y = [i_{sd} \ i_{sq} \ i_{rd} \ i_{rq}]^T \text{ and } U = [V_{sd} \ V_{sq} \ V_{rd} \ V_{rq}]^T.$$

$$A = \begin{bmatrix} -a_1 & aw + w_s & a_3 & a_5w \\ -aw - w_s & -a_1 & -a_5w & a_3 \\ a_4 & -a_6w & -a_2 & -\frac{w}{\sigma} + w_s \\ a_6w & a_4 & \frac{w}{\sigma} - w_s & -a_2 \end{bmatrix} \quad (2)$$

$$B = \begin{bmatrix} b_1 & 0 & -b_3 & 0 \\ -aw - w_s & -a_1 & -a_5w & a_3 \\ -b_3 & 0 & b_2 & 0 \\ 0 & -b_3 & 0 & b_2 \end{bmatrix} \quad (3)$$

$$C = \begin{bmatrix} 1 & 0 & 0 & 0 \\ 0 & 1 & 0 & 0 \\ 0 & 0 & 1 & 0 \\ 0 & 0 & 0 & 1 \end{bmatrix} \quad (4)$$

With:

$$\begin{aligned} a &= \frac{1-\sigma}{\sigma}; \quad a_1 = \frac{R_s}{\sigma L_s}; \quad a_2 = \frac{R_r}{\sigma L_r}; \quad a_3 = \frac{R_r M}{\sigma L_s L_r}; \quad a_4 = \frac{R_s M}{\sigma L_s L_r}; \\ a_5 &= \frac{M}{\sigma L_s}; \quad a_6 = \frac{M}{\sigma L_r}; \quad b_1 = \frac{1}{\sigma L_s}; \quad b_2 = \frac{1}{\sigma L_r}; \quad b_3 = \frac{M}{\sigma L_s L_r}; \\ \sigma &= 1 - \frac{M^2}{\sigma L_s L_r} \end{aligned}$$

The stator and rotor flux as a function of currents are given as:

$$\begin{bmatrix} \varphi_{sq} \\ \varphi_{sd} \\ \varphi_{rq} \\ \varphi_{rd} \end{bmatrix} = \begin{bmatrix} L_s & 0 & L_o & 0 \\ 0 & L_s & 0 & L_o \\ L_o & 0 & L_r & 0 \\ 0 & L_o & 0 & L_r \end{bmatrix} \begin{bmatrix} I_{sq} \\ I_{sd} \\ I_{rq} \\ I_{rd} \end{bmatrix} \quad (5)$$

With,  $L_s = L_{ls} + L_o$  and  $L_r = L_{lr} + L_o$ .

Moreover,  $R_s$  and  $R_r$  denote the stator and rotor resistance, respectively.  $L_s$  is the stator and  $L_r$  the rotor self-inductances, where the quantities  $L_{ls}$  and  $L_{lr}$  are the stator and rotor leakage inductances, respectively, and  $L_o$  denote the magnetizing inductance. The mechanical equations of the system can be determined by [24]:

$$J \frac{d\Omega}{dt} = T_{em} - T_l - f\Omega \quad (6)$$

Where, The electromagnetic torque is as follows:

$$T_{em} = p \cdot \frac{M}{L_s} (\varphi_{sq} i_{rd} - \varphi_{sd} i_{rq}) \quad (7)$$

With,

$p$ : number of poles pairs;  $M$ : mutual inductance;

$J$ : moment of inertia;  $T_{em}$ : electromagnetic torque;

$T_l$ : load torque.

### B. DC-AC Converter modelling

Three-phase voltage inverter with two levels is a device based on IGBT transistors consisting of three arms. So, it is used to convert three DC phase input voltage into AC phase output. The switching functions are defined as follows :

$$S_{jk} = \begin{cases} 1 \rightarrow S_{jk} \text{ Closed} \\ 0 \rightarrow S_{jk} \text{ Open} \end{cases} \quad (8)$$

With :  $j \in \{1,2,3\}$  and  $k \in \{1,2\}$

The switches pairs  $T_{11}$  and  $T_{12}$ ,  $T_{21}$  and  $T_{22}$ ,  $T_{31}$  and  $T_{32}$  must be controlled complementarily to ensure currents continuity. The three phase output voltages  $v_a$ ,  $v_b$  and  $v_c$  can be synthesized in terms of switching functions  $S_{jk}$  by the following equation :

$$\begin{bmatrix} v_a \\ v_b \\ v_c \end{bmatrix} = \frac{v_{dc}}{3} \begin{bmatrix} S_1 \\ S_2 \\ S_3 \end{bmatrix} \quad (9)$$

$v_{dc}$ : supply voltage

## III. FAULTS DETECTION AND ISOLATION METHOD

The method used for faults detection and identification is based on the analysis of current vector. Park's (d-q) vector is a mathematical transformation, which simplifies three-phase circuit. It allowing to move from three-phase representation to the equivalent two-phase representation. Under the ideal conditions, it is assumed that:

$$i_a + i_b + i_c = 0 \quad (10)$$

Where  $i_a$ ,  $i_b$  and  $i_c$  are the stator currents of the induction motor. Consequently, the three phase sinusoidal current system can be written as [7, 14]:

$$i_n = \begin{cases} i_a = i \cdot \sin(\omega_s + \varphi) \\ i_b = i \cdot \sin\left(\omega_s - \frac{2\pi}{3} + \varphi\right) \\ i_c = i \cdot \sin\left(\omega_s + \frac{2\pi}{3} + \varphi\right) \end{cases} \quad (11)$$

where “ $i$ ” is the current maximum amplitude,  $\omega_s$  is the motor current frequency, and  $\varphi$  is the initial phase angle and  $n=a, b, c$ . The Park's vector components can be expressed by the following equations [11, 15]:

$$i_d = \frac{2}{3} i_a - \frac{1}{3} i_b - \frac{1}{3} i_c \quad (12)$$

$$i_q = \frac{1}{\sqrt{3}} (i_b - i_a) \quad (13)$$

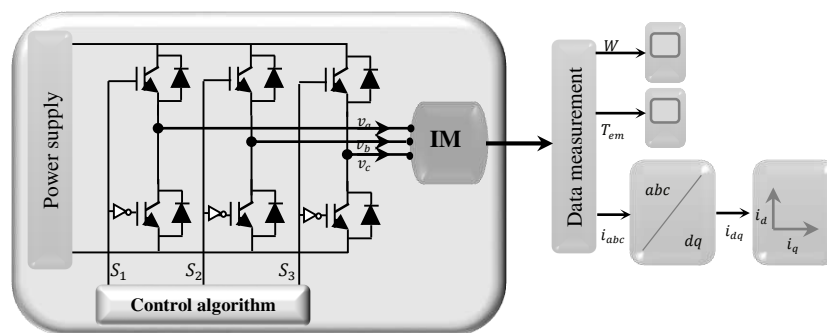


Fig. 2. Block diagram diagnosis method

Using d-q transformation, we can detect open circuit switches faulty situation of inverter. A normal operation is represented by a circle centered at the origin. If an open switch fault has occurred, there is a change in the phase current value at the location of fault. Indeed, a change in the circle shape illustrates the occurrence of an open fault condition. Figure 2 represents the structure of the diagnosis block diagram method that we have developed in this work.

#### IV. SIMULATION RESULTS

Fig. 3 presents the current waveform of three-phase current  $i_a$ ,  $i_b$  and  $i_c$  with switch open circuit of  $T_5$ , applied at  $t=1s$ . We can observe that when the fault is applied, two phases vary in the same direction and the third varies in the opposite direction. Then, we deduce that there is a fault.

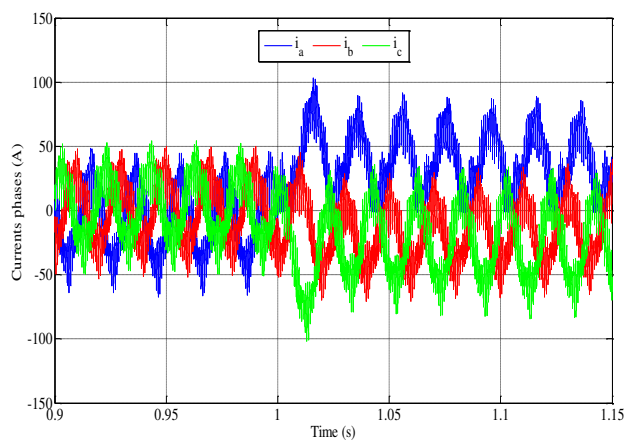


Fig. 3. Three phase trajectories under open switch fault (switch T22)

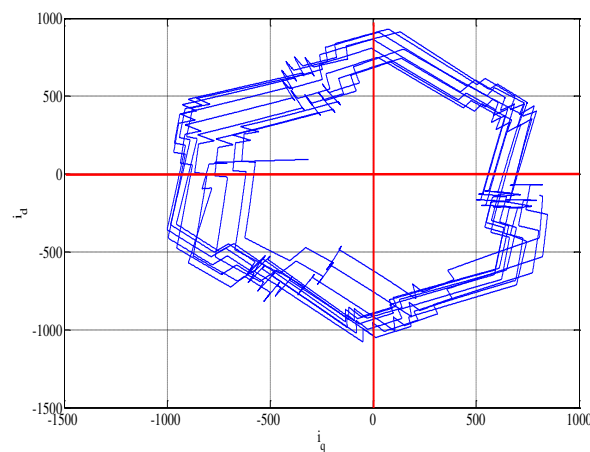


Fig. 4. d-q current trajectories 'without fault'

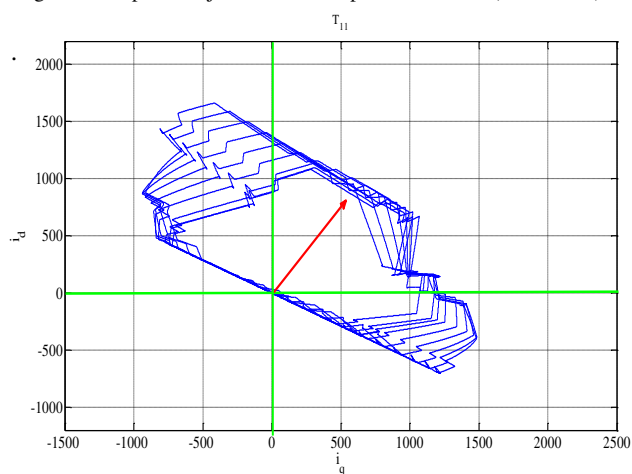


Fig. 5. d-q current trajectories under open switch fault 'switch T11'

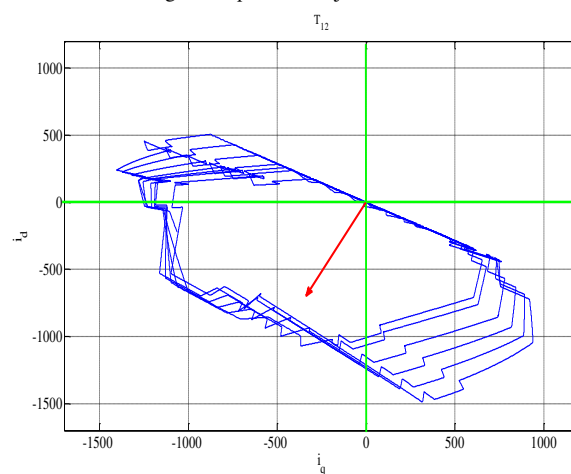


Fig. 6. d-q current trajectories under open switch fault 'switch T12'

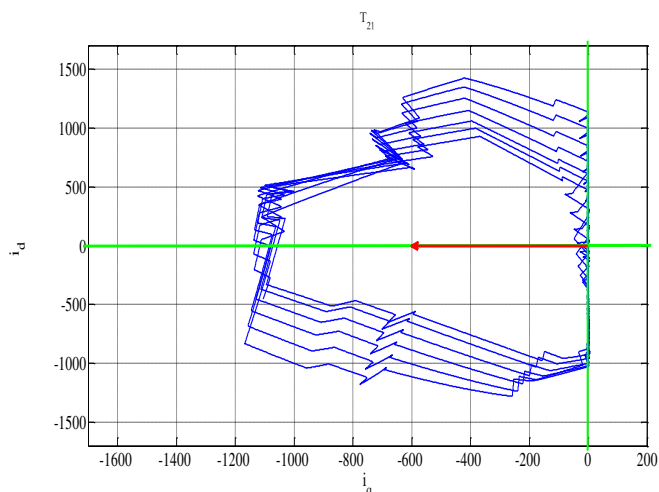


Fig. 7. d-q current trajectories under open switch fault 'switch  $T_{21}$ '

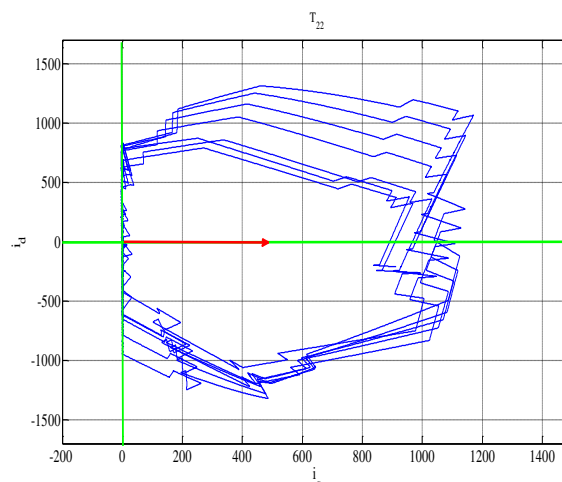


Fig. 8. d-q current trajectories under open switch fault 'switch  $T_{22}$ '

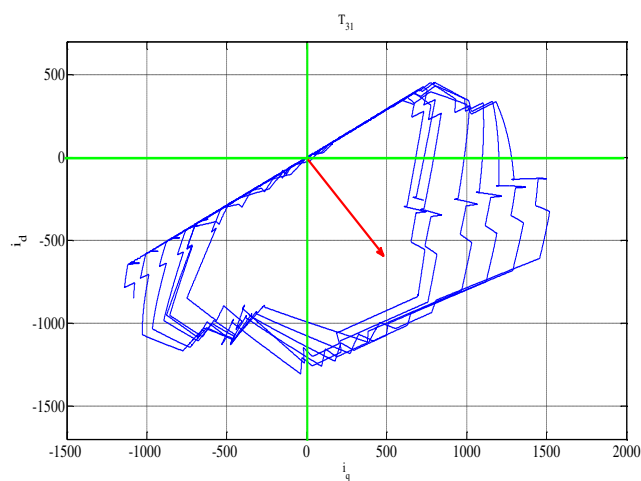


Fig. 9. d-q current trajectories under open switch fault 'switch  $T_{31}$ '

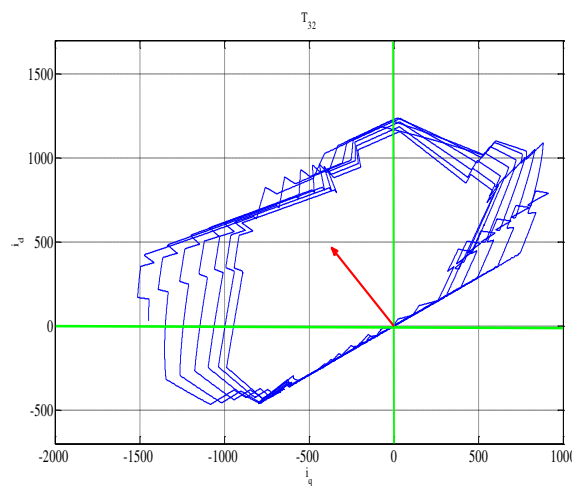


Fig. 10. d-q current trajectories under open switch fault 'switch  $T_{32}$ '

In a normal state (without fault), the current phase trajectory is a circle. Figure 4 to 10 show d-q transformation for normal and faulty phase current of three phase inverter, respectively. In the case when the switches  $T_{21}$  is failing, we notice a half-ellipse oriented to the left at the negative extension of the axis "d", and when the switch  $T_{22}$  is damaged we note that the half-ellipse is moved to the right of the axis "d". Indeed, the two half ellipses of  $T_{21}$  and  $T_{22}$  are separated by an angle of  $180^\circ$ . The analysis of the other switches ( $T_{11}$ ,  $T_{12}$ ) and ( $T_{31}$ ,  $T_{32}$ ) gave the same result. Suppose the fault is in the upper part of the inverter ( $T_{11}$ ,  $T_{21}$ ,  $T_{31}$ ), their corresponding half ellipses are separated by an angle of  $120^\circ$  and even if we consider the switches damage of the inverter lower position ( $T_{12}$ ,  $T_{22}$ ,  $T_{32}$ ), angle of separation between the half-ellipses is  $120^\circ$ .

## V. CONCLUSION

In this paper, we are interested in detection and isolation of IGBT semiconductor open switch faults of a three-phase converter based on park's current vector analysis. This technique concerns the tracking of park contour path to detect and to identify opening faults of MLI converter. Indeed, we considered the analysis of the simulation results for the case of induction machine fed by a three-phase converter without faults, and then, the case of IGBT opening fault. The obtained curves make it possible to detect and isolate easily the defective IGBT. The analysis of Park's contours in the repository. d-q is an effective tool for the diagnosis of semiconductor defects. Moreover, if the fault remains, the protection systems will have already reacted to stop the process.

## REFERENCE

- [1] Ribrant J, Bertling L. Survey of failures in wind power systems with focus on Swedish wind power plants during 1997–2005. *IEEE Trans Energy Convers.*, vol. 22, pp. 167–173, 2007.
- [2] Hahn, B., Durstewitz, M., Rohrig, K. Reliability of wind turbines. In : *Wind energy*. Berlin, Heidelberg: Springer, pp. 329–32. ISBN 978-3-540-33865-9, 2007.
- [3] Lin Y, Tu L, Liu H, Li W. Fault analysis of wind turbines in China. *Renew Sustain Energy Rev.*, vol. 55, pp. 482–90, 2016.
- [4] Freire NMA, Estima JO, Marques Cardoso AJ. Open-circuit fault diagnosis in PMSG drives for wind turbine applications. *IEEE Trans Ind Electron.*, vol. 60, pp. 3957–67, 2013.
- [5] Freire N, Estima J, Cardoso A. Converters fault-diagnosis in PMSG drives for wind turbine applications. In : *Proceedings of the IECON 2010 – 36th annual conference on IEEE industrial electronics society*, pp. 403–408, 2010.
- [6] Fuchs F. Some diagnosis methods for voltage source inverters in variable speed drives with induction machines – a survey. In : *Proceedings of the 29th annual conference of the IEEE on industrial electronics society (IECON'03)*; vol. 2, 2003, p. 1378–85.
- [7] H. Merabet, T. Bahi, K. Bedoud, and D. Drici, Real-Time Switches Fault Diagnosis for Voltage Source Inverter Driven Induction Motor Drive, *Int. J. Elec. & Elecn. Eng. & Telcomm.* vol. 8, n°. 2, pp. 103–107, 2019. doi: 10.18178/ijeetc.8.2.103-107
- [8] Sethom, H.B.A., Ghedamsi, M.A.: ‘Intermittent misfiring default detection and localization on a PWM inverter using wavelet decomposition’, *J. Electr. Syst.*, vol. 4, pp. 1–12, 2008.
- [9] Yang, S., Bryant, A., Mawby, P., *et al.*: ‘An industry-based survey of reliability in power electronic converters’, *IEEE Trans. Ind. Appl.*, vol. 47, pp. 1441–1451, 2011.
- [10] Yang, S., Xiang, D., Bryant, A., *et al.*: ‘Condition monitoring for device reliability in power electronic converters – a review’, *IEEE Trans. Power Electron.*, vol. 25, pp. 2734–2752, 2010.
- [11] Hongshan Zhao, Liangliang Cheng, Open-circuit faults diagnosis in back-to-back converters of DF wind turbine, *IET Renew. Power Gener.*, vol. 11, pp. 417–424, 2017.
- [12] Lee, J.S., Lee, K.B., Blaabjerg, F.: ‘Open-switch fault detection method of a back-to-back converter using NPC topology for wind turbine systems’, *IEEE Trans. Ind. Appl.*, vol. 51, pp. 325–335, 2015.
- [13] Jlassi, I., Estima, J.O., El Khil, S.K., *et al.*: ‘Multiple open-circuit faults diagnosis in back-to-back converters of PMSG drives for wind turbine systems’, *IEEE Trans. Power Electron.*, vol. 30, pp. 2689–2702, 2015.
- [14] M. R. Ubale, R. B. Dhumale, S. D. Lokhande, Open switch fault diagnosis in three phase inverter using diagnostic variable method, *International Journal of Research in Engineering and Technology*, vol. 02, 2013, <http://www.ijret.org>.
- [15] Won-Sang Im, J.S Kim, J.M. Kim, D.C. Lee, and K.B. Lee, Diagnosis Methods for IGBT Open Switch Fault Applied to 3-Phase AC/DC PWM Converter *Journal of Power Electronics*, vol. 12, N°. 1, 2012, <http://dx.doi.org/10.6113/JPE.2012.12.1.120>, pp. 120–127.
- [16] Blaabjerg, F., Ma, K.: ‘Future on power electronics for wind turbine systems’, *IEEE J. Emerging Sel. Top. Power Electron.*, vol. 1, pp. 139–152, 2013.
- [17] K. Bedoud, T. Bahi, S. Vaidyanathan and H. Merabet, Control of Matrix Converter Fed Induction Motor Drive, vol. 10, N°. 2, pp 881–890, 2017.

# The influence of Mn in structure of hydrotalcite-derived catalysts on the activity of dry reforming of methane

F. Touahra<sup>1</sup>, F. Bali<sup>\*2</sup>, B. Djebbari<sup>3</sup>, N. Aider<sup>4</sup>, Z. Abdelsadek<sup>3</sup>, K. Bachari<sup>1</sup>, D. Halliche<sup>2</sup>

<sup>1</sup>Centre de Recherche Scientifique et Technique en Analyses Physico-chimiques (CRAPC), BP 384-Bou-Ismaïl-RP 42004, Tipaza-Algérie.

<sup>1</sup>ftouahra@gmail.com

<sup>6</sup>bachari2000@yahoo.fr

<sup>2</sup>Laboratory of Natural Gas Chemistry, Faculty of Chemistry (USTHB), BP 32 16111 Algiers, Algeria.

<sup>2</sup>balifer@gmail.com

<sup>7</sup>dhallliche@yahoo.fr

<sup>3</sup>Department de Chimie, Faculty of sciences, University of M'hamed Bougara, Independence Avenue, 35000 Boumerdès, Algeria.

<sup>3</sup>djebbaribaya@gmail.com

<sup>5</sup>zoulisabrina@yahoo.fr

<sup>4</sup>Département de Chimie, Faculté des Sciences (UMMTO), Tizi-ouzou, Algérie

<sup>4</sup>n\_aider@yahoo.fr

**Abstract**— The NiAl-HDL and NiAlMn-HDL hydrotalcite-like compounds, were successfully synthesized following co-precipitation method at pH = 12. A several characterization techniques including XRD, N<sub>2</sub> adsorption and desorption, H<sub>2</sub>-TPR, SEM-EDX and TEM, were utilized to determine the structure function relationship for the obtained catalysts. These catalysts were evaluated in the reforming of methane reaction under continuous flow with CH<sub>4</sub>/CO<sub>2</sub> ration equal to 1, at atmospheric pressure and a temperature 700 °C. The Mn addition to the NiAl-LDH showed improved resistance to coke deposition.

**Keywords**— Syngas, Hydrotalcite, Mn, Co-precipitation, Methane dry reforming.

## I. INTRODUCTION

Dry Reforming of Methane (DRM, CH<sub>4</sub>+ CO<sub>2</sub> → 2CO + 2H<sub>2</sub>), is nowadays considered as a perspective alternative for the production of syngas (H<sub>2</sub> + CO) involving the valorization of CO<sub>2</sub>, coming either from capture or naturally present in the reactant gas, i.e. such in biogas. Furthermore, the H<sub>2</sub>/CO molar ratio in DRM-syngas, equal to 1, makes it applicable for Fischer-Tropsch synthesis [1]. One of the main drawbacks confronted during the process of CO<sub>2</sub> reforming of methane, is the poor stability of the catalyst over prolonged period of times, this is mainly associated with carbon deposited on the catalyst's Surface [2]. Several studies have been proposed to limit the formation of coke such as, the incorporation of the active phase in well-defined structures such as perovskites, hydrotalcites, etc., maybe on stream or (pre)reduction, resulting in a higher dispersion of the active phase species which leads to a good compromise between stability and catalytic activity. In this context, the purpose of the present work was to prepare efficient NiAl-LDH and

NiAlMn-LDH catalyst derived from hydrotalcite for dry reforming of methane.

## II. EXPERIMENTAL

### A. Catalysts preparation

The NiAl-LDH and NiAlMn-LDH hydrotalcite-derived catalysts were prepared *via* co-precipitation method with molar ratio (nNi<sup>2+</sup>/nAl<sup>3+</sup>) = 2, in order to induce the formation of hydrotalcite structures. The aqueous solutions of nitrate metals were added dropwise to a vigorously stirring solution of NaOH (2M) at room temperature while pH was maintained at 12. The obtained slurry was heated at 80 °C, kept under stirring for 15 hours for maturation, and then filtered, washed with water and finally dried at 100 °C in oven overnight. The physico-chemical properties of the synthesized materials were characterized using various techniques such as ICP, XRD, BET, TPR-H<sub>2</sub>, SEM-EDX, TEM and TPO-O<sub>2</sub>.

### B. Catalytic activity

Catalytic testing experiments were carried out in a continuous flow system at atmospheric pressure using a fixed-bed tubular quartz reactor. Prior to catalytic reaction, 100 mg of each sample was reduced in-situ under constant hydrogen flow at 700 °C for one hour. After that, the temperature was cooled down to the initial reaction's temperature and a feed gas mixture containing CH<sub>4</sub>:CO<sub>2</sub>: Ar in a ratio of 20:20:60 was passed through. The total gas flow rate was set to 20 mL/min. The effluent gases were analyzed using a gas chromatograph (Delsi), equipped with a thermal conductivity detector (TCD).



### III. RESULTS AND DISCUSSION

#### A. X-ray diffraction analysis

Fig. 1A shows the X-ray diffractograms of uncalcined samples (NiAl-LDH and NiAlMn-LDH). The corresponding X-ray diffractograms for NiAl-LDH, and NiMnAl-LDH are consistent with those expected for hydrotalcite-like with sharp and symmetric reflections for (003), (006), (110) and (113) planes and broad asymmetric for (012), (015) and (018) [JCPDS file 15-0087]. The results of XRD experiments for the calcined samples (at 800°C) are presented in Fig. 2B. As can be seen, after thermal treatment, the hydrotalcite structure of the samples was destroyed. On the NiAl-cal sample, XRD patterns showed the formation of NiO species [JCPDS file 47-1049] and NiAl<sub>2</sub>O<sub>4</sub> spinel [JCPDS file 10-0339], an amorphous aluminum oxide phase should be also formed (not detected in XRD)[3]. The Mn-containing samples exhibited peaks corresponding to NiO, NiAl<sub>2</sub>O<sub>4</sub> and Mn<sub>3</sub>O<sub>4</sub> [JCPDS file 24-0734].

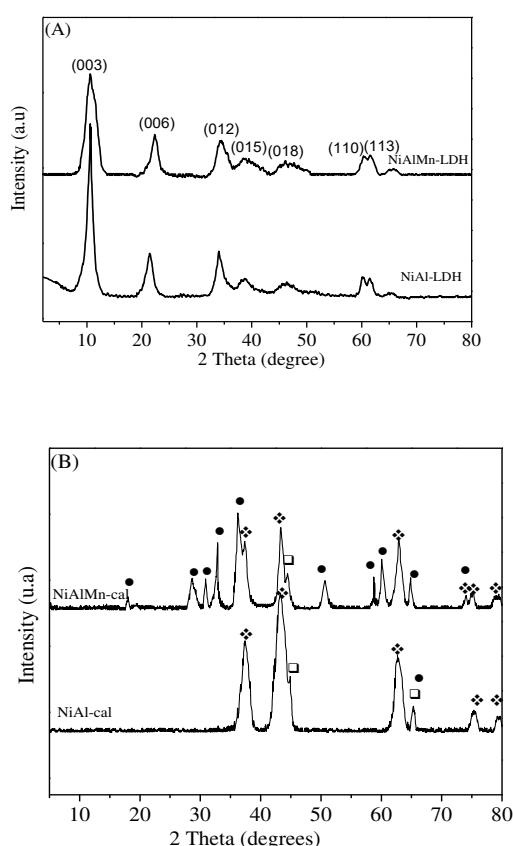


Fig.1 XRD of Precursors samples (A) and Mixed oxides (B)  
 ● Mn<sub>3</sub>O<sub>4</sub>, ♦ NiO and □ NiAl<sub>2</sub>O<sub>4</sub>

#### B. Measurement of specific surface areas

Table 1 shows the specific surface area values ( $S_{BET}$ ) of the NiAl-LDH and NiAlMn-LDH solids before calcination and after calcination at 800 °C.

TABLE I  
 SPECIFIC SURFACES OF THE NiAl-LDH AND NiAlMn-LDH

Samples	BET Surfaces area (m <sup>2</sup> /g)			
	Precursors	Calcined	Reduced	Used
NiAl-LDH	79	105	98	75
NiAlMn-LDH	90	121	114	101

Analyses of the obtained data revealed that the surface areas of two calcined solids are relatively high. We also note that  $S_{BET}$  of two materials have increased after calcination (Table 1) associated with the removal of water, nitrate and carbonate from the interlayer space of the hydrotalcite structures.

#### C. Temperature programmed reduction (TPR)

The TPR profiles obtained for all the samples are plotted in Fig. 2. The TPR of NiAl-cal sample showed a profile with a main peak at 530 °C, which can correspond to the reduction of free or NiO weakly interacting with Al<sub>2</sub>O<sub>3</sub>. A broad peak was observed around 677 °C; it is well known that the species that reduce at higher temperatures may correspond to species with high interaction with the surface. This high temperature reduction peak may be corresponding to the reduction of nickel species in NiAl<sub>2</sub>O<sub>4</sub> phase which observed previously by XRD analysis. Therefore, TPR of NiMnAl and NiAl-MnY showed three reduction peaks. The first peak was observed respectively around 450 and 470°C, which can attributed to the reduction of free NiO or weakly bound to the Al<sub>2</sub>O<sub>3</sub> and the second peak was observed respectively at 645 and 650°C, which can correspond to reduction of nickel in NiAl<sub>2</sub>O<sub>4</sub> phase. The last peak centered at 775 and 780°C is assigned to the reduction of Mn<sub>3</sub>O<sub>4</sub> to MnO according to previous reports that indicate that Mn<sub>3</sub>O<sub>4</sub> reduction occurs in a single step [4], [5].

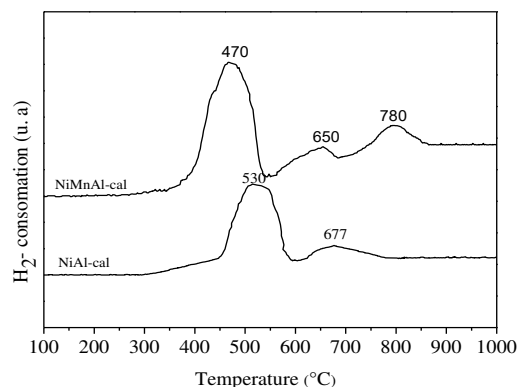


Fig.2 Reduction temperature profiles (5% H<sub>2</sub> / Ar) of the solids calcined at 800 °C.

### C. X-ray diffraction after reduction

In the case of two sample Fig. 3, The XRD patterns obtained after reduction show the presence of Ni<sup>0</sup> [JCPDS file 04-0850], identified by the diffraction lines located at 2θ = 44.50°, 51.84° and 76.01°. In addition, XRD profile of the catalyst after reduction demonstrated the presence of NiO. In the case of Mn-containing sample, MnO and Mn<sub>3</sub>O<sub>4</sub> were also observed.

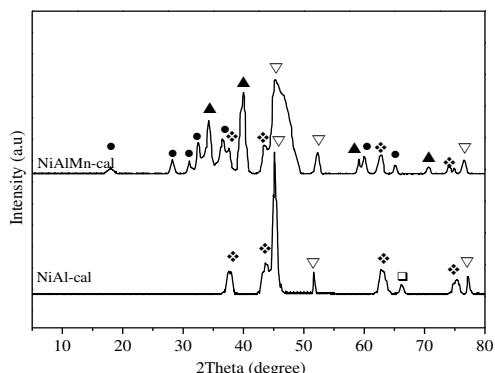


Fig. 3 XRD of reduced catalysts at 750°C. ●Mn<sub>3</sub>O<sub>4</sub>, ♦NiO, ▽Ni<sup>0</sup>, ▲MnO et □ NiAl<sub>2</sub>O<sub>4</sub>.

### D. BET surface of reduced samples

Evaluation of the specific surface area of all catalysts after reduction was also studied. Indeed, data shown in Table 1 demonstrated that the reduction step lead to a small decrease in the specific surfaces areas.

### E. SEM & TEM analyses after reduction

The morphology of NiAl-cal and NiAlMn-cal after reduction was analyzed by SEM-EDX and TEM (Fig. 4 and Fig. 5, respectively). Following reduction, catalysts demonstrated the presence of smaller and evenly distributed Ni particles on the surface of the catalysts. The Ni<sup>0</sup> particle have been confirmed by the EDX analysis.

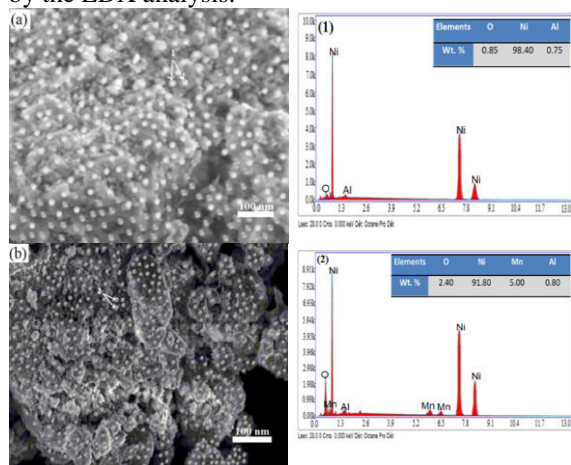


Fig. 4 SEM-EDX for the reduced samples (a) NiAl-cal and (b) NiMnAl-cal.

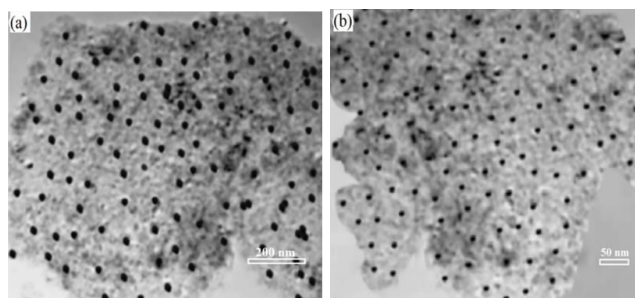
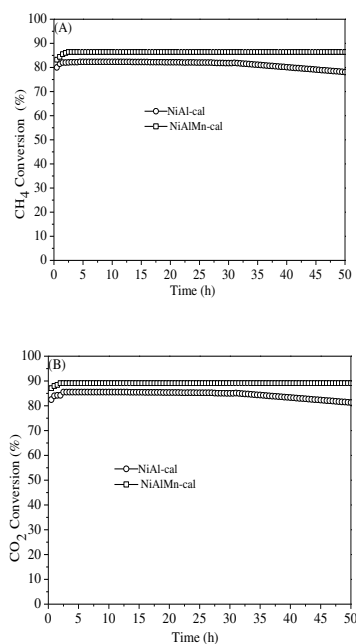


Fig. 5 TEM for the reduced samples for the reduced samples (a) NiAl-cal and (b) NiMnAl-cal.

### F. Catalytic activity tests

The catalytic performances of the synthesized catalysts were evaluated at 700°C in methane dry reforming reaction, after an ‘in situ’ H<sub>2</sub> reduction at 750 °C for 1 h. The catalytic performances and selectivity results are presented in Fig. 6, including both conversions of CH<sub>4</sub> and CO<sub>2</sub>, and H<sub>2</sub>/CO molar ratio. As can be seen, the Mn-based catalysts showed higher catalytic activity than NiAl-cal. The conversion of CH<sub>4</sub> increased from 82 % (NiAl-cal) to 86 % (NiAlMn-cal), whereas CO<sub>2</sub> conversion increased from 86 % (NiAl-cal) to 88 % in the case of NiAlMn-cal. This result is due to the incorporation of Mn in Ni-based catalyst which plays a good role in promoting a synergistic effect that further stabilizes the catalyst. In addition, previous work by our group also elucidated the possibility of deposited carbon being oxidized in the presence of manganese oxide (Mn<sub>3</sub>O<sub>4</sub>) to release carbon monoxide CO:  $(Mn_3O_4 + C \leftrightarrow 3 MnO + CO)$  [4]. This was confirmed by the presence of Mn<sub>3</sub>O<sub>4</sub> and MnO species prior to and after reaction, respectively.



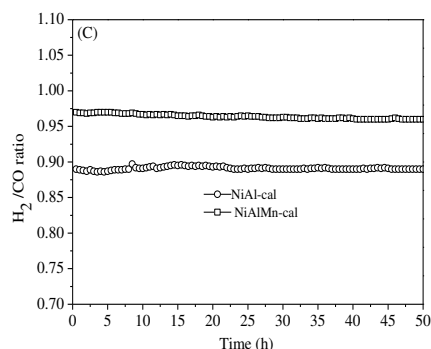


Fig. 6 (A) CH<sub>4</sub> conversion, (B) CO<sub>2</sub> conversion and (C) H<sub>2</sub>/CO ratio obtained during DRM.

#### G. Temperature programmed oxidation TPO-O<sub>2</sub>

TPO-O<sub>2</sub> curves of two catalysts after reaction are shown in Fig. 7. The TPO-O<sub>2</sub> profile of the spent catalyst shows the presence of a broad peak between 450°C -700 °C in the case of NiAlMn-cal catalyst. On the other hand, TPO of NiAl-cal sample showed a broad peak with high intensity around 600 °C. The only oxidation peak appearing in the TPO-O<sub>2</sub> profile of the spent catalysts was attributed to the oxidation of one type of carbonaceous species (filamentous carbon) on the surface of both samples [6]. As can be seen, the addition of Mn within NiAl-LDH, prompted less carbon deposition during the reaction of CO<sub>2</sub> reforming of methane.

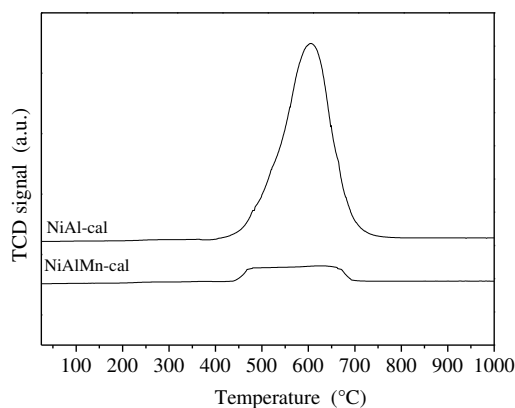


Fig. 7 TPO profiles of catalysts after DRM reaction.

#### IV. CONCLUSIONS

The solids NiAl-LDH and NiAlMn-LDH have been prepared by co-precipitation method. The synthesized catalysts were successfully characterized using XRD, BET, TPR-H<sub>2</sub>, SEM-EDX and TEM analysis, and applied for syngas production from CO<sub>2</sub> reforming of methane at 700 °C. NiAlMn-cal catalyst exhibited high activity and selectivity, but also high stability and good resistance to carbon deposition; this could be related to the capacity of manganese oxide in oxidizing carbon deposition forming CO as by-product.

#### ACKNOWLEDGMENT

The authors would like to thank Centre de Recherche Scientifique et Technique en Analyses Physico-Chimiques (CRAPC), Algeria, for the financial support.

#### REFERENCES

- [1] A.S. Al-Fatesh, M.A. Naem, A.H. Fakeeha and A.E. Abasaed, *Bull. Chem. Soc. Jpn.*, vol. 86, pp. 742, 2013.
- [2] M. Usman, W.W. Daud and H.F. Abbas, *Renew. Sust. Energ. Rev.*, vol. 45, pp. 710, 2015.
- [3] B. Djebbari, V. Gonzalez-Delacruz, D. Halliche, K. Bachari, A. Saadi, A. Caballero, J.P. Holgado and O. Cherifi, *React. Kinet., Mech. Cat.*, vol.111, pp. 259-275, 2014.
- [4] F. Touahra, M. Sehalia, D. Halliche, K. Bachari, A. Saadi and O. Cherifi, *Int. J. Hydrogen Energy*, vol. 41, pp. 21140-21156, 2016.
- [5] P. Arnoldy and J.A. Moulijn, *J. catal.*, vol. 93, pp. 38-54, 1985.
- [6] M. Rezaei, *Iranian J. Hydrogen Fuel Cell.*, vol. 2, pp. 215-226, 2016.

# Design of a Permanent Magnet Synchronous Generator for Wind Turbines

Zina Larabi<sup>#1,2</sup>, Kaci Ghedamsi<sup>\*3</sup>, Djamel Aouzellag<sup>\*4</sup>

<sup>#1</sup>*Electrotechnics Department, Mouloud Mammeri University  
15000, Tizi-Ouzou, Algeria*

<sup>#2</sup>*Electrical systems engineering Departement, M'Hamed Bougara University  
Avenue de l'indépendance, 35000, Boumerdes, Algeria*

<sup>1</sup>[zinalara@gmail.com](mailto:zinalara@gmail.com), <sup>2</sup>[z.larabi@univ-boumerdes.dz](mailto:z.larabi@univ-boumerdes.dz)

<sup>\*</sup>*Laboratoire de Maitrise des Energies Renouvelables  
Faculté de Technologie, Université de Bejaia, Algérie*

<sup>3</sup>[kghedamsi@yahoo.fr](mailto:kghedamsi@yahoo.fr)

<sup>4</sup>[aouzellag@hotmail.com](mailto:aouzellag@hotmail.com)

**Abstract**— The objective of this work is the design of a surface permanent magnet synchronous generator (SPMSG) with a large number of poles to be used in the conversion of wind energy. The design of the SPMSG is performed by three steps. The first step is the geometrical design which is performed analytically according to the imposed technical specifications and constraints. The second step is the verification and the examination of the electromagnetic behavior of the designed SPMSG using a finite elements method under Ansys Maxwell RMXpert software. Finally, with the third step, the main performances of the generator connected to an infinite bus are investigated and the steady state parameters of the SPMSG are also calculated.

**Keywords**— Design; SPMSG; Ansys Maxwell RMXpert; Finite Elements Method; Wind Energy

## I. INTRODUCTION

Among the renewable energy sources, the wind power has notably increased in the last decade [1-2] and the main two types of electrical machines used in the conversion of wind energy are the doubly fed induction generators and synchronous generators [1], but the tendency is the use of the direct drive generators with a better efficiency due to the elimination of the gearbox which is prone to complications such as generation of noise, regular maintenance, increased losses, and is responsible for high percentage of outage time.

Several types of these generators and geared drives have been presented, discussed and compared by many authors to address the effects of each concept.

Among the conversion technologies presented in [3], it appears that the direct-drive technology offers good performance with respect to reliability, maintenance, energy extraction, and grid power quality.

In [4], the authors compared five different generator systems, namely doubly-fed induction with three stages (DFIG3G) and with single-stage gearbox (DFIG1G), permanent magnet generator with single-stage gearbox (PMSG1G), direct drive generator with electrical excitation (DDSG) and direct drive permanent magnet generator

(DDPMG). The authors concluded that all of the geared generators have high losses in the gearbox which reduce the energy yield, DDSG is the heaviest and most expensive alternative, and that there is important copper losses in the stator and the rotor. DDPMG does not have a gearbox and electrical excitations which reduce the losses and improve the energy yield.

The authors in [5] compared the embedded magnets with the surface mounted magnet machine. The study showed that higher torque is achieved with surface mounted magnet machine and it needs less magnet material compared to embedded magnets. Five types of rotor structures are presented and discussed in [6] to determine the suitable rotor structure with high power for a PMSG. And it is concluded that the surface permanent magnet (SPM) structure with a magnet width/pole pitch of 90% is the most suitable rotor structure for high efficiency, low voltage, and high power output.

According to different comparisons, discussions and presentations of the direct drive generators given in the literature, our choice is focused on the design of a surface permanent magnet synchronous generator (SPMSG). It has various advantages, such as higher efficiency, larger power density and higher reliability which reduce operation and maintenance costs [7-9].

The direct-drive generators are designed with a large diameter and small pole pitch to increase the efficiency, to reduce the active material and to keep the end winding losses small [10], [11]. The air-gap should not exceed a few millimetres to avoid excessive magnetization requirements [10]. A design procedure of a direct drive low speed surface mounted permanent magnet (SMPM) machine is presented in [12], The result showed that the higher the pole number, the lower the weight for the same amount of copper losses, and the concentrated winding, with a number of slots per pole per phase  $q=0.5$  are more advantageous than a distributed winding with  $q=1$ , the weight and the torque ripple are lower, and the torque is higher for the same amount of copper losses.

In this paper the design of SPMSG is presented in three sections. Firstly, analytical design concerning the calculation of the principal dimensions of SPMSG is performed. Secondly, internal modelling concerning the electromagnetic behaviour of the generator is simulated in Ansys Maxwell RMXpert software. Finally, external modelling concerning the dynamic performance of the generator connected to an infinite bus is illustrated.

## II. ANALYTICAL DESIGN

In this section, a direct drive SPMSG with 64 pole pairs, 660 kW rated power and 46.875 rpm rated mechanical speed is analytically designed. The principal dimensions of the generator are calculated using classical equations given in literature [13-20].

The geometry of the SPMSG including the parameters of the geometrical dimensions is shown in the fig. 1.

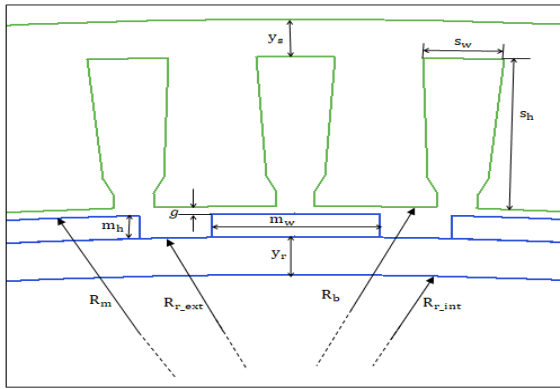


Fig. 1 Geometrical parameters of the SPMSG studied design

The bore radius ( $R_b$ ) and the active length ( $L$ ) of the generator are given by [13-15]:

$$R_b = \left( \frac{2r_{r1}P_n}{\pi^2 K_{w1} \hat{B}_{g1} \hat{A}_1 \Omega \cos \varphi} \right)^{1/3} \quad (1)$$

$$L = \frac{R_b}{r_{r1}} \quad (2)$$

Where  $r_{r1}$  is the ratio of the radius bore to the active length ( $L$ ),  $P_n$  is the rated power,  $K_{w1}$  is the stator fundamental winding factor,  $\hat{B}_{g1}$  is the fundamental air gap flux density,  $\hat{A}_1$  is the linear current density,  $\Omega$  is the rated speed and  $\cos \varphi$  is the rated power factor.

The gap length ( $g$ ), the stator yoke ( $y_s$ ) and the rotor yoke ( $y_r$ ) are expressed by [14], [16-17]:

$$g = 0.001 + 0.003\sqrt{R_b L} \quad (3)$$

$$y_s = y_r = \frac{\pi R_b \hat{B}_{g1}}{2p B_y} \alpha_m \quad (4)$$

Where:  $p$ : The number of pole pairs;  $B_y$ : The flux density in the iron core;  $\alpha_m$ : The rotor pole embrace.

The height ( $s_h$ ) and the width ( $s_w$ ) of the stator slot are given by [14-15] and [18]:

$$s_h = \frac{A_1}{J_s K_r K_s} \quad (5)$$

$$s_w = \frac{\pi R_b}{Q_s} \quad (6)$$

With:  $J_s$ : The current density;  $K_r$ : The stator slot fill factor;  $K_s$  is the slot proportion;  $Q_s$  is the number of stator slots.

The height ( $m_h$ ) and the width ( $m_w$ ) of the permanent magnet are expressed by [18-20]:

$$m_h = K_c g \frac{\mu_r}{\frac{B_r}{B_{g1}} - 1} \quad (7)$$

$$m_w = \frac{0.7(\pi(R_b - m_h - g))}{p} \quad (8)$$

Where:  $\mu_r$  and  $B_r$ : The relative permeability and the residual flux density of the permanent magnet.

The imposed technical specifications and constraints which must be fulfilled by the generator are given in the table 1, and the results calculations are summarized in the table 2.

TABLE I  
 TECHNICAL SPECIFICATION AND CONSTRAINTS OF THE SPMSG

Rated power	$P_n$	660	kW
Rated speed	$\Omega$	4.9	rad/s
Number of phases	$m$	3	-
Frequency	$f$	50	Hz
Rated power factor	$\cos \varphi$	0.95	-
Number of pole pairs	$P$	64	-
Linear current density	$A$	60e3	A/m
Surface current density	$J_s$	4e6	A/m <sup>2</sup>
Winding factor	$K_{w1}$	0.95	-
Permanent magnet type	NdFeB	-	-
Residual flux density	$B_r$	1.1	T
Relative permeability	$\mu_r$	1.05	-
Ratio of the radius bore to the active length	$r_{r1}$	5	-

TABLE II  
 DESIGN RESULTS FOR THE SPMSG

Bore radius	$R_b$	1.466	m
Active length	$L$	0.293	m
Stator yoke	$y_s$	14.4	mm
Rotor yoke	$y_r$	14.4	mm
Height of slot	$s_h$	56.7	mm
Width of slot	$s_w$	24	mm
Gap length	$g$	3	mm
Height of permanent magnet	$m_h$	8.7	mm
Width of permanent magnet	$m_w$	50	mm

### III. NUMERICAL DESIGN

To verify and validate the analytical design obtained in the section 2, it is necessary to perform a numerical design with Ansys Maxwell RMXpert software.

The numerical design concerns the internal modeling of the SPMSG using a finite elements method to analyze its electromagnetic behavior, and the external modeling of SPMSG to analyze its dynamic performances.

#### A. Concept of the Finite Elements Method(FEM)

The basic concept of the FEM is the discretization of the model to small elements where equilibrium equations are formulated. The combination of these equations gives us the equation for the whole structure. The boundary conditions are then imposed and the equations of equilibrium are solved.

In this study, a magnetodynamic analysis is considered, and the basic equation is given by:

$$\text{rot} \left( \frac{1}{\mu} \text{rot} \vec{A} \right) + \sigma \frac{\partial \vec{A}}{\partial t} = \vec{J} + \text{rot} \vec{M} \quad (9)$$

In two dimensional analysis, the magnetic vector potential  $\vec{A}$  and the permanent magnets magnetization  $\vec{M}$  are reduced to the z axes scalar  $A_z$  and the (x,y) axes scalars  $M_x, M_y$ , respectively. The equation 9 becomes:

$$\frac{\partial}{\partial x} \left( \frac{1}{\mu} \frac{\partial A_z}{\partial x} \right) + \frac{\partial}{\partial y} \left( \frac{1}{\mu} \frac{\partial A_z}{\partial y} \right) - \sigma \frac{\partial A_z}{\partial t} = -J_{sz} - \left( \frac{\partial M_y}{\partial x} - \frac{\partial M_x}{\partial y} \right) \quad (10)$$

Where:  $\mu$ : The absolute permeability;  $\vec{J}$ : The current density;  $\sigma$ : The electric conductivity.

#### B. Maxwell 2D RMXpert Model

Firstly, the analytical design is imported to the RMXpert environment to verify it and then, to the Ansoft Maxwell 2D software to perform the magnetodynamic analysis. The geometric model of the generator under RMXpert environment is represented in the fig.2.

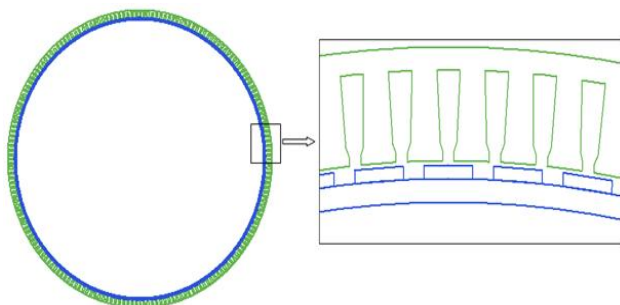


Fig. 2 SPMSG design

The different materials selected in the RMXpert material library are: NdFeBr35 for the permanent magnets, Steel\_1010 for the stator and the rotor core, and Copper for the stator winding. The B-H curve of the Steel\_1010 is shown in the fig. 3.

A fractional double layer winding used is represented in the fig. 4. This type of winding leads to easier manufacture

and lower cost of coils and the short pitching can be used to reduce cogging and certain harmonics [16].

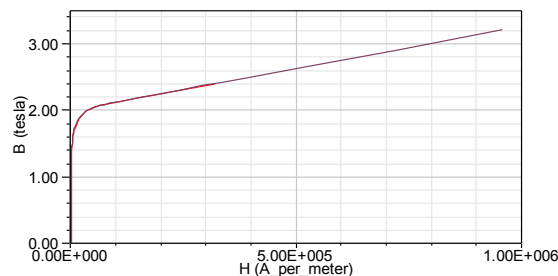


Fig. 3 B-H curve of steel\_1010

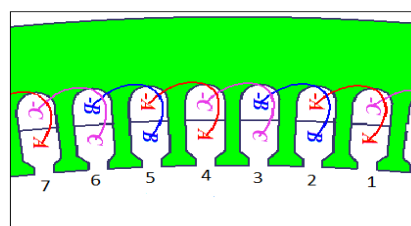


Fig. 4 Double layer fractional winding distribution

Because of the big size of the obtained SPMSG, and to minimize the simulation time, only two poles of the model simulation is considered. The finite elements discretization realized in Ansoft Maxwell software is shown in fig. 5.

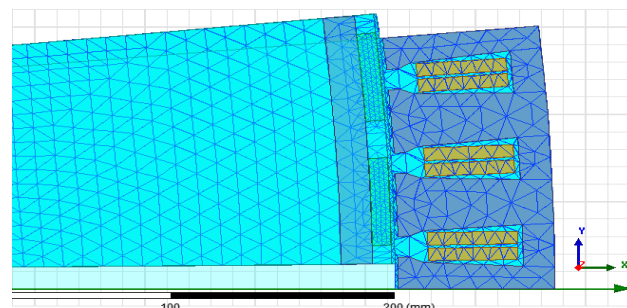


Fig. 5 Mesh analysis for the designed SPMSG

The flux lines path and the flux density distribution are shown in fig.6 and fig.7, respectively. These results are obtained at 0.4s which correspond to the position of the rotor 113.054 degrees, and at the rated speed 46.875 rpm.

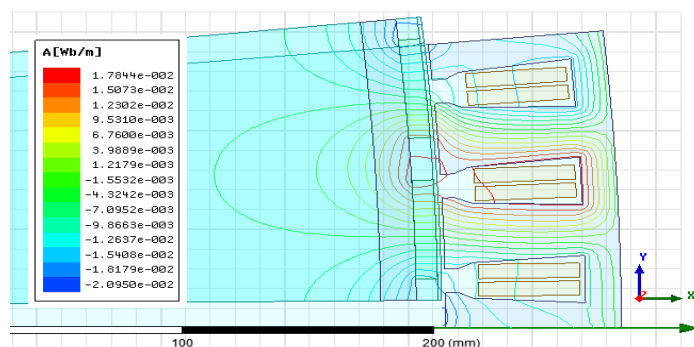


Fig. 6 Flux lines path of the SPMSG

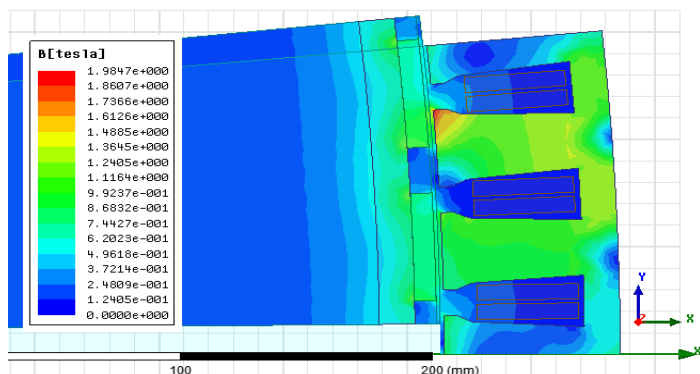


Fig. 7 Flux density distribution

### C. Performance Analysis

The SPMSG is directly driven by the wind turbine torque (mechanical input energy) which is converted into electrical output energy [22-23], and then delivered to the infinite bus. The system is simulated in Ansoft Maxwell 2D RMXpert software under the conditions given in the table 3.

TABLE III  
 CONDITIONS OF THE ANALYSIS

Operating type	Generator
Load type	Infinite bus
Rated output power	660 kW
Rated speed	46.875 rpm
Operating temperature	75°C

The main performances of SPMSG obtained in the Ansoft Maxwell 2D RMXpert simulation are the winding voltage and currents under load, the air gap flux density, the air gap power versus power angle and the transient plots of the moving torque and the current winding. The results are shown in fig. 8 to fig. 13.

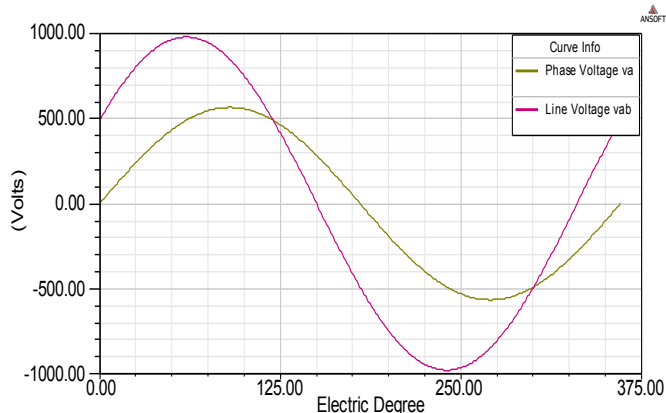


Fig. 8 Winding voltage under load

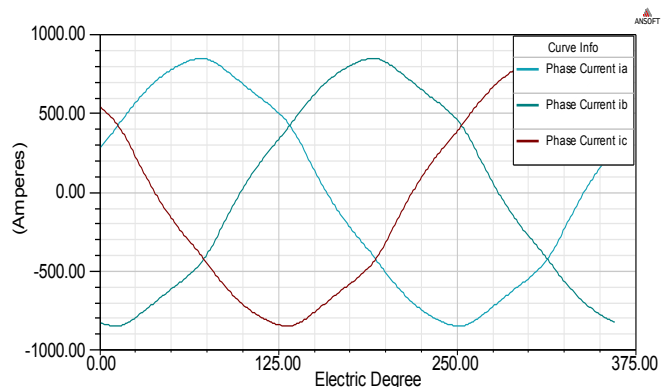


Fig. 9 Winding currents under load

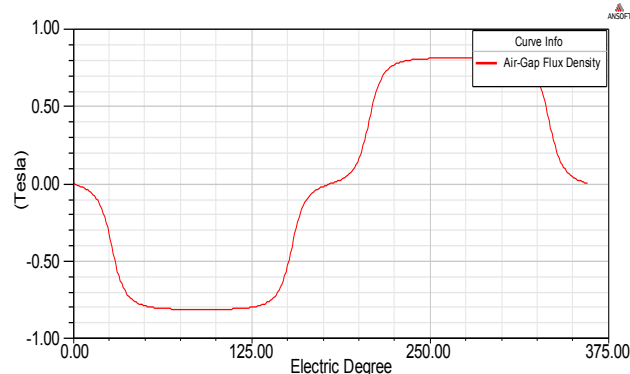


Fig. 10 Air gap flux density

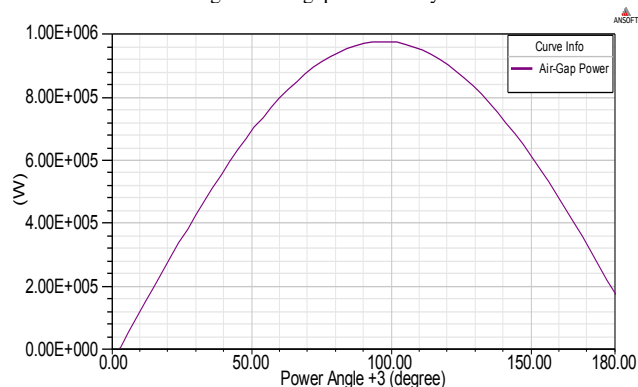


Fig. 11 Air gap power versus power angle

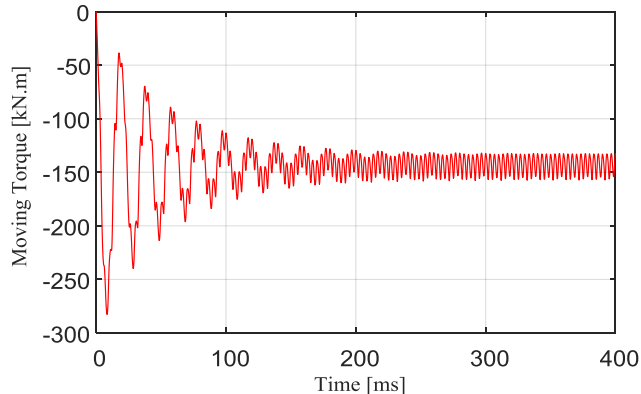


Fig. 12 Moving torque

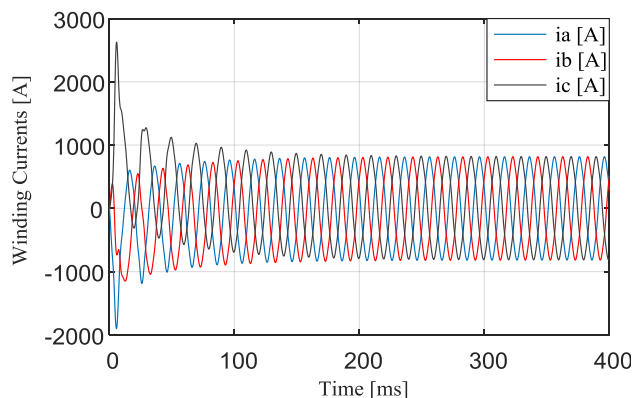


Fig. 13 Winding currents

The results show that, the voltage and the current winding have the waveform with a root mean square (RMS) values of 400V for the phase voltage and 582 A for the current phase as shown in fig.8 and fig. 9 respectively. The variation of the air gap flux density versus the electric degree is illustrated in the fig. 10, it has a wave form with a peak value of 0.81 T. As shown in fig. 11, the air gap power versus power angle is presented with a rated value of 660 kW which is reached at 47.11 deg of the power angle. The transient plots of the moving torque and the current winding are illustrated in fig. 12 and fig. 13 respectively. After the transient period, the current phase reaches its root mean square (RMS) value 582 A and the moving torque reaches its average 141 kN.m.

Moreover, the no-load and the full load characteristics and the steady-state parameters of the SPMSG are also calculated in Maxwell RMXpert software. They are summarized in table 4, table 5 and table 6, respectively.

TABLE IV  
 NO LOAD CHARACTERISTICS OF THE SPMSG

Stator teeth flux density	1.49	T
Stator yoke flux density	1.51	T
Rotor yoke flux density	1.51	T
Air gap flux density	0.81	T
Stator teeth ampere turns	148.33	At
Stator yoke ampere turns	60.28	At
rotor yoke ampere turns	56.59	At
Air gap ampere turns	2249.88	At
Magnet ampere turns	-2540.68	At
Fundamental back emf	789.42	V
THD of back emf	14.30	%

TABLE V  
 FULL LOAD CHARACTERISTICS OF THE SPMSG

RMS line current	582.34	A
RMS phase current	582.34	A
Input power	691.866	kW
Output power	660.187	kW
Maximum output power	870.823	kW
Armature copper loss	31.678	kW
Iron core loss	11.507e-5	kW
Total loss	31.679	kW
Efficiency	95.421	%
Rated torque	141	kN.m

TABLE VI  
 STEADY STATE PARAMETERS OF THE SPMSG

D-Axis reactive inductance $L_{ad}$	0.618	mH
Q-Axis reactive inductance $L_{aq}$	0.618	mH
D-Axis inductance $L_1+L_{ad}$	1.965	mH
Q-Axis inductance $L_1+L_{aq}$	1.965	mH
Armature leakage inductance $L_1$	1.347	mH
Armature phase resistance $R_1$	0.031	Ohm
D and Q axis time constant	0.019	s

#### IV. CONCLUSION

A direct drive surface permanent magnet synchronous generator is designed and analyzed using analytical and numerical methods. The analytical design concerning the calculation of the principal dimensions of SPMSG is performed according to the imposed technical specifications and constraints. The obtained design is verified and validated using a numerical method under Ansys Maxwell RMXpert software. A finite elements method is used for the internal modeling of the designed generator in order to analyze its electromagnetic behavior. The dynamic performances of the generator are also verified and presented in this paper.

The obtained results are satisfying, and respond to the imposed technical specifications and constraints. it shows and



proves the effectiveness and the feasibility of the designed generator for the wind turbine.

For the future work, it is desirable to comfort the obtained results in this paper with the experimental by realizing a prototype of the designed SPMSG.

#### REFERENCES

- [1] T. P. M. Bazzo, J. F. Kolzer, R. Carlson, F. Wurtz, L. Gerbaud. "Multidisciplinary design optimization of direct-drive PMSG considering the site wind profile". *Electric Power Systems Research*. Volume 141. Pp 467-475, 2016.
- [2] T. P. M. Bazzo, J. F. Kolzer, R. Carlson, F. Wurtz, L. Gerbaud, « Multidisciplinary Design Optimization of a Direct-Drive PMSG including the Power Converter Cost and Losses », *IEEE*, pp 1909-1914, January 2016.
- [3] M. R. Dubois., H. Polinder, J. A. Ferreira "Generator Topologies for Direct Drive Wind Turbines and adapted Technology for Turbines Running in Cold Climate", proceeding of the conference on wind energy in cold climate, Matane, Canada, 2001.
- [4] H. Polinder, F.F.A. van der Pijl, G.J. de Vilder, P. Tavner, "Comparison of direct-drive and geared generator concepts for wind turbines", *IEEE Trans. Energy Conversion*, Vol. 21, pp. 725-733, September 2006.
- [5] P. Salminen, J. Pyrhönen, M. Niemelä "II-17. a comparison between surface magnets and embedded magnets in fractional slot wound pm motors", *ISEF 2003 – 11th International Symposium on Electromagnetic Fields in Electrical Engineering* Maribor, Slovenia, September 18-20, 2003.
- [6] H. Haraguchi, S. Morimoto and M. Sanada, "Suitable design of a PMSG for a small-scale wind power generator," 2009 International Conference on Electrical Machines and Systems, Tokyo, 2009, pp. 1-6.
- [7] P. Xu, K. Shi, Y. Sun, H. Zhua, « Effect of pole number and slot number on performance of dual rotor permanent magnet wind power generator using ferrite magnets », *AIP Advances* 7, 056631, January 2017.
- [8] A. Hebala, W. A. M. Ghoneim, H. A. Ashour, "Different Design Approaches of Surface Mounted High Performance PMSG », *IEEE*, 41458, ACCS'017& PEIT'017, Alexandria, Egypt 2017.
- [9] K. Sindhya, A. Manninen, K. Miettinen, J. Pippuri, "Design of a Permanent Magnet Synchronous Generator using Interactive Multiobjective Optimization », *Transactions on Industrial Electronics*, DOI 10.1109/TIE.2017.2708038, *IEEE*.
- [10] Msc. Zoran Ivanovski " Direct - Drive Wind Turbines" *International Journal of Scientific & Engineering Research* Volume 2, Issue 10, Oct-2011, ISSN 2229-5518
- [11] D. Bang, H. Polinder, G. Shrestha and J. A. Ferreira, "Promising Direct-Drive Generator System for Large Wind Turbines," 2008 Wind Power to the Grid - EPE Wind Energy Chapter 1st Seminar, Delft, 2008, pp. 1-10.
- [12] F. Libert and J. Soulard, "Design Study of Different Direct-Driven Permanent-Magnet Motors for a Low Speed Application", in *Proceedings of the Nordic Workshop on Power and Industrial Electronics (NORpie)*, Trondheim, Norway, June 2004.
- [13] A. Lebsir, A. Bentounsi, R. Rebbah, S. Belakehal and M. E. H. Benbouzid, "Comparative study of PMSM and SRM capabilities," 4th International Conference on Power Engineering, Energy and Electrical Drives, Istanbul, 2013, pp. 760-763.
- [14] S. Belakehal "Conception & Commande des Machines à Aimants Permanents Dédiées aux Energies Renouvelables », Thèse de Doctorat en sciences, Electrotechnique, Université de Constantine, Algérie 2010.
- [15] T. Wu, T. Camarano, J. Zumberge, M. Wolff, E. S. Lin, H. Huang, X. Jia, "Electromagnetic Design of Aircraft Synchronous Generator with High Power-Density », 50th AIAA Aerospace Sciences Meeting including the New Horizons Forum and Aerospace Exposition, 09 - 12 January 2012, Nashville, Tennessee.
- [16] A. abdelli « Optimisation multicritère d'une chaîne éolienne passive », Thèse de Doctorat en génie électrique, Institut Polytechnique de Toulouse (INPT), France 2007.
- [17] M. Belatel, H. Benalla « Etude par CAO d'une machine synchrone à aimant permanent pour la production d'énergie éolienne », *Revue des Energies Renouvelables* Vol. 11 N°2 (2008) 167 – 180.
- [18] S. Mouty « Conception de machines à aimants permanents à haute densité de couple pour les éoliennes de forte puissance », Thèse de Doctorat en génie électrique, Université de Franche – Comté, Ecole doctorale Sciences pour l'ingénieur et microtechniques, France 2013.
- [19] L. Drouen, F. Scuiller, J.F. Charpentier, E. Smail, S. Clenet, « Modèle analytique de pré-dimensionnement de machines lentes à aimants de grand diamètre et a grand nombre de poles », *Conférence EF 2007, ENSEIHT, Toulouse*, 6-7 Septembre 2007.
- [20] S. Arslan, E. Kurt, O. Akizu, J. M. Lopez-Guede "Design optimization study of a torus type axial flux machine", *Journal of Energy Systems*, 2(2), 2018, pp. 43-56.
- [21] B. Kundrotas, A. Petrovas, R. Rinkeviciene, A. Smilgevicus "Research of Six-Phase Induction Motor Windings", *Electronics and Electrical Engineering*. Vol. 20, 2014, PP. 93-96.
- [22] T. Z. Htet, Z. Zhao, Q. Gu, J. Li, "Modelling and Analysis of Radial Flux Surface Mounted Direct-Driven PMSG in Small Scale Wind Turbine", *Advances in Science, Technology and Engineering Systems Journal* Vol. 2, No. 6, 94-99 (2017).
- [23] N. Fazli and J. Siahbalaee, "Direct torque control of a wind energy conversion system with permanent magnet synchronous generator and Matrix Converter," 2017 8th Power Electronics, Drive Systems & Technologies Conference (PEDSTC), Mashhad, 2017, pp. 166-171.

# Characterization of Protease milk clotting Obtained from Turkey proventriculus (*Meleagris gallopavo*)

MEKHANEG B.\*<sup>1</sup>, GIRARDET J-M. <sup>#2</sup>, BELLAL M-M. <sup>#1</sup>

(1) ENSA Ecole Nationale Supérieure d'Agronomie, Laboratoire de Technologie Alimentaire  
(2) URAFPA, équipe protéolyse et biofonctionnalités des protéines et peptides (BP2P), Nancy-Université

\*Corresponding author: E-mail: b.mekhaneg@yahoo.fr  
Ecole Nationale Supérieure d'Agronomie (ENSA) El Harrach, (16000) Alger, Algérie

**Abstract\_Valorization of avian by-products such as turkey (*Meleagris gallopavo*) proventriculus in the preparation of milk clotting enzymes constitutes an alternative to commercial rennet. The clotting enzyme of *Meleagris gallopavo* has been prepared by ammonium sulfate at 50% saturation followed by purification by cation-exchange fast protein liquid chromatography (FPLC), and determination of the clotting protease activity performed on milk incubated at 35 °C. Electrophoresis analysis revealed a band with apparent molecular mass of 36.5 kDa.**

**Keywords:** clotting activity, *Meleagris gallopavo*, protease proventriculus, turkey

## I. INTRODUCTION

The increase of calf rennet price led to investigate new milk clotting enzymes able to adequately replace calf rennet in the manufacture of dairy products [1], when possible. Different microbial alternatives are used for the production of chymosin, but these techniques are not too suitable for quality cheese production because they produce a bitter taste [2].

Several coagulating enzymes have been identified in different plant species; however many of enzyme preparations are deemed unsuitable because they produce extremely bitter cheeses [3]

However, there is little information on the purification and characterization of turkey's pepsin enzyme (*Meleagris gallopavo*). It is thus interesting to investigate such a pepsin enzyme from turkey as rennet for cheese preparation from cow's milk. The aim of the present study was to purify and characterize clotting enzyme from turkey's proventriculus, a by-product to valorise.

## II. MATERIALS AND METHODS

### 2.1. Biological Materials

Raw proventriculi were extracted from the digestive system of the turkey (*Meleagris gallopavo*). The study focused on 500 g of fresh sample rid of its fat, washed several times in distilled water, cut and conditioned in sealed plastic bags and, finally, stored at -18 °C until used.

### 2.2. Enzyme Extraction

The extraction was performed according to the method of [4] with some modifications. The proventriculus tissue was milled in 5% NaCl and 0.2% boric acid in a ratio 1/2 w/v

(weight/volume) of extraction mixture, frozen at -18 °C for 24 h, then thawing and macerating at 4 °C under gentle agitation for 24 h, and the mixture obtained was filtered on a gauze strip and the filtrate was centrifuged at 3200 g at 4 °C for 20 min and finally, the recovered supernatant was filtered on filter paper. The pH of the crude enzymatic extract was adjusted to 2.0 with 0.1 M HCl and left to stand for 15 min at room temperature and then readjusted to pH 5.0 with 0.1 M NaOH.

### 2.3. Fast protein liquid chromatography (FPLC) and electrophoretic control

The pre-purification was carried out with successive steps of ammonium sulfate precipitation at 25, 50, and 75% saturation (100% saturation corresponds to 760 g/L of ammonium sulfate at 25 °C) on crude enzyme extract. The pellet obtained with 50% of ammonium sulfate saturation was suspended in the sodium formiate at pH 3.5, then purified by FPLC onto a cation-exchange Hi-Trap SP-FF column connected to an ÄKTA-Purifier apparatus and a 0–0.5M NaCl gradient was applied for 20 min at a flow rate of 1 mL min<sup>-1</sup>. Coagulating fractions were analyzed by sodium dodecyl sulfate polyacrylamide gel electrophoresis (SDS-PAGE) on a 12% acrylamide resolving gel according to the method of [5] carried out with a Mini-Protean Tetracell (Bio-Rad Laboratories Inc., Hercules, CA, USA).

### 2.4. Determination of protein concentration

The protein concentration was determined according to the method of [6] with bovine serum albumin as the standard.

### 2.5. Determination of the enzymatic activity

The milk clotting activity expressed as rennet unit (RU) was determined according to [7]. Briefly, 1 mL of crude extract or fractions was added to 10 mL of Berridge substrate (12 g low heat spray dried skim milk powder in 100 mL of 0.01 M CaCl<sub>2</sub>), mixed thoroughly and incubated at 30 °C. The time required for the first appearance of the particles was discernible recorded. One unit of milk clotting activity was defined as the amount of enzyme required to clot 10 mL of milk in 100 s at 30 °C.

$$= \frac{10V}{T_c Q} \quad (1)$$

Where:

RU: Rennet Unit; V: volume of standard substrate (mL);  
Q: volume (mL) of crude gastric extract (CGE) or chromatographic fraction; T<sub>c</sub>: clotting time (s).

## III. RESULTS AND DISCUSSION

Poultry viscera, especially turkey proventriculus, are a source of milk coagulant proteases, currently under-exploited and easy to obtain throughout the year and require a better valuation in the cheese industry, unlike ruminant rennet, the availability of which is lower and the cost is greater.

Pepsin is one of the animal origin that has been tested for potential use as substitutes of rennet [8]

In this study, turkey proventriculus was used to purify milk clotting enzyme, the purification procedure developed in this study resulted in an active band with apparent molecular mass of 36.5 kDa that is consistent with the molecular mass reported by [9]. Both animal and microbial milk clotting proteases belong to a class of acid aspartate proteases and have molecular masses between 30000 to 40000 Da. However, the purification of the enzyme using ammonium sulfate is recommended for the enzyme preparation with excellent milk clotting properties. The presence of one active band of purified enzyme might be indicative of monomer protease. The specific activity in the crude extract increases from 1.2 to 4.6 after FPLC purification; this is explained by the elimination of the inactive proteins in the crude extract.

### 3.1. Purification of turkey's milk clotting enzyme

Purification of the clotting protease from proventriculus of turkey is summarized on **Table 1**. The extraction of crude extract was performed by maceration of the proventriculus in 5% (w/v) NaCl and displayed a clotting activity of 11.1 RU.

The process of extraction of milk clotting proteases from *Cynara Cardunculus* L. in saline medium was already reported by [4] and confirmed by [10]. NaCl can play a role in

the recovery of the enzyme. In fact, [8] obtained a clotting activity for the crude extract of 2.43 U mL<sup>-1</sup> for a concentration of 5% NaCl, whereas [11] obtained a clotting activity of 7.83 U mL<sup>-1</sup> for a concentration of 10% NaCl. These results suggest that the appropriate method for the extraction of coagulating enzymes greatly depends on the NaCl concentration.

The purification was achieved by flocculation of clotting materials from the crude extract with ammonium sulfate at 50% saturation, as the fraction precipitated at 25% saturation of ammonium sulfate presented no clotting activity, and as the fraction precipitated at 75% showed only a low activity of 0.1 RU. In the present work, the extract precipitated in 50% ammonium sulfate displayed a clotting activity of ca. 3.2 RU and specific activity of 1.5 RU mg<sup>-1</sup> higher than the initial specific activity of the crude extract of 1.2 RU mg<sup>-1</sup> (purification factor of 1.26 and purification yield of 29%). [12] obtained a clotting fraction precipitated by ammonium sulfate between 40 and 60% saturation from the viscera of boliti fish (*Tilapia nilotica*), with a specific activity of 0.25 U mg<sup>-1</sup> protein, a purification factor of 4.16, and a purification yield of 42%. Similarly, [13] have prepared a clotting enzyme extract by ammonium sulfate precipitation between 20 to 60% saturation from sea bream (*Sparus latus Houttuyn*), with a specific activity of 3.0 U mg<sup>-1</sup> protein, a purification factor of 1.4, and a purification yield of 64%.

The chromatographic profile obtained by cation-exchange FPLC (**Fig. 1**) showed 4 peaks, and clotting activity was found in the collected fractions 12–16 eluted at 0.4–0.5 M NaCl and corresponding to materials the most strongly adsorbed on the column (fourth peak). The active fractions were analyzed by SDS-PAGE (**Fig. 1**) and a single band with an apparent molecular mass of 36.5 kDa was unveiled, and agreed well with the results of [14], who found a same apparent molecular mass of 36 kDa for a clotting enzyme partially purified.

## IV. CONCLUSIONS

In the present study, a fraction of enzyme was purified for the first time from proventriculus of turkey. A fraction highly enriched in clotting enzyme was recovered with high purity by chromatography methods and turkey enzyme can advantageously replace calf rennet as it displayed a milk clotting activity. Its apparent molecular mass was 36.5 kDa. Future investigations will focus on the molecular characterization of the coagulating enzyme.

Table 1

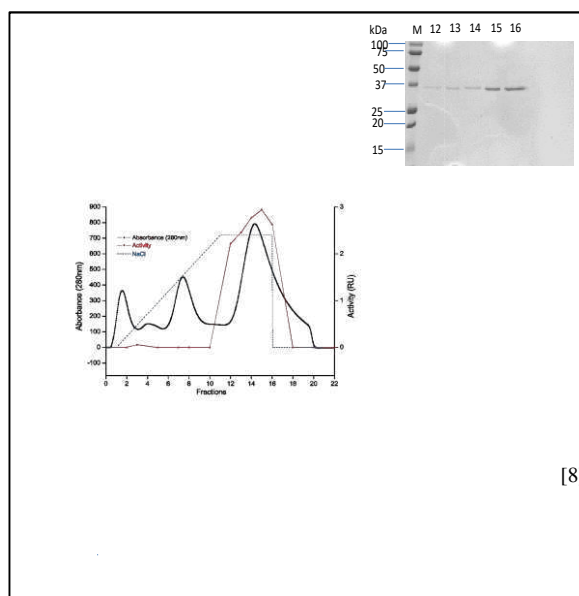
Summary of purification steps of pepsin-like enzyme of turkey (*Meleagris gallopavo*)

Purification step	Clotting activity (RU)	Amount of total protein (mg mL <sup>-1</sup> )	Specific Activity (RU mg <sup>-1</sup> )	Purification Factor	Purification Yield (%)
Crude extract	11.11	9.2	1.2	1	100
Ammonium sulfate (50%)	3.22	2.11	1.52	1.26	28.98
<b>Cation-exchange FPLC</b>					
Fraction 12	2.22	1.14	1.94	1.27	68.94
Fraction 13	2.38	0.95	2.5	1.28	107.2
Fraction 14	2.77	1.08	2.56	1.02	116.38
Fraction 15	2.94	1.41	2.08	0.81	106.13
Fraction 16	2.63	0.95	2.76	1.32	89.45

REFERENCES

- [1] M.M. Grozdanovic, L.Burazer and M Gavrovic-Jankulovic, Kiwifruit (*Actinidia deliciosa*) extract shows potential as a low-cost and efficient milk-clotting agent. *International Dairy Journal*, 32, 46–52, 2013.
- [2] A.Kumar, J. Sharma, A Kumar Mohanty, S.Grover and V. Kumar Batish, Purification and characterization of milk clotting enzyme from goat (*Capra hircus*). *Comparative Biochemistry and Physiology Part B: Biochemistry and Molecular Biology*, 145, 108–113, 2006.
- [3] M. Beigomi, M.A Mohammadifar, M Hashemi, M.G. Rohani, K Senthil and M Valizadeh, Biochemical and Rheological Characterization of a Protease from Fruits of *Withania coagulans* with a Milk-clotting activity. *Food Sci. Biotechnol*, 23, 1805–1813, 2014.
- [4] J. Tsouli, Etude comparée de l'activité enzymatique de 3 variétés d'artichauts du genre *Cinara Cardunculus* L sur la coagulation du lait. *Le Lait*, INRA Editions, 54, 415–421, 1974.
- [5] U.K. Laemmli, Cleavage of structural proteins during the assembly of the head of bacteriophage T4. *Nature*, 227, 680–685, 1970.
- [6] M.M. Bradford, A rapid and sensitive method for the quantitation of microgram quantities of protein utilizing the principle of protein-dye binding. *Anal Biochem*, 72, 248–254, 1976.
- [7] N.J. Berridge, The purification and crystallization of rennin. *Biochem J*, 39, 179–187, 1945.
- [8] F.A. Benyahia-Krid, F.Adoui, O. Aissaoui-Zitoun, H. Boughellout, E-H. Siar, A. Zikiou, and M.N. Zidoune, Effect of Sodium Chloride and Incision on the Chicken Pepsin Coagulant Activity Extracted from Proventriculus, Dried Under Partial Vacuum. *Advances in Dairy Research*, 5:3, 2017.
- [9] M.B. Rao, A.M., Tanksale, M.S Ghatge and V.V.Deshpande, Molecular and Biotechnological Aspects of Microbial Proteases. *Microbiol Mol Biol Rev*, 62, 597-635, 1998.
- [10] R.G. Beka, F.Krier, M. Botquin, V.D. Guiama, P.Donn, D.G Libouga, C.M Mbofung, K.Dimitrov, M.C. Slomianny, D.Guillochon, and D. Vercaigne-Marko, Characterization of a milk-clotting extract from *Balanites aegyptiaca* fruit pulp. *International Dairy Journal*, 34, 25–31. 2014.
- [11] H.Temiz , E.Okumus, U.Aykut, M., Dervisoglu and F.Yazici, Partial Purification of pepsin from turkey proventriculus. *World Journal of Microbiology and Biotechnology*, 24, 1851–1855, 2008.
- [12] A.E. El-Beltagy, T.A. El-Adawy, E.H. Rahma and A.A. El-Bedawey, Purification and characterization of an acidic protease from the viscera of bolti fish (*Tilapia nilotica*). *Food Chemistry*, 86, 33–39. 2004.
- [13] Q. Zhou, X.P Fu, L.J. Zhang, W.J. Su and M.J. Cao, Purification and characterization of sea bream (*Sparus latus Houttuyn*) pepsinogens and pepsins. *Food Chemistry*, 103, 795–801, 2007.
- [14] H. Temiz, U. Aykut, E. Okumus, and S. Turhan, The partial purification and properties of pepsin obtained from Turkey proventriculus. *Biotechnology and Bioprocess Engineering*, 12, 450–456, 2007.

Fig1



[8]

**Fig 1.** Elution profile onto cation-exchange column Hi-Trap SP-FF of clotting extract prepared from turkey's proventriculus after precipitation with ammonium sulfate at 50% saturation and SDS-PAGE control of the active fractions 12–16.

# Voltage Control of a Self Excited Induction Generator in a Wind Turbine: Implementation and Simulation

Rachid El Bachtiri<sup>#1</sup>, Imane Idrissi<sup>#2</sup>, Mohamed Salhi<sup>\*3</sup>, Tariq Riouch<sup>#4</sup>

<sup>#</sup> PERE Lab. EST School, USMBA University, Fez, Morocco

<sup>1</sup>rachid.elbachtiri@usmba.ac.ma

<sup>2</sup>imane.idrissi@usmba.ac.ma

<sup>3</sup>tariq.riouch@gmail.com

<sup>\*</sup> ENSAM School, UMI University, Meknes, Morocco

<sup>3</sup>salhi.ensam@yahoo.fr

**Abstract**— This paper proposes an automatic solution to control voltage and frequency, in spite of load variations, for an induction machine used as a generator and excited by a capacitor bank. Our solution consists in developing a mathematical formula that allows the calculation of the necessary capacity for a given resistive load. This formula has been determined based on the single-phase equivalent model of the generator. A test rig located in our laboratory has been used to carry out experimental achievements. First tests allow us to determine electrical characteristics of the induction machine, and to deduce equivalent model parameters. Second tests allow us to determine capacitance values under no-load and resistive load conditions. Furthermore, the control curves of the generator are obtained by modeling and simulating the studied system in the Matlab & Simulink software. Experimental and simulated results are compared and the similarity of results has been demonstrated.

**Keywords**— Wind Turbine, Self-Excited Induction Generator, Voltage Control, Magnetization

## I. INTRODUCTION

Nowadays, the asynchronous machine is increasingly utilized as a generator in isolated power systems, as in wind turbines installed in remote areas. In these regions, the electricity production is known to be difficult and expensive.

The extensive use of the asynchronous machine over conventional alternators, is justified by its enormous advantages such as: mechanical and electrical simplicity, rugged construction, low cost, power generation capability at varying speed, and easy maintenance. However, to operate as a generator, it requires reactive power to produce magnetizing current responsible of its excitation.

When the reactive power is supplied by the electrical grid, the induction generator is called Grid-Connected Induction Generator; while it is named Self-Excited Induction Generator (SEIG) or the Off-grid Induction Generator, when the reactive power is provided by a capacitor bank.

For the SEIG, a capacitor bank is star or delta connected across the stator terminals, while the rotor is driven by the wind turbine. In the case of delta connection, each single capacitor

has the line voltage at its terminals; while in the case of star connection, each single capacitor has a phase voltage at its terminals. However, it is well-known that delta connection of the capacitor bank gives more merits than the star one. Indeed, it enables the same self-excitation conditions with a three times smaller value of the capacitance [1].

The major drawback of the self-excited induction generator is poor voltage and frequency regulations [2]. The variable frequency depends on the load level and the variable voltage is produced by the excitation capacitor value, magnetization characteristics, the electrical load and its power factor [3].

When a driven asynchronous generator is self-excited by capacitors, a voltage is produced. However, if a resistive load is connected to the terminals of this SEIG, its voltage drops. Therefore, the load cannot operate under its rated voltage. So, in order to ensure that the load operates at its rated voltage, it is necessary to compensate the drop. For practical use, it is necessary to maintain the terminal voltage constant. That issue is known as the excitation automation of the self-excited generator. This automation consists of maintaining SEIG voltage constant, regardless of the load variations.

The values of the capacitance required to excite the SEIG were analyzed by [4]. Several methods are proposed for calculation of minimum capacitance value, required for self-excitation of an isolated three-phase self-excited induction generator (SEIG). In [5], the minimum capacitance value is determined under various conditions as variable load and variable rotor speed. This developed technique uses Adaptive Particle Swarm Optimization (APSO) technique, devoted for the non-linear equations. For Wind turbine driven Self-excited induction generators, an algorithm of fixed capacitor selection is proposed by [6], which is able to increase annual energy captured by the Wind Energy Conversion System (WECS).

In this paper, we propose an automatic solution which enables the compensation of the voltage drop to maintain constant the terminal voltage in spite of load variations. It is based on a model we will establish. We will develop a mathematical formula to compute the value of the necessary capacity for a given resistive load value.

This work is supported by the CNRST center, Rabat, Morocco (GISER Project)

The outline of this paper is given as follows: In section 2, a mathematical model of SEIG is presented. Then, the excitation automation of the asynchronous generator is developed in section 3. Section 4 shows the implementation of the system and experimental results. Furthermore, the simulation results, performed in the Matlab & Simulink software, are presented in section 5 and the conclusion is given in section 6.

## II. MODELING OF SEIG

Firstly, the single phase equivalent circuit of the asynchronous generator is shown in Fig. 1.  $R_s$  and  $L_s$  are the resistance and leakage reactance respectively of the stator,  $R_r$  and  $L_r$  are the resistance and leakage reactance of the rotor,  $R_\mu$  and  $L_\mu$  are respectively the iron core-loss resistance and the magnetizing reactance.  $I_s$  and  $I_r$  are respectively the stator current and the rotor current referred to the stator,  $I_\mu$  is the sum of magnetizing and core-loss current components and  $s$  is the slip machine factor.

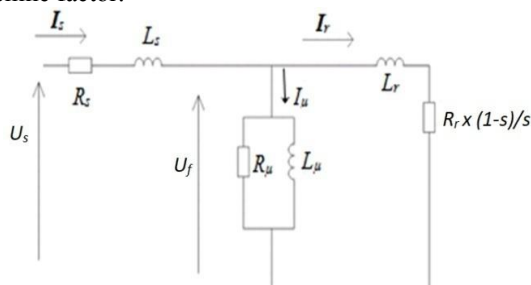


Fig.1. Single phase equivalent circuit of the asynchronous generator

To operate as a generator, an asynchronous machine requires reactive power for its excitation. Since the generator does not have an excitation circuit, the magnetizing power is provided by connecting the machine stator to the electrical grid or to a capacitor bank in the case of stand-alone use. The Fig. 2 presents the Single phase equivalent model of an asynchronous generator connected to a capacitor bank.

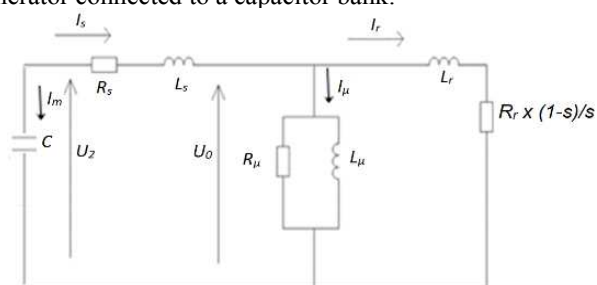


Fig.2. Single phase equivalent model of an asynchronous generator connected to a capacitor bank.

In our case of study, the excitation must be sufficient to enable the stator to generate voltage at its terminals with a constant magnitude and at constant frequency.

## III. EXCITATION AUTOMATION OF THE INDUCTION GENERATOR

### A. Self-Excitation Process of SEIG

The voltage buildup process of the three-phase induction generator is shown in Fig. 3. There is generation of small voltage 'oa', due to the remanent induction, generated when the rotor runs. This voltage 'oa' produces a capacitor current 'ob'.

This later produces a flux which gives voltage 'bc' across stator terminals. Voltage 'bc' generates current 'od' which engenders the voltage 'de'. This voltage buildup process continues till the magnetization curve of the induction generator cuts the capacitor load line. Intersection point is marked as 'f' in the Fig. 3.

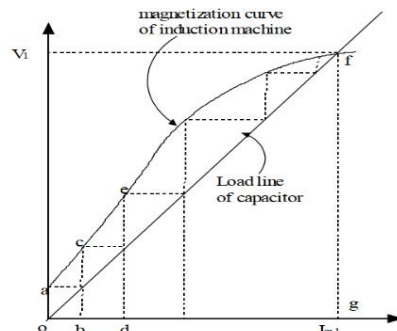


Fig.3. Voltage built-up in a 3-phase induction generator [7]

The voltage build-up depends upon the value of capacitor. It means that when the value of capacitance is high, the voltage build-up is greater.

For this test, the generator has no load, and rotor runs at synchronous speed. For drawing magnetization, one can simply measure stator voltages and corresponding currents.

The operating point is the intersection between the magnetization curve of the induction machine and the load line of capacitor, which has the following equation:

$$V_s = \frac{I_s}{C\omega} \quad (1)$$

Where,  $I_s$  is the stator line current,  $V_s$  is the phase voltage,  $C$  is the capacitance and  $\omega$  is the angular frequency.

### B. Problem Formulation

When an induction generator is utilized to produce electricity in isolated areas, for instance in wind turbine; it requires reactive power from an external supply system for its magnetization. This reactive power can be provided by a capacitor bank. However, when the asynchronous generator is feeding a load, voltage drops, and the load cannot operate under its nominal voltage. Then, in order to compensate the voltage drop, and provide constant voltage and frequency to the load, the automation of the induction generator excitation is necessary.

### C. Automation of the Induction Generator Excitation

The proposed solution aims to maintain constant voltage across the load. To achieve this objective, we have established a formula from the equivalent model of the self-excited induction generator coupled to the load, which allows to automatically compensate the voltage drop once the load (resistance) value is known. Therefore, the suitable value of the capacitance value can be determined.

The per-phase equivalent model of the induction generator, coupled to the resistive load and excited by the capacitor bank, is shown in the following figure:

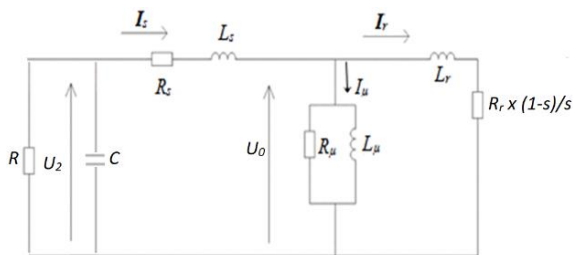


Fig.4. Per-phase equivalent model of an asynchronous generator connected to a capacitor bank and coupled to a resistive load.

From the figure and according to the voltage mesh law, we have:

$$U_2 = U_0 - \sqrt{3} \cdot I_s \cdot (R_s \cdot \cos\varphi + X_s \cdot \sin\varphi) \quad (2)$$

The following simplifying assumptions have been taken into account:

Resistive load:  $\cos\varphi = 1$  ;  $\sin\varphi = 0$ ,

Constant output voltage:  $U_0 = U_s = 380$  [V]

Star connected capacitors:  $U_2 = \frac{3 \cdot I_m}{\sqrt{3} \cdot C \cdot \omega}$

Therefore, the equation (2) becomes:

$$U_2 = U_0 - \sqrt{3} \cdot \frac{U_s}{R} \cdot (R_s \cdot \cos\varphi + X_s \cdot \sin\varphi) \quad (3)$$

$$\frac{3 \cdot I_m}{\sqrt{3} \cdot C \cdot \omega} = 380 - \sqrt{3} \cdot \frac{380}{R} \cdot R_s \quad (4)$$

By measuring  $I_m$  ( $I_m = 5,112$  A), determining  $R_s$  ( $R_s = 0.8 \Omega$ ) and  $\omega$  ( $\omega = 100\pi$ ), we have:

$$C = \frac{0,02822}{380 - 562,54/R} \quad (5)$$

From the equation (5), we can clearly notice that the load variations cause the variation of capacitance value if the constant output voltage (380V in our case of study). However, this solution remains valid as long as the load power factor is unity.

#### IV. IMPLEMENTATION OF THE EXCITATION SYSTEM FOR THE INDUCTION GENERATOR

To achieve the experimental task, a test rig located in our laboratory has been used, shown in Fig. 5, which consists of wound rotor asynchronous motor with rings. Its nominal power is 4,5 kW. It is driven by a 3 kW DC motor with separated excitation reproducing the mechanical effect of the wind turbine rotor.



Fig.5. Experimental test rig: Asynchronous generator(4,5 kW), DC motor (3kW)

Nameplates of the DC motor and of the asynchronous generator are given respectively in Fig. 6 and Fig. 7.

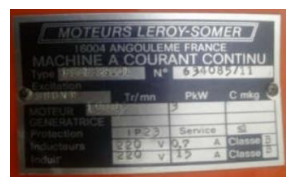


Fig.6. DC motor nameplate



Fig.7. Wound rotor asynchronous machine nameplate

The first step was the electrical parameters determination of the considered machine equivalent model (Fig. 1); which are: the stator resistance  $R_s$  and the stator inductance  $L_s$ , the rotor resistance  $R_r$  and the rotor inductance  $L_r$ , the iron loss resistance  $R_\mu$  and the magnetizing inductance  $L_m$ .

#### A. Determination of Electrical Parameters in the Induction Machine Equivalent Model

- Stator resistance ( $R_s$ ) measurement:  
 The DC test is performed to calculate the stator winding resistance  $R_s$ ; a DC voltage is applied to the stator windings of the asynchronous generator with opened rotor circuit. Both the current in the stator windings and voltage across the two phases of the generator are measured.

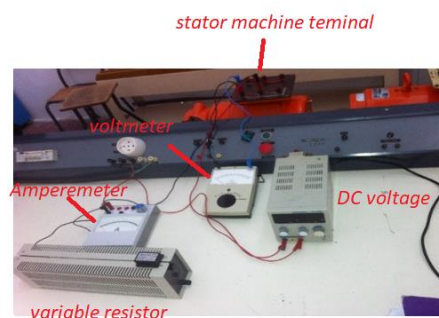


Fig.8. Manipulation scheme for  $R_s$  measurement

By using Ohm's Law:

$$R_s = \frac{U_s}{2} \cdot I_s \quad (6)$$

Where  $U_s$  the measured phase-to-phase voltage;

$I_s$  the measured current;

Thus,  $R_s = 0.8 \Omega$

- Rotor resistance ( $R_r$ ) measurement:

To measure the rotor resistance, the same manipulation scheme as before is performed with a short circuited rotor this time.

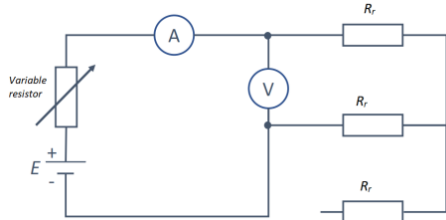


Fig.9. The performed manipulation scheme for  $R_r$  measurement

Therefore,  $R_r = 0,55 \Omega$

- $R_\mu$  and  $L_\mu$  measurement:

The elements of the magnetic circuit ( $R_\mu$  and  $L_\mu$ ) are calculated from the synchronism test of the asynchronous machine.

When the machine is operating in the synchronous mode, its rotor speed  $N$  is equal to the synchronism speed  $N_s$ . Therefore, the slip  $s$  equals zero and we have  $R_r/s$  tends to the infinity limit. For this reason, we have considered that the rotor branch is open-circuit so we determined the value of  $R_\mu$  and  $L_\mu$  from calculation of joules losses and iron losses.

- Calculation of  $R_\mu$ :
 
$$R_\mu = \frac{3 \cdot (V - R_s \cdot I_{syn})^2}{P_{syn}} \quad (7)$$

Where,  $V$  is the phase to neutral stator voltage,  $I_{syn}$  is the line current flowing in the stator winding, measured in the synchronism test,  $P_{syn}$  is the synchronism power.

Then,  $R_\mu = 439,66 \Omega$

- Calculation of  $L_\mu$ :

From the per phase equivalent model of the asynchronous machine (figure 1), we have:

$$U_f = R_\mu \cdot I_{\mu a} = X_\mu \cdot I_{\mu r} \quad (8)$$

$$X_\mu = \frac{R_\mu \cdot I_{\mu a}}{I_{\mu r}} \quad (9)$$

With:

$$I_{\mu a} = I_{syn} \cdot \cos\varphi \quad (10)$$

$$I_{\mu r} = I_{syn} \cdot \sin\varphi \quad (11)$$

And, we have:

$$X_\mu = 2 \cdot \pi \cdot f \cdot L_\mu \quad (12)$$

$$L_\mu = \frac{X_\mu}{2 \cdot \pi \cdot f} \quad (13)$$

Therefore,  $L_\mu = 138 \text{ mH}$

- Stator leakage reactance ( $L_s$ ) measurement:

This parameter was determined through the synchronism test. In fact, the reactive power in the synchronism test, noted

$Q_{syn}$ , is consumed only at the level of the circuit stator and the magnetic stator. Then, the following equation can be written:

$$\frac{Q_{syn}}{3} = X_\mu \cdot I_{\mu r}^2 + X_s \cdot I_{syn}^2 \quad (14)$$

$$X_s = \left( \frac{Q_{syn}}{3} \right) - X_\mu \cdot I_{\mu r}^2 / I_{syn}^2 \quad (15)$$

$$X_s = 2 \cdot \pi \cdot f \cdot L_s \quad (16)$$

Therefore,  $L_s = 6,17 \text{ mH}$

- Rotor leakage reactance ( $L_r$ ) measurement:

This parameter was determined from the blocked rotor test of the asynchronous machine. This test consists of star-coupling the machine and then feeding it using a balanced three-phase voltage. We gradually increased the value of the supply voltage until the rotor shaft began to rotate, at which point we blocked the shaft with pliers to bring the speed back to 0. In this test, the reactive power, noted  $Q_{sc}$ , is consumed by both the rotor and at the stator because the current flowing through the magnetic circuit is negligible. This allows us to write the equation below:

$$\frac{Q_{sc}}{3} = X_s \cdot I_{s-sc}^2 + X_r \cdot I_{r-sc}^2 \quad (17)$$

$$X_r = \left( \frac{Q_{sc}}{3} \right) - X_s \cdot I_{s-sc}^2 / I_{r-sc}^2 \quad (18)$$

$$X_r = 2 \cdot \pi \cdot f \cdot L_r \quad (19)$$

With:  $I_{s-sc}$  is the stator current in the short circuited test,

$I_{r-sc}$  is the rotor current in the sort circuited test.

Therefore,  $L_r = 1,45 \text{ mH}$ .

The following table summarizes the calculated electrical parameters of the asynchronous machine:

TABLE I. ELECTRICAL PARAMETERS OF THE ASYNCHRONOUS GENERATOR

$R_s(\Omega)$	$R_r(\Omega)$	$R_\mu(\Omega)$	$L_s(\text{mH})$	$L_r(\text{mH})$	$L_\mu(\text{mH})$
0,8	0,535	439,66	6,17	1,45	138

### B. Self-Excitation of the Induction Generator

- No-load test:

With the aim to produce a constant voltage equal to 380 volts, the stator of the asynchronous machine was coupled to a capacitor bank able to provide the sufficient reactive power for the magnetization of the machine. The bank capacitor has been connected in star arrangement and the capacitance value is:  $C_{exc} = 65,65 \mu\text{F}$  for rotor speed  $N = 1510 \text{ rpm}$  and frequency  $f = 50\text{Hz}$ .

The following figure presents the manipulation scheme of the studied test:



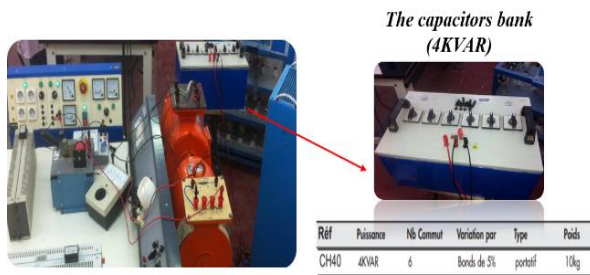


Fig.10. The performed manipulation scheme for self excitation of the induction machine (no load test)

• Resistive load test:

After having excited the asynchronous machine by the capacitor bank, a variable resistive load is coupled to the system. Figure below shows the manipulation scheme:



Fig.11. The performed manipulation scheme for self excitation of the induction machine (resistive load test)

The following table presents the obtained results of the resistive load test:

TABLE II. RESULTS OF THE RESISTIVE LOAD TEST OF THE SEIG

Load (W)	none	200	600	1400	2000
Capacity ( $\mu F$ )	65,65	77,58	91,51	125,33	167,11
Voltage (V)	385	385	377	374	374
Current (A)	5,18	5,3	5,5	5,98	6,63
Power (W)	30	180	580	1370	1990

The capacitance value is calculated according to the equation (5).

V. SIMULATION RESULTS

In order to compare experimental results to the simulated ones, the studied system is modeled and simulated in the Matlab & Simulink software.

For the no-load test, the Simulink scheme is shown in the following figure:

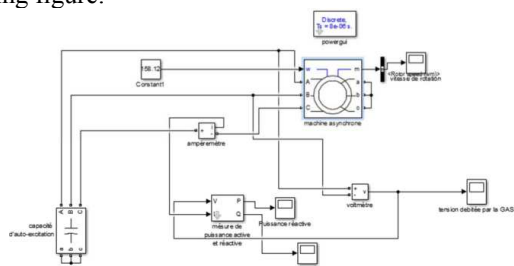


Fig.12 Simulink scheme of the no-load test of the asynchronous generator

We have fixed the rotor speed at 1510 rpm, the powers obtained from experimental test are  $P = 2870 W$  and  $S =$

3337.12 VA,  $\cos\phi = 0.86$ , the capacitance value  $C = 67.63\mu F$ . The output voltage of the generator is shown in this figure:

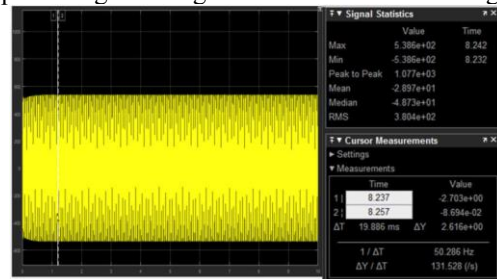


Fig.13 Delivered voltage by the generator in the no load test

From this figure, we notice that the magnitude voltage is equal to:  $U = 380.4 V$  ( $RMS = 3.804e+2$ ) and the frequency is equal to:  $f = 50.286 Hz$ . It is therefore concluded that the capacitance value which provides a voltage of 380.4 V ( $f = 50.286 Hz$ ) is  $C = 67.63\mu F$ . For the resistive load test, the load value is chosen so that the generator produces its nominal power. Therefore, the resistance  $R$  is fixed at  $32 \Omega$ . the manipulation scheme performed in Simulink is given by the figure below:

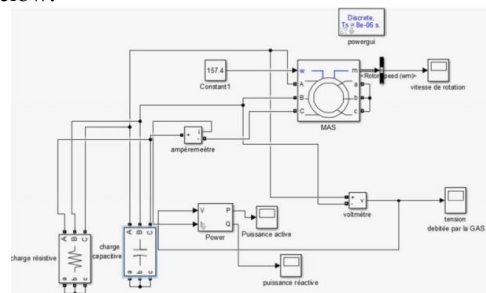


Fig.14 Simulink scheme of the resistive load test of the asynchronous generator

When the capacitance value is maintained at  $C = 67.63 \mu F$ , the delivered voltage has dropped across the load. (from 380.4V to 225.4V, which gives a voltage drop of 155V. Moreover, the frequency is decreased ( $f = 49.369 Hz$ ). For this reason, we have applied the proposed solution of excitation automation given by the equation (5) and the capacitance value  $C$  becomes  $C = 77.62 \mu F$  for  $R = 32 \Omega$ . The obtained voltage is given as follows:

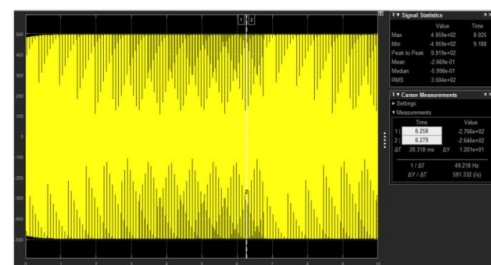


Fig.15 Output voltage by the generator with the nominal resistive load

From the figure, it is clear that the new value of the output voltage is 350.4V and the frequency  $f$  is equal to 49.218 Hz. However, these results do not meet our objectives, which are 380V and 50 Hz.

To overcome this problem, we have drawn two control curves. These curves allow the determination of the capacitance

values which excite continuously the generator to deliver a fixed voltage of 380 V and a constant frequency of 50 Hz. The first control curve plots the capacity variation along with the resistive load while fixing the rotor speed  $N$  of the generator. For instance, when  $N$  is equal to 1503 rpm, we get this curve:

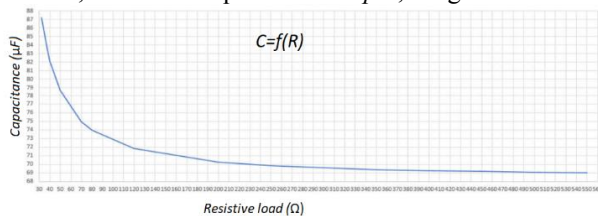


Fig.16 Capacitance value variation as function of resistive load for  $N = 1503$  rpm

For  $N = 1528$  rpm, we have:

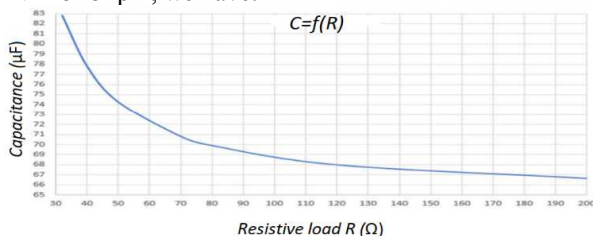


Fig.17 Capacitance value variation as function of resistive load for  $N = 1528$  rpm

Therefore, we can conclude that the capacitance value is inversely proportional to the resistive load.

The second control curve plots the capacitance variation as function of the rotor speed of the generator while maintaining the load constant (nominal load  $R = 32\Omega$ ). This scenario occurs for variable speed turbines with fixed loads. The obtained curve is presented below:

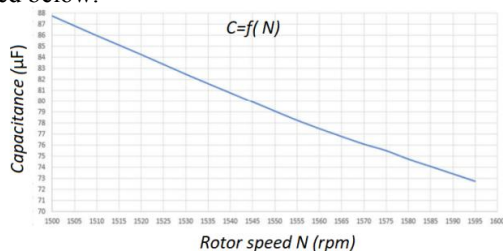


Fig.17 Capacitance value variation as function of rotor speed of the generator

The obtained curve is a linear regression line, which shows that when the rotor speed decreased, the capacitance value increased. Furthermore, when the generator is operating at the synchronous speed of rotation, the capacitance value reaches its maximum.

The following table presents the comparison between the simulation results and those obtained from the experimental tests:

TABLE III. SIMULATED AND EXPERIMENTED RESULTS COMPARISON

Operating conditions	Simulation results	Experimental results
-No load test -Constant rotor speed $N = 1510$ rpm	$C = 67.63 \mu\text{F}$ $U = 380$ V	$C = 65.65 \mu\text{F}$ $U = 385$ V

-Resistive load test -Constant load $R = 710.645 \Omega$	$C = 77.58 \mu\text{F}$ $U = 413.7$ V	$C = 77.58 \mu\text{F}$ $U = 385$ V
--	--	--

From this table, we conclude that the simulation results consolidate the experimented ones.

## VI. CONCLUSION

The use of induction machine as a generator is becoming popular in renewable energy systems such as wind turbines. The induction generator has the possibility to operate independently from the grid utility since the reactive power necessary needed for its excitation is provided by an external source, which is in most of the time, a capacitor bank connected to the generator stator windings. However, the major problem of this technology is the control of the output voltage under variable loads and variable rotor speeds. To solve this problem, an automatic solution of voltage drop compensation so as to maintain constant voltage under load variations, is proposed. This method consist sin developing a mathematical formula, which determines the necessary capacitance value for a given resistive load. To carry out the implementation of the induction generator excitation, a test rig composed of wound rotor asynchronous motor driven by DC motor with separated excitation, has been used. Firstly, we have determined the electrical parameters of the induction generator equivalent model. Secondly, the excitation of the induction generator has been ensured by means of connecting a capacitor bank to the generator stator windings, under no-load and resistive load conditions. The necessary capacitance value has been determined in the two cases with the objective to obtain a constant output voltage of 380 V. Then, the control curves of the generator obtained from experimental results are compared to those got by modeling and simulating the studied system in the software Matlab & Simulink. The comparison established has demonstrate the similarity between simulated and experimented results.

## REFERENCES

- [1] Levi, E., & Liao, Y. W. (2000). An experimental investigation of self-excitation in capacitor excited induction generators. *Electric Power Systems Research*, 53(1), 59-65.
- [2] Shah, M., & Somkun, S. (2017). Efficiency Evaluation of Three Phase and Single Phase C2C Self-Excited Induction Generator for Micro Hydro Power Application. *Energy Procedia*, 138, 193-198.
- [3] Borkowski, D. (2016). Voltage and frequency control of A stand-alone induction generator using sVPWM converter in a small reservoir hydropower plant. *Czasopismo Techniczne*, 2016(Elektrotechnika Zeszyt 3-E 2016), 51-63.
- [4] Capelo, B., Pérez-Sánchez, M., Fernandes, J. F., Ramos, H. M., López-Jiménez, P. A., & Branco, P. C. (2017). Electrical behaviour of the pump working as turbine in off grid operation. *Applied energy*, 208, 302-311.
- [5] Chatterjee, H. S., & Mahato, S. N. (2016, January). Calculation of minimum capacitance of isolated three phase induction generator using adaptive PSO technique. In *2016 International Conference on Microelectronics, Computing and Communications (MicroCom)* (pp. 1-4). IEEE.
- [6] Fernandes, J. F., Pérez-Sánchez, M., da Silva, F. F., López-Jiménez, P. A., Ramos, H. M., & Branco, P. C. (2019). Optimal energy efficiency of isolated PAT systems by SEIG excitation tuning. *Energy conversion and management*, 183, 391-405.

# Preparation and characterization of nickel-based catalysts deposited on ZrO<sub>2</sub> for methane steam reforming.

Akila BELHADI<sup>#1</sup>, Ouiza CHERIFI<sup>#2</sup>

<sup>#</sup> Laboratoire de chimie du Gaz Naturel, Faculté de Chimie, U.S.T.H.B, BP 32, Alger, Algérie.

<sup>1</sup> sarakila@yahoo.fr

<sup>2</sup>second.author@second.com

**Abstract**—The activity and stability of NiO (4wt%) catalysts supported on ZrO<sub>2</sub> were investigated for the methane steam reforming between 475 and 700 °C at atmospheric pressure. The catalysts were prepared by the impregnation method. They have been characterized by various physical methods like atomic absorption, BET technique, X-ray diffraction. According to the catalyst, the activity can be due, not only to the interaction nickel-support but also to the physico-chemical properties of the support.

**Keywords**— Methane, steam reforming, nickel, coke, supports oxides

## I. INTRODUCTION

Among the advanced research and the existing processes in the area of chemical conversion of natural gas, the classical methane steam reforming (MSR) is an indirect conversion via synthesis gas and remains extensively used [1]. The hydrogen is a clean energy that could play a key role as energetic source for fuel cells and for the environmental protection [2].

Among the catalysts based on transition elements, used in the steam reforming of methane, nickel is the most studied element [3]. It has been reported that nickel presents good catalytic performances when supported on Al<sub>2</sub>O<sub>3</sub> doped by MgO and CaO [4]. Mixed oxides such as Al<sub>2</sub>O<sub>3</sub>-ZrO<sub>2</sub>, prepared by sol-gel method, or by grafting zirconium on the surface of the alumina.

The major problem with nickel based catalysts, is carbon deposition to form coke which deactivates the catalysts. To remedy this inconvenient, some authors examined the use of the nickel promoted by an alkaline oxide [5] in sweeter conditions.

The aim of the present work is to compare the activity, the selectivity and the carbon formation of two series of nickel based catalyst (4 wt. %) supported on ZrO<sub>2</sub> during the MSR reaction. The catalysts have been characterized after

calcination and reaction by BET, atomic absorption, X-ray diffraction (XRD).

## II. EXPERIMENTAL

### A. Catalysts preparation

The solids Ni/ ZrO<sub>2</sub> were prepared by impregnation of the support ZrO<sub>2</sub> with Ni(NO<sub>3</sub>)<sub>2</sub>·6H<sub>2</sub>O (1 M) (Merck). The solution was stirred during 2 h, and then evaporated at 80 °C under agitation. The solid was dried at 80 °C (12 h), calcined during 2 h at 300 °C and 2 h at 500 °C at a heating rate of 4 °C/mn, in air flow (1.2 L h<sup>-1</sup>). The catalysts were then sieved to have a particle diameter less than 0.16 mm.

### B. Catalysts characterization

The solids were analyzed by atomic absorption thanks to a spectrometer type Perkin-Elmer 1100 B. The specific surface areas were determined by the BET method using an analyzer of surface type (Coultronics 2100E). The crystal structures were identified by XRD with a diffractometer ( $\theta/2\theta$  CGF) provided with a proportional detector and using K $\alpha$  molybdenum anticathode ( $\lambda=0.70930$  Å). The X-ray patterns were obtained for  $2\theta$  values ranging from 20° to 70°. The apparent size of nickel oxide (nickel) particles was calculated by the Scherrer formula,  $L = 0.9\lambda/\beta\cos\theta$ , where  $\beta$  is the width of the most intense NiO peak at half-height, and  $\theta$  is the corresponding Bragg angle.

### C. Reactivity

The catalytic tests were carried out in a quartz reactor fixed bed ( $L=65$  cm,  $\varnothing=1$  cm) under atmospheric pressure. The catalyst (0.1 g) is pre-reduced at 500 °C under hydrogen flow (1.2 L h<sup>-1</sup>) before introduction of the gas mixture (H<sub>2</sub>O/CH<sub>4</sub> = 3.3) diluted in argon flow and obtained by crossing of a mixture CH<sub>4</sub> (10 %)/Ar, in a saturator with a thermostated bath (65 °C, 1.2 L h<sup>-1</sup>). The

reactants and the products (CO, CO<sub>2</sub> and CH<sub>4</sub>) were analyzed by gas chromatography thanks to TCD chromatograph (Hewlett-Packard 5730) on a carbosieve B column, 100-200 mesh, of 2 m of length, using hydrogen as vector gas.

Before each analysis, the reactants and products pass through a water-trap at 0 °C to remove water. The conversion of CH<sub>4</sub> and product selectivities are calculated using following formulas:

$$\text{Conversion}_{\text{CH}_4} (\%) = \frac{n_{\text{CH}_4}^{\text{in}} - n_{\text{CH}_4}^{\text{out}}}{n_{\text{CH}_4}^{\text{in}}} \times 100$$

$$\text{Selectivity}_{\text{CO}} (\%) = \frac{n_{\text{CO}}^{\text{out}}}{n_{\text{CH}_4}^{\text{in}} - n_{\text{CH}_4}^{\text{out}}} \times 100$$

$$\text{Selectivity}_{\text{CO}_2} (\%) = \frac{n_{\text{CO}_2}^{\text{out}}}{n_{\text{CH}_4}^{\text{in}} - n_{\text{CH}_4}^{\text{out}}} \times 100$$

$$\%C = (n_{\text{CH}_4}^{\text{in}} - (n_{\text{CH}_4}^{\text{out}} + n_{\text{CO}}^{\text{out}} + n_{\text{CO}_2}^{\text{out}})) \times 100$$

n : number of moles

### III. RESULTS AND DISCUSSION

#### A. Catalytic systems characterization

The physical characteristics of the solids are summarised in Table I. The atomic absorption analysis shows that the composition of the systems is very close to the theoretical one.

TABLE I  
 CHARACTERISTICS OF Ni/SUPPORT SYSTEMS

Samples	SBE m <sup>2</sup> /g	Ni <sub>exp</sub> wt%	Ni <sub>theo</sub> wt %	XRD results			
				d <sup>a</sup> (nm) NiO	d <sup>a</sup> (nm) Ni	before reaction	After reaction
ZrO <sub>2</sub>	93						ZrO <sub>2</sub>
4% Ni/ZrO <sub>2</sub>	86	4.3	4	35.8	21.5	NiO, ZrO <sub>2</sub>	Ni <sup>0</sup> , ZrO <sub>2</sub>

[a]: Evaluated from the full width β at half maximum of the most intense XRD peak using the Scherrer relation.

The specific surface areas of 4wt %Ni/ZrO<sub>2</sub> are 86 m<sup>2</sup>/g, slightly lower than that of the ZrO<sub>2</sub> support (93m<sup>2</sup>/g).

The crystallite size was calculated from X-ray line broadening of NiO and that of Ni peaks (2θ= 19.5° and 20° respectively) using the Scherrer equation. The results show that the support influence significantly the average size of Ni particles with ca. 22 nm for Ni/ZrO<sub>2</sub>, while for the NiO particles, the value is ca. 36 nm for carriers.

After calcination at 500 °C, the XRD pattern of 4 wt% and after MSR reaction, the presence of Ni<sup>0</sup> metallic species and that of support are visible in the patterns of Ni/ZrO<sub>2</sub> (Table 1), The absence of peaks corresponding to carbon in presence of Ni/ZrO<sub>2</sub> catalyst could be due to an amorphous form of carbon.

#### B. Methane Steam reforming reaction

The catalytic performances of supported Ni systems in the MSR reaction were examined in the temperature range (475–700 °C), after reduction pretreatment under hydrogen flow at 500 °C (1.2 L/h). The MSR reaction over the catalysts leads to the formation of CO, CO<sub>2</sub>, H<sub>2</sub> and carbon and the results are reported in Figures 2, 3

#### C. Variation of the catalytic activity over the reaction time

For the preparation of 4%Ni/ZrO<sub>2</sub> sample, two calcination temperatures (500 and 700°C) were used to examine their effect on the catalytic performance. Figure 1 shows methane conversion as a function of reaction temperature.

After reduction pre-treatment (H<sub>2</sub>/500 °C/overnight), 4%Ni/ZrO<sub>2</sub> system leads to similar evolution of the methane conversion with reaction temperature for calcinations temperatures 500 and 700 °C. when the catalyst is calcined at 500 °C, the CO<sub>2</sub> formation is favoured at low reaction temperatures ( > 650 °C), the CO selectivity is favoured at high temperatures( < 550 °C). This result shows that the used calcination temperature, during the catalyst preparation, does not have a significant effect on the conversion whereas CO formation is favored when the calcination temperature is 500 °C. So, the calcination temperature was fixed at 500°C for all studied systems.

TABLE II  
 CATALYTIC ACTIVITIES OF NiO/ZrO<sub>2</sub>

Catalysts	Temp (°C)	Conv (%)	Select CO (%)	Select CO <sub>2</sub> (%)	% C	H <sub>2</sub> 10 <sup>-6</sup> (mol/g h)
4%Ni/ZrO <sub>2</sub>	475	22	12	42	46	-
	500	33	30	23	47	17.0
	550	49	46	6	48	17.2
	600	62	42	traces	58	17.4
	650	75	41	0	59	17.5
	700	82	41	0	59	17.5

The catalytic activity of 4%wt NiO/ZrO<sub>2</sub> in the MSR reaction was examined in the temperature range (475–700 °C) after in-situ pre-treatment of the catalyst under hydrogen flow at 500 °C overnight. Similar evolutions of the methane conversion as a function of time-on-stream were obtained at different temperatures for 4%wt NiO/ZrO<sub>2</sub> catalyst. Steady-state was reached at the beginning of reaction for all temperatures indicating a good stability of this system. The catalytic activity of 4%wt NiO/ZrO<sub>2</sub> became stable in less

than 3 h for reaction temperatures below 700 °C. The methane conversion increases from ca.20 to ca. 85% in presence of 4%wt NiO/ZrO<sub>2</sub> with increasing of reaction temperature from 475 to 700 °C, reflecting the endothermic nature of MSR reaction.

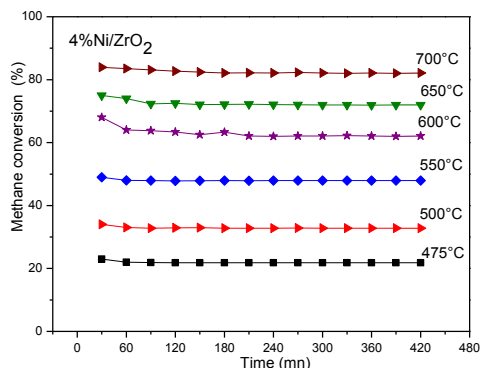


Fig. 1: Methane conversion vs. reaction time, for catalysts 4% Ni/ZrO<sub>2</sub> at different temperatures, m= 0.1 g, Tred= 500 °C/H<sub>2</sub>/overnight, d= 1.2 L h<sup>-1</sup>, H<sub>2</sub>O/CH<sub>4</sub>= 3.3.

The evolution of the methane conversion with time shows that a stationary regime is reached after ~ 3 h (Fig. 1). The setting in mode is accompanied by the formation of CO<sub>2</sub> which strongly decreases with the profit of the CO formation as one approaches the stationary regime. This indicates an incomplete reduction of catalysts during the pre-treatment in H<sub>2</sub> (500 °C) and thus the reactional mixture produces species on surfaces more reduced than hydrogen itself [6]. We note an important carbon deposition at 600 °C on catalysts. This result is agreement with the literature, according to Nielsen [7] who found that carbon deposition, on nickel catalyst has different temperature regimes: usually, ~ 550 °C, the activation energy of coke formation changes to a negative value.

The testing results show that catalytic performances of Ni/ZrO<sub>2</sub> are very sensitive to temperature from 500 to 700 °C, and conversions varying between 22 - 82 % (Fig 2) and CO selectivity varying between 12 - 41% (table II). We notice an important carbon deposition at 600 °C on catalyst (table II).

The best hydrogen production is at temperature between 650-700°C (17.5%) (fig 3).

Moreover, we noticed no diffusional limitation (effect of mass, flow etc...). The experimental conditions of the reaction are chosen so that they are as optimal as possible. It appears that the catalyst is more active. This is can be due to a better dispersion of the active phase for the weakly charged catalyst, a result in agreement with the literature data.

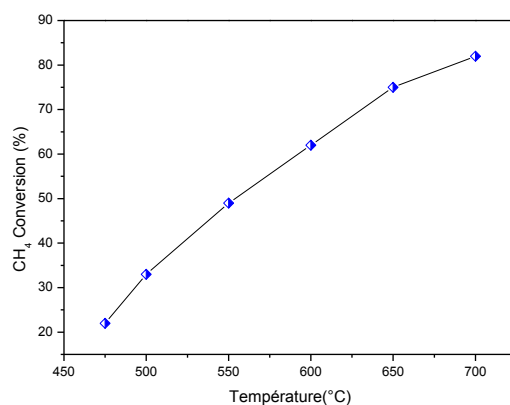


Fig. 2 Conversion of the methane versus temperature for nickel-based catalysts with ratios of 4% NiO/ZrO<sub>2</sub> at different temperatures, m= 0.1 g, Tred= 500 °C/H<sub>2</sub>/overnight, d= 1.2 L h<sup>-1</sup>, H<sub>2</sub>O/CH<sub>4</sub>= 3.3.

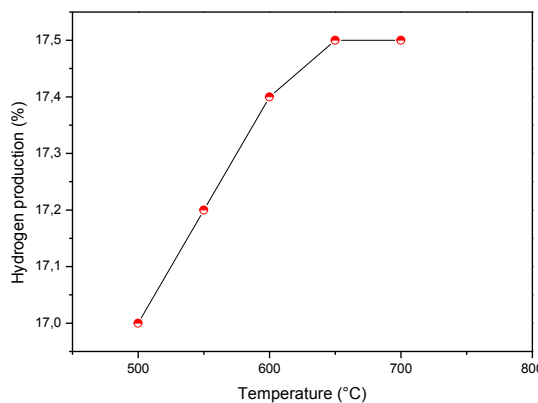


Fig.3 : Production of hydrogen according to the temperature on the nickel-based catalysts, with ratios of 4% NiO/ZrO<sub>2</sub> at different temperatures, m= 0.1 g, Tred= 500 °C/H<sub>2</sub>/overnight, d= 1.2 L h<sup>-1</sup>, H<sub>2</sub>O/CH<sub>4</sub>= 3.3.

#### IV. CONCLUSIONS

The reactivity, of CH<sub>4</sub>/H<sub>2</sub>O reaction, for synthesized Ni-based catalysts (4 % of NiO) supported on ZrO<sub>2</sub> was investigated at temperatures ranging from 475 to 700 °C with the aim of facilitating the formation of synthesis gas. It has been shown that:

The catalyst is more active. This result can be explained by a better dispersion of the active phase for the lower charged catalysts.

#### REFERENCES

- [1] Sanbing Zhang, Jiankang Wang, Xiaolai Wang, *Journal of Natural Gas Chemistry* 2008, 17:179.

- [2] Shinku Lee, Joongmyeon Bae, Sungkwang Lim, Joonguen Park, *J Power Sources*, 2008, 180:506.
- [3] K. O. Christensen , D. Chen, R. Lødeng, A. Holmen. *Appl Catal A: General*, 2006, 314(1): 9.
- [4] Tadeusz Borowiecki, Wojciech Gac, Andrzej Denis, *Appl. Catal. A: Gen.* 2004, 270:27.
- [5] N. Martin, M. Viniegra, E. Lima, G. Espinosa, *Ind. Eng. Chem. Res.*, 2004, 43 : 1206.
- [6] A. Belhadi, O. Cherifi; *J. Soc. Alger. Chim.*, 2009; 19(1), 49-62.
- [7] J.R. Rostrup-Nielsen, in *Catalysis Science and Technology*, eds, J.R. Anderson and M. Boudart (Springer-Verlag, New York), 1984, Vol. 5:1.

Amri Khaoula<sup>a\*</sup> and Alkama Djamel<sup>b</sup>

<sup>a1</sup> *PhD student, Laboratory ETAP:*

*Environment and Technology for Architecture  
and Cultural Heritage, University Blida1,  
Algeria;* <sup>b</sup>*Professor, University of Guelma,  
Algeria.*

amrikhaoula12@gmail.com\*corresponding author

**Abstract:**

The following study focuses on the investigation of climatic performance of the vernacular architecture in hot context, in order to prove the positive behaviour of this heritage without recourse to mechanical solutions of climatisation ; it aims also to extracting a sum of recommendations forming alternatives to promote local ecological architecture. The methodology followed is based on an experimental analysis, presented by a series of measurements on three determining factors: temperature, relative humidity and air velocity. The sample examined preserves the traditional architectural typology, with the principle of centrality and introversion towards courtyard, covered by elongated vaults and built with local materials (gypsum and sand rose stone). The tests were carried out in hot period. The results obtained show the famous adaptability between architectural solutions chosen and climatic implications, it proves the performance of this heritage in terms of thermal comfort and climatic adaptability.

**Keywords:** Adaptability, Arid context, Climate, Durability, Vernacular Architecture.

**Introduction:**

Nowadays, the problem of over-consumption of energy has become a major challenge for modern lifestyles. Among other things, it is a question of developing an architecture that is eco-responsible, functional, comfortable, economical in raw materials and respectful of the environment. However, this multiplicity of responses is not new: the study of vernacular constructions proves the multitude of solutions that can provide users with the necessary comfort, while respecting the integrity of the territory and the particularities of each region. The latter is surprisingly diverse, strongly influenced by the local context, cultural traits and the impact of physical environments. These forms, materials and techniques have always been dictated by the microclimate and the advantages offered by locally available resources.

In Algeria, urban and Saharan architecture is developing. The pace of construction is being challenged by the continuous increase in demand for housing, due to the constant increase in the urban population, with traditional materials giving way to cinder blocks. Sand-colored plasters are neglected and local architecture is marginalized in favor of impersonal and



standardized designs [1]. As a result, the desert city has lost its originality and bioclimatic qualities. Based on this observation, the study of vernacular experiences focused on understanding climate adaptation methods and tools, particularly in difficult and hostile contexts, provides an opportunity to acquire knowledge and information. For this reason, this research aims to study the influence of the architectural typology of the housing unit and its construction materials on the improvement of the thermal atmosphere of the spaces, through the comparison between vernacular and contemporary buildings, as in the case of the Oued Souf, which is part of south-east Algeria, based on its specific typology built in vaults and domes, as well as its specific local materials: rose bush and gypsum. The interpretation of the information collected during the survey shows the performance of vernacular knowledge and the fact that the choice of such a typology is not random but the result of the combination of a multitude of factors.

- **Method and technique:**

The study is structured in two main parts. The first part describes the general geomorphological context of the region, as

well as the particularities of vernacular typology from the point of view of spatial organization and construction materials. A second one consists of a series of measurements applied to sample in the hot season, precisely in August, using an anemometer measuring the three factors: temperature, humidity and air speed for one day. All the measurements are presented in graphs.

## **2. Presentation of the study region:**

### **2.1. Situation and delimitation:**

The study area is part of the Algerian lower Sahara, located in the south-east, on the northern borders of the eastern Erg. It is limited in the North by the Melghir and Merouane mountain peaks, in the South by the extension of the Grand Erg Oriental, in the West by the immense oasis of Oued Righ and in the East by the Tunisian borders [2]. **Figure .1.**



**Figure.1.** General Situation of the region.

### **2.2. Geographical character:**

In contrast to important regions of the Algerian lower Sahara, which have long acted as relays along an itinerary, have

been driven by trans-Saharan trade; the Souf region is different. This territory, for which the large Erg was an obstacle to caravan traffic, was for a long time a blind spot and a meeting place for groups seeking a place of refuge. Jean Brunhes described these regions as "Lost in the middle of the sands, and separated from all the other groups of oases by several days of walking, they constitute a small world apart"[3]. For generations, the inhabitants of this region have struggled and reflected on the best way of life, despite an environment characterized by poor vegetation, dry air and a considerable lack of surface water. The existence of an oasis system created by cratering has made life in the region possible. This system consists of digging deep excavations at the bottom of which the palms are planted, so the roots are in direct contact with the water table, this original technique has given the region a strictly typical physiognomy by shaping the natural landscape in the form of a set of funnels .**Figure. 2.**



**Figure.2.** Agrarian system (Ghout)

### 2.3. Climate context:

The study area is characterized by a dry desert Saharan-type climate with: dry atmosphere, high temperature, scarcity of bad weather and strong sand winds. Summers are scorching, arid and open and winters are chilly, dry and open overall. During the year, the temperature generally varies from 5°C to 40°C [4]. Metrological data show that: The very hot season lasts months, with a maximum average temperature of 45°C and a minimum temperature of 27°C. While the cool season extends from November to March, with a minimum average temperature of 5°C and a maximum of 16°C. Indeed, the region is exposed to a movement of active winds almost all year round, the most violent is the Sirocco (Chehili) very hot and dry, it blows from the south and causes very significant damage (drying out, dehydration).**Figure.3.**

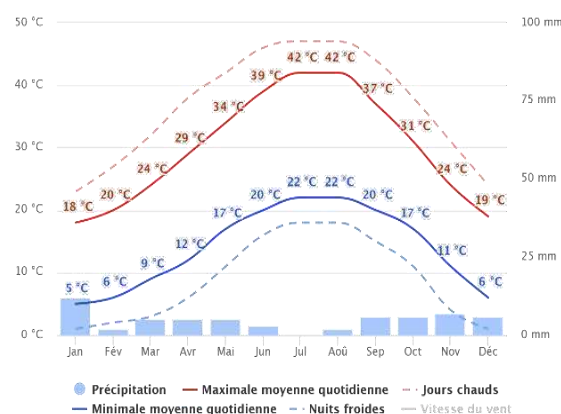


**Figure.3:** Climatological data of the region

### 3. The vernacular typology:

#### 3.1. The housing organisation:

The overall structure of the housing unit follows the shape of the plot; all the units are joined together beside each other, limited to a single ground floor, forming a compact and homogeneous structure. It is presented with blind walls, the continuity of which is interrupted only by small openings placed at the top and a single intimate door. The first reading of the typical plan of the house allowed us to observe that this unit takes up in its spatial organization the classical model of the Maghreb house with the principle of centrality, a courtyard in the center, named (haouch) and the rooms around, called (diars). Nevertheless, there are some particularities, one linked to the existence of a space particular to the region called (sabat), (Marc cote, 2005). Which is a relaxation space semi-open to the courtyard, the other concerns the denomination of the spaces. It also has a (skiffa), a chicane space of great symbolic value, used to keep the courtyard away from outside view. **Figure.4.**

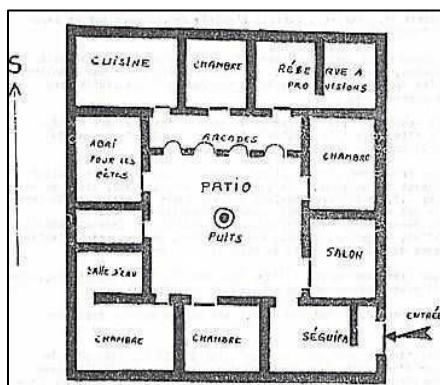


**Figure.4.** housing typology. [3].

### 3.2. Construction materials:

#### *Local materials:*

Given the nature of the soil and subsoil, which excludes the use of wood, ashlar and clay, only the exploited local materials are used: *louss* (sand rose) and *tafza* (gypsum). The first is a very hard gypsum concretization, which in free form gives sand roses, but in continuous sedimentation gives a resistant slab; this material constitutes the construction stones of walls and basements

#### **.Figure.05.a.**

The second is a lighter and more reliable coating which, once fired, gives a good plaster, once dried it constitutes a very resistant binder, found buried under the sand in the form of parts or plates in the northern part of the region, this stone is removed and burned in incinerators. The development of this industry to promote the creation of traditional ovens called (*kusha*). These burnt stones are struck with a kind of drumstick until they become a powder. **Figure.05.b.**



**Figure.05.a.** the sand rose stone (*louss*).

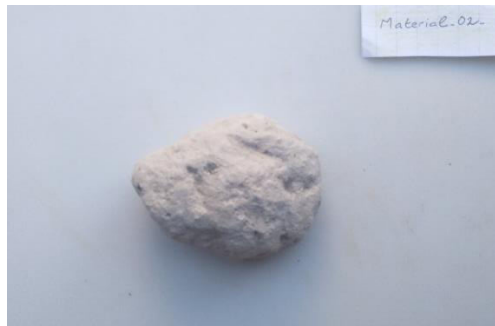


**Figure.05.b.** Gypsum plaster stone (Tafza).

#### 4. Investigation phase:

To assess the thermal performance and examine the behaviour of dwellings in the face of climatic constraints, a measurement campaign was carried out on two samples during the summer period of 2018, precisely during the month of August. Measurements were carried out between 6am and 9pm using an anemometer measuring the three parameters: indoor temperature "c°", relative humidity "%", air velocity "m/s". [5]. as well as the outdoor temperature at street level. The two rooms chosen are: the sabat room and the living room with a one-hour interval between measurements.

#### 4.1. Description of the instrument:

The instrument used is an anemometer of type: TMA5 amp with one: capacitive humidity sensor and one with precision thermistor, and an external temperature sensor to measure the temperature of walls and floors. **Figure .06.** The instrument is placed at a height of 1.40 m

in the centre of the chamber [6], the air flow sensitive fan is directed towards the door. the measured values are displayed with an accuracy of (0.00) unit.



**Figure.6:** The instrument used during the campaign.

#### 4.2. Description of sample:

The sample is presented by a vernacular house, built of local materials: sand rose stone and gypsum plaster. Overall, this unit retains its original appearance with a central courtyard and surrounding rooms, 50 cm thick walls made of sand rose stones and gypsum mortar, all covered by low-profile vaults pierced by ventilation holes. Measurements were taken in the living room and in the sabat room.

**Figure.07.**

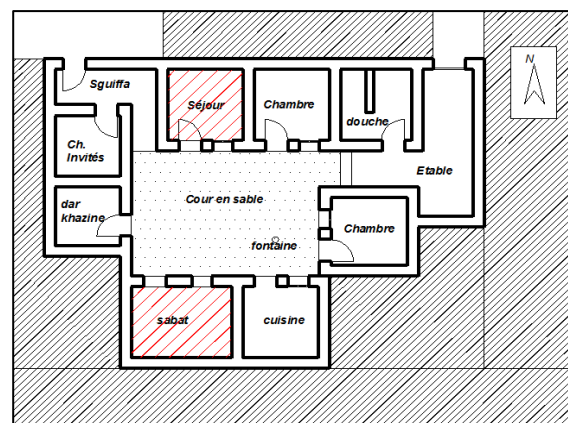




**Figure 07:** view of the sample

## 5. Result and discussion:

### Temperature measurements inside the rooms:

The thermal investigation shows different thermal behaviours during the 24 hours of measurement, governed by variations in external temperatures, solar incident power and human activity. Indeed, considering that the type of thermal transfer is carried out by convection through the external walls as well as the roof.

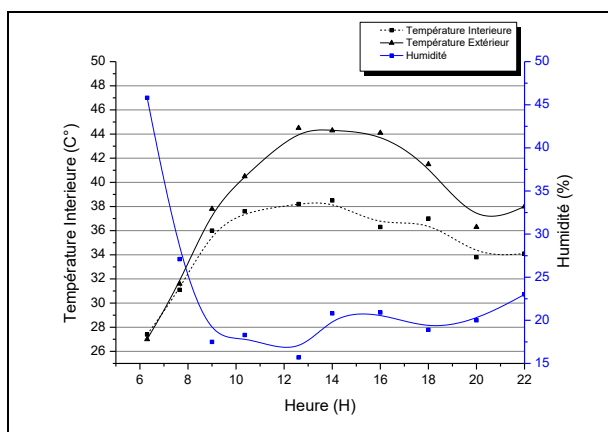


**Figure.08.**Evolution of the temperature and relative humidity inside the summer room(*Sabat*) as well as the outside temperature at the street level, 05 August 2018,(Vernacular housing).

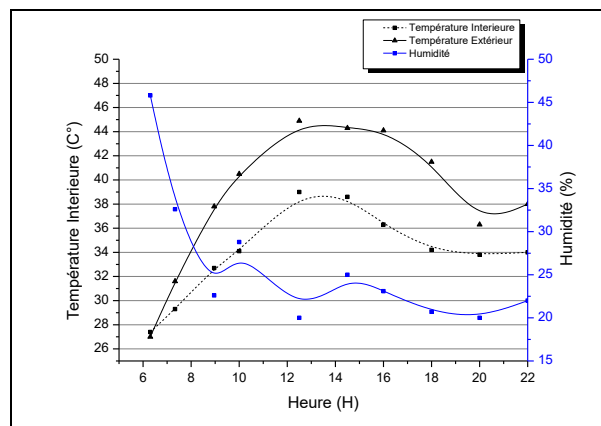


**Figure.09.** Evolution of the temperature and relative humidity inside the living room as well as the outside temperature at the street level, 05 August 2018 , (Vernacular housing). The diagrams on **figures .07.08.** show positive behaviour, especially during the critical period, especially between 12:00 and 16:00 hours. Measured temperature increases over time but it keeps a range of 8.9 C° between the outside and the inside, because it reaches a maximum of 38.5 C° at 12.30h and 14h while outside the maximum measured temperature is 44.9 C°. Overall, we can distinguish 3 decisive periods:

*From 6am to 10am:* a humidity level is too high caused by the accumulation of heat released during the night, (50%), with the beginning of human activity and the opening of windows the air begins to renew this level begins to decrease with a slight increase in temperature inside.

*From 12 noon:* during this period the indoor temperature rises rapidly and reaches its peak at 1:30 p.m. influenced by outside temperature fluctuations and the change in

human behaviour from 12 a.m. onwards: all openings are closed except that the doors are opened and protected by shades that encourage the renewal of air with the central courtyard. Nevertheless, there is a slight difference between the two diagrams: the summer chamber (*Sabat*) .**Figure.08**, which faces northwest has a uniform variation with an interval of less than two degrees compared to the living room which faces southeast, mainly due to the orientation effect and the number of walls in contact with the outside environment.

*From 4pm to 8pm:* the temperature measured inside begins to gradually decrease with a slight increase in humidity caused by the watering of the sand covering the rooms and the central courtyard

*During the night:* walls release the heat stored during the day towards the interior [7]and consequently the interior temperature increases, this justifies the return of temperature increase from 22 h. the thing that explains the nomadism of the occupants during the night towards the yard to sleep.

The interval of temperature between inside and outside is mainly justified by the large mass and thickness of walls, which measures 45 cm, built of gypsum stone, which have good thermal insulation, used to store heat throughout the day and decrease its direct transfer. It insulates the interior and maintains a

steady temperature inside the rooms. The shape and height of the roof also plays a very important role, the vaults serve to break the sun's rays and increase the shade area by its longitudinal shape. This reduces the intensity and amount of heat exposure. From the inside, the hollowed shape is used to accumulate the hot air at the top to evacuate it through the ventilation holes. Roof ventilation has been shown to be the most effective because the roof surface is the warmest being the most exposed and therefore the suction effect is more accelerated

In addition, there are no openings that lead directly to outside. All the rooms in the house open onto the inner courtyard, which in turn serves regulate the temperature of the rooms by the ventilation ticket eventually with the existence of a water source.

## 6. Conclusion

Vernacular architecture has proven its performance, whatever the time and place of construction, an intuitive approach to notions of sustainability and respect for places; it represents a whole knowledge, acquired through secular experience. At the end of this article, we will conclude that a set of information has been found around this vernacular heritage and can be summarized as follows:

Despite the natural obstacles and difficult climatic conditions, the scarcity of water resources, the unavailability of varieties of materials, the need for housing and stabilization has led Soufi humain to acquire and perfect knowledge and skills. Subtle and adapted to the local context. This acquisition was manifested through different aspects: access to water and exploration of the territory, farming methods, architectural typology as well as ancestral construction techniques. All these elements have contributed to give a specific character and identity to the region.

The architectural and experimental analysis of the housing unit according to both climatic and material levels shows that behind the modesty of the form and materials used, there are deep and significant causal relations. This is expressed by the adoption of a typology specific to the region, dictated by climatic criteria as well as by the needs of society and locally available materials. Generate a powerful and comfortable design. This architectural wealth of this vernacular heritage constitutes a source of inspiration and references for sustainable architecture with the possibility of investing these performances in contemporary architectural design.

### 1. References:

1.Cote Marc, La ville et le désert, le bas Sahara algérien, (Karthala et Ireman. Paris, 2005), pp.141-143.

2.André Voisin, Le Souf monographie d'une région saharienne, (El Walid, 1985), pp113-117.

3.Jean Brunhes, Les Oasis du Souf et du M'zab comme types d'établissements humain. In : Bulletin de la société des géographes, tome V, one Semestre, (Masson ET Cie éditeurs. Paris, 1902), pp.7-14.

4. Organisme Technique de Mise en valeur des Richesse du sous-sol Saharienne, présentation du Souf, (Le Porodon-Hydra. Alger. 1971), pp.02.

5. Givoni B, L'homme, l'architecture et le climat, (Edition de Moniteur), pp.21.

6. Amar Bennadji. Adaptation climatique ou culturelle en zones arides. Cas du sud-est algerien. Geography. Université de Provence - Aix-Marseille I, 1999, p 113-121-131.

7. Liébrard A. De herde A, Traité d'architecture et d'urbanisme bioclimatique. Concevoir, édifier et aménager avec le développement durable, (Le moniteur, 2005), pp181.

# Biogas production from algal wastes

Nadjla CHAIB<sup>#1</sup>, Sabrina LAMRAOUI<sup>#2</sup>, Sabrina DZIZI<sup>\*#3</sup>

<sup>#</sup>Department of Petrochemistry and Process Engineering, Faculty of Technology, University 20 august 1955 – Skikda (Algeria)

<sup>1</sup>n.chaib@univ-skikda.dz

<sup>2</sup>s.lamraoui@univ-skikda.dz

<sup>\*</sup>Laboratoire de recherche sur la physico-chimie des surfaces et interfaces (LRPCSI), University 20 august 1955 – Skikda (Algeria)

<sup>3</sup>s.dzizi@univ-skikda.dz

**Abstract**— Over the last few years, scientists emphasized their researches on biogas production harder than ever to encounter the energy needs. In particular, biogas crowdsourced by algal wastes became a tendency research field due to the high content of volatile solids in algae. The primary objective of the present study is to assess the biogas productivity from algal wastes and explore temperature and granulometry parameters effects on biogas yield. However, the biogas was produced of freshwater macroalgae (*Oedogonium sp.*) and microalgae (*Thalassiosira sp.* and *Chaetoceros sp.*) wastes. It was found that algal biogas yields are directly proportional to temperature and inversely proportional to granulometry. Optimal conditions for biogas production from algal wastes were determined as the temperature of 55 °C, a granulometry of 200 µm, a residence time of 21 days and an alga–inoculum ratio of 1:2 (w:w). Highest biogas yield obtained under these conditions was found as 342.59 cm<sup>3</sup> CH<sub>4</sub> g<sup>-1</sup> volatile solids (VS) from *Oedogonium sp.*, and 287.65 cm<sup>3</sup> CH<sub>4</sub> g<sup>-1</sup> VS from *Thalassiosira sp.* Followed by *Chaetoceros sp.* (254.37 cm<sup>3</sup> CH<sub>4</sub> g<sup>-1</sup> VS). It may be concluded that algal biomass is a good source for future biogas production, albeit more studies are required to enhance biogas yield and properties.

**Keywords**— Biogas, algal wastes, biogas yield, temperature, granulometry.

## I. INTRODUCTION

Algae that have come into prominence for biofuel production in the last decade are considered a third generation biofuel feedstock [1, 2]. They are classified as macroalgae and microalgae and they can be also used in many areas, such as food, cosmetics and pharmaceutical industries. Although algae sources contain very valuable compounds, especially macroalgae are treated as wastes in many coastal areas and costly procedures are applied for their disposal [3]. In this paper, the biogas production potential from macro-algal wastes *Oedogonium sp.*, and micro-algal wastes (Diatoms: *Thalassiosira sp.* and *Chaetoceros sp.*), and the effect of temperature and granulometry parameters on biogas yield were investigated. *Oedogonium* is very suitable for the biofuel production [4], and as a result, a lot of waste is generated after the extraction process [5]. The experimental results of this study will enhance bibliographic database [6-11] and will guide future research.

## II. MATERIAL AND METHODS

The green filamentous macroalga was provided by a treatment plant in the Refinery R1K (Skikda, Algeria). It was removed from the sludge thickeners stored at room temperature and in the dark.

The brown microalgae (diatoms) were collected by brushing some artificial substrates (glass plates of 10 cm<sup>2</sup>), immersed in the same basin of decantation of the treatment plant. Two dominant microalgae were identified and growing in vitro in fed-batch bioreactors, to obtain larger amounts for the production of biogas.

The batch reactors for anaerobic digestion experiments were set up in 5L glass bottles (**Fig. 1**). Two parameters were monitored during the experiment that are Temperature and blending provided with a heating magnetic agitator. The amount of biogas produced was measured volumetrically by evacuation of the liquid.



- 1- Flexible tube
- 2- Two valves for connection
- 3- Glass bottle
- 4- Bicycle inner tube

Fig. 1 Batch reactors for anaerobic digestion

The reactors are maintained in mesophilic to thermophilic conditions (25 to 60°C) in a water bath heated and regulated by a thermostat.

The production of biogas is the main goal of digestion anaerobic. During the anaerobic digestion process, The volume of biogas produced is measured regularly daily frequencies, the volume of biogas is measured using system hydraulics (liquid displacement), or the gas produced in the exit of the digester, recovered in an inner tube, which is immersed in the water in a graduated bowl, which will move the level of the liquid contained in the bowl and thus indicates the volume of the produced gas.



To determine the influence of temperature and granulometry for biogas yield, the temperatures were selected as 25°C, 35°C, 45°C, 55°C, and 60°C; grain sizes were selected as 0.25mm, 0.55mm, 0.75mm and 1mm. Several studies showed that the biogas production diminishes with increasing the ratio algae–inoculum [12, 13]. Therefore, several ratios of (w:w) algal biomass and inoculum were added to the reactors and then distilled water was added to the final volume of 5L.

After that, the reactors were airtight-capped with silicone plugs and placed on heating magnetic agitators. Moreover, all the anaerobic digestion experiments were repeated in triplicate.

Total solids (TS), volatile solids (VS), moisture content, lipids, pH of the mixture algae/inoculum, and the biogas composition (CH<sub>4</sub>, CO<sub>2</sub>, O<sub>2</sub>, H<sub>2</sub> and H<sub>2</sub>S content) were investigated [14], to assess the yield of the biogas produced.

### III. RESULTS AND DISCUSSION

#### A. Characterization of raw materials

The characterization results of algae wastes and inoculum used in our experiments are shown in Table 1.

TABLE 1. CHARACTERISATION OF ALGAE-INOCULUM WASTES

Parameter	<i>Oedogonium sp.</i>	<i>Thalassiosira sp.</i>	<i>Chaetoceros sp.</i>
TS %	72.6	58.64	48.21
VS %	83.92	72.41	66.48
pH	6.7	6.5	6.5
Lipids %	56.13	25.32	21.57
Moisture content %	33.67	22.5	18.4

Total solids and volatile solids measured for filamentous green macroalga '*Oedogonium sp.*' are higher than those of microalgae (brown diatoms) *Thalassiosira sp.* and *Chaetoceros sp.* This can be explained by its high large amount of lipids and nutrients content more than most micro-algal biomasses [4]. Subsequently, this macroalga is more suitable to be used as a potential energy crop field for biogas production.

Moisture content is also higher for *Oedogonium sp.* than those of *Thalassiosira sp.* and *Chaetoceros sp.*; this can be explained by the fact that macroalgae have generally higher water content than that of many terrestrial crops [15, 16]. pH values are maintained in optimal neutrality conditions.

#### B. Measurement of the main biogas

The main components of the produced biogas from macro- and micro-algal wastes are represented in table 2.

TABLE 2. CHARACTERISATION OF BIOGAS PRODUCED FROM DIFFERENT ALGAE-INOCULUM WASTES

Parameter	<i>Oedogonium sp.</i>	<i>Thalassiosira sp.</i>	<i>Chaetoceros sp.</i>
H <sub>2</sub> O%	16.9	13.2	12.9
H <sub>2</sub> %	<0.002	<0.002	<0.002
CO <sub>2</sub> %	15.91	32.05	27.31
CH <sub>4</sub> %	78	65.2	64.14

CO ppm	11	23	26
N <sub>2</sub> %	4.08	6.15	5.28
H <sub>2</sub> S ppm	18	12	13

The measured concentrations of the main compounds (CO<sub>2</sub>, CH<sub>4</sub>) correspond exactly to the values of the bibliography [7]. The concentrations of CH<sub>4</sub> and CO<sub>2</sub> are higher than those found in the bibliography [14, 17 - 19], which is explained by a very low H<sub>2</sub> content compared to the average concentration found in the bibliography (20%) [20]. The H<sub>2</sub>S content is close to the average of treatment plants [21].

#### C. Effect of temperature on biogas production yields

An investigation of the experimental data was performed taking into account residence time and heating temperature, to estimate the biogas (Methane) production efficiency in cm<sup>3</sup> CH<sub>4</sub> g<sup>-1</sup> VS (Fig. 2).

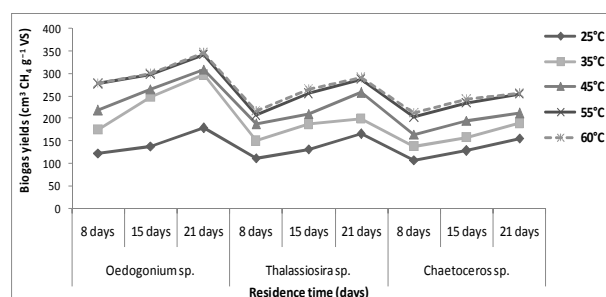


Fig. 2 Produced biogas yields according to experimental temperature conditions and residence time for different algae-inoculum wastes

It can be seen from the results presented in Figure 2 that biogas production yields vary proportionally with temperature and residence time. They are higher at the temperatures 55°C and 60°C after a residence time of 21 days. Biogas production yields are thus higher for the macroalga *Oedogonium sp.* (342.59 to 345.68 cm<sup>3</sup> CH<sub>4</sub> g<sup>-1</sup> VS respectively at 55°C and 60°C), than for those produced by microalgae *Thalassiosira sp.* and *Chaetoceros sp.*, at the same temperatures (287.65 to 290.54 cm<sup>3</sup> CH<sub>4</sub> g<sup>-1</sup> VS and 254.37 to 256.81 cm<sup>3</sup> CH<sub>4</sub> g<sup>-1</sup> VS respectively) after 21 days of residence.

#### D. Effect of granulometry on biogas production yields

The same experiments were carried out to produce biogas from algal-inoculum wastes, taking into account the grain size of the crushed algae after drying and sieving.

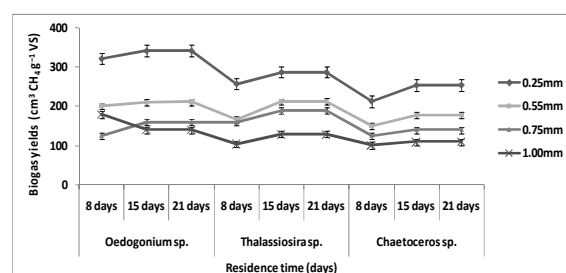


Fig. 3 Produced biogas yields according to granulometry and residence time for different algae-inoculum wastes.

The obtained results illustrated in Fig. 3, show that the biogas production yields vary inversely with the grain size of the algal particles, for the three types of wastes.

The highest production yields are measured for *Oedogonium sp.* ( $342.59 \text{ cm}^3 \text{ CH}_4 \text{ g}^{-1} \text{ VS}$ ) after a residence time of 21 days and for a grain size of 0.25 mm. This yield is followed by those of *Thalassiosira sp.* ( $287.65 \text{ cm}^3 \text{ CH}_4 \text{ g}^{-1} \text{ VS}$ ), and *Chaetoceros sp.* ( $254.37 \text{ cm}^3 \text{ CH}_4 \text{ g}^{-1} \text{ VS}$ ) under the same conditions.

#### E. Effect of alga-inoculum ratio

Simultaneously, we realized the same experiments taking into account the mass ratio (w:w) alga: inoculum. These experiments were carried out under the same temperature and particle size conditions after a residence time of 21 days, which proved to be the best corresponding to the highest yield of biogas production. The results obtained are illustrated in figures 4 and 5.

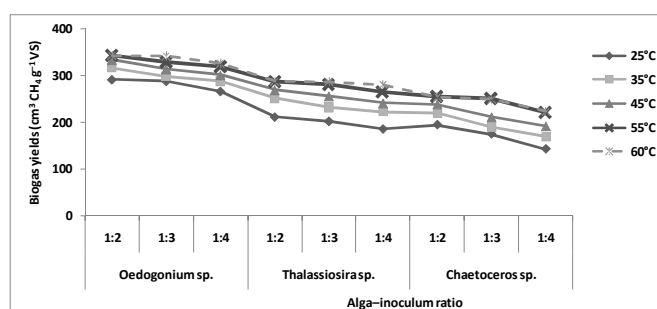


Fig. 4 Produced biogas yields according to experimental temperature conditions and alga-inoculum ratio for different algae wastes.

The results obtained show that the production of biogas (methane) varies inversely with the increase in the mass ratio of alga: inoculum. The best yields of biogas obtained were measured for the 1:2 ratio for the three types of algae. The highest yields are obtained for *Oedogonium sp.* ( $342.59 \text{ cm}^3 \text{ CH}_4 \text{ g}^{-1} \text{ VS}$  à  $55^\circ\text{C}$ ).

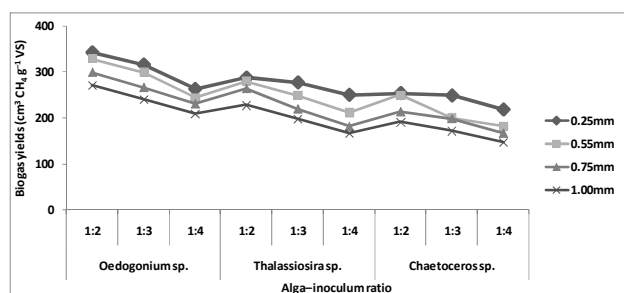


Fig. 5 Produced biogas yields according to granulometry and alga-inoculum ratio for different algae-inoculum wastes.

Biogas yields obtained by using smaller granulometry (0.25 mm) are higher than that produced by big grain size. All correspond in our case to alga: inoculum mass ratio of 1:2.

The highest yields were obtained for *Oedogonium sp.* ( $342.59 \text{ cm}^3 \text{ CH}_4 \text{ g}^{-1} \text{ VS}$ ), then *Thalassiosira sp.* ( $287.65 \text{ cm}^3 \text{ CH}_4 \text{ g}^{-1} \text{ VS}$ ) followed by *Chaetoceros sp.* ( $254.37 \text{ cm}^3 \text{ CH}_4 \text{ g}^{-1} \text{ VS}$ ).

#### IV. CONCLUSIONS

In this study, algal wastes were used in biogas production and the effects of some parameters on biogas yield were investigated. The maximum biogas production for all algal wastes was found for the process in thermophilic conditions ( $55^\circ\text{C}$ ). Also, it was found that the smaller granulometry (0.25 mm) caused the faster biomass hydrolysis, because the hydrolysis enzymes bind to the substrates more easily. This ensures that biogas production was faster and more efficient. In addition to this, the extraction process seems to accelerate the biogas production as it breaks down the cell walls of microalgae. The highest biogas yields were obtained after 21 days of time residence in the optimal conditions of temperature and granulometry. Subsequently, the highest yields were obtained from *Oedogonium sp.* ( $342.59 \text{ cm}^3 \text{ CH}_4 \text{ g}^{-1} \text{ VS}$ ), then *Thalassiosira sp.* ( $287.65 \text{ cm}^3 \text{ CH}_4 \text{ g}^{-1} \text{ VS}$ ) followed by *Chaetoceros sp.* ( $254.37 \text{ cm}^3 \text{ CH}_4 \text{ g}^{-1} \text{ VS}$ ).

From a technical point of view, it has been demonstrated that the production of biogas through the use of algal wastes is both sustainable and ecological. However, the efficiency and quality of produced biogas should be enhanced through further studies. In this sense, biogas quality and efficiency can be increased by various physical, chemical and biological pretreatments and anaerobic co-digestion with different wastes. Biogas production from the waste algal biomass should be developed in parallel to the algae bio-economic market to support the economy and environment.

#### ACKNOWLEDGMENT

This paper covers some of the results obtained by a university research project (PRFU) under the code: A16N01UN210120180002.

We are grateful to the editor, and the anonymous reviewers for their criticism and comments that improved the final manuscript.

#### REFERENCES

- [1] J. Baeyens, Q. Kang, and L. Appels, "Challenges and opportunities in improving the production of bio-ethanol," *Progress in Energy and Combustion Science*, vol. 47, pp. 60-88, 2015.
- [2] Q. Kang, L. Appels, and T. Tan, "Bioethanol from Lignocellulosic biomass: Current findings determine research priorities," *The Scientific World Journal*, vol. 13, 2014.
- [3] D. Özçimen, B. İnan, and S. Akış, "Utilization alternatives of algal wastes for solid algal products," *In: Algal Biorefineries. Springer*, pp. 393-418. 2015.
- [4] N. CHAIB, S. DZIZI, F. NOUNE, and H. KADDECHE, "Production of 3rd generation biofuel from green microalgae : *Oedogonium nodulosum*," *International Journal of Control, Energy and Electrical Engineering (CEEE)*, vol. 9, pp. 10-14, 2019.
- [5] J. Singh and S. Gu, "Biomass conversion to energy in India—A critique," *Renewable Sustainable Energy Review*, vol. 14, pp.1367-1378, 2010.
- [6] A. T. Koçer and D. Özçimen, "Investigation of the biogas production potential from algal wastes," *Waste Management & Research*, pp. 1-6, 2018
- [7] A. Karlsson, X. B. Truong, and B. H. Svensson, "Anaerobic treatment of activated sludge from Swedish pulp and paper mills -Biogas production

- potential and limitations,” *Environmental Technology*, DOI: 10.1080/09593330.2010.543932, Source: PubMed, 2011.
- [8] L. Appels, J. Lauwers, and J. Degreve, “Anaerobic digestion in global bioenergy production: potential and research challenges,” *Renewable Sustainable Energy Review*, Vol. 15, pp. 4295–4301, 2011.
- [9] R. Ramaraj, Y. Unpaprom, and N. Dussadee, “Potential Evaluation of Biogas Production and Upgrading Through Algae,” *International Journal of New Technology and Research*, vol. 2(3), pp. 128-133, 2016.
- [10] D. Hughes, M. S. Kelly and K. D. Black, “Biogas from Macroalgae: is it time to revisit the idea?” *Biotechnology for Biofuels*, vol. 5, pp. 86. 2012.
- [11] M. Hannon, J. Gimpel, and M. Tran, “Biofuels from algae: Challenges and potential,” *Biofuels*, vol. 1, pp. 763–784, 2010.
- [12] Y. Chen, J. J. Cheng, and K. S. Creamer, “Inhibition of anaerobic digestion process: A review,” *Bioresources Technology*, vol. 99, pp. 4044–4064. 2008.
- [13] G. Migliore, C. Alisi, and A. Sprocati, “Anaerobic digestion of macroalgal biomass and sediments sourced from the Orbetello lagoon, Italy,” *Biomass and Bioenergy*, vol. 42, pp. 69–77, 2012.
- [14] C. H. Vanegas and J. Bartlett, “Green energy from marine algae: biogas production and composition from the anaerobic digestion of Irish seaweed species,” *Environmental Technology*, DOI: 10.1080/09593330.2013.765922, 2013.
- [15] R. Rajkumar, Z. Yaakob, and M. S. Takriff, “Potential of the micro and macro algae for biofuel production: A brief review,” *BioResources*, vol. 9, pp. 1606–1633, 2013.
- [16] D. Zhou, L. Zhang, and S. Zhang, “Hydrothermal liquefaction of macroalgae *Enteromorpha prolifera* to bio-oil,” *Energy Fuels*, vol. 24, pp. 4054–4061, 2010.
- [17] J. Poullot, “Caractérisation des BIOGAZ Bibliographie : Mesures sur sites,” *INERIS DRC-02-27158-AIRE-n°316b-JPo*, 2002.
- [18] J. De Vrieze, L. Raport, and B. Willems, “Inoculum selection influences the biochemical methane potential of agro-industrial substrates,” *Microbial Biotechnology*, vol. 8, pp. 776–786, 2016.
- [19] D. Yadav, L. Barbora, and L. Rangan, “Tea Waste and Food Waste as a Potential Feedstock for Biogas Production,” *Environmental Progress & Sustainable Energy*, DOI 10.1002/ep.12337, 2016.
- [20] A. Melis, “Green alga hydrogen production: progress, challenges and prospects,” *International Journal of Hydrogen Energy*, vol. 27, pp. 1217-1228, 2002.
- [21] V. Alonso, A. Martin, and R. Borja, “Anaerobic treatment of wastewater produced in the manufacture of cellulosic pulp from wheat straw,” *Environmental Technology*, vol. 14, pp. 1145-1153, 1993.

# Preparation and characterization of nickel-based catalysts deposited on vanadium oxide for hydrogen production by methane steam reforming

A. Belhadi<sup>#1</sup>, A. Boudjemaa<sup>\*1,2</sup>, S. Boumaza<sup>#2</sup>, M. Trari<sup>♦3</sup>, O. Cherifi<sup>#3</sup>

<sup>(1)</sup>Laboratory of Chemistry of Natural Gas, Faculty of Chemistry (USTHB), BP 32, 16111 Algiers, Algeria  
[ouizac@yahoo.fr](mailto:ouizac@yahoo.fr)

<sup>(2)</sup>Centre de Recherche Scientifique et Technique en Analyses Physico-Chimiques (CRAPC), BP 384, Siège ex-Pasna Zone Industrielle, Bou-Ismaïl CP 42004, Tipaza, Algérie.

<sup>(3)</sup>Laboratory of Storage and Valorisation of Renewable Energies, Faculty of Chemistry (USTHB), BP 32, 16111 Algiers, Algeria.

**Abstract**— In this work, we are interested in the preparation of nickel-based materials deposited on vanadium oxide. Our solid are elaborated by impregnation method and characterized by different physico-chemical analysis techniques such as: Atomic absorption, BET, X-ray diffraction, Chemical analysis. The results of XRD analyses carried out showed the presence of the NiO phase for the solid. The reaction of steam reforming of methane, in the presence of nickel-based catalysts (4% nickel) deposited on vanadium oxide, is carried out at atmospheric pressure between 500 and 650 °C.

**Keywords**—NiO, V<sub>2</sub>O<sub>4</sub>, hydrogen, steam reforming.

## I. INTRODUCTION

Today, alternative and sustainable solutions are proposed to replace fossil fuels. Hydrogen is an alternative energy source for the future. It can be produced by electrolysis (4%) and essentially by reforming of fossil fuels (95%). Natural gas, consisting mainly of methane, propane and butane, is a fairly abundant and widely available raw material in the world. The preferred route of its recovery is its transformation into synthesis gas (CO + H<sub>2</sub>). It can be converted into many products usually derived from petrochemistry (ammonia, methanol, higher alcohols, aldehydes, carboxylic acids, gasoline...).

Steam methane reforming is the most common and economical way to make hydrogen. There are two primary reactions: the reforming reaction (1) and the water gas shift

reaction (2) to produce synthesis gas according to the following reactions:



Due of the endothermic reaction, it operates that under severe conditions pressure and temperature (15 - 30 bar and 850-900°C) in order to increase the conversion to methane. The syngas (CO + H<sub>2</sub>) obtained has a defect in carbon monoxide. In these reactions, the supported catalysts are largely used. The support is not necessarily inert, there are metal-support interactions that exalt the activity of the catalysts [1]. The reactivity and stability of Ni /SiO<sub>2</sub> catalysts are investigated in the steam reforming reaction at 565 °C. The results showed a great dependence on the steam-reforming according the ratio  $R = \text{H}_2\text{O} / \text{CH}_4$ .

Steam reforming of hydrocarbons is an industrial process of high temperature during which a serious operational problem arises namely the deposit of carbon. To overcome this problem, Zhuang et al. [3] have shown that carbon deposition decreases on Ni catalysts promoted by cerium oxide CeO<sub>2</sub>, the latter contributes to a better dispersion of Ni and increases its activity. Thus, the addition of promoters (alkaline or alkaline-earth metal) to methane steam reforming catalysts generally suppresses carbon deposition [4].

In this work, the search for catalysts that is more efficient, available and less costly for used in CH<sub>4</sub> + H<sub>2</sub>O reaction on nickel-based catalysts deposited on vanadium. Various parameters that influenced on the catalytic activity are investigated.

## II. EXPERIMENTAL

### II.1. Catalysts preparation

The solid  $\text{Ni/V}_2\text{O}_4$  with a nickel percentage of 4 wt.% was prepared by impregnation of the support  $\text{V}_2\text{O}_4$  with  $\text{Ni}(\text{NO}_3)_2 \cdot 6\text{H}_2\text{O}$  (1 M) (Merck)[5-6]. The solution was stirred during 2 h, and evaporated at 80 °C under agitation. Then solid was dried at 80 °C (12 h), and calcinated at 300 °C (2 h) and 500 °C(6h) with a heating rate of 4 °C/mn (1.2 L h<sup>-1</sup>). The solids were sieved to have a particle diameter less than 0.16 mm.

### II.2. Catalysts characterization

The solids were analysed by atomic absorption using a Perkin Elmer 100 B spectrometer. The specific surface areas were determined by the BET method using an area analyzer (Coultronics 2100E). The crystal structures were identified by XRD with a diffractometer ( $\theta/2\theta$  CGF) provided with a proportional detector and using  $\text{K}\alpha$  molybdenum as anticathode ( $\lambda=0.70930 \text{ \AA}$ ). The X-ray patterns were obtained for  $2\theta$  values ranging from 20 to 70°. The apparent size of nickel particles was calculated by the Scherrer formula,  $L = 0.9\lambda/\beta\cos\theta$ , where  $\beta$  is the width of the most intense NiO peak at half-height, and  $\theta$  is the corresponding Bragg angle.

### II.3. Reactivity

The catalytic tests were carried out in a quartz reactor fixed bed ( $L= 65 \text{ cm}$ ,  $\varnothing= 1 \text{ cm}$ ) under atmospheric pressure. The catalyst (0.1 g) is pre-reduced at 500 °C under hydrogen flow (1.2 L h<sup>-1</sup>) before introduction of the gas mixture ( $\text{H}_2\text{O}/\text{CH}_4= 3.3$ ) diluted in argon flow and obtained by crossing of a mixture  $\text{CH}_4$  (10 %)/Ar, in a saturator with a thermostated bath (65°C, 1.2 L h<sup>-1</sup>). The reactants and the products ( $\text{CO}$ ,  $\text{CO}_2$  and  $\text{CH}_4$ ) were analysed by gas chromatography using a TCD chromatograph (Hewlett-Packard 5730) on a carboxisieve B column(100-200 mesh,2 m), with hydrogen as vector gas.

The conversion rates and the  $\text{CO}_2$  and  $\text{CO}$  selectivities were calculated from the following formulas:

Total transformation rate:

$$TTG(\%) = \frac{n_{\text{CH}_4}(\text{converted})}{n_{\text{CH}_4}(\text{total})} \times 100$$

Transformation rate in compound « i » :

$$TTi(\%) = \frac{n_i}{n_{\text{CH}_4}} \times 100$$

Selectivity in compound « i » :

$$S_i(\%) = \frac{n_i}{n_{\text{CH}_4}(\text{converted})} \times 100 = \frac{TTi}{TTG} \times 100$$

with :

i :  $\text{CO}$ ,  $\text{CO}_2$ .

ni : number of moles of compound «i».

$n_{\text{CH}_4}$  : number of moles of methane.

Carbone balance:

$$\text{Xc}(\%) = [n_{\text{CH}_4}^e - (n_{\text{CH}_4}^s + n_{\text{CO}_2}^s + n_{\text{CO}}^s)] \times 100$$

## III. RESULTS AND DISCUSSION

### A. Materials characterization

The physical characteristics of the solids are regrouped in the Table1

TABLE I  
 CHARACTERISTICS OF Ni/V<sub>2</sub>O<sub>4</sub> SYSTEMS

materials	Ni (%)		Surface area (m <sup>2</sup> /g)	XRD
$\text{V}_2\text{O}_4$	-	-	15	$\text{V}_2\text{O}_4$
$\text{Ni/V}_2\text{O}_4$	4	3.95	5.8	NiO $\text{V}_2\text{O}_4$

The atomic absorption analysis shows that the Ni composition is very close to the theoretical one. The specific surface areas of 4wt %Ni/V<sub>2</sub>O<sub>4</sub> is slightly lower than the  $\text{V}_2\text{O}_4$  support (See table 1).

The XRD pattern of 4 wt% Ni/V<sub>2</sub>O<sub>4</sub> shows peaks assigned to NiO and  $\text{V}_2\text{O}_4$  (Fig 1).

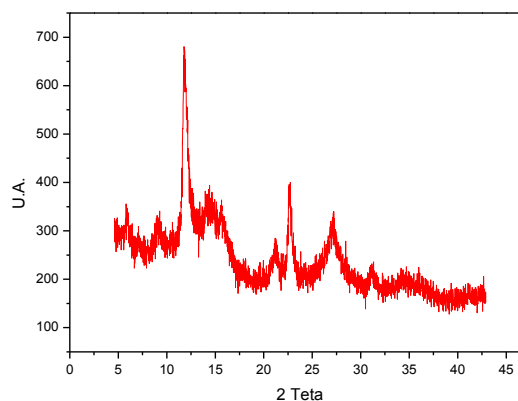


Fig 1 XRD patterns of NiO/V<sub>2</sub>O<sub>4</sub>

### B. Methane Steam reforming reaction (MSR)

The catalytic performances of supported material were examined in the temperature range (500–650 °C). After, 03hrs of reaction,  $\text{CO}$ ,  $\text{CO}_2$ ,  $\text{H}_2$  were formed (Table II and fig I) and the  $\text{CH}_4$  conversion was varied from 40 to 60 % depend on the temperature of reaction.

Also, the carbon was formed with a yield less than 15%.

TABLE III: Catalytic activities of Ni/V<sub>2</sub>O<sub>4</sub> at different reaction temperatures, T<sub>cal</sub>=500°C, CH<sub>4</sub>/H<sub>2</sub>O =3.3

T (°C)	TTG (%)	S <sub>CO<sub>2</sub></sub> (%)	S <sub>CO</sub> (%)	C (%)	H <sub>2</sub> (%)
500	44	17	05	3	78
550	52	16	21	5	63
600	61	11	31	8	58
650	60	11	67	13	22

The evolution of the CH<sub>4</sub> conversion versus time shows that a stationary regime is reached after ~ 3 h. The setting in mode is accompanied by the formation of CO<sub>2</sub> which strongly decreases with the profit of CO formation as one approaches the stationary regime. This indicates an incomplete reduction of catalysts during the pre-treatment in H<sub>2</sub> (500 °C) and thus the reactional mixture produces species on surfaces which are more reduced than hydrogen itself [6].

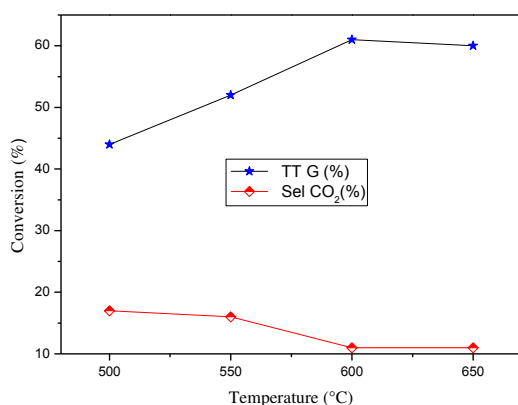


Fig 2: Conversion of the methane and selectivity of CO<sub>2</sub> versus temperature for 4%Ni/V<sub>2</sub>O<sub>4</sub> nickel-based catalyst.

The testing results show that catalytic performances of Ni/V<sub>2</sub>O<sub>4</sub> are very sensitive to temperature from 500 to 650 °C, and conversions varying between 44 and 60 % and CO selectivity varying between 5 and 67%. We notice an important carbon deposition at 600 °C on catalysts. This result is in agreement with the literature, according to Nielsen [7] who found that carbon deposition, on nickel catalyst has different temperature regimes: usually, ~ 550 °C. The activation energy of coke formation changes to a negative value.

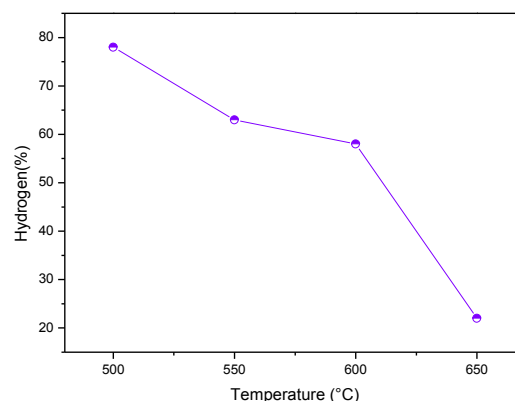


Fig 3: Production of hydrogen according to the temperature for 4%Ni/V<sub>2</sub>O<sub>4</sub> nickel-based catalysts

The best hydrogen production is at low temperature (500 °C (78%)) because of the formation of carbon (fig 3).

Moreover, no diffusional limitation (effect of mass, flow etc...) is observed. The experimental conditions of the reaction are chosen after optimization. It appears that catalyst elaborated with 4% of Nickel is active. It can be owed to a better dispersion of the active phase for the weakly charged catalyst. This result is in agreement with the literature data.

#### IV. CONCLUSIONS

The reactivity of CH<sub>4</sub>/H<sub>2</sub>O reaction for Ni/V<sub>2</sub>O<sub>4</sub> catalyst was investigated at temperatures ranging from 500 to 650 °C with the aim of facilitating the formation of synthesis gas. It has been shown that: -The NiO phase is observed.

The catalyst remains stable for more than 7 hours, and the steady state is obtained after 3 hours, which suggests a synergy between the nickel and the support. The best production of H<sub>2</sub> in obtained at 650 °C for the yield (≈ 60%).

#### REFERENCES

- [1] S. Lee, J. Bae, S. Lim, J. Park, J Power Sources, 2008, 180:506.
- [2] K O. Christensen, D. Chen, R. Lødeng, A. Holmen. Appl Catal A: General, 2006, 314(1): 9.
- [3] T. Borowiecki, W. Gac, A. Denis, Appl. Catal. A: Gen. 2004, 270:27.
- [4] N. Martin, M. Viniegra, E. Lima, G. Espinosa, Ind. Eng. Chem. Res., 2004, 43 : 1206.
- [5] A. Belhadi, O. Cherifi; J. Soc. Alger. Chim., 2009, 19(1), 49-62.
- [6] A.BELHADI, L. BOUDJELLAL, S. BOUMAAZA , M. TRARI" Hydrogen production over the hetero-junction MnO<sub>2</sub>/SiO<sub>2</sub> " Int. J. Hyd. Energy; 2018 (43), 3418-3423.
- [7] J.R. Rostrup-Nielsen, J.R. Anderson and M. Boudard (editors). Catalysis- Science and Technology, Vol.5, Springer Verlag, Heidelberg (1984), 1

# An air cooler system for retrofitted PV panels in a Mediterranean climate

Amel F. Boudjabi<sup>#\*1</sup>, Abderrahmane Dib<sup>#2</sup>, Thabet Lebeche<sup>#</sup>, Kamal Rezgui<sup>#</sup>, Chafik Tamrabet<sup>#</sup>

<sup>#</sup>*Faculty of Sciences and Applied Sciences, University of Oum El Bouaghi  
BP 358, Route de Constantine, Oum El Bouaghi, 04000, Algeria*

<sup>1</sup>[boudjabi.af@gmail.com](mailto:boudjabi.af@gmail.com)

<sup>2</sup>[abderrahmanedib@yahoo.fr](mailto:abderrahmanedib@yahoo.fr)

<sup>\*</sup>*Energy & Environment Laboratory, University of Constantine3  
Ali Mendjli, 25016, Algeria*

**Abstract**— Investigations attempt to increase the photovoltaic systems' performance by the development of new materials, conversion process and design. The studies have shown inter alia, that the electrical/solar radiation ratio decreases under cells warming. Efforts are made to develop the hybrid photovoltaic thermal solar collectors in buildings. In order to investigate the potential of these systems in a high plateau site in Algeria, an air cooling system is designed and fixed at the backside of a solar module. A series of measurements have been conducted to evaluate the effect of temperature and inclination angle on the uncooled and retrofitted panels. The results have shown these parameters affect the electrical energy generated and the power conversion efficiency.

**Keywords**— solar energy conversion, hybrid PV/T collector, air cooling system, inclination angle, electrical efficiency.

## I. INTRODUCTION

Approximately, 98 Gigawatts PV power was completed in 2017 worldwide to achieve a total photovoltaic production capacity of 402 GW, as indicated in the renewable 2018 global status report [1]. Indeed, Photovoltaics constitutes an important challenge in the world production of electricity and the PV technology continues to progress very fast. Despite the available huge solar energy, only a small fraction of the world's electricity production is photovoltaic, owing to the kWh cost and the low cells' efficiency. The electrical efficiency of a PV depends on solar radiation and cells temperature; the best ratio does not exceed 15% to 18% for crystalline cells [2,3]. Solar panels convert into electricity only a small fraction of the solar radiation, most of the energy is dissipated as heat (infrared spectrum), causing cells overheating and efficiency drop [4, 5]. Indeed, water or air cooling systems can be used to remedy this warm-up problem [6, 7, 8]. The conversion of solar radiation into both electricity and thermal energy on the same module could be an appropriate solution to generate energy for the consumers. Wherefore, hybrid technology combines an electrical generation with heat systems. Thus, Zondag et al. [6] carried out an experimental and simulation study on a combined panel, with water circulation, where a conventional PV

multicrystalline cells was connected to a sheet-tube collector. Their 1D model well agreed with the measurements. The thermal and electrical efficiencies obtained were 33% and 6.7% respectively, as compared to 54% for a thermal collector and 7.5% for a PV panel in the same conditions. Krauter [9] developed an experimental apparatus using a water film flow over the PV front. The author obtained an energy gain of 10.3 % during the test, while, Rossi et al. performed numerical simulation and experimental study on retrofitted photovoltaic panels [9,10]. Their adjustment had increased the electrical efficiency. Similarly, heat exchangers in aluminium were fixed at the rear of PV panels by De Rosa et al. [11], their model was in very good agreement with the experiment for static and dynamic water conditions. Popovic et al. [12] proposed a simulation study of hybrid panels using vertical airflow channel, they obtained an increasing electrical efficiency with this ventilation system. In a numerical model with Ansys Fluent software validated by experiments, Pauly et al [13] demonstrated the effect of flow mass rate and duct depth on the performance of the solar hybrid PV/T collector, the results were that the overall performance raised by 20%. The study of Nizetic et al. [14] concerned the air convection on the backside of a PV/T. They confirmed that heat transfer in the PV-T collector is complex and depends on the variable surrounding conditions. The authors noted an increase of temperature in specific regions.

Energy exchanges in PV/T collectors are very complex due to the interaction with surrounding conditions, hence, an experimental comparison between uncooled and retrofitted panels is proposed in this paper. The impact of panel temperature and inclination on the energy produced and the power conversion efficiency are verified in a Mediterranean climate site.

## II. EXPERIMENTAL SETUP

### A. Location description

Different tests have been conducted in the site, located in a high plateau city in the northeast of Algeria with 891m elevation, 35.80° latitude angle and 7.39° longitude angle.

The site has an annual sunshine duration average of more than 11 hours and 7600 - 8000 Wh/m<sup>2</sup> annual solar radiation<sup>1</sup>.

A comparative study of two photovoltaic modules behaviour, operating under the same climatic and technical conditions, is described in this paper; the objective is to propose a simple design to improve the efficiencies of an installed PV system. One of the two conventional panels was adapted by integrating a novel air cooling system at its backside. The experimental investigation consisted in measuring actual received solar radiation and corresponding supplied electricity.

### B. Setup

The panels used in the experiment have the electrical characteristics shown on Table 1.

TABLE I  
 OPERATING PARAMETERS OF THE PV PANELS

Module	Siemens M75 <sup>2</sup>
Number of cells	33
Panel area A	0.33 m <sup>2</sup>
Peak power Wc	48W
Empty voltage	19.8 Voc
Short circuit current	3.35 A
Load voltage	15.9 V
Charging current	3.02 A

The first module “panel A” was combined with an air cooling device at its rear to recover the dissipated heat from solar cells. This ventilation system was designed using a forced air circulation, through a 3 cm gap between the panel and the protection box. The latter consists of an insulating cover of 2 cm polystyrene and a protective wooden box which serves as a support for the fans. Four fans are used to extract the heated air in contact with the PV module. The box protection and polystyrene are perforated so that ambient air enters the system through holes of 8 mm diameter, distributed at regular and sufficient distances around the fans. The second module “panel B” was used as a reference panel.

The experimental apparatus is shown on Fig. 2 and Fig. 3. The measurement of the electrical photovoltaic load corresponds to the consumption of the four (04) fans (DC 12V, 0.14 A) and a lamp of 21W.

A front view of the photovoltaic panels is presented on Fig.1. For the sake of inclination, wooden pedestals have been used. The panels were oriented due south and inclined at a selected angle to the horizontal plane. During measurement days, tilt angles of 36° (site latitude), 20° and 50° were tested.



Fig. 1 Front view of the experiment setup

Fig. 2 indicates the backside of the panels, the air heat exchanger and the autonomous electrical system.

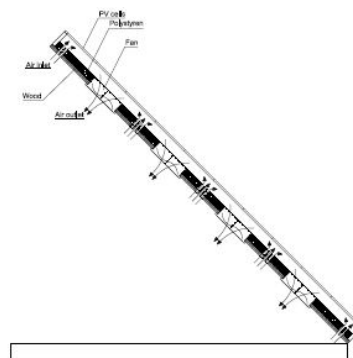


Fig.2. Backside view of the panels

### III. RESULTS AND DISCUSSION

The tests were performed for 05 days (from 22 May 2018), by clear short periods. The electrical power conversion efficiency and the temperature of the two panels have been analysed for the different tilt angles and the same electrical load. All paragraphs must be justified, i.e. both left-justified and right-justified.

The first graph (Fig.3) describes the evolution of the solar radiation with time for the representative measurement period. The curves show that the panels received a greater amount of energy with tilt angles of 36° and 20°. The solar radiation for these two cases was greater than 950 W, while for the angle of 50°, the values were between 700 and 800 W.

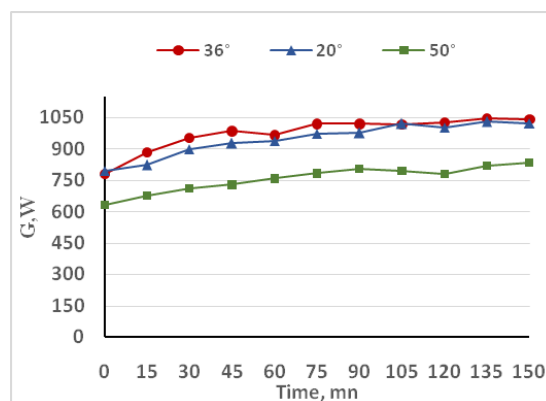


Fig.3. Solar radiation during measurement period

<sup>1</sup> Atlas Solaire Algérien, EISSN/ ISSN 1112-3850 ,2002.

<sup>2</sup> The panels are formed of 33 high-power monocrystalline Si solar cells.



**A. Power conversion efficiency**

A photovoltaic system is determined according to its electrical efficiency at standard conditions [2]. The linear correlation between the temperature and electrical efficiency is expressed in previous studies [8, 15] by the equation:

$$\eta = \eta_{stc} [1 - \beta(T - 298)] \tag{1}$$

Where :

- $\eta$  is the Power conversion efficiency ;
- $\eta_{stc}$  is the electrical efficiency in standard conditions ;
- $\beta$  is the efficiency correction coefficient for temperature.

The value of  $\beta$  is usually taken equal to 0.0045 1/°C for crystalline Si cells [6]. For the current study,  $\eta_{stc}$  and  $\beta$  were estimated from measurements. The electrical efficiency at standard conditions for the PV M75 is 14, 55% while  $\beta$  was deduced from the electrical efficiency results of the different cases. It was estimated at 0, 0112 .

For the first angle of 20° as observed on Fig.4., the mean rate of increase in the power conversion efficiency between the retrofitted panel A and the conventional panel B was about 0.88%. The ratio is nearly 12% for the panel A and equal to 11-11,25% for the panel B.

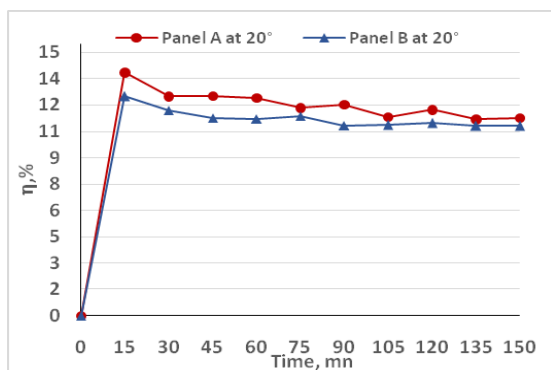


Fig.4. Electrical power conversion efficiency

The mean rate in the second case for an inclination angle of 36°, is equal to 1,039 %. The ratio is about 11,5-12% in panel A and close to the 11% value for panel B. The difference between the two curves is quite steady.

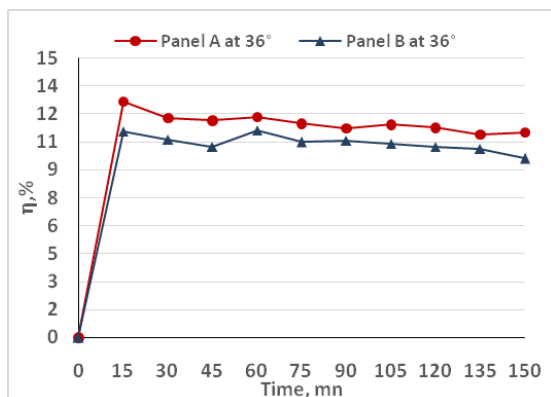


Fig.5. Electrical power conversion efficiency

Then, the electrical efficiency in the case of the 50° inclination angle is presented on Fig.6. It increased for the ventilated panel with a rate of 0.54% on average. The difference is very small and the ratio for the two cases is almost the same after 60 minutes of operation. At the last measure time, the ratio decreased of about 2%, this is due to the important temperature of the panel.

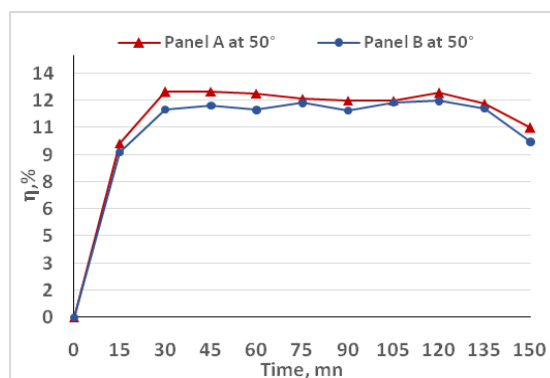


Fig.6. Electrical power conversion efficiency

**B. Panel temperature measurements**

During the tests, the temperature difference between conventional and ventilated panels for the three inclinations is shown in Fig. 7, Fig. 8 and Fig.9.

The temperature at the beginning of measurements was greater for the "panel A". The fans were not turned on, so, the module was more heated at the backside because of the insulated box, but with the fans switched on, cooling started and the panel temperature decreased in few minutes. For the first case on Fig.7, the difference recorded was - 4°C at first and 12° C as a maximum value, with a mean difference of 8 degrees. The temperature of the combined system was approximately steady around 35° C and below the 40° C graduation.

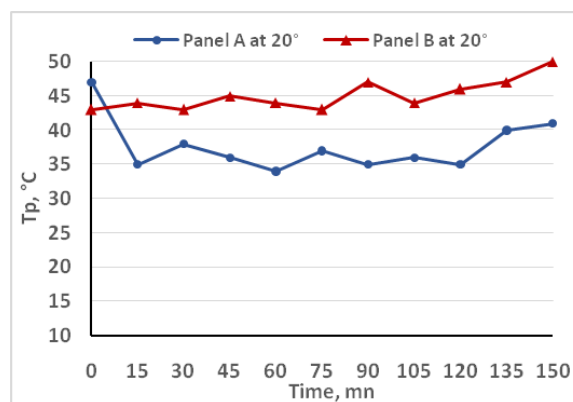


Fig.7. Panel temperature at 20° inclination

For the 36° inclination, as seen on Fig.8, the temperature difference varies between 5 and 12 degrees with an approximate mean value of 7 °C. The ventilated panel was

fairly well cooled with a relative temperature distribution interval around 5 degrees in the most measurement instants, while the conventional panel temperature was rising.

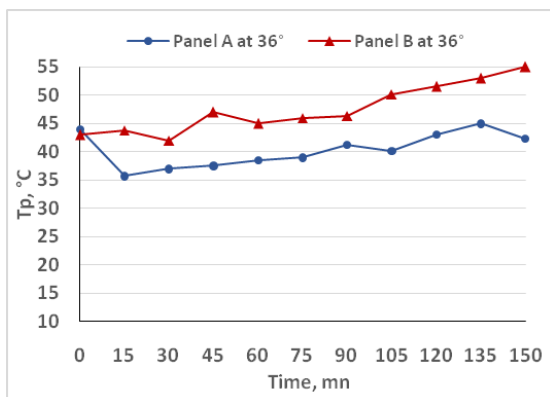


Fig.8. Panel temperature at 36° inclination

At the 50° inclination angle on Fig.9, the mean temperature drop between the Panels A and B was about 5 degrees, with a temperature generally close to 40° C. It varied between 38 and 44 degrees, as compared to the uncooled module which was at 42 to 53 °C.

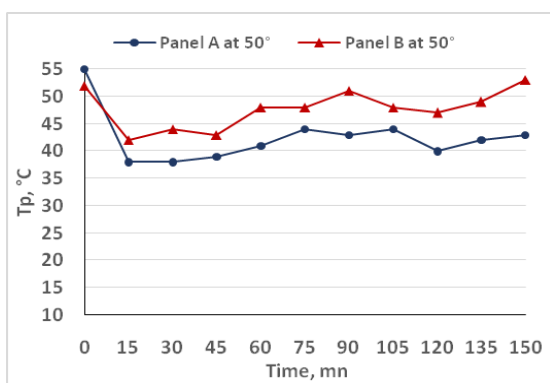


Fig.9. Panel temperature at 50° inclination

### C. Air temperature measurements

Air temperatures were measured using an anemometer at different points at inlets near the holes and outlets nearby the fans, mean temperatures are taken into account in calculations.

In the other test periods, an increase of temperature of the extracted air was observed. For the panel A inclined of 20°, the temperature difference between the incoming air and the outgoing air was of 1 degree up to 4 degrees as maximum, seeing that on Fig.10. It should be noted that the heat extraction was more significant, indeed, the temperature of the panel was higher and the temperature of the ambient air was low comparing to other cases, this encouraged thermal convection inside the exchanger.

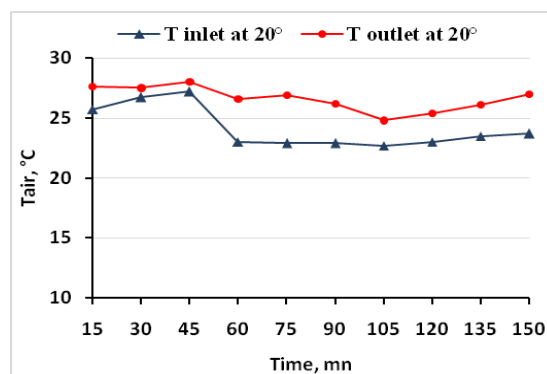


Fig.10. Air temperature at 20° inclination

At 36° inclination, the air temperature differences have reached a maximum of 3 degrees (e.g. Fig.11). The difference was almost steady after 90 minutes of operation.

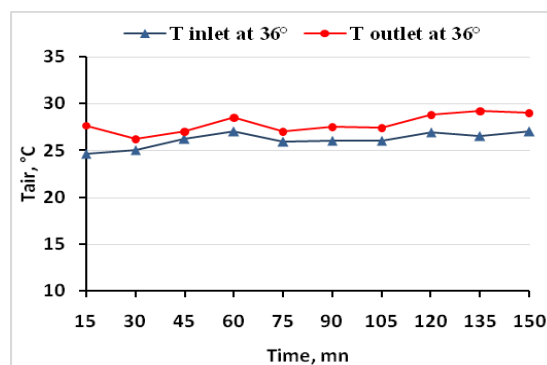


Fig.11. Air temperature at 36° inclination

For the last angle 50°, as it appears on Fig.12, the inlet air temperature which was nearly the same of the ambient temperature is high compared to the previous tests, the difference values varied from 0.5 degrees to 2.5 degrees. After the 90 first minutes, the cooling system became inefficient.

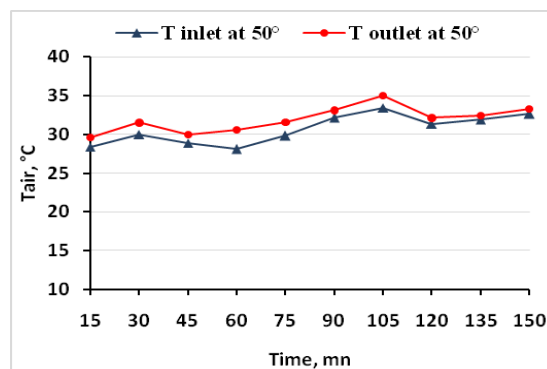


Fig.12. Air temperature at 50° inclination

## IV. CONCLUSIONS

The carried out experimental study confirmed the impact of cooling the photovoltaic panel. The panel without ventilation had a lower power conversion efficiency compared to the panel provided with an air convector, which

ensures a quite steady cells temperature against an increasing temperature for a conventional PV. The angle of inclination equal or below the latitude of the site considered is more favourable, where the performance turned out better for the measurement period. For the angle greater than the latitude, the electrical energy and conversion power efficiency declined due to the lower amount of solar energy absorbed by the cells.

#### REFERENCES

- [1] Renewables 2018 – Global status report, REN 21(2018).
- [2] Martin A. Green. Progress In photovoltaics Research And Applications 17 (2009)183.
- [3] A. Goetzberger, V.U. Hoffman, Photovoltaic Solar Energy Generation, Springer. Berlin Heidelberg, ed. New York ( 2005).
- [4] Martin A. green, Yoshihiro Hishikawa, Ewan D. Dunlop, Dean H. Levi, Jochen Hohl- Ebinger, Anita W. Y. Ho-Baillie. Wiley progress in Photovoltaics, (2017).
- [5] Wisam A. M. Al- Shohami, Raya Al-Dadah, Saad Mahmoud. Applied thermal engineering 109 (2016) 475.
- [6] H.A. Zondag, D.W.De Vries, W.G.J. Van Helden, R. J.C. Van Zolingen, A..A. Van Steenhoven. Solar Energy72 (2002) 113.
- [7] H.A. Zondag, D.W.De Vries, W.G.J. Van Helden, R. J.C. Van Zolingen, A..A. Van Steenhoven.. Solar Energy 74 (2003) 253.
- [8] Stephan Krauter. Solar Energy Materials and Solar Cells,82(2004),131
- [9] Rossi C, Tagliafico LA, Scarpa F, Bianco V. 76 (2013)634
- [10] Rossi C, De Rosa M, Bianco V, Scarpa F, Tagliafico LA. . MECHANICS '14: 10th International Conference on Applied and Theoretical Mechanics, Salerno, Italy, 2014,
- [11]De Rosa Mattia, Romano Giorgio, Rossi Cecilia, Scarpa Federico, Tagliafico Luca A., Energy Procedia 81(2015)345.
- [12]Cătălin George Popovici, Sebastian Valeriu Hudișteanu, Theodor Dorin Mateescu, Nelu-Cristian Cherecheș., Energy Procedia 85 (2016) 425.
- [13] Lippin Pauly, L. Rekha, Christy V. Vazhappilly, Melvinraj C.R. Procedia technology 24 (2016) 513.
- [14] S. Nizetic , F. Grubisic-Cabo, I. marinic-Ktagic, A.M. Papadopoulos.. Energy 111(2016)211.

#### ACKNOWLEDGMENTS

The authors wish to thank the laboratory technician for his collaboration.

# CFD analysis of wind loads on Linear Fresnel Concentrator

H.Bendjebbas and A.Mezidi

Unité de Développement des Équipements Solaires. UDES. /Centre de Développement des Energies Renouvelables .CDER. Bou-Ismaïl.42415.w.Tipaza. Algerie.

hbendjebbas@gmail.com

**Abstract**— the design of structures and tracking system must necessarily go through the knowledge of maximum pressures. in order to quantify the pressures caused by the wind on the linear Fresnel concentrators, we carried out a CFD study to determine the most sensitive LFR sides to wind loads.

This has allowed us to find that the 30° wind direction generates the most significant pressures on LFR mirrors.

**Keywords**— CSP, Linear Fresnel, Wind loads, CFD

## I. INTRODUCTION

Rapid growth of the solar industry is challenging engineers and building officials to develop appropriate wind load estimation and structural design approaches, given a current lack of building code provisions directly applicable to solar installations [1]. The need to understand and quantify wind loading effects on individual and fields of tracking solar collectors has emerged as an important design and development issue. This understanding is important in the cost effective design of both conventional concentrators and innovative low-cost concepts which can be considerably less robust than their conventional counterparts. Moreover, to aid in the development of that understanding, methods for the adequate modeling and simulation of wind loading on individual concentrators within the actual field environment are needed [2].

It is important to determine the wind loads on individual modules within an array because the aggregate flow field is influenced by adjacent modules. This is especially true if mutual interactions between modules were such as to augment wind loads compared to those that would occur on a single concentrator at equivalent wind free-stream conditions. Some information is available for photovoltaic and parabolic-trough arrays [3].

The present study is a three-dimensional numerical simulation of wind loads effect around linear Fresnel reflector at different wind directions.

## II. MODEL PRESENTATION

For this study, a three-dimensional steady-state model using a “ $k-\epsilon$ ” turbulent flow has been implemented in the Comsol Multiphysics® software. The geometry study has been limited to a simplified linear Fresnel module. The model in the current example represents twelve LFR concentrators with different tilt angle for each mirror.

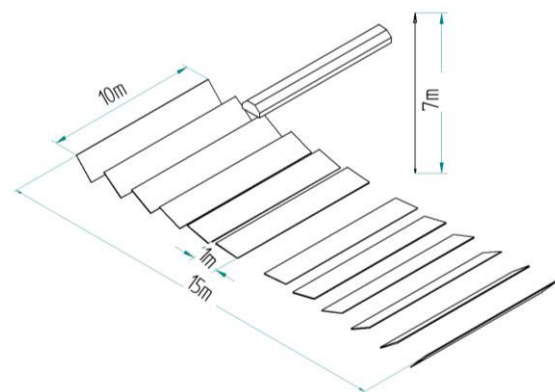


Fig.1. LFR geometry

As illustrated in Fig.1, a simplified model of a Fresnel linear concentrator was used in this work with twelve mirrors 1m width and 10m length, the receiver is 7m from the ground and the total length of the model is 15m.

The numerical simulation consists in studying the effect of the wind on the LFR by varying the direction of the wind with respect to the LFR at 0°, 30°, 60° and 90° respectively (Fig.2). The direction of 0° corresponds to a vertical direction of the wind relative to the surface of the mirrors of the LFR.

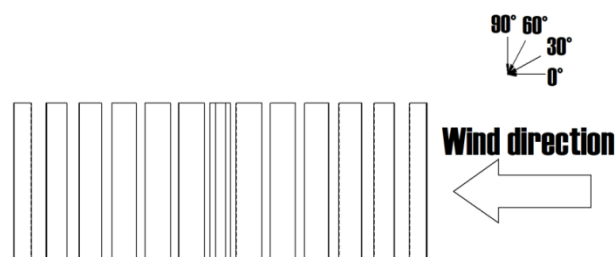


Fig.2. Wind direction

Winds of interest design have some characteristics near the ground. Mean (time averaged) wind speed increases with height above ground, and winds have gusts of short duration which are significantly higher than the mean and which define peak wind loads. Both the variation of speed with height and the turbulence must be accounted for in the design of LFR [6]. For the assessment of wind loads on structures, the power-law profile has been used most widely because of its simplicity [7] and it can be written as:

$$\frac{U_z}{U_{zref}} = \left(\frac{z}{z_{ref}}\right)^\alpha$$

The value of the exponent “ $\alpha$ ” refers to the profile of the mean velocity over uniform level surfaces equal to 1/7 in open areas.  $U_z$  is the mean wind velocity,  $U_{zref}$  is the reference velocity at reference height  $z$ .

Three cases of reference velocity (reference height of 10m) were considered: 30m/s, 40m/s and 50m/s respectively.

The result of a numerical calculation is dependent on the mesh that is used. A too coarse mesh will give a high error in the result and as the mesh size gets finer this error should decrease. However, if the size of the mesh elements is small enough so that the numerical result is close to the real solution, a further decrease of the element size should not affect the solution significantly since the result is already correct.

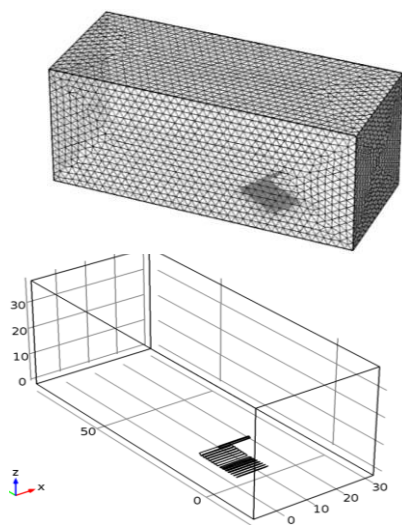


Fig.3. Entire domain meshing and calculating domain

When this situation occurs the solution is said to be mesh-independent and this should always be achieved when performing a simulation. Mesh design (including the height of the first mesh cell) is critical to obtain a valid and accurate CFD solution, leading to very thin boundary layer. Complete mesh consists of 254768 domain elements, 21204 boundary elements, and 3186 edge elements.

The dimensions of the calculation domain and meshing are given in Fig. 3 with a total length of 100m, a height of 40m and a depth of 40m. The LFR model is placed at 30m from the win inlet velocity.

### III. NUMERICAL PROCEDURE

#### A. Governing equations

The The  $k-\varepsilon$  turbulence model is the most widely used and tested two-equation model, with many improvements incorporated over the years [4]. The formulation of this model is as follow [5]: The Reynolds stresses  $\overline{u_i u_j}$  are related to the shear stress of the flow  $\tau_{ij}$  by the following equation:

$$\tau_{ij} = \overline{\rho u_i u_j}$$

Where  $\rho$  is the density of the fluid. We can find the value for  $\tau$ , and hence  $\overline{u_i u_j}$  from the following equation:

Where  $\rho$  is the density of the fluid. We can find the value for  $\tau$ , and hence  $\overline{u_i u_j}$  from the following equation:

$$\tau_{ij} = \mu_t \left( \frac{\partial \overline{u_i}}{\partial x_j} + \frac{\partial \overline{u_j}}{\partial x_i} \right) - \frac{2}{3} \rho k \delta_{ij}$$

Where  $\mu_t$  is the turbulent viscosity. In the case of  $k-\varepsilon$  turbulence model, turbulence viscosity is defined as:

$$\mu_t = \rho C_\mu \frac{k^2}{\varepsilon}$$

Where  $C_\mu$  is the model constant [3].

TABLE I  
 VALUES OF  $k-\varepsilon$  TURBULENCE MODEL CONSTANTS [3]

	$C_\mu$	$C_{\varepsilon 1}$	$C_{\varepsilon 2}$	$\sigma_\varepsilon$	$\sigma_k$
COMSOL and ANSY CFX	0.09	1.44	1.92	1.3	1.0

By solving the following differential equations for the turbulent kinetic energy,  $k$ , and the turbulent dissipation rate,  $\varepsilon$ , we can find a value for  $\mu_t$  [5]:

$$\frac{D(\rho k)}{Dt} = \frac{\partial}{\partial x_j} \left( \left( \mu + \frac{\mu_t}{\sigma_k} \right) \frac{\partial k}{\partial x_j} \right) + \tau_{ij} \frac{\partial \overline{u_i}}{\partial x_j} - \rho \varepsilon$$

$$\frac{D(\rho \varepsilon)}{Dt} = \frac{\partial}{\partial x_j} \left( \left( \mu + \frac{\mu_t}{\sigma_\varepsilon} \right) \frac{\partial \varepsilon}{\partial x_j} \right) + C_{\varepsilon 1} \frac{\varepsilon}{k} \tau_{ij} \frac{\partial \overline{u_i}}{\partial x_j} - C_{\varepsilon 2} \rho \frac{\varepsilon^2}{k}$$

Where  $\sigma_k$ ,  $\sigma_\varepsilon$ ,  $C_{\varepsilon 1}$ ,  $C_{\varepsilon 2}$  and  $C_\mu$  are all empirical model constants. The default values for these constants in most commercial CFD softwares, including ANSYS CFX and COMSOL are shown in Table 1.

#### B. Boundary conditions

- Inlet velocity profile:

$$u = u_{zref} \cdot \left(\frac{z}{z_{ref}}\right)^\alpha$$

$$h_{ref} = 10m$$

$U_{ref}=30m/s, 40m/s \text{ and } 50m/s$

$$\alpha = \frac{1}{7} \text{ in open areas.}$$

- Outlet:

$$\frac{\partial P}{\partial x} = \frac{\partial u}{\partial x} = \frac{\partial v}{\partial x} = 0$$

In this study, a comparison between pressure evolution on the FLR flat mirrors in the considered domain was performed with three different -velocities (30m/s, 40m/s and 50m/s) varying in each case the wind direction (0°, 30°, 60° and 90°).

#### IV. RESULTS AND DISCUSSION

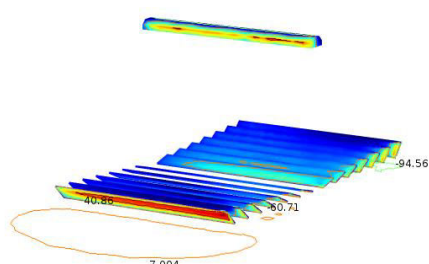


Fig.4. Pressure on LFR components (wind direction at 0°)



Fig.5. Wind velocity isosurfaces at 7m/s, 14m/s and 21m/s respectively

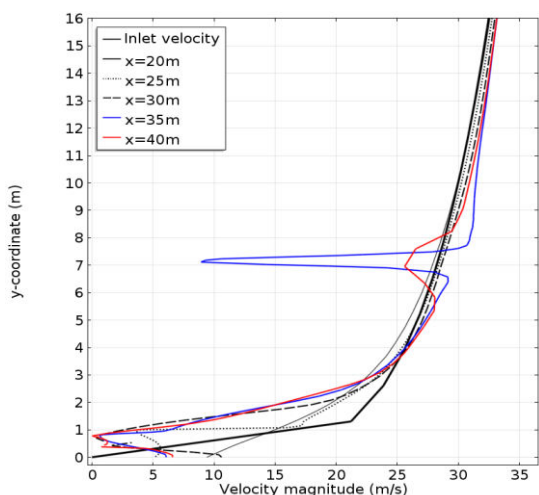


Fig.6. Wind velocity vertical profiles

A 3-D numerical simulation was performed to predict and estimate the effect of wind loads on linear Fresnel concentrator. Numerical computation was made for wind speed of 30 m/s, 40m/s and 50m/s respectively by varying wind direction of 0°, 30°, 60° and 90° respectively.

Fig.4 is an example for the pressure distribution on the flat mirrors of FLR module.

Fig.5 illustrates the Wind velocity iso-surfaces at 7m/s, 14m/s and 21m/s respectively.

Vertical Velocity magnitude profiles for different vertical position in the considered domain are illustrated in Fig.6

Fig.7 demonstrates the pressure distribution in the case of 30° wind direction where the maximum values of pressure are located in the first four of mirrors (dawn) and the last four mirrors (top).

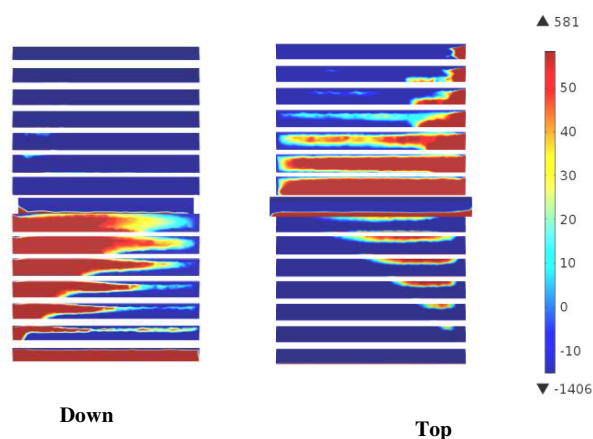


Fig.7. Pressure on the top and down of FLR in the case of 30°Wind direction (30m/s).

The pressure caused by strong winds on this type of solar collector is a tool for dimensioning mirrors structures and electric motors of tracking system.

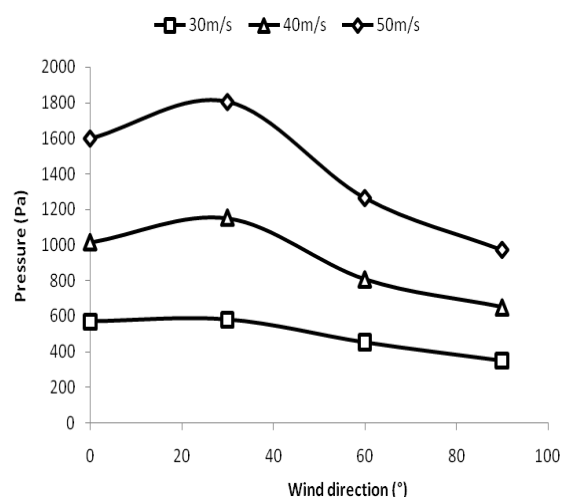


Fig.8. Pressure with wind direction

The wind direction of 30° generates the most important pressures on the mirrors. Fig.8 representing the maximum pressures exerted by the wind on the FLR mirrors with different directions shows that the maximum pressure is when the wind speed is 50 and a wind direction of 30°

## V. CONCLUSIONS

The present work is a CFD analysis of wind loads effect on linear Fresnel flat mirrors. Preliminary results show that the mirrors in direct contact with the wind are affected considerably compared with internal mirrors. For the vertical profile of the wind, and according to Fig.6, there are significant fluctuations throughout the collector which causes recirculation zones between mirrors. The pressure caused by strong winds on this type of solar collectors is used for sizing the load-bearing structures of the FLR.

## REFERENCES

- [1] Andreas Schellenberg, Joe Maffei, Karl Telleen, Rob Ward. Structural analysis and application of wind loads to solar arrays. *J. WindEng.Ind.Aerodyn.*123(2013)261–272
- [2] J. A. Peterka, N. Hosoya, B. Bienkiewicz, J. E. Cermak. *Wind Load Reduction for Heliostats*. Solar energy rethacherch institute. U.S department of energy. 1986
- [3] e. j. roschke. *wind loading on solar concentrators: some general considerations*. Jet propulsion laboratory pasadena, california. 1984
- [4] Argyropoulos CD, Markatos NC. Recent advances on the numerical modeling of turbulent flows. *J Appl Math Model* 2015;39:693-732.
- [5] Gillas Serge, Glover Nina, Malki-Apshtein Liora. Bayesian calibration of the constants of the k-epsilon turbulence model for a CFD model of street canyon flow. *Comput Methods Appl Mech Eng* 2014; 279:536-553
- [6] H. Bendjebbas, A. Abdellah El-Hadj and M. Abbas, Full scale, wind tunnel and CFD analysis methods of wind loads on heliostats: A review. *Renewable and Sustainable Energy Reviews*, 54 (2016); 452-472
- [7] Q.S. Li, Zhi Lunhai and Hu Fei, Boundary layer wind structure with from observations on a 325m tower. *Journal of wind engineering and industrial aerodynamics*, 98(2010); 881-832

# Optimization of two level production distribution systems with stock and transportation costs

Bensakhria Mohamed<sup>#1</sup>, Samir Abdelhamid<sup>#2</sup>

<sup>#</sup>*Department of industrial engineering*

*University of Batna 2, Batna, Algeria*

<sup>1</sup>m.bensakhria@univ-batna2.dz

<sup>2</sup>samir\_abdel@hotmail.com

**Abstract**— In this paper we address the optimization of production, distribution, and routing decisions to adapt retailers' demand with the general objective of optimizing the total cost. This work aims at implementing a solution that is related to production, replenishment, inventory allocation and transportation for a combined optimization of stock and transportation costs. The methodology adopted to tackle this issue is based on two heuristics greedy and genetic algorithms. The results demonstrate that the proposed heuristics are effective and performs impressively in terms of computational efficiency and solution quality.

**Keywords**— Optimization, Production-distribution systems, Routing decision, Inventory, Genetic Algorithms.

## I. INTRODUCTION

Over the recent years modeling and simulation of production routing problems (PRP) has been well developed, given the huge role it plays in the analysis of the discrete behavior of this type of systems, this later combines lot-sizing decisions, inventory management and routing. In the PRP within each period production facility must determine whether or not to make the product and decide the corresponding quantity in which this product can be inventoried at the retailers, Considering production setup cost and variable cost, transportation and routing costs [4, 2].

According to recent studies, integrated supply chain planning problems consider the optimization of stock and transport costs separately which is significant and cannot be neglected, Li et al. [1] a supply chain may be seen as a composed layers. Deliveries are made between each pair of layers. Each pair represents one level of the distribution network; transportation is considered the building block of any supply chain. Many shipment policies have been proposed in literature for this problem. For instance, a current trend in the application of freight distribution systems involving two or more levels where at first freight travels using ships and then is loaded on trucks to distribute it over the warehouses or retailers [3]. The reminder of this paper organized as follows: section 2 presents the notation used throughout the paper and introduces the literature concept of the PRP. Mathematical formulation presented in section 3. Section 4 a two phase algorithm is presented to solve the proposed model and. The experimentation and results are

provided in section 5. Finally Section 6 provides the conclusions drawn and future research lines.

## II. STATE OF THE ART

In the research literature these four decisions can be found in Bhatnagar et al. [8], Sarmiento and Nagi [9]. Regarding the large number of studies in this area different tools and techniques have been used in past publication for the optimization of the PRP problem. Mathematical techniques which have been widely used in the past include heuristic procedures. Several metaheuristics, such as Boudia using memetic algorithm with dynamic population management for an integrated production distribution problem [10], GRASP [12], tabu search [13, 14], and ALNS [18]. Ettl et al [11] they considered a queuing network model with constraint nonlinear optimization to minimize the inventory cost while satisfying customer service level requirements, the main disadvantage of this approach is that it does not consider the production capacity, which is a key constraint in the PRP systems. Chang et al. [15] discussed a serial production system with finite storage space that follows a base-stock policy. They developed a phase-type approximation to estimate the effective arrival rate of customers in which they can determine the optimal base-stock level. Bard et al [17] they presented a comparative analysis of a series of heuristics for an inventory routing problem (IRP) using branch-and-price framework. Golden et al [16] were the first to investigate the interrelated problem of inventory allocation and vehicle routing. They developed a heuristic for designing an integrated delivery planning system aimed at comparing the distribution rule used by the company with their approach.

Recently, new forms of relationships in the supply chain have been adopted. One of these is called vendor managed inventory (VMI), Archetti et al [7] have introduced a particular policy, known as deterministic order up to level policy, the problem is to evaluate for each time period the quantity to ship to each retailer and the vehicle route, they present a mixed integer linear programming model with additional valid inequalities to strengthen the linear relaxation. Chitsaz et al [5] presented a general model for the assembly routing problem (ARP). The problem formulated as a mixed-integer linear program and they proposed a three-phase decomposition matheuristic that relies on the iterative solution of different subproblems. Leopoldo et al [6] developed a



heuristic algorithm to solve the selective and periodic inventory routing problem. They proposed to reduce and optimize approach with the introduction of a new inequality.

In this paper, the problem is mathematically formulated by a MILP model. Due to the complexity of the problem which was shown to be NP-hard by Arkin et al. [19], two well-known heuristics available in the literature of PRP (Genetic Algorithm (GA) and Greedy Algorithm (GA)), are first adapted to (LSP) then (VRP). To more effectively solve larger problems, a two-phase algorithm is also presented to solve the proposed model. The algorithm is greedy considering at each step, several alternatives are generated and the best one is selected. To evaluate the model performance, different numerical experiments were performed. The results show the model and the heuristics are effective for the problem.

### III. PROBLEM DESCRIPTION

In this research proposal we aim to address the identified points; we will evaluate the inventory cost by integrating production, inventory, and routing decisions that minimize total costs, while ensuring that all demands are met. We consider a set of retailers'  $r = \{1 \dots R\}$  geographically dispersed around the production facility, products delivered to retailers along a planning discrete time horizon  $t = \{1 \dots T\}$ . Each retailer  $r$  has a fixed nonnegative deterministic demand  $d_{rt}$  that must be satisfied over a time horizon  $t$ . back orders are not permitted a limited amount of the end product can be restocked from the production facility, the storage capacity at the retailers are limited to  $C_r$  with unit holding cost  $h_r$  which depends on the retailer.

A product quantity is produced or made available at the production facility and a quantity is consumed at retailer, no capacity limit is assumed on production site but the amount produced per item in each period is restricted to  $P_{max}$ , the storage capacity is limited to  $C_p$  with a holding cost  $h_p$ . A fixed production setup cost  $F_{pc}$  and a variable setup cost  $V_{pc}$  is incurred. A fleet of  $Z$  homogeneous vehicles with capacity  $Q$  capable of serving several retailers on the same route is responsible for shipping the product from the production facility to retailers. A cost of  $C_{ij}$  is realized when the link among two pair  $i$  and  $j$  is traversed. VRP must be solved daily to determine which customers to visit and how much product to deliver to each retailer. From the comparative study of different extensions of the PRP problems and our objectives the problem can be formulated as a mixed integer linear programming (MILP) with a multi-heuristics based approach.

#### Indexes

- $t = 1 \dots T$  : set of periods
- $r = 1 \dots R$  : set of retailers
- $z = 1 \dots Z$  : set of vehicles
- $d_{rt}$  : demand of retailer  $r$  in period  $t$
- $C_r$  : storage capacity of retailer  $r$
- $C_p$  : storage capacity of production facility

- $P_{max}$  : production capacity
- $h_r$  : inventory holding cost of retailer  $r$
- $h_p$  : inventory holding cost of production facility
- $Q$  : vehicle capacity
- $F_{pc}$  : fixed setup cost
- $V_{pc}$  : variable setup cost
- $C_{i,j}$  : fixed transportation cost

#### Decision variables

- $D_{rzt}$  : The quantity to be delivered to retailer  $r$  using vehicle  $z$  in period  $t$
- $I_p^t$  : Inventory level at production facility in planning period
- $I_r^t$  : Inventory level at retailer  $r$  in planning period  $t$
- $P_t$  : quantity to be produced in period  $t$
- $Z_t$  : Production quantity in planning period  $t$
- $Y_t$  : Binary variable equal 1 if there is production on planning period  $t$ , otherwise equal 0
- $X_{rzt}$  : Binary variable equal 1 if vehicle  $Z$  is used in planning period  $t$  to serve retailer  $r$  in period  $t$ , otherwise equal 0
- $U_{rzt}$  : Binary variable equal 1 if retailer  $r$  is served by vehicle  $z$  in planning period  $t$ , otherwise equal 0

$$\text{Min} = \sum_{t=1}^T (F_{pc} \cdot Y_t + V_{pc} \cdot Z_t + h_p \cdot I_p^t + \sum_r h_r \cdot I_r^t + \sum_r \sum_z C_{ij} \cdot X_{rzt}) \quad (1)$$

$$I_p^t = I_p^{t-1} + P_t - \sum_r \sum_z D_{rzt} \quad \forall r \in R, z \in Z, t \in T \quad (2)$$

$$I_r^t = I_r^{t-1} + \sum_z D_{rzt} - d_{rt} \quad \forall r \in R, z \in Z, t \in T \quad (3)$$

$$I_p^t \leq C_p \quad \forall t \in T \quad (4)$$

$$I_r^t \leq C_r \quad \forall t \in T \quad (5)$$

$$P_t \leq P_{max} \cdot Y_t \quad \forall t \in T \quad (6)$$

$$D_{rzt} \leq Q \cdot U_{rzt} \quad \forall r \in R, z \in Z, t \in T \quad (7)$$

$$\sum_r D_{rzt} \leq Q \quad \forall r \in R, z \in Z, t \in T \quad (8)$$

$$\sum_z U_{rzt} \leq 1 \quad \forall z \in Z, t \in T \quad (9)$$

$$\sum_r U_{rzt} \leq 1 \quad \forall r \in R, t \in T \quad (10)$$

$$\sum_r U_{rzt} \leq Q \cdot X_{rzt} \quad \forall z \in Z, t \in T \quad (11)$$

$$X_{rzt} \cdot Y_t \cdot U_{rzt} \in \{0,1\} \quad \forall r \in R, z \in Z, t \in T \quad (12)$$

$$P_t, I_p^t, I_r^t, D_{rzt} \geq 0 \quad \forall r \in R, z \in Z, t \in T \quad (13)$$

The mathematical formulation for the proposed problem is presented as follows:

The objective function given in (1) used to minimize the overall costs of production setup, transportation, holding costs at the production facility and the retailers. Constraints (2) relates to the inventory balance equations at production facility, where the inventory level at the end of period  $t$  can be obtained by adding the inventory level at the end of period  $t-1$ . Similarly inventory balance equations at the retailer  $r$ , as shown in constraints (3), is equal to the inventory level in period  $t-1$ , by adding the total quantity shipped in period  $t$  and subtracting the total quantity shipped to the other retailers.

Constraints (4) and (5) guarantee the upper bounds on inventory levels at production facility or retailers. Constraints (6) confirm that the inventory level of the production facility does not exceed the maximum level. Constraints (7) link the continuous variable  $D_{rzt}$  to the binary variable which means if there is a delivery to a retailer in planning period  $t$ , then it must be 1. Constraints (8) define the vehicle capacity. Constraints (9) ensure that each retailer is visited at most once in a given period. Similarly, constraints (10) guarantee the vehicle loading and routing restrictions used mostly once per planning period. Constraints (11) define number of trips during planning horizon. Finally, constraints (12) and (13) are variable definitions.

Initial attempts to solve instances of this size with CPLEX 8.1 were not encouraging. This was not surprising since the model is NP-hard, to deal with such a complex problem is to decompose it into smaller problems of reduced complexity for which optimal or near optimal solutions can be determined.

#### IV. PROPOSED METHOD

Optimally solving such a convenient problem is in general difficult due to its combinatorial nature that integrates two well known problems, lot sizing and vehicle routing problems. We present a solution procedure based on a two phase algorithm to solve the proposed model, decomposition and integration. The initial phase solves the shortest path constraints for the production facility submodel, which contains all the original constraints. Resulting solutions to this phase is always feasible but not optimal and thus gives an upper bound solution to our problem. Successfully solving this problem determines production quantities, quantities to be delivered to each retailer and each retailer that must be visited at each time period. Fixing the routing decisions in the initial phase define the number of retailers to be visited and the quantity to be delivered at each time period. Consequently, in the next phase we propose a heuristic to solve the routing problem in the distribution submodel. In the next iteration the results of the distribution submodel considered as an inputs to update the routing decisions for the next iteration. The procedure continues this iterative solve feedback solve until a stopping criterion is achieved or attain a fixed number of iterations. The main steps of the iterative method illustrated in algorithm 1.

##### Algorithm 1

###### Begin

**Step 1:** Estimate demand and production quantity for each retailer that needs delivery in period  $t$

**Step 2:** Solve production problem using Greedy algorithm

**Step 3:** Solve the routing problem using Genetic algorithm

**Step 4:** Calculate sol and set best sol = sol

###### Repeat

###### Repeat

**Step 5:** Update demand and production quantity for each retailer

**Step 6:** Run diversification mechanism

**Step 7:** Solve production problem using retailers' updated costs using Greedy algorithm

**Step 8:** Solve routing problem using Genetic algorithm

**Step 9:** Update sol if necessary

Until a stopping criterion in met

**Step 10:** Calculate the sol

**If** (sol < best sol)

Set best sol = sol

**End if**

**Until** a stopping criterion in met

**End.**

With the aim to simplify our solution, we set some goals based on the retailer's demand and the vehicles capacity, to be more precise the sum of retailers' demands in planning period  $t$  (Drt). The production unit model is demonstrated in relations (14) to (19):

$$\text{Min} = \sum_{t=1}^T (F_{pc} \cdot y_t + V_{pc} \cdot Z_t + h_p \cdot I_p^t) \quad (14)$$

$$I_p^t = I_p^{t-1} + P_t - D_t \quad \forall r \in R, z \in Z, t \in T \quad (15)$$

$$I_p^t \leq C_p \quad \forall t \in T \quad (16)$$

$$P_t \leq P_{\max} \cdot Y_t \quad \forall t \in T \quad (17)$$

$$Y_t \in \{0,1\} \quad \forall r \in R, z \in Z, t \in T \quad (18)$$

$$P_t, I_p^t \geq 0 \quad t \in T \quad (19)$$

Then the algorithm proceeds to the second phase that require all the routing decisions which include retailers that has served by each vehicle at each time period. Given that the initial phase allocates retailers to vehicles and considering vehicle capacity. Relations (20) to (30) demonstrate the distribution model. The sum of the production quantities  $P_t$  work as an update for the next iteration of the second phase. The routing phase model is:

$$\text{Min} = \sum_{t=1}^T (\sum_r \sum_z C_{ij} \cdot X_{rzt} + \sum_r h_r \cdot I_r^t) \quad (20)$$

$$I_r^t = I_r^{t-1} + P_t - \sum_r \sum_z D_{rzt} \quad \forall r \in R, z \in Z, t \in T \quad (21)$$

$$I_r^t = I_r^{t-1} + \sum_z D_{rzt} - drt \quad \forall r \in R, z \in Z, t \in T \quad (22)$$

$$I_r^t \leq C_r \quad \forall t \in T \quad (23)$$

$$D_{rzt} \leq Q \cdot U_{rzt} \quad \forall r \in R, z \in Z, t \in T \quad (24)$$

$$\sum_r D_{rzt} \leq Q \quad \forall r \in R, z \in Z, t \in T \quad (25)$$

$$\sum_z U_{rzt} \leq 1 \quad \forall z \in Z, t \in T \quad (26)$$

$$\sum_r U_{rzt} \leq 1 \quad \forall r \in R, t \in T \quad (27)$$

$$\sum_r U_{rzt} \leq Q \cdot X_{rzt} \quad \forall z \in Z, t \in T \quad (28)$$

$$X_{rzt}, U_{rzt} \in \{0,1\} \quad \forall r \in R, z \in Z, t \in T \quad (29)$$

$$P_t, I_p^t, I_r^t, D_{rzt} \geq 0 \quad \forall r \in R, z \in Z, t \in T \quad (30)$$

Given the fact that during the initial tests that we performed to solve the production submodel problem a greedy search algorithm attempts to generate a feasible solutions, we found that this heuristic solutions are unlikely to perform well and even when they can be adapted, they may not be able to find good optimal feasible solutions in a reasonable time. This implies the alternative of applying extended heuristics, genetic algorithms. Hence the question which needs to be asked is how to adapt two different heuristics in an effective way

**A. PROPOSED GENETIC ALGORITHM**

In the first phase chromosomes are created for an optimal size that we describe the routing phase, in which corresponds in calculating vehicle routes at each period. A chromosome is a sequence of nodes, indicating the order in which vehicles must visit all retailers. In this case we consider a set of retailers to be served by a fleet of identical vehicles in planning periods; we set a two dimensional matrix that each cell contains the retailer’s demand in a given time period.

The binary variables Urzt that imply if a vehicle z is used in planning period t to serve a retailer r is the main issue to identify the other decision variables. The above procedure is repeated until a stopping criterion is achieved. The details of the basic genetic algorithm are given below in algorithm 2

**Algorithm 2**

**Begin**

- Step 1:** Population size (p)
- Step 2:** Number of generations (n)
- Step 3:** Create a delivery with a random order of retailers
- Step 4:** Do this for p times to create a population
- Step 5:** Select the best delivery from the population
- Step 6:** Set the initial feasible solution as local best solution and global best solution

**Genetic algorithm**

```

Run for n times
Loop1
Run for p times
Loop2
Select a random set of delivery from the population
Get the fittest and return
//Crossover
Parent1 = roulette wheel selection ()
Parent2 = roulette wheel selection ()
Child = Crossover (Parent1, Parent2)
//Mutation
Swap random two retailers in the child
endLoop2
//New population is created
Calculate the fitness value for each individual
Sort the population by their fitness values
Update local best Solution and global best Solution
endLoop1
final local solution = local best Solution
final global solution = global best Solution
    
```

**End**

**B. Genetic operators**

The mechanism for generating the initial population allows the production of individuals’ population as the basis for future generations. The choice of the initial population is important because it can make more or less fast the convergence to the global optimum.

*1) Selection and crossover*

The first step in genetic algorithm it starts with selection in which individuals are selected for crossover according to their relative fitness, in this way the selection step implemented in practice by the creation of a mating pool for the next generation. The choice of a selection technique in the suggested genetic algorithm is the roulette wheel operator which used to select the initial population to create new children, the probability of choosing an individual depends directly on its fitness.

In the next step the crossover occurs when two members of a population (chromosomes) are selected for reproduction, and is usually based upon their relative fitness in solving the problem. Two parents P1 and P2 are selected randomly we use the order crossover (OX) with slightly modification, it starts by choosing two crossover points then applying sliding motion to fill up the left out holes by sending the mapped positions. It copies the portion of permutation elements between the crossover points from the cut string directly to the offspring, placing them in the same absolute position. An example of offspring generation is illustrated in Fig 1

*2) Mutation*

Mutation may be defined as a small perturbation to prevent the genetic algorithm converging to a local minimum; we opted to use the operator left to right flip for the mutation process. An example of mutation consists of choosing randomly two genes from the chromosome and exchanging their values is illustrated in Fig 2. As noted to escape such a point we implemented a diversification mechanism. The rule we adopt it captures, for each retailer, the complementarities with the other retailers served in the same route. Our principle of correction is to start by calculate the total sum of the quantity transported by vehicles .After that, we have to browse each group gene by gene and if it is higher than the maximum available vehicle capacity, we must search in the next sequence of group’s nodes which succeed this position of excess capacity, a retailer who has not been served and its insertion does not cause overload of vehicle we insert it in the next position.

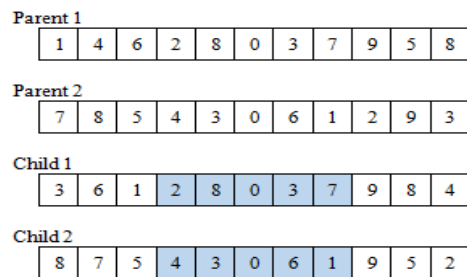


Fig 1. Order crossover operator

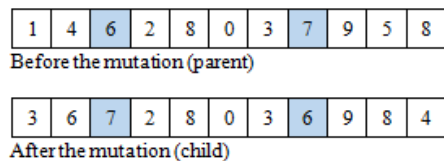


Fig 2. Mutation operation

V. EXPERIMENTAL RESULTS

Our algorithms are implemented in Matlab environment. We used IBM ILOG CPLEX 12.6 with the default settings to solve the proposed problem. All experiments were performed on an Intel Core 2Duo processor, with 4096Ko of memory cache, 4GB of RAM and a frequency of 3.0 GHz using the Windows 7 operating system. Problem instances are created by randomly generating parameters as follows:

Number of periods (T), retailers (R), vehicles (V), production capacity ( $P_{max}$ ) and vehicle capacity (Q)

- (i) Demand quantities  $d_{rt} = U [5, 25]$
- (ii) Variable production setup costs  $V_{pc} = U [50, 100]$
- (iii) Fixed production setup costs  $F_{pc} = U [500, 1000]$
- (iv) Inventory holding costs in production facility and retailers  $h = U [5, 10]$
- (v) Fixed transportation costs  $C_{ij} = U [200, 300]$
- (vi) Vehicle capacity  $2\alpha, 1.5\beta (\alpha = \sum_{r,t} d_{rt} / R \times T)$
- (vii) Production capacity  $2\alpha, 1.5\beta (\beta = \sum_{r,t} d_{rt} / R \times T)$

A. Computational results on the small and large sets of instances

Let us first compare the effectiveness of the iterative method proposed in this paper on the small size of instances. In the latter part we present our best solutions and average results on random test problems. A summary of the results for small size test problems is reported in Table 1. In columns 2-4 a comparison of objective functions of the IBM ILOG CPLEX 12.6, Proposed Genetic Algorithm (PGA) then the optimal solution or the best solution is determined by the standard solver IBM ILOG CPLEX 12.6 after one hour.

In terms of average optimal solutions the PGA is able to produce better results at the beginning afterward could not further improve the solution quality due to the algorithm sensitivity to the number of periods (T) and the increase number of vehicles. whereas PGA algorithm could provide better average results for 13 out of 32 test problems and consequently on the overall number of instances solved to optimality , 252 of 648 (39%).

TABLE 1: COMPARISON OF OBJECTIVE FUNCTIONS OF PGA AND IBM ILOG CPLEX ON SMALL INSTANCES

Problem N T K	CPLEX 1h	PGA	Optimal solutions
4 5 2	23465	23465	6
4 5 3	24158	24158	6
4 10 2	34028	34101	3
4 10 3	42919	43899	2
6 5 2	61520	61520	6
6 5 3	56676	56676	6
6 10 2	55318	55318	6
6 10 3	45297	45297	6
8 5 2	65754	65890	2

8 5 3	63378	66524	2
8 10 2	73985	74520	4
8 10 3	55550	55550	6
10 5 2	74586	77002	3
10 5 3	91357	100211	1
10 10 2	86542	100254	0
10 10 3	86524	99652	0
<b>Average</b>	<b>58816.06</b>	<b>61502.31</b>	<b>3</b>

TABLE 2: COMPARISON OF OBJECTIVE FUNCTIONS OF PPGA, MGA AND IBM ILOG CPLEX ON LARGE INSTANCES

Problem N T K	CPLEX 2h	PGA average	PGA worst
30 10 10	163560	179965	182569
30 10 15	215766	236524	245879
30 15 10	310026	356900	365852
30 15 15	383894	425696	440652
40 10 10	523088	536265	575632
40 10 15	179534	193654	199652
40 15 10	257486	280654	290652
40 15 15	335069	340259	391368
50 10 10	466532	500256	520236
50 10 15	559502	625438	643652
50 15 10	307254	350236	364258
50 15 15	284769	312589	343560
60 10 10	402569	480659	499856
60 10 15	501394	576301	601254
60 15 10	665841	758963	796502
<b>Average</b>	<b>383805</b>	<b>428395.06</b>	<b>451883.50</b>

Again the results for large instances are similar to those observed on the objective function in table 2. The table illustrates again how PGA determines solutions of good quality compared to the standard solver IBM ILOG CPLEX 12.6, which is the most successful approach on large instances. The standard solver sometimes cannot find feasible solutions whereas both heuristics find one.

VI. CONCLUSIONS AND FUTURE WORK

We have proposed a two-phase iterative method based on two heuristics to solve the PRP. In the first phase, a lot-sizing problem is solved using a greedy heuristic. The first phase decides when and how much to produce at each period, when to visit retailers, and how much to deliver at each visit. The second phase takes routing decision into account using genetic algorithm approach. In the GA construction phase, a randomized version of a previously developed construction heuristic is used. Which involves two random neighborhood search mechanisms, the crossover and mutation operations, suitable designs are developed. In order to validate the performance of proposed method, a number of randomly generated test problems are used. We have tested these approaches on small and large size instances. The results show that the proposed method can provide optimal solutions. On average, proposed genetic algorithm outperforms the standard solver IBM ILOG CPLEX 12.6 and generates solutions that are within 2% from the optimal solution.

Our next step is to develop and test different meta-heuristics or other hybrid methods. Then, many more iterations would be possible and more elaborated diversification schemes.

REFERENCES

- [1] LI, J., SAVA, A., and XIE, X. Performance evaluation and optimization of a two-stage production-distribution system with batch orders and finite transportation time. The 16th world congress of IFAC, Prague.2005
- [2] Thomas DJ, Griffin PM Coordinated supply chain management. *Eur J Oper Res* 94(1):1–15. 1996
- [3] Infante D, Paletta G, Vocaturo F. A ship-truck intermodal transportation problem. *Marit Econ Logist*; 11:247–59. 2009
- [4] Geoffrion AM, Powers RF. 20 years of strategic distribution system design: an evolutionary perspective. *Interfaces* 25(5): 105–127. 1995
- [5] Masoud Chitsaz, Jean-François Cordeau, and Raf Jans. A unified decomposition metaheuristic for assembly, production, and inventory routing. *INFORMS Journal on Computing*, 31(1):134–152, 2019.
- [6] Leopoldo Eduardo Cárdenas-Barrón, José Luis González-Velarde, Gerardo Treviño Garza, and Dagoberto Garza-Nuñez. Heuristic algorithm based on reduce and optimize approach for a selective and periodic inventory routing problem in a waste vegetable oil collection environment. *International Journal of Production Economics*, 211:44–59, 2019.
- [7] Archetti C, Bertazzi L, Laporte G, Speranza MG. A branch-and-cut algorithm for a vendor managed inventory routing problem. *Transp Sci*; 41(3):382–91. 2007
- [8] Bhatnagar R, Chandra P, Goyal SK. Models for multi-plant coordination. *Eur J Oper Res* 67(2):141–160. 1993
- [9] Sarmiento AM, Nagi R. A review of integrated analysis of production-distribution systems. *IIE Trans* 11(3):1061–1074. 1999
- [10] Boudia M, Prins C. A memetic algorithm with dynamic population management for an integrated production-distribution problem. *Eur J Oper Res*; 195 (3) :703–15. 2009
- [11] Ettl, M., Feigin, G. E., Lin, G.Y. and Yao. D.D. "A Supply Network Model with Base-Stock Control and Service Requirements", *Operations Research*, Vol. 48/2, 2000. pp. 216-232.
- [12] Boudia M, Louly MAO, Prins C. A reactive GRASP and path relinking for a combined production-distribution problem. *Comput Oper Res*; 34 (11):3402–19. 2007
- [13] Armentano VA, Shiguemoto AL, Løkketangen A. Tabu search with path relinking for an integrated production-distribution problem. *Comput Oper Res*; 38(8):1199–209. 2011
- [14] Bard JF, Nananukul N. The integrated production-inventory-distribution-routing problem. *J Sched*; 12(3):257–80. 2009
- [15] Chang K-H, Lu Y-S. Inventory management in a base-stock controlled serial production system with finite storage space. *Math Comput Model* 54:2750–2759. 2011
- [16] Golden, B., Assad, A., Levy, L., and Gheysens, F. (1984). The fleet size and mix vehicle routing problem. In *Computers and Operations Research*, 11:49–66.
- [17] J. F. Bard and N. Nananukul, Heuristics for a multiperiod inventory routing problem with production decisions, *Computers and Industrial Engineering*, vol. 57, no. 3, pp. 713–723, 2009.
- [18] Adulyasak Y, Cordeau J-F, Jans R. Optimization based adaptive large neighborhood search for the production routing problem. *Transp Sci*; 48(1):20-45. 2014
- [19] Arkin E, Joneja D, Roundy R (1989) Computational complexity of uncapacitated multi echelon production planning problems. *Oper Res Lett* 8(2):61–66

# Olive pomace steam gasification for production of syngas/hydrogen : sensitivity analysis

Rim Tilouche<sup>#1</sup>, Raoudha Garma<sup>#2</sup>, Doniazed Sioud<sup>#3</sup>, Housam Binous<sup>#4</sup>, Ahmed Bellagi<sup>#5</sup>

<sup>#</sup>*L.R. Thermique & Thermodynamique des Procédés Industriels*

*Ecole Nationale d'Ingénieurs de Monastir-ENIM, University of Monastir, Monastir, Tunisia*

<sup>1</sup>rimtilouch@gmail.com

<sup>2</sup>raoudhagarma83@gmail.com

<sup>3</sup>siouddoniazed@gmail.com

<sup>4</sup>ahmedbellagi@yahoo.fr

**Abstract**— This paper presents a thermodynamic simulation model of the olive pomace gasification process intended to produce hydrogen rich syngas.

The considered gasification process is simulated using the flow-sheeting software ASPENTECH.

The performance of gasification process is investigated by varying the gasification temperature, pressure and the steam to biomass ratio  $R$  in the feed.

Results show that for all investigated pressures, the produced hydrogen increases with temperature, reaches a maximum and then decreases.

We also noted that the parameter  $R$  has a large effect on the  $H_2/CO$  ratio in the exiting gas in the temperature range between 900 and 1300°C. The  $H_2/CO$  molar ratio is at its maximum with a value of two.

**Keywords**— Olive pomace gasification, hydrogen production, steam/biomass ratio, biomass, Aspen plus.

## I. INTRODUCTION

The increase in energy consumption in all economic sectors and the expected depletion of fossil fuel resources lead to a shortage of hundreds of tonnes of fossil fuels. This insist the use of other alternative and renewable energy resources such as solar photovoltaic, biomass, wind and hydroelectric power generation. To meet this energy demand, combustion processes, which are currently the most used for transport and industry, the tertiary sector or the residential sector, will have to evolve in stages and be substantially improved. They will have to diversify from fuel by introducing a growing share of biomass, and waste products.

Also, as we face the problem of global warming and greenhouse gas emission from conventional fuels via anthropogenic actions, extensive research and development focused on the use of biomass as auxiliary to fossil fuels. Biomass is an attractive renewable energy source with minimum negative environmental impact as compared to fossil fuels, because of its low sulphur content and its carbon dioxide neutral emissions [1, 2].

Gasification converts biomass through partial oxidation into an energy rich gaseous mixture, small quantities of char and condensable compounds. It is considered as one of the

most efficient way of converting the energy embedded in biomass, and it is becoming one of the best alternatives for the reuse of waste solids [3].

Biomass gasification process produces very low levels of particulates and very little amounts of  $NO_x$  and  $SO_x$  when compared with fossil fuels [4]. It can also be used as a source to produce various chemical species. The addition of steam in the gasification process can enhance hydrogen production. [5, 6]

Extensive research has been carried out in biomass gasification using different reactor configurations, operating condition and gasification agents.

Thermodynamic models constitute valuable investigation tools for prediction of produced gas composition under various gasification operating conditions, in particular as it is the case in the present paper, for prediction of the expected  $H_2/CO$  ratio.

Olive oil extraction processes widely used by oil mills are conventional pressure processes, either in batch mode (super press) or in continuous mode (centrifugation). These processes produce, apart from olive oil, by-products such water as olive pomace.

The thermal recovery of olive cake is the most relevant alternative for the reduction of these olive by-products. Thermal processes convert these pomaces into usable energy in different forms. The three main thermochemical conversions of olive pomace commonly developed correspond to combustion, pyrolysis, and gasification.

The objective of this paper is to investigate the hydrogen and syngas production using steam gasification of olive pomace.

The study is carried out assuming the establishment of the thermodynamic equilibrium in the gasifier at the prevailing conditions of temperature and pressure set. The composition of the gas is calculated by minimizing the free enthalpy of the mixture, taking into account mass and energy balances. For the following simulations, the mass flow rate of olive pomace was set at 1000 kg/hr while the flow rate of water vapour was varied from 100 to 1000 kg/hr. The temperature range

investigated is 500 -1500°C and the pressure range, between 1 to 250 bar.

## II. DESCRIPTION OF THE FEED

### 1) Characterization of the biomass

The origin of the raw olive pomace is a semi-traditional unit of olive oil extraction unit using a three-phase continuous system. The agricultural waste was composed of a mixture of olive skins, pulp residues, core fragments, water and a quantity of residual oil. The biomass is generally dried in open air and with solar energy [7, 8]. The treatment of the biomass is largely affected by the biomass composition and particle size.

In Tunisia, most olive pomace goes through a solvent treatment to recover the residual oil. Other value chains for olive pomace are cattle feed and use as fuel in oil mills for heating water [9].

### 2) Ultimate and proximate analysis

Raw olive pomace requires characterization for the design of an adequate system for their conversion (gasifier in the case of this study). In a first step, proximate analysis is performed to determine the amount of volatile matter (VM), fixed carbon (FC), moisture (M) and ash). The analysis of the organic matter content of the pomace investigated was carried out gravimetrically using a muffle furnace set at 550°C. Moisture is also measured gravimetrically at 105°C. The results obtained show an organic matter content of 75.28%, 23.45% humidity and 1.27% ash.

Thermogravimetric analysis (GTA) consists of measuring the mass variation of a sample as a function of temperature. Such an analysis presupposes a good precision for the three measures: weight, temperature and temperature variation. Two tests were realized in a furnace raised at two different temperatures to monitor the continuous variation in the mass loss of the contained pomace. This type of test allows to have a rough idea about the kinetics of gasification in the perspective of using a gasifier with continuous fuel supply. The results of these two tests are given in Table I.

As for the ultimate analysis, it is important to determine the weight percentage (wt %) of the elemental composition (Carbon: C, Hydrogen: H, Oxygen: O, nitrogen: N, sulphur: S) of olive pomace.

Raw olive pomace has a significant high heating value (HHV), 22.50 MJ/kg, The HHV of this residue is comparable with that of wood, which up to now is the biomass most appreciated and the most used even if its calorific value does not exceed 19.10 MJ/kg [10].

The high heating value of the biomass is calculated by the unified correlation developed by Channiwala and Parikh (2002) and based on 15 existing correlations and 50 fuels, including biomass.

$$HHV = 349.C + 1178.3H + 100.5S - 103.4O - 15.1N - 21.1ASH \text{ kJ / kg}$$

TABLE I  
 ULTIMATE AND PROXIMATE ANALYSIS OF THE BIOMASS [11]

Proximate analysis (wt%)	
Organic material	75.28
Moisture content	23.45
Ash	1.27
Ultimate analysis (wt%)	
C	53.6
H	6.93
O	37.98
N	1.48

Were C, H, S, O, N and ASH are percentage of carbon, hydrogen, sulphur, oxygen, nitrogen and ash determined by ultimate analysis on dry basis.

## III. PROCESS DESCRIPTION OF BIOMASS GASIFICATION

### A. Process description

Figure 1 illustrates the gasification process composed of four operations: (1) grinding (not presented in figure), (2) drying and flashing (DRY REAC and SEPARATE), (3) gasifying (DECOMP and GASIFIER) and (4) gas treatment (CYCLONE).

Firstly, the biomass is fed into the DRYREAC in parallel with a stream of nitrogen at high temperature. In this reactor, the elimination of moisture takes place. The nitrogen is thereafter eliminated by flashing and the biomass is converted into DRY-BIOM. DRY-BIOM is then introduced into the pyrolysis reactor, DECOMP. In this reactor, the biomass is converted according its ultimate analysis into simple species including carbon, oxygen, hydrogen, nitrogen and ash. This mixture, named FEED in Fig. 1 is then fed to the gasifier. Concurrently, steam is injected into this reactor. In the gasifier section, the biomass is converted into gaseous products (combustible gases, tars and volatiles matters) and solids products, mainly ash and. Finally, PRODUCTS coming from the GASIFER reactor passes to the CYCLONE for separating of GASES and SOLIDS from the main stream. As a result of this separation the product gas (SYNGAS) is obtained.

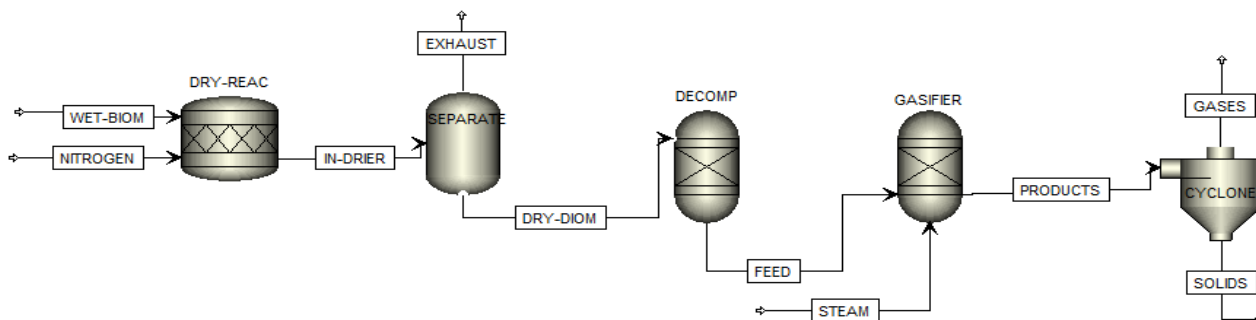


Fig. 1 Schematic diagram of the gasification process

The whole gasification process (pyrolysis in the decomposer then gasification in the gasifier) includes a set of consecutive and parallel reactions summarized in Table II [13].

TABLE II  
 CHEMICAL REACTIONS IN GASIFICATION PROCESS

Reaction	Reaction Name	$\Delta H_{25^\circ\text{C}}$ (kJ/mol)
<b>Combustion</b>		
$\text{C} + 0.5\text{O}_2 \leftrightarrow \text{CO}$	Partial oxidation	-111
$\text{CO} + 0.5\text{O}_2 \leftrightarrow \text{CO}_2$	CO Oxidation	-284
$\text{H}_2 + 0.5\text{O}_2 \leftrightarrow \text{H}_2\text{O}$	Hydrogen combustion	484
<b>Reduction</b>		
$\text{C} + \text{CO}_2 \leftrightarrow 2\text{CO}$	Boudourad reaction	172
$\text{C} + \text{H}_2\text{O} \leftrightarrow \text{CO} + \text{H}_2$	Steam reforming	131
$\text{C} + 2\text{H}_2 \leftrightarrow \text{CH}_4$	Methane formation	-74
$\text{CO} + \text{H}_2\text{O} \leftrightarrow \text{CO}_2 + \text{H}_2$	Water gas shift	-42
$\text{CH}_4 + \text{H}_2\text{O} \leftrightarrow \text{CO} + 3\text{H}_2$	Methane reforming	206
$\text{CH}_4 + \text{CO}_2 \leftrightarrow 2\text{CO} + 2\text{H}_2$	CO <sub>2</sub> Reforming of methane	247

## B. Model development

### 1) Thermodynamic equilibrium model

Equilibrium models have mainly two approaches: stoichiometric and non-stoichiometric. The stoichiometric approach requires a clearly defined reaction set that incorporates all chemical reactions and species involved. In the non-stoichiometric approach, no particular reaction routes considered in the numerical simulation. The only input requested is the component set at equilibrium and the elemental composition of feed, obtained from ultimate

analysis data. This approach is based on the minimization of the Gibbs energy of the reactanting mixture [12].

### 2) Process modelling

The simulation are performed using ASPENTECH. In this platform there is no especial gasification model ready for use. Therefore the modelling of the whole process is decomposed into blocks. The main unit operations involved in gasification are drying, pyrolysis or decomposition, gasification, combustion and finally, gas separating. These operations are represented by blocks simulating their functions, namely reactor block RSTOIC, flash block FLASH2, reactor block RYIELD, adiabatic reactor block RGIBBS and cyclone separator block SSPLIT.

As this study is based on an equilibrium approach, the reaction kinetic parameters are not needed.

The following assumptions were contemplated in modelling the gasification process:

- Steady state;
- Residence time for reactants sufficient to reach chemical equilibrium;
- Tar formation not considered;
- Char is 100% carbon;
- Biomass volatilization instantaneous and volatile products consist mainly of H<sub>2</sub>, CO, CO<sub>2</sub>, CH<sub>4</sub> and H<sub>2</sub>O [14].

The main objective of this paper is to investigate the effect of various operating parameters (Temperature, pressure, and R, steam/biomass ratio) on the gasification process's performance.

The effect of temperature on the syngas composition is studied from 500 to 1500°C. Pressure is set respectively at 1, 50, 150, 250 bar. For R we consider just two values in the simulation, R = 0.5 and R = 1.0.

Gasification conditions summarized in Table III.



TABLE III  
 OPERATING PARAMETERS FOR GASIFICATION PROCESS

Feed rate (kg/hr)	1000
Steam/biomass ratio, R	0.5 – 1.0
Gasification temperature (°C)	500 -1500
Pressure (bar)	1 - 250

#### IV. RESULTS AND DISCUSSION

The results are represented in Figures 2-9. They show that when the pressure increases, the maximum amount of produced hydrogen shifts to higher temperatures (cf. also table III).

##### A. Effect of temperature

Temperature is one of the most important operating parameter influencing biomass gasification. It has a significant effect on the composition of the producer gas.

To study the effect of the temperature, several simulations were performed. For the investigated temperature range, the H<sub>2</sub> composition of the product gas are relatively high. Further, the composition of H<sub>2</sub> increases with gasification temperature and reaches its maximum at 1500°C. This effect is probably due the endothermicity of the steam reforming reaction favored by higher temperatures.

The concentration of CO increases with gasification temperature while CO<sub>2</sub> concentration followed an opposed trend. The CH<sub>4</sub> concentration decreases as the gasification temperature increases.

##### B. Effect of pressure

Pressure is also an important factor which affects the composition of syngas production and gasification process. As the simulation results show, lower pressures for fixed gasifier temperature favour the amount of H<sub>2</sub> and CO. Opposite effect is observed for the concentration of CO<sub>2</sub> and CH<sub>4</sub> : they increase with pressure. Le Chatelier's law may explain these trends: chemical equilibrium at higher pressure evolves in a direction that favours the decreasing of the gas phase, enhancing so reactions consuming gas reactants.

##### C. Effect of steam/biomass ratio R

Steam to biomass ratio R is a key parameter in gasification on account of its influence on the syngas composition, yield and heat content [15].

Increasing R results in larger H<sub>2</sub> yield, due to water–gas shift, reforming, and cracking reactions. However, this effect is confined to a specific range of R. Beyond a certain limit, any increase in this ratio results in an excess steam in the

syngas. Steam is an important source of hydrogen, but energy contained in excess steam along with enthalpy losses in generating this steam results in low process efficiency. An optimal ratio R is to be determined to ensure thermal efficiency of the gasification process.

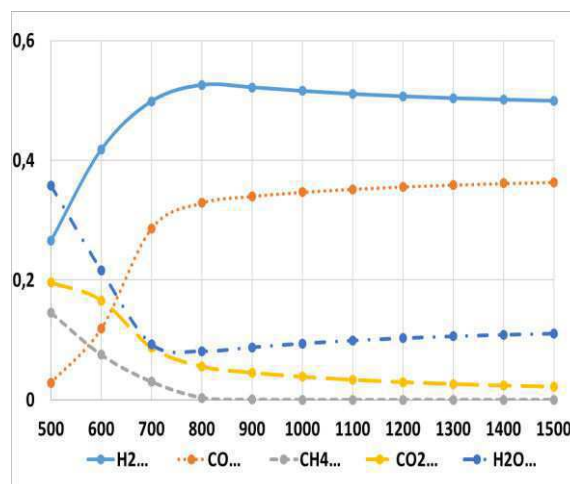


Fig. 2 Exit gas composition vs. temperature (R=0.5, P=1bar)

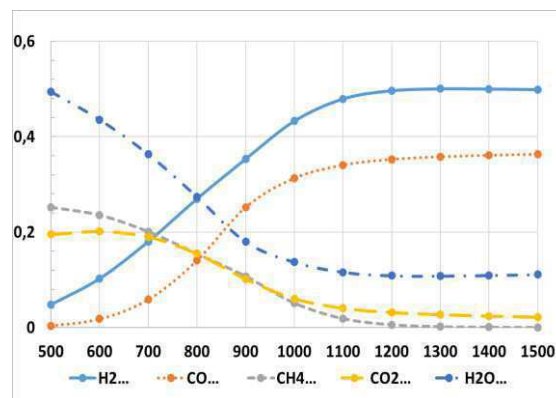


Fig 3: Exit gas composition vs. temperature (R=0.5, P=50bar)

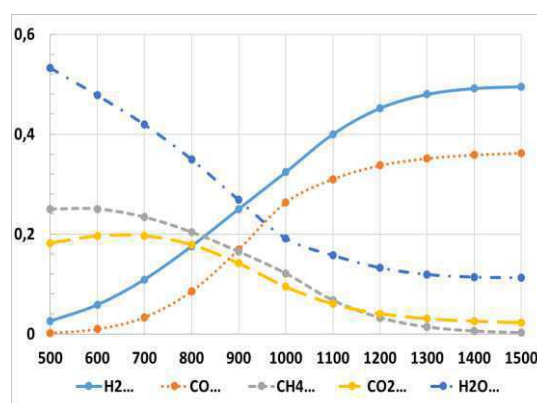


Fig 4: Exit gas composition vs. temperature (R=0.5, P=150bar)

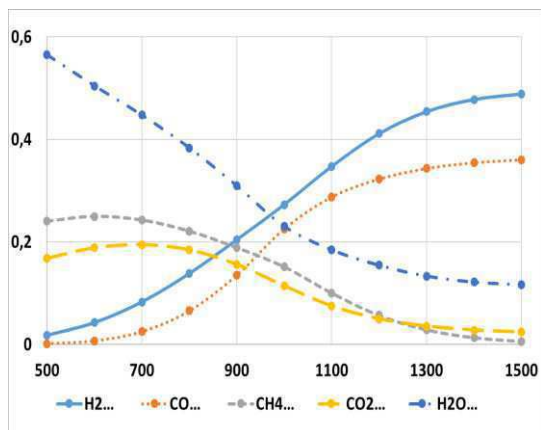


Fig 5: Exit gas composition vs. temperature (R=0.5, P=250bar)

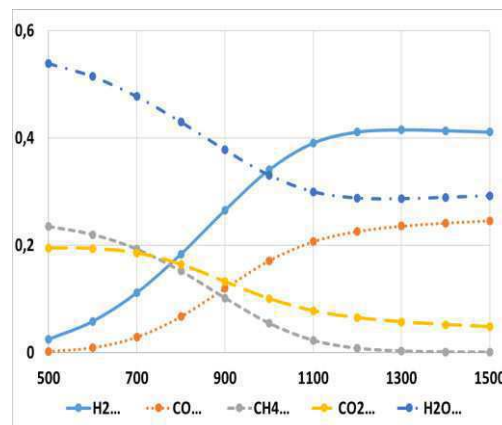


Fig 6: Exit gas composition vs. temperature (R=1, P=150bar)

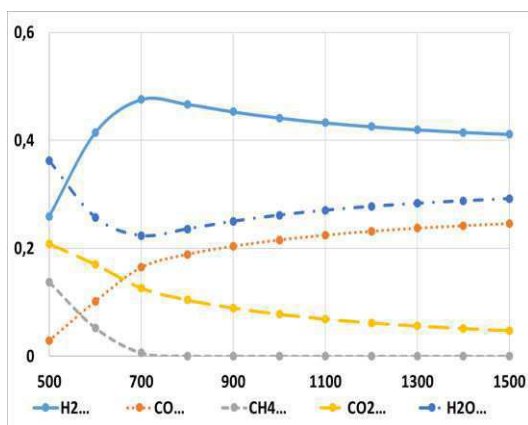


Fig 7: Exit gas composition vs. temperature (R=1, P=1bar)

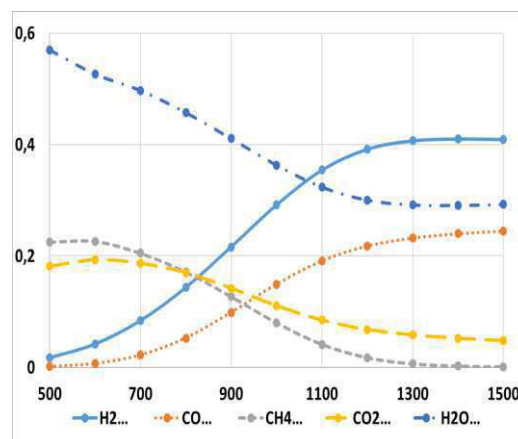


Fig 8: Exit gas composition vs. temperature (R=1, P=250bar)

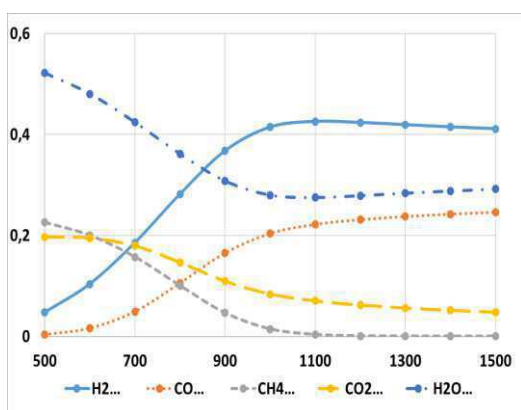


Fig 9: Exit gas composition vs. temperature (R=1, P=50bar)

### C. Conclusion

A thermodynamic equilibrium model of olive pomace gasification in a fixed bed gasifier is developed. Process simulations using AspenPlus are performed in order to investigate the effect of pressure, temperature and biomass to steam ratio on the composition of produced gas. High hydrogen amounts are observed by the highest considered temperature. Lower pressure favours the production of H<sub>2</sub>. The steam to biomass ratio R is to be optimized to ensure the energy efficiency of the gasification process.

TABLE IV  
 SIMULATED CHARACTERISTICS VALUE OF MAXIMUM  
 HYDROGEN PRODUCED

R=0.5		
Pressure [bar]	Maximum hydrogen produced	Temperature [°C]
1	0.5	800
50	0.5	1100
150	0.5	1400
250	0.5	1500
R=1		
1	0.5	700
50	0.4	1100
150	0.4	1300
250	0.4	1300

## REFERENCES

- [1] K. Maniatis, and G.Guiu, J.Riesgo, "Pyrolysis and gasification of biomass and waste, proceeding of an expert meeting", *The European commission perspective in biomass and waste thermochemical conversion.*, pp. 1–18, Nov. 2002.
- [2] Lin Y, Tanaka S. "Ethanol fermentation from biomass resources: current state and prospects," *Appl Microbiol Biotechnol*, paper 42, pp. 69-627, 2006,
- [3] Maria Puig- Arnavat, Joan Carlos Bruno, Alberto Coronas, "Review and analysis of biomass gazification models," *Renewable and Sustainable Energy Reviews* 14 pp.2841-2851, 2010.
- [4] (2002) The IEEE website. [Online]. Available: <http://www.ieee.org/>
- [5] M. Shell. (2002) IEEEtran homepage on CTAN. [Online]. Available: <http://www.ctan.org/tex-archive/macros/latex/contrib/supported/IEEEtran/>
- [6] Moflih A.Adnan, Herri Susanto, Housam Binous, Oki Muraza. "Feed composition and gasification potential of several biomasses including microalgae: a thermodynamic modelling approach", *International journal of hydrogen energy* 42, pp.17009-17019, 22 June 2017.
- [7] Mohammed Alae Bennini, Abdelghani Koukouch, Ilias Bakhtari, Mohamed asbik, Benoit Cagnon, Sylvie Bonnamy. "Characterization and combustion of olive pomace in a fixed bed boiler: Effect of particle size" *International journal of Heat and technology.* paper 37, pp. 229-238, Mach, 2019.
- [8] Koukouch A, Idlimam A, Asbik M, Sarh B, Izrar B, Bostyn S, Bah A, Ansari O, Zegaoui O, Amine A. "Experimental determination of the effective moisture diffusivity and activation energy during convective solar drying of olive pomace waste". *Renewable Energy* 101: pp.565-574, 2017.  
<http://doi.org/10.1016/j.renene.2016.09.006>
- [9] Koukouch A, Idlimam A, Asbik M, Sarh B, Izrar B, Bah A, Ansari O. "Thermophysical characterization and mathematical modeling of convective solar drying of raw olive pomace". *Energy Conversion and Management* paper 99, pp 221-230. 2017  
<http://doi.org/10.1016/j.enconman.2015.04.044>
- [10] Chouchene A, Jeguirim M, Khiari B, Trouvé G, Zagrouba F. "Study on the emission mechanism during dévolatilisation/char oxidation and direct oxidation of olive solid waste in a fixed bed reactor". *Journal of Analytical and Applied Pyrolysis* paper.87, pp.168-174, 2010.  
<http://doi.org/10.1016/j.jaap.2009.11.008>
- [11] H.Dhaouadi, Mounastir science Faculty, Cours. "Les procédés de gazéification" vol 7, pp20-27.
- [12] Mohammed Alae Bennini, Abdelghani Koukouch, Ilias Bakhtari, Mohamed asbik, Benoit Cagnon, Sylvie Bonnamy. "Characterization and combustion of olive pomace in a fixed bed boiler: Effect of particle size" *International journal of Heat and technology.* paper 37, pp. 229-238, Mach, 2019.
- [13] Maria Puig- Arnavat, Joan Carlos Bruno, Alberto Coronas, "Review and analysis of biomass gazification models," *Renewable and Sustainable Energy Reviews* 14 pp.2841-2851, 2010.
- [14] M. B. Nikoo and N. Mahinpey, "Simulation of biomass gasification in fluidized bed reactor using Aspen Plus," *Biomass and Bioenergy*, vol.32, pp. 1245-1254, Feb. 2008.
- [15] Vineet Sikarwar, Ming Zhao, "Biomass Gasification", pp.1-14, Chapter · December 2017DOI  
<https://www.researchgate.net/publication/315849347>
- [16] Housam Binous, Ahmed Aheed, Mouhamed M.Housain. "Haber process and steam coal gasification: two standard thermodynamic problems elucidated using two distinct approaches". pp.1-13, 26 May 2015



# METHANE DECOMPOSITION over NICKEL SUPPORTED on ACID TREATED HZSM-5

Lilia ALALGA, Aicha BENAMAR

*Laboratoire d'Etude Physico-Chimique des Matériaux et Application à l'Environnement  
, Faculté de Chimie, U S T H B, BP32, El-Alia, Bab-Ezzouar, 16111, Alger, Algérie.*

alalga.lilial@gmail.com  
aichabenamar2000@yahoo.fr

**Abstract:** In this work, we have studied the effect of acid treatment of a commercial HZSM-5 zeolite (HZ, Si/Al=11.5) on the production of CO<sub>x</sub>-free hydrogen and nano carbon material deposited during the catalytic decomposition of methane (CDM) at 520 °C and 1 bar over pre-reduced 20 wt. % Ni-catalysts supported on HZ and HZ-a sample resulting from the acid treatment. Both catalysts, prepared by impregnation, are characterized by XRD, FTIR, N<sub>2</sub>-sorption, H<sub>2</sub>-TPR, SEM, EDX, XPS, Raman, and potentiometric titration for acidity measurement. The catalysts display close catalytic behaviour due to the slight structural and textural modifications of HZ-a. TEM images of both catalysts after 4 h of CDM show nano fibres of carbon with Ni<sup>0</sup> at their tip, while XRD patterns indicate a better crystallinity of the ZSM-5 phase and metallic Ni particles with HZ-a support.

**Keywords:** CH<sub>4</sub>, CDM, Ni, ZSM-5 dealumination, H<sub>2</sub>, CNFs.

## I. INTRODUCTION

Methane is the major component of natural gas, and this latter resource is the one's world abundant. Hydrogen is considered as a large-scale carrier for renewable energy. The catalytic decomposition of methane (CDM) is an alternative and promising route, compared to conventional processes, in the recent years to generate CO<sub>x</sub>-free H<sub>2</sub> for many applications such as the fuel cells [1-11]. In addition, valuable by-products such as carbon nanotube (CNT: SWCNT, MWCNT) and carbon nanofibers (CNF) which have exceptional electrical, chemical and mechanical properties [1-11]. The decomposition reaction is as follow:

$$\text{CH}_4(\text{g}) \xrightarrow{\text{Catalyst}} 2 \text{H}_2(\text{g}) + \text{Carbon}(\text{s}) \quad \Delta H^\circ = 75.6 \text{ kJ mol}^{-1}$$

Without catalyst, cracking of the strong covalent C-H bonds occurs at temperatures >1200 °C and amorphous carbon is obtained [11]. These temperatures are reduced by using transition metal (Fe, Co and Ni) and especially Ni supported on conventional oxides, zeolites and ordered mesoporous silicates [1-11]. Ni-catalysts are the most active in CDM reaction at temperature <600 °C. Ni metal contains partially filled 3d orbitals ([Ar] 3d<sup>8</sup> 4s<sup>2</sup>) which improve the dissociation of CH<sub>4</sub> molecules through partially accepting electron [1]. But, the drawback of Ni-catalysts for CDM is their rapid deactivation due to sintering and encapsulation of nickel particles by the nano carbon. Addition of a second metal such as Cu by creation of Ni-Cu alloys improves not only H<sub>2</sub> production but also graphitization degree of

nanocarbon formed at reaction temperature >600 °C [1, 2]. Metallic Ni<sup>0</sup> particles are the active species in the decomposition of CH<sub>4</sub> and nano carbon growth [12]. It is well known that the catalyst supporting material play an important role in the dispersion of the active phase such as Ni crystallites, their size and surface areas and in the metal-support interactions which affect catalytic properties of Ni-catalysts in the CDM [12]. Among Ni-catalysts supported on conventional oxides like Al<sub>2</sub>O<sub>3</sub>, SiO<sub>2</sub>, TiO<sub>2</sub>, MgO, ZrO<sub>2</sub>, SiO<sub>2</sub> is found as the best performing material [12] while Ni supported on HY zeolite is the most active and stable in the CDM compared to Ni supported on USY, SiO<sub>2</sub>, and SBA-15 [13]. Ni-catalysts supported on HZSM-5 zeolites are found promising catalysts in CDM process [4, 5]. The ordered mesoporous silicates (MCM-41) used as supports improve Ni dispersion and carbon diffusion during methane decomposition [2]. When HZSM-5 zeolites with different Si/Al ratios (40, 150, 300 and 485) are used as supports of 30 wt. % Ni based catalysts, the one with a ratio of 150 exhibits a better H<sub>2</sub> yield and longevity for the CDM carried out at 550 °C under flow of pure methane. Best results are obtained (H<sub>2</sub>:171 Nm<sup>3</sup> mol<sub>Ni</sub><sup>-1</sup>) for 20 wt. % Ni/HZSM-5 (Si/Al=150) [5]. The authors [5] related the superior performance of this catalyst to the higher Ni metal surface area and a direct correlation between Ni loading, H<sub>2</sub> yield and Ni metal surface area was deduced from their results. Awadallah et al. [4] compared catalytic performances of 40 wt. % Ni supported on Z-25, Z-400 (Z=HZSM-5, number=Si/Al ratio) and amorphous silica (AS), and found that the texture, morphology, pore topology, crystalline structure of the support affect catalytic performances for the H<sub>2</sub> production and nature of carbon deposited. The crystallite size and dispersion of NiO are influenced by the crystalline structure and pore geometry of the supports. Thus, Ni/Z400 exhibits higher metal Ni<sup>0</sup> dispersion, higher specific surface area, smaller Ni particles and better catalytic performance for the CDM compared to Ni/Z-25 and Ni/AS.

In this work, we tried to modify a commercial HZSM-5 (HZ) with low Si/Al ratio of 11.5 by an acid treatment. The resulted HZ-a sample along with HZ are used to prepare Ni/HZ and Ni/HZ-a catalysts (Ni: 20 wt. %). The effectiveness of the post-synthesis treatment of the bare support on H<sub>2</sub> yield and nano carbon deposited during

decomposition of methane at 520 °C is studied. Catalysts are characterized by several techniques to see any correlation with catalytic performances.

## II. EXPERIMENTAL

### II.2.1 Catalysts preparation

The support HZSM-5, denoted HZ, is prepared by calcination of a commercial NH<sub>4</sub>ZSM-5 (CBV 2314, Si/Al=11.5) at 500 °C for 5 h under air flow. A sample of HZ is treated, under stirring and reflux at 80 °C for 5 h, in 2 M HCl aqueous solution (20 mL HCl/zeolite). The resultant HZ-a solid, after thorough washing, is oven-dried at 120 °C overnight, and then calcined in air at 500 °C for 5 h. Ni/HZ and Ni/HZ-a catalysts (Ni: 20 wt. %) are prepared by the wet impregnation procedure using Ni (NO<sub>3</sub>)<sub>2</sub>.6H<sub>2</sub>O as precursor.

### II.2.2 Catalyst characterization

The crystalline phases are analysed by XRD in the 2θ range of 10°-80°. The textural properties of the fresh catalysts are obtained from the data of N<sub>2</sub> adsorption-desorption isotherms carried out at -196 °C. The morphology of the samples is characterized by SEM and carbon formed by TEM, XRD and Raman spectroscopy. The reducibility of catalysts and interaction metal-support can be obtained from the H<sub>2</sub>-TPR profiles which are carried out in a home-made pulsed set-up.

### II.2.3 Decomposition of methane

Catalytic methane decomposition reaction is carried out at 520 °C and 1 bar in a fixed bed glass reactor with a catalyst mass of 0.2 g and CH<sub>4</sub> flow of 30 mL/min. Prior to the reaction, the catalyst is reduced at 520 °C for 2 h with H<sub>2</sub> (30 mL/min). The outflow gas is directly injected via a 6-way valve (sample loop: 0256 mL) into the HP chromatograph equipped with a 13 X column and TCD detector using Ar as a carrier. The concentrations of H<sub>2</sub> and CH<sub>4</sub> are evaluated using calibrated data. Hydrogen formed is calculated from the formula:

$$H_2 \text{ (mol. \%)} = \frac{n_{H_2}}{n_{H_2} + n_{\text{unconsumed } CH_4}} \times 100$$

## III. RESULTS AND DISCUSSION

### III. 3.1. Characterization results

Two HZSM-5 samples are used as supports of Ni catalysts. The first one, denoted HZ, is obtained by calcination of a commercial NH<sub>4</sub>-ZSM-5 (Si/Al=11.5), and the second, denoted HZ-a, results from acidic treatment of HZ.

The XRD pattern of the calcined HZ and HZ-a samples are shown in Fig. 1. HZ exhibits the ZSM-5 characteristic reflections at 2θ = 7.95°, 8.89°, 23.13°, 23.70°, 23.94° and

24.39° [14]. More detailed analysis of the XRD patterns reveals that all reflections of HZ-a are slightly shifted to higher values of 2θ (Δθ = 0.08-0.10°), indicating a very slight dealumination, although Al rich zeolites (Si/Al<20) are known to be refractory to dealumination and desilication in acidic and alkaline solutions, respectively [15]. This is confirmed by a slight increase in the Si/Al molar ratio from 11.5 for HZ to 14.5 for HZ-a (EDX analysis) and by a crystallinity loss of 5 % by comparison to that of HZ taken as reference, hence 100 % crystalline. For the same Si/Al ratio, the topology of the zeolite plays an important role during a post-synthesis treatment. Thus, BEA zeolite is more sensitive than HZSM-5. As can be seen in Table 1, the crystallite size of HZ-a is slightly smaller than that of HZ with values of 52 and 55 nm, respectively. This indicates a slight contraction of the unit cell of HZ-a

**Table 1.** Physico-chemical properties of the bare zeolites and calcined and reduced 20 wt. % Ni-catalysts.

Sample	(Si/Al) <sup>a</sup>	Cryst. <sup>b</sup> (%)	H <sup>+</sup> <sup>c</sup> μmol/g	Particle size (nm) <sup>d</sup>		
				Zeolite	NiO	Ni
HZ	11.5	100	1061	55.0	-	-
NiO/HZ	11.5	79	539	63.0	25	-
Ni/HZ	11.5	26	-	17.5	-	18
HZ-a	14.5	100	909	52.0	-	-
NiO/HZ-a	14.5	90	212	64.0	23	-
Ni/HZ-a	14.5	38	-	17	-	17

<sup>a</sup>: Framework Si/Al ratio.

<sup>b</sup>: Crystallinity (%) of zeolite = (ΣI sample/ΣI reference sample)x100.

<sup>c</sup>: Number of Brønsted acid sites determined by potentiometric titration.

<sup>d</sup>: particle size calculated via the Scherrer formula.

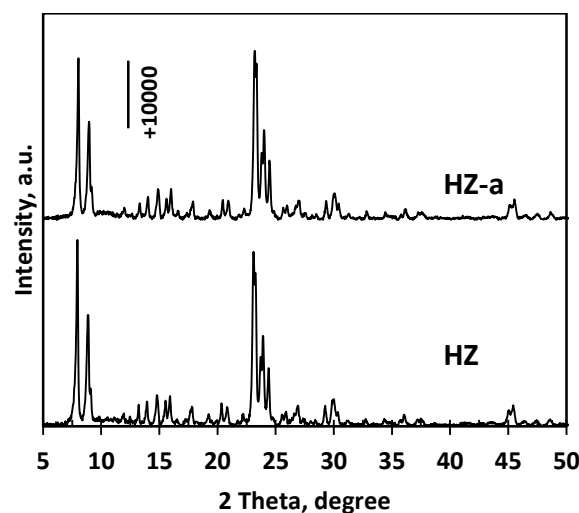


**Fig. 1:** XRD patterns of fresh bare zeolites.

Fig. 2 shows the XRD patterns of the fresh calcined 20 wt. % supported HZ material is the most affected. Reflections of metallic Ni particles and their crystallites size are slightly higher for reduced Ni/HZ-a compared to Ni/HZ (Table 1).

Fig. 2 shows the XRD patterns of the fresh calcined 20 wt. % Ni supported on HZ and HZ-a samples which both exhibit diffraction reflections of crystalline NiO cubic phase at  $2\theta = 37.3^\circ, 43.3^\circ, 62.9^\circ, 75.5^\circ$  and  $79.4^\circ$  [JCPDS n° 01-1239] along with clear reflexions of the HZSM-5 phase. Nickel oxide such as Ni<sub>2</sub>O<sub>3</sub> and NiSiO<sub>4</sub> and Ni<sub>2</sub>Al<sub>2</sub>O<sub>4</sub> phases are not detected. So, calcined catalysts are denoted NiO/HZ and NiO/HZ-a while the reduced forms as Ni/HZ and Ni/HZ-a. The crystallite size of NiO decreases from 42 nm with loaded HZ to 35 nm for HZ-a (Table 1) while the crystallinity of HZ-a support is slightly higher than that of supported HZ. A drastic loss in the crystallinity of loaded zeolites, by comparison to their unloaded counterparts, is expected after Ni loading [4, 5], but here it is only of 10 and 21 % for HZ-a and HZ samples, respectively. Large NiO particles located at the outer surface of the supports and not interacting with them could explain this relatively good crystallinity. But, SEM images and Ni 2p XPS spectra indicate more NiO species at the external surface of HZ-a. With a high Ni loading of 20 wt. %, a great part of NiO species will be located at the external surface of the zeolite support, and this for both catalysts. Interaction between the support and NiO species can limit the aggregation of the latters. According to Awadallah et al. [4], the use of HZSM-5 with well-defined porosity as support limits aggregation of NiO species in 40 wt. % Ni-catalysts by comparison to amorphous silica.

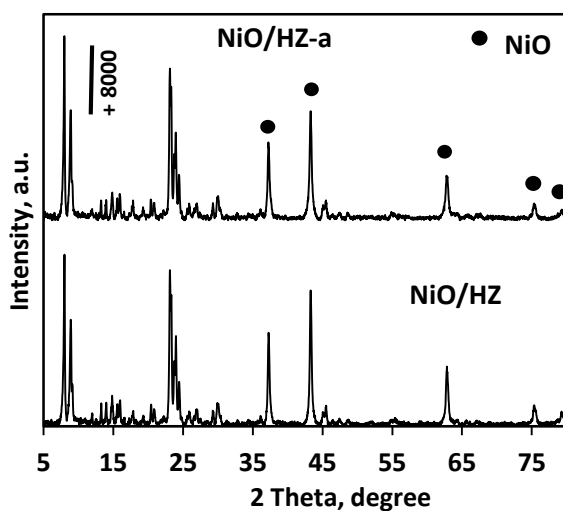


Fig. 2 XRD patterns of fresh calcined NiO-catalysts.

The XRD patterns of reduced 20 wt. % Ni loaded on HZ and HZ-a fresh samples show the reflections at  $2\theta = 44.6^\circ, 51.9^\circ$  and  $76.6^\circ$  pertaining to crystalline Ni cubic phase and successively indexed to the [111], [200] and [220] crystal planes [JCPDS n° 87-0712]. Minor diffraction lines of HZSM-5 phase are also observed as reported in the literature [4, 5]. Fig. 3 show clearly that the crystallinity of both supports is mainly affected after the reduction process and the

supported HZ material is the most affected. Reflections of metallic Ni particles and their crystallites size are slightly higher for reduced Ni/HZ-a compared to Ni/HZ (Table 1).

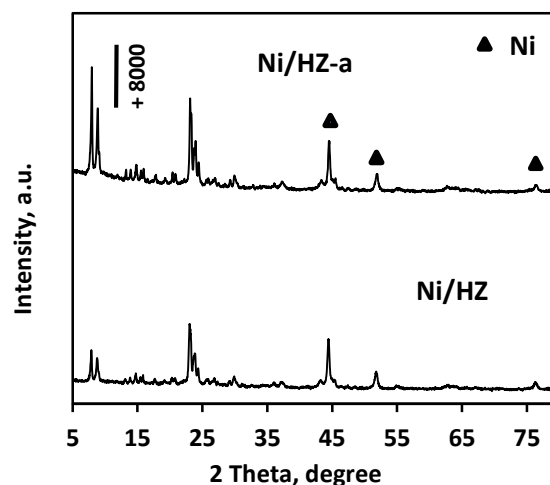


Fig. 3 XRD patterns of fresh reduced Ni- catalysts.

Fig. 4a and 4b show SEM images of the fresh calcined NiO/HZ and NiO/HZ-a catalysts, respectively. The latter catalyst seem to have more NiO species with smaller size at the external surface of the HZ-a support. A greater aggregation of NiO species seems to occur at the external surface of HZ. Similar trend is observed by SEM for metallic Ni species. All these observations must be confirmed by TEM analysis.

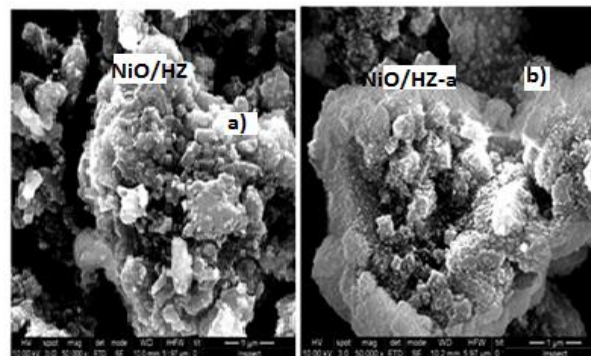


Fig. 4 SEM images of fresh a) NiO/HZ and b) NiO/HZ-a catalysts.

The specific surface area ( $S_{BET}$ ), and pore volumes measurements of the unloaded zeolites and their calcined 20 wt. % Ni loaded counterparts are given in Table 1. The data taken from the N<sub>2</sub>-isotherms (I type) for unloaded samples are typical of microporous ZSM-5 zeolite. The BET surface area of the fresh HZ-a decreases by 19 % compared to HZ. Both fresh zeolites display very similar values of total ( $V_p$ ), micro- ( $V_{micro}$ ) and mesopore ( $V_{meso}$ ) volumes. Liquid total pore volume  $V_p$  is taken from the N<sub>2</sub>-adsorption isotherm at

$P/P_0=0.99$ . The micropore volume ( $V_{micro}$ ) is calculated via the t-plot method and the mesopore ( $V_{meso}$ ) is obtained by subtracting  $V_{micro}$  from  $V_p$ . As expected, after Ni loading of a zeolite, the specific surface of its loaded counterpart decreases by 37 and 14 % for HZ and HZ-a. This is in agreement with the XRD results. Table 1 shows clearly that only  $V_{micro}$  of the loaded supports is affected by a partial blocking by NiO species mainly located outside the pores. The decrease in  $V_{micro}$  leads to that of Brønsted acid sites located inside the pores by 50 and 70 % for HZ and HZ-a supports, respectively.

**Table II.** Characteristics of the calcined samples.

Sample	$S_{BET}$ ( $m^2/g$ )	$V_p^a$	$V_{micro}^b$ ( $cm^3/g$ )	$V_{meso}^c$	Pore size (nm) <sup>d</sup>
HZ	390	0.180	0.13	0.05	1.85
HZ-a	316	0.176	0.11	0.07	2.23
NiO/HZ	245	0.176	0.08	0.09	2.88
NiO/HZa	271	0.160	0.07	0.07	2.36

<sup>a</sup>: Total pore volume determined at  $P/P_0=0.99$ .

<sup>b</sup>: Micropore volume determined by the t-plot method.

<sup>c</sup>:  $V_{meso} = V_p - V_{micro}$

<sup>d</sup>: Pore diameter calculated from  $4 V_p/S_{BET}$  formula.

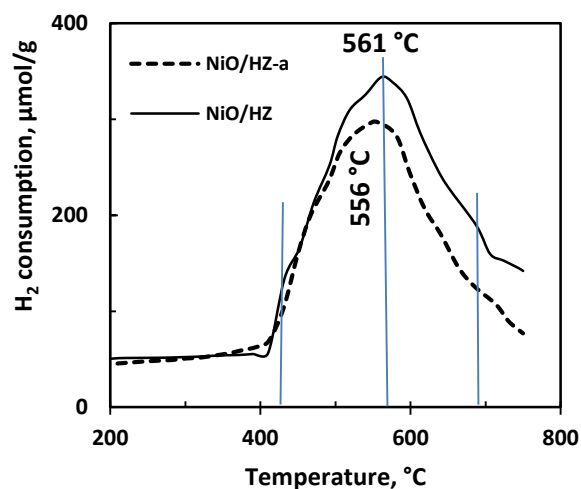


**Fig. 5** TPR profiles of the catalysts.

$H_2$ -TPR profiles are carried out in order to determine the reduction behavior of the metal and metal-support interactions of the catalyst and to have any information about the effect of the support since both catalysts were prepared with the same Ni content of 20 wt. %. The  $H_2$ -TPR profiles of fresh calcined NiO-catalysts are shown in Fig. 5. Both catalysts display similar profiles with a large  $H_2$  consumption peak centered at 556 °C and 561 °C for NiO/HZ and NiO/HZ-a catalysts, respectively. The weak shoulder peak at around 435 °C could

be assigned to the reduction of free NiO species having very weak interaction with the supports and located on the external surface of the latters. The intense peak at 556-561 °C is due to the reduction of bulk NiO. The weak shoulder reduction peaks at  $T > 561$  °C could be assigned to the reduction of NiO deposited in the zeolite channels and also to large sized NiO clusters [4, 5].  $H_2$  consumed, given by the total area below the curves, is slightly lower with HZ-a support. Both catalysts are totally reduced for  $T \geq 700$  °C.

### III.3.2. Catalytic results

The unloaded HZ and HZ-a samples are inactive in the catalytic decomposition of methane (CDM) at 520 °C under atmospheric pressure and pure flow of  $CH_4$ . According to the literature [ ] and from our results, the active species for this reaction are metallic Ni<sup>0</sup> particles [ ], and when NiO species are not totally reduced, undesirable CO<sub>x</sub> products are formed in the  $H_2$  stream [ ]. Tested in the same operating conditions and Ni loading (20 wt. %), the CDM reaction over pre-reduced Ni/HZ and Ni/HZ-a catalysts leads to CO<sub>x</sub>-free hydrogen and solid nano carbon according to the endothermic reaction:  $CH_4(g) \longrightarrow H_2(g) + C(s)$ . So, if differences in the catalytic performances are observed, they could be due to the supports. According to Anjaneyulu et al. [5], there is a direct relation between particle size and surface area of metallic Ni particles and hydrogen yield.  $H_2$  formation is favored with smaller Ni particles, a high dispersion and high metal surface area. The support play a very important role in the characteristics of Ni particles. Comparing a series of Ni/HZSM-5 (Si/Al =40, 150, 300, 485; Ni: 30 wt. %; Si/Al=150 and Ni: 10, 20, 30 and 50 wt.%) in the CDM at 550 °C, a catalyst with optimized values of Si/Al ratio (150) and Ni content (20 wt. %) is selected. Ni/HZSM-5 samples are found to be promising catalysts for the CDM to pure  $H_2$  and CNFs. For 40 wt. % Ni-catalysts, large NiO particles are found with amorphous silica support, while very small particles are observed with HZSM-5 having a Si/Al ratio of 400 by comparison to its counterpart with a ratio of 25 [4]. According to these authors, aggregation of Ni species is limited when using zeolites with a well-defined crystalline structure and pore topology.

Fig. 6 compares hydrogen formed with reaction time of both pre-reduced Ni/HZ and Ni/HZ-a catalysts. The slight differences observed in their catalytic behavior can be related to the very close values of Ni<sup>0</sup> particles ((17-18 nm, Table 1) of the fresh reduced catalysts. Hydrogen is formed at the first contact (first 2 min) with catalyst surface. An induction phase is observed during the first ten minutes of CDM before to increase to a certain value after 1 h. Then, the amount of  $H_2$  increases slightly and progressively for Ni/HZ catalyst while decreasing in similar manner for Ni/HZ-a. A slight improvement in the  $H_2$  formation observed during the first 40



min of reaction time with HZ-a support can be related to more accessible Ni<sup>0</sup> particles. However, more coke is deposited on Ni/HZ catalyst

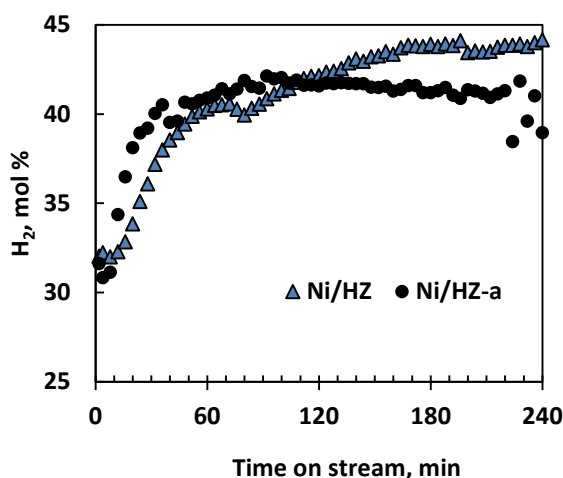


Fig. 6 H<sub>2</sub> production (mol %) over pre-reduced Ni-catalysts.

Fig. 7 shows TEM images of carbon deposits after 4 h of reaction. Carbon nanofibers (CNFs) with Ni<sup>0</sup> at their tip are formed regardless of the support. Their growth follows the tip growth mode [7, 8], suggesting weak metal-support interactions in both catalysts. On the basis of the Raman spectra (not shown), the graphitization degree of CNFs formed is relatively low. Indeed, the relative intensity of the D band to G band ( $I_D/I_G$ ) is of 1.06 and 1.07 for reacted Ni/HZ and Ni/HZ-a catalysts, respectively. The graphitic structure increases with that of G band. The latter at 1574 cm<sup>-1</sup> has been attributed to the in-plane carbon-carbon stretching vibrations of graphite layers and the D band at 1344 cm<sup>-1</sup> to the structural default of graphite.



Fig. 7 TEM images of used catalysts in CDM at 520 °C for 4 h.

Fig. 8 exhibits the XRD patterns of both Ni-catalysts after methane decomposition at 520 °C for 4 h. Carbon deposited has a graphitic structure as evidenced by the characteristic peak at  $2\theta = 26^\circ$  (101). The latter is more intense for the reacted Ni/HZ compared to Ni/HZ-a. The large peaks indicate small crystallites of carbon for both catalysts (6 nm). On the

other hand, the characteristic diffraction peaks of metallic Ni phase along with those of ZSM-5 are clearly seen in Fig. 8, notably for the reacted Ni/HZ-a, indicating weak metal-support interactions for this catalyst. Both Ni and ZSM-5 phases are drastically affected for Ni/HZ sample, indicating likely a recovery by the carbon. A slight higher accumulation of carbon is observed for the latter catalyst.

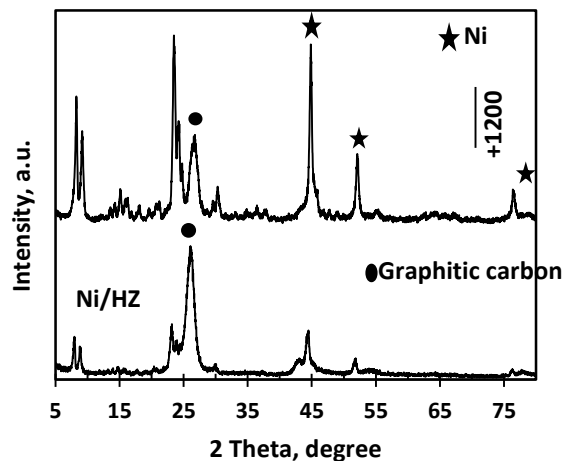


Fig. 8 XRD patterns of Ni-catalysts after 4 h of CDM reaction at 520 °C.

#### IV. CONCLUSION

The acid treatment of a commercial HZSM-5 zeolite (HZ) with a low Si/Al ratio of 11.5 leads to a very slight dealumination of the resulted HZ-a sample (Si/Al=14.5). HZ and HZ-a resulting from acid treatment are used as supports of 20 wt. % Ni- catalysts. Over both pre-reduced catalysts, CH<sub>4</sub> molecules are decomposed into pure H<sub>2</sub> and carbon nanofibers. The catalytic behaviour of both catalysts is close owing to the slight modifications in the proprieties in HZ-a compared to HZ. But analysis of reacted catalysts shows that the ZSM-5 and metallic Ni phases are less affected by carbon deposit with HZ-a support. A steam treatment of rich Al zeolites followed by post-synthesis treatments are intended to deeply change textural and structural properties of the resulted zeolite in order to improve H<sub>2</sub> production and quality of the nano carbon deposits in the CDM.

#### REFERENCES

- [1] D. Torres, J.L. Pinilla, I. Suelves, Screening of Ni-Cu bimetallic catalysts for hydrogen and carbon nanofilaments production via catalytic decomposition of methane, *Appl. Catal. A*, vol 559, pp 10-19, 2018.
- [2] N. Gutta, V. Kumar Velisoju, Anjaneyulu C.,V. Boosa, James Tardio, Jim Patel, and Venugopal A.kula, Promotional effect of Cu and influence of surface Ni-Cu alloy for enhanced H<sub>2</sub> yields from CH<sub>4</sub>

- decomposition, Energy Fuels, 2018, DOI: 10.1021/acs.energyfuels.7b03363.
- [3] Srilatha, K., Bhagawan, D., Shiva Kumar, S., Himabindu, V., Sustainable Fuel Production by Thermocatalytic Decomposition of Methane – A Review, South African Journal of Chemical Engineering, vol 24, pp 156-167, 2017.
- [4] A. E. Awadallah, D.S. El-Desouki, N.A.K.Aboul-Gheit, A.H. Ibrahim, A. K. Aboul-Gheit, Effect of crystalline structure and pore geometry of silica based supported materials on the catalytic behavior of metallic nickel particles during methane decomposition to CO<sub>x</sub> – free hydrogen and carbon nanoparticles, Int. J. Hydrogen Energy, vol.41, pp.16890-16902, 2016.
- [5] C. Anjaneyulu, G. Naresh, V. V. Kumar, A. H. Padmasri, J. Tardio, S. K., Bhargava, A. Venugopal, Ni/H-ZSM-5 as a stable and promising catalyst for CO<sub>x</sub> free H<sub>2</sub> production by CH<sub>4</sub> decomposition, RSC Adv., vol. 6, pp. 34600-34607, 2016.
- [6] Ashik UPM, Wan Daud WMA, Abbas HF, Production of greenhouse gas free hydrogen by thermocatalytic decomposition of methane- a review, Renew Sustain Energy Rev., vol. 44, pp. 2221-2256, 2015
- [7] B. Michalkiewicz, J. Majewska, Int. Diameter-controlled carbon nanotubes and hydrogen production J. Hydrogen Energy, vol 39, pp 4691-4770,2014.
- [8] J. Majewska, B. Michalkiewicz, Carbon nanomaterials produced by the catalytic decomposition of methane over Ni/ZSM-5: Significance of Ni content and temperature *New Carbon Materials*, vol 29, pp 102-108, 2014..
- [9] Ashraf M. Amin , Eric Croiset , William Epling, Review of methane catalytic cracking for hydrogen production, Int. J. hydrogen Energy vol 36, pp 2904-2935, 2011.
- [10] Hazzim F. Abbas\*, W.M.A. Wan Daud, Hydrogen production by methane decomposition: A review, Int. J. hydrogen Energy, vol 35, pp 1160, 2010.
- [11] N. Muradov, F. Smith, C. Huang, A.T. Raissi, Autothermal catalytic pyrolysis of methane as a new route to hydrogen production with reduced CO<sub>2</sub> emissions, Catal. Today, vol 116, pp 281-288, 2006.
- [12] J. Ashok, S. Naveen Kumar, A. Venugopal, V. Durga Kumari, M. Subrahmanyam, CO<sub>x</sub>-free H<sub>2</sub> production via catalytic decomposition of CH<sub>4</sub> over Ni supported on zeolite catalysts, Journal of Power Sources, vol 164, pp 809–814, 2007.
- [13] J. Ashok , S. N. Kumar, M. Subrahmanyam, A. Venugopal, Production of CO<sub>x</sub> Free Hydrogen by Catalytic Decomposition of Methane Over Ni/HY Catalysts, Catal Lett, vol 118, pp 139-145, 2007.
- [14] L. Zhang, H. Liu, X. Li, S. Xie, Y. Wang, W. Xin, S. Liu, L. Xu, Differences between ZSM-5 and ZSM-11 zeolite catalysts in 1-hexene aromatization and isomerisation, Fuel Processing Technology, vol. 91, pp. 449-455, 2010.
- [15] S. Yang, C. Yu, L. Yu, S. Miao, M. Zou, C. Jin, D. Zhang, L. Xu, S. Huang, Brindging dealumination and desilication for the synthesis of hierarchical zeolites, Angew Chem Int Ed Engl., vol 56, pp 12553-12556, 2017.

# Hybrid Power System Optimization of the Emission Antenna of Beni Chograne FM-Radio (Cherb-Errih, Mascara, Algeria)

Hamza SIYOUCEF <sup>#\*1</sup>, Benameur AFIF <sup>#2</sup>, HabibAllah BOUHAMIDA <sup>#\*3</sup> and Boualem MERABET <sup>#4</sup>

<sup>#1,2,3,4</sup>Fac. Sciences And Technology, University – Mustapha Stambouli of Mascara, Algeria,

<sup>1</sup> [siyoucef.hamza@univ-mascara.dz](mailto:siyoucef.hamza@univ-mascara.dz)

<sup>2</sup> [b.afif@univ-mascara.dz](mailto:b.afif@univ-mascara.dz), [afifafif22@yahoo.fr](mailto:afifafif22@yahoo.fr)

<sup>3</sup> [habib.bouhamida@univ-mascara.dz](mailto:habib.bouhamida@univ-mascara.dz)

<sup>4</sup> [boualem19985@yahoo.fr](mailto:boualem19985@yahoo.fr)

\* LSTE Laboratory, M.S Mascara University, BP 305, Mascara 29000, Algeria

**Abstract**— Electricity originating from solar is nowadays one of the main contributors of electrical power to energy systems in the future, but solar technology needs support to find its way to the market. Since photovoltaic electricity always involves very high costs compared to electricity from other sources, a striking question is: how can photovoltaic achieve competitiveness? There are different strategies for promoting applied photovoltaic electricity generation around the world. In this work, we simulated and designed a 40Kwp injected photovoltaic power plant, evaluating the energy of the incident photon flux, the energy produced by the photovoltaic panels and the energy injected into the electricity grid. And this is to judge whether the installation.

**Keywords**— Photovoltaic system, grid injection, solar inverter, photon energy, injected energy.

## I. INTRODUCTION

Energy sources like wind, solar or hydro became more and more popular mainly because they don't produce emissions and are inexhaustible. PV energy is the fastest growing renewable source with a history dating since it has been first used as power supply for space satellites. Currently, electricity is almost entirely supplied to cold rooms by conventional hydroelectric or thermal power plants [1]. Greenhouse gas emissions and other environmental pollution issues, for ex., are of increasing concern [2]. Renewable energy technologies, such as photovoltaic cells, are recommended for electricity production [1]. The photovoltaic (PV) systems performances depend on geographical locations and types of PV modules

used [4]. PV systems are useful in areas highly exposed to incident solar radiation [5]. **Designing an**



Fig. 1 Geographical parameters of Chareb-Errih (radio relay) solar resource.

**optimal hybrid (Wind/PV), a standalone system has been analysed, based on environmental and economic aspects. When such design is accepted our findings are so as CO<sub>2</sub> emission can be mostly reduced, compared to other existing Diesel-only systems [6-8]. Different configurations types have been analysed, showing that based on the energy cost, a hybrid PV-Diesel-Battery system is more cost-efficient than Diesel only and PV-Diesel without storage [9-11]. It has also shown that a rural village is economically best suited for a PV-Diesel power generation system when energy storage systems are absent [12-14]. To identify an optimum model of PV-Diesel-Battery system in various climatic areas, we developed other models (not studied here) using Homer software.**

## II. SIMULATION MODEL

HOMER model is used here to size the proposed system and determine the optimum configuration [15]. HOMER, due to its flexibility, is useful in evaluating design issues in the planning and early decision-making phase of rural electrification projects. It evaluates a range of equipment options over varying constraints and sensitivities to optimize small power systems [16-19]. HOMER's optimization and sensitivity analysis algorithms make it easier to evaluate many possible system configurations. To use this software, the model is provided with inputs, which describe technology options, component costs, and resource availability [20-22]. These inputs are used by HOMER to simulate system configurations (or combinations of components) and generate results that can be seen as a list of feasible configurations sorted by net present cost. It also displays simulation results, compares configurations and evaluates them on economic and technical basis. When we need to explore changes' effects in resource availability and economic conditions might have on the cost-effectiveness of different system configurations, it is possible to use the model to perform sensitivity analyses [23-25]. Sensitivity analysis results can be used to identify the factors that have the greatest impact on the design and operation of a power system. HOMER Pro is used to design and find optimized configurations of a hybrid power system in terms of stability, low cost, size and number of components, prior to installation. Fig. 2 shows a schematic of the System architecture.

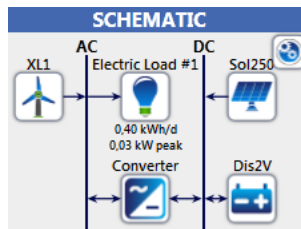


Fig. 2 Schematic of the System Architecture (parameters are listed below).

TABLE I.  
 SYSTEM ARCHITECTURE PARAMETERS

01	Solar World 250 SW 250 Mono (0.145 KW)
02	Discover 2VRE – 1600TG (2.00 strings)
03	System Converter (0.0371 kW)
04	Homer Combined Dispatch

## III. RESULTS AND DISCUSSIONS

Concerning the average variation solar irradiation confirms an excellent compatibility with the changing seasons of the region the maximum irradiation during summer and the minimum during winter as shown in the figure below:



Fig. 3 Monthly average solar global horizontal irradiance (ghi) data. the annual average (kWh/m<sup>2</sup>/day) is 4. 80.

According to the simulation of the studied system, which is shown in Table II, where the results show different configurations of combinations between the main PV, wind and storage components. The sensitivity cases are:

TABLE II.  
 SIMULATION OF THE STUDIED SYSTEM

Architecture				
Sol250 (kW)	XL1	Dis2V	Converter (kW)	Dispatch
0,145	2	0,0371	CD	

To optimize our results, the architecture of our system is as shown in Tables III, IV and V, below.

TABLE III.  
 ARCHITECTURE OF THE OPTIMIZED SYSTEM

Architecture				
Sol250 (kW)	XL1	Dis2V	Converter (kW)	Dispatch
0,145	2	0,0371	CD	
	1	1	0,0648	CD
0,117	1	1	0,104	CD

TABLE IV. RESULTS OF THE OPTIMIZED SYSTEM

Component	Discover 2VRE-1600TG	Homer Combined Dispatch	Solar world 250 SW 250 Mono	System Converter	System
Capital (DA)	60000.00	160000.00	55084.32	556.12	275640.43
Replacement (DA)	89156.84	0.00	0.00	784.46	89905.30
OM (DA)	6534.18	1966025.43	473.59	0.00	203033.21
Salvage(DA)	73827.27	0.00	0.00	-304.12	-74131.39
Total (DA)	81863.76	356025.43	55557.91	1000.45	494447.55

TABLE V. OTHER RESULTS

Discover 2VRE-1600TG	Capital (DA)	Replacement (DA)	OM (DA)	Salvage (DA)	Total (DA)
Discover 2VRE-1600TG	60000.00	89156.84	6534.18	-73827.27	81863.76
Homer Combined Dispatch	160000.00	0.00	1966025.43	0.00	356025.43
Solar world 250 SW 250 Mono	55084.32	0.00	473.59	0.00	55557.91
System Converter	556.12	784.46	0.00	-304.12	1000.45
System	275640.43	89905.30	203033.21	-74131.39	494447.55

Here, we have chosen the optimal choice for our study is the use of solar panels with batteries. The system architecture (SolarWorld250SW 250 Mono (0.145kW)) is so that 0.0371 kW was converted, using Homer Combined Dispatch (Discover 2VRE-1600TG (2.00 strings)). Total costs (such as NPC) are as follows :

- Total NPC :494447,60DA,
- Levelized COE : 102.83DA,
- Operating Cost : 6697.31DA.

The total net present cost (NPC) of a system is the present value of all the costs the system incurs over its lifetime, minus the present value of all the revenue it earns over its lifetime. Costs include capital costs, replacement costs, O&M costs, fuel costs, emissions penalties, and the costs of buying power from the grid. Revenues include salvage value and grid sales revenue. HOMER calculates the total NPC by summing the total discounted cash flows in each year of the project lifetime. The total NPC is HOMER's main economic output, the value by which it ranks all system configurations in the optimization results, and the basis from which it calculates the total annualized cost and the levelized cost of energy. To calculate the COE, HOMER divides the annualized cost of producing electricity (the total annualized cost minus the cost of serving the thermal load) by the total electric load served, using the following equation (1):

$$COE = \frac{C_{ann,tot} - C_{boiler}H_{served}}{E_{served}} \quad (1)$$

Where,  $C_{ann, tot}$ ,  $C_{boiler}$ ,  $H_{served}$  and  $E_{seved}$  are the total annualized and boiler marginal costs, and total

thermal and electrical load served, respectively. The second term in the numerator is the portion of the annualized cost that results from serving the thermal load. In systems, such as wind or PV, that do not serve a thermal load ( $H_{thermal}=0$ ), this term is zero. COE is a convenient metric with which to compare systems, but HOMER does not rank systems based on COE. Operating costs are annualized values of all costs and revenues other than initial capital costs.

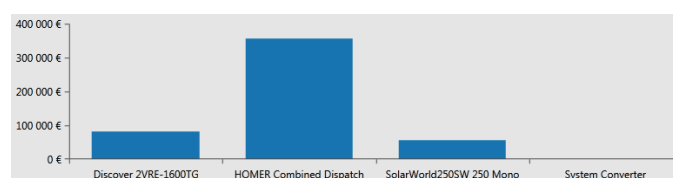


Fig. 4 Total NPC for hybrid PV/storage system.

The current net cost for 25 years is 494447.60 DA (Fig. 4) and a COE is 102.83 DA, the battery takes first place, with a cost of 60 00000,00 DA, the second place the control cost (Combined Dispatch CD) 160 000.00 DA; the PV system with a cost of 55 084.32 DA. The last place converter with a cost of 556.12 DA. Economically, Fig. 5 gives the results

	Architecture				Cost	
	Sol250 (kW)	XL1	Dis2V	Converter (kW)	NPC (د.ج)	Initial capital (د.ج)
Base system	0,183	1	0,168	494 913 د.ج	261 994 د.ج	
Current system	0,145	2	0,0371	494 448 د.ج	275 640 د.ج	

Fig. 5 Economic results.

Different parameters originating from the simulation are obtained: the present and annual worths are 465 € and 14€ respectively, the return on investment is – 1.4%, internal rate of return (%) is *n/a*, simple and discounted payback (a year) are respectively 13.50 and 13.39. Results of electrical production and consumption are listed in Table VI, below :

TABLES VI. OUTPUT PARAMETERS

Production	kWh/y	%
Solar World 250 SW 250 Mono	221	100
<b>Total</b>	<b>221</b>	<b>100</b>

Consumption	kWh/y	%

AC Primary Load	147	100
DC Primary Load	0	0
<b>Total</b>	<b>147</b>	<b>100</b>

<b>Quantity</b>	<b>kWh/y</b>	<b>%</b>
Excess Electricity	45.4	20.5
Unmet Electric Load	0.0342	0.0232
Capacity Shortage	0.0589	0.0400

<b>Quantity</b>	<b>Value</b>
Renewable Fraction	100
Max. Renew. Renetration	1089

The mean monthly electricity production of our PV system is shown in Fig. 5 and Tables VII, below.

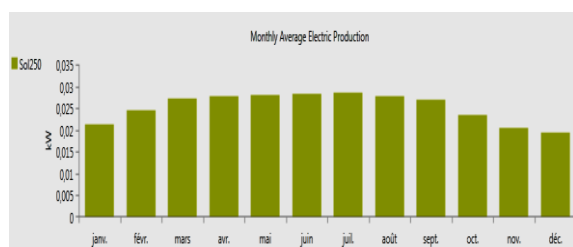


Fig. 5 Average monthly electricity production of the PV system.

TABLES VII. OTHER OUTPUT PARAMETERS

<b>Capacity-based metrics</b>	<b>Value</b>	<b>Units</b>
Nominal Renewable capacity divided total nominal capacity	100	%
Usable Renewable capacity divided total capacity	100	%

<b>Energy-based metrics</b>	<b>Value</b>	<b>Units</b>
Total Renewable production divided by load	150	%
Total Renewable production divided by generation	100	%
One minus total nonrenewable production divided by load	100	%

<b>Peak values</b>	<b>Value</b>	<b>Units</b>
Renewable output divided by load ( Homer standard)	150	%
Renewable output divided by total generation	100	%
One minus nonrenewable output divided by total load	100	%

#### IV. CONCLUSIONS

In this paper a solution to the lack of electricity and energy conversion technologies is proposed. HOMER was found to be a very helpful tool for the microgrid planning and dispatching, so that distributed sources of energy. Analysis reveal that although a fully renewable-based microgrid, which has no carbon footprint, is the most preferred, the net present cost (NPC) is higher. It is worth to mention that when the microgrid is connected to the external grid, it is the most economically favorable option. Also, the most environmentally friendly microgrid is the renewable energy microgrid, and there is still much work to be done in terms of renewable energy and mixed system development, because of their high initial capital and replacement costs. Allowing a small amount of annual load to be left unmet makes the microgrid more cost-effective. Also, the break-even distance presented in this work shows that for isolated microgrids, far away from the external grid connectivity point, the mixed microgrid, is the most economic optimal choice. **In this paper we analysed a hybrid system that can be used as a guideline on designing and implementing grid-connected PV-based power systems in Algeria. Similar approaches could be applied to other regions in this country, so that optimum results might be different from the current ones depending on the local data.**

#### REFERENCES

- http://magazine.ieee-pes.org/latest issue May/June 2019.
- V. Fthenakis, Point of View, Vol. 103, No. 3, March 2015 Proceedings of the IEEE.
- I. M. Kirpichnikova, A. A. Maliugina, 2<sup>nd</sup> International ICIEAM Conference, Chelyabinsk, Rev. Roum. Sci. Techn. – Électrotechn. Et Énerg., doi: 10.1109/ICIEAM.2016.7911464, pp. 1–3 (2016).
- K. Attari, A. Elyakoubi, A. Asselman, Energy Reports, 2, 261-266 (November 2016).
- M. R. Maghami, H. Hizam, C. Gomes, M. A. Radzi, M. I. Radzi, S. Hajighorbani, Renewable and Sustainable Energy Reviews, 59, 1307-1316 (June 2016).
- Cherechi Ndukwe, Tariq Iqbal “Sizing and dynamic modelling and simulation of a standalone PV based DC microgrid with battery storage system for a remote community in Nigeria” , Journal of Energy Systems, Volume 3, Issue 2, Published:30.06.2019, pp 67-85
- G. Alamri and T. Iqbal, “Sizing of a hybrid power system for a house in Libya,” in 2016 IEEE 7th Annual Information Technology, Electronics and Mobile Communication Conference (IEMCON), pp. 1–6, Vancouver, BC, Canada, 2016. View at Publisher · View at Google Scholar · View at Scopus
- MD. NURUNNABI, NARUTTAM KUMAR ROY, EKLAS HOSSAIN, HEMANSHU ROY POTA “Size Optimization and Sensitivity Analysis of Hybrid Wind/PV Micro-Grids- A Case Study for Bangladesh” Received September 12, 2019, accepted September 27, 2019, date of publication October 7, 2019, date of current version

- October 28, 2019. Digital Object Identifier 10.1109/ACCESS.2019.2945937, VOLUME 7, 2019,
- [9] S. K. Nandi and H. R. Ghosh, "Prospect of wind PV-battery hybrid powersystem as an alternative to grid extension in Bangladesh," *Energy*, vol. 35, no. 7, pp. 3040–3047, 2010. doi: 10.1016/j.energy.2010.03.044.
- [10] HOMER Analysis of Micropower System Options. Accessed: Oct. 20, 2017. Online]. Available: <https://analysis.nrel.gov/homer/>
- [11] T. M. Taw k, M. A. Badr, E. Y. El-Kady, and O. E. Abdellatif, "Optimization and energy management of hybrid standalone energy system: A case study," *Renew. Energy Focus*, vol. 25, pp. 48–56, Jun. 2018. doi:10.1016/j.ref.2018.03.004.
- [12] Y. Z. Alharthi, M. K. Siddiki, and G. M. Chaudhry, "Resource assessment and techno-economic analysis of a grid-connected solar PV-wind hybrid system for different locations in Saudi Arabia," *Sustainability*, vol. 10, no. 10, p. 3690, 2018. doi: 10.3390/su10103690.
- [13] Aung Ze Ya, "An Innovative Zero-Emission Energy Model for a Coastal Village in Southern Myanmar" *Global Journal of Researches in Engineering: F Electrical and Electronics Engineering Volume 18 Issue 2 Version 1.0 Year 2018 Type: Double Blind Peer Reviewed International Research Journal Publisher: Global Journals Online ISSN: 2249-4596 & Print ISSN: 0975-5861*
- [14] DEPARTMENT OF RURAL DEVELOPMENT (DRD), LIST OF ELECTRIFIED VILLAGES WITH THE STAGE/REGION BY THE END OF FY 2016-2017, NATIONAL ELECTRIFICATION PROJECT", NAY PYI TAW, MYANMAR, 2018.
- [15] M. A. Matinn, A. Deb, A. Nasir, "Optimum Planning of Hybrid Energy System using HOMER for Rural Electrification," *International Journal of Computer Applications (0975 – 8887) Volume 66– No.13, March 2013*.
- [16] Vergura, V. de J. Lameira, *Revista Eletrônica Sistemas & Gestão*, Vol. 6, pp 210-220, 2011.
- [17] [www.irena.org/Publications](http://www.irena.org/Publications), "Renewable Power Generation costs in 2012: An Overview" IRENA 2013.
- [18] N. Kumar Malik, J. Singh, R. Kumar, N. Rathi, *International Journal of Innovative Technology and Exploring Engineering (IJITEE)* Vol. 3, No. 1, pp. 116-119, June 2013.
- [19] Yinghao Chu, "Review and Comparison of Different Solar Energy Technologies" *Global Energy Network Institute (GENI)*, August 2011.
- [20] Sunil Kumar Mahapatro, *International Journal of Engineering Research & Technology (IJERT)*, Vol. 2 No. 5, pp. 1810-1821, May 2013
- [21] S. Sinha and S.S. Chandel, "Review of software tools for hybrid renewable energy systems.", *Renewable and Sustainable Energy Reviews* Vol 32, pp. 192-205. (2014)
- [22] Walid Ouled Amor, Hassen Ben Amar, Moez Ghariani "Energetic and Cost Analysis of Two Conversion Systems Connected To The Grid By Using Homer Pro", *International journal of renewable energy research*, vol.5, no.3, pp. 226- 236. 2015
- [23] Cherechi Ndukwe, Tariq Iqbal "Sizing and dynamic modelling and simulation of a standalone PV based DC microgrid with battery storage system for a remote community in Nigeria ", *Journal of Energy Systems* Volume 3, Issue 2, pp. 67-85, 30.06.2019
- [24] Y.M.Irwan, A.R.Amelia1, Z. Syafiqah, M.Irwanto, Fareq.M, W.Z.Leow, S. Ibrahim " Design the Balance of System (BOS) for Photovoltaic Application at CERE Building for Low Load Application: An Application of HOMER Pro" , *Applied Mechanics and Materials* Vol. 785 (2015) pp 571-575
- [25] Eodia Tasik Sedan Lobo, Rombe "Modeling and designing hybrid wind- solar energy", *International Journal of Research in Engineering and Technology*, Volume: 06 Issue: 09 | Sep-2017 pp133-137.

# A two dimensional numerical study of an evaporative cooler with a wet return surface

Amel F. Boudjabi<sup>#a1</sup>, Chadi Maalouf<sup>\*2</sup>, Kamal Rezgui<sup>a</sup>, Fabien Beaumont<sup>\*</sup>, Guillaume Polidori<sup>\*</sup>, Djamila Rouag<sup>#</sup>

<sup>#</sup>*Energy and Environment Laboratory, Constantine3 University  
Salah Bounider University Constantine3, 25016, Ali Mendjli, Algeria*

<sup>a</sup>*Sciences and Applied Sciences Faculty, University of Oum El Bouaghi  
University of Larbi Ben M'hidi of Oum El Bouaghi, BP 358 Oum El Bouaghi, 04000, Algeria*

<sup>1</sup>boudjabi.af@gmail.com

<sup>\*</sup>*ITheMM, SFR Condorcet FR CNRS 3417, University of Reims Champagne Ardenne  
51687 Reims, Cedex 2, France*

<sup>2</sup>Chadi.maalouf@univ-reims.fr

**Abstract**—In this study, a two dimensional heat and mass transfer numerical simulation based on species transport and discrete phase model on CDF code Ansys/Fluent is presented for a dew point evaporative cooler. The air supply temperature along the channel obtained is lower than previous numerical data by 3.39% and 3.45% for the exhaust air temperature, while the moisture content and relative humidity give a discrepancy of 1.35% and 2.28% respectively. The parametric analysis allowed examining the effect of working air ratio where wet bulb effectiveness was greater than 120% for ratios up to 0.7 and the dew point effectiveness reached more than 80% for this values. For an increase of 15 °C in air inlet temperatures, the wet bulb effectiveness and the dew point effectiveness dropped of about 12.69% and 25.26 %.

**Keywords**— dew point evaporative cooler, dry/wet channel, product air, working air, wet bulb/dew point efficiency.

## I. INTRODUCTION

Nowadays, evaporative coolers' investigations are trying to optimize the design of the cooler in order to reach lower air temperatures. Indeed, the usual evaporative systems (direct and indirect) have some disadvantages related to the humidity for the direct systems and the limited efficiency for the indirect ones. In both cases, the supply air temperature cannot be lower than the wet bulb temperature of the air [1]. In hot and dry climate regions, the dew point evaporative coolers can be energy efficient and even with a low environmental impact [2]. Ala Hasan [3] has carried out a 1D numerical study. He has considered four patterns of evaporative cooler with one and two stages, co and counter current and cross flow systems. The author has obtained 116% wet bulb efficiency for the case of one indirect stage with a wet return surface.

In another paper, Riangvilaikul and Kumar [4] have conducted a numerical and experimental study of a vertical configuration of dew-point evaporative system for different conditions. Their results show that at: air velocity below 2.5

m/s, channel gap less than 5 mm, channel height larger than 1 m and working air ratio around 35–60%, a wet bulb effectiveness greater than 100% is obtained. Lee et al. [5] have used a counter-current system with a wet return surface; they achieved the model using an aluminum plate supporting a wet media to activate heat transfer. For an air inlet temperature of 30°C and a relative humidity of 50%, they found an air supply temperature of 22°C, 1.7 °C lower than the wet bulb air temperature. A 3D numerical study of laminar airflow of a counter-current evaporative cooler has also been proposed by Pengfei Liu and Xinyu Li [6]. The authors used Ansys software to simulate a 200 mm length system: a dry channel for the product air, a wet channel and a dry channel for the working air with holes on the wet return surface. They obtained a dew point efficiency of 71.2%. In a 3D numerical simulation using, C++ language, Hamoon Jafarian et al. [7] considered a modified boundary condition on the separating wall surface (symmetry condition). Their results predicted the prototype performance to  $\pm 3.53\%$  and the authors deduced a maximum error between 2D and 3D models less than 4.5%.

In an experimental and numerical work [8], the authors used a new method based on NTU-LE-R model and a 2D numerical simulation on software COMSOL for a vertical dew point evaporative cooler. The discrepancy was about 6% between experimental and numerical data. Guangya Zoo et al. [9] identified the influential parameters on the Maisotsenko cycle exchanger and proposed a dew point effectiveness correlation. Compared with numerical simulations and experimental data, the deviations were 2.35% and 6.75% respectively. Ali Pakali et al. [10] examined the cooler using a 1D model and a 3D simulation with COMSOL multiphysics, which agree well with the experimental results within 8.5% and 10% respectively.

The aim of this paper is to investigate numerically a dew point evaporative cooler for the Mediterranean climate applicability. A 2D numerical model is developed in CFD



code ANSYS/ fluent and the results are discussed with reference to other works in the literature.

## II. SYSTEM DESCRIPTION

The counter current flow evaporative cooler has two channels separated by a return wet surface. A working air ratio varying between 30 and 80% is applied. The product air supplies the building as shown on Fig.1. The dry and wet channels have a gap  $H$  of 3.5 mm each, a system length of 500 mm and a plate of aluminium covered of water film (0.5 mm height) is used for the heat and mass transfer between the dry product air and the wet working air.

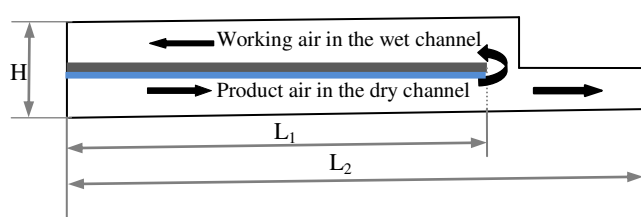


Fig. 1 The dew point evaporative cooler design

### A Mathematical model

A numerical simulation of two-dimensionnal configuration is released using the commercial CFD code ANSYS/ fluent. The transport equations of the air flow are resolved by finite volume method. The airflow is supposed laminar because of the very thin gap compared to length [7,10].

For the water evaporation model, the species transport equation and the discrete phase model are used. The governing equations are:

- The Continuity equation

$$\nabla \cdot u = 0 \quad (1)$$

- The Momentum conservation equations

$$\rho u \nabla u = -\nabla P + \mu \nabla^2 u \quad (2)$$

The energy conservation equation

- $\rho C_p u \nabla T + \nabla \cdot (-k \nabla T) = 0 \quad (3)$

- The Species transport equation

$$\rho u \nabla c + \nabla \cdot (-\rho D \nabla c) = 0 \quad (4)$$

Where :  $u$  is the velocity vector ( $m \cdot s^{-1}$ ),  $P$  is the pressure (Pa),  $\rho$  is the density ( $kg \cdot m^{-3}$ ),  $\mu$  is the dynamic viscosity (Pa.s),  $T$  is the temperature (K),  $C_p$  is the specific heat ( $J \cdot kg^{-1} \cdot K^{-1}$ ),  $c$  is the species concentration and  $D$  is the diffusion coefficient ( $m^2 \cdot s^{-1}$ ).

The assumptions considered are:

- Steady -state of the airflow and heat and mass transfer ;
- The water injection temperature is constant;
- Laminar airflow is in the longitudinal direction;
- Air and water properties are set uniform.

### B Mesh analysis

A structured mesh with quadrilateral elements is generated. A refinement method is applied around the interfacial surface and in the return region. Several size elements of mesh were tested in order to reach grid independence results: 42500, 54600, 66700, 90250, 152300 and finally 260400 cells. From the mesh repartition of 66700 to 260400 elements, the results were very close, therefore, the 90250 elements' mesh was chosen for the rest of the simulation.

## III. MODEL VALIDATION

A two dimensional numerical model is considered for a dew point evaporative cooler similar to the system used in Hasan [3] and Maalouf et al. [11] papers. Table I shows the influential parameters of the airflow in the device.

TABLE I  
COOLER PARAMETERS

Parameter	Hasan[3]	Current case
Channel length (m)	0.5	0.5
Channel gap (m)	0.0035	0.0035
Air inlet velocity (m/s)	0.676	0.676
Working air ratio (-)	0.7	<b>0.7</b> , 0.2 0.3, 0.5, 0.8
Air inlet temperature (°C)	30	30, 35, 40, 45
Inlet moisture content (g/kg air)	9	9

Fig.3 shows the streamlines in the two channels. It illustrates a laminar air flow without recirculation zones.

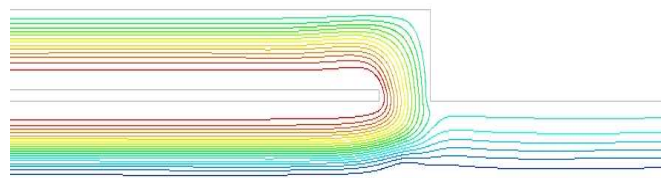


Fig. 3 Stream function contours

Because of the very small gap of the channels compared to their length, contours temperature are indicated on three representative regions of the airflow: at the air inlet/ exhaust working air, at the middle length of the system and at air supply outlet/ return zone.

As observed on the Fig. 4, the temperature in the dry channel drops progressively into the system, while the temperature in the wet channel increases; this is due in a large part to the latent heat of water evaporation.

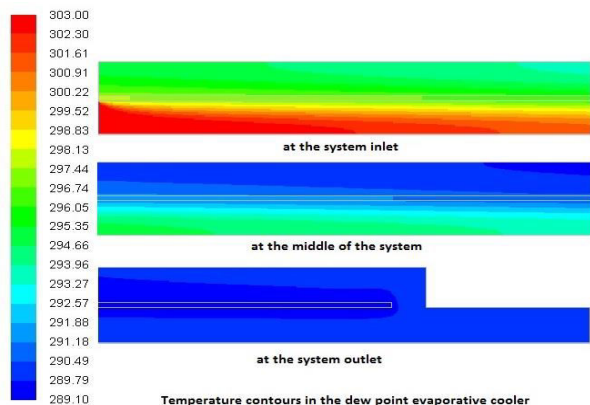


Fig. 4 Temperature contours ( in Kelvin) for the validation case

Because of heat transfer from the dry channel, water evaporates and allows a temperature drop of product air (supply air). At exhaust, the wet air moisture content reaches about 14.67 g/kg of air (humidity ratio contours not illustrated here).

Both the results of the air supply temperature and the absolute humidity are in fair agreement with the literature data, in the finite difference model of Hasan [3] and the parametric study of Maalouf et al. [11].

As shown on the curves in Fig. 5 the product air temperature decreases from the outdoor temperature of 30 °C to a mean temperature of 17.11°C of the supply air. The working air is rejected at a mean temperature of 22.8 °C. The comparison of the temperature profiles between our results and those of Hasan [3] shown on Fig.5, confirm a discrepancy of 3,39% and 3,45 % for the product air and the working air temperatures along the two channels, respectively.

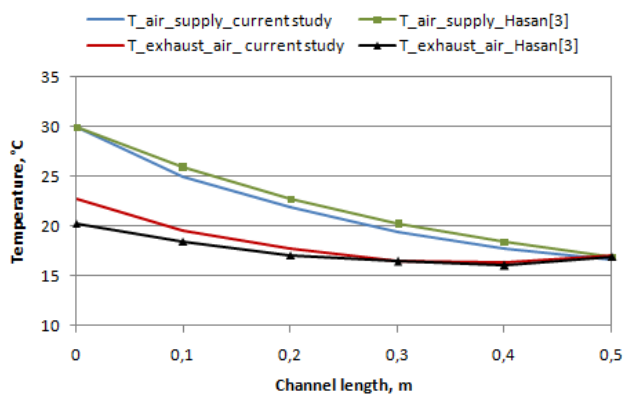


Fig. 5 Temperature profiles

The same observation is done on Fig. 6, for the moisture content profiles which are compared to those given by Maalouf et al. [11].

Our results present a deviation of about 1.35% for the absolute humidity and 2.28% for the relative humidity.

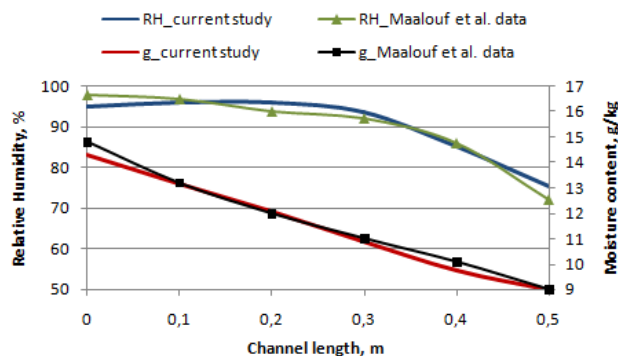


Fig. 6 Relative humidity (RH) and moisture content ( $q_v$ ) profiles

#### IV. PARAMETRIC STUDY

In this section, a parametric study is accomplished to highlight the effect of some influential parameters, as working air ratio or air inlet temperature on the cooler performance.

##### A Effect of the working air ratio

The working air ratio is varied from 0.2 to 0.8. The inlet airflow temperature is 30°C, its absolute humidity is 9 g/kg of air and the velocity is equal to 0.676 m/s.

To achieve the analysis, the wet bulb and dew point effectiveness' equations (5) and (6) are used:

$$\varepsilon_{wb} = \frac{T_{in} - T_{out}}{T_{in} - T_{wb}} \quad (5)$$

$$\varepsilon_{dp} = \frac{T_{in} - T_{out}}{T_{in} - T_{dp}} \quad (6)$$

Where  $T_{wb}$  and  $T_{dp}$  are air wet bulb and dew point temperatures and  $\varepsilon_{wb}$ ,  $\varepsilon_{dp}$  are wet bulb and dew point effectiveness respectively.

Fig. 7 shows the air supply temperature and the effectiveness evolutions with the working air ratio. For values higher than 0.7, the growth is limited suggesting that there is no need to go further as system cooling power would decrease with the decrease in air supply flow rate. For a working air ratio of 0.7, the dew point effectiveness is close to 80% and the wet bulb effectiveness is around 122%.

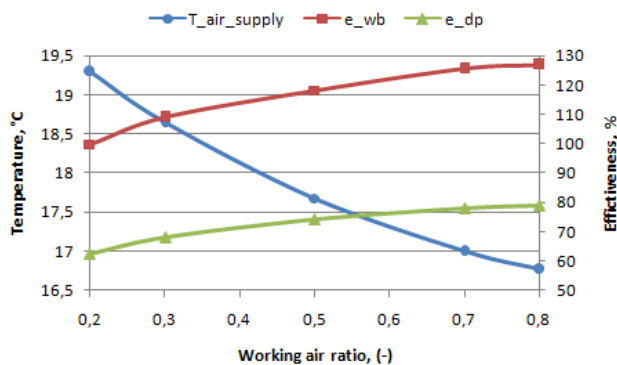


Fig.7 Effect of working air ratio on cooling effectiveness and air supply temperature

### B Effect of the air inlet temperature

In the second analysis, the Fig. 8 illustrates the effect of air inlet temperature on the cooler performance. The air outlet temperature increases from 17 °C to 26° when the air inlet temperature rises of 15°C, so, the cooler loses about 12.7% of its wet bulb effectiveness and 25.26 % of its dew point effectiveness. These results are in good agreement with the literature.

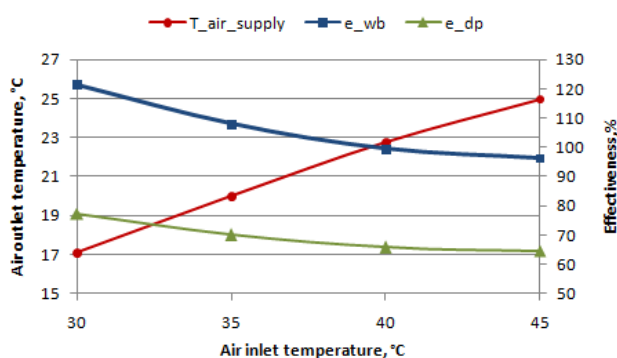


Fig. 8 Effect of air inlet temperature on the air supply temperature and cooler effectiveness.

## V. CONCLUSION

This paper investigated numerically the thermal performance of a dew point cooler. The results are validated by previous numerical data. It is found that a working intake air ratio greater than 50% of the total inlet airflow, is more efficient giving a wet bulb effectiveness above 100% and a dew point effectiveness close to 80%. Considering outdoor temperature, the system performance decline is not very important for high temperatures which encourages using the

dew point evaporative cooler in hot climates like Algeria. Further investigations will be done to improve the cooler design, the effect of other influential parameters as the cooler length, the channel gap, the evaporation model...

## ACKNOWLEDGMENT

This work is the result of a scientific cooperation between France and Algeria. Authors wish to acknowledge the support of the Hubert Curien Partnership (PHC TASSILI).

## REFERENCES

- [1] J.R. Camargo, C.D. Ebinumca, J.L. Silveira. "Thermoeconomic analysis of an evaporative dissicant air conditioning system". Applied Thermal Engineering, vol. 23 , pp. 1537-1549, 2003.
- [2] N. Lechner, heating, Cooling, Lighting, Sustainable Design Methods for Architects, 3<sup>rd</sup> ed. New jersey, U.S.A. Wiley, 2009.
- [3] A. Hasan. " Indirect evaporative cooling of air to a sub-wet bulb temperature", Appl. Therm. Eng., vol. 30, pp. 2460-2468, 2010.
- [4] B. Riangvilaikul, S. Kumar. " An experimental study of a novel dew point evaporative cooling system". Energy Buid., vol. 42, pp. 637-644, 2010.
- [5] Pengfei Liu, Xinyu Li. Simulation on Three Dimensional Laminar Properties of Dew Point Evaporative Cooling in Plate Heat Exchanger. 3rd International Conference on Mechanical Engineering and Intelligent Systems, ICMEIS, Singapore , 2015.
- [6] J. Lee, D.Y Lee. "Experimental study of a counter flow regenerative evaporative cooler with finned channels". Int.J.Heat Mass Transf., vol. 65 , pp. 173-179, 2013..
- [7] Hamoon Jafarian, Hoseyn Sayyaadi, Farschad Torabi. "A numerical model for a dew point counter-flow indirect evaporative cooler using a modified boundary condition and reconsidering effects of entrance regions". International Journal of Refrigeration, vol. 84, pp. 33-51, 2017.
- [8] Yangda Wan, Jie Lin, Kian Jon Chua, Chengqin Ren." A new method for prediction and analysis of heat and mass transfer in the ounter-flow dew point evaporative cooler under diverse climatic operating and geometric conditions". International Journal of heat and Mass transfer, vol. 127, pp. 1147-1160, 2018.
- [9] Guangya Zhu, Weiwei Chen, Shihua Lu."Modelling of a dew point effectiveness correlation for Maisotsenko cycle heat and mass transfer". Chemical Engineering & Processing: Process Intensification, vol. 145, 107665, 2019.
- [10] Ali Pakari, Saud Ghani." Compari\_son of 1D and 3D heat and mass transfer models of a counterflow dew point evaporative cooling system: Numerical and experimental study". Inetrnational Journal of refrigeration, vol. 99, pp. 114-125, 2019.
- [11] Chadi maalouf, Tala Moussa, Amel Ferial Boudjabi, Djallel Abada, Guillaume Polidori, Saffidine Djamilia Rouag, Ernest Wultz. " Numerical study and design of a dew point evaporative cooler for buildings". Conference EENVIRO 2018, Cluj Napoca, Romania, October 2018.

# Comparative Study on Modeling of Heavy Duty Gas Turbines

Djamila Talah<sup>1</sup>, Hamid Bentarzi<sup>2</sup>

*Electrical and Electronic Institute, M'hamed Bougara, University*

*Boumerdes, Algeria*

<sup>1</sup>tlhdjamil@yahoo.fr

<sup>2</sup>lss@univ-boumerdes.dz

**Abstract**— Industrial heavy duty gas turbines (HDGT) are specially designed for power generation. They are specified with long life and higher reliability compared with other types of gas turbines. Therefore, modeling and simulation of their behaviors, under realistic operating conditions, play a key role for efficient design as well as reliable manufacturing practice. In this aspect, several gas turbine models have been developed based on the different parts of heavy duty gas turbine as well as their important functions in the gas turbine plants: the speed governor, the fuel system, the combustion chamber, temperature control and the turbine. Recently there has been growing interest in the study of heavy duty gas turbines models with different degrees of difficulty and merit. This paper presents modeling and analysis of the behavior of heavy duty gas turbine to understand the power system problems. This is achieved by a complementary and comparative analysis of the response of different dynamic models published in different journals. In this paper, two models have been chosen using Matlab/Simulink simulation. The frequency dependant model (FD) and the modified Rowen's model of heavy duty gas turbines have studied taking into consideration the effectiveness and accuracy. In order to apply the same conditions of simulation as Rowen's model, simple time delays are integrated in the FD model in our approach.

**Keywords**— *Gas Turbine; Modeling and simulation; Mathematical modeling; Electric Power plants.*

## I. INTRODUCTION

Due to their specific characteristics, gas turbines (GT) are adopted worldwide for power generation, especially in countries endowed with huge natural gas resources. On the other hand, owing to their longer life cycle coupled with a higher availability factor, heavy duty gas turbines (HDGT) are well targeted for power generation on industrial scale. However, an accuracy study in modeling and simulation of the gas turbines is necessary because of their dynamics which is the most important in a power plant. A great number of studies [1-9] has been published on gas turbines model. Although there are no guidelines regarding the model construction methodology, most of the published models stem from the Rowen's seminal model. This GT model account for the size as well as the characteristic features of the underlying power system as reported in [3]. Nonetheless, whatever the

adopted GT model, there are two main quantities that determine the turbine behavior, namely the output torque and the exhaust gas temperature [4, 5, 8,9]. These quantities come along with two control loops: the speed governor control loop and the exhaust temperature control loop. The current study focuses on two considered basic models: Rowen's Model and Frequency Dependent (FD) Model including time delays. These time delays are introduced in feedback control loop. They are articulated by exponential functions  $e^{-as}$ . In this case study, a 265 MW single shaft HDGT is considered. For this purpose, brief descriptions of the above mentioned models are given, along with the predicted simulation results. In order to investigate the model performance at rated load, the considered HDGT model is simulated under nominal conditions operation without acceleration control loop. Speed reference is equal to one pu during all the simulations. In order to apply the same conditions of simulation as Rowen's model, simple time delays are introduced in the FD model. Three different situations of simulation are studied: a turbine step speed response, -3% turbine speed deviation, and 20% load step increase. The parameters of 265 MW HDGT using in the simulation models are defined in [6].

## II. ROWEN'S MODEL

In 1983, W.I.Rowen provided a model of gas turbine that can be used for dynamic performance studies of power system [5, 6, 9, 10]. Rowen's model consists of a set of algebraic equations describing the steady-state characteristics of gas turbine thermo-dynamics, simple time delays, and a few related controls including temperature control, governor, and acceleration control. The model is suitable for a wide range of ambient temperatures, and the influence of axial flow compressor variable inlet guide vanes (IGVs) is included in the models as appropriate to the actual machinery configuration [8-11].

The control system includes speed control, temperature control, axial flow compressor inlet guide vane control, and upper and lower fuel limits [11, 12]. The IGVs controller is affected by exhaust gas temperature, while the minimum value of temperature and load / frequency

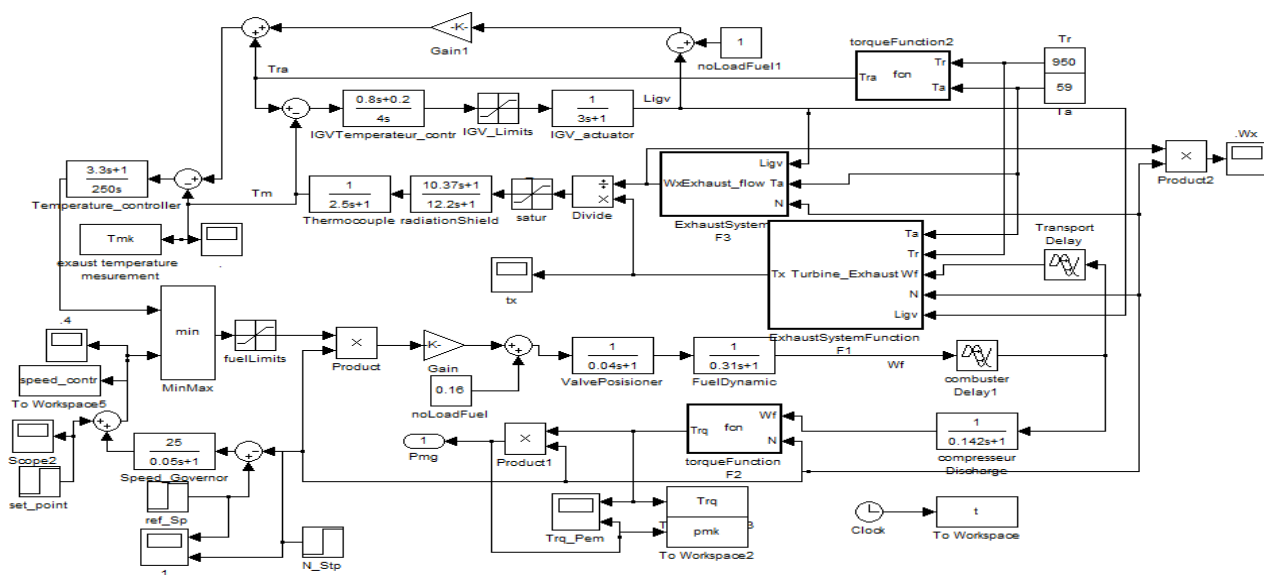


Fig.1. The simulated model based on Rowen's model

control leads to generation of the fuel demand signal. The exhaust flow is proportional to a slightly non-linear function of inlet guide vanes position multiplied by the rotor speed and corrected for ambient temperature [13, 14]. Exhaust flow is provided as an output from the model for use in heat recovery system simulations. The duty of IGVs is to keep the output temperature at a design point which is held at a more or less constant value by regulating the flow of air mass into the compressor. The IGVs are in operation only during the startup and shut down of a simple operating gas turbine without any heat recovery [5, 11,13]. Rowen's model equations are given as follows:

A. Turbine exhaust temperature calculation

$$f_1 = T_x = \left( \frac{1}{1+0.0050(15-T_a)} \right) [(T_R - 453 (N^2 - 4.21N + 4.42) 0.82 (1 - W_f)) + 722 (1 - N) + 1.94 (MaxIGV - IGV)] \quad (1)$$

B. Turbine torque calculation

$$f_2 = [1.16 (W_f - 0.133)]/N \quad (2)$$

C. Turbine exhaust flow calculation

$$f_3 = W_x = N \left[ \frac{519}{T_a + 460} \right] (Ligv^{0.257}) \quad (3)$$

where:

- Ligv = Per Unit Inlet Guide Vane Actuator Stroke
- IGV = Actual Inlet Guide Vane Angle - Circular Degrees
- Ta = Site Ambient Temperature (F)

III. FREQUENCY DEPENDENT MODEL (FD MODEL)

The FD model presents a process that may enable parameter estimation of the frequency dependency from

the output power of the turbine and ambient temperature [9, 10, 12]. As mentioned in [5, 15], a new formulation of the gas turbine thermodynamic characteristics has been developed in order to reveal the effects of shaft speed. This model is based on mathematical equations which are deduced from physical principles. The structure of the FD model, is given in [5, 14, 16].

A. Air flow equations

$$W_a = q(T_a, P_a) U(\Delta N) \frac{\sin(\theta_{IGV} - \theta_0)}{\sin(\theta_{Max} - \theta_0)} \quad (4)$$

$$q(T_a, P_a) = \left( \frac{P_a}{P_{a0}} \right) \sqrt{T_{a0}/T_a} \quad (5)$$

$$U(\Delta N) = 1 + (A_0 \Delta N) + (A_1 \Delta N^2) + (A_2 \Delta N^3) \quad (6)$$

$$\Delta N = N(\sqrt{T_{a0}/T_a}) - 1 \quad (7)$$

where: Ta=288K: The ambient temperature

Pa=1 atmosphere

B. Compressor Pressure Ratio (CPR) equation

$$CPR = (A_5 W_a + A_6 W_f) \left( \frac{P_{a0}}{P_a} \right) + A_7 \quad (8)$$

C. Exhaust temperature Equation

$$T_x = T_a + \frac{A_3 \left( \frac{P_a}{P_{a0}} \right) + A_4 W_f}{W_a} \quad (9)$$

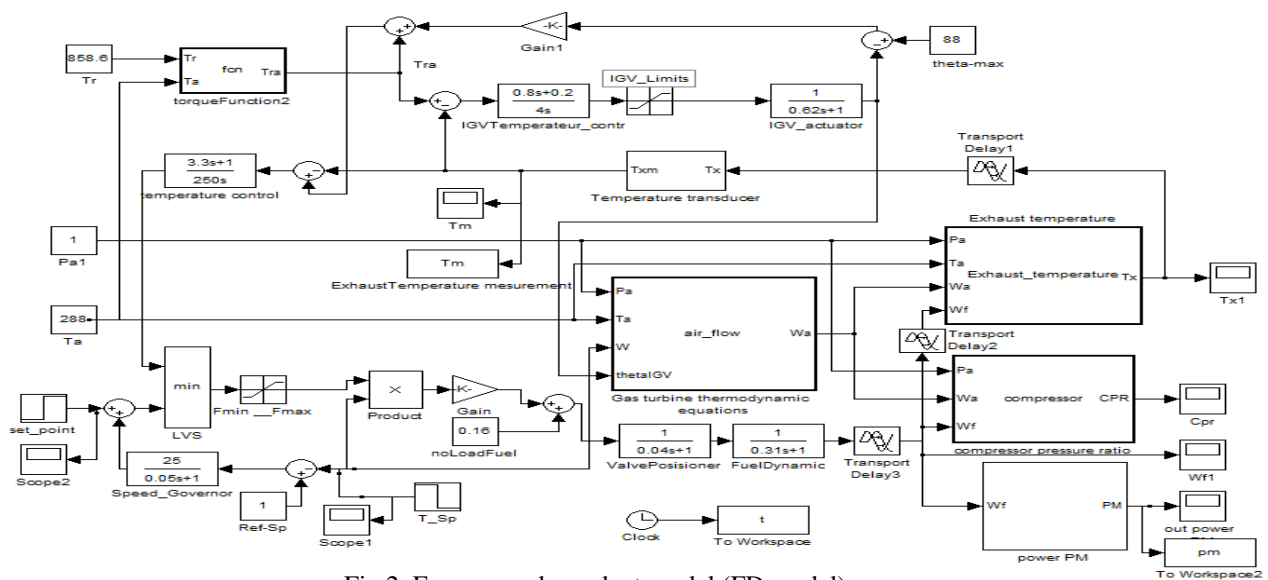


Fig.2. Frequency dependent model (FD model)

D. Output power equation

$$P_m = \frac{P}{1 + T_{trb} \cdot S} \quad (10)$$

$$P = \frac{W_f - W_{f0}}{1 - W_{f0}} \quad (11)$$

where,

$A0 = 0.945, A1 = -7.8, A2 = 39, A3 = 126.7, A4 = 461.6, A5 = 11.6$   
 $A6 = 4.64, A7 = -0.85,$   
 $\theta_0 = 8.73^\circ, \theta_{max} = 88^\circ,$   
 $T_{a0} = 288^\circ K, P_{a0} = 1 \text{ atmos.},$   
 $W_{f0} = 0.23, T_{trb} = 0.2 \text{ sec.}$

However, the parameters (A0, A1, and A2) can be estimated. In [16, 17], we can find more details about the structure of the model and the mathematical equations used in FD model. Furthermore, most of the parameters of the gas turbine thermodynamics can be estimated from loading test data in the steady state characteristics, except for their frequency dependency [14, 17].

Air flow may be regulated by Inlet Guide Vanes (IGVs) and is also a function of ambient air temperature (Ta), ambient pressure (Pa), and shaft speed (N). CPR is defined as the discharge pressure of the compressor divided by the inlet air pressure [14, 16, 17].

IV. SIMULATION RESULTS AND DISCUSSION

Simulations are done for three cases:

1. In the first case, a step turbine speed is applied, shown in fig.3. and fig.4.
2. In the second case, a 3% step turbine speed is applied at 100 sec, shown in fig.5. and fig.6.

3. In the last case, a 20% step increase of load is applied at 100 sec, with the results shown in Fig.7. and fig.8.

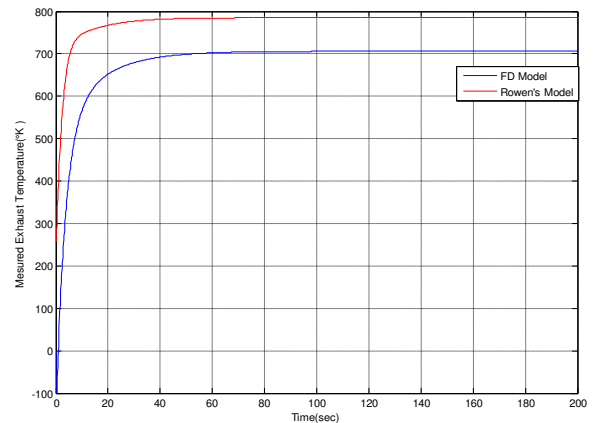


Fig.3. The behavior of Exhaust temperature (step response)

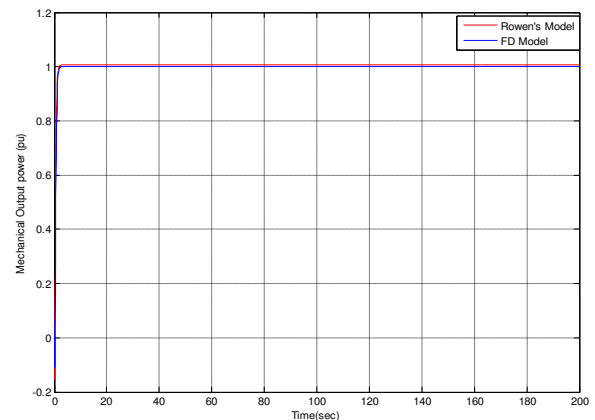


Fig.4. The behavior of the output power (step response)

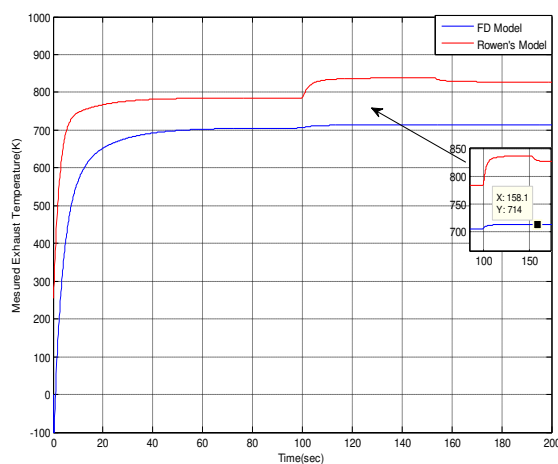


Fig.5. Exhaust temperature, for a droop speed by 3% at 100 sec.

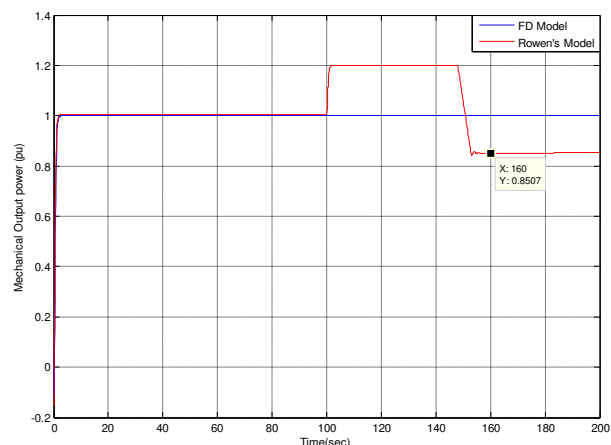


Fig.8. The behavior of the output power, for a 20% step increase of load at 100 sec.

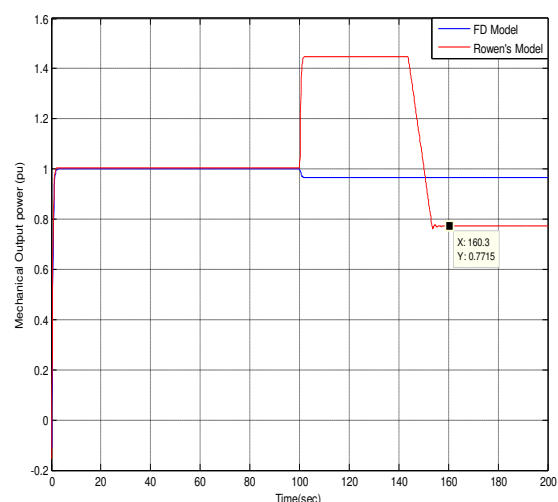


Fig.6. Mechanical output power, for a droop speed by 3% at 100 sec.

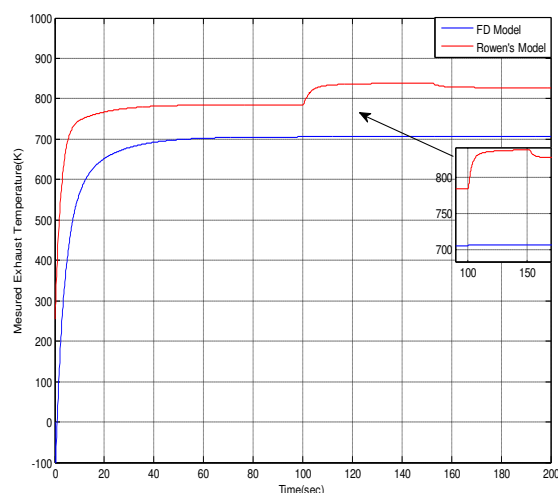


Fig.7. Exhaust temperature, for a 20% step increase of load at 100 sec.

As presented in the figures, the Rowen's model dynamic responses are highly affected by each situation. First, we noted that the exhaust temperatures and also the mechanical output power follow the rated values, which are  $783^{\circ}\text{K}$  (we noted  $784^{\circ}\text{K}$ ) and 1pu, respectively. In the second and third situation, the mechanical output power and the measured exhaust temperature are affected by each change, from 100sec to 160sec approximately. At this time (160 sec), the temperature control and the IGV controller are activated and takes the exhaust temperature down to  $828^{\circ}\text{K}$  approximately, and the power output remains constant (0.85 pu approximately). This behavior shows that temperature control plays a vital role in this model.

On the other hand, the FD model dynamic responses are not much affected by this change in different cases. In the first scenario, where the turbine speed is a step, it can be noted that the exhaust temperature is stabilized at  $705.5^{\circ}\text{K}$ , and does not follow the rated speed which is  $858.6^{\circ}\text{K}$ . In the second situation, where the step speed drop by 3% was applied, we noted that the exhaust temperature and also the output power lightly are affected by this change. The mechanical output power decreases from 1 pu to 0.97 pu and the exhaust temperature increases from  $705.5^{\circ}\text{K}$  at 100 sec to  $713.7^{\circ}\text{K}$ . In the last case, a final steady state of  $705.8^{\circ}\text{K}$  is observed for the measured exhaust temperature. So, the temperature control and the IGV position are not activated during the simulation. However, an increase of 20% in load would cause the temperature control to be activated. Besides, it can be noted that the mechanical output power remains around 1 pu.

## V. CONCLUSION

The main aim of this paper is to present an overview of existing gas turbine models and explore the relationship between Rowen's model and FD model. As mentioned earlier, simple time delays are included in the FD model, in order to apply the same conditions of simulation as Rowen's model. These models present considerable level of accuracy since the IGVs controller is considered. It can be concluded that the

obtained simulations results highlight the usefulness and accuracy of the Rowen's model compared to the frequency dependent model that cannot be well tuned for a large amount of disturbances. However, Rowen's model, owing to its simplicity and accuracy, has been widely utilized for diverse purposes and studies.

## REFERENCES

- [1] Khormali, I. Yousefi, H. Yahyaei, Sh. M. Aliyari. "Identification of an industrial gas turbine based on Rowen's model and using multi-objective optimization method", International Conference On Robotics And Mechatronics (ICROM), 2015.
- [2] N. Kakimoto, K. Baba, "Performance of gas turbine-based plants during frequency drops". IEEE Transactions on Power Systems, vol. 18, No 3, August 2003.
- [3] L. Meegahapola, "Characterisation of gas turbine dynamics during frequency excursions in power networks", IET Generation, Transmission and Distribution, Vol. 8, (10) pp. 1733-1743, 2014.
- [4] J. Mantzaris, C. Vournas, "Modeling and stability of a single-shaft combined cycle power plant". International Journal of Thermodynamics Vol. 10, No. 2, pp. 1-9, June 2007.
- [5] W.I ROWEN, "Simplified mathematical representation of heavy duty gas turbines". Journal of Power, vol 105, pp. 865-869, October 1983.
- [6] H. AsgarI, X. Q. Chen, R. Sainudiin , " Modelling and simulation of gas turbines", International Journal of Modelling, Identification and Control, Vol. 20, No.3, pp. 253-270,2013.
- [7] M. Khalilpour, K. Valipour, H. Shayeghi, N. Razmjooy, "Designing a robust and adaptive PID controller for gas turbine connected to the generator", Research Journal of Applied Sciences, Engineering And Technology, Vol. 5, N°. 5, pp. 1544-1551, 2013
- [8] S. K. Yee, J. V. Milanovic, F. M. Hughes, "Overview and comparative analysis of gas turbine models for system stability studies", IEEE Transactions on Power Systems, Vol. 23, No. 1, 0885-8950, February 2008.
- [9] M. R. Bank Tavakoli, B. Vahidi, and W. Gawlik, "An educational guide to extract the parameters of heavy duty gas turbines model in dynamic studies based on operational data". IEEE Transactions on Power Systems, Vol. 24, No. 3, 2009.
- [10] B. Vahidi, M. R. Bank Tavakoli, and W. Gawlik, "Determining parameters of turbine's model using heat balance data of steam power unit for educational purposes". IEEE Transactions on Power Systems, vol. 22, no. 4, pp. 1547-1553, 2007.
- [11] H. Emam Shalan, M. A. Moustafa Hassan, a. B. G. Bahgat, "Parameter estimation and dynamic simulation of gas turbine model in combined cycle power plan based on actual operational data". Journal of American Science, 7(5), pp.303-310, 2011.
- [12] L. Meegahapola, D. Flunn, "Gas turbine modelling for power system dynamic simulation studies", Power Factory Applications for Power System Analysis, pp 175-195, 2014.
- [13] S. O. Oyedepo, O. Kilanko, " Thermodynamic analysis of a gas turbine power plant modeled with an evaporative cooler", International Journal of Thermodynamics, vol. 17 (no. 1), pp. 14-20, 2014.
- [14] K. Kunitomi, A. Kurita, Y. Tada, S. Ihara, W. W. Price, I. M. Richardson, and g. Smith, "modeling combined-cycle power plant for simulation of frequency excursions". IEEE Transactions on Power Systems, vol. 18, no. 2, pp. 724-729, 2003.
- [15] W. I. Rowen, "Simplified mathematical representations of single shaft gas turbines in mechanical drive service". International Gas Turbine and Aeroengine Congress and Exposition Cologne, Germany, 1992.
- [16] K. Kunitomi, A. Kurita, H. Okamoto, Y. Tada, S. Ihara, P. Pourbeik, and W. W. Price, " Modeling frequency dependency of gas turbine output". IEEE Power. Eng. Soc, winter meeting, Columbus, vol. 2, 2001.
- [17] H. E. Shalan, M. A. Moustafa hassan, A. B. G. Bahgat, "comparative study on modeling of gas turbines in combined cycle power plants" Paper ID 317, December 2010.



# Improved absorbance of the mixed $\text{Fe}_2\text{O}_3 / \text{V}_2\text{O}_5$ PSi structure

H. Cheraga, S. Friha, S. Achacha  
Silicon technology research center for energy  
Algiers Algeria  
hcheraga2002@yahoo.fr

**Abstract**— Mixed oxides such as  $\text{SiO}_2\text{-TiO}_2$  were used by K. Chhor and all the  $\text{V}_2\text{O}_5\text{-Fe}_2\text{O}_3$  in the photocatalytic degradation of phenol and salicylic acid as a function of the calcination temperature [01]. The materials were prepared by sol-gel. The amount of hydroxyl present on the surface of the materials strongly modifies the adsorption of the molecular oxygen (and thus modifies the photocatalytic activity).

The sol-gel process has been widely used for depositing metal oxide films because of its many advantages, such as its low cost, large area deposition and the ease of metal doping.

**Keywords :** Mixed oxides, sol-gel, FTR, spectrometry UV-IR .

## I. INTRODUCTION

Generally, deposits of iron oxides and vanadium oxides are done by the electrochemistry or immersion coating and by Spin coating; the deposition is followed by annealing in an oven at a temperature of 300 to 600 ° C for several hours in order to crystallize the layer.

We already know that some types of materials (substrate) are too sensitive to any temperature variation. Our work consists of producing iron oxide and vanadium oxide layers, using the in situ dip coating (gel sol) technique by immersing the substrate in the solution for few second. The solution is heated at temperature of 100 and 150 and, which gave satisfactory results.

### A. Results and discussion

The film deposition technic and the conditions of preparation determines its morphology, its quality, and crystalline degree, it also impacts the degree of disorder, and the stoichiometry, other parameters such as the ambient atmosphere, the temperature acts also. The exploitation of the specific properties of thin layers has become one of the most important pathways of technological progress [2]. The mastery of this type of technology requires a thorough characterization at all stages of the process. Optical spectroscopy in the UV-Visible-NIR range is one of the most used techniques for analyzing the optical properties of thin films.

The main characterization of our samples is realized by UV-IR spectrometry, FTIR, SEM and DRX. The layers of

$\text{Fe}_2\text{O}_3 / \text{V}_2\text{O}_5$  have been deposited on glass and on silicon, the thickness varies between 20 and 110 nm, measured by the profilometer D600

the UV-Vis spectra of the samples indicate that in the near-UV region ( $\lambda = 300\text{-}800$  nm) the light reflectance spectrum of the modified samples tends to move towards the region of the longest lengths of the light wave and the trend is very big. The spectral lines of the specimens have an absorbance effect on the UV-Vis spectrum and a slightly less light absorption in shorter wavelength. This means that the samples are also able to absorb photons in the visible region and have lower energy values of the band gap. However, the light absorption capacity in the Visible and Ultraviolet region of the samples is 85% and for samples that have undergone the heat treatment (heated solution) at 100 ° C is the same, and also for porous silicon sample. Between ( $\lambda 800 - 2500$ ) nm, it is found that the reflectance is almost 60% identical for the sample treated at 100 ° C and also for the porous silicon sample, we observed the disappearance of interferences in porous silicon subtract due to the deposited layer.

for the layer treated at 150 ° C a slight increase in the reflectance and decrease in absorbance in some UV regions and visible at 60%, for the IR region the reflectance decreases and the absorbance increases at an average of 65% for the  $\text{Fe}_2\text{O}_3 / \text{V}_2\text{O}_5 / \text{PSi}$  structure

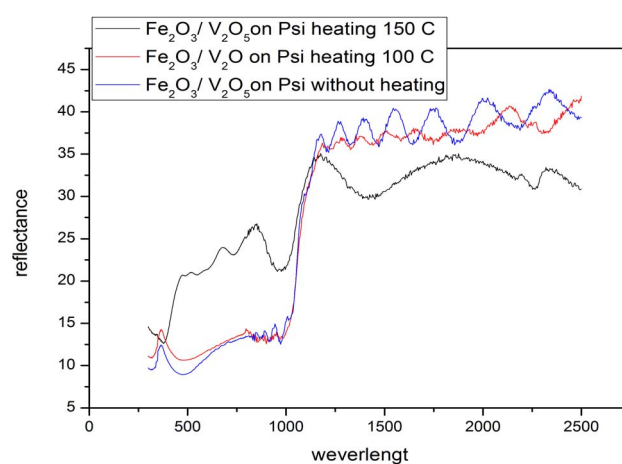


Fig .1 layer reflectance  $\text{Fe}_2\text{O}_3/\text{V}_2\text{O}_5 / \text{PSi}$  realized in situ.

Figure. 2 avec le spectre de transmittance pour les structures réalisées sur verre, nous pouvons calculer la bande interdite. La progression de la bande interdite de 3,23 eV a été estimée pour l'échantillon non chauffé, les échantillons de 3,66 eV chauffés à 100 ° C et de 3,95 eV pour l'échantillon chauffé à 150 ° C.

In FIG. 4 (a), (c) and (e) (d) the morphology of the two layers of  $\text{Fe}_2\text{O}_3$  and  $\text{V}_2\text{O}_5$  of the sample is clearly observed with a porous and granular layer (a) (c) and nanoparticles which is in the form of agglomerates (d) (e). These layers deposited successively by dip coating technique (solution heated to 150 °C)., Fig 4 (b) Note an opaque and granulated layer of the sample solution heated to 100°

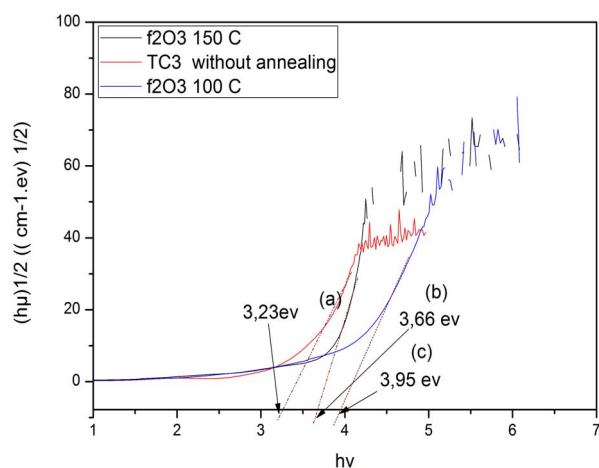


Fig .2 »the Gap layer  $\text{Fe}_2\text{O}_3/\text{V}_2\text{O}_5/\text{PSi}$  realized in situ

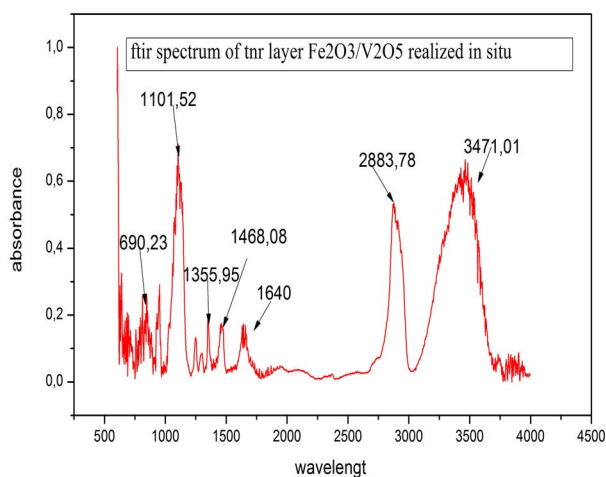


Fig .3. FTIR spectrum of  $\text{Fe}_2\text{O}_3/\text{V}_2\text{O}_5 / \text{PSi}$  layer

We used the Fourier transform infrared spectroscopy "Thermo-Nicolet", equipped with a detector DTGM KBr. All the spectra were collected in a transmission mode in the area of the average infrared 4000-400  $\text{cm}^{-1}$ . The FTIR spectrum shown in fig.5 represents the ferrite  $\text{Fe}_2\text{O}_4$  with characteristic peak of  $\text{Fe}_2\text{O}_3$  at  $527\text{cm}^{-1}$  and  $601.25\text{ cm}^{-1}$ , attributed to the Fe O bond modes.

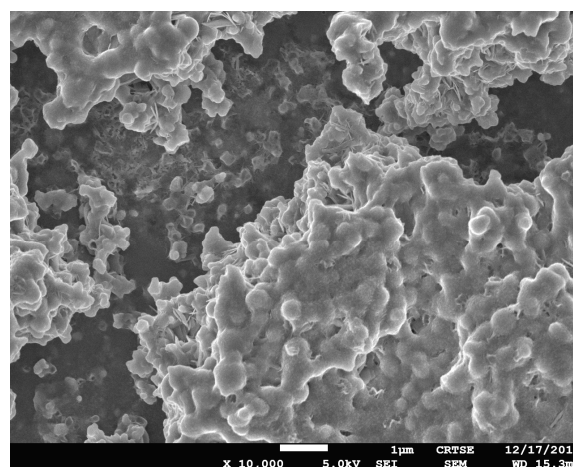
The band centered at  $3471\text{cm}^{-1}$  is characterized to the OH vibration mode,

The band located at  $1351.91\text{ cm}^{-1}$  corresponds to the deformation movement in the plane Fe H

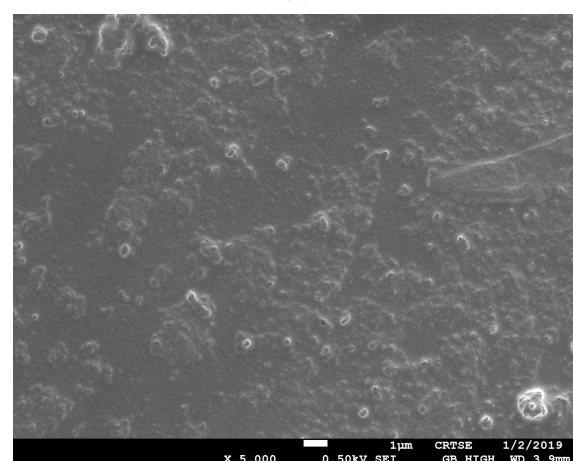
The peak at about  $1001\text{ cm}^{-1}$  is related to the stretching band of Si- O- Si.

In the band in the range  $990\text{-}1270\text{ cm}^{-1}$  is attributed to the elongation vibrations of the Si-O-Si band, confirming the formation of an oxide on the surface.

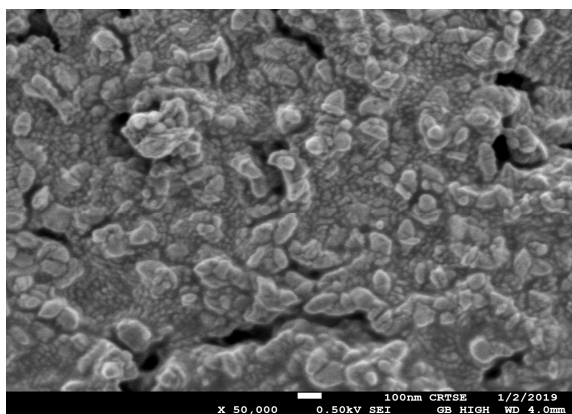
The elongation vibrations of the Si-H, Si-H2, Si-H3 bands are centered around  $2083\text{cm}^{-1}$ .



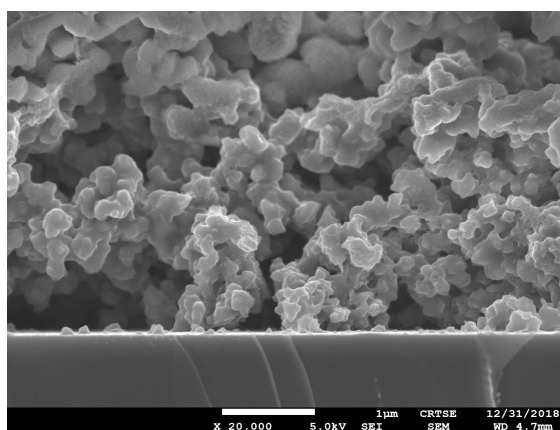
(a)



(b)



(c)



(d)

Fig 3 SEM images of the  $\text{Fe}_2\text{O}_3/\text{V}_2\text{O}_5/\text{PSi}$  surface

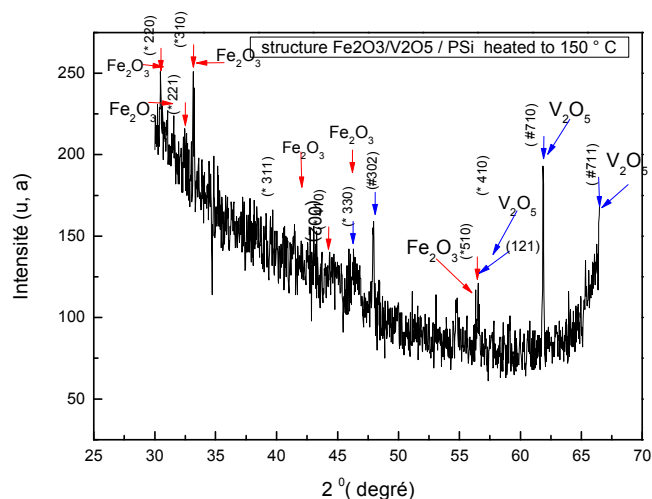


Fig .4 XRD layer  $\text{Fe}_2\text{O}_3/\text{V}_2\text{O}_5/\text{PSi}$  deposit obtained by dip coating technique

Fig.5 X-ray diffraction pattern of iron vanadium FIG. 5 shows the X-ray diffraction patterns of the  $\text{Fe}_2\text{O}_3/\text{V}_2\text{O}_5/\text{PSi}$  structure prepared by the dip coating technique in the  $\text{Fe}_2\text{O}_3$  and  $\text{V}_2\text{O}_5$  in heated solutions for 1 min. It highlights the characteristic diffraction peaks that can be indexed on the Fe plane (220) (cfc) (JCPDS, file number 00-001-1267). The presence of weak diffraction characteristic peaks at  $2\theta = 30.39^\circ$  (220) and  $33.10^\circ$  (310), corresponding to the formation of  $\text{FeSi}_2$  and Sharp phase diffraction peaks at  $2\theta = 61.98^\circ$  (221), corresponding to the  $\text{FeSi}$  and  $\text{VO}$  phases were observed. Fig. 5 also shows the characteristic diffraction peaks corresponding to the Si substrate used as the working electrode which can be identified (JCPDS, card No. 01-080-0018).

#### REFERENCES

- [1] H. S. Nalwa, Handbook of Thin Film materials (Academic Press, 2002).
- [2] J. Singh, Optical Properties of Condensed Matter and Applications ( John Wiley & Sons, 2006).
- [3] M. Gholami, J. Basic. Appl. Sci. Res. 2, 3563 (2012).

# IoT and lighting control for smart greenhouse

Anouar BELKADI <sup>#1</sup>, Dhafer MEZGHANI <sup>#1</sup>, Abdelkader MAMI <sup>#3</sup>

<sup>#</sup> UR-LAPER, Faculty of Sciences of Tunis  
University of Tunis El Manar Tunis, Tunisia

<sup>1</sup>anouar.belkadi@gmail.com

<sup>2</sup>Dhafer.mezghanii@gmail.com

<sup>3</sup>Abdelkader.mami@gmail.com

**Abstract**— This article presents the development of an optimal lighting system for greenhouses, allowing uniform illumination over the entire greenhouse surface and meeting the plants' needs in terms of PFFD. Our work aims to develop a control system that is based on the use of a light sensor, a dimmable luminaire, a RASPBERRY PI 3 and a web application. The brightness management is done in an autonomous and/or manual way according to the user's choice, the automatic control uses the data from the lighting sensors, However, the user can opt for the manual control to vary the luminous intensity of the luminaires. The system was designed, prototyped, and tested in Tunis province of Tunisia. Our contribution through this work represents the management of agriculture through digital innovation (IoT) to optimize the lighting energy used in greenhouses through the use of the Daylight system control technique and the combination of biological parameters that define tomato lighting requirements and DLI to analyze the measured data to choose the best control mode. All this has allowed us not only to supervise, control and reduce the energy cost of lighting, but also to improve the productivity and quality of tomatoes.

**Keywords**— IOT; LED luminaire; Raspberry Pi; Smart Greenhouse; Web application.

## I. INTRODUCTION

Digitation and the technical evolution of systems have made very remarkable progress during this decade, they have quickly penetrated into our daily lives as well as into several sectors of activity such as industrial activities, transport, medical, agriculture, etc...

Especially in the field of greenhouse agriculture, digitation has enabled its users to improve the productivity and profitability of their systems.

Greenhouses are traditionally controlled by ON/OFF buttons through the control panel which is usually placed inside the greenhouse however this traditional method is not efficient and requires the presence of the user to perform the control.

The technology subsequently evolved through the use of time-delay systems [1-3] but unfortunately, this method does not provide accurate, reliable and efficient control, nor does it allow data to be recorded in order to be able to analyse them and detect more effective control methods.

The Greenhouse Control Mode underwent a radical evolution a few years later using programmable controllers or microcontrollers connected to sensors for data acquisition and has relays for control [4-9]. Unfortunately, this method

remains limited and ineffective as it has not solved the problem of data recording and management as mentioned by [10-12].

Nowadays greenhouse control is done through the Internet of Things (IoT).

The IoT is essentially composed of three main technologies:

- (1) a sensor for data acquisition,
- (2) a network for data communication between the connected objects and the computer.
- (3) the computer that ensures the analysis and intelligent processing of the various data to convert them into control actions.

The IoT has covered almost all areas of agriculture (irrigation, temperature control, humidity control, etc.).

In irrigation, a system has been created to control the water pumps when the humidity level decreases in relation to the user's set point by using sensors for reading the humidity, relays for activating and deactivating the pumps [13].

In temperature and humidity control, [14] has developed a system using an Arduino board capable of monitoring and controlling the ambient humidity, soil moisture, and temperature of a greenhouse in the Valeriana jatamansi area.

In the control and monitoring of air quality and CO<sub>2</sub> [15] has implemented a system that automatically monitors and controls air quality parameters and co<sub>2</sub> inside greenhouses.

All these systems have improved the efficiency of greenhouse control and monitoring, however, there are a few parameters that haven't been considered in the works of the majority of author and which has, directly and indirectly, impact on the energy balance of the greenhouse and which require more emphasis such as lighting, we have shown in a previous article[16] that this parameter is essential to ensure optimal plant growth and that we can make significant energy savings if we manage to optimise the monitoring and control of this factor and this is the subject of our study and contribution.

## II. METHODOLOGY

### A. System Overview

We aim to design and implement a lighting control system using sensors spread over nine different locations in the greenhouse, to collect the different levels of illumination and

transmit them to the RASPBERRY PI who will process this data and the stocks in the web application database.

The farmer will then be able to handle the greenhouse remotely through a control panel designated to communicate with the RASPBERRY PI, the control panel is a web application accessible via the Internet or via the local network of the greenhouse that offers several features for better accessibility to the greenhouse,

we can present an overview of our system as shown in Figure.1.

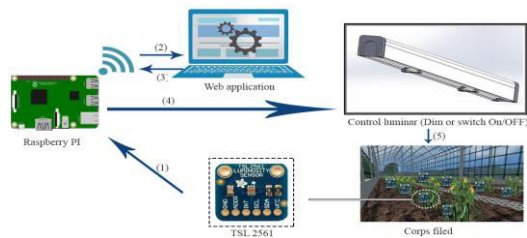


Figure.1. System Overview

### B. System Design

Our system is essentially composed of 3 components:

- The TSL2561 illuminance sensors, which measure illuminance in real-time.
- The RASPBERRY PI which allows controlling the luminous intensity of the luminaires inside the greenhouse.
- The web application: allows us to monitor and manage IoT information in real-time.

#### 1) IoT devices

During our design we used the TSL2561 sensor which is a very light-sensitive sensor and allows to calculate the amount of visible and infrared light, it communicates with the RASPBERRY PI through the i2c bus.

The characteristics of the TSL2561 sensor are shown in Table I.

TABLE I: TSL2561 CHARACTERISTICS

Power supply	2,7 à 3,6 Vcc
Interface	I2C
Measuring range:	0,1 à 40000 Lux
T° of service:	-30 à +80 °C

#### 2) Design of the control system (RASPBERRY PI):

The control system is developed with the PYTHON language and the MYSQL language,

The control system can communicate with the database peripherals, as well as actuators:

- Interaction control unit /database:

The control system communicates with the database in order to extract the necessary information for good management of the greenhouse however the MYSQLDB library allows to interact with the database management

system, the interaction activity diagram of the control unit /database is presented as shown in Figure.2.

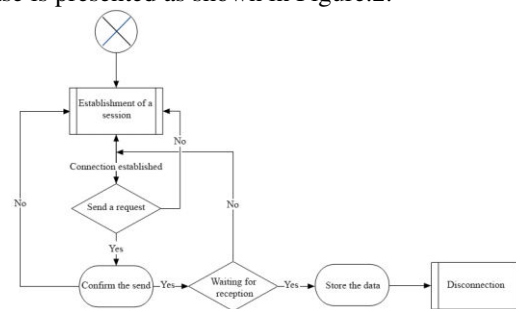


Figure 2. Activity diagram interaction of the control unit/database

- Interaction control unit/peripherals:

The manipulation of hardware resources such as communication buses, input/output ports requires the use of libraries to communicate with external devices, the interaction activity diagram of the control unit/peripherals is presented as shown in Figure.3.

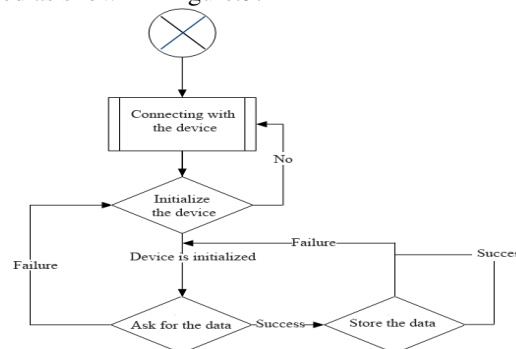


Figure 3. Activity diagram interaction of the control unit and peripherals

- Interaction control unit/actuators:

The control system uses the data retrieved from the database to control the actuators, the figure .4. presents the interaction activity diagram of the control unit/actuators.

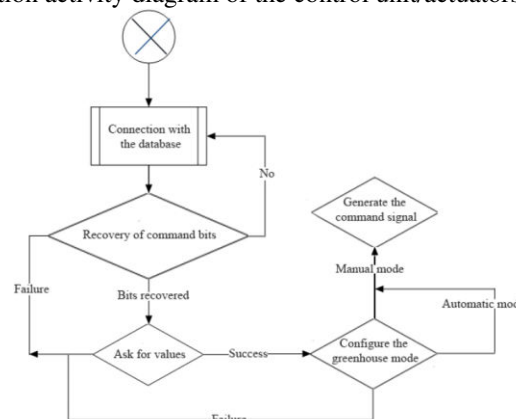


Figure 4. Activity diagram interaction of the control unit/actuator

to simplify all this, we can present the use case diagram of our control system as shown in Figure 5.

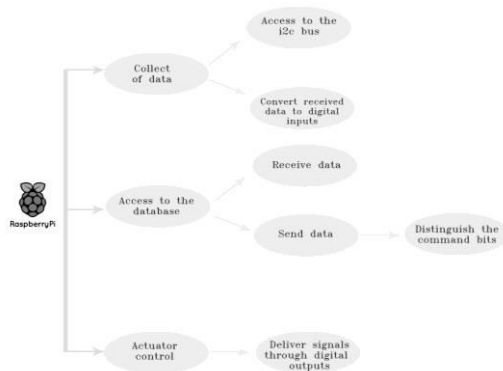


Figure.5. RASPBERRY PI user case diagram

### 3) Design of the web application

The SMART GREENHOUSE web application was developed with HTML5, CSS3, JAVASCRIPT, PHP5 languages, and to accelerate the application development process and obtain an ergonomically optimized web application, we have used BOOTSTRAP which is a FRAMEWORK of CSS and JAVASCRIPT in order to well organize the different parts of the web pages, we have also used a FRAMEWORK of JAVASCRIPT called JQUERY and which is very useful to interact with web servers as well as to execute a diversity of events according to the results received from the server.

The interaction with the database server is an essential task, and to do this it is necessary to develop files called server files with the PHP language that allows being an intermediary between the client and the server, there is also some functionality that uses JQUERY libraries or PHP libraries in order to trace curve and to generate PDF files containing greenhouse data. We can present the case diagram of our application and its graphical interface as shown respectively in Figures 6-9.

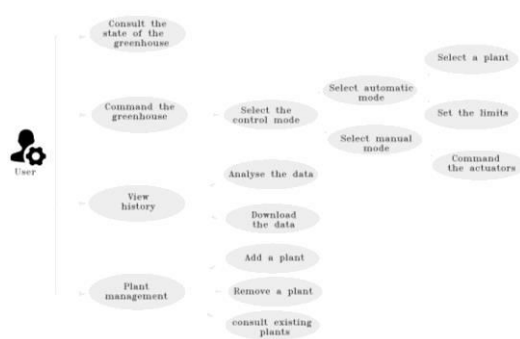


Figure.6. The control panel of the application

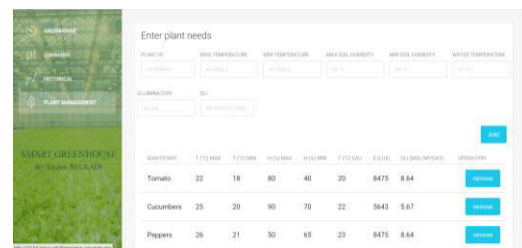


Figure.7. Plant management

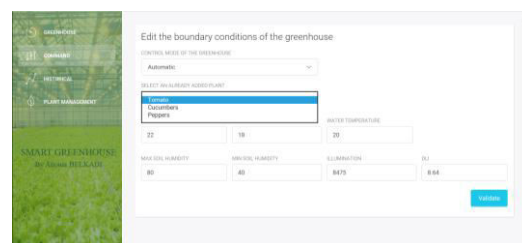


Figure.8. Control mode of the greenhouse

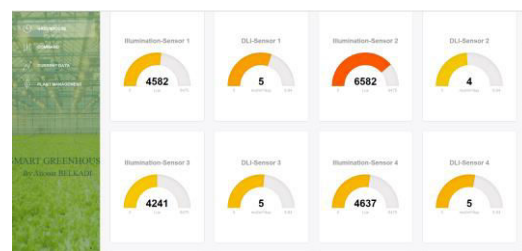


Figure.9. The dashboard of the web application

### C. Implementation

In our study we used nine TSL2561 light sensors which are associated respectively to nine luminaires group as shown in Figure 10., and which are connected to a RASPBERRY PI3 in order to transmit the value of the illumination in real-time, the RASPBERRY PI stores this data and the data. processed to calculate the difference between the daylight and our target which is 8475 LUX [16] in order to control the luminaire to obtain a uniform illumination equal to the desired value at any time "t".

As detailed in our previous article [16] the luminaire will be switched of while the target is achieved and to be turn on (60w) when the illumination is 0 lux and dimmed if the illumination is ]0 – 8475[.

The RASPBERRY PI 3 will control the luminaires through a PWM signal control to attenuate or increase their light intensities for a duration of 16h as long as the DLI is lower than the target value of the tomato plant [16] but once the DLI is reached RASPBERRY PI controls the fixture group associated with this sensor to be in the off state,

The figures 11-13 represent a practical test on the behavior of the system for a single sensor to show the different real-time measurements such as power [w], lighting [lux], ect ...



Figure.10. Distribution of sensors and luminaire groups inside the greenhouse

Figure 10 represents the position and the associated number of each sensors and luminaire groups inside the greenhouse.

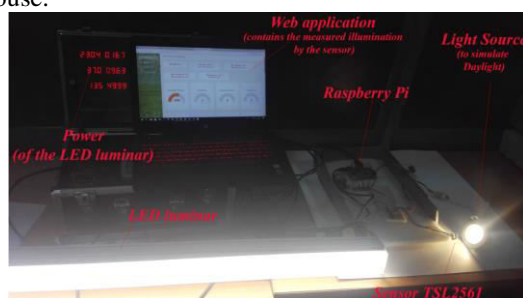


Figure.11. System Implementation



Figure.12. Measurement of the illumination and the power consumption of the luminaire – Test 1.

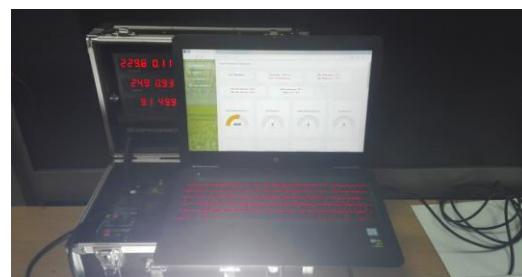


Figure.13. Measurement of the illumination and the power consumption of the luminaire – Test 2.

Figure 11 represent the practical test used for the measurement of the illumination measured by the sensor and the power consumption of the controlled luminaire.

Figure 12 and Figure 13 represent two simple test, where the first one shows an illumination of 3248 Lux for a power consumption of 37w and the second one an illumination of 4949 Lux for a power consumption of 25w, these results are expected and confirms that's our system is working correctly.

#### System data analysis

The illumination data of each sensor are recorded and stored in a daily manner, Figure 14 shows the illumination data measured for the various sensors during 16h while Figure 15 represents the data of the DLI.

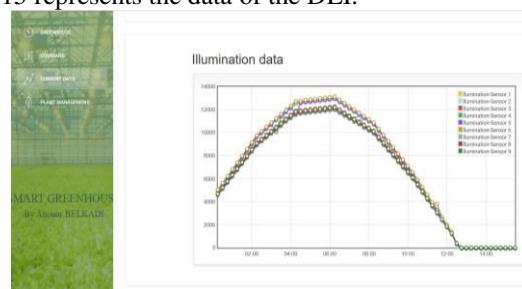


Figure.14. Evolution of the illumination from 7h:00 to 21h:00 for the day 15-06-2019

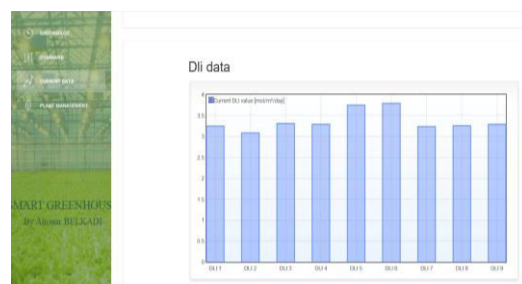


Figure.15. Evolution of the measured DLI from 7h:00 to 12h:15 for the day 15-06-2019

Figures 14 and 15, represent the evolution of the illumination from 7:00 am to 9:00 pm and the DLI measured up to 12:15 in the nine different zones, it is clear that we do not have the same measurements and this is expected, as the value of the illumination is not the same as a function of time and place, the difference can reach 12% by comparing the results obtained by the sensors 5 and 6 with those measured by the sensor 2, these values depend essentially from several parameters such as the shape of the greenhouse, the angle of inclination of the sun, the position and direction of the

greenhouse, altitude, latitude, etc. This difference has a direct effect on the consumption of fixtures and indirectly on the energy balance of the greenhouse as we have shown in a previous article [16]. This difference has a direct effect on the consumption of luminaires and an indirect effect on the greenhouse balance energy as we have shown in a previous article [16]. To compare the daily consumption of the lighting system by adapting traditional lighting control systems with our IoT control system,

Traditional control systems generally use timers that adopt one of these two control strategies (control scenario 1 and control scenario 2) respectively:

Light one hour before the sunset until midnight [17] i.e. from 6:30 p.m. until midnight, which means a total of 5h:30 of additional lighting,

Light 4-5 hours of sunset until 1h after the sunrise [17], i.e. from 23:30 to 5:30 am, which mean a total of 6h:30 of additional lighting,

In order to deduce the energy gain, we have superimposed the consumption curves relating to the traditional control modes 1 and 2 as well as the groups of luminaires associated with the sensor 2 and 6 as represented in figure.16.

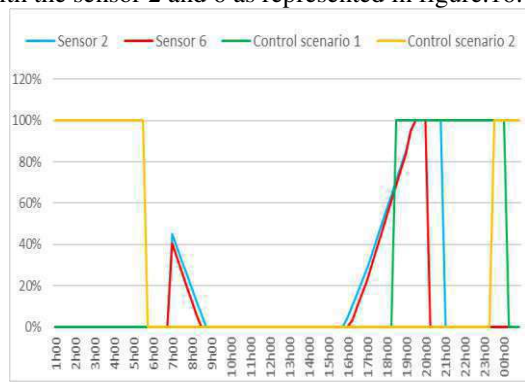


Figure.16. Lighting Power consumption [%]

According to Figure 16, we notice that the group of luminaires associated with sensor 6 consumes less than the “1/5” of the energy required compared to the groups of luminaires associated with the sensor 2, we also note that through our system, we can save up to 58% of energy compared to traditional control mode. We have therefore not only succeeded in satisfying the DLI condition and guaranteeing the same growth rate of the various plants but also in optimising the energy consumption of the luminaires.

### III. CONCLUSION

This research has shown that the supervision and control of lighting can improve the efficiency of our greenhouse in terms of consumption and quality of products. We have naturally drawn the following conclusions:

- The average illumination differs from one area to another and this has been shown through the installation of nine sensors inside our greenhouse, this difference is essentially due to several parameters such as (greenhouse position, altitude, latitude, geometric shape of the greenhouse, angle of inclination of the sun, etc.....) [16].

- The control of the luminaires allowed us to have a uniform illumination and distributed in the same way in order to guarantee a better quality of product and which has the same growth.
- Our system, allows us to control our greenhouse manually and/or automatically, it eventually solved the data logging problem which will allow us to analyze the data in real-time and gives us the opportunity to improve our system in a continuous way.
- Our contribution on the reduction of the energy consumption of luminaires and hours of operation has allowed us to reduce the consumption of 12% from one zone to another (zone 5 and zone 6 Versus zone 2) and 58% compared to traditional control mode (Zone 6 Vs control scenario 2).

### ACKNOWLEDGEMENTS

I gratefully acknowledge the support and generosity of BBL institute, without which the present study could not have been completed.

### REFERENCES

- [1] O. J. Smith. (1957) Closer Control of Loops with Dead Time. *Chemistry Engineering Progress*, Vol. 53, No. 5, pp. 217-219.
- [2] MARSHALL, J.E. (1979) *The Control of Time-Delay Systems*, Peter Peregrinus, I.E.E. Control Engineering Series.
- [3] Marshall J.E. (1980) Identification strategies for time-delay systems. In: Unbehauen H. (eds) *Methods and Applications in Adaptive Control*. Lecture Notes in Control and Information Sciences, vol 24. Springer, Berlin, Heidelberg.
- [4] Ventzas, D. (1998). MC68HC11 Microcontroller Control of a Greenhouse Environment as a Time Delay System. *IFAC Proceedings Volumes*, 31(12), pp.239-244.
- [5] van Straten, G. (1998). Acceptance of Optimal Operation and Control Methods for Greenhouse Cultivation. *IFAC Proceedings Volumes*, 31(12), pp.11-18.
- [6] Young, P., Price, L., Berckmans, D. and Janssens, K. (1998). Recent Developments in the Modelling and Control of Climate and Ventilation in Agricultural Buildings. *IFAC Proceedings Volumes*, 31(12), pp.3-10.
- [7] Hampel, J. and Wilkie, D. (1980). A MICROPROCESSOR BASED PROCESS CONTROLLER FOR INTERACTIVE CONTROL APPLICATIONS. *Digital Computer Applications to Process Control*, pp.457-463.
- [8] Udink ten Cate, A. and van de Vooren, J. (1977). Digital adaptive control of a glasshouse heating system. *IFAC Proceedings Volumes*, 10(16), pp.505-512.
- [9] Ameer, S., Laghrouche, M. and Adane, A. (2001). Monitoring a greenhouse using a microcontroller-based meteorological data-acquisition system. *Renewable Energy*, 24(1), pp.19-30.
- [10] Wolfert, S., Ge, L., Verdouw, C. and Bogaardt, M. (2017). Big Data in Smart Farming – A review. *Agricultural Systems*, 153, pp.69-80.
- [11] Pham, X. and Stack, M. (2018). How data analytics is transforming agriculture. *Business Horizons*, 61(1), pp.125-133.
- [12] Kamilaris, A., Kartakoullis, A. and Prenafeta-Boldú, F. (2017). A review on the practice of big data analysis in agriculture. *Computers and Electronics in Agriculture*, 143, pp.23-37.
- [13] Karan Kansara et al “Sensor based Automated Irrigation System with IOT: A Technical Review”, *International Journal of Computer Science and Information Technologies*, Vol. 6 Issue 6 , pp. 53315333, 2015.
- [14] Thakur, D., Kumar, Y., Kumar, A., Kumar, P. and Singh, V. (2018). Real Time Monitoring of Valeriana Jatamansi Plant for Growth Analysis. *Procedia Computer Science*, 132, pp.507-517.



- [15] Li, Y., Ding, Y., Li, D. and Miao, Z. (2018). Automatic carbon dioxide enrichment strategies in the greenhouse: A review. *Biosystems Engineering*, 171, pp.101-119.
- [16] Belkadi, A., Mezghani, D. and Mami, A. (2019). Energy Design and Optimization of a Greenhouse: A Heating, Cooling and Lighting Study. *Engineering, Technology & Applied Science Research*, Vol. 9 issue 3, pp. 4235-4242.
- [17] Ted Goldammer, 2018, "Greenhouse Management: A Guide to Operations and Technology," Apex Publishers, First Edition, ISBN (13): 978-0-9675212-9-9.
- [18] Damers D.A., Dorais M, C.Wien, A. Gosselin, 1998, "Effects of supplemental light duration on greenhouse tomato (*Lycopersicon esculentum* Mill.) plants and fruits yields. *Scientia Hort*, 74, pp. 295-306.

# Robust Speed Control of a Doubly Fed Induction Motor

Lekhchine Salima <sup>#1</sup>, Bahi Tahar <sup>\*2</sup>

<sup>#</sup> *Department of Electrical Engineering, 20 August University Skikda, 21000, Algeria*

<sup>1</sup> [slekhchine@yahoo.fr](mailto:slekhchine@yahoo.fr)

<sup>\*</sup> *Automatic and Signals Laboratory LASA, Badji Mokhtar University Annaba, 23000, Algeria*

<sup>2</sup> [tbahi@hotmail.fr](mailto:tbahi@hotmail.fr)

**Abstract**— This work presents a analysis of the performance of the proportional integral controller and artificial neural network controller using for the control of doubly fed induction machine speed. However, Direct Torque Control is using to obtain high performance torque control but due to the sensitivity of proportional integral regulators to parametric variations because their coefficients are calculated according to these parameters. In this paper , we propose the replacement the speed PI regulator of double fed induction motor by a regulator based on artificial intelligence especially neuronal controller to improve the tuning performance. A complete simulation model for the proposed drive is developed using MATLAB/Simulink. The effectiveness of the proposed drive is verified at different dynamic operating conditions by simulation results. Indeed , the simulation results showed that the proportional integral controller is sensitivity to motor parameter variations but the artificial neural network controller ensures the best performances in rotor resistance and load variations and better dynamic characteristics

**Keywords**— *Variable speed; Doubly fed induction machine; DTC; controllers; artificial neural network; simulation.*

## I. INTRODUCTION

The electric motors of industrial systems operate generally at variable speed. Since long time, the induction motors (IMs) are often used for induction drives because they are unquestionably an advantage over to the machine the DC machine [1,2] because of this simple and robust structure, high torque to weight ratio, higher reliability and ability to operate in hazardous environments. However, induction motors are difficult to control for several reasons as their dynamics are intrinsically nonlinear and multivariable, not all of the state variables and not all of the outputs to be controlled may be available for feedback and there are critical parameters which may considerably vary during operations [3]. For example, the resistance change due to temperature particularly at low speeds. Therefore, the use of a robust control is necessary, in this context; our contribution proposes a regulator based on neural networks to improve the tuning performances. In addition, the Direct Torque Control (DTC) is used to obtain

high performance torque control of the doubly fed induction machine (DFIM). DTC improves the induction machine controller dynamic performance and reduces the influence of the parameter variation during the operation [4] .

The Direct Torque Control (DTC) method was introduced, especially for asynchronous machines in 1985 by Takahashi and Depenbrock [5]. This control technique is based on a decoupling of the flux and the motor torque by orientation of the magnetic field of the stator and he is known to have a simple control structure with comparable performance to that of the field-oriented control (FOC) techniques developed by [6] . The DTC have several advantages over its competitor field oriented control. It is utilizes hysteresis band controllers for both stator flux linkage and motor developed torque controls. Unlike FOC, the DTC scheme does not need any coordinate transformation, pulse width modulation (PWM) and current regulators. Unlike FOC methods, DTC techniques require utilization of hysteresis band comparators instead of flux and torque controllers [7]. The fact that the DTC directly controls the switches without going through regulators, greatly improves its dynamic performance compared to other controls.

The present paper is arranged as follows: in Section 2, the dynamic model of doubly fed induction machine based on DTC is introduced. Section 3 we define the doubly fed induction machine and inverter models. The proportional integral speed and neural control are presented in Section 4. Simulation results are given and discussed, and finally in Section 5 and concluding remarks are given in Section 6.

## II. DOUBLE STAR INDUCTION MOTOR MODEL

The DFIM with the distributions of its windings and its own geometry is very complex. Therefore to analyse it, its exact configuration is taken into account. It is then necessary to adopt the following simplifying assumptions in order to develop a simple model [8] . and the air gap is constant; the magnetic circuit is not saturated and it is perfectly aminated, with the result that the iron losses and hysteresis are negligible and only the windings are driven



$$B = \begin{bmatrix} \frac{1}{\sigma L_s} & 0 & \frac{-L_m}{\sigma L_s L_r} & 0 \\ 0 & \frac{1}{\sigma L_s} & 0 & \frac{-L_m}{\sigma L_s L_r} \\ \frac{-L_m}{\sigma L_s L_r} & 0 & \frac{1}{\sigma L_r} & 0 \\ 0 & \frac{L_m}{\sigma L_s L_r} & 0 & \frac{1}{\sigma L_r} \end{bmatrix} \quad (12)$$

$$C = \begin{bmatrix} 1 & 0 & 0 & 0 \\ 0 & 1 & 0 & 0 \\ 0 & 0 & 1 & 0 \\ 0 & 0 & 0 & 1 \end{bmatrix} \quad (13)$$

The dynamical equation and electromagnetical torque are given by (8) and (9), respectively:

$$J \frac{d\Omega}{dt} = T_{em} - T_l - k_f \Omega \quad (14)$$

$$T_{em} = p \cdot L_m (i_{qs} \cdot i_{dr} - i_{ds} \cdot i_{qr}) \quad (15)$$

The DTC based on hysteresis comparators and switching tables provides a fast torque response. However, in steady state the torque has large ripples, due to the switching frequency of the inverter caused by the hysteresis bands. DTC requires accurate knowledge of the amplitude and angular position of the controlled flux with respect to the stationary stator axis in addition to the angular velocity for the torque control purpose [9]. The principle of DTC operation can also be explained by analyzing the stator voltage equation in the stator flux reference frame [10].

$$\vec{u}_s = R_s \dot{\vec{i}} + \frac{d\vec{\phi}}{dt} + j\omega_s \vec{\phi}_s \quad (16)$$

If this expression is separated into the direct ( $\alpha$ ) and the quadrature component ( $\beta$ ) of the stator voltage, the following expression can be obtained:

$$u_{s\alpha} = R_s i_{s\alpha} + \frac{d\phi_{s\alpha}}{dt} \quad (17)$$

$$u_{s\beta} = R_s i_{s\beta} + \frac{d\phi_{s\beta}}{dt} \quad (18)$$

The following torque expression:

$$T_{em} = \frac{3 \cdot p \cdot \phi_{s\alpha}}{2 \cdot R_s} (u_{s\beta} - \omega_s \phi_{s\alpha}) \quad (19)$$

Electromagnetic torque can be controlled by means of the component of the stator voltage, under adequate decoupling of the stator flux. DTC requires the estimation of stator flux and torque, which can be performed by means of two different phase currents, the state of the VSI and the voltage level in the DC voltage bus. This work uses a DTC schemes for an induction motor fed by two-level voltage source inverter (VSI).

### III. PI AND ARTIFICIAL NEURAL NETWORK CONTROLLER

Where the speed controller is a proportional integral (PI), the proportional action (P) ensures the performance criteria required by speed loop. So the integral action (I) cancel the error in study state. By neglecting, the load torque ( $T_l=0$ ), the transfer function is [11]:

$$\frac{\omega_r}{\omega_r^*} = \frac{\frac{K_{p\omega l}}{K_{i\omega l}} P + 1}{\frac{J}{p \cdot K_{i\omega l}} P^2 + \frac{K_{p\omega l} + \frac{K_f}{K_{i\omega l}}}{K_{i\omega l}} P + 1} \quad (20)$$

Where,  $K_{p\omega l} = K_{p\omega} K_e$ ,  $K_{i\omega l} = K_{i\omega} K_e$  and  $K_e = K_m \Phi^*$

By identification with the canonical form:

$$G(s) = \frac{\omega_r}{\omega_r^*} = \frac{1}{\frac{1}{\omega_n^2} P^2 + \frac{2\xi}{\omega_n} P + 1} \quad (21)$$

We obtained:

$$\begin{cases} K_{i\omega} = \frac{J\omega_n^2}{p \cdot K_e} \\ K_{p\Omega} = \left( \frac{2\xi K_{i\omega} - \frac{k_f}{p}}{\omega_n} \right) \frac{1}{K_e} \end{cases} \quad (22)$$

We chose the coefficients for  $\xi = 1$  and response time ( $T_{rep}=20ms$ ) at 5%.

The control speed use a controller based on ANN (20 multiphases). The multi layer preceptor, the number of hidden layers and hidden neurons is not known a priori. Furthermore, there is no general rule for predicting the number of hidden scheme of neural fuzzy-speed control. neurons necessary to achieve a specified performance of the model. One of the most popular programs is the back-propagation. So for the proposed application, an ANN with a single layer with activation function tansig type is used. In this step, the authors execute several tests and analyzing the performance of the system [12-13]. The neural network controller considered have two neurons in input layer, 30 neurons in hidden layer and one neuron in output layer.

#### IV. RESULTS AND DISCUSSION

The proposed ANN controller for the DFIM drive is tested using a Matlab/Simulink. The scheme system consists of the following elements: three-phase doubly fed induction machine, voltage-source inverter.

In order to evaluate the performances of the proposed control scheme at different operating conditions. The control system operated properly according for starting and reversing of motor rotation, taking into account, the variation of the load torque, the simulated responses are shows in Fig.1 and Fig.2. Rotor speed, electromagnetic torque, rotor flux, and stator current are shown in Fig. 1(a, b and c), respectively. Moreover, the system is tested for low speed (see Fig. 2). It can be seen that the proposed controller gives regulated responses in terms of fast tracking, small overshoot, and zero steady-state errors. The rotor flux has successfully followed the rotor command flux, while the rotor speed increases linearly to its rated value. The Fig.1 (a) and Fig. 2 (a) shows that the speed converges to  $\pm 100$ rad/s and  $\pm 30$  rad/s, and the electromagnetic torque is shown in Fig.8 (b) and Fig.2 (b). Also, the rotor flux value shown in Fig.8(c) and Fig. 2(c) converges to its reference properly. By comparing the simulation test results, it can be stated that the intelligent control required performances for the DFIM drive. Another important advantage of the proposed intelligent controller is that it is relatively easy to tune the gain parameters of the controllers effectively and efficiently for high-performance DFIM drive systems. The rotor speed has successfully tracked the command speed while the rotor flux is fixed at its reference value.

Fig. 3, Fig. 4 represent zooms which show the effect of the variation of the rotor resistance of the machine on the performances of both types of speed controllers utilized. To this effect, to study the effect of change in rotor resistance, we visualized in Fig. 3 and Fig. 4 zoom that shows the evolution of variables at the time of application and removal of the load. This for the case of a PI controller (Fig. 3) and artificial neural network controller (Fig. 4). The results show clearly that the NN controller is insensitive of parameter variations because it is designed for models that do not require to know the parameters.

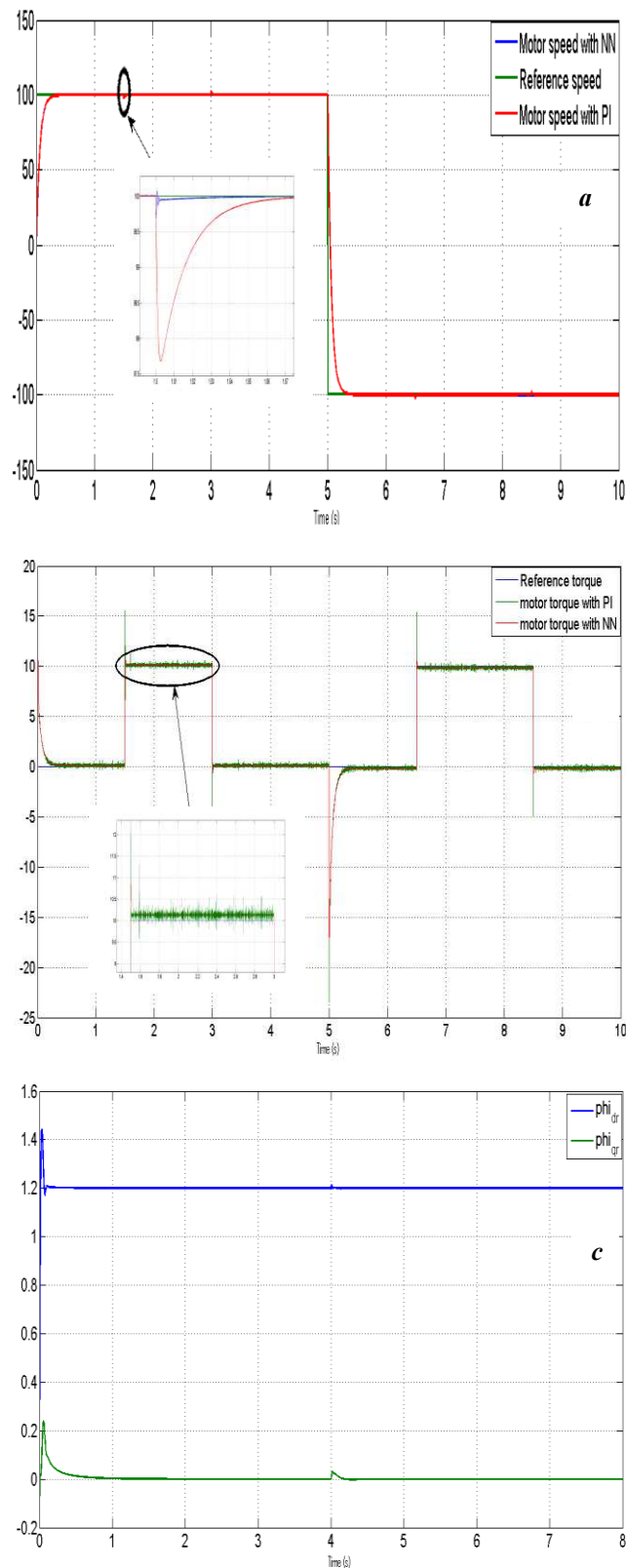


Fig. 1. Speed, torque and flux with PI and NN

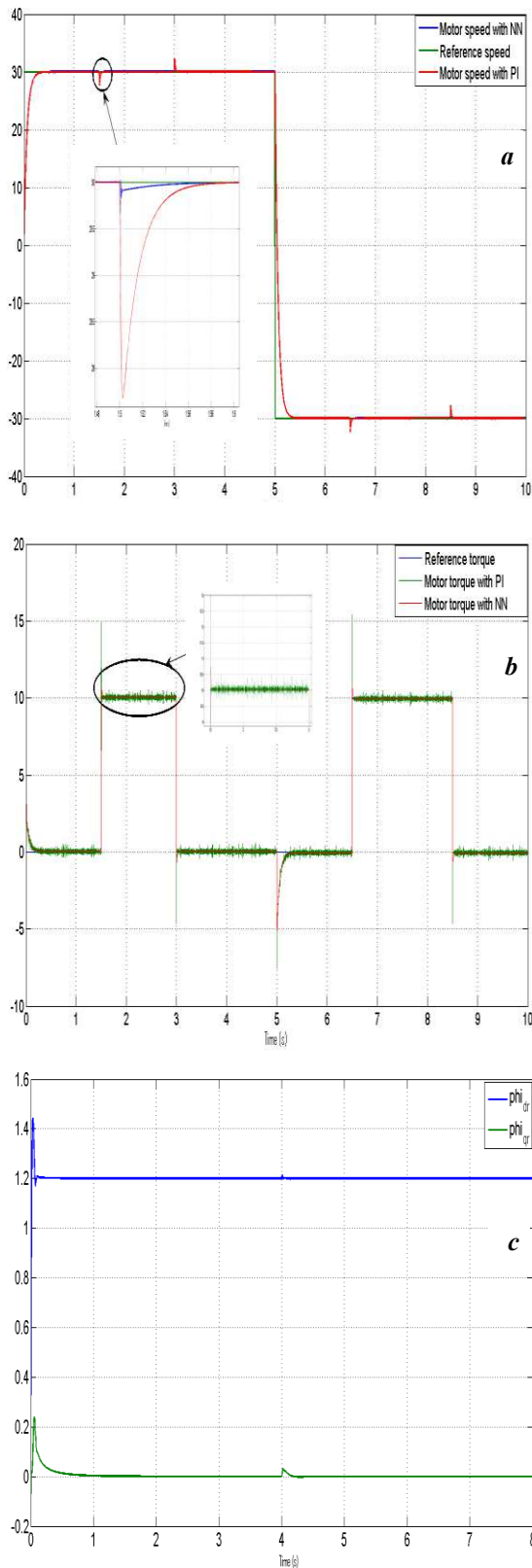


Fig. 2. Results for lower speed reference

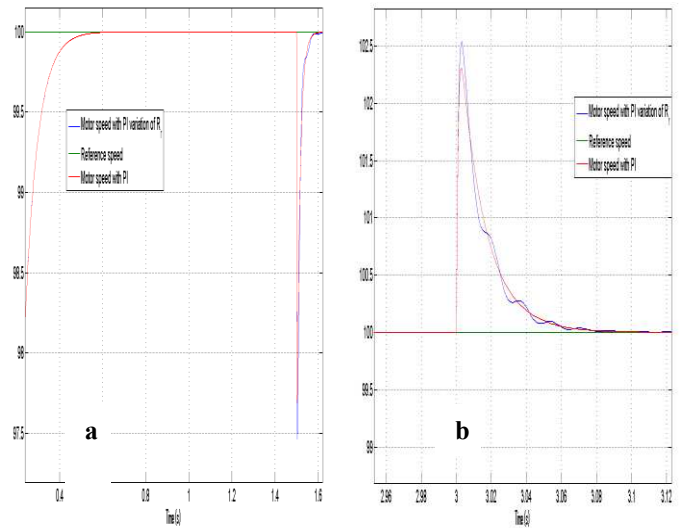


Fig. 3. Zoom with PI controller and resistance variation

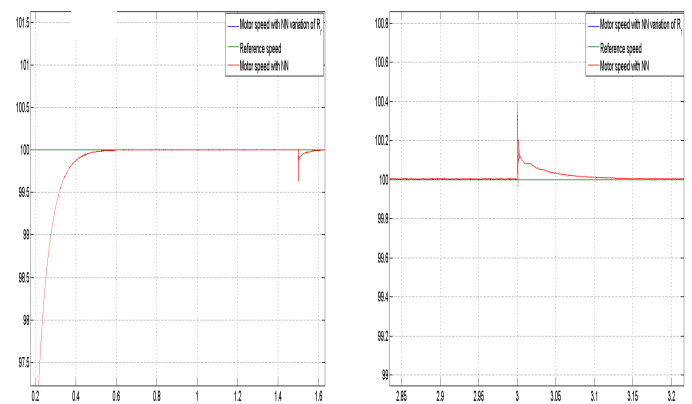


Fig. 4. Zoom with ANN controller and resistance variation

## V. CONCLUSION

This work has presented a study to show improvement obtained by using ANN controller for the DFIM drive. The system is tested also for low speed. The results shows the proposed controller gives regulated responses in terms of fast tracking, small overshoot, and zero steady-state errors and good control performance in terms of robustness and adaptability. Another important advantage of the proposed intelligent controller is that it is relatively easy to tune the gain parameters of the controllers effectively and efficiently for high-performance DFIM drive systems. The intelligent technique can be easily adopted for industrial applications.

## REFERENCES

- [1] M. F. Benkhoris and A. Gayed, "Discrete sliding control technique of DC motor drive," *IEE Power Electronics and Variable Speed Drives, Conference*, Publication No. 429, pp. 81-86, 1996.
- [2] Y. Y. Hsu and W. C. Chan, "Optimal Variable Structure Controller for DC Motor Speed Control", *Proc IEE*, Vol. 131, Pt. D, No. 6, pp. 233-237, Nov. 2009.
- [3] S. Lekhchine et al " Fuzzy Sliding Mode Control of Induction Motor Drive, International conference of renewable energies, Tunisi, 2015.
- [4] El Hassan I., Westerholt E. V., Roboam X., De Fomel B., Comparison of different state models in Direct Torque Control of induction machines operating without speed sensor. *IEEE*, 2000, p. 1345-1352..
- [5] Takahashi I., Noguchi T., A New Quick-Response and High-Efficiency Control Strategy for an Induction Motor. *IEEE Trans. Ind. Appl.*, 1986, 22(5), p. 820-827.
- [6] Blaschke F., The Principle of Field Orientation as Applied to the New Transvector Close-Loop Control System for Rotating-Field Machines. *Siemens Review*, 1972, 1(34), p. 217-220.
- [7] Mei C. G., Panda S. K., Xu J. X., Lim K. W., Direct Torque Control of Induction Motor-Variable Switching Sectors. *IEEE Int. Conf. Power Electron. and Drive Sys., PEDS'99, Hong Kong, 1999*, p. 80-85. [4] *Leonardo Journal of Sciences ISSN 1583-0233 Issue 12, January-June 2008* p. 34-56
- [8] Levi E. Recent developments in high performance variable-speed multiphase induction motor drives. Sixth international symposium nikola tesla , Belgrade, SASA, Serbia ; October 18–20, 2006.
- [9] Field Oriented Control Of a Dual Star Induction Machine» , *International Journal of Electrical Power and Energy Systems, IJEPES, Revue Elsevier*, 57 (2014): 206-211.
- [10] Hadiouche D, Razik H, Rezzoug A. On the modelling and design of dual-stator windings to minimize circulating harmonic currents for VSI fed AC machines. *IEEE Trans Ind Appl* 2004;40(2):506–15.
- [11] Merabet E, Amimeur H, Hamoudi F, Abdessemed R. Self-tuning fuzzy logic Controller for a dual star induction machine. *J Electr Eng Technol* 2011;6(1) :133–138.
- [12] Andriamalala R.N, Razik H, Sargos F.M. Indirect-rotor-field-oriented-control of a double-star induction machine using the RST controller. *IEEE Xplore*; 2008.
- [13] Masiala M, Vafakhah B, Salmon J, Knight A. Fuzzy self-tuning Speed control of an indirect field-oriented control induction motor drive. *Proceedings of IEEE Ind. Appl. Soc. Ann. Meet* ; 2007: 1008-1014.

# Effects of the Cl-edge shape and the width on the structural, electronic and magnetic properties of silicene nanoribbons

M. T. Kadri<sup>1</sup>, I. Djabri<sup>1</sup>, H. Belkhir<sup>1</sup>

<sup>1</sup>Laboratory Studies of Surface and Interfaces of Solid Materials (LESIMS), Department of Physics, Faculty of Sciences, University B

adji Mokhtar, P.O. Box 12, Annaba 23000, Algeria

medtahar.kadri@univ-annaba.dz

djabri\_issam@yahoo.fr

Hafid.belkhir@yahoo.com

**Abstract**— Based on the density functional theory (DFT), the structural, electronic and magnetic properties of bare silicene nanoribbons (SiNRs) with either zigzag edge (ZSiNRs) or armchair edge (ASiNRs) and the effect of Cl-termination on the properties of the two types SiNRs are studied. The optimized structural parameters were in good agreement with the experimental and theoretical values. The results show that both bare zigzag and armchair are always metallic. The effect Cl-termination clearly on the electronic and magnetic properties of SiNRs with either zigzag edge (ZSiNRs) or armchair edge (ASiNRs). We observed a nearly degenerate flat edge-state band appears at the Fermi level  $E_f$ , which give rise to a very large density of states (DOS up and DOS down) at  $E_f$ , demonstrating magnetic properties for Cl-terminated 5-ZSiNR. For Cl-terminated 7-ASiNR the width between the top of the valance band or the bottom of the conduction band representing a direct semiconducting and nonmagnetic because of the  $\sigma$ - $\pi$  mixing. The total density of states (DOS) and projected density of states (PDOS) analyses show that the top of the valance band or the bottom of the conduction band for the 7-ASiNR is mainly contributed by Cl atoms. The charge density distributions show that there is covalent bonding between all sorts of the Si-Si bonds, ionic bonding resulted between the edge Cl atom and the nearest Si atom. This because the electro-negativity of Si atoms is smaller than that of Cl atoms.

**Keywords**— silicene nanoribbons, DFT calculations, Cl-termination, electronic properties

## I. INTRODUCTION

Graphene is a form of carbon which has a two-dimensional honeycomb structure [1]. Due to their fascinating properties and potential applications in nanoelectronics such as zero band gap semi metal, very high carrier mobility [2], graphene attracted much attention in recent years [3]. Quasi one-dimensional (1D) derivatives of graphene, called graphene nanoribbons have been a subject of interest because of thier electronic and magnetic properties dependent on their size [4], geometry [5], and edge-passivation pattern [6]. The discovery of graphene also stimulates interest on two-

dimensional honeycomb structures formed by other elements, such as silicene [7-8]. Silicene is a two-dimensional hexagonal lattice of silicon (Si) atoms. The electronic structure of the two-dimensional silicene is similar to that of graphene, with zero gap and linear energy dispersion near the K point [9], but contrary to graphene, silicene has a buckled atomic structure (0.44 Å) [9]. However, silicene also possesses some unique properties which carbon has not [10-11]. For example, the graphene is not easily compatible for the Si-based electronics industry.

In recent years, A new material, quasi one-dimensional (1D) derivatives of silicene, called Silicene nanoribbons (SiNRs), (namely, graphene-like Si [12]) have been the subject of numerous experimental and theoretical studies [13-14]. The Silicene nanoribbons was successfully epitaxially grown on Ag surface [14-15-16-17]. The electronic and magnetic properties of SiNRs with H-terminated and F-terminated have been synthesized and expected to possess unusual electronic and magnetic properties dependent on their width, edge shape and termination [18-19]. The first-principle numerical methods showed all the H-terminated and F-terminate with the armchair edges ASiNRs are nonmagnetic semiconductors with a direct gap and the band gaps present an oscillation behavior with a period of 3 dimers when ribbon width increases, and the H-terminated and F-terminate with the zigzag edges (ZSiNRs) have stable antiferromagnetic states.

In this paper, the structural, electronic and magnetic properties of bare silicene nanoribbons (SiNRs) with either zigzag edge (ZSiNRs) or armchair edge (ASiNRs) and the effect of Cl-termination on the properties of the two types SiNRs are examined using the density functional calculations (DFT). This paper is organized as follows. The calculation method and models of the two types of Cl-terminated SiNRs are given in section 2, the energy band structures, the density of states (DOS) and the charge density of the systems are analyzed in section 3 and conclusions are presented in section 4.



## II. CALCULATION METHODS AND MODELS

The present calculations have been performed by using the Vienna ab initio simulation package (VASP) [20, 21], which is based on the spin-polarized density functional theory [22, 23]. Ultrasoft Vanderbilt-type pseudopotentials [24] were used to describe the interactions between ions and electrons. The exchange correlation functional is treated within the generalized gradient approximation (GGA), in the form of Perdew and Wang 91 (PW91) [25]. The cut-off energy for the plane waves is chosen to be 350 eV. The  $2s^2 2p^3$ , and electrons are taken as the valence electrons for Si and Cl atoms, respectively. Supercells are used to simulate the isolated nanostructures, and the distance between images is chosen to be 15 Å in order to avoid interactions between the ribbon and its periodic images. The sampled k points in the Brillouin zone are generated by the Monkhorst–Pack scheme [26] with  $\Gamma$ -centred grids. The convergence of the total energy is chosen to be 0.0001 eV and all atomic positions and unit cells are optimized until the atomic forces are less than 0.02 eV/Å with a Gaussian smearing broadening of 0.2 eV. Pressures on the lattice unit cell are decreased to values less than 1 kbar. We investigate for infinitely long single-layer SiNRs and set the periodicity of the SiNR along the ribbon axis. The width of ZSiNR is classified by the number of the zigzag chains ( $N_z$ ) across the ribbon width and the width of ASiNR is classified by the number of dimer lines ( $N_a$ ) across the ribbon width. Thus we refer a ZSiNR with  $N_z$  chains as  $N_z$ -ZSiNR and an ASiNR with  $N_a$  dimer lines as  $N_a$ -ASiNR. Figure 1 presents the geometry for (a) 6-ZSiNR and (b) 7-ASiNR with Cl atoms termination. The mandarin and green balls represent Si and Cl atoms, respectively.

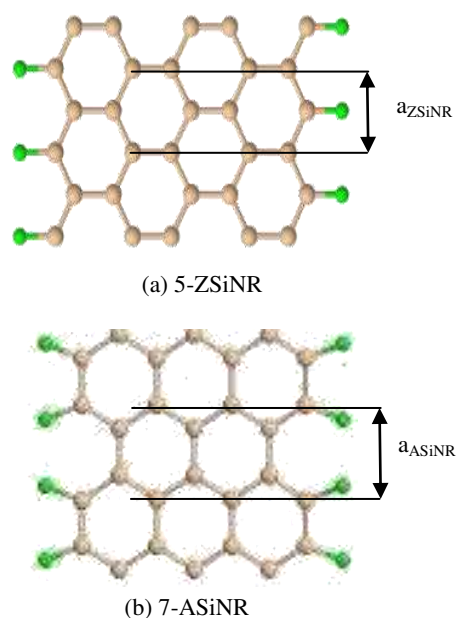


**Fig. 1** The geometry structures of (a) 5-ZSiNR and (b) 7-ASiNR terminated with Cl atoms. The mandarin and green balls represent Si and Cl atoms balls, respectively. The area between two black lines represents the lattice constant of SiNR.

## III. RESULTS AND DISCUSSION

### III.1 STABILITY AND STRUCTURAL PROPERTIES

Taken 5-ZSiNR and 7-ASiNR with Cl-terminated as example, we first make the full structure optimizations. We find that the lattice constant of nanoribbons for 6-ZSiNR and (b) 7-ASiNR are  $a_{ZSiNR} = 3.88956 \text{ \AA}$  and  $a_{ASiNR} = 6.72357 \text{ \AA}$  respectively. The Si–Si lengths and Si–Cl bonds in 6-ZSiNR and 7-ASiNR with Cl-terminated are shown in Figure 2. (a) and (b), respectively. For both SiNRs with Cl-terminated the length of the Si–Cl bond is always  $2.06 \text{ \AA}$ , but the Si–Si lengths are varying between  $2.22 \text{ \AA}$  and  $2.29 \text{ \AA}$ .

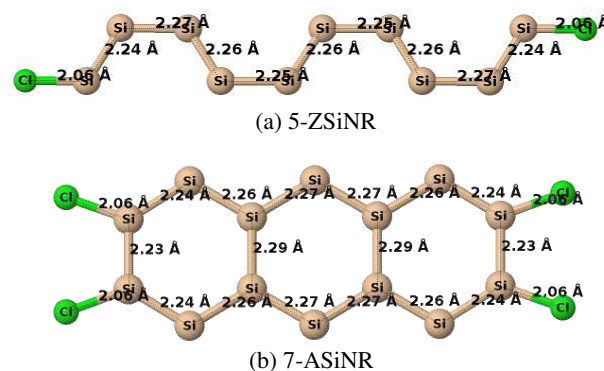


**Fig. 2** Optimized lengths ( $\text{Å}^0$ ) of Si–Si, and Si–Cl bonds in (a) 5-ZSiNR and (b) 7-ASiNR terminated with Cl atoms. The mandarin and green balls represent Si and Cl atoms balls, respectively.

The fully optimized structural parameters of 7-ASiNR and 5-ZSiNR are summarized in Table 1 and compared to experimental values of Kara et al. [17] and theoretical calculations of C. Lian et al. [27] and N. Gao et al [28]. The Lattice constants  $a_{SiNR}$  (in Å), the length of the Si–Cl bond  $L_{Si-Cl}$  and width of nanoribbons  $d_{width}$  (in Å). We define the width of nanoribbons  $d_{width} = d_{distance} + d_{diameter}$ , where  $d_{diameter}$  is the diameter of the silicon atom, which is  $2.2 \text{ \AA}$  and  $d_{distance}$  is the distance between the center of silicon atoms on both edges. It shows that the 7-ASiNRs have 15% difference and 5-ZSiNRs have 17% difference with the experimental ones. The deviations of our results with others are reasonable.

**Table 1** Geometric parameters of 5-ZSiNR and 7-ASiNR, compared to experimental data of Kara et al. [17] and calculations of Lian et al. [27] and Gao et al [28].

Parameters	Present work	Theory <sup>a,b</sup>	Exp <sup>c</sup>
$a_{ZSiNR}$	3.88956	(3.868) <sup>a</sup>	
$a_{ASiNR}$	6.72357	(6.7) <sup>a</sup>	
$d_{width}$ 5-ZSiNR	15.72	(16.6) <sup>a</sup>	16
$d_{width}$ 7-ASiNR	13.77	(14.7) <sup>a</sup>	16
$L_{Si-Cl}$ SiNR	2.06	(2.085) <sup>b</sup>	

<sup>a</sup> Ref. [27]

<sup>b</sup> Ref. [28]

<sup>c</sup> Ref. [17]

**III.2 ELECTRONIC PROPERTIES** For getting insights the electronic structure of bare 5-ZSiNR and 7-ASiNR, their band structures are shown in Figure.3 (a) and (b), respectively. It can be seen that the band structures the dangling bonds introduce one or several bands crossing the Fermi level

accompanied with an up shift of all bands. So that both bare 5-ZSiNR and 7-ASiNR are always metallic. It also agrees with the experimental and theoretical results [31, 18]. The spin polarized total density of states plots of bare 5-ZSiNR and 7-ASiNR are presented in Figure.4 (a) and (b), respectively. It can be clearly seen the spin polarized DOS for the spin up channel is significantly different from the spin down channel, indicating distinct magnetism in both SiNRs conformer. We find that the total magnetic moment per supercell of bare 7-ASiNR approaches to  $\mu=1.04\mu_B$  is higher than of the total magnetic moment per supercell of bare 5-ZSiNR approaches to  $\mu=0.64\mu_B$ , respectively.

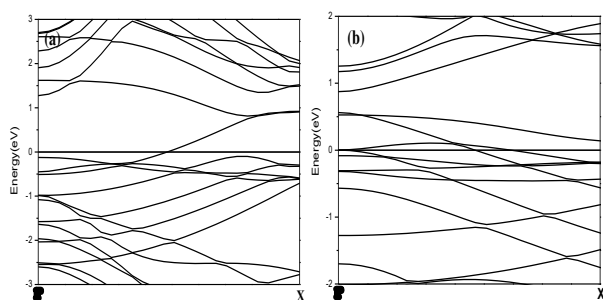


Fig. 3 The band structures of bare (a) 5-ZSiNR and (b) 7-ASiNR, respectively. The Fermi level  $E_f$  is set to zero and is indicated by the horizontal lines.

We examine the effect of Cl-termination on the electronic and magnetic properties properties of 5-ZSiNR and 7-ASiNR. The band structures and spin polarized total density states of Cl-terminated 5-ZSiNR are shown in Figure.5 (a) and (b), respectively. It can be seen that around the Fermi level the highest valence band and the lowest conduction band are coincide near the X point and there is a degenerate flat edge-state band at the Fermi level ( $E_f$ ), which give rise to a very large density of states (DOS up and DOS down) at  $E_f$ . This DOS (spin up and spin down) peak at the Fermi level  $E_f$  is remarkable, which therefore provides the magnetic properties of Cl-5-ZSiNR. This phenomenon has been found in ZGNRs [29, 30] and ZSiNRs [18]. The value of the total magnetic moment per super cell has declined to become  $0.16\mu_B$ .

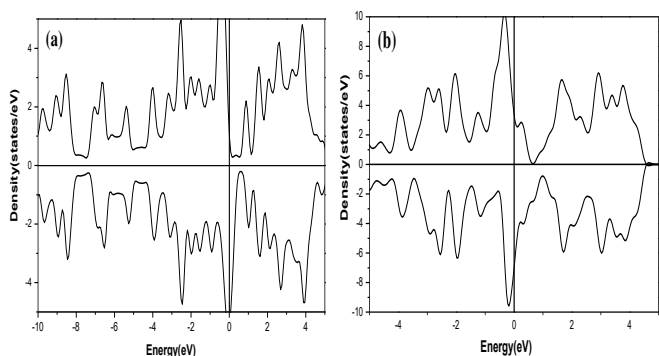


Fig. 4 The spin polarized total density states of (a) 5-ZSiNR and (b) 7-ASiNR, respectively. The Fermi level  $E_f$  is set to zero and is indicated by the vertical lines.

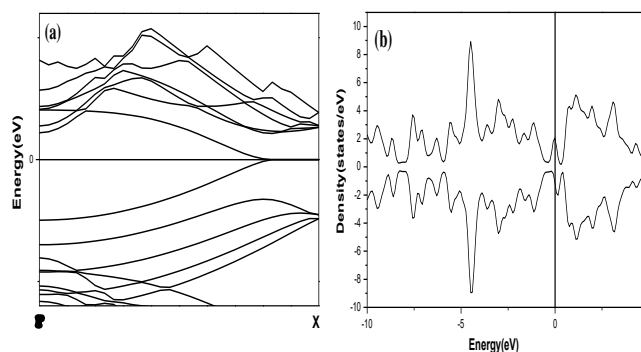


Fig. 5 The band structures of (a) 5-ZSiNR with Cl-terminated. The Fermi level  $E_f$  is set to zero and is indicated by the horizontal line. The spin polarized total density states of (b) 5-ZSiNR. The Fermi level  $E_f$  is set to zero and is indicated by the vertical lines.

The band structures of Cl-terminated 7-ASiNR is shown in Figure. 6. It can be seen that the bottom of the conduction band and the top of the valance band appeared at  $\Gamma$  point are separated. So that the Cl-terminated 7-ASiNR is nonmagnetic semiconductors with a direct band gap approaches to  $0.12\text{ eV}$ .

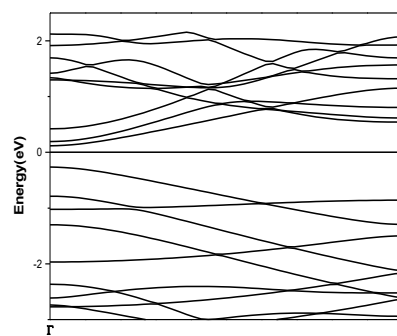


Fig. 6 The band structures of 7-ASiNR with Cl-terminated. The Fermi level  $E_f$  is set to zero and is indicated by the horizontal lines.

The total density of states (DOS) (a) and projected density of states (PDOS) on Si 3p atom (b) and Cl 3p atom (c) of Cl-terminated 7-ASiNR given in Figure. 7. It can be seen that, the p states of Cl atom contributes and affects the width between the top of the valance band or the bottom of the conduction band.

This is because the  $\sigma$ - $\pi$  mixing effect[32-33], the interaction between non-bonding 3p electrons of Cl atoms and 3p state of Si atoms, produce an important orbital mixing with the  $\sigma$  valence electrons. Such a phenomena was also observed by S.Y.You et al. in the Si halides nanowires[34] and Y.-NYang et al in F-terminated ZSiNRs[19]. DFT calculations have shown that the different terminations can affect the electronic properties of SiNRs. The Cl- terminated SiNRs has a advantage because of its narrower band gap compared to the SiNRs with H-terminated and F-terminated.

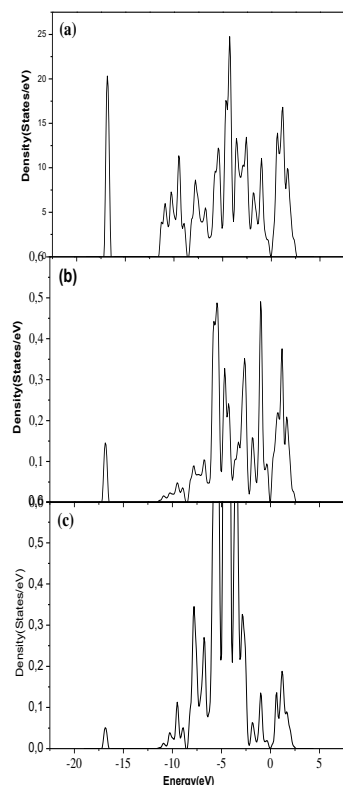
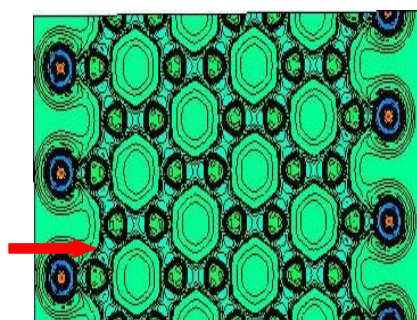
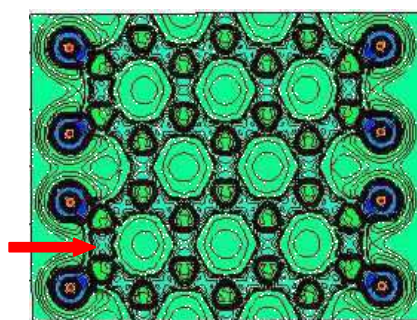


Fig. 7 The total density of states (DOS) (a), projected density of states (PDOS) on Si 3p atom (b) and Cl 3p atom (c) of Cl-terminated 7-ASiNR. The Fermi level  $E_f$  is set as energy zero.

The charge-densities contours of 5-ZSiNR and 7-ASiNR terminated with the Cl atoms in the (0 0 1) crystallographic plane respectively, are presented in Figure 8.



(a) 5-ZSiNR



(b) 7-ASiNR

Fig. 8 The charge density contours of (a) 5-ZSiNR and (b) 7-ASiNR terminated with Cl atoms.

The electro-negativity of Si atoms is smaller (1.8) than that of Cl atoms (3.16), where the Si atoms lose the electrons while the Cl atom gain the electrons in both SiNRs. So that the charge density distribution indicates that there is covalent bonding between all sorts of the Si-Si bonds, ionic bonding resulted between the edge Cl atom and the nearest Si atom. The values of the charge density distribution of the edge zigzag Si-Si bond (indicated by the red arrow) for 5-ZSiNR is smaller than that of the edge dimer Si-Si bond (indicated by the black arrow) for 7-ASiNR. This is because the edge zigzag Si-Si bond with only one adjacent Cl atom but the edge dimer Si-Si bond with two adjacent Cl atoms, the bond direction of the nanoribbon axis, the bond position from the nanoribbon edge and the flatband that appeared in 5-ZSiNR but does not appear in 7-ASiNR terminated with the Cl atoms at the Fermi level  $E_f$ .

**IV CONCLUSIONS** The structural, electronic and magnetic properties of the both bare SiNR with either zigzag  $N_Z$  - ZSiNR or armchair  $N_A$  - ASiNR edges with  $N_Z=5$  and  $N_A=7$  were investigated based on the density functional calculations under GGA. It has been demonstrated that, firstly, the both bare 5-ZSiNR and 7-ASiNR having metallic character with magnetic moment. It also agrees with the experimental and theoretical results. Secondly, we examine the effect of Cl-termination on the electronic and magnetic properties of the two types SiNRs. The Cl-terminated 5-ZSiNR having zero gap, also a nearly degenerate flat edge-state band appears at the Fermi level  $E_f$ , which give rise to very large spin-polarized total density of states density of states (up and down) at  $E_f$ . This DOS peak demonstrating magnetic properties of Cl-5-ZSiNR. The value of the total magnetic moment has declined. However, the Cl-terminated 7-ASiNR is nonmagnetic semiconductors with small direct band gap. Because of the  $\sigma$ - $\pi$  mixing effect, the interaction between non-bonding 3p electrons of Cl atoms and 3p state of Si atoms, produce an important orbital mixing with the  $\sigma$  valence electrons. The DOS and PDOS analyses show that the top of the valence band or the bottom of the conduction band for the 7-ASiNR is mainly contributed by Cl atoms. The bonding features are analyzed by using the charge-densities contours in the (0 0 1) crystallographic plane. We found that covalent bonding between all sorts of the Si-Si bonds, ionic bonding resulted between the edge Cl atom and the nearest Si atom.

#### REFERENCES

- [1] K. S. Novoselov, A. K. Geim, S. V. Morozov, D. Jiang, Y. Zhang, S. V. Dubonos, I. V. Grigorieva, and A. A. Firsov, *Science* 306, 666 (2004).
- [2] J.H. Chen, C. Jang, S. Xiao, M. Ishigami and M.S. Furher, *Nanotechnology* 3, 206 (2008).
- [3] A. H. Castro Neto, F. Guinea, N. M. R. Peres, K. S. Novoselov, and A. K. Geim, *Rev. Mod. Phys.* 81, 109 (2009).
- [4] Y.W. Son, M.L. Cohen and S.G. Louie, *Phys. Rev. Lett.* 97, 216803 (2006).
- [5] V. Barone, O. Hod and G.E. Scuseria, *Nano Lett.* 6, 2748 (2006).

- [6] M. Wang and C.M. Li, *Nanoscale* 3, 2324 (2011).
- [7] B. Aufray, A. Kara, S. Vizzini, H. Oughaddou, C. Landri, B. Ealet and G. Le Lay, *Appl. Phys. Lett.* 96, 183102 (2010).
- [8] A. Kara, H. Enriquez, A. P. Seitonen, L. C. Lew Yan Voon, S. Vizzini, B. Aufray, and H. Oughaddou, *Surf. Sci. Rep.* 67, 1 (2012).
- [9] S. Cahangirov, M. Topsakal, E. Aktürk, H. Sahin and S. Ciraci, *Phys. Rev. Lett.* 102, 236804 (2009).
- [10] M. Zhang, Y.H. Kan, Q.J. zang, Z.M. Su and R.S. Wang, *Chem. Phys. Lett.* 379 (2003) 81.
- [11] H. Lee, Y. W. Son, N. Park, S. Han, and J. Yu, *Phys. Rev. B* 72,174431 (2005).
- [12] G.G. Guzman- Verri, and L.C. Lew Yan Voon, *Phys. Rev. B* 76, 075131(2007).
- [13] Y. Ding and J. Ni, *Appl. Phys. Lett.* 95, 083115 (2009).
- [14] A. Kara, S. Vizzini, C. leandri, B. Ealet, H. Oughaddou, B. Aufray, and G. Le Lay, *J. Phys. Condens. Matter* 22, 045004 (2010).
- [15] Y. Ding and J. Ni, *Appl. Phys. Lett.* 95, 083115, (2009).
- [16] P. De Padova, C. Léandri, S. Vizzini, C. Quaresima, P. Perfetti, B. Olivieri, H. Oughaddou, B. Aufray, and G. Le Lay, *ibid.* 8, 2299 (2008).
- [17] A. Kara, C. Léandri, M. E. Dàvila, P. De Padova, B. Ealet, H. Oughaddou, B. Aufray, and G. Le Lay, *J. Supercond. Novel Magn.* 22, 259 (2009).
- [18] Y.L. Song, Y. Zhang, J.M. Zhang and D.B. Lu, *Appl. Surf. Sci.* 256, 6313-6317 (2010).
- [19] Yan-Ni Yang, Jian-Min Zhang and Ke-Wei Xu, *Physica E* 57, 21–27 (2014).
- [20] G. Kresse and J. Furthmüller, *Physical Review B* 54, 11169 (1996).
- [21] G. Kresse and D. Joubert, *Physical Review B* 59, 1758 (1999).
- [22] P. Hohenberg, and W. Kohn, *Physical Review B* 136, 864 (1964).
- [23] W. Kohn and L.J. Sham, *Physical Review A* 140, 1133, (1965).
- [24] D. Vanderbilt, *Physical Review B* 41, 7892, (1990).
- [25] J.P. Perdew, J.A. Chevary, S.H. Vosko, K.A. Jackson, M.R. Pederson, D.J. Singh and C.Fiolhais, *Phys. Rev. B* 46, 6671(1992).
- [26] H J Monkhorst and J D Pack, *Phys. Rev. B* 13, 5390 (1976).
- [27] C. Lian and J.Ni, *Physica B* 407, 4695–4699, (2012).
- [28] N. Gao, W. T. Zheng and Q. Jiang, *Phys. Chem. Chem. Phys.* 14, 257–261. (2012).
- [29] Y. Miyamoto, K. Nakada and M. Fujita, *Phys. Rev. B* 59, 159858 (1999).
- [30] K. Nakada, M. Fujita, G. Dresselhaus, M.S. Dresselhaus, *Phys. Rev. B* 54, 17954,(1996).
- [31] P. De Padova, C. Quaresima, P. Perfetti, B. Olivieri, C. Leandri, B. Aufray, S. Vizzini and G. Le Lay, *Nano Lett.* 8, 271 (2008).
- [32] H. Motoyama, K Takeda and K Shiraishi, *Pro. Mat. Res. Soc. symp.* 486, 385 (1997).
- [33] D. B. Lu, Y L Song, Z X Yang and G Q Li, *Appl. Surf. Sci.* 256, 6313 (2010).
- [34] S. Y. You and Y Wang, *Chin. J. Semiconductors* 27, 1927. Chinese (2006).

# ETANOLYSIS OF SUNFLOWER OIL OVER HOMOGENEOUS AND HETEROGENEOUS HETEROPOLYACID CATALYSTS

Yasmina Idrissou<sup>1,2</sup>, Tassadit Mazari<sup>3</sup>, and Chérifa Rabia<sup>1\*</sup>

<sup>1</sup>Laboratoire de Chimie du Gaz Naturel, Faculté de Chimie, Université des Sciences et de la Technologie Houari Boumediene (USTHB), BP 32, El-Alia, 16111 Bab-Ezzouar, Alger, Algeria.

<sup>2</sup>Ecole Normale Supérieure Kouba (ENS)-Alger

<sup>3</sup>Laboratoire de Chimie Appliquée et de Génie Chimique (LCAGC). UMMTO, Tizi Ouzou 15000, Algérie

(\*) corresponding author: [c\\_rabia@yahoo.fr](mailto:c_rabia@yahoo.fr)/[crabia@usthb.dz](mailto:crabia@usthb.dz)

**Abstract**—  $H_3PW_{12}O_{40}$  and  $H_4SiW_{12}O_{40}$  were used as catalysts for the sunflower oil ethanolysis as bulk and supported on silica,  $SiO_2$  with (30wt%). The fatty acid ethyl esters, reaction products, were analyzed and quantified by gas chromatography. The influences of ethanol/oil molar ratio (14,5/1 -58/1), temperature (35 or 70°C) and reaction time (30-180min) on biodiesel yield and moles number of fatty acid ethyl esters formed were examined.

Both acids in bulk form are more effective for sunflower ethanolysis than those in supported form and the SiW based catalyst is more effective than those based PW.  $H_4SiW_{12}O_{40}$  is the most performant catalyst with 55% of biodiesel yield at 70°C with a reaction time of 3 hours and an alcohol/oil ratio of 29/1 and also, the most active for the ethanolysis of palmitic acid.

**Index Terms**— Biodiesel; Ethanolysis; Sunflower oil; Ethyl esters; Heteropolyacids.

## I. INTRODUCTION

The greenhouse gas emission increase into the environment caused by the fossil fuel combustion has encouraged researchers to find an alternative. Biodiesel, composed of alkyl esters, could be a promising fuel because it comes from a renewable source, vegetable oils as sunflower, castor, soybean ....., or animal fats. In addition, the biodiesel has a very low toxicity, a biodegradability and a flash point lower than diesel from fossil fuel. On the other hand, contrarily to homogeneous catalysis, the heterogeneous catalysis presents some advantages as easy separation catalyst/reaction mixture, catalyst reuse and reducing wastes.

Several studies have reported biodiesel production from vegetable oil methanolysis in heterogeneous systems using bases as calcium oxide [1], dolomite [2,3], Alumina/silica supported  $K_2CO_3$  [4], sodium silicate [5] and hydrotalcite [6]. Although, basic catalysis leads to high biodiesel yields, it causes a saponification reaction. To overcome this disadvantage, authors have proposed an acid catalysis that has

the advantage of activating both esterification and transesterification of fatty acids and, in addition, the water presence in the reaction mixture is not a barrier.

Among the acid solid catalysts examined in the vegetal oil transesterification as  $SO_4-ZrO_2$  [7] and  $WO_3-ZrO_2$  [8,9], emerge the tungsten based Keggin-type polyoxometalates (POMs) in their acid or salt form. Their effectiveness is due to their Bronsted acidity stronger than conventional acids as  $H_2SO_4$  and  $HNO_3$ . Thus, the insoluble salts as  $(NH_4)_xH_3-xPW_{12}O_{40}$  were used for palmitic acid esterification [10],  $(Cs)_xH_3-xPW_{12}O_{40}$  for used vegetable oil transesterification [11] and for  $Ag_xH_3-xPW_{12}O_{40}$  castor oil transesterification [12]. In its acid form,  $H_3PW_{12}O_{40}$  was supported on  $Nb_2O_5$  [13],  $SiO_2$  [14] and MCM-41 [15] and tested for palmitic acid esterification and transesterification of sunflower oil and waste cooking, respectively [16].

In the above-mentioned works, the most widely used alcohol is methanol because of its low price; in recent years, however, the production increase of ethanol from agricultural biomass (beet, corn, sugar cane and starch) has led to lower prices. On the other hand, it can be noted that ethanol is a renewable alcohol when it is derived from biomass compared to methanol obtained from hydrocarbons. Ethanol in concentrated and hydrated form is used as a biofuel and also as an additive to fossil fuels. Few studies have focused on the ethanol use in the transesterification of vegetable oils, although the ethyl esters are more biodegradable in water than methyl esters [17,18] (Boehman, 2005; Makareviciene and Janulis, 2003). They present also a higher cetane index and heating power (Clark et al., 1984) [19] and lower cloud, cold filter plugging, and pour points (Encinar et al., 2007). [20].

Production of fatty acid ethyl esters from rubber seed oil in hydrodynamic cavitation reactor in the presence of sulfuric acid (4,0 wt.%) led to 92,5% of biodiesel yield,

obtained with a 6:1 ethanol:oil molar ratio [21]. The soybean oil transesterification with ethanol using sulfonated activated carbon from corn cobs as a catalyst and a microwave-assisted process has proven to be a promising, less energy-intensive solution [22].

In this context, we were interested in the sunflower oil ethanolysis in the presence of  $H_3PW_{12}O_{40}$  and  $H_4SiW_{12}O_{40}$  in homogeneous and heterogeneous phases. The used support is silica,  $SiO_2$ , with (30wt%)  $H_3PW_{12}O_{40}$  (noted S30) and (30wt%)  $H_4SiW_{12}O_{40}$  (noted S'30). The preparation of the supported materials was previously reported [14]. The influences of ethanol /oil molar ratio (14,5/1-58/1), temperature (35 or 70°C) and reaction time (30-180min) on biodiesel yield and moles number of fatty acid ethyl esters were examined.

## II. EXPERIMENTAL

The refined sunflower oil ethanolysis reaction was carried out at 35 or 70°C, atmospheric pressure under reflux conditions with constant stirring (300 rpm) and a ethanol/oil molar ratio varying between 14,5/1 and 58/1. In a catalytic test experiment, 2,61 g of sunflower oil were taken in the glass reactor with a given ethanol volume, after heating to 35 or 70°C, and a given catalyst mass was then added to reaction mixture. After 3h of reaction and adding 10ml of distilled water through the refrigerant, to recover all of the ethanol, the reaction mixture was put in a separating funnel (the catalyst was separated by filtration in the case of supported catalysts). Then 20 ml of chloroform were added for better visibility of two layers of liquid (aqueous and organic phases) and therefore better separation by decantation. After decantation, the chloroform phase, containing the FAEEs (ethyl linoleate, ethyl oleate, ethyl stearate and ethyl palmitate), was recovered and the aqueous phase was washed 2 times with 10 ml of chloroform to extract all esters. Then, the chloroform was removed using a rotary evaporator and the FAEEs recovered were dried over anhydrous  $Na_2SO_4$  and concentrated under vacuum. The ester content was analyzed and quantified using a gas chromatograph. Peak identification was achieved by comparing the retention time between the samples and a standard and the compositions were calculated as wt% based on the peak areas of each component.

GC gas chromatograph (Agilent Technologies 7890A) equipped with a flame ionization detector was used under the following conditions: capillary column, carbowax (30 m x 0,25 mm) with nitrogen as a carrier gas (flow rate: 1 ml/min) and injection temperature 260 °C. Product separation was obtained using temperature ramps: from 120 to 180°C with a rate of 10°C/min, and from 180 to 260°C with a rate of 7°C/min. The temperature is then maintained at 260°C.

The ethanolysis products were identified using a GC-MS (GC 6890 plus, MSD 5973, Hewlett Packard-5MS) with HP-INNOWAX column (30 m x 0,25 mm x 0,25 µm). The mass analysis is of Quadripôle type (150°C). Purified helium was

used as the carrier gas with a flow rate of 0,5 ml min<sup>-1</sup>. The samples were diluted with hexane. Initial oven temperature was set at 90 °C for 5 min, then ramped to 280 °C at 4 °C.min<sup>-1</sup> and kept at the highest temperature for 5 min. Injector temperature and injector volume were 250 °C and 0,2 µl, respectively. The split ratio was 20:1. The ionization source (electronic impact) temperature was kept at 230 °C and that of the interface at 280 °C.

The biodiesel yield was calculated from the content of analyzed ethyl esters using the following equation [14]:

$$\text{Biodiesel Yield (\%)} = \frac{\text{mol FAEEs number} \times 100}{3 \times \text{mol oil number}}$$

## III. RESULTS AND DISCUSSION

In the sunflower oil composition presented in Table I, the major fatty acids are linoleic (C18:2) and oleic (C18:1) followed of palmitic (C16:0) and stearic (C18:0) and less than 1% of linolenic (C18:3), arachidic (C20:0) and behenic (C22:0).

TABLE I  
FATTY ACID COMPOSITION OF SUNFLOWER OIL

Fatty acid nature	Chemical formula	Form	Weight(wt.%)
palmitic	$C_{16}H_{32}O_2$	C16 :0	7,0
stearic	$C_{18}H_{36}O_2$	C18 :0	4,6
oleic	$C_{18}H_{34}O_2$	C18 :1	35,5
linoleic	$C_{18}H_{32}O_2$	C18 :2	52,5

### A. Ethanolysis and methanolysis of sunflower oil

The sunflower oil ethanolysis was carried out at 70°C with a reaction time of 3h and an alcohol/oil molar ratio of 29/1 in a homogeneous and heterogeneous phases in the presence of  $H_3PW_{12}O_{40}$  and  $H_3PW_{12}O_{40}/SiO_2$  (noted S30) respectively. For comparison, the methanolysis reaction was carried out in the same conditions.

The obtained results (Table II) from ethanolysis and methanolysis showed that both reactions are sensitive to the alcohol nature and fatty acid composition. Thus, regardless homogeneous or heterogeneous phase, the formation of methyl esters is favored to that of ethyl esters, particularly with unsaturated fatty acids. The methanolysis led to biodiesel yield superior to that of ethanolysis with 63 against 37%, in homogeneous system and 60 against 21% in heterogeneous system. The decrease in biodiesel yield would be related to the difference in molecule size between the two alcohols and to the decrease in polarity that would induce a decrease of the transesterification rate. [23].

The distribution of the different esters is also sensitive to the nature of alcohol, fatty acid and phase-type. In a homogeneous system, ethanolysis of oleic acid (C18:1) did not take place contrary to that of the methanolysis that led to the formation of  $11,41 \times 10^{-4}$  moles of methyl oleate. While,

in heterogeneous system, S30 reacted and led to  $2,39 \times 10^{-4}$  moles of ethyl oleate and  $11,78 \times 10^{-4}$  moles of methyl oleate. Methyl linoleate (C18:2) was obtained with  $35,37 \times 10^{-4}$  and  $34,01 \times 10^{-4}$  moles and ethyl linoleate with  $24,04 \times 10^{-4}$  and  $13,45 \times 10^{-4}$  moles in homogeneous and heterogeneous phases, respectively.  $5,63 \times 10^{-4}$  mole of methyl palmitate and  $4,02 \times 10^{-4}$  moles of methyl stearate and  $5,51 \times 10^{-4}$  moles of ethyl palmitate and  $3,20 \times 10^{-4}$  moles for ethyl stearate in homogeneous phase were obtained. In heterogeneous phase, the formation of these products is less favoured with  $3,80 \times 10^{-4}$  mole of methyl palmitate and  $4,02 \times 10^{-4}$  moles of methyl stearate and  $2,47 \times 10^{-4}$  moles of ethyl palmitate and  $2,18 \times 10^{-4}$  moles for ethyl stearate. From these results, it can be observed that whatever the fatty acid nature, methanolysis is more favoured than ethanolysis both in homogeneous and heterogeneous systems.

TABLE II  
 EEAGs MOLES NUMBER AND BIODIESEL YIELD (%) OBTAINED WITH METHANOLYSIS AND ETHANOLYSIS REACTION IN THE HOMOGENEOUS AND HETEROGENEOUS PHASE

Type of Catalysts	Type of Alcohol	EEAGs moles number *10 <sup>4</sup>				Biodiesel yield (%)
		C16:0	C18:0	C18 :1	C18 :2	
HPW	méthanol	5,63	4,02	11,41	35,37	63
HPW	éthanol	5,51	3,20	0,00	24,04	37
S30	méthanol	3,80	4,02	11,78	34,01	60
S30	éthanol	2,47	2,18	2,39	13,45	21

### B. Effect of ethanol/oil molar ratio

Table III shows the moles number of formed EEAGs and biodiesel yield as function of ethanol/oil molar ratio. The sunflower oil ethanolysis was carried out at 70°C in the S30 presence with a reaction time of 3h. The results showed that biodiesel yield and ester ethyl formation are sensitive to ethanol/oil molar ratio variation. Thus, the biodiesel yield increases from 11 to 29% with the increase of the ethanol/oil molar ratio from 14,5/1 to 43,5/1 and then decreases from 29 to 24% for a ratio of 58/1. The decrease in biodiesel yield observed with an excess alcohol could be explained, as in the case of methanolysis, either by poor glycerol settling and consequently poor ester-glycerol separation and/or a shift in the equilibrium towards the direction of triglyceride formation or to an emulsification effect during biodiesel washing that would be favoured with an amount alcohol increase in the reaction medium [24, 25].

The number of moles of C18:0 and C18:1 ester ethyl ( $0,67 \times 10^{-4}$  –  $2,18 \times 10^{-4}$  and  $1,39 \times 10^{-4}$  –  $2,80 \times 10^{-4}$ , respectively) appears to be little affected by the rise ethanol/oil molar ratio from 14,5/1 to 58/1 unlike to C16:0 ester ethyl that display  $13,33 \times 10^{-4}$  moles for a ethanol/oil molar ratio of 43,5/1 against  $2,47 \times 10^{-4}$  –  $7,57 \times 10^{-4}$  moles for other ethanol/oil molar ratios. C18:2 ester ethyl that presents a mole number of  $13,45 \times 10^{-4}$  for a ethanol/oil molar ratio of 29/1

against  $4,93 \times 10^{-4}$  –  $10,25 \times 10^{-4}$  for other ethanol/oil molar ratios. C18:2 ethanolysis of toward ethyl linoleate was favored with a ratio of 29/1 and that of C16:0 to ethyl palmitate, with a ratio of 43,5/1. Ethanol is very little active with respect to the transesterification of C18:0 and C18:1 fatty acids.

From these results, it can be observed that the highest biodiesel yield (29%) was obtained with a molar ratio of 43,5/1 and a reaction time of 180 min from sunflower oil ethanolysis carried out at 70°C. However, there is not a significant difference between the obtained biodiesel yields (21-29%) for molar ratios of 29/1, 43,5/1 and 58/1. for this reason, the ethanol/oil molar ratio will be fixed at 29/1 for the followed study.

TABLE III  
 EEAGs MOLES NUMBER AND BIODIESEL YIELD (%) AS A FUNCTION OF THE ALCOHOL/OIL MOLAR RATIO (CATALYST: S30, REACTION TEMPERATURE: 70°C, REACTION TIME: 3H)

C	Molar ratio alcohol / oil	EEAGs moles number *10 <sup>4</sup>				Biodiesel yields (%)
		C16:0	C18:0	C18:1	C18:2	
Effect of temperature	14,5/1	4,08	0,67	1,39	4,93	11
	29/1	2,47	2,18	2,39	13,45	21
	43,5/1	13,33	1,61	2,06	10,25	29
	58/1	7,57	1,94	2,80	11,98	24

### ture and time reaction

The figures 1 and 2 show the biodiesel yields and the number of ethyl ester moles formed, as time reaction function respectively, at 35 and 70°C. The sunflower oil ethanolysis carried out at in the presence of S30 with a molar ratio of 29/1. The variation in the reaction temperature has a strong influence on both the biodiesel yield and the number of ethyl ester moles formed. Thus, whatever the reaction time, biodiesel yields increase from 12-27% to 11-46% with the reaction temperature from 35 to 70°C. The highest biodiesel yield (46%) was obtained after 150min of ethanolysis. It is noted that with a reaction time of 90min, the highest biodiesel yield (27%) was obtained at 35°C and the lowest (11%) at 70°C. According with the observed results at 180min and 35°C, where a strong decrease of the biodiesel yield was obtained (from 24 to 12%), it is the same with 180min and 70°C (from 46 to 21%).

The results obtained highlight the importance of temperature and reaction time on the displacement of the ethanolysis equilibrium of sunflower oil. Thus, a temperature increase of 35 to 70°C also makes it possible to reach the activation energy necessary to initiate the reaction, to reduce the viscosity of the oil (immiscible reagent) and thus to make the mixing between the reagents more efficient and consequently to displace the equilibrium towards the formation of ethyl esters of fatty acids [26]. These results also show that 90 min are not enough to displace the

equilibrium to ethanolysis, a time of 180min favours, in addition of the formation of ethyl esters, to that of glycerol which induces a bad separation of these products, so it would seem that 150min is the ideal time to obtain a maximum biodiesel yield. The influence of time has already been reported by some authors [24, 27-29].

As the biodiesel yield, ester ethyl formation is sensitive to both time and temperature of sunflower ethanolysis reaction. Ethyl palmitate (C16:0) is the major product for both temperatures (35 and 70°C. At 70°C, the reaction times favoring ethyl palmitate formation are 60min ( $23,37 \times 10^{-4}$  moles), 120min ( $17,50 \times 10^{-4}$  moles) and 150min ( $27,36 \times 10^{-4}$  moles) and at 35°C, a reaction time of 150min ( $16,50 \times 10^{-4}$  moles).

Ethyl stearate (C18:0) is obtained with a moles number inferior at  $2,2 \times 10^{-4}$ . C18:1 ethanolysis was only observed for a reaction time of 30 min at 35°C and 180min at 70°C with the same moles number of  $0,24 \times 10^{-4}$ . Ethyl linoleate formation is favored at 70°C for times of reaction of 120min ( $13,31 \times 10^{-4}$  moles), 150min ( $11,86 \times 10^{-4}$  moles) and 180min ( $13,48 \times 10^{-4}$  moles). At low temperature (35°C), the number of moles does not exceed  $6 \times 10^{-4}$ , unlike ethyl palmitate, where the number of moles varies between  $7,6 \times 10^{-4}$  and  $16,5 \times 10^{-4}$ .

These results suggest that the ethanolysis of palmitic acid is more favored than that of linoleic acid; although this latter represents 52,5 against 7% of the sunflower oil composition. The biodiesel is essentially composed of ethyl palmitate.

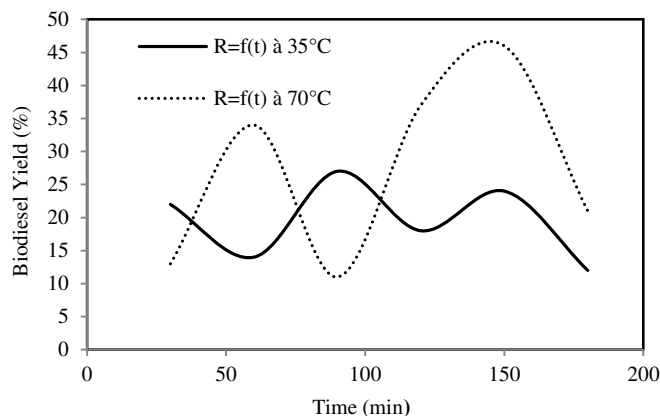


FIG. 1. BIODIESEL YIELD AS FUNCTION OF TEMPERATURE AT 35°C AND 70°C (CATALYST : S30, ETHANOL/OIL : 29/1)

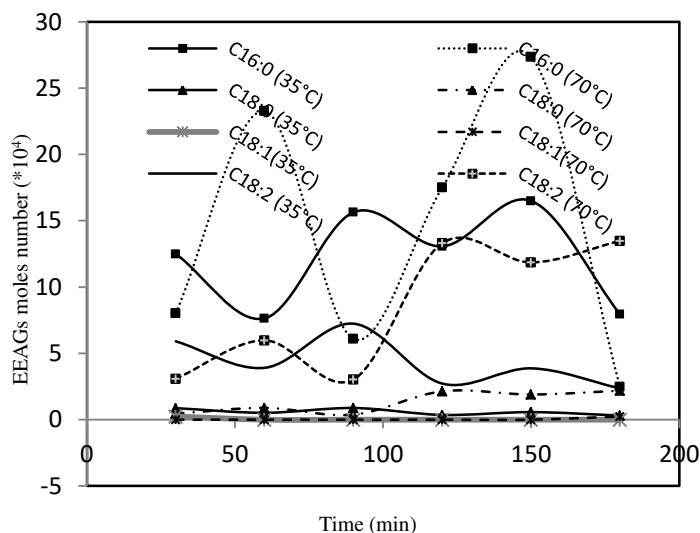


FIG. 2. EEAGS MOLES NUMBER AS A FUNCTION OF TIME (CATALYST: S30, REACTION TEMPERATURE: 70°C, ETHANOL/OIL: 29/1)

#### D. Effect of the nature catalyst

For comparison, both  $H_3PW_{12}O_{40}$  and  $H_4SiW_{12}O_{40}$  as bulk and supported on silica with wt30% noted S30 and S'30, respectively, were tested in the sunflower oil ethanolysis at 70°C with a reaction time of 3 hours and an alcohol/oil ratio varying between 14,5/1 and 58/1. Table IV displays the biodiesel yields and the number of ethyl ester moles obtained from the ethanolysis of different fatty acids composing the sunflower oil.

The biodiesel yield obtained with an alcohol/oil ratio of 29/1, in the presence of  $H_4SiW_{12}O_{40}$  is higher than that obtained in the presence of  $H_3PW_{12}O_{40}$ , with 55 versus 37%, suggesting that transesterification depends much more on the proton number than on the acidity strength. It is known that  $H_3PW_{12}O_{40}$  is a stronger acid than  $H_4SiW_{12}O_{40}$  [30-32]. This latter is also very active towards palmitic acid ethanolysis compared to that of  $H_3PW_{12}O_{40}$ , with  $27,78 \times 10^{-4}$  moles against  $5,51 \times 10^{-4}$  moles of ethyl palmitate, while they have the same catalytic behavior towards linoleic acid ethanolysis, with an ethyl linoleate moles number of  $18,52 \times 10^{-4}$  and a similar catalytic behavior towards stearic acid ethanolysis, with an ethyl stearate moles number of  $2,70 \times 10^{-4}$  and  $3,19 \times 10^{-4}$ .

In heterogeneous systems, S30 and S'30 led to biodiesel yields inferior to those of  $H_3PW_{12}O_{40}$  and  $H_4SiW_{12}O_{40}$ , bulk, respectively, with 21 and 19% against 37 and 55%. Expected result, given that acid sites active in homogeneous phase are more accessible to reagents than those in heterogeneous phase.

Supported on silica, both heteropolyacids, were also found to be less active towards the ethanolysis of C16:0, C18:0, C18:1 and C18:2 fatty acids. The difference in the number of moles of ethyl esters corresponding to C16:0 and C18:2 acids is more pronounced in the case of the  $H_4SiW_{12}O_{40}$  bulk use with  $27,78 \times 10^{-4}$  moles and  $18,52 \times 10^{-4}$  moles against  $8,16 \times 10^{-4}$  moles and  $7,86 \times 10^{-4}$  moles,



respectively, for S'30. This observation seems to suggest that the ethanolysis of both acids (C16:0 and C18:2) is more favored when the protons are more available.

While, in the case of the  $H_3PW_{12}O_{40}$ , similar behavior towards of the formation of ethyl esters regardless of fatty acid nature was observed for bulk and supported (S30).

Supported heteropolyacids were tested at different alcohol/oil molar ratios. Excepted for the ratio of 58/1, where the biodiesel yield obtained with S30 is superior to that obtained with S'30 (24 against 16%), similar biodiesel yields were observed for both supported catalysts, for each ratio (11-12% for 14,5/1, 21-19 for 29/1, and 29 for 43,5/1). The palmitic acid ethanolysis is more favored in the presence of S'30 compared to S30, with  $5,99 \times 10^{-4}$  against  $4,08 \times 10^{-4}$ ,  $8,16 \times 10^{-4}$  against  $5,51 \times 10^{-4}$  and  $16,31 \times 10^{-4}$  against  $13,33 \times 10^{-4}$  of ethyl palmitate moles for alcohol/oil ratios of 14,5/1, 29/1 and 43,50/1, respectively. However, the opposite was observed for the alcohol/oil ratio of 58/1 ( $7,57 \times 10^{-4}$  against  $1,01 \times 10^{-4}$  of ethyl palmitate moles).

Contrarily, to the ethyl palmitate formation, that of ethyl linoleate is promoted by S30 catalyst, whatever the alcohol/oil ratio ( $4,9 \times 10^{-4}$  -  $13,45 \times 10^{-4}$  against  $3,75 \times 10^{-4}$  -  $11,92 \times 10^{-4}$  ethyl linoleate moles). S'30 is inactive and S30 is few active towards the oleic acid ethanolysis. S30 and S'30 have a similar catalytic behavior for stearic acid ethanolysis with ethyl stearate moles number inferior at  $3,2 \times 10^{-4}$ .

TABLE IV  
EEAGS MOLES NUMBER AND BIODIESEL YIELD (%) AS A FUNCTION OF THE CATALYST COMPOSITION NATURE AND ALCOHOL/OIL MOLAR RATIO (REACTION TEMPERATURE: 70°C, REACTION TIME: 3H)

Molar ratio ethanol /oil	Catalyst	EEAGs moles number * 10 <sup>4</sup>				Biodiesel yield (%)
		C16:0	C18:0	C18:1	C18:2	
14,5/1	S30	4,08	0,67	1,39	4,93	11
	S'30	5,99	0,56	0	3,75	12
29/1	$H_3PW_{12}O_{40}$	5,51	3,19	0	18,52	37
	S30	2,47	2,18	2,39	13,45	21
	$H_4SiW_{12}O_{40}$	27,78	2,70	0,45	18,52	55
	S'30	8,16	1,16	0	7,86	19
43,5/1	S30	13,33	1,61	2,06	10,25	29
	S'30	16,31	2,12	0	7,37	29
58/1	S30	7,57	1,94	2,80	11,98	24
	S'30	1,01	1,72	0	11,92	16

#### IV. CONCLUSION

The biodiesel production, composed of alkyl esters, from sunflower oil transesterification was carried out using  $H_3PW_{12}O_{40}$  and  $H_4SiW_{12}O_{40}$  as bulk and supported on silica with 30wt% (noted S30 and S'30 respectively), as catalyst and ethanol as alcohol. The biodiesel yield and the ethanolysis activity of fatty acids that constitute the oil are very sensitive to the to temperature and time reaction an substrat/ethanol ratio. For comparison, the methanolysis was studied bulk and  $H_3PW_{12}O_{40}$ .

The bulk and supported heteropolyacids proved to be active catalysts in the transesterification of sunflower oil. Regardless homogeneous ( $H_3PW_{12}O_{40}$ ) or heterogeneous ( $H_3PW_{12}O_{40}/SiO_2$ ) phase, the formation of methyl esters is favored to that of ethyl esters, whatever the fatty acid nature.

Both acids in bulk form are more effective for sunflower ethanolysis than those in supported form and the SiW based catalyst is more effective than those based PW.

The ethanolysis of palmitic acid (C16:0) is more favored than those of C18:0 acids. Therefore, ethyl palmitate is the main component in the biodiesel.

#### ACKNOWLEDGMENT

The author would like to thank Pr. Chérifa Rabia, for its help and support in making this work possible. This work is carried out in the Natural Gas Laboratory, Faculty of Chemistry, University of Science and Technology Houari Boumediène (USTHB), Algiers. Funded by the Minister of Research.

#### V. REFERENCES

- [1] Ming-Chien Hsiao b, Chin-Chiuan Lin a, Yung-Hung Chang. Microwave irradiation-assisted transesterification of soybean oil to biodiesel catalyzed by nanopowder calcium oxide, Fuel 90 (2011) 1963–1967.
- [2] Oguzhan Ilgen. Dolomite as a heterogeneous catalyst for transesterification of canola oil. Fuel Processing Technology 92 (2011) 452–455.
- [3] Shuang Zhao, Shengli Niu, Hwei Yu, Yilin Ning, Xiangyu Zhang, Ximing Li, Yujiao Zhang, Chunmei Lu, Kuihua Han. Experimental investigation on biodiesel production through transesterification promoted by the La-dolomite catalyst. Fuel 257 (2019) 116092.
- [4] I. Lukic', J. Krstic', D. Jovanovic', D. Skala. Alumina/silica supported  $K_2CO_3$  as a catalyst for biodiesel synthesis from sunflower oil. Bioresource Technology 100 (2009) 4690–4696.
- [5] Feng Guo a,b, Ning-Ning Wei a, Zhi-Long Xiu a, Zhen Fang b is within the limits prescribed by the standard. Transesterification mechanism of soybean oil to biodiesel catalyzed by calcined sodium silicate. Fuel 93 (2012) 468–472.
- [6] Amornmart Chantrasaa, Nisarath Phlernjaia, James G. Goodwin Kinetics of hydrotalcite catalyzed transesterification of tricaprilyn and methanol for biodiesel synthesis. Jr. Chemical Engineering Journal 168 (2011) 333–340.
- [7] Petchmala A, Laosiripojana N, Jongsomjit B, Goto M, Panpranot J, Mekasuwandumrong O, et al. Transesterification of palm oil and esterification of palm fatty acid in near and super-critical methanol with  $SO_4-ZrO_2$  catalysts. Fuel 89 (2010) 2387–3239.

- [8] Jiménez-López A, Jiménez-Morales I, Santamaría-González J, Maireles-Torres P. Biodiesel production from sunflower oil by tungsten oxide supported on zirconium doped MCM-41 silica. *Journal of Molecular Catalysis A: Chemical* 335 (2011) 205–209.
- [9] S. Furuta, H. Matsushashi, K. Arata. Biodiesel fuel production with solid superacid catalysis in fixed bed reactor under atmospheric pressure. *Catalysis Communications* 5 (2004) 721–723.
- [10] B.Y. Giri, K. Narasimha Rao, B.L.A. Prabhavathi Devi, N. Lingaiah, I. Suryanarayana, R.B.N. Prasad, P.S. Sai Prasad. Esterification of palmitic acid on the ammonium salt of 12-tungstophosphoric acid: The influence of partial proton exchange on the activity of the catalyst. *Catalysis Communications* 12 (2005) 788-792
- [11] Hee-Yong Shin, Seung-Hwan An, Rizwan Sheikh, Yeung Ho Park, Seong-Youl Bae. Transesterification of used vegetable oils with a Cs-doped heteropolyacid catalyst in supercritical methanol. *Fuel* 96 (2012) 572–578.
- [12] A. Zieba, L. Matachowski, J. Gurgul, E. Bielanska, A. Drelinkiewicz. Transesterification reaction of triglycerides in the presence of Ag-doped  $H_3PW_{12}O_{40}$ . *Journal of Molecular Catalysis A: Chemical* 316 (2010) 30–44.
- [13] L. Pesaresi a,c, D.R. Brown b, A.F. Lee a, J.M. Montero a, H. Williams b, K. Wilson a. Cs-doped  $H_4SiW_{12}O_{40}$  catalysts for biodiesel applications. *Applied Catalysis A: General* 360 (2009) 50–58.
- [14] Yasmina Idrissou, Tassadit Mazari, Siham Benadji, Maamar Hamdi and Cherifa Rabia. Homogeneous and heterogeneous sunflower oil methanolysis over 12-tungstophosphoric, sulfuric and boric acids. *Reaction Kinetics, Mechanisms and Catalysis* 119 (1) (2016) 291-304.
- [15] Srilatha K, Lingaiah N, Prabhavathi Devi BLA, Prasad RBN, Venkateswar S, Sai Prasad PS. Esterification of free fatty acids for biodiesel production over heteropoly tungstate supported on niobia catalysts. *Applied Catalysis A: General* 365 (2009) 28-33.
- [16] Sukriti Singh, Anjali Patel. Mono lacunary phosphotungstate anchored to MCM-41 as recyclable catalyst for biodiesel production via transesterification of waste cooking oil. *Fuel* 159 (2015) 720–727.
- [17] Boehman, L. Biodiesel production and processing. *Fuel Processing Technology* 86 (2005) 1057–1058.
- [18] Makareviciene, V., Janulis, P. Environmental effect of rapeseed oil ethyl ester. *Renewable Energy* 28 (2003) 2395–2403.
- [19] Clark S.J, Wagner L, Schrock M.D, Pienaar P.G. Methyl and ethyl soybean esters as renewable fuels for diesel engines. *Journal American Oil Chemical Society* 61(1984) 1632–1638.
- [20] Encinar, J.M, González, J.F, Rodríguez-Reinares, A. Ethanolysis of used frying oil. Biodiesel preparation and characterization. *Fuel Processing Technology* 88 (2007) 513–522.
- [21] Olusegun D. Samue, Modestus O. Okwu, Semiu T. Amosun, Tikendra Nath Verma, Sunday A. Afolalu. Production of fatty acid ethyl esters from rubber seed oil in hydrodynamic cavitation reactor: Study of reaction parameters and some fuel properties. *Industrial Crops & Products* 141 (2019) 111658.
- [22] Pablo D. Rocha, Leandro S. Oliveira, Adriana S. Franca. Sulfonated activated carbon from corncobs as heterogeneous catalysts for biodiesel production using microwave-assisted transesterification. *Renewable Energy* 143 (2019) 1710-1716.
- [23] Ji et al (2006).
- [24] A. Phan et T. Phan. Biodiesel production from waste cooking oils. *Fuel* 87 (2008) 3490-3496.
- [25] H. Berna, Thèse Doctorat. Université Claude Bernard – Lyon1 (2009).
- [26] Zelatical J. Predojevic. The production of biodiesel from waste frying oils : A comparison of different purification steps. *Fuel* 87 (2008) 3522-3528.
- [27] S. AWAD, Thèse Doctorat. Université de NANTES (2011).
- [28] Alok Kumar Tiwari, Akhilesh Kumar, Hifjur Raheman. Biodiesel production from jatropha oil (*Jatropha curcas*) with high free fatty acids: An optimized process. *Biomass and Bioenergy* 3 (2007) 569-575.
- [29] H. Raheman, S.V. Ghadge. Performance of compression ignition engine with mahua (*Madhuca indica*) biodiesel. *Fuel* 86 (2007) 2568-2573.
- [30] M. Misono. Heterogeneous Catalysis by Heteropoly Compounds of Molybdenum and Tungsten. *Catalysis Reviews Science and Engineering* 29 (1987) 269-321.
- [31] T. Okuhara, N. Mizuno, M. Misono. Catalytic Chemistry of Heteropoly Compounds. *Advances in Catalysis* 41 (1996) 113-252.
- [32] IV. Kozhevnikov. Catalysis by HeteropolyAcids and Multicomponent Polyoxometalates in Liquid-Phase Reactions. *Chemical Review* 98 (1998) 171-198.



# Modeling of transport phenomena in laser welding of dissimilar metals Al/Mg

Sabrine Ben Halim<sup>1</sup>, Sana Bannour, Kamel Abderrazek, Wassim Kriaa, Michel Autric<sup>2</sup>

<sup>1</sup>Laboratoire de Thermique et Thermodynamique des Procédés Industriels, Ecole Nationale d'Ingénieurs  
Monastir, Tunisia

sabrinebenhalim8@gmail.com

kriaawass@yahoo.fr

<sup>2</sup>Aix-Marseille Univ, CNRS, IUSTI  
Marseille, France

michel.autric@univ-amu.fr

**Abstract.** The laser welding appears a promising process to several industrial fields due to the possibility of assembly of dissimilar materials while preserving the characteristics of this technology: low heat input, narrow and deep weld bead, high welding speed, etc. In this study, the transport phenomena (heat transfer, fluid flow and species distributions) are numerically modeling for the case of laser welding of dissimilar metals Al/Mg with the finite volume software, Ansys-Fluent. In order to understand the complex physical phenomena involved, a three-dimensional transient model has been developed based on the solution of the equations of mass, momentum, energy conservation and solute transport in weld pool. Transient temperature distribution and thermal cycles at different locations are obtained. The distribution of alloy elements and composition profile (Al and Mg) are also present. It is found that the heat transfer and the mass transport are two main phenomena in the formation of a heterogeneous mixture in the fusion zone. Corresponding experiments are performed using the same parameters as in the computations, showing a good qualitative agreement between the two results.

**Keywords:** dissimilar metals, numerical modeling, heat transfer, fluid flow, mass transport.

## I. INTRODUCTION

Nowadays, several manufacturers in the automotive and aeronautics fields have studied the use of light metal alloys in different welding processes. This would allow them to reduce the weight of their mobile gear, or the reduction of energy consumed, and therefore the emission of gaseous pollutants. Recently, the use of magnesium and aluminum alloys has invaded the transportation industries thanks to their interesting characteristics. Aluminum alloys are characterized by low density, good corrosion resistance, high thermal and electrical conductivity [1, 2], potential recovery, durability, inexpensive maintenance [3] and recyclability [4]. For Magnesium alloys, they have high strength [5], good moldability, hot forming and recycling [6]. However, it has been found that the assembly of dissimilar metals Al and Mg presents difficulties because of

the difference in thermal and physical properties, the formation of brittle intermetallic compounds extremely fragile in the transition zone between the two materials and the presence of cracks in the joint [7,8].

Several dissimilar material welding techniques such as electron beam welding [9], MIG welding [10, 11], resistance spot welding [12], bonding diffusion [13, 14] have been studied. Other studies have focused on laser welding. For example, Chen et al. [15] studied experimentally and numerically the laser welding of Titanium / Aluminum joints. They have highlighted more particularly the inhomogeneous mixture which can be formed during the welding process. G. Casalino et al. [16] studied numerically fiber laser welding of Ti6Al4V and AA5754-T40 materials using the Ansys Parametric Design Language (APDL). They studied the effect of some welding conditions on thermal behavior.

In this paper, numerical and experimental studies of laser welding of dissimilar Aluminum / Magnesium alloys have been carried out. For the simulation, a three-dimensional model was developed using Ansys, Fluent software to predict weld bead dimensions and to simulate heat transfer and mass transport during laser welding and then results were discussed. It also gives an idea of the mass contents of Aluminum and Magnesium in different areas of the weld.

## II. EXPERIMENTAL PROCEDURE

In this modeling work, the Aluminum alloy (A5754) and the Magnesium alloy (AZ31) were used as base materials and were arranged one on the other, Figure 1. The chemical composition and the thermo-Physical properties of the base materials are shown in table I and table II, respectively. The experiments were carried out with a continuous Yb: YAG laser with a wavelength of 1032 nm. The radius of the laser beam is 0.45 mm [17]. An Argon shielding gas with a flow rate of 20 l / min was used to protect the weld bead from oxidation. The operating parameters adopted in this study are shown in Table III.

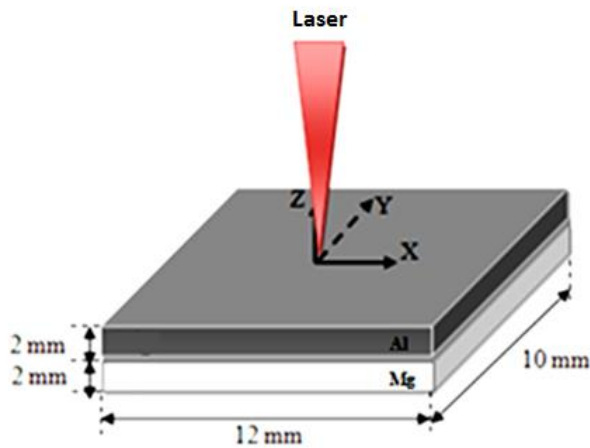


Fig.1 Lap joint configuration Al/Mg

TABLE I. Chemical composition of base metals

Chemical Elements	Mg	Al	Mn	Zn	Fe	Cu	Si
Magnesium	96.67	2.65	0.17	0.52	...	...	...
Aluminum	2.68	96.63	...	...	0.4	0.14	0.13

TABLE II. Characteristics of base materials

Property	Magnesium	Aluminum
Density (solid) [kg/m <sup>3</sup> ]	1810	2880
Thermal conductivity (solid) [W/m·K]	146	202
Specific heat (solid) [J/Kg·K]	1020	728
Solidus temperature [k]	880	740
Liquidus temperature[k]	933	923

TABLE III. Welding parameters adopted

Configuration	Laser power (w)	Welding velocity (m/s)
Al/Mg	2500	0.66

### III. NUMERICAL SIMULATION

Heat transfer, fluid flow, and mass transport during Laser lap welding of dissimilar couple Aluminum / Magnesium were simulated by 3D transient numerical model developed using ANSYS FLUENT software. The domain used for modeling is  $12 \times 10 \times 4 \text{ mm}^3$  (length  $\times$  width  $\times$  thickness). The calculation

was carried out with a mesh composed of 1170,000 cells. We have adopted a uniform mesh over the entire area of computation and refined mesh near the heat source. The workpiece moves with a constant speed  $U_x$ .

The assumptions adopted are as follows:

- The thermo-physical properties vary with temperature and mass fraction.
- Fluid flow in the weld pool is incompressible and laminar.
- The model is unsteady.
- The free surface of the weld pool is flat.

### IV. EQUATIONS

This study is based on the resolution of conservation equations presented as follows [9]:

Mass conservation

$$\frac{\partial(\rho)}{\partial t} + \nabla \cdot (\rho \vec{v}) = 0 \quad (1)$$

Where  $\vec{v}$  is the speed following the respective directions.

Momentum conservation

$$\frac{\partial(\rho \vec{v})}{\partial t} + \nabla \cdot (\rho \vec{v} \vec{v}) = -\nabla p + \nabla \cdot (\mu \nabla \vec{v}) + \rho \vec{g} + \vec{S} \quad (2)$$

Where  $p$  is the pressure,  $\mu$  is the viscosity and  $\vec{S}$  is the source term.

Energy conservation

$$\frac{\partial(\rho H)}{\partial t} + \nabla \cdot (\rho \vec{v} H) = \nabla \cdot (k \nabla T) + S_E \quad (3)$$

Where  $H$  is enthalpy and  $S_E$  is the energy source term.

Species conservation

$$\frac{\partial(\rho C)}{\partial t} + \nabla \cdot (\rho \vec{v} C) = \nabla \cdot (\rho D \nabla C) \quad (4)$$

Where  $C$  is the concentration and  $D$  is the mass diffusivity.

The heat transfer and fluid flow models were coupled with a melting and solidification model. Melting and solidification of the weld pool was simulated with an enthalpy-porosity formulation. It indicates the liquid fraction in the

welding pool. The mushy region (partially solidified region) was treated as a porous medium.

The momentum sink due to the reduced porosity in the mushy zone can be expressed as:

$$\vec{S} = - \left( \frac{A(1-\beta)^2}{\beta^3 + b} \right) \vec{v} \quad (5)$$

Where  $\varepsilon$  is the liquid fraction,  $A$  is the mushy zone constant (a large number, say  $10^8$ ) and  $b$  is an arbitrary small number to prevent division by zero ( $10^{-3}$ ).

#### V. BOUNDARY AND INITIAL CONDITIONS

At time  $t = 0$ , the entire domain was considered to be in the solid state with a temperature of 300 K and the gravitational acceleration was assumed to be  $9.81 \text{ ms}^{-2}$ ,

At the flat free surface of the liquid, shear force due to surface tension (Marangoni force) is expressed as:

$$\mu \frac{du}{dz} = \beta \frac{\partial \sigma}{\partial T} \frac{\partial T}{\partial x} + \beta \frac{\partial \sigma}{\partial C} \frac{\partial C}{\partial x} \quad (6)$$

$$\mu \frac{dv}{dz} = \beta \frac{\partial \sigma}{\partial T} \frac{\partial T}{\partial y} + \beta \frac{\partial \sigma}{\partial C} \frac{\partial C}{\partial y} \quad (7)$$

Where  $\sigma_T$  is thermal surface tension coefficient.

The heat loss by convection heat transfer and radiation is given by,

$$q_{\text{rad}} = \varepsilon \sigma (T^4 - T_0^4) \quad (8)$$

$$q_{\text{conv}} = h_{\text{conv}} (T - T_0) \quad (9)$$

Where  $h_{\text{conv}}$  is the convection coefficient,  $\sigma$  is the Stefan-Boltzmann constant and  $\varepsilon$  is the emissivity of the surface radiation.

#### VI. RESULTS AND DISCUSSION

To validate the model developed in this study, the simulated weld bead geometry was compared to that obtained experimentally. The weld bead profile is in good agreement with the experimental results, as shown in Figure 1.

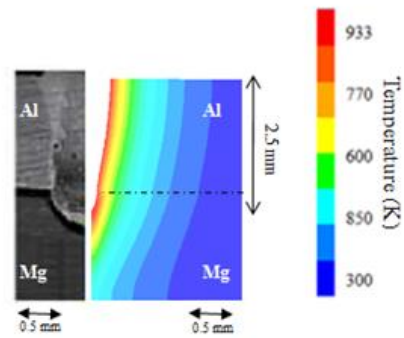


Fig. 1 Comparison of weld bead profile with calculated and experimental results

Figure 2 shows the distribution of the isotherms of the surfaces of a dissimilar weld joint. These isotherms are connected to thermal fusion-solidification cycles characteristic of laser welding. From this figure, we distinguish the melt and basic metal zones. The discontinuity of the physical properties of the base materials such as the melting temperature, the specific heat capacity and the thermal diffusivity affect the dimensions of the weld pool, especially the depth of penetration.

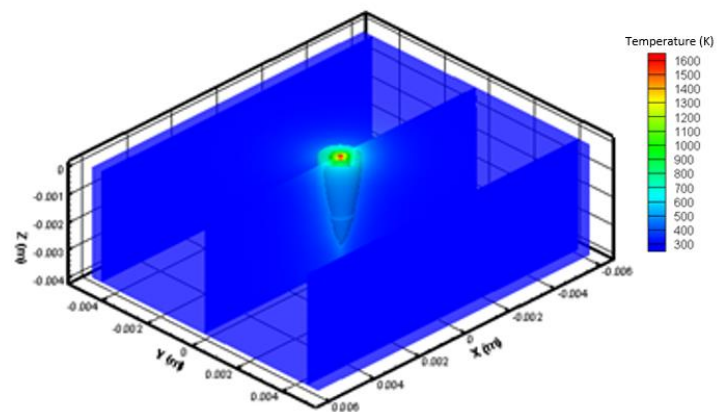


Fig. 2 Isotherms in the workpiece

The hydrodynamic movements shown in Figure 3 are important at the free surface than at the interface between the two metals. This is due to the dominant Marangoni force at the surface of the weld pool where the fluid velocity is maximum. This force depends strongly on the gradient of the surface tension which itself depends on the temperature gradient at the laser-material impact point.

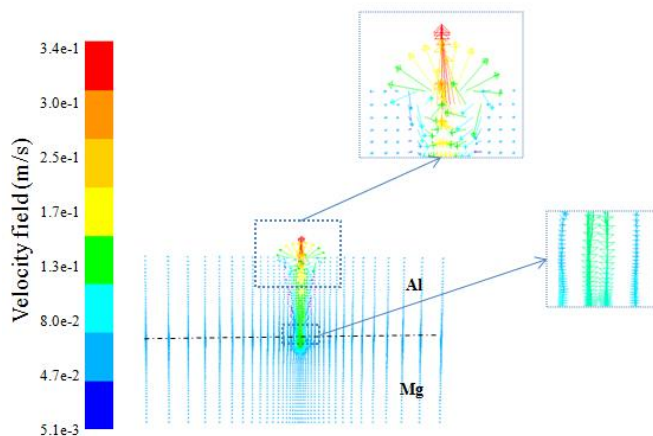


Fig. 3 Contour of velocity field vectors: view (y-z)

Figure 4 shows the evolution of the mass fraction of Aluminum during laser welding. The formation of a heterogeneous mixing zone formed both of Aluminum and Magnesium where the molten Al descends into the bottom of the weld bead through the hydrodynamic movements generated in the molten pool. In addition, the diffusion phenomenon of Al and Mg elements contributes to the transport of the molten metal.

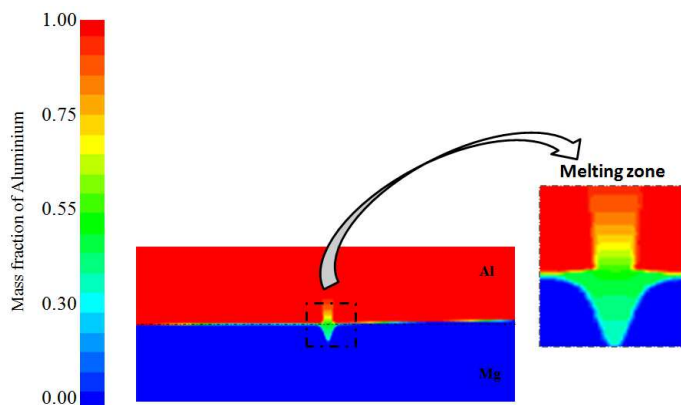


Fig. 4 Cross section of the mass fraction of Aluminum

Figure 5 shows the chemical distribution of Aluminum and Magnesium in the fusion zone (L). This figure confirms what has been shown previously; there is a variation of Aluminum composition in the weld bead. The mass percentage of Al decreases as it passes from base metal (100%) to the melting zone. For the Magnesium content, it increases in the fusion zone. This is due to the hydrodynamic movements created in

the molten pool. The results of the numerical study are in agreement with the experimental results.

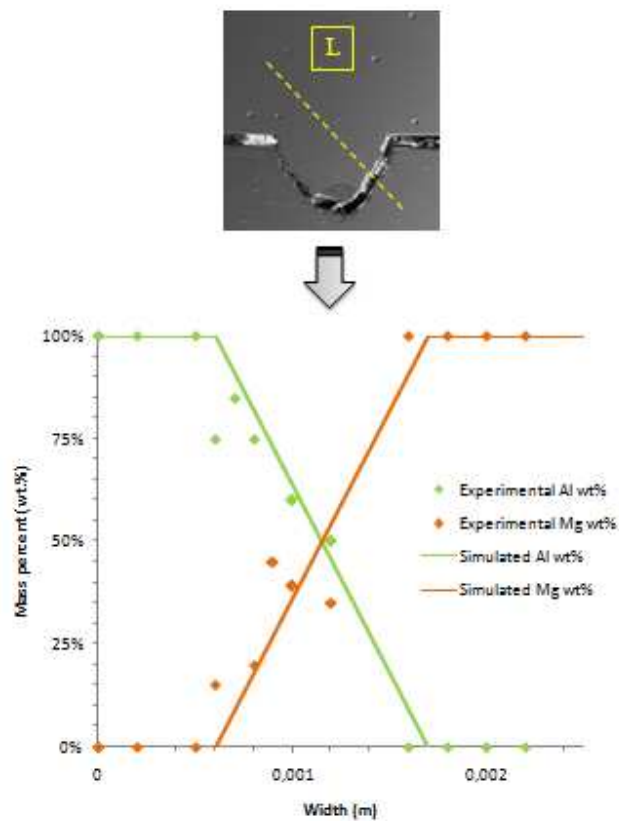


Fig. 5 Experimental and simulated profile line of Mg and Al distributions

## VII. CONCLUSION

This paper presents a study on heterogeneous welding between Aluminum alloys and Magnesium alloys. The numerical model makes it possible to predict the thermal cycle, the alloying elements distribution and the geometry of the weld bead. The experimental results validate the profile of the weld seam in terms of depth of penetration and the distribution of chemical elements from numerical simulation. They agree well with those obtained numerically.

## REFERENCES

- [1] R. S. Rana, Rajesh Purohit, and S Das, Reviews on the Influences of Alloying elements on the Microstructure and Mechanical Properties of Aluminium Alloys and Aluminium Alloy Composites, International Journal of Scientific and Research Publications, 2 (2012) Issue 6.
- [2] Toros S, Ozturk F and Kacar I 2008 J. Mater. Process. Tech. 207(1-3) 1-12
- [3] Hayat F 2011 Mater. Design. 32(4) 2476 – 2484.
- [4] Casalino G 2007 J. Mater. Process. Tech. 191(1-3) 106-110.

- [5] Liu C C, Chen D L, Bhole S, Cao X and Jahazi M 2009 *Mater. Charact.* 60(5) 370-376.
- [6] Carrino L., Squillace A., Paradiso V., Ciliberto S., Montuori M., Superplastic forming of friction stir processed magnesium alloys for aeronautical applications: A modeling approach, *Materials Science Forum* 735 (2013) 180-191.
- [7] Liu C C, Chen D L, Bhole S, Cao X and Jahazi M 2009 *Mater. Charact.* 60 (5) 370-376
- [8] Liu L M, Tan J H, Zhao L M and Liu X J 2008 *Mater. Charact.* 59(4) 479-483.
- [9] C.-T. Chi, C.-G. Chao, T.-F. Liu, C.-H. Lee, Aluminium element effect for electron beam welding of similar and dissimilar Magnesium–Aluminium–Zinc alloys, *Scr. Mater.*, 56 (2007) 733–736.
- [10] M Ishak and M R Islam. Weldability of A7075-T651 and AZ31B dissimilar alloys by MIG welding method based on welding appearances, *Journal of Physics*, 2014.
- [11] Zhang H T and Song J Q 2011 *Mater. Lett.* 65(21-22) 3292-3294.
- [12] F. Hayat, The effects of the welding current on heat input, nugget geometry, and the mechanical and fractural properties of resistance spot welding on Mg/Al dissimilar materials, *Mater. Des.*, 32 (2011) 2476–2484.
- [13] Jian Zhang, GuoqiangLuo, Yiyu Wang, QiangShen, Lianmeng Zhang, An investigation on diffusion bonding of aluminum and magnesium using a Ni interlayer, *Materials Letters* 83 (2012) 189–191.
- [14] Carrino L., Paradiso V., Franchitti S., Squillace A., Russo S., Superplastic forming/diffusion bonding of a titanium alloy for the realization of an aircraft structural component in multi-sheets configuration, *Key Engineering Materials* 504-506 (2012) 717-722.
- [15] Chen S, Li L, Chen Y, Huang J. Joining mechanism of Ti/Al dissimilar alloys during laser welding-brazing process, *Journal of Alloys and Compounds*, 891–898, 2011.
- [16] G. Casalino, M. Mortello, P. Peyre. FEM analysis of fiber laser welding of Titanium and Aluminum, *Procedia CIRP*, 992 – 997, 2016.
- [17] S. Bannour, K. Abderrazak, S. Mattei, J. E. Masse, M. Autric, H. Mhiri. The influence of position in overlap joints of Mg and Al alloys on microstructure and hardness of laser welds, *journal of laser applications*, 2013.



# Feasibility study of a solar brackish water desalination system plant in Algeria.

Mohamed Abbas<sup>1</sup>, Asma Adda<sup>2</sup>, Djilali Tassalit<sup>1</sup>, Hanane Aburdeh<sup>1</sup> and Zahia Tgrine<sup>1</sup>

<sup>1</sup> *Unité de Développement des Equipements Solaires. UDES. /Centre de Développement des Energies Renouvelables .CDER. Bou Ismail.42415.w.Tipaza.Algérie*

<sup>2</sup> *Yahia Fares University, Medea, Algeria*

Email : [abbasdreams@gmail.com](mailto:abbasdreams@gmail.com)

**Abstract**—The southern regions in Algeria are suffering from fresh water shortage due to their climate severity and the geographic situation. These areas have access to brackish groundwater and significant potential of solar energy. The combination of solar energy with desalination processes, such as reverse osmosis systems, presents possible solution to satisfy the fresh water needs for the population living in these remote areas. This paper presents a technical and economic evaluation of a small-scale brackish water reverse osmosis desalination unit powered by solar photovoltaic systems for fresh water production under Algerian arid climate conditions. In the first part of this paper, a mathematic model has been developed for design and sizing the photovoltaic field, taking into account two configuration; power system with batteries and without batteries. The photovoltaic system model is coupled to reverse osmosis model to determine the overall system performance (water production, Specific Energy Consumption...) and an optimization is performed in order to determine the suitable configuration. In the second part, the economic feasibility study of use solar energy has been done using some economic parameters such as, Levelized Water Costs (LCOW) Net Present Value (NPV) and Internal Rate of Return (IRR). The investigation also includes a discussion on the sensitivity of cost of unit of produced fresh water to some parameters such as the useful life of reverse osmosis system, cost of solar photovoltaic pannels and other associated parameters. The results of this investigation can be used also as indicators to identify the best locations for solar powered desalination plant implementation for fresh water production in Algeria.

**Keywords:** Desalination, Brackish water, Solar Energy, Photovoltaic.

## 1. INTRODUCTION

Algeria, like other southern Mediterranean countries suffers from the water shortage that will worsen in the years to come, with more than 42 million inhabitants and it's among most exposed to water stress by 2030. With less than 500 m<sup>3</sup> per inhabitant per year of drinking water, Algeria has less than 50% of the theoretical scarcity threshold set by the World Bank at 1000 m<sup>3</sup> per inhabitant per year [1,2]. Desalination of seawater or brackish water is one of the possible responses to adapt to the growing scarcity of water resources. Currently, Reverse osmosis membrane

technology dominates the industry of desalination and brackish water treatment in Algeria and in all world countries. The Algerian government has launched a huge desalination program to build 13 big desalination plants in several regions of northern Algeria and even in the south for the brackish water treatment. For the moment, the desalination of seawater contributes, in Algeria, to 17% in the national supply of drinking water and we will exceed 25% once the units in progress put into service [1,2]. However, while desalination techniques are now well controlled, their implementation requires large amounts of energy, in the form of heat or electricity, costly and potential sources of greenhouse gas emissions. In addition to the coastal areas, these features allow a very fast installation and a perfect adaptation to the specific needs of arid and semi-arid regions suffering from a deficiency of drinking water, emphasizes. In the last few years, the solar power desalination technology of brackish water being considered as one of the promising way for fresh water production in order to satisfy the water demand growing. In this work, we present a technical and economic evaluation of a small-scale brackish water reverse osmosis desalination unit powered by solar photovoltaic systems RO/PV for fresh water production under Algerian arid climate conditions. The coupling of RO/PV using the MATLAB software has been modelled. The modelling has to be done, taking into account the types of systems used, as well as the territorial, environmental and economic stakes involved in their coupling.

## 2. WATER RESOURCES STATE IN ALGERIA

Due to its geographic location in the MENA region, Algeria is a water scare country. For this reason, it is considered among the poorest countries in Africa and in the World in term of water resources. The water is obtained from different sources which include rainfall, surface water resources (dams and very small rivers), non-conventional water resources, i.e. desalination and wastewater stations, and underground water resources. The Algerian territory is divided into five hydro-geographic basins comprising the 19 watersheds in the country. The water potentials in Algeria are estimated at 15.37 Billion Cubic Meters (BCM) annually, distributed as follow:

\* 10 BCM annually in the north, of which 7.4 BCM of surface water and 2.6 BCM of groundwater (80% are mobilized by wells and boreholes)

\* 5.37 BCM annually in the south, of which 0.37 BCM of surface water and 5 BCM of groundwater.

Hereinafter, a brief overview of the available water resources is provided ( only desalination status):

### 3. DESALINATION IN ALGERIA

In order to take advantages of its coastline stretching over 1200 km, Algeria has moved towards mobilization of non-conventional water resources using seawater desalination and brackish water demineralization process.

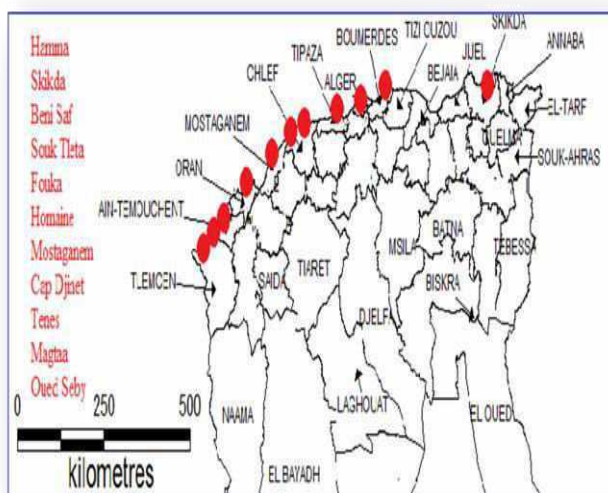


Figure 1. Desalination plants Map in Algeria

Since 2000, Desalination has become an imperative and inevitable solution for Algeria to overcome its current shortage of potable water. For this, more than 11 seawater desalination Mega plants have been installed in the coaster region of the country with a total daily capacity of 21.1 million m3, see figure 1.

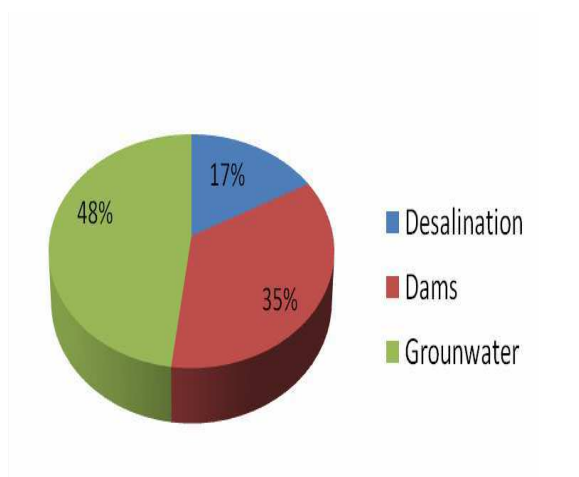


Figure 2. Water consumption resources contained in Algeria

The daily capacity of these plants ranges between 100,000 and 500,000 m3 each, in addition to the 21 monobloc desalination plants with an daily average capacity of 2500 to 5000 m3 each and a total daily capacity of 57,500 m3.

It's worth mentioning that the desalination plants in Algeria supply nearly 15% of total water consumption per year, as indicated on figure 6. The total water production is estimated at 8.24 Million per day or 3.3 Billion M3 per year.

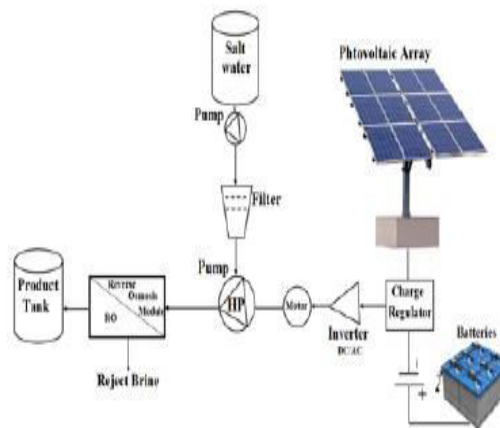


Figure 3. Schematic diagram of the PV powered RO system

## 4. MATERIALS AND METHODS

### 4.1. PV/RO modeling

To determine the performance of the proposed system (figure 3), a global model of the water transformation (brackish water-drink water) and the solar field is performed in MATLAB in which the system is divided into two components. The first is for reverse osmosis unit while the second one is dedicated to solar photovoltaic pannels and batteries.

The required energy production by the desalination system is given by :

$$P_{PV / RO} = \frac{P_p}{\frac{t_{hd}}{24} + \left(1 - \frac{t_{hd}}{24}\right) a_{bch} a_{bcdh}}$$

( kWh/day)

Where :

$P_p$  Energy produced by solar cells (kWh),

$t_{hd}$  : Average hours of daylight,  $a_{bch}$  : The charging efficiency of the battery,  $a_{bcdh}$  : the discharging efficiency of the battery .

In our case we took  $a_{bch} = 0,2$  and  $a_{bcdh} = 0,8$ .

The total number of modules needed to feed the electrical energy of RO system is :

$$P_{PV} / RO = \frac{1}{\frac{t_{hd}}{24} + \left(1 - \frac{t_{hd}}{24}\right) a_{bch} \cdot a_{bcdh}} \cdot \frac{P_p}{P_{PVM}}$$

Where :

$P_{PVM}$  : Average daily production of energy by PV (kWh/day)

#### 4.2. Economic study

The desalination plant incorporates two elements; the capital cost and the annual operating costs. The capital costs cover Equipment purchasing cost, auxiliary equipment and installation charges. In our case, the land cost is not taken into account because it's offered by the state. Annual operating cost represents the total yearly costs of owning and operating a desalination plant. These, include amortization or fixed charges, operating and maintenance costs, energy costs and membrane replacement costs. Our investigation take into consideration only stand alone plant in isolated areas in the southern region of Algeria. The levelized Water Cost (LWC) is generally used to compare different desalination plant technologies. In this economic calculation approach, the annual capital costs (fixed and variable annual costs of RO plant and of solar photovoltaic plant) are divided by the total annual fresh water production.

The economical considerations of utilizing the solar energy for fresh water production by desalination are most important aspects in selecting the proper desalination processes to be used in any project and also to choose the location where the plant will be implemented. To study the economic feasibility of a power system, different methods could be used to evaluate different figures of merit of the systems. Each method has its own advantages, disadvantages, limitations and some conditions to be satisfied so that it can be applied [14]. For the evaluation of the investment, the two following indicators have been used:

The following equation is used to calculating the LEC:

$$LWC = \frac{C_{inv} + C_{chem} + C_{staff} + C_{maint} + C_{mem}}{Q_{water}}$$

(\$/m<sup>3</sup>)

Where:

$C_{inv}$ : The total investment costs of the reverse osmosis and Photovoltaic plants (\$/y),  $C_{chem}$  is the annual cost of chemicals (\$/y),  $C_{staff}$  is the annual cost of staff (\$/y),  $C_{maint}$  is the annual maintenance costs (\$/y),  $C_{mem}$  is the annual costs of membrane replacement (\$/y) and  $Q_{water}$  is the annual fresh water production ( m<sup>3</sup>/y).

#### 4.3. Environmental analysis

The CO<sub>2</sub> saving in the proposed system calculated from the CO<sub>2</sub> emissions factor per kWh generated (C), take in the account the transmission and distribution losses (T&D). The saving can be calculated as below equation:

$$CO_{2\text{saving}} = \text{Annual Energy Saving} \times (1 + T \& D) \times C$$

In Algeria, the C is assumed to 0.7 kg CO<sub>2</sub>/kWh and the T&D losses are 15%.

### 5. RESULTS AND DISCUSSIONS

The type of membrane used in the considered pilot is the SW30HR380 FILMTEC. This membrane has a high flux and a good boron rejection results (99%). The operating pressure ranges between 10 and 15 bars (brackish water).

Table 1 : Characteristics of the RO unit are shown in table 1.

Characteristics	Value
Permeate Flow (l/h)	84
Feed water flow (l/h)	165
Pump Efficiency (%)	75
Solar field capacity ( kW)	3

Table 2 Component replacement rate

Component	Lifetime (years)
Photovoltaic pannels	25
Control Electronics	10
Membrane	05
Pumps	10

The system life is assumed at 25 years and the interest rate is about 4%. The system capital costs and maintenance costs are considered. We don't consider the following costs ; land, site preparation, system assembly, brine disposal and water distribution. The average replacement rate are shown on table 2.

### 6. CONCLUSION

Solar desalination is a promising way of meeting water demand in remote areas and as a way to reduce the carbon footprint of commercial desalination. Reverse osmosis process is currently the most cost-competitive solar desalination technologies approaching conventional desalination water costs.

The investigated proposed plant in this study shows that using PV systems for brackish water desalination at current electricity tariff is not economically feasible in the high plateau regions.

The investigated proposed plant in this study shows that using PV systems for brackish water

desalination is economically feasible in the remote areas ( extreme south).

There are environmental benefits for the proposed system, as Green House Gases reduction..

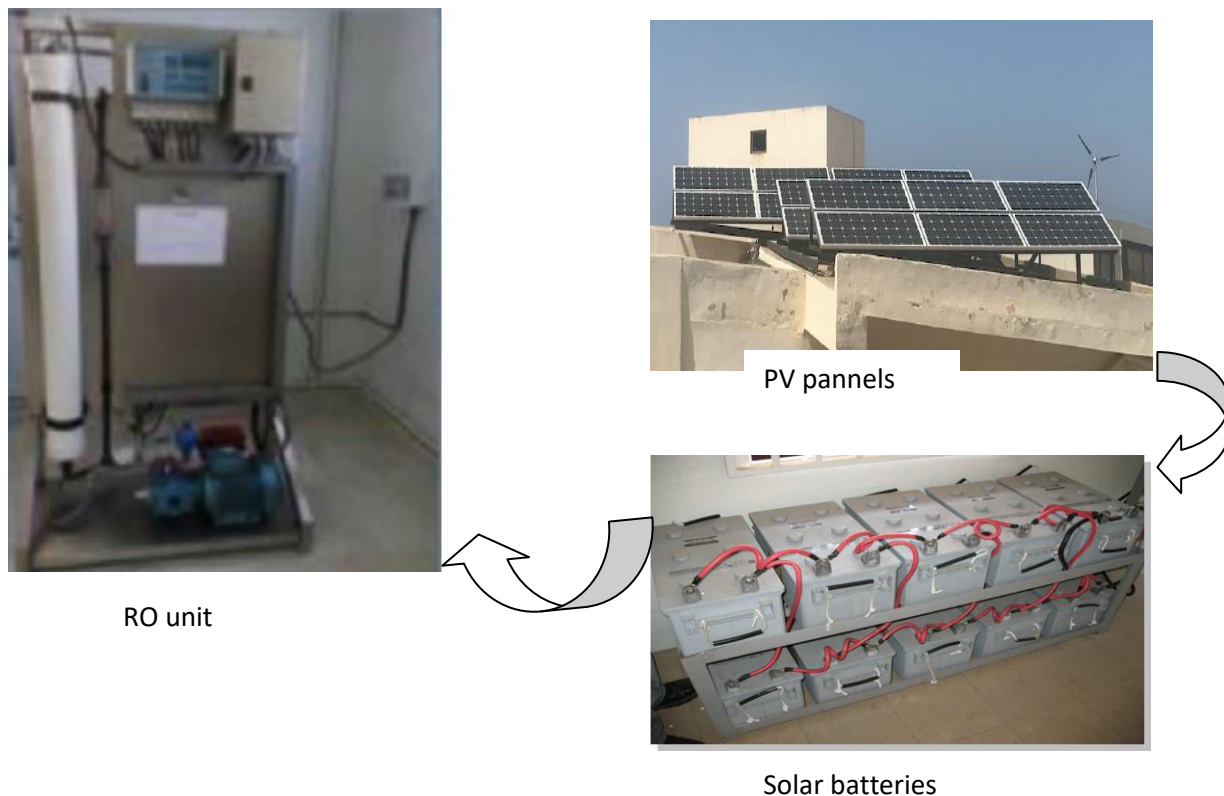


Figure 4: The studied solar desalination unit

## 7. REFERENCES

1. Algerian Ministry of Water Resources .  
<http://www.mree.gov.dz>.
2. Z. Tigrine, H. Aburideh, M. Abbas, S. Hout, N. Kasbadji Merzouk, D. Zioui, M. Khateb: Membrane Desalination Technology in Algeria: Reverse Osmosis for Coastal Areas. Chapter In book: Exergy for A Better Environment and Improved Sustainability. Green Energy and Technology book series (GREEN), 2. 197-218, 2018.
3. Ali Al-Karaghoul, Lawrence L. Kazmerski, Energy consumption and water production cost of conventional and renewable-energy-powered desalination processes. *Renewable and Sustainable Energy Reviews*, 24, 343-356, 2013.
4. Bilton, A.M. Wiesman, R. Arif, A. F. M. Zubair, S. M. & Dubowsky, S. On the feasibility of community-scale photovoltaic-powered reverse osmosis desalination systems for remote locations. *Renewable Energy*, 2011, 36, pp.3246–3256.

# Modeling and Simulation of Low Voltage Power MOSFET for DC-DC Converter Applications

Smail toufik

Unité de Développement des Equipements Solaires,  
UDES/Centre de Développement des Energies  
Renouvelables, CDER, Bou Ismail, 42415 W. Tipaza,  
Algeria.  
smaïl.toufik77@gmail.com

Belmili hocine

Unité de Développement des Equipements Solaires,  
UDES/Centre de Développement des Energies  
Renouvelables, CDER, Bou Ismail, 42415 W. Tipaza,  
Algeria.  
belmilih@yahoo.fr

**Abstract**— In this paper, a new behavioral electro-thermal (ET) model for low voltage power MOSFET is improved and implemented in the PSpice software environment. The (ET) model couples a thermal (RC) network model with the electrical model by the interaction between the junction temperature ( $T_j$ ) and the total power loss ( $P_{total}$ ). The parameters of the (RC) thermal network model are extracted from the data provided by the manufacturer's datasheet using particle swarm optimization (PSO) method for constructing the transient thermal impedance ( $Z_{th}$ ). The (ET) model procedure is discussed and the comparisons between simulations and with those provided by the manufacturer's datasheet for the static and thermal characteristics behaviors to validate the proposed model are presented. Further, dynamic study of the ( $T_j$ ) and the junction temperature fluctuation ( $\Delta T_j$ ) is also performed by considering the variation of the switching frequency ( $f_{sw}$ ), this process demonstrates the good performance of the proposed model. In order to show the efficiency of the (ET) model in estimating the ( $T_j$ ), a dc/dc buck converter is used as a case study. Finally, the power source obtained using dc/dc buck converter is efficient and allowing the power loss reduction.

**Keywords**—*Electro-Thermal Model; Transient Thermal Impedance ; MOSFET; Junction Temperature; Particle Swarm Optimization; dc/dc buck converter.*

## I. INTRODUCTION

Power electronic DC-DC converters are used in many applications, such as, renewable energy generators, power systems and hybrid electric vehicles to manage power flow and to regulate voltage. With the development of distributed renewable energy generation, Small-scale inverter becomes a focus of research. Being able to convert all kinds of distributed energy into a unified DC/DC power, the grid connected inverter extensively broadens the application range of renewable energies, and thus acts as an indispensable role in the renewable energy generation system [1,2]. In renewable energy applications, DC/DC converters can be used to obtain a well-regulated output voltage from low voltage power source, such as, photovoltaic array and wind turbine. The DC/DC converter is based on MOSFET devices, the characteristics and performance of a MOSFET can be considerably affected by junction temperature ( $T_j$ ). Therefore, a fast and precise transient thermal model based on the junction temperature dependence of the power loss is critical for proper thermal management of

power devices. This is particularly significant at a high power level when operating at low fundamental frequencies or with large load variations when the junction temperature is at a level close to the operating bounds. So, it is substantial to carry out a thermal analysis of the devices, in order to determine if they are performing within the maximum allowed physical limits. Generally, three methods can be used to establish the thermal model for power electronic devices. The first approach is based on analytical methods, which is achieved by solving analytical 1D or 2D heat condition diffusion equation [3]. In this method, the estimation of the heat spreading effect might be obtained inaccurately, involving a typical heat spreading angle of  $45^\circ$  [4]. The second approach is based on numerical methods. It is mainly based on the finite elements method (FEM) that uses a detailed model of the device, and at the same time, it takes into consideration the material properties and layers [5-6]. Providing the exact solution is the success key advantage of this method, nevertheless, it is characterized by its low computation speed in case where different system components with various time scales are present. This results in a difficult evaluation of the junction temperature evolution in real duty cycle or operating condition. The third approach, the most commonly used one, is the thermal resistor-capacitor (RC) network where circuit simulators are used to estimate the instantaneous junction temperature [7-8]. As a result of representing the process by a heat transfer coefficient value, this method might not provide a good estimation of the heat convection from the cold plate to the coolant. The aim of this paper is the improvement of electro-thermal (ET) model for a low voltage power MOSFET for estimating the junction temperature ( $T_j$ ). Firstly, a thermal model for the (ET) is improved on the basis of its transient thermal impedance ( $Z_{thjc}$ ), the parameters of the ( $Z_{thjc}$ ) are extracted from the data provided by the manufacturer's datasheet using particle swarm optimization (PSO) method. Thereafter, an electrical model of the (ET), which provides accurate predictions of the junction temperature ( $T_j$ ) dependent electrical characteristics, this (ET) model is implemented in PSpice circuit simulator. Furthermore, dynamic study of the junction and case temperature is performed by considering the variation of the switching frequencies ( $f_{sw}$ ) which shows the good electro-thermal performance of the proposed model. Finally, to better illustrate the capability and attractiveness of the electro-thermal model in estimating the junction temperature, a dc/dc buck converter is used as case study.

## II. MOSFET (ET) COUPLING SIMULATION

The diagram of the (ET) simulation model of power MOSFET model is shown in Fig. 1. The total power losses model are composed of the conduction losses and switching losses. The total power losses model is interfaced with the thermal model as shown in Fig. 1. The current, voltage profiles and switching frequency is first translated into power loss by the device total power loss model. This power loss serves as an input of the thermal model, which calculates the (Tj), which is then fed back to the total loss model.

## III. POWER LOSSES OF MOSFET MODEL

The power efficiency of power MOSFET can be divided in three groups: conduction loss (Pco), blocking losses (Pbl), normally being neglected and switching loss (Psw). Therefore, the total power loss (Ptotal) can be calculated by combining the conduction loss and the switching loss are given by:

$$P_{total} = P_{bl} + P_{co} + P_{sw} \approx P_{co} + P_{sw} \quad (1)$$

### A. Conduction Losses

The MOSFET conduction losses (Pco) are generated by the on-state drain-source voltage drop VDS across the power device and the instantaneous value of the current ID, which is flowing through it, as shown in Fig. 2, are calculated as:

$$P_{co}(t) = \frac{1}{T_{on}} \int_{T_{off}}^{T_{off}+T_{on}} V_{DS}(t) \cdot I_D(t) dt \quad (2)$$

Therefore, the instantaneous value of the MOSFET conduction losses is:

$$P_{coM}(t) = V_{DS}(t) \cdot I_D(t) = R_{DSon} \cdot I_D^2(t) \quad (3)$$

Integration of the instantaneous power losses over the switching cycle gives an average value of the MOSFET conduction losses:

$$P_{coM} = \frac{1}{T_{sw}} \int_0^{T_{sw}} P_{coM}(t) dt = R_{DSon} \cdot I_{Drms}^2 \quad (4)$$

where  $I_{Drms}$  is the rms value of the MOSFET on-state current.

### B. Switching losses

Switching loss (Psw) is the power dissipated during the turn-On and turn-Off switching transitions. These losses are related to the off-state blocking voltage VDD, the instantaneous drain current ID, the switching frequency fsw and the (Tj). They are calculated using the equation (5).

$$P_{sw} = (E_{on} + E_{off}) \cdot f_{sw} \quad (5)$$

where Eon and Eoff represent the turn-on and turn-off energies respectively. The estimation of the Eon and Eoff is done by:

$$E_{on} = \int_0^{t_{ri}+t_{fv}} V_{DS}(t) \cdot I_D(t) dt = V_{DD} \cdot I_D \frac{t_{ri}+t_{fv}}{2} + Q_{rr} \cdot V_{DD} \quad (6)$$

$$E_{on} = \int_0^{t_{rv}+t_{fi}} V_{DS}(t) \cdot I_D(t) dt = V_{DD} \cdot I_D \frac{t_{rv}+t_{fi}}{2} \quad (7)$$

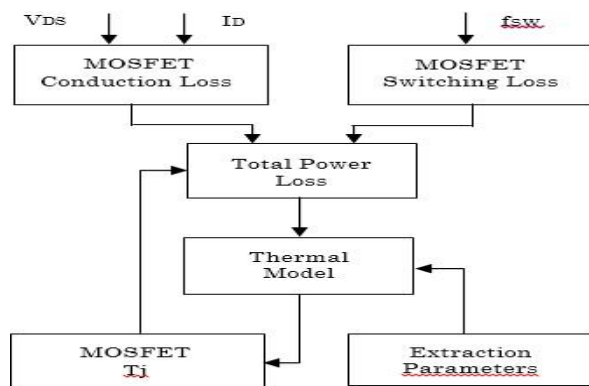


Fig. 1. Diagram of the (ET) coupling simulation.

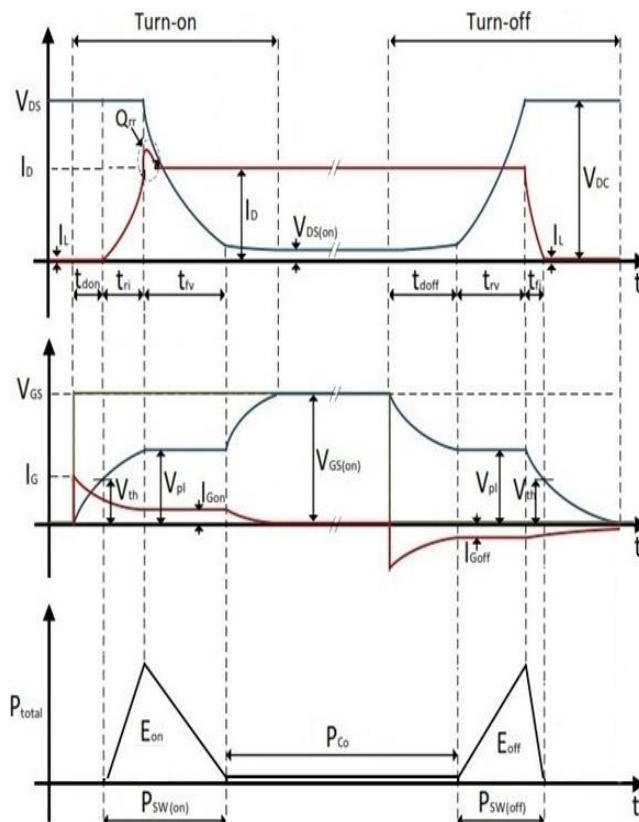


Fig.2. Current, voltage and Energy losses characteristic at turn-on and turn-off of the device

#### IV. ELECTRICAL MODEL

An equivalent power electrical MOSFET circuit is used for modeling. It includes of a voltage control current source (MOSFET level-3), reverse body diode, junction capacitors that vary with voltage, and parasitic components. The Equation (8) and (9) are used to describe the MOSFET model.

Cutoff Region ( $V_{GS} < V_{th}$ )

$$I_{DS} = 0 \quad (8)$$

On Region ( $V_{GS} > V_{th}$ )

$$I_{DS} = \mu_n C_{ox} \frac{W}{L} \left( V_{GS} - V_{th} - \frac{1+f_b}{2} V_{DS} \right) V_{DS} \quad (9)$$

The proposed model is validated with manufacturer's datasheet for the static characteristics. Fig. 3 illustrates the simulated and the datasheet by the manufacturer from transfer characteristics at different temperatures (-55°C, 25°C and 125°C). From the figure, we can see that these comparisons demonstrate good agreement. Moreover, the validity of the model from I-V characteristics is verified for different gate voltages at the same temperature. It can be observed from Fig. 4 that the model shows a good agreement at different gate drive voltages.

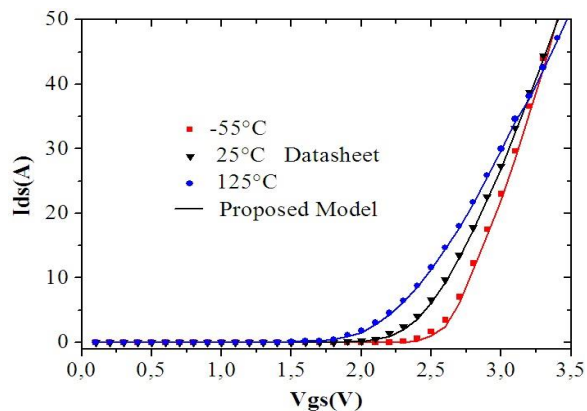


Fig. 2. Transfer characteristics comparison between the simulation results and datasheet at different temperatures.

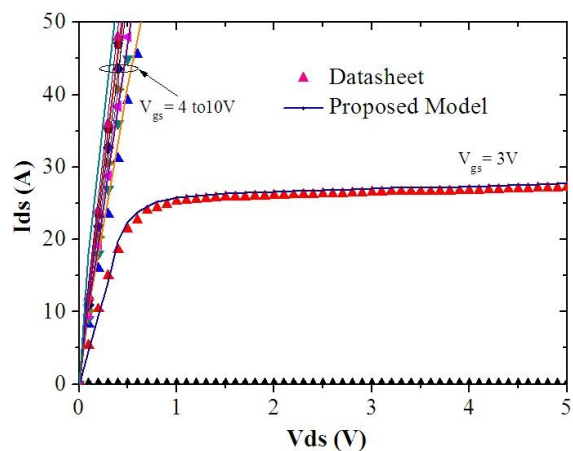


Fig. 1. I-V output characteristics comparison between the simulation results and datasheet for various  $V_{gs}$  values at  $T$  25 °C.

#### V. THERMAL MODEL

##### A. Thermal RC Networks

The (RC) thermal model is a lumped parameter network represented with R thermal resistance, C thermal capacitance and current source equivalent to the heating source. The behavior based (RC) network model solves the conflict between fast calculating speed and high calculating accuracy. It can also be easily integrated to circuit simulator PSpice or Sabre to conduct (ET) simulation. There are two common types of (RC) thermal models namely, the Foster and Cauer models [9-11]. These models provide excellent accuracy over a wide dynamic range, without simulation times or model complexity. A Foster network is constructed using thermal resistance and thermal capacitance parameters from the device datasheet and the parameters do not have physical meanings. In thermal modeling, the Foster RC network is preferred even though it is purely mathematical. The Foster RC network can only predict the junction temperature instead of the temperature distribution. In order to improve the Foster thermal networks based models, algorithms are developed for the conversion of Foster networks to an equivalent Cauer type thermal network with the same pair number of RC lumps [12]. The Cauer network relates better to the real physical thermal system because each node represents a real temperature and can be used to describe the temperature distribution inside the packaging [13].

##### B. Transient Thermal Impedances $Z_{th}(t)$ model

The transient thermal behavior of an Metal Oxide Semiconductor Field Effect Transistor (MOSFET) model is characterized by a transient thermal impedance  $Z_{th-jc}(t)$  between the junction and case temperature [14], can be written as:

$$Z_{th-jc}(t) = \frac{T_j(t) - T_c(t)}{P_d} \quad (10)$$

where  $T_j(t)$  is the junction temperature,  $T_c(t)$  the case temperature and  $P_d$  is the average dissipated power. When using the Foster network, the transient thermal impedance curve can be fitted into a series consisting of a finite number of exponential terms as given in (11).

$$Z_{th-jc}(t) = \sum_{i=1}^n R_i \left( 1 - \exp\left(-\frac{t}{\tau_i}\right) \right) \quad (11)$$

with  $\tau_i$  is the thermal time constant.

$$\tau_i = R_i C_i \quad (12)$$

##### C. Particle Swarm Optimisation

PSO (Particle Swarm Optimization), is a population-based heuristic optimization algorithm which it was proposed by [15-16] is inspired in the study of animal flocks such as bird flocking and fish schooling it has been used to solve optimisation problems in different fields [17-18]. PSO is conceptually simple and computationally efficient. The

following equations define the Particle Swarm Optimization behavior are:

$$v_i^{(K+1)} = K \left( w_i v_i^K + c_1 rand_1 \times (pbest_i - x_i^K) + c_2 rand_2 \times (gbest - x_i^K) \right) \quad (13)$$

$$x_i^{(K+1)} = x_i^K + v_i^{(K+1)} \quad (14)$$

where K is the constriction factor of the search, c1 and c2 are positive constants classed as acceleration coefficients, w is the inertia weighting factor and rand1, rand2 are two functions that generate the inherent randomness in the PSO. xi represents the position of the i<sup>th</sup> particle, pbesti is the best previous position of xi and gbest is the best previous position among the members of the population chosen at random as informants. vi is the velocity of particle xi.

#### D. Implementation of the PSO Algorithm

In the present work, the 4rd order thermal equivalent (RC) Foster model pair parameters are extracted by fitting the step response equation given in (11) to the Zth curves. The (PSO) curve fitting algorithm is used for this purpose. The Ri and τi parameters are determined (11) using PSO algorithm with set population size as 10; inertia weight as between 0.4 and 0.9; and acceleration factors c1 and c2 have been taken as equal to 2 with a maximum iteration set to 500. In order to estimate the thermal impedance curve provided in the device datasheet according to Fig.5 the results showing a very good matching between the proposed method and the data provided by the manufacturer's datasheet. The extracted parameters of the Foster model are listed in Table 1.

TABLE I. LIST OF EXTRACTED PARAMETERS USING PSO ALGORITHM.

No	R <sub>i</sub> (°C / W)	τ <sub>i</sub> (s)
1	235.2314 10 <sup>-6</sup>	76.3912 10 <sup>-6</sup>
2	812.3754 10 <sup>-3</sup>	1.7798 10 <sup>-3</sup>
3	1.2408	17.5243 10 <sup>-3</sup>
4	1.1465	6.8955 10 <sup>-3</sup>

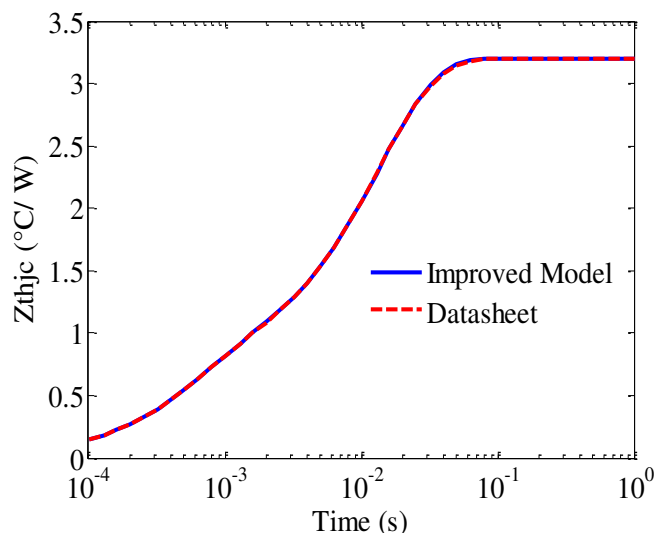


Fig. 5. The improved simulated transient thermal impedance curve and the datasheet curve.

The convergence characteristic of the proposed PSO is shown in Fig 6. From this figure, it is can be observed that fitness function before 200 iterations is unstable; After 200 iterations, no significant improvement is observed, thus the optimized fitness function parameters can be obtained prior to the total training time taken (76.79 sec).

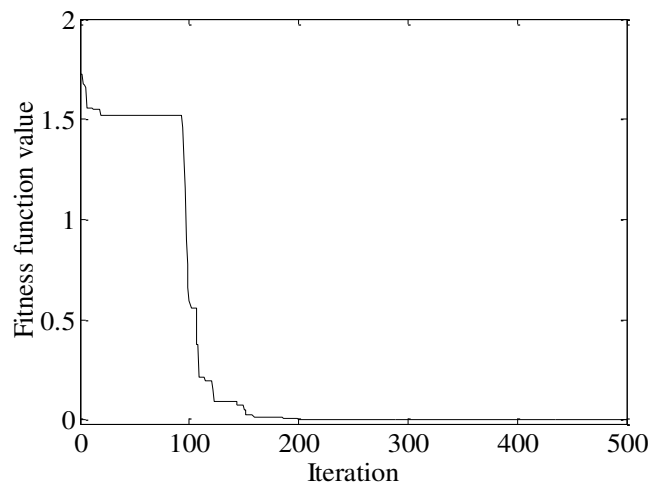


Fig. 6. PSO convergence characteristic.



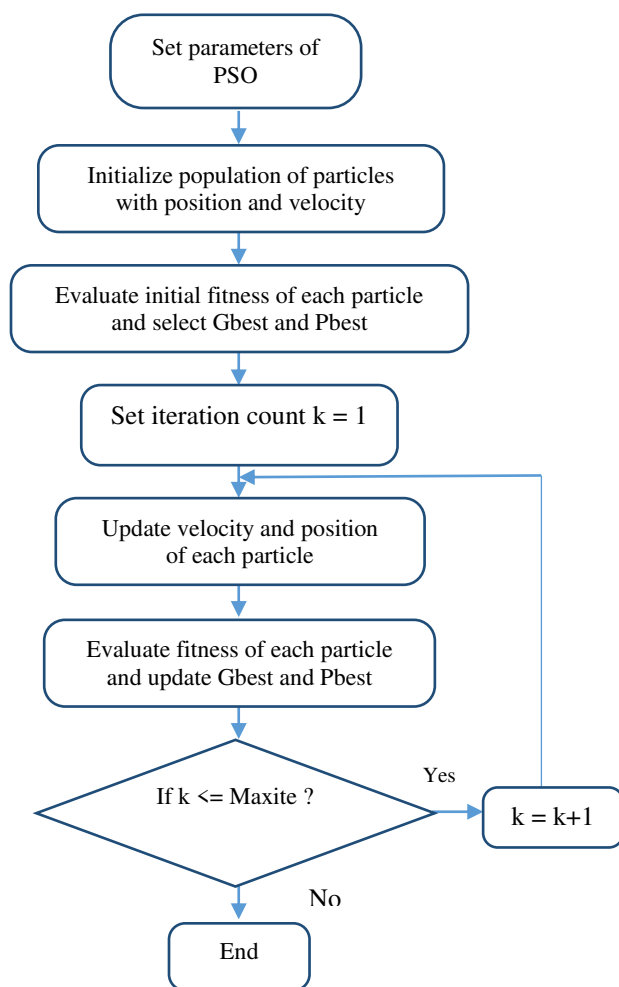


Fig. 7 – Flowchart for particle swarm optimization algorithm.

### VI. ESTIMATION OF JUNCTION TEMPERATURE

To provide a realistic power loss waveform for junction temperature evaluation, a dc/dc buck converter is constructed in the PSpice software environment, using the electro-thermal model, as shown in Fig. 8. The buck converter circuit, used during the simulation, has been designed to operate at the gate voltage  $V_{GS} = 4.5V$ , the input voltage of buck converter  $V_{in} = 15V$ , the Switching frequency of 10 kHz, duty ratio  $D = 50\%$ , the inductance  $L = 50 \mu H$ , the output capacitance  $C = 50 \mu F$ , and the electrical resistance  $R = 4 \text{ ohm}$ . The power loss profile and the corresponding junction temperature variations during the first 300  $\mu s$  of simulation time are shown in Fig.9.

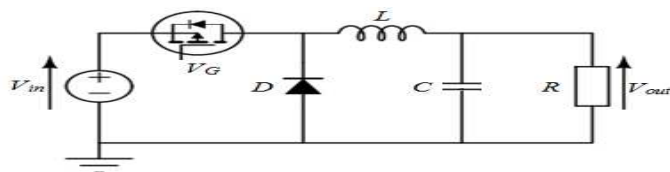


Fig. 8. Coupled electro-thermal simulation for a dc/dc buck converter.

The dynamic behavior of the junction temperature ( $T_j$ ) and the corresponding power loss profile based on the proposed electro-thermal model are shown in Fig. 9. It can be observed

that the junction temperature is proportionate to the power loss oscillates at the fundamental frequency, the maximum junction temperature  $T_{jmax} = 150^\circ C$  and the junction temperature fluctuates  $\Delta T_j = 7^\circ C$ . The abrupt rise of the junction temperature ( $T_j$ ) at the very beginning and the junction temperature fluctuations ( $\Delta T_j$ ) during the whole simulation are mainly caused by the small thermal time constant of the MOSFET.

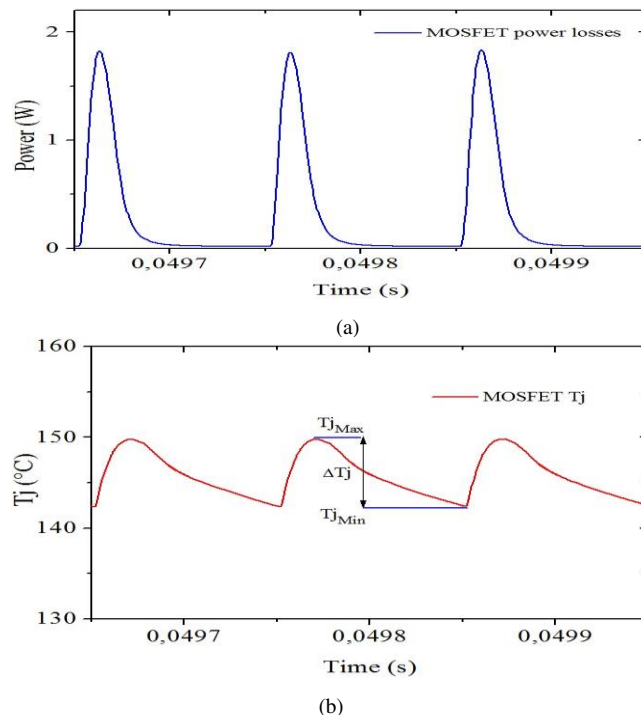
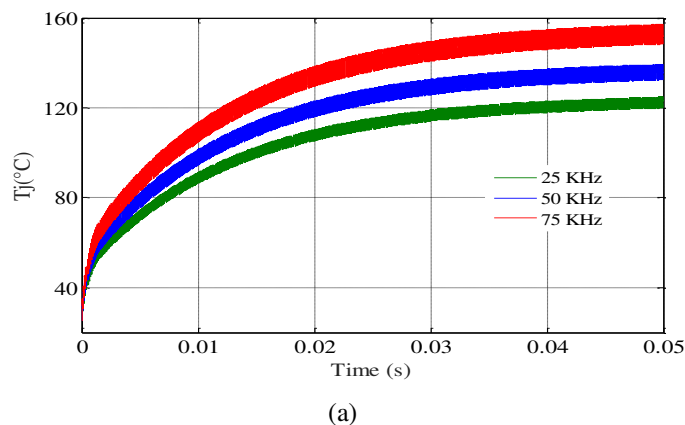


Fig. 9. The power dissipated in the MOSFET (a), the MOSFET junction temperature estimates estimated (b).

Fig. 10 shows that for a switching frequency ( $f_{sw}$ ) less than 50 kHz, the proposed model is not override the maximum admissible ones of junction temperature. If the switching frequency ( $f_{sw}$ ) is increased up to 70 kHz, the amplitude of the temperature fluctuation becomes larger and the thermal limitations of the device are exceeded, this involving device failure. Fig. 11 presents the maximum junction temperatures ( $T_{jmax}$ ) and swinging amplitudes ( $\Delta T_j$ ) of the junction temperatures of the proposed (ET) model. Both the maximum junction temperatures and their swinging amplitudes ( $\Delta T_j$ ) appear to increase linearly with increasing of the switching frequency ( $f_{sw}$ ).



(a)

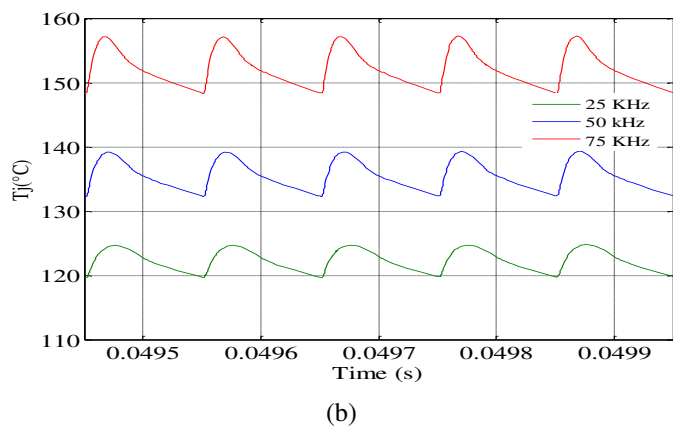


Fig. 10. (a) Junction temperature waveforms under different switching frequencies (b) Zooming in to the Junction temperature in 0.55ms.

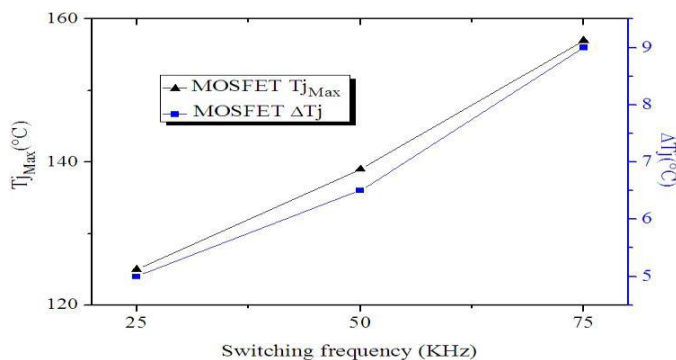


Fig. 11. The steady (ET) simulation results: maximum junction temperatures and fluctuates of the junction temperatures.

## VII. CONCLUSION

In this paper, the transient electro-thermal (ET) model of a low voltage power MOSFET based converter is improved and implemented in Pspice simulator. The particle swarm optimization (PSO) algorithm was applied to extract the thermal model. Transient analysis was done for this model and compared with the datasheet in order to prove the effectiveness of the extraction method used. Based on the electrical model and thermal model, the fully coupled transient simulation of the converter was performed and the dynamic performances of the junction temperature under different operating conditions was observed. Finally, the improved (ET) model can predict the junction temperature and can also guarantee the accuracy of the estimated junction temperature fluctuation. This simulation model will provide crucial information for the thermal management system and for evaluating the reliability of the MOSFET model and use it in PV applications.

## REFERENCES

- [1] Faranda, R.S.; Hafezi, H.; Leva, S.; Mussetta, M.; Ogliari, E. The optimum PV plant for a given solar DC/AC converter. *Energies* 2015, 8, pp.4853–4487, 2015.
- [2] Han, Y.; Chen, W.; Li, Q. Energy Management Strategy Based on Multiple Operating States for a Photovoltaic/Fuel Cell/Energy Storage DC Microgrid. *Energies*, 10, 136, 2017.
- [3] M. Ayadi, S. Abid, and A. Ammous. "Thermal simulations of multichips modules." In Proc. IEEE International Conference on Electronics, Circuits and Systems, Gammarth, Tunisia, pp.1-4, Dec. 2005.
- [4] M. Ishiko, T. Kondo. "A Simple Approach for Dynamic Junction Temperature Estimation of IGBTs on PWM Operating Conditions." In Proc. IEEE Power Electronics Specialists Conference, Orlando, FL, pp.916-920, June. 2007.
- [5] I. Swan, A. Bryant, P. A. Mawby, T. Ueta, T. Nishijima, and K. Hamada, "A fast loss and temperature simulation method for power converters, part II: 3-D thermal model of power module," *IEEE Transactions on Power Electronics*, vol. 27, no. 1, pp. 258–268, Jan. 2012.
- [6] T. K. Gachovska, B. Tian, J. L. Hudgins, W. Qiao, and J.F. Donlon, "A Real-Time Thermal Model for Monitoring of Power Semiconductor Devices," *IEEE Trans. Ind. Appl.*, vol. 51, no. 4, pp. 3361 - 3367, Jul/Aug. 2015.
- [7] A. S. Bahman, K. Ma, P. Ghimire, F. Iannuzzo and F. Blaabjerg, "A 3-D-Lumped Thermal Network Model for Long-Term Load Profiles Analysis in High-Power IGBT Modules," *IEEE J. Emerg. Sel. Topics Power Electron.*, vol. 4, no. 3, pp. 1050-1063, Sept. 2016.
- [8] J. Nelson, G. Venkataramanan, and A. M. EL-Refaeie, "Fast thermal profiling of power semiconductor devices using Fourier techniques," *IEEE Transactions on Industrial Electronics*, vol. 53, no. 2, pp. 521– 529, April. 2006.
- [9] Y. Xu, H. Chen, S. Lv, F. F. Huang, and Z. T. Hu, "Thermal model for power converters based on thermal impedance," *Journal of Power Electronics*, vol. 13. no. 6, pp. 1080-1089, Nov. 2013.
- [10] J. O. Krahn and C. Klarenbac, "On-line semiconductor junction temperature estimation for frequency inverters," in Proc. International Exhibition and Conference for Power Electronics, Intelligent Motion and Power Quality, Nuremberg, Germany, pp. 424 -431, Jun. 2010.
- [11] A. Nejadpak and O. A. Mohammed. "A physic-based, dynamic electro-thermal model of silicon carbide power IGBT devices," in Proc. 28 IEEE Applied Power Electronics Conference and Exposition(APEC), Long Beach, CA, pp. 201-206, Mar. 2013.
- [12] Z. Luo, H. Ahn, and M. A. El Nokali, "A thermal model for insulated gate bipolar transistor module," *IEEE Transactions on Power Electronics*, vol. 19, no. 4, pp. 902–907, Jul. 2004.
- [13] M. Rencz and V. Szekely, "Dynamic thermal multiport modeling of IC packages," *IEEE Trans. Compon. Packag. Technol.*, vol. 24, no. 4, pp. 596–604, Dec. 2001.
- [14] M. März and P. Nance, *Thermal modeling of power electronics systems*. Munich: Infineon Technologies; 2000.
- [15] J. Kennedy, R. Eberhart, Particle swarm optimization, in: *IEEE International Conference on Neural Networks*, Vol. 4, pp. 1942-1948, 1995.
- [16] R. Eberhart, J. Kennedy, A new optimizer using particle swarm theory, in: *IEEE Proceedings of the Sixth International Symposium on Micro Machine and Human Science*, pp. 39-43, 1995.
- [17] Ganguly, S., Sahoo, N.C., Das, D.: 'Multi-objective particle swarm optimization based on fuzzy-Pareto-dominance for possibilistic planning of electrical distribution systems incorporating distributed generation', *Fuzzy Set Syst.*, 213, pp. 47–73, 2013.
- [18] Tsekouras, G.E., Tsimikas, J.: 'On training RBF neural networks using input– output fuzzy clustering and particle swarm optimization', *Fuzzy Set Syst.* 221, pp. 65–89, 2013.

# Evaluation of wind park performances located At Algerian East Highlands

A. Mezidi<sup>#1</sup>, H. Bendjebbas<sup>\*2</sup>, K. Mohammedi<sup>#3</sup>

<sup>#</sup> *Unité de Développement des Equipements Solaires-UEDES/CDER  
Bou Ismail, Tipasa- Algérie*

<sup>1</sup>mazidiahmed@yahoo.fr

<sup>#</sup> *Unité de Développement des Equipements Solaires-UEDES/CDER  
Bou Ismail, Tipasa- Algérie*

<sup>2</sup>hbendjebbas@gmail.com

<sup>#</sup> *Unité de Recherche Matériaux Procédés et Environnement-U.M.B.B*

Université M'Hamad Bougara Boumerdès- Algérie

<sup>3</sup>mohammedik@yahoo.com

**Abstract**— this work deals with a technico-economic study of the production of the 5.1 MW wind farm located in Tebessa region. The wind potential available at the Tebessa site used the 03-year wind data from the measurements taken by the National Meteorological Office (NOM) during the period 2014-2016. This evaluation of the wind potential was carried out using the WAsP OWC software, and a study of the wind potential assessment available in another region of the Algerian East Highlands Region was carried out. The results were used to predict the performances of wind farms that would be located in this selected site. The obtained results were then used to calculate the cost of the kilowatt-hour wind generated in this site.

**Keywords**— wind Park, WAsP, arid areas and economics

## I. INTRODUCTION

Wind energy is one of the most developed renewable energy resources. According to the Bloomberg New Energy Finance Institute's (BNEF) report, cumulative global production of solar and wind energy reached 1 TW in 2018, with a slight dominance of wind power by 54%. The installed wind capacity currently in the world is appreciable and reached 539 Gigawatt at the end of 2018. This growth is mostly due to the decrease of the cost of electricity from renewable sources, mainly electricity from solar PV and wind. Moreover, as reported by (Amine Akbi et al. 2016), it is recognized that the use of renewable energies can significantly reduce carbon dioxide or equivalent (CO<sub>2</sub>eq) emissions compared to their fossil equivalents [2]. Therefore, wind energy is clean and sustainable; it does not release hazardous substances into the environment and does not generate waste, wind energy can contribute to mitigate climate change. a brief overview of the main recent scientific work related to the analysis of meteorological data and the determination of available wind resources in a site, study by Boudia and Guerri (2015) [3] and Belabes et al. (2015) [4] who evaluated the available wind potential in different regions of northern Algeria and

Highlands using 10-year data. An estimate of the cost per kilowatt hour of wind was given in both books.

Tran and Chen (2016) [5] used data collected between 2005 and 2011 (7-year data) to assess wind potential available on Phuquoc Island in Vietnam and to calculate the theoretical energy production of a farm of 75 MW. Recently, Abdeslame et al. (2017), [6] used 10-year data to estimate electricity production wind farms installed on four windy sites in the Algerian highlands. Jourdir and Drobinski (2017), [7] used four-year observations to examine the Weibull distribution in assessments of wind resources and energy efficiency. Ramadan (2017), [8] used two-year data to measure wind Firm. Energy and Resource Assessment in the Sinai Peninsula, Egypt. Our vast country is subdivided into two distinct geographical areas. The North Mediterranean is characterized by a coastline of 1200 km, the two mountainous chains of the Atlas and the vast region of southern Algeria, characterized by the Saharan climate. Curb the rural exodus to the north and set populations. In view of solar energy potentials, geothermal and wind farms in southern Algeria, these regions are generally suitable for the implementation of energy systems based on renewable energies. The selected site is Tebessa and the wind data used are records of 3 years of measurements carried out between 2014 and 2016. The wind potential assessment is carried out using the WAsP OWC utility based on the statistical distribution of Weibull. The results were used to predict the performance of wind farms that would be located in this selected site. The obtained results were then used to calculate the cost of the kilowatt-hour wind generated in this site.

## II. METHODOLOGY

### A. wind data analysis

The WAsP allows spatial interpolation from ground-based data while taking into account topography, roughness and obstacles. It has been used to establish wind atlas of several countries and the European wind atlas [8] reported that the prediction model of the wind resource implemented by the wind speed  $f(V)$  given by Equation (1) [10] and [11].

$$f(v) = \left(\frac{k}{A}\right) \left(\frac{V}{A}\right)^{k-1} \exp\left(-\left(\frac{V}{A}\right)^k\right) \quad (1)$$

- Com is the operation, maintenance and repair costs (O&M costs)
- S is a scrap factor

### B. WIND TURBINE PERFORMANCE ANALYSIS

The expected annual production (AEP) of the wind turbines are evaluated using the WASP software, the wind turbine power curves given by the manufacturer and the results of the statistical wind data analysis. Power loss considered in the WASP software is only due to wake loss. However, according to the European Association for wind energy [11] power loss are also due to blade soiling, electrical losses, and machine downtime and yaw mechanism.

The wind turbine capacity factor (CF) is defined as the ratio between the wind turbine annual production and one-year theoretical wind farm production [12]

$$C_f = \frac{AEP_{net}}{8760 \cdot P_n} \quad (2)$$

Where  $P_n$  is the wind turbine rated power ( $P_n = 850$  kW).

### C. Wind turbine full load hours.

The wind turbine full load hours (NH) is also used to analyse the performance of a wind turbine or a wind farm installed in a specific site. This parameter is calculated using the following relationship [13]

$$NH = \frac{AEP_{mean}}{P_n} \quad (3)$$

### D. Economic analysis

The present value cost (PVC) method is adopted in this work for the computation of wind energy cost because (i) it considers the dynamic development of the relevant economic factors and (ii) different occurrences of costs and income are taken into account regardless of whether the money has been or will be paid or received in the past or in the future through deduction of accrued interest (discounting) of all payments flows to a common reference time [14]

$$PVC = I + C_{om} \cdot \left(\frac{1+i}{1+r}\right) \cdot \left[1 + \left(\frac{1+i}{1+r}\right)^t\right] - s \cdot \left(\frac{1+i}{1+r}\right)^t \quad (4)$$

Where:

- I is the CAPEX (Capital Expenditure) or the investment cost. It comprises wind turbine price and other initial costs, including provisions for civil work, land, infrastructure, installation and grid integration.
- r and i are the interest and inflation rate, respectively
- t is machine lifetime

## III. DATA USED

### A. Presentation OF THE STUDIED SITE

The selected region in this study called Tebessa IS LOCATED IN the extreme east of Algeria, bordering Tunisia. It is characterized by its location in the border area of the Eastern Highlands of the country. The total size is 13,878 km<sup>2</sup>, it is limited by:

- To the north by the region of Souk-Ahras
- North-West by the region of Oum-El Bouaghi and Khenchela
- To the East by Tunisia (over 300 kms of borders)
- South by the region of El-Oued

### B. Geographical and Meteorological Data

In the present work, we precede to the evaluation of the wind resources of Tebessa. Table I gives the geographical features of the studied site.

TABLE I GEOGRAPHIC DATA OF TEBESSA SIT

stations	Longitude	Latitude	Altitude[m]
Cheikh Larbi Tebessi	08° 07' 32" E	35° 25' 57" N	811.1

### C. Wind turbine data

The wind turbines selected in this wind park consists of 06 GAMESA G52-850 KW Wind turbines. The main wind turbine characteristics are summarized in table II.

TABLE II: TECHNICAL SPECIFICATIONS OF THE G52-850KW GAMESA WIND TURBINE

Nominal power: Pn [KW]	850
Rotor diameter: D [m]	52
Pylon height: H [m]	55
Starting speed: Vd [m/s]	4
Rated speed: Vn [m/s]	15
Stop speed: Vs [m/s]	25

## IV. RESULTATS

### A. WIND DATA STATISTICS

The results obtained at 10m height above the ground level are depicted fig. 1. It is found, that for the site of Tebessa, the average wind speed is of the order of 4.44 m/s with the north and North-West as dominant sector and a power equal to 120w/m<sup>2</sup>.

**B. WIND DATA STATISTICS AND TECHNICAL ANALYSIS RESULTS**

Fig.2 illustrates the annual change in mean wind speed and power density at 10 m above ground level, for the Tebessa site. This figure shows that during three years, worth of data acquisition from 2014 to 2016, a decreasing of these quantities was recorded. The average wind speed varies from a maximum of 5.56 m/s in 2014 to 4.32 m/s in 2016. With regards to the power density, this figure shows that it varies from 174 W / m<sup>2</sup> with a maximum value in 2014 at 1120W/m<sup>2</sup> in 2016.

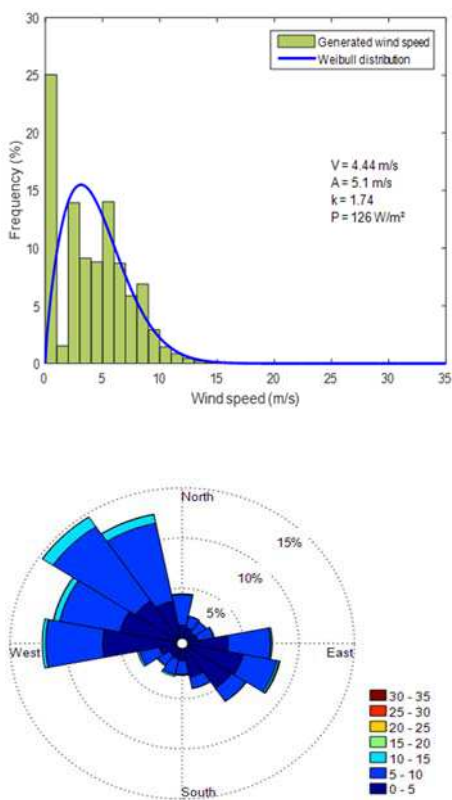


Fig.1 Wind speed histogram (left) and wind rose (right) of the four area at 10 m a.g.l.

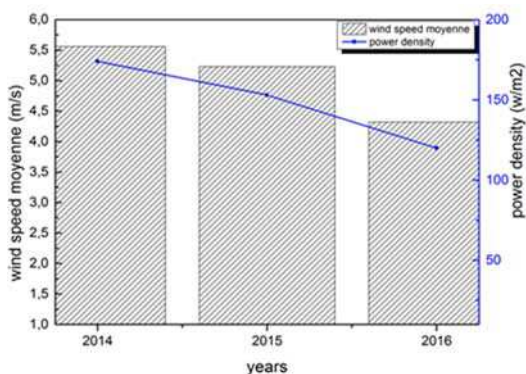


Fig.2 Variation of the annual mean wind speed and density of power in E Oued area, at 10m a.g.l

**C. WIND MAP:**

Fig 3 obtained by using the WAsP software illustrates the map of the wind speed at 55 m above ground level (Wind turbine height), of the wind turbine at the study site. The average annual wind speed varies from 3.5 to 9 m/s.

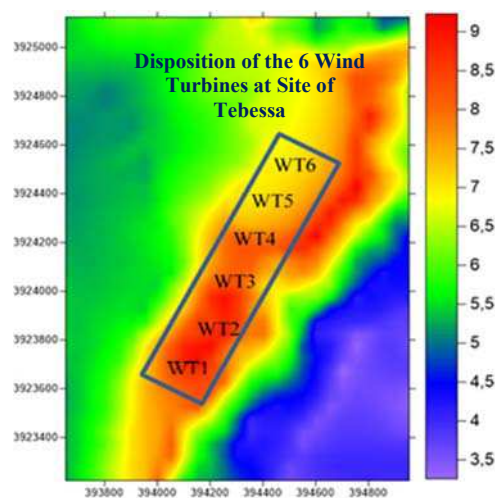


Fig.3 Wind speed maps at 10 m a.g.l. for Tebessa site

**D. PERFORMANCE OF THE WIND FARM INSTALLED IN TEBESSA**

In table 3, the wind park AEP net takes a value of 20725. Concerning the wind farm mean speed, it is about 8.79m/s. The power density of the wind park takes the value of 846 W/m<sup>2</sup>.

TABLE .III THE PERFORMANCE OF THE WIND FARM

AEP Gross [GWh]	AEP net [GWh]	Proportional wake loss [%]	Mean speed [m/s]	Power density [W/m <sup>2</sup> ]
20.852	20.725	0.61	8.79	846

**E. ECONOMIC ANALYSIS RESULTS:**

The PVC of wind energy is computed for the study areas with the following assumptions:

The wind turbines cost varies with their nomina279 l power. According to the specific costs suggested by [11] and [12] in this work, the wind turbines specific costs is set to vary between 1240 and 1600 USD/kW.

- Civil engineering costs and other costs are estimated at 20% of the wind turbines cost.

- The lifetime of wind turbines is 20 years
- Operating and maintenance costs are estimated at 25% the initial investment cost (equipment cost/lifetime).
- Inflation and interest rates are estimated at 8% and 6% respectively.
- The value of the parameter S is set to 10% of the investment cost.

The LCOE of wind energy produced in the site study varies between **3.28 to 4.23 c\$/kW**

## V. CONCLUSIONS

The WASP software allowed to evaluate the wind farm of the studied site, by drawing the wind maps, the wind speeds distribution rose, the frequency histogram of the real wind speeds, the interpolation curves of the wind Weibull, as well as the assessment of the electrical powers of the Tebessa wind farm.

The results obtained showed that in this region of Tebessa, the wind resources are appreciable. But further investigations must be made before considering the development of wind farms such as the study of the possibility of installing larger wind farms, the optimization of the power and the number of wind turbines to install, the possibility of hybridization of existing diesel plants and the possibility of integrating fluctuating energy into the local electricity grid.

As a result, the results obtained in this study can contribute to an important scientific support to invest projects in this field of renewable energies in the Tebessa region of the highlands of Algeria. Indeed, it is the moment for the decision makers in collaboration with the investors, to implement projects similar to the only wind farm in Algeria with a capacity of 10.2 megawatts installed in the region of kabertene (Adrar).

## References

- [1] A. Amine, N. Yassaa, R. Boudjema, and B. Aliouat, "A new method for cost of renewable energy production in Algeria : Integrate all benefits drawn from fossil fuel savings," vol. 56, pp. 1150–1157, 2016.
- [2] Barry DBarry DBarthe A et al, "The wind turbine - energy rediscovered."
- [3] S. M. Boudia and O. Guerri, "Investigation of wind power potential at Oran , northwest of Algeria," *ENERGY Convers. Manag.*, vol. 105, pp. 81–92, 2015.
- [4] B. Belabes, A. Youcefi, O. Guerri, M. Djamai, and A. Kaabeche, "Evaluation of wind energy potential and estimation of cost using wind energy turbines for electricity generation in north of Algeria," *Renew. Sustain. Energy Rev.*, vol. 51, pp. 1245–1255, 2015.
- [5] V. T. Tran and T. H. Chen, "Wind energy resources on Phuquoc Island, Vietnam," *Energy Sources, Part A Recover. Util. Environ. Eff.*, vol. 38, no. 11, pp. 1612–1619, 2016.
- [6] D. Abdeslame, N. Kasbadji Merzouk, S. Mekhtoub, M. Abbas, and M. Dehmas, "Estimation of power generation capacities of a wind farms installed in windy sites in Algerian high plateaus," *Renew. Energy*, vol. 103, pp. 630–640, 2017.
- [7] B. Jourdir and P. Drobinski, "Errors in wind resource and energy yield assessments based on the Weibull distribution," pp. 691–700, 2017.
- [8] H. S. Ramadan, "Wind energy farm sizing and resource assessment for optimal energy yield in Sinai Peninsula , Egypt," *J. Clean. Prod.*, vol. 161, pp. 1283–1293, 2017.
- [9] L. Petersen, D. Version, and L. Petersen, *European Wind Atlas*. 1989.
- [10] D. Solyali, M. Altunç, S. Tolun, and Z. Aslan, "Wind resource assessment of Northern Cyprus," *Renew. Sustain. Energy Rev.*, vol. 55, pp. 180–187, 2016.
- [11] M. Benmemdejahed and S. Mouhadjer, "Evaluation of Wind Energy Cost and Site Selection for a Wind-Farm in the South of Algeria," vol. 30001, 2016.
- [12] A. Mezidi, O. Guerri, S. Mohammed, and K. Mohammadi, "Influence of wind data temporal variation in wind resource assessment . Two case studies in the southern part of Algeria," 2018.
- [13] A. Mezidi, O. Guerri, "Evaluation of Wind Turbine Performances Located in Two Sites of The Algerian Sahara." 2019 .
- [14] B. Belabes, A. Kaabache, O. Guerri, B. B. Dz, and B. Belabès, "Evaluation du coût de production d'électricité d'origine éolienne. Cas de deux sites des hauts plateaux Algériens," *Rev. des Energies Renouvelables*, vol. 17, pp. 1–117, 2014.



# Energy Flow Management for a Standalone Hybrid PV/Wind Power System

Sabri Boulouma<sup>#1</sup>, Hachemi Rahmani<sup>#2</sup>, Boualem Bendib<sup>#3</sup>, Hocine Belmili<sup>#4</sup>, Naoual Seddaoui<sup>#5</sup>

*<sup>#</sup>Unité de développement des Equipements Solaires, UDES/ Centre de Développement des Energies Renouvelables, CDER, Bou-Ismaïl, 42415, W. Tipaza, Algeria*

<sup>1</sup>sab\_blm@yahoo.fr

<sup>2</sup>rhachemi8@yahoo.fr

<sup>3</sup>bendib1427@yahoo.fr

<sup>4</sup>belmilih@yahoo.fr

<sup>5</sup>nawelseddaoui@yahoo.com

**Abstract**— Hybrid power systems are effective and reliable energy sources; they can better cover electricity demands for remote and small areas. However, the difficulty in energy management between different energy sources, the storage system and the load is more challenging. This paper outlines the development of an energy management control scheme for a standalone hybrid photovoltaic/wind power system. The system under study is based on a real experimental platform. Seen from the photovoltaic part, a sliding mode controller is developed to ensure an optimal operation for the whole system under different possible generation and load profiles. The scenarios considered are when the load demand is satisfied and when the demand is not satisfied, in the first case the controller should provide PV energy to keep the charging mode of battery optimal and to ensure energy balance while in the second case, the controller should ensure maximum power capture to remedy the insufficiency of the load demand. Simulation results using real meteorological data from the site and load profile from the laboratory are conducted to show the effectiveness of the proposed control strategy.

**Keywords**— Hybrid PV/Wind, Distributed generation, Energy management, Sliding mode, Buck converter.

## I. INTRODUCTION

Electrical energy is an essential factor for the human development and welfare [1]. Conventional electrical energy generation is mainly based on fossil fuel resources, However the exhaustive nature of these resources, their negative impact on the environment and their increasing prices have somehow weakened their reliability [2,3]. In this context, the interest in renewable energy sources (RES: photovoltaic modules, wind turbine, biomass, geothermal, etc.) has increased since these technologies can remedy the drawback of conventional energy generation sources. One main drawback of renewable energy sources is the intermittent nature of the resources such as wind speed and insolation [2,3,4].

Hybrid power systems (HPS), which combine multiple renewable and possibly conventional energy sources with storage elements (batteries, inertial wheels, fuel cells, etc.) are very interesting in terms sustainable and reliable electrical energy production as well as the reduction of environmental impacts [3]. According to experts, a HPS that combines solar and wind electric technologies offers several advantages over either single system [3,4]. In other words, HPSs, can provide an economic, environment friendly and reliable supply for

electricity [3,5]. Instead of using power from wind energy alone or solar energy alone, combining both sources provides a better and more reliable system.

Generally speaking, HPS can be stand-alone or grid-tied. In standalone systems, both sources together can supply power and if any decrease in power occurs, in any one, the other source can compensate for the first. Also, both systems together can supply higher loads if required. Whenever the generated power is in excess, it can also be stored in a battery. For reliable supply of power in remote locations or inaccessible rural areas, it is necessary to design and set up hybrid system, which combined the advantage of two different energy technologies. These could be either two renewable technologies or a renewable and a conventional energy or fossil fuel technology [5,6].

The main challenge in standalone PV/Wind HPSs is the management of the power flow between renewable sources, the battery system and the load [2,4,5,6]. An efficient energy flow management strategy should be able to ensure maximum power delivery when there is a scarcity of production and large load demand. Besides, it should ensure optimal battery operation to optimize its lifecycle.

The energy flow management in renewable HPS has been studied by many researchers from the industrial and academic fields as can be witnessed by the abundant research literature. In fact, many research papers and deal with the control and energy management of hybrid standalone and grid-tied power systems, these methods are based on classical and nonlinear control such as sliding mode [3,4] or based on soft computing techniques such as neural networks such as in [2,5,6].

This paper presents an energy flow management control strategy for a standalone PV/Wind multi-source power system with a 4kW PV array and a 2kW Wind subsystem. For this purpose, the sliding mode methodology is applied to the photovoltaic side to ensure optimal operation for different scenarios (surplus or a deficit of energy). The proposed controller should be able to decide the operating mode and to fulfil the control specifications for each mode. The paper is organized as follows, in section II, the nonlinear model of the HES is developed and the control objective is outlined, in section III, the operational modes of the system and controller strategy developed, in section IV, simulation results using the parameters of the real system along with real measured



meteorological data is carried out and the results are discussed, section V presents conclusions on this work and perspectives for future works.

## II. HYBRID POWER SYSTEM DESCRIPTION AND MODELLING

In this section the dynamic state space model of the HPS (PV/Wind) is developed. The model is based on the PV/Wind platform installed on the roof of the SMS laboratory in the UDES at Bou-Ismaïl in Algeria (Fig. 1).

### A. Hybrid Power System Description

The HPS is built around a 48V DC bus topology, it is made up of the following subsystems (Fig. 2):

- Photovoltaic array based on STP-135 Suntech, STP 135 tb modules, the array arranged into 5 parallel strings, each string consists of 6 series modules connected to the 48v DC bus via Tristar DC/DC converters.
- Wind energy conversion system (WECS) based on 2 Whisper 200 wind turbines (WT), these WT are based on a PMSG with a rated power of 1kW, they are connected to the 48V DC bus via dedicated Whisper controllers.
- Storage subsystem, based on 24 series connected Classic OPzS 200 Lead Acid batteries with 2 V for each cell.
- Domestic and laboratory AC loads connected to the 48V DC bus via a DC/AC converter (XTH-8000-48 Steca inverter).

In the following, mathematical models for each subsystem and the whole HPS will be derived.



Fig. 1 The experimental PV/Wind HPS (UDES, Bou-Ismaïl)

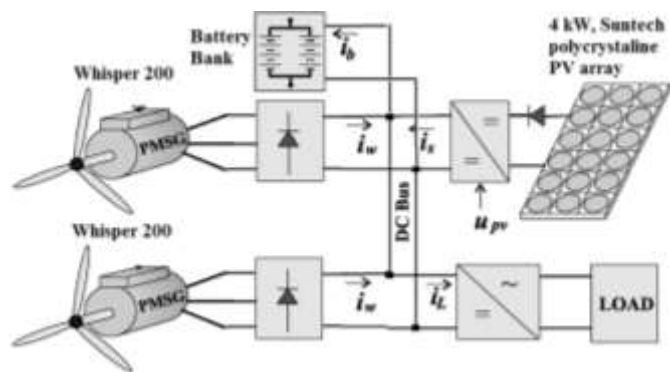


Fig. 2 Schematic diagram of the HES under study

### B. Photovoltaic subsystem modelling

The photovoltaic subsystem converts solar radiation from the sun into electricity, the I-V characteristic of a solar cell is given by [7,8]:

$$i_{pv} = I_{ph} - I_{rs} \left( e^{q(v_{pv} + i_{pv} R_s) / AKT_c} - 1 \right) \quad (1)$$

where  $q$  is the electron charge in coulombs,  $A$  is the diode's ideality factor,  $K$  is the Boltzmann's constant and  $T_c$  is the cell's temperature,  $I_{ph}$  is the photocurrent under a given insolation, and  $I_{rs}$  is the cell reverse saturation current given respectively by:

$$I_{ph} = (I_{sc} + K_i (T_c - T_{ref})) G \quad (2)$$

$$I_{rs} = I_0 \left( T_c / T_{ref} \right)^3 e^{qE_g (1/T_{ref} - 1/T_c) / KT_c} \quad (3)$$

where  $I_{sc}$  is the cell's short circuit current at reference temperature and insolation,  $K_i$  is the short-circuit temperature coefficient,  $T_c$  is the cell's temperature in kelvin and  $G$  is the insolation measured in kW/m<sup>2</sup>.

The PV subsystem is our HES composed of  $N_p$  parallel strings, with  $N_{ss}$  series modules in each string, each module is composed of  $N_{sc}$  series cells, this makes a total of  $N_{ss} \times N_{sc}$  series cells, thus the I-V curve for the whole system:

$$i_{pv} = N_p I_{ph} - N_p I_{rs} \left( e^{q(v_{pv} + i_{pv} R_s) / N_{sc} N_{ss} AKT_c} - 1 \right) \quad (4)$$

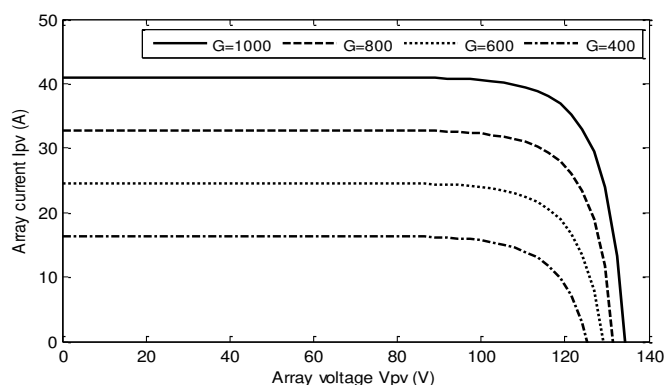


Fig. 3 Current vs. voltage curve of the HES PV array

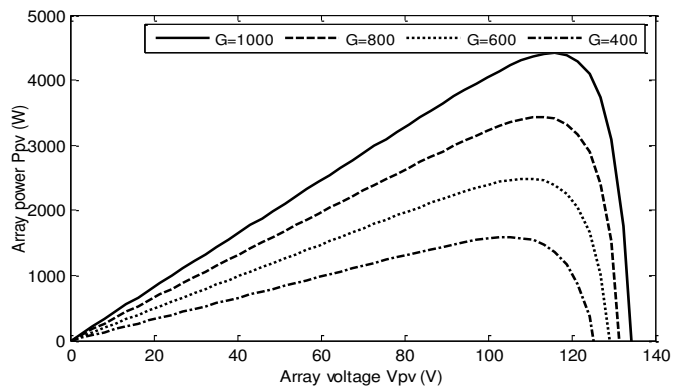


Fig. 4 Power vs. voltage curve of the HES PV array

And the corresponding power will be given by

$$p_{pv} = v_{pv} \left( N_p I_{ph} - N_p I_{rs} \left( e^{q(v_{pv} + i_{pv} R_s) / N_{cs} N_{ss} A K T_c} - 1 \right) \right) \quad (5)$$

Typical I-V and P-V curves for the PV subsystem under different conditions of insolation and a cell temperature of 20° are shown in figures Fig. 3 and Fig.4 respectively.

### C. Wind subsystem modelling:

The wind subsystem consists of 2 Whisper 200 wind turbines (WTs), each one has rated power of 1 kW. The power generated by a WT is related to the wind speed by [1,9,10]:

$$p_{wt} = \frac{1}{2} \rho \pi R^2 C_p V^3 \quad (6)$$

where  $V$  is the wind speed,  $C_p$  is the WT power coefficient,  $\rho$  is the air density and  $R$  is the rotor radius. The power coefficient  $C_p$  describes the conversion efficiency of with turbine, it has a theoretical limit of 0.69 called the Betz limit [1]. Notice that in real WTs, this limit is never reached, typical values for this limit are around 0.4 [1,9], for the case of our Whisper 200 turbine, the variation of  $C_p$  is shown in Fig.5, it has a limit around 0.39, which is inferred from the manufacturers datasheet.

Usually, wind turbines are usually characterized by their power curves, the typical power curve for the Whisper 200 wind turbine is shown in Fig. 5. For our study, The WT model consists of a look-up table generated from the power curves given in the manufacturer's data-sheet.

### D. Battery and Converter System Modelling:

The HPS is built around a 48V DC bus, the battery is directly connected to the 48V bus, for the purpose of our study, the battery is modelled as a shown in Fig.6. ,it consists of a voltage sources  $E_b$  connected in series with a resistance  $R_{b1}$  a resistance  $R_{b2}$  and capacitance  $C_b$ , the battery voltage is : [11]

$$v_b = E_b + v_c + i_b R_{b2} \quad (7)$$

where  $i_b$  is the battery current which is positive when the battery is charging and negative when the battery is discharging, it is given as follows:

$$i_b = i_s + i_{w1} + i_{w2} - i_L \quad (8)$$

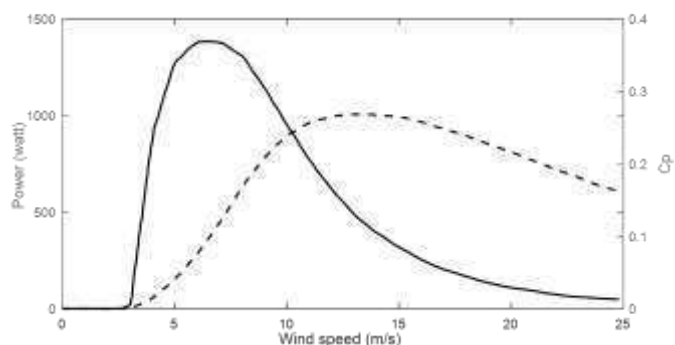


Fig. 5 Power curve and power coefficient of the Whisper-200 WT

the wind subsystem is connected to the DC bus via whisper controller, the load is connected via an inverter and the PV subsystem is connected via DC/DC buck converter as outlined in Fig. 5. The switched dynamic model for the buck converter can be written as:

$$\dot{v}_{pv} = \frac{i_{pv}}{C} - \frac{i_0}{C} u_{pv} \quad (9)$$

$$\dot{i}_s = -\frac{v_b}{L} + \frac{v_{pv}}{L} u_{pv} \quad (10)$$

$$\dot{v}_c = \frac{1}{C_b} i_b - \frac{1}{C_b R_{b2}} v_c \quad (11)$$

where the different electric variables and parameters are illustrated in Fig.5. with their values in the appendix. The battery voltage is given in (7).

Equations (7)-(11) can be assembled together to build the complete nonlinear state space model of the HES as follows

$$\dot{x} = f(x) + g(x)u \quad (12)$$

with:

$$x = \begin{bmatrix} v_{pv} \\ i_s \\ v_c \end{bmatrix}, f(x) = \begin{bmatrix} i_{pv}/C \\ -v_b/L \\ i_b/C_b - v_c/C_b R_{b2} \end{bmatrix}, g(x) = \begin{bmatrix} -i_s/C \\ v_{pv}/L \\ 0 \end{bmatrix}$$

The control objective is to design a control law for the IGBT gate trigger  $u_{pv}$  of the DC/DC buck converter in order to meet an optimal energy balance between the storage system (battery bank), the load and sources (PV and Wind generators) [4].

### III. ENERGY MANAGEMENT CONTROL DESIGN

In this section the control law is design in order to ensure the energy balance between the different constituents of the HES, for this purpose the required operation specifications are first outlined, then the control law is derived, notice the control law a slightly modified version of that presented in [4].

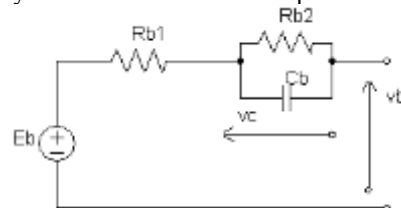


Fig.6 Thevenin equivalent circuit for the battery [11]

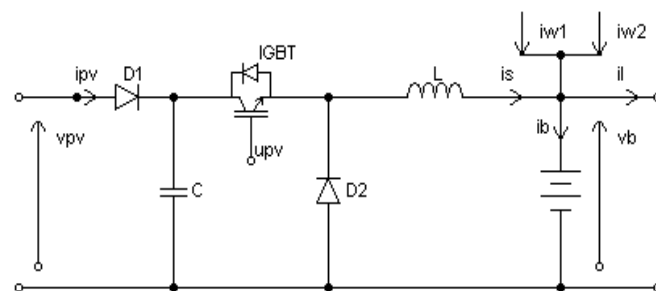


Fig. 7 Schematic of the DC bus of the HPS

### A. Required Operational Specifications

The control objective is focused on the PV subsystem, the aim is to fulfil the total energy balance between the different renewable energy sources (PV system and wind subsystem), the storage subsystem and the load.

In addition, the battery should be operated at a charging current that is related to its state of charge (SOC) in order to prevent it from damage and lengthen its lifespan. For this purpose, we consider two situations: first, if the battery is fully charged it will be charged with a small reference current  $I_{b,ref} = 2A$ , this is usually called the float mode, however if the battery is below a certain charge, it will be charged with a large reference current  $I_{b,ref} = 20A$ , this is called the bulk mode of operation of the battery [ref, ref].

According to the developments presented in [4], the system should operate according to two modes of operation as follows:

The first mode of operation occurs when there is enough energy generation from the resources that satisfy the demand imposed by the load. In this case, the PV power generation from the PV subsystem has to be regulated in order to ensure a power balance, in this way, the power generated from the resources must be equal to the power fed to the load and the battery, that is:

$$P_{pv,ref} + P_{w1} + P_{w2} = P_L + P_{b,ref} \quad (13)$$

where  $p_{pv,ref}$  is the PV reference power that should be delivered by the PV subsystem,  $p_{w1}$  and  $p_{w2}$  are the power produced by the wind turbines,  $p_L$  is the power consumption from the load and  $p_{b,ref}$  is the power for the battery charging which is defined as

$$P_{b,ref} = I_{b,ref} \cdot V_b \quad (14)$$

From (15), the energy balance in the first mode can be expressed by the following sliding surface which should be kept as small as possible:

$$s_1 = P_L + P_{b,ref} - P_{w2} - P_{w2} - P_{pv,ref} \quad (15)$$

The second mode of operation is when the photovoltaic and wind generators are unable to satisfy the load demand, in this case, the photovoltaic subsystem should be operated at its maximum power point (MPP). According to the power curve of the PV subsystem, the power reaches its maximum at a certain operation voltage, thus:

$$\frac{\partial p_{pv}}{\partial v_{pv}} \Big|_{mpp} = 0 \quad (16)$$

Given that  $p_{pv} = v_{pv} i_{pv}$ , equation (18) the following

$$\frac{\partial (i_{pv} v_{pv})}{\partial v_{pv}} \Big|_{mpp} = v_{pv} \frac{\partial i_{pv}}{\partial v_{pv}} \Big|_{mpp} + i_{pv} \Big|_{mpp} = 0 \quad (17)$$

Therefore, for the second mode of operation, the sliding manifold that should be regulated around zero can be derived from (19) as follows:

$$s_2 = v_{pv} \frac{\partial i_{pv}}{\partial v_{pv}} + i_{pv} \quad (18)$$

It is worth notice that the operation mode is dictated by the reference power  $p_{ref}$  that would be produced if the PV systems is at MPP, if this power by the PV subsystem as follows:

### B. Energy flow management algorithm

Under the light of the above development, the control strategy that ensures an optimal operation of the HES can be summarized as follows:

The operational mode is decided by comparing the reference power  $P_{ref}$  with the power the would be produced at the MPP, therefore we have the following control scheme:

If  $P_{ref} + \frac{\partial i_{pv}}{\partial v_{pv}} v_{pv}^2 < 0$  (first mode of operation), then

$$u = \begin{cases} 1 & \text{if } s_1 \geq 0 \\ 0 & \text{if } s_1 < 0 \end{cases} \quad (19)$$

Else if  $P_{ref} + \frac{\partial i_{pv}}{\partial v_{pv}} v_{pv}^2 \geq 0$  (Second mode of operation) then

$$u = \begin{cases} 0 & \text{if } s_2 \geq 0 \\ 1 & \text{if } s_2 < 0 \end{cases} \quad (20)$$

In this way, the PV system will produce only the needed power if there is enough energy for the load, it will be pushed to its MPP when there is insufficient power for the load.

## IV. SIMULATION RESULTS AND DISCUSSION

In this section, numerical simulation is carried out to access the effectiveness of the described power management strategy. The numerical values for the PV, wind, converter and battery are summarized in the appendix. For the meteorological data, real measurements for 5 minutes from the station installed on the roof of the SMS Laboratory in the Unit of Development of Solar Equipment's in Bou-Imail, where the hybrid Standalone PV/Wind system is installed. The measurements are taken for the day of at midday, The Irradiance and module temperatures are shown in figures Fig. 6, Fig.7 and Fig.8 respectively. For the load profile, we assume the profile shown in Fig. which is based on the devices existing inside the SMS Laboratory is fed by the HPS.

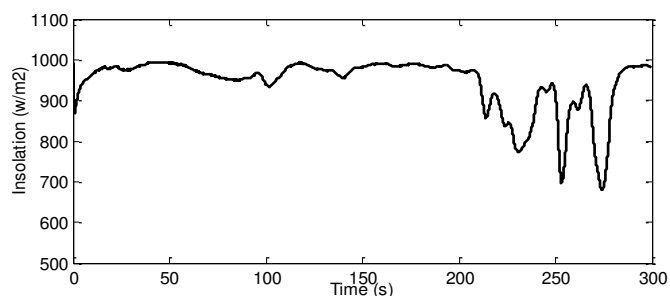


Fig. 10 Measured insolation curve for 5 minutes

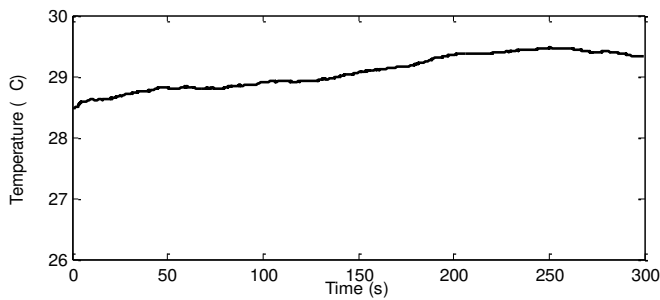


Fig. 11 Measured temperature variation for 5 minutes

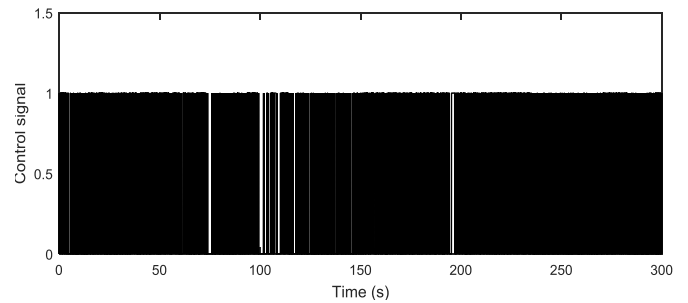


Fig. 14 Gate trigger signal variations

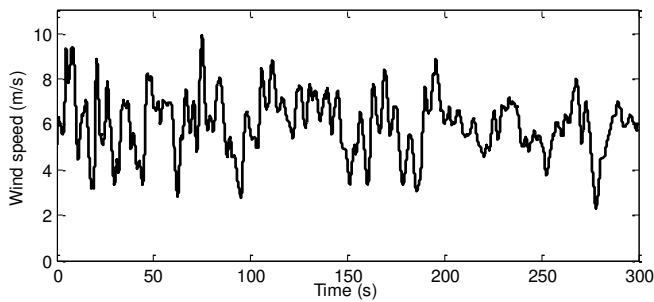


Fig. 12 Measured wind speed for 5 minutes

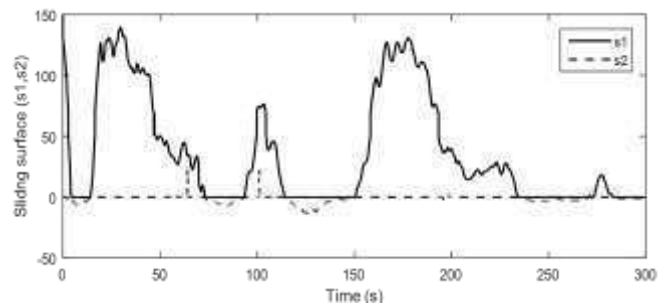


Fig. 15 Variations of the sliding surfaces  $s_1$  and  $s_2$

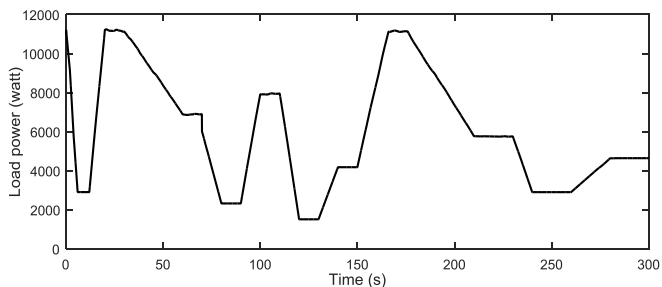


Fig. 13 Load power profile variations for 5 minutes

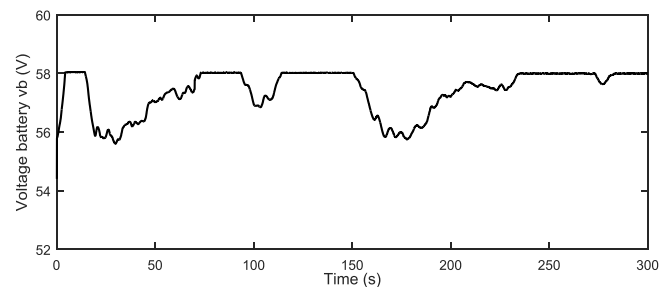


Fig. 16 DC bus (battery) voltage variations

The simulation results using these measured data are shown in Figures Fig.14 – Fig.19. Fig.14 shows the switching signal for the converters Gate, it can be seen that pulse width varies to ensure an optimal operation as required by the two modes of operation stated above.

Fig.15 shows the variations of the two sliding manifolds  $s_1$  and  $s_2$ , we see that for the first mode of operation  $s_1$  is kept around zero while  $s_2$  is disregarded while in the second mode of operation,  $s_2$  is kept around zero and  $s_1$  is disregarded, which is in accordance with the control algorithm. Fig.16, shows the battery voltage variation, when there is a surplus of energy production, the battery will be charged to its full state (58 V) and when there is a power deficit, it will be drawn from the battery which lead to its discharge. Fig.17 really describes the behaviour of our control strategy, we see that the operating point for the PV system swings back and forth between the two modes of operation depicted by the two distinct regions in the power curve.

Figures Fig.18 and Fig.19 shows the energy balance between the produced energy from the PV and Wind systems and the power consumption from the load and the power fed to or from the battery. We see that our controller ensures an energy balance in the first scenario where the production tracks the needed power. While in the second mode of operation, even though, the system is operated at its MPP, the energy balance is not always satisfied when the needs for the load are very high. There is always an energy deficit. This energy deficit can be practically talked by a proper sizing of the whole HPS. Since in our study we used a theoretical profile for the load we cannot conclude as if the system is property sized or not.

In conclusion we see that the proposed control architecture is elegant and efficient. and can ensure an optimal operation of the system in both modes of operation, it has the ability to automatically decide the required operational mode and switch to it so that the design requirements are satisfied. Besides, the simplicity of the proposed control scheme encourages its experimental implementation on the real system existing on the SMS lab in the UDES, Bou-Ismaïl.

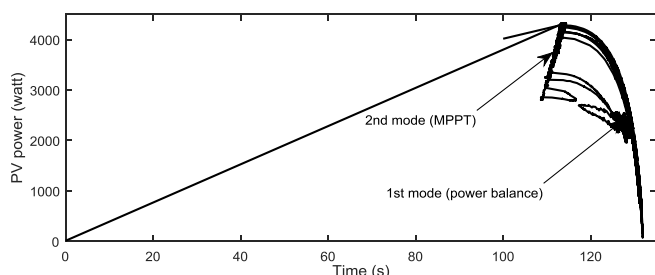


Fig. 17 Variations of the PV operating point between the two modes

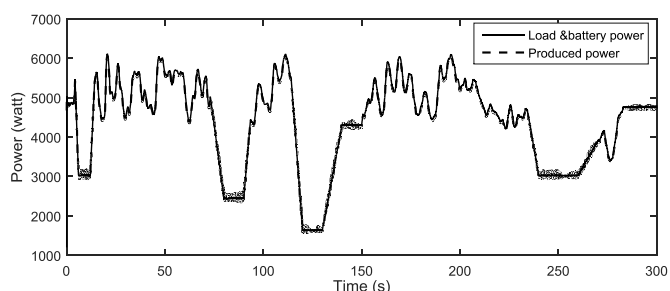


Fig. 18 Produced power vs needed power

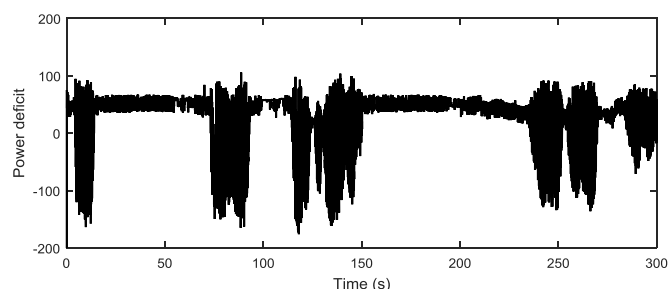


Fig. 19 Power deficit between needed and produced

## V. CONCLUSION

In this paper, a sliding mode control strategy is proposed and applied to a standalone PV/Wind HPS in order to ensure an optimal energy flow within the system. The control is focused on the photovoltaic subsystem. Two possible modes of operation are considered. In the first mode, the load demand is satisfied, therefore the PV subsystem should be regulated to produce only the needed power. In the second mode, the load demand is not satisfied, in this case the PV subsystem should be operated at its maximum power to draw the best from the PV modules. For both modes, a sliding manifold is constructed and the sliding mode technique is used to keep these manifolds around zero. The control strategy is applied to a real experiment HPS with real measurements. As a future perspective for our system, we consider the total implementation of the controller on a DC converter and the introduction of a state observer to estimate the states of the model in case they are not available for measurement.

## REFERENCES

- [1] I. Munteanu, A. I. Bratcu, N. A. Cutululis, and E. Ceanga, *Optimal Control of Wind Energy Systems: Towards a Global Approach*, Springer, 2008.
- [2] S. Sumathi, L., A. Kumar and P. Surekha, *Solar and Wind Energy Conversion Systems*, Springer, 2015.
- [3] Jan Moravek, Petr Mastny, "Hybrid Renewable Energy System-Configuration and Control", *Recent Researches in Electric Power and Energy Systems, Electrical Engineering Series*. Chania, Crete Island, Greece: p. 87-92, 2013.
- [4] F. Valenciaga, P. F. Puleston and P. E. Battaiotto, "Power Control of a Photovoltaic Array in a Hybrid Electric Generation System using Sliding Mode Techniques", *IEEE Proceedings-Control Theory and Applications*, Vol. 148 Issue: 6, 2001.
- [5] S. Zerkaoui, AK El Hajjaji, J. Bosche, "On-line Control Strategy for instantaneous Power Management of Hybrid Power System Based on Dynamic Fuzzy Logic Controller", in the *7th IEEE Conference on Industrial Electronics and Applications (ICIEA)*, 2012.
- [6] A. Gligor, C. D., Dumitru and H. S., Grif, "Artificial intelligence solution for managing a photovoltaic energy production unit", *Procedia Manufacturing*, Vol. 22, pp. 626-633, 2018.
- [7] J. Khanam, S. Y. Foo, "Modeling of a Photovoltaic Array in Matlab Simulink and Maximum Power Point Tracking using Neural Network", *Electrical and Electronic Technology Open Access Journal*, Vol. 2, Issue 2, pp.40-46, 2018.
- [8] H. Tsai, C. Tu, and Y. Su, "Development of Generalized Photovoltaic Model Using MATLAB/SIMULINK", in *Proceeding of the World Congress on Engineering and Computer Science*, San Francisco, USA, 2008.
- [9] N. Bounar, S. Labdai, A. Boulkroune, M. Farza and M. M'Saad, "Adaptive Fuzzy Control Scheme for Variable-Speed Wind Turbines Based on a Doubly Fed Induction Generator", *Iranian Journal of Science and Technology-Transactions of Electrical Engineering*, October, 8th, 2019. <https://doi.org/10.1007/s40998-0.19-00276-6>.
- [10] Jan. Moravek, Petr Mastny, "Model of PMSG Wind Turbine in Hybrid Energy System", in *Proceedings of the 15th International Scientific Conference on Electric Power Engineering*, Czech Republic, 2014
- [11] B. S. Borowy and Z. M. Salameh, "Dynamic Response of a Standalone Wind Energy Conversion System with Battery Energy Storage to a Wind Gust", *IEEE Transactions on Energy Conversion*, Vol. 12, N. 1, pp.73-78., 1997.

## APPENDIX

TABLE I  
 NUMERICAL VALUES FOR SIMULATION

Parameter name and symbol	Value
Nbr of series cells per module ( $N_{sc}$ )	36 Cells
Nbr of series modules per string ( $N_{ss}$ )	06 Modules
Nbr of parallel strings in the array ( $N_p$ )	05 Strings
Electron charge ( $q$ )	$1.6 \times 10^{-19}$ C
Boltzmann constant ( $K$ )	$1.3805 \times 10^{-23}$ Nm/K
Diode ideality factor ( $A$ )	1.2
Short circuit current at reference ( $I_{scr}$ )	8.20 A
Open circuit voltage at reference ( $V_{ocr}$ )	22.3 V
Cell's Series resistance ( $R_s$ )	0.00685 Ohm
Converter inductance ( $L$ )	4 mH
Input shunt capacitance ( $C$ )	1 mF
Converter switching frequency ( $F_{sw}$ )	20 000 Hz
Battery voltage ( $R_b$ )	48 V
Battery resistances ( $R_{b1}$ and $R_{b2}$ )	0.02 Ohms
Battery Capacity ( $C_b$ )	180 000 F



